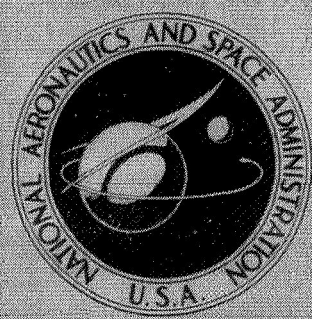


N71-12211



NASA CONTRACTOR
REPORT

NASA CR-1644

NASA CR-1644

CASE FILE
COPY

DYNAMIC DISTORTION AT THE EXIT OF A SUBSONIC DIFFUSER OF A MIXED COMPRESSION INLET

*by Arnold W. Martin, Leonard C. Kostin,
and Sidney D. Millstone*

Prepared by
NORTH AMERICAN ROCKWELL CORPORATION
Los Angeles, Calif.
for Ames Research Center

1. Report No. NASA CR-1644	2. Government Accession No.	3. Recipient's Catalog No.	
4. Title and Subtitle "DYNAMIC DISTORTION AT THE EXIT OF A SUBSONIC DIFFUSER OF A MIXED COMPRESSION INLET"		5. Report Date December 1970	6. Performing Organization Code
		8. Performing Organization Report No.	
7. Author(s) Arnold W. Martin, Leonard C. Kostin and Sidney D. Millstone		10. Work Unit No.	
9. Performing Organization Name and Address North American Rockwell Los Angeles California		11. Contract or Grant No. NAS 2-4667	
		13. Type of Report and Period Covered Contractor Report	
12. Sponsoring Agency Name and Address National Aeronautics and Space Administration Washington D.C. 20546		14. Sponsoring Agency Code	
		15. Supplementary Notes	
16. Abstract Dynamic distortion characteristics at the engine face station of a 20 in. diameter axisymmetric inlet were investigated at M = 2.6 and 3.0. Inlet operation modes included (1) stationary geometry and tunnel conditions, (2) sinusoidal exit area disturbances, (3) simulated engine transients, (4) sinusoidal external flow disturbances, (5) simulated clear air turbulence. Inlet-induced turbulence is composed of random and nonrandom pressure oscillations. The basic turbulence generating mechanism appears to be boundary layer/shock interaction. Regions of maximum turbulence correspond with regions of maximum pressure recovery. Instantaneous (msec) spatial distortions appreciably exceed steady state distortions during highly supercritical inlet operation.			
17. Key Words (Selected by Author(s)) Axisymmetric inlet Engine-face distortion Dynamic distortion Instantaneous distortion Inlet turbulence		18. Distribution Statement Unclassified-Unlimited	
19. Security Classif. (of this report) Unclassified	20. Security Classif. (of this page) Unclassified	21. No. of Pages 343	22. Price* \$3.00

TABLE OF CONTENTS

CONTENTS	Page
SUMMARY	1
INTRODUCTION	2
MODEL DESCRIPTION	3
Inlet Configuration	3
Instrumentation	4
TEST PROCEDURES	7
Steady-State and "Steady-State Dynamics" Test	7
Exit Area Disturbance Tests	7
External Disturbance Tests	8
Shock Control Tests	8
Inlet Unstarts	9
TUNNEL AIRFLOW TURBULENCE AND INSTRUMENTATION NOISE	9
Capped Probe Data	9
Electrical Noise	9
Wind Tunnel Airflow Turbulence	10
STATISTICAL CHARACTERISTICS OF STEADY-STATE ENGINE FACE DATA	11
Probability Density	11
Stationarity	11
Ergodicity	12
DYNAMIC DISTORTION AT THE ENGINE FACE STATION	13
Instantaneous Spatial Distortion	13
Instantaneous Average Total Pressure Recovery	14
Time-Averaged Distortion Characteristics	15
Steady-State Distortion Characteristics	16
Inlet Unstart	16
Inlet Restart	17

Contents	Page
STEADY-STATE OPERATION TURBULENCE CHARACTERISTICS	18
Engine Face Turbulence	18
Turbulence Variation With Station	20
HYPOTHETICAL MODEL OF THE TURBULENCE-GENERATING PROCESS	21
Hypothetical Model	21
Comments on the Hypothetical Model	23
STEADY-STATE OPERATION POWER SPECTRAL DENSITY AND COHERENCE CHARACTERISTICS	24
Power Spectral Density Characteristics	24
Coherence Characteristics	26
TERMINAL SHOCK CONTROL SYSTEM TESTS	28
Shock Excursion Comparisons	29
Control System Effects on Turbulence	30
CONCLUSIONS AND RECOMMENDATIONS	30
Test Procedures and Equipment	30
Data Recording and Analysis Techniques	31
Steady-State Dynamics Distortion	32
Dynamic Distortion With Internal and External Disturbances	32
Recommendations	33
APPENDIX A - SERVO CONTROL SYSTEM AND DISTURBANCE MECHANIZATION	35
Component Positioning Control System	35
Internal Disturbances	36
External Disturbances	36
APPENDIX B - SHOCK POSITION CONTROL SYSTEM	39
Shock Position Sensing Parameter	39
Control System Analysis	40

Contents	Page
APPENDIX C - TOTAL PRESSURE PROBE TRANSDUCER FAILURES AND PROTECTIVE CONFIGURATIONS	41
Original Probe Configuration	41
APPENDIX D - DYNAMIC-DISTORTION TEST RUN SUMMARY, TEST 87-255	45
APPENDIX E - COHERENCE CALCULATIONS	53
APPENDIX F - DETERMINATION OF TRANSFER FUNCTIONS FROM STATISTICAL PARAMETERS	73
REFERENCES	75

LIST OF TABLES

Table	Title	Page
I	RMS/ P_{t0} Measurements for Different Sections of a 5-Second Interval, $M_0 = 3.0$, $\bar{P}_{t2}/P_{t0} = 0.877$	77
II	RMS/ P_{t0} Measurements for Three 5-Second Intervals in a 7-Minute Run, $M_0 = 3.0$, $\bar{P}_{t2}/P_{t0} = 0.877$	78
III	RMS/ P_{t0} Measurements for Different Sections of a 5-Second Interval, $M_0 = 3.0$, $\bar{P}_{t2}/P_{t0} = 0.565$	79
IV	RMS/ P_{t0} Measurements for Three 5-Second Intervals in a 7-Minute Run, $M_0 = 3.0$, $\bar{P}_{t2}/P_{t0} = 0.565$	80
V	Coherence Functions for Pairs of In-Line Probes, $M_0 = 3.0$	81
VI	Coherence Functions for Pairs of Static and Total Pressures at MS47.30 and MS66.70.	81
VII	Control System Test Summary of Shock Travel	82
VIII	Cat Filter Transfer Functions	83
IX	Transfer Function Calculations.	84

LIST OF ILLUSTRATIONS

Figure	Title	Page
1	Inlet and external rakes	85
2	Inlet and external disturbance vane	86
3	Supersonic inlet configuration	87
4	Inlet cross-sectional area variation - NASA Ames axisymmetric inlet	88
5	Bleed configuration	89
6	Bypass valve schematic	90
7	Translating sleeve/plug valve	91
8	External disturbance vane	92
9	External flow field rake	93
10	Engine face dynamic pressure instrumentation	94
11	Inlet duct dynamic instrumentation	95
12	Typical installations of dynamic static pressure instrumentation	100
13	Tape recorder channel listings - vane installed	101
14	Tape recorder channel listings - no vane	102
15	Conical probe configuration	103
16	Inlet duct steady-state instrumentation	104
17	Metering nozzle and instrumentation	110
18	Tunnel flow power spectral density, probe 802, $M_0 = 2.6, \bar{P}_{t2}/P_{t0} = 0.918$	111
19	Tunnel flow power spectral density, probe 802, $M_0 = 3.0, \bar{P}_{t2}/P_{t0} = 0.877$	112
20	Tunnel flow power spectral density, probe 802, $M_0 = 3.0, \bar{P}_{t2}/P_{t0} = 0.565$	113
21	Tunnel flow power spectral density with vane installed, probe 802, $M_0 = 3.0, \bar{P}_{t2}/P_{t0} = 0.785$	114
22	Tunnel flow power spectral density with vane installed, probe 804, $M_0 = 3.0, \bar{P}_{t2}/P_{t0} = 0.785$	115
23	Typical turbulence values, external rake pressure probes	116
24	Engine face total pressures vs time, $M_0 = 3.0,$ $\bar{P}_{t2}/P_{t0} = 0.877$	117
25	Engine face total pressures vs time, $M_0 = 3.0,$ $\bar{P}_{t2}/P_{t0} = 0.565$	118
26	Probability density, probe P870, $M_0 = 3.0$	119
27	Probability density, probe P874, $M_0 = 3.0$	121
28	Statistical data intervals	123
29	Probability density functions for different 5-second intervals, $M_0 = 3.0, \bar{P}_{t2}/P_{t0} = 0.877$	124

Figure	Title	Page
30	Probability density functions for different 5-second intervals, $M_0 = 3.0$, $\bar{P}_{t2}/P_{t0} = 0.565$	127
31	Power spectral density at different 5-second intervals, $M_0 = 3.0$, $\bar{P}_{t2}/P_{t0} = 0.877$	130
32	Power spectral density at different 5-second intervals, $M_0 = 3.0$, $\bar{P}_{t2}/P_{t0} = 0.565$	133
33	Instantaneous average and individual engine face total pressure comparisons , $M_0 = 3.0$, $\bar{P}_{t2}/P_{t0} = 0.877$	136
34	Instantaneous average and individual engine face total pressure comparisons, $M_0 = 3.0$, $\bar{P}_{t2}/P_{t0} = 0.565$	137
35	Instantaneous <u>total</u> pressure ratio contours, $M_0 = 3.0$, $\bar{P}_{t2}/P_{t0} = 0.877$	138
36	Instantaneous <u>total</u> pressure ratio contours, $M_0 = 3.0$, $\bar{P}_{t2}/P_{t0} = 0.565$	141
37	Instantaneous <u>total</u> pressure ratio contours, $M_0 = 2.6$, $\bar{P}_{t2}/P_{t0} = 0.918$	153
38	Instantaneous <u>total</u> pressure ratio contours, $M_0 = 2.6$, $\bar{P}_{t2}/P_{t0} = 0.642$	156
39	Instantaneous <u>spatial</u> distortion versus time, $M_0 = 3.0$, $\bar{P}_{t2}/P_{t0} = 0.877$	167
40	Instantaneous <u>spatial</u> distortion versus time, $M_0 = 3.0$, $\bar{P}_{t2}/P_{t0} = 0.565$	168
41	Instantaneous <u>spatial</u> distortion versus time, $M_0 = 2.6$, $\bar{P}_{t2}/P_{t0} = 0.918$	169
42	Instantaneous <u>spatial</u> distortion versus time, $M_0 = 2.6$, $\bar{P}_{t2}/P_{t0} = 0.642$	170
43	Instantaneous <u>average</u> pressure recovery versus time, $M_0 = 3.0$, $\bar{P}_{t2}/P_{t0} = 0.877$	171
44	Instantaneous <u>average</u> pressure recovery versus time, $M_0 = 3.0$, $\bar{P}_{t2}/P_{t0} = 0.565$	172
45	Instantaneous <u>average</u> pressure recovery versus time, $M_0 = 2.6$, $\bar{P}_{t2}/P_{t0} = 0.918$	174
46	Instantaneous <u>average</u> pressure recovery versus time, $M_0 = 2.6$, $\bar{P}_{t2}/P_{t0} = 0.642$	175
47	Time-averaged <u>total</u> pressure ratio contours, 0.002-second span, $M_0 = 3.0$, $\bar{P}_{t2}/P_{t0} = 0.877$	176
48	Time-averaged <u>total</u> pressure ratio contours, 0.005-second span, $M_0 = 3.0$, $\bar{P}_{t2}/P_{t0} = 0.877$	177
49	Time-averaged <u>total</u> pressure ratio contours, 0.010-second span, $M_0 = 3.0$, $\bar{P}_{t2}/P_{t0} = 0.877$	178
50	Time-averaged <u>total</u> pressure ratio contours, 0.040-second span, $M_0 = 3.0$, $\bar{P}_{t2}/P_{t0} = 0.877$	179

Figure	Title	Page
51	Steady-state total pressure ratio contour, $M_o = 3.0$, $\bar{P}_{t2}/P_{t0} = 0.877$	180
52	Time-averaged total pressure ratio contours, 0.002-second span, $M_o = 3.0$, $\bar{P}_{t2}/P_{t0} = 0.565$	181
53	Time-averaged total pressure ratio contours, 0.005-second span, $M_o = 3.0$, $\bar{P}_{t2}/P_{t0} = 0.565$	183
54	Time-averaged total pressure ratio contours, 0.010-second span, $M_o = 3.0$, $\bar{P}_{t2}/P_{t0} = 0.565$	185
55	Time-averaged total pressure ratio contours, 0.040-second span, $M_o = 3.0$, $\bar{P}_{t2}/P_{t0} = 0.565$	187
56	Steady-state total pressure ratio contour, $M_o = 3.0$, $\bar{P}_{t2}/P_{t0} = 0.565$	188
57	Typical steady-state total pressure ratio contours and profiles, $M_o = 3.0$	189
58	Typical steady-state total pressure ratio contours and profiles, $M_o = 2.6$	190
59	Engine face total pressure during unstarts	191
60	Instantaneous total pressure ratio contours during inlet unstart, $M_o = 2.6$	192
61	Cowl-induced inlet unstart time history, $M_o = 2.6$, $\bar{P}_{t2}/P_{t0} = 0.918$	198
62	Instantaneous total pressure ratio contours during inlet unstart, $M_o = 2.9$, $\bar{P}_{t2}/P_{t0} = 0.873$	199
63	Cowl-induced inlet unstart time history, $M_o = 2.9$, $\bar{P}_{t2}/P_{t0} = 0.873$	204
64	Instantaneous total pressure ratio contours during inlet unstart, $M_o = 2.9$, $\bar{P}_{t2}/P_{t0} = 0.741$	205
65	Cowl-induced inlet unstart time history, $M_o = 2.9$, $\bar{P}_{t2}/P_{t0} = 0.741$	211
66	Duct pressures during inlet restart	212
67	Engine face turbulence variation with recovery $M_o = 3.0$	213
68	Engine face turbulence variation with recovery, $M_o = 2.6$	217
69	Engine face turbulence and total pressure ratio contour comparisons	221
70	Engine face turbulence and total pressure ratio radial profile comparisons	223
71	Steady-state distortion versus average turbulence of individual probes	225
72	Steady-state distortion versus average turbulence	226
73	Turbulence variation with distortion, individual probes, $M_o = 3.0$	227

Figure	Title	Page
74	Turbulence variation with distortion, individual probes, $M_O = 2.6$	231
75	Upstream rake effect on engine face turbulence, $M_O = 3.0$	235
76	Engine face turbulence variations with angle of attack, $M_O = 3.0$	236
77	Turbulence variation with station, $M_O = 3.0$	237
78	Turbulence variation with station, $M_O = 2.6$	239
79	Hypothetical model of turbulence	241
80	Power spectral density variation with recovery, $M_O = 3.0$, $\alpha_O = 0$ degrees, engine face inboard total pressure probe 875	246
81	Power spectral density variation with recovery, $M_O = 3.0$, $\alpha_O = 0$ degrees, engine face outboard total pressure probe 884	247
82	Power spectral density variation with recovery, $M_O = 3.0$, engine face annulus center total pressure probe 882	248
83	Power spectral density variation with recovery, probe 870, $M_O = 2.6$	249
84	Power spectral density variation with circumferential angle, $M_O = 3.0$, $\bar{P}_{t2}/P_{t0} = 0.877$	250
85	Power spectral density variation with circumferential angle, $M_O = 3.0$, $\bar{P}_{t2}/P_{t0} = 0.565$	251
86	Power spectral density variation with radius, $M_O = 3.0$, $\bar{P}_{t2}/P_{t0} = 0.877$	252
87	Power spectral density variation with radius, $M_O = 3.0$, $\bar{P}_{t2}/P_{t0} = 0.565$	253
88	Power spectral density variation with angle of attack, probe 884, $M_O = 3.0$	254
89	Power spectral density variation with angle of attack, probe 882, $M_O = 3.0$	255
90	Power spectral density variation with angle of attack, probe 880, $M_O = 3.0$	256
91	Power spectral density variation with angle of attack, probe 885, $M_O = 3.0$	257
92	Power spectral density variation with angle of attack, probe 887, $M_O = 3.0$	258
93	Power spectral density variation with angle of attack, probe 889, $M_O = 3.0$	259
94	Total pressure power spectral density variation with station, $M_O = 3.0$, $\bar{P}_{t2}/P_{t0} = 0.877$	260
95	Total pressure power spectral density variation with station, $M_O = 3.0$, $\bar{P}_{t2}/P_{t0} = 0.565$	261

Figure	Title	Page
96	Static pressure power spectral density variation with station, NASA/Ames axisymmetric inlet, $M_0 = 3.0$, $\bar{P}_{t2}/P_{t0} = 0.877$	262
97	Static pressure power spectral density variation with station, $M_0 = 3.0$, $\bar{P}_{t2}/P_{t0} = 0.565$	263
98	Power spectral densities at rake MS 47.30, $M_0 = 3.0$, $\bar{P}_{t2}/P_{t0} = 0.877$	264
99	Power spectral densities at rake MS 47.30, $M_0 = 3.0$, $\bar{P}_{t2}/P_{t0} = 0.565$	265
100	Power spectral densities showing effect of disturbance vane, probe 802, $M_0 = 3.0$	266
101	Power spectral densities showing effects of disturbance vane, probe 804, $M_0 = 3.0$	267
102	Power spectral densities showing effects of disturbance vane, probe 807, $M_0 = 3.0$	268
103	Power spectral density showing effects of disturbance vane, probe 885, $M_0 = 3.0$	269
104	Power spectral densities showing effects of disturbance vane, probe 887, $M_0 = 3.0$	270
105	Power spectral densities showing effects of disturbance vane, probe 889, $M_0 = 3.0$	271
106	Engine face coherence, $M_0 = 3.0$	272
107	Engine face coherence, $M_0 = 2.6$	277
108	Average coherence function - 13 engine face pairs	282
109	Coherence functions for adjacent probes on the same rake	283
110	Coherence function for equiradius probes on different rakes, $M_0 = 3.0$	285
111	Coherence function inversion, $M_0 = 2.6$	286
112	Engine face coherence between static and total pressures, $M_0 = 3.0$, $\bar{P}_{t2}/P_{t0} = 0.565$	287
113	Subsonic diffuser coherence function for probes on opposite sides of duct, MS 76.35, $M_0 = 3.0$	288
114	External to engine face total pressure coherence with clear air turbulence, $M_0 = 3.0$, $\bar{P}_{t2}/P_{t0} = 0.785$	289
115	Shock position control system performance with sinusoidal exit area disturbances, $M_0 = 3.0$	290
116	Shock position control system performance with sinusoidal vane angle disturbances, $M_0 = 3.0$	291
117	Turbulence levels with sinusoidal exit area disturbances, $M_0 = 3.0$, $\bar{P}_{t2}/P_{t0} = 0.846$	292
118	Turbulence levels with sinusoidal vane angle disturbances, $M_0 = 3.0$, $\bar{P}_{t2}/P_{t0} = 0.778$	293

Figure	Title	Page
119	Power spectral densities for 0, 2, and 14 Hz sinusoidal exit area disturbances, $M_o = 3.0$, $\bar{P}_{t2}/P_{t0} = 0.846$. . .	294
120	Effect of control on PSD for a 2 Hz sinusoidal exit area disturbance, $M_o = 3.0$, $\bar{P}_{t2}/P_{t0} = 0.846$	295
121	Effect of control on PSD for a 10 Hz sinusoidal exit area disturbance, $M_o = 3.0$, $\bar{P}_{t2}/P_{t0} = 0.846$	296
122	Effect of control on PSD for a 14 Hz sinusoidal exit area disturbance, $M_o = 3.0$, $\bar{P}_{t2}/P_{t0} = 0.846$	297
123	Control system interfaces	298
124	Position control system computer	299
125	Control system amplifier outputs versus actuator position	300
126	Control panel wiring diagram	301
127	Interface between TR-10A and model-mounted actuators . . .	302
128	Interface between TR-10A and disturbance vane actuator . .	303
129	Flow properties in the wake of a 25-degree leading edge and a 7.5-degree trailing edge wedge	304
130	Flow properties in the near wake of a 25-degree leading edge and a 7.5-degree trailing edge wedge	305
131	Flow angle in the near wake of the disturbance wedge . . .	306
132	Sinusoidal disturbance tape recording setup	307
133	CAT power spectral density, $M_o = 2.6$	308
134	CAT power spectral density, $M_o = 3.0$	309
135	CAT input recording setup	310
136	Shock position control system block diagram	311
137	Shock position pressure ratio versus shock position . . .	312
138	Shock position control system linear mathematical model. .	313
139	Shock control system hardware tie-in simulation	314
140	Shock position control system responses to a 2-inch step change in ΔX_S hardware tie-in simulation . . .	315
141	Shock position control response to sinusoidal shock position disturbances, hardware tie-in simulation	316
142	Kulite CPL-125-25 pressure sensor	317
143	Engine face rake total pressure probe	318
144	Centerbody probes	319
145	Damaged diaphragm, pinhole failure	320
146	Damaged diaphragm, "complete" failure	321
147	Probe modifications	322
148	Frequency calibration curve	324
149	Shock position parameter, power spectral density, 10 Hz excitation	325

Figure	Title	Page
150	Plug position parameter, power spectral density, 10 Hz excitation	326
151	Cross power spectral density, 10 Hz excitation	327
152	Linear transfer function - $\frac{\text{shock position pressure change}}{\text{exit area voltage change}}$.	328
153	Normalized transfer function - $\frac{\text{shock position change}}{\text{zero frequency shock position change}}$	329

LIST OF ABBREVIATIONS

<u>Abbreviation</u>	<u>Description</u>
CAT	Clear air turbulence
Co CPSD	Coherent component of cross power spectral density
MS	Model station
PSD	Power spectral density
Qu CPSD	Quadrature component of cross power spectral density

LIST OF SYMBOLS

<u>Symbol</u>	<u>Description</u>	<u>Units</u>
K_I	Adjustable integrator gain	
K_S	Adjustable system gain	
K_σ	CAT control system gain	
K_{α_W}	Disturbance vane angle control system gain	
L	Turbulence scale	feet
M_0	Free stream Mach number	
M_x	Mach number at station upstream of terminal shock	
M_y	Mach number downstream of terminal shock	
ΔP	Pressure variation from the mean	psi
PR	Shock position parameter pressure ratio	psi/psi
P_{tmax}	Maximum total pressure at the engine face station	psi
\bar{P}_{tmax}	Maximum total pressure at the engine face station determined from steady-state instrumentation	psi
P_{tmin}	Minimum total pressure at the engine face station	psi
\bar{P}_{tmin}	Minimum total pressure at the engine face station determined from steady-state instrumentation	psi
P_{tx}	Total pressure at station upstream of terminal shock	psi
P_{ty}	Total pressure downstream of terminal shock	psi
P_{t0}	Free stream total pressure	psi
P_{t2}	Instantaneous total pressure for engine face probe	psi
\bar{P}_{t2}	Average steady-state total pressure at engine face	psi

<u>Symbol</u>	<u>Description</u>	<u>Units</u>
P_{t2avg}	Instantaneous average total pressure at engine face	psi
	Average total pressure at engine face over specified time interval	psi
RMS	Root mean squared value of pressure amplitude variation	psi
S	Laplace transform variable	
U	Aircraft velocity	ft/sec
X	Position variable - location denoted by subscript	in.
X_S	Shock position	in.
X_p	Exit area	sq in.
α_W	Disturbance vane	deg
σ_ω^2	Mean squared gust velocity intensity	(ft/sec) ²
$\phi_X(\omega)$	Input power spectrum to CAT filter	
$\phi_Y(\omega)$	Output power spectrum from CAT filter	
ω	Frequency	radians/sec
Ω	Reduced frequency = $\frac{\omega}{U}$	radians/ft

DYNAMIC DISTORTION AT THE EXIT OF A SUBSONIC
DIFFUSER OF A MIXED COMPRESSION INLET

By Arnold W. Martin, Leonard C. Kostin, and Sidney D. Millstone

Los Angeles Division of
NORTH AMERICAN ROCKWELL CORPORATION
Los Angeles, California

SUMMARY

A 20-inch diameter, axisymmetric, external-internal shock compression inlet was tested at Mach numbers from 2.6 to 3.0 to obtain inlet dynamic distortion data. High-response instrumentation was used to obtain dynamic pressure data during inlet operation with (1) fixed inlet geometry and tunnel conditions, (2) sinusoidal exit area disturbances, (3) simulated engine transients, (4) sinusoidal external flow disturbances, and (5) simulated clear air turbulence. A portion of the test program was conducted with a simple terminal shock control system.

Analog and digital data analysis procedures were used to obtain instantaneous pressure patterns, turbulence levels, probability density curves, cross correlations, power spectral densities, cross power spectral densities, and coherence functions.

Data analyses indicate that inlet-induced turbulence is a combination of random and nonrandom pressure oscillations, the nonrandom components becoming more apparent as inlet operation becomes more supercritical. The basic turbulence-generating mechanism appears to be boundary layer/shock interaction which creates a time-varying pattern of boundary layer detachment and oblique and normal shock waves. Maximum excursions in pressure in the turbulence process are toward the high-pressure side; regions of maximum turbulence correspond generally with the regions of maximum pressure recovery.

Instantaneous engine face spatial distortions are quite large during highly supercritical inlet operation, and appreciably exceed the values that would be measured by conventional steady-state instrumentation. Large changes in distortion occur within a millisecond. Instantaneous total pressure recovery averaged over the engine face annulus also varies with time during "steady-state" operation, but at a generally lower rate than the variations in spatial distortion.

The terminal shock control system was reasonably effective in reducing terminal shock excursions induced by exit area disturbances. Shock excursions induced by external flow disturbances were increased by the shock control system. Inlet turbulence levels were affected by the control system only as the terminal shock position was affected.

INTRODUCTION

During propulsion system wind tunnel and flight tests of both the turbojet-powered XB-70 and the turbofan-powered F-111, a number of engine stalls were encountered which could only be explained by turbulent flow at the engine face. Characteristically, the probability of such inlet turbulence-induced stalls increased as the turbulence amplitude increased; however, individual stalls appeared to be random with time, particularly at marginal turbulence levels. That is, an engine might stall immediately upon reaching a given inlet operating condition, or it might not stall for many seconds or even minutes. This observation suggested the use of statistical techniques in analyzing inlet dynamic distortion data; much of this investigation has been based on such techniques.

Resolution of dynamic distortion problems requires a two-sided approach, one relative to the engine, the other relative to the inlet. On one side, knowledge is required as to what dynamic distortion characteristics are critical to an engine. On the other side, methods must be developed for defining, predicting, and possibly eliminating inlet dynamic distortion.

Determining what dynamic distortion characteristics are critical to an engine was not a part of this program. However, other investigations have indicated the following:

(1) A major cause of turbulence-induced stall is spatial distortion at the compressor/fan face sustained for sufficient time to act as steady-state distortion. There must be a low-pressure area of appreciable size sustained for some minimum time, in the order of 5 milliseconds.

(2) One-dimensional pressure oscillations (a major portion of the engine face pressures varying in phase) can induce stall in different ways depending on the frequency as well as the amplitude. At low frequencies, such relatively slow-response items as the fuel control, exhaust nozzle area, and rotor speeds coupled with the combustor and tailpipe volume dynamics can result in excursions of the engine operating point exceeding the surge limit. At high frequencies, the interstage volume dynamics can result in changing stage-by-stage matching so that the apparent compressor characteristics differ from the steady-state values.

There were a number of objectives in this exploratory investigation of inlet dynamic distortion ranging from the general to the quite specific. These included:

- (1) Developing a better understanding of the general nature of inlet-induced turbulence
- (2) Defining turbulence for a specific inlet in terms of statistical parameters
- (3) Determining the transport properties of turbulence
- (4) Determining the scale of turbulence (the distance over which pressures vary in unison)
- (5) Determining the presence of discrete and/or preferred frequencies and their dependence on inlet geometry
- (6) Determining the pattern and magnitude of engine face spatial distortion and their variation with time
- (7) Determining whether an inlet amplifies or attenuates external flow disturbances such as clear air turbulence
- (8) Determining the effectiveness of an automatic shock position control in reducing terminal shock excursions due to either internal or external flow disturbances

MODEL DESCRIPTION

Inlet Configuration

The inlet model tested was an axisymmetric, mixed-compression inlet having a cowl leading edge diameter of 20 inches. It was originally designed and constructed as an approximately one-third scale model of a Mach 3.0 supersonic transport inlet by the Lockheed Company. A detailed description of the model can be found in references 1, 2 and 3. Steady state performance characteristics are given in reference 2.

Figures 1 and 2 are photographs of the model installed in the NASA Ames Unitary 8 x 7 Wind Tunnel. Figure 3 shows the general configuration of the inlet and its internal lines. Cross-section area as a function of model station is presented in figure 4. The boundary layer bleed configuration and compartmentation are illustrated in figure 5.

Variable model components. - Remotely variable components on the inlet model included a translating cowl, a rotating sleeve bypass valve, and a translating sleeve which, in combination with a fixed position plug, varied duct exit area. A hydraulically powered servo control system, discussed in Appendix A, was used to control the variable components.

Translating cowl: The translating cowl was used to start the inlet and to obtain the desired contraction ratio for each run.

Bypass valve: The rotating sleeve bypass valve is shown schematically in figure 6. Flow passage areas were enlarged relative to the initial model construction to insure that the exit area controlled by the rotating sleeve was the flow regulating area. During the "automatic control" portion of the test program, bypass area was varied to control terminal shock position as sensed by inlet throat static pressures. The control system characteristics are described in Appendix B.

Sleeve/plug valve: The sleeve/plug valve (figure 7) was positioned either through manual input or through input from magnetic tapes prerecorded to produce either sinusoidal exit area variations or exit area variations simulating engine transients.

Attention is called to the fact that the sleeve/plug valve minimum area is well downstream of the simulated engine face station. Construction of the model made it impractical to locate the sonic section of the flow control valve near the engine face station.

External flow disturbance vane: A two-dimensional vane forward and above the inlet model was used to generate disturbances in the external flow. Figure 8 is a schematic diagram of the vane which completely spanned the tunnel. Vane angle variations to produce sinusoidal disturbances and clear air turbulence (CAT) were commanded by prerecorded magnetic tape inputs to a PACE TR-10 analog computer as described in Appendix A.

Instrumentation

Instrumentation consisted of high-frequency response pressure probes for measuring transient pressures, steady-state pressure probes for establishing the steady-state external flow and inlet performance characteristics, and potentiometers to measure the positions of the translating cowl, the bypass sleeve, the exit area sleeve, and the external disturbance vane angle. Tunnel instrumentation was used to measure model angle of attack.

Transient pressure instrumentation.-

External rakes: Figure 9 shows the location and typical configuration of the 12 probes constituting the external flow field transient pressure rake. Satham PA222 transducers were used in the rake.

Internal rakes: Total pressure instrumentation in the model consisted of four rakes at the engine face station, and two boundary layer rakes at different stations but in-line in the subsonic diffuser. In addition, single total pressure probes were located (1) on the center body external conical spike, (2) just upstream of the inlet throat section, and (3) at the diffuser exit plug station. The total pressure probes just upstream of the inlet throat and on the external spike were removed early in the test program because of the disturbances generated in the downstream flow. Locations of the probes at the engine face station are shown in figure 10. Locations of probes at other stations are shown in figure 11.

Details of a typical total pressure probe are presented in Appendix C. Screens of 27-percent porous material having 0.0055-inch-diameter holes were used to protect the 0.125-inch-diameter Kulite transducers from particle impact damage. Initially, the Kulite transducers were mounted with the diaphragms exposed directly to the airstream. During the first few minutes of tunnel operation (which followed a period of tunnel maintenance), 30 of the 32 total pressure probe transducers failed. The failures, and the methods developed to protect the transducers and the resultant dynamic characteristics, are described in Appendix C.

The dynamic instrumentation for measuring static pressures consisted of 4 static pressure probes at the engine face station (figure 10) and 40 static pressure taps located as shown in figure 11. Typical configuration details of the static taps are shown in figure 12. Satham PA222 transducers were used where space permitted; Kulite CPL-125-25 transducers were used when a smaller size was required.

Dynamic pressure recording: Transient pressures were recorded both on magnetic tape and oscillographs. The latter were used for guidance in conducting the test program and to check the magnetic tape data validity. Nine 14-channel tape recorders were used to record the frequency-modulated signals. Figures 13 and 14 list, respectively, the parameters on each recorder with and without the external disturbance vane installed.

Time-dependent analog data analyses such as cross correlations and cross-power spectral densities could be made only with those parameters recorded on a single tape. Consequently, certain key parameters were repeated on several recorders.

An IRIG B time code signal was recorded on each tape to permit time correlation of data from different tapes providing that the FM analog data were converted to digital data.

Dynamic pressure reference system: To obtain the maximum accuracy and signal-to-noise ratio, most of the steady-state component of each pressure was eliminated in one of two ways. Where the absolute instantaneous pressure was of concern (engine face total pressures, for example) the steady-state component was eliminated by maintaining a reference tank pressure close to the average pressure. Where only the time and magnitude of pressure change were of concern (duct static pressure taps, for example) the steady-state pressure component was eliminated by an electrical bias. The method used for each pressure is noted in figures 13 and 14.

Steady-state pressure instrumentation.-

External flow rake: An external flow rake was mounted on the cowl as illustrated in figure 9. The rake consisted of three identical conical probes for measuring flow angle, Mach number, and total pressure. The conical probe configuration is shown in figure 15.

Internal rakes and static pressure taps: Figure 16 gives the locations of the steady-state total pressure probes and static pressure taps.

Flow metering nozzle: The flow metering nozzle and the associated pressure instrumentation are shown in figure 17.

Pressure recording: All steady-state pressures were recorded using the tunnel pressure data system.

Position instrumentation. - Linear potentiometers were used to measure the position of the inlet cowl, the bypass ring, the exit plug valve sleeve position, and the external disturbances vane angle.

During operation where either the exit sleeve or the external vane was cycled about the same midposition at frequencies above 4 Hz, the potentiometer signals became extremely noisy, and frequent replacement or cleaning of the potentiometers was necessary.

TEST PROCEDURES

Test procedures fell into six general categories. These were:

- (1) Operating at various inlet cowl positions, angles of attack, and mass-flow ratios to define steady-state performance
- (2) Operating at selected "steady-state" conditions to obtain inlet turbulence measurements
- (3) Operating with exit area disturbances
- (4) Operating with external flow disturbances
- (5) Operating with identical input disturbances with the automatic shock control system operative and with it inoperative
- (6) Inducing inlet unstarts and buzz either by exit area reduction or throat area reduction

Steady-State and "Steady-State Dynamics" Tests

Steady-state and "steady-state dynamics" data were recorded after the angle of attack, cowl position, and mass-flow ratio had been set. During the "steady-state dynamics" tests, several seconds of oscillograph data and up to 400 seconds of magnetic tape data were recorded at each run condition. The runs and data recorded are summarized in Appendix D.

Exit Area Disturbance Tests

Inputs to a PACE TR-10 analog computer from prerecorded magnetic tapes were used to schedule exit sleeve position to provide either sinusoidal variations in exit area or variations simulating engine transients. The magnetic tape command data were shaped to account for the kinematics and dynamics of the servo control system as described in Appendix A. The taped sinusoidal inputs were 1/2, 1, 2, 4, 6, 8, 10, 12, and 14 cycles per second for the large amplitude disturbances (± 4 square inches for most tests), and 1/2, 1, 2, 4, 6, 8, 10, 12, 14, 16, 18, and 20 cycles per second for the small amplitude disturbances (± 2 square inches).

External Disturbance Tests

Inputs from prerecorded tapes were used to drive the external vane so that either sinusoidal disturbance or simulated clear air turbulence was generated. Because the vane cannot accurately simulate the combination of flow direction, Mach number, total pressure, and density (or temperature) that an aircraft will encounter flying through a turbulent atmosphere, an arbitrary decision was made to simulate flow direction. Two input tapes were generated for both the sinusoidal disturbances and the clear air turbulence simulation, one tape scheduling flow angle versus time, the other tape scheduling vane angle versus time. The vane angle tapes were used in the actual tests because vane angle was directly measurable, and because flow angularity was not uniform over the face of the inlet.

Sinusoidal disturbances.- Both small-amplitude disturbances, ± 3.5 degrees about a midpoint of 10 degrees and large-amplitude disturbances, ± 7.5 degrees about a midpoint of 10 degrees, were input at frequencies of 1/2, 1, 2, 4, 6, 8, 10, ... 28, and 30 cycles per second. Appendix A shows the approximate variations of the several flow parameters with wedge angle at free stream Mach numbers of 3.0 and 2.6.

Clear air turbulence.- Tests were run with both large-amplitude (3 RMS \sim 6 degrees) and small-amplitude (3 RMS \sim 2.5 degrees) clear air turbulence. The mechanization and definition of the clear air turbulence inputs are discussed in Appendix A.

Shock Control Tests

A portion of the test program was run with a relatively simple terminal shock control system. No attempt was made to optimize the system. Rather, the objectives were to see if the control system performed according to analytical predictions, to see whether internal and external disturbances were increased or decreased by the control, and to compare turbulence levels with and without the control.

The control system mechanization is described in Appendix B. Basically, the bypass area was varied to control shock position as indicated by four inlet throat static pressure taps.

The test procedure consisted of operating the inlet with either exit area or external flow disturbances first with the control system inoperative, then with it operative. The inlet operating point and input disturbances were identical with and without the control system except for a small bias in the operating point introduced when the control system was activated.

Inlet Unstarts

In runs to obtain dynamic distortion characteristics during inlet unstart and buzz, (1) the inlet operating point was set, (2) the data recording systems were turned on, and (3) the inlet was unstarted either by reducing exit area or translating the cowl forward. Exit area unstarts were induced at Mach 2.6 and 3.0. Cowl-induced unstarts were induced at Mach 2.6 and 2.9. Cowl travel was inadequate to unstart the inlet at Mach 3.0. Transient data were also recorded for a fast and a slow restart at each of these test conditions.

TUNNEL AIRFLOW TURBULENCE AND INSTRUMENTATION NOISE

Wind tunnel airflow turbulence, transducer vibrations, and electrical noise contribute to the transient pressure measurements. Analyses indicate that, with the occasional exception of electrical noise, these extraneous contributions are appreciably smaller than the turbulence levels of concern to an engine.

Capped Probe Data

Because transducers act to some degree as accelerometers, total pressure probe outputs were recorded during wind tunnel operation with the total pressure probes capped. Power spectral density (PSD) plots of these data suggest mechanical vibration inputs at 40, 215, 330, and 603 Hz for the external rakes, and at 330 and 603 Hz for the engine face rakes. Signal levels are so low that the apparent absolute levels are questionable.

Electrical Noise

The major contributor to extraneous signals was 60 Hz electric current. These inputs were introduced during both data recording and data analysis, and their magnitude varied from run to run. Part of this variation can be explained in terms of signal levels, data recording, and analysis systems gains. Part is most easily attributed to gremlins.

Data components associated with 60 Hz electric current are readily apparent in that they show up as multiples of 60. Because they are so apparent, no attempt was made to filter out those components associated with 60 Hz electric current. This minimized the possibility of distortion or elimination of valid pressure data.

Wind Tunnel Airflow Turbulence

Pressure transients associated with the tunnel airflow were measured by the external flow field rakes. Data were analyzed at Mach 2.6 and 3.0 without the external disturbance vane installed, and at Mach 3.0 with the vane installed.

Turbulence levels without the disturbance vane.-

Mach 2.6: Figure 18 is a PSD plot for the external rake total pressure probe P802 at an inlet total pressure recovery of 0.918. Discrete peaks not associated with 60 Hz electrical inputs are apparent at approximately 285, 333, 605, 645, and 680 Hz. The peak frequencies of 333 and 605 Hz correspond to those observed with capped probes, and may be associated with or amplified by mechanical vibration frequencies. Peaks at the other frequencies are believed to be characteristic properties of the tunnel flow.

Peak PSD values were less than 7×10^{-9} . PSD values, excluding the discrete frequency peaks, ranged from 1×10^{-10} to 5×10^{-10} . Tunnel turbulence levels were, therefore, well below inlet turbulence levels of concern to a propulsion system.

Mach 3.0: Figures 19 and 20 present PSD plots for probe P802 at inlet pressure recoveries of 0.877 and 0.565, respectively. Associated turbulence levels ($6 \text{ RMS}/P_{t0}$) were less than 0.01. Discrete frequency peaks are apparent at 285, 333, 605, 640, and 680 Hz; the 333 and 605 Hz frequencies again correspond to those observed with the probes capped. Peak PSD values at Mach 3.0 were typically less than 4×10^{-9} . Average values, excluding the discrete peaks, ranged from 1×10^{-10} to 5×10^{-9} .

Turbulence levels with the disturbance vane installed.- The appreciable increase in turbulence when the vane is installed in the tunnel is shown by comparison of the PSD curve of figure 21 with those of figures 19 and 20. The data of figure 21 were obtained with the vane installed at zero degree angle of attack.

Turbulence also varied appreciably with location behind the disturbance vane. This difference can be seen by comparison of the PSD curves of figures 21 and 22 for external rake probes P802 and P804, respectively. The probe-to-probe variation in turbulence with the vane installed is further illustrated in figure 23.

Although turbulence levels were higher with the disturbance vane installed, they were well below the levels of concern for an inlet.

STATISTICAL CHARACTERISTICS OF STEADY-STATE ENGINE FACE DATA

Probability Density

Engine face total pressure versus time traces are presented in figures 24 and 25 for Mach 3.0 operation at high- and low-pressure recoveries, respectively. Data are from the 45-degree rake. Probability density curves for each of the two recovery levels are presented in figure 26 for the inner probe, and in figure 27 for the outer probe.

Comparison of high and low recovery probability density functions for the inboard probe, P870, shows little difference, both patterns being essentially Gaussian with a slight skewness to the negative side. In figure 27, the difference in the probability density plots with recovery for the outer engine face total pressure probe, P874, is more extreme. At the high recovery, the essential Gaussian characteristics of the data from probe P874 are indistinguishable from those of the data from probe P870 at either recovery level. At the low recovery, however, the skewness is more marked, and the curve has a considerably thinner bell shape and an appreciably higher peak value. Figures 24 and 25 show that this distortion is associated with the relatively greater amplitude of the positive spikes for P874 at low recovery.

In summary, the probability density determinations show the steady-state data to consist of basically Gaussian random noise plus randomly occurring positive discrete spikes. The spikes increase the peak amplitude above the pure Gaussian peak amplitude of 0.394, make thinner the standard bell shape, and skew the curve to the left. However, for the most part, probability density is not a sensitive parameter. The presence of spikes, for example, is more easily detectable from the original pressure data. In general, significant changes in the data that occur with changes in operating conditions are not readily determinable from probability density analyses.

Stationarity

When time averages are calculated over some fundamental minimum interval, the data are said to have the property of stationarity when these averages are independent of the particular time interval selected. For the engineer, stationarity of inlet turbulence data is of concern (1) in determining the data recording requirements at each test condition, (2) in determining the number and length of data records to be analyzed, and (3) in determining the validity of the statistical analyses.

As a check of the degree of stationarity of the inlet turbulence data, statistical properties have been computed for several increments of several

lengths and in different portions of a 7-minute data record. This procedure is illustrated in figure 28 which shows the three 5-second time intervals in the 7-minute run and the four 0.05-second intervals within one of the 5-second intervals for which statistical data were obtained.

Table I presents RMS values obtained at a Mach 3.0, high-pressure recovery condition. Data are compared for four 0.05-second intervals and a 5-second interval which included the 0.05-second intervals. The RMS values for the 0.05-second intervals were computed from digital data; the 5-second interval values were measured by an RMS meter. Table II presents RMS values for three 5-second intervals in the Mach 3.0, high recovery run.

Tables III and IV present RMS values for intervals similar to those of tables I and II but for a Mach 3.0, low recovery point.

Probability density functions for the Mach 3.0 high recovery condition are presented in figure 29 for three 5-second intervals for each of three engine face total pressure probes. Figure 30 presents similar data for the Mach 3.0 low recovery condition.

PSD plots corresponding to the aforementioned probability density curves are presented in figures 31 and 32.

The preceding tables and figures indicate stationarity of the 5-second-interval data within most engineering requirements. Even the 0.05-second-interval data show reasonable stationarity at the high recovery conditions. There is considerable variation, however, in the low recovery, 0.05-second-interval data, particularly for such probes as P873 and P874.

The generally lower digital data RMS values, as compared to the corresponding analog values, are probably an indication that the 2,000-per-second sampling rate is too low to catch the spike peaks.

Ergodicity

Whenever statistical information is obtained by taking time averages, the assumption that such information is valid is called the ergodic hypothesis (reference 4). For the inlet system, the statement of the ergodic hypothesis implies that if 1,000 identical inlets operating under identical steady-state conditions have an instantaneous pressure measurement taken at the same point in each inlet, the statistical distribution of this data is the same as if 1,000 measurements are made at equal intervals of time at the same point in one inlet. A test for ergodicity involving 1,000 independent observations on

identical systems is obviously impractical. Consequently, in dealing with practical processes, the truth of the ergodic hypothesis is generally accepted as a matter of convenience, and averages over time are taken to provide statistical information.

While it is impractical to verify the ergodic hypothesis, a check of a somewhat analogous "spatial ergodicity" is possible. That is, the instantaneous average of a number of engine face probes can be compared with the time average of all these probes. Figure 33 presents the spatial average of 20 engine face probes as a function of time at a Mach 3.0, high recovery condition. Also shown are the time histories of two typical probes showing their appreciably larger excursions with time. Similar data are presented in figure 34 for a low recovery condition. At the high recovery condition, the instantaneous spatial average does approach the time average, even with the limited number of probes. At the low recovery condition, however, there is an appreciable variation with time of the instantaneous spatial average. That is, the pressures at the 20 different probe locations are not independent. The degree of dependence of the 20 probe pressures becomes more apparent in the discussion of engine face coherence.

DYNAMIC DISTORTION AT THE ENGINE FACE STATION

A known cause of engine stall is spatial total pressure distortion at the engine face. Dynamic instrumentation shows that even during "steady-state" operation, spatial distortion changes rapidly with time, and that short-duration distortion values can appreciably exceed those measured by conventional steady-state instrumentation.

The distortion data presented in this section were obtained by digitizing the analog pressure data recorded on magnetic tape. Data were digitized for each of 20 dynamic engine face total pressure probes at intervals of 0.0005 second. That is, there were 2,000 instantaneous time slices per second.

Instantaneous Spatial Distortion

Instantaneous total pressure ratio contours are presented in figures 35 through 38 for instantaneous time cuts 0.0005 second apart. Additional data presented are the instantaneous spatial average total pressure recovery, the minimum and maximum individual total pressure readings, and the instantaneous distortion parameter, $\frac{P_{t \max} - P_{t \min}}{P_{t2 \text{ avg}}}$, where $P_{t2 \text{ avg}}$ is the engine face

instantaneous spatial average total pressure. Figures 35 and 36 present data recorded at high- and low-pressure recovery conditions, respectively, at Mach 3.0. Figures 37 and 38 present similar data for Mach 2.6. Note that the low-pressure recoveries are much lower than would be anticipated for an actual aircraft installation. Turbulence characteristics are exaggerated and are therefore more easily detected at these exceptionally low recoveries.

Figures 35 through 38 show that large changes in the engine face total pressure contours take place in 0.0005 second, the changes being markedly greater at the low-pressure recoveries. Although the model was presumably axisymmetric, a preferred pattern of distortion can be seen.

An interesting characteristic revealed by the instantaneous time-cut data is that the variation with time of the maximum local pressure in the engine face annulus is greater than the variation in the minimum local pressure. For example, the maximum local pressure ratio in figure 36 varied from 0.625 to 0.881; the minimum local pressure ratio varied from 0.451 to 0.508.

The instantaneous spatial distortion parameter, $\frac{P_{t \max} - P_{t \min}}{P_{t \text{ avg}}}$, is presented as a function of time in figures 39 through 42. All values in the parameter are instantaneous values for that time cut.

Comparison of figures 39 and 40, high recovery at Mach 3.0 and low recovery at Mach 3.0, respectively, show that both the distortion parameter and its excursions with time are an order of magnitude higher for the low recovery condition. Similar trends at Mach 2.6 are shown in figure 41 and 42.

Instantaneous Average Total Pressure Recovery

The instantaneous average pressure recovery at the engine face station (spatial average) is shown as a function of time in figures 43 through 46.

At the Mach 3.0, high recovery condition (figure 43), there are relatively small changes in the instantaneous average recovery with time. However, as "steady-state" pressure recovery decreases, the variations in instantaneous average pressure recovery become much larger as shown in figure 44. The oscillation in instantaneous average pressures shown in figure 44 would be seen by an engine as absolute pressure transients of approximately 14 percent.

The same general trends observed at Mach 3.0 are shown at Mach 2.6 in figures 45 and 46.

Some interesting characteristics are revealed when the spatial average pressure recovery history of figure 44 is compared to the distortion parameter history of figure 40. The distortion parameter appears to have little more than a random relationship with the instantaneous average recovery. Particularly interesting are the lower frequency "beat note" spatial average total pressure oscillations that become more prominent at low recovery conditions. The typical "beat note" period shown in the bottom portion of figure 44 is nearly identical to the organ-pipe frequency of the model, assuming that the terminal shock and the choked sleeve/plug valve act as closed ends.

Time-Averaged Distortion Characteristics

Because of volume dynamics and flow inertia, there is some minimum time required before a distortion pattern or pressure oscillations result in compressor (fan) stall. Volume dynamics in particular tend to average out extremely short-duration pressure transients. Figures 47 through 50 and 52 through 55 present pressure ratio contours, average pressure recovery, and distortion values obtained by averaging the instantaneous time-cut data over various lengths of time.

The data presented in figures 47 through 50 for the high recovery Mach 3.0 condition were obtained using the individual probe pressures computed by averaging the instantaneous time-cut pressure ratios of figure 35 over time spans of 0.002, 0.005, 0.010, and 0.040 second. Times given for each plot are those for the initial cut of data used in the averages. The corresponding steady-state data are presented in figure 51.

Mach 3.0 low recovery total pressure ratio contours and distortion parameters are presented in figures 52 through 55 for time-averaging periods of 0.002, 0.005, 0.010, and 0.040 second, respectively. Two sets of data are presented for each time-averaging period: one beginning at 42.000 seconds and one beginning at 42.0420 seconds. The time-average values were computed from the instantaneous time-cut pressure ratios of figure 36. The corresponding contours, distortion parameter, and pressure recovery computed from the steady-state instrumentation are presented in figure 56.

As might be expected, the maximum values of distortion and recovery are reduced as the instantaneous time-cut data are averaged over longer periods of time. In the data presented for the Mach 3.0 low recovery condition, for example, the maximum distortion values were 0.5948, 0.4347, 0.4272, 0.3986, and 0.3670 for the instantaneous point and for time-averaging periods of 0.0020, 0.0050, 0.010, and 0.040 second, respectively. The steady-state value was 0.3464. Similarly, the total pressure contours approach the steady-state values as the time-averaging increment is increased.

The time-averaged parameters were computed for consecutive increments of the selected time span. Inspection of plots, such as figures 40 and 44, show that the high-frequency pressure and distortion oscillations are superimposed on lower frequency oscillations. Thus, except for very long time-averaging periods, peak values of time-averaged parameters are dependent on the initial time selected. This dependency of the peak values on the initial time could be eliminated by computing a running average. That is, at each time slice, the data from, say, the preceding and following 10 slices would be averaged. This process would be repeated for each time slice point.

Steady-State Distortion Characteristics

The steady-state total pressure ratio contours for Mach 3.0 high and low recovery operations presented in figure 51 and 56 are compared to the more conventional radial profile plots in figure 57. Similar plots for Mach 2.6 high and low recovery operations are shown in figure 58. The figures show a migration of the maximum pressure region from the outer portion of the annulus towards the hub as pressure recovery decreases. This characteristic is typical of the inlet at both Mach 3.0 and 2.6.

Inlet Unstart

Inlet unstarts and buzz are accompanied by changes in spatial distortion as spectacular as the pressure transients. Data for a Mach 2.6 unstart induced by reducing exit area and for two Mach 2.9 unstarts induced by forward translation of the cowl are presented in figures 59 through 65.

Figure 59 shows engine face total pressure traces for the unstarts.

Figure 60 presents total pressure ratio contours beginning with the steady-state values prior to initiating the Mach 2.6 unstart and continuing with instantaneous time cuts through the unstart transient. Instantaneous distortion values and total pressure ratios are also presented for each time cut. These data are further presented in figure 61 as plots of

$\frac{P_{t \max} - P_{t \min}}{P_{t2 \text{ avg}}}$, $\frac{P_{t2}}{P_{t0}}$, and $\frac{P_{t \max} - P_{t \min}}{P_{t0}}$ versus time. The distortion

parameter, $\frac{P_{t \max} - P_{t \min}}{P_{t2 \text{ avg}}}$, increases rapidly during the unstart. The

second distortion parameter, $\frac{P_{t \max} - P_{t \min}}{P_{t0}}$, has an appreciably smaller

increase during the unstart inasmuch as P_{t0} does not change.

Data similar to that presented for the Mach 2.6 unstart are presented in figures 62 and 63 for a Mach 2.9, 0.873 initial recovery unstart, and in figures 64 and 65 for a Mach 2.9, 0.741 initial recovery unstart. Trends are generally similar to those observed for the 2.6 Mach number unstart.

The Mach 2.9 unstarts exhibit an unusual buzz cycle of approximately 77 cycles per second. Fully developed buzz cycles normally have periods similar to that for the unstart cycle, and analytic calculations predict a buzz frequency of approximately 19 cycles per second. (On close inspection, the presence of this "normal" buzz cycle can be seen in the high recovery unstart oscillograph traces.) The high-frequency buzz of approximately 77 cycles per second corresponds closely to calculated organ-pipe frequency when the terminal shock and the choked plug exit valve are considered to be closed ends.

The fully developed "normal" buzz cycle is triggered by separation of the throat region boundary layer which initiates a duct emptying process. When the emptying process has reduced duct pressures sufficiently, the boundary layer reattaches, and a filling cycle is initiated. It would appear that a higher frequency boundary layer separation and reattachment cycle is triggered by the organ pipe pressure pulsations and is superimposed on the lower frequency empty-fill cycle.

Inlet Restart

Figure 66 presents oscillograph traces recorded during a transition from buzz to started operation at Mach 2.6. Shown are three engine face total pressures, three static pressures measured downstream of the inlet throat (see figure 11), and the exit sleeve position. The approximate time when the cowl translation began is also shown.

During the initial buzz operation, both the empty-fill and the organ-pipe frequencies previously discussed are clearly evident, the organ-pipe frequency being particularly distinctive in the throat region. As the exit area increases, the low-frequency buzz vanishes.

Upon restart, the terminal shock moves downstream of the throat static pressure taps. Engine face total pressure increases relatively smoothly but then shows the turbulence characteristic of excessively supercritical operation. The latter is to be expected for an open-loop restart where the exit area and throat area are opened by arbitrary amounts to ensure inlet restart. A closed-loop restart control which would increase bypass flow only by the amount required for the restart would largely eliminate the engine face total pressure turbulence during the restart.

STEADY-STATE OPERATION TURBULENCE CHARACTERISTICS

Turbulence values have been computed as a function of operating conditions, location, and steady-state distortion. Herein, turbulence is defined as $6 \text{ RMS}/\bar{P}_{t2}$ where RMS is the measured true root mean square voltage of the given pressure transducer signal, and \bar{P}_{t2} is the average steady-state engine face total pressure. This expression can be interpreted physically as the width of a band which would bound the nondimensionalized pressure oscillation trace for all but an infrequent, abnormally high-amplitude oscillation.

Engine Face Turbulence

Turbulence variation with recovery.- Figures 67 and 68 present turbulence as a function of total pressure recovery for each of the engine face total probes at Mach 2.6 and 3.0. The data were obtained during steady-state operation at zero degrees angle of attack.

As pressure recovery drops (terminal shock strength increases), turbulence increases sharply, as does the probe-to-probe variation on a given rake. The discontinuity, at approximately 78 percent recovery for the Mach 3.0 operation in figure 67, is believed to reflect a change in the wall boundary layer conditions. These data and total pressure ratio contour data suggest separation of the outerwall boundary layer at the lower recoveries.

To be noted is the fact that turbulence values differ by several-fold from location to location at a given operating condition. For example, turbulence ranged from 0.04 to 0.07 at Mach 3.0 high recovery, from 0.03 to 0.11 at Mach 2.6 high recovery, from 0.20 to 0.85 at Mach 3.0 low recovery, and from 0.24 to 0.85 at Mach 2.6 low recovery. Obviously, the turbulence level computed from a single probe does not define the overall turbulence level. Other test data show not only a several-fold variation in turbulence level between probes, but also that the location of the probe(s) having the highest turbulence level often changes as changes are made in the inlet operating condition.

Turbulence and total pressure ratio contour similarity.- When engine face station turbulence contours and radial profile plots were examined, a striking similarity to the corresponding total pressure ratio plots was noted. This similarity is illustrated in figures 69 and 70. Figure 69 compares contour plots of turbulence and total pressure ratio. Figure 70 compares radial profile plots of turbulence and total pressure ratio. In particular, it can be seen that the regions of maximum turbulence coincide with the regions of maximum total pressure ratio. Further, minimum turbulence regions are those near the outer and inner walls of the flow annulus.

As would be expected for an axisymmetric configuration, the turbulence variation is primarily radial. Somewhat lower values of turbulence were observed for the probes on the 45-degree rake. The two boundary layer rakes upstream of the 45-degree engine face rake (figure 11) may have changed the flow pattern and characteristics enough to lower the turbulence values.

Turbulence variation with steady-state distortion parameter.- As steady-state total pressure recovery decreases, both turbulence and steady-state distortion increase. Figures 71 through 74 show the relationship of turbulence and the steady-state distortion parameter, $\frac{\bar{P}_{t \max} - \bar{P}_{t \min}}{\bar{P}_{t2}}$.

Curves of distortion versus the numerical average of turbulence at Mach 3.0 and 2.6 are presented in figure 71. The turbulence value is the numerical average for 20 engine face total pressure probes.

Figure 72 is similar to figure 71 except that the average turbulence was computed as the square root of the sum of the squares of the 20 engine face total pressure turbulence values. This parameter gives greater weight to high turbulence values.

Figures 73 and 74 present distortion versus individual probe turbulence values for Mach 3.0 and Mach 2.6, respectively. The large probe-to-probe variation in turbulence, previously noted with respect to figures 67 and 68, is again clearly evident.

Circumferential variation in turbulence.- Comparison of the turbulence levels for probes at the same radius on different rakes in figures 67 and 68 and the turbulence contour plots of figures 69 and 70 shows reasonable but not complete axisymmetry of the engine face total pressure turbulence. Part of the nonaxisymmetry is undoubtedly associated with the instrumentation effects on the flow.

Upstream rake effects on engine face turbulence.- Engine face rake turbulence values obtained in two test runs are compared in figure 75. The runs differed in that the two single-probe rakes installed in the 315-degree plane in the supersonic flow portion of the inlet for the first run were removed for the second run. Engine face total pressure turbulence is higher in the 45-, 135-, and 225-degree planes with the rakes installed, but lower in the 315-degree plane behind the upstream rakes.

Turbulence variation with angle of attack.- Figure 76 shows the variation in turbulence with angle of attack at Mach 3.0 for low recovery operating conditions (high recovery operation was not possible at 8 degrees angle of attack). The data were all obtained with the 315-degree plane rakes installed. The variation in turbulence with angle of attack clearly is dependent on the total pressure probe location.

Turbulence Variation With Station

Total pressure turbulence.- Turbulence variation both with inlet station and with radial location are illustrated in figures 77 and 78. Data are for Mach 3.0 and 2.6, respectively, at three recovery levels. Also shown are the approximate terminal shock positions. All the data are from the 45-degree plane instrumentation.

With few exceptions, the total pressure turbulence decreases with distance downstream of the terminal shock. The few exceptions are believed to be a function of the radial location of the instrumentation.

The relatively higher total pressure turbulence near the centerbody at MS 47.50, particularly when the nominal shock position is downstream of the rake, possibly indicates unsteady separation of the boundary layer triggered by the rake strut shock.

Static pressure turbulence.- With an occasional exception within the data accuracy, wall static tap turbulence values decrease with distance downstream of the terminal shock. This characteristic is consistent with data from several other inlet configurations and is believed to be associated with (1) increased mixing length and damping in the wall boundary layer, and (2) decreasing Mach number with distance downstream of the shock. In addition, where an appreciable organ-pipe component exists, much higher pressure oscillations would be expected near the terminal shock and the choking station, i.e., the node points. (The choking station for this model is well downstream of the engine face station.)

Static pressure turbulence measured at the wall tap, MS 76.35, is consistently higher than that measured in the airstream by the engine face static pressure probes. Turbulence values at the two locations differed by as much as a factor of 2.

Turbulence levels at the same station but different circumferential locations are reasonably similar as would be expected for an axisymmetric inlet. For example, turbulence levels are as follows for two wall static pressure taps 90 degrees apart at station MS 76.35:

$\underline{M_o}$	$\underline{\bar{P}_{t2}/P_{t0}}$	$\underline{315^\circ}$	$\underline{45^\circ}$
3.0	0.877	0.018	0.017
3.0	0.565	0.131	0.121
2.6	0.918	0.022	0.019
2.6	0.642	0.182	0.138

Some difference is to be expected because of the two rakes forward of the 45-degree pressure tap; it can be seen that turbulence levels are somewhat lower in the 45-degree plane, particularly at the higher turbulence levels.

HYPOTHETICAL MODEL OF THE TURBULENCE-GENERATING PROCESS

Hypothetical Model

Several observations from this and other tests suggest a hypothetical model for turbulence generated by boundary layer-shock interaction during supercritical operation.

Observations suggesting the hypothetical model include the following:

- (1) Turbulence levels increase as the inlet operation becomes increasingly supercritical, that is, as terminal shock strength and boundary layer thickness increase. This is illustrated by figures 67 and 68.
- (2) During highly supercritical operation, the terminal shock is not a planar normal shock. Rather it consists of a train of oblique and normal shocks which are in continual motion.
- (3) Turbulence contour maps tend to correspond to total pressure contour maps. Specifically, as indicated in figures 69 and 70, the regions of maximum pressure recovery correspond generally to the regions of maximum turbulence.

(4) Pressure versus time traces such as in figure 25 show that the time that total pressures are near their minimum exceeds that for which they are near their maximum. Further, the greatest and most erratic excursions are forward the high-pressure direction.

(5) The peak pressures during these excursions appreciably exceed those that can be computed assuming a single normal shock loss at the apparent quasisteady terminal shock position.

The hypothetical turbulence model is based on cyclical separation and reattachment of the boundary layer. The separation and reattachment of the boundary layer is both caused by and causes changes in the terminal shock structure. Figure 79 shows sequential shock and boundary layer separation patterns. To obtain a qualitative understanding for the magnitude of the total pressure changes with time that can result, several arbitrary assumptions have been made.

(1) The flow is essentially two-dimensional and is symmetrical about a reflection centerplane. (The flow annulus height is small compared to its diameter.)

(2) Flow Mach number upstream of the Station e shock position is 2.2, and the ratio of effective area at Station a to that at Station e is 1.05 when the boundary layer is attached.

(3) When the boundary layer detaches, it forms an effective ramp angle of 13 degrees relative to the flow.

Consider now the conditions for each of the shock patterns of figure 79.

Figure 79(a): The boundary layer is initially attached, and the terminal normal shock is at Station a. Except for flow in the boundary layer, total pressure recovery is essentially uniform. For the assumed conditions, the total pressure ratio across the terminal shock system, P_{ty}/P_{tx} , will be 0.606 for streamtubes 1, 2, and 3.

Figure 79(b): The strong static pressure gradient with the normal shock at Station a caused the boundary layer to separate. The separated boundary layer generates an oblique shock which is reflected from the centerplane. The converging area and continuity considerations cause the normal shock to move forward to b where quasisteady-state total pressure ratios are 0.825 for streamtube 1, 0.825 for streamtube 2, and 0.925 for streamtube 3.

Figure 79(c): The terminal shock moves upstream to Station c. Quasisteady-state total pressure ratios, P_{ty}/P_{tx} , are 0.825 for all three stream tubes.

Figure 79(d): When the terminal normal shock reaches Station d, total pressure ratios are 0.825 for streamtubes 1 and 2 and 0.628 for streamtube 3.

Figure 79(e): With the terminal shock at Station e, the total pressure ratio for streamtubes 1, 2, and 3 will be 0.628. The contours formed by the detached boundary layer will cause the subsonic flow behind the terminal shock to be reaccelerated, perhaps to supersonic Mach numbers. The associated static pressure gradients will cause reattachment of the separated boundary layer, the terminal shock will move aft, and a new cycle may be initiated.

Comments on the Hypothetical Model

The hypothetical model is in good agreement with experimental observations. The center and normally higher recovery streamtubes undergo the most frequent and highest amplitude changes in total pressure. Quite high peaks in total pressure occur for short periods. Finally, there are large total pressure changes in a given streamtube.

Generally, the boundary layer separation and reattachment patterns and processes would not be expected to be symmetrical nor in phase from one part of a duct to another. An exception might be when essentially one-dimensional pressure waves were moving through the duct. Such waves, associated with organ-pipe or Helmholtz resonance, for example, could trip a cyclical and relatively symmetrical boundary layer separation which, in turn, would add energy to the resonance process.

A factor further contributing to measured pressure transients during the boundary layer detachment and reattachment process is the fact that the streamtubes shift laterally while the pressure probes remain stationary. Lateral displacements of streamtubes of different total pressure are therefore seen as pressure transients by a dynamic probe. This factor is, of course, strongest in regions of high total pressure gradients.

STEADY-STATE OPERATION POWER SPECTRAL DENSITY AND COHERENCE CHARACTERISTICS

Power Spectral Density Characteristics

The distribution of turbulence energy with respect to frequency is best seen in power spectral density (PSD) curves. The area under the PSD curve is proportional to the square of the turbulence parameter, $6 \text{ RMS}/P_{t2}$, if the upper and lower frequency limits used in the data processing are identical.

Units of the PSD curves presented herein are $(\Delta P/\bar{P}_{t2})^2/\text{Hz}$. That is, the pressure oscillations are nondimensionalized by the engine face average total pressure. Unless otherwise noted, a constant filter bandwidth of 5 Hz was used in the PSD determinations.

Power spectral density variation with recovery.- The typical increase in engine face total pressure PSD's with decreasing recovery is shown in figures 80 through 83. Figures 80 through 82 present Mach 3.0 PSD's for inner, outer, and middle probes, respectively. Figure 83 consists of Mach 2.6 PSD's for an inner probe. It can be seen that PSD levels varied as much as a thousandfold over the test range of recoveries.

Typically, the PSD curves slope down to the right. As recovery drops and turbulence increases, a disproportionate part of the energy increase is in the low-frequency range. For example, in figure 82 the increment in PSD between the low and high recovery condition is approximately 5×10^{-6} at 1,000 Hz and 38×10^{-6} at 100 Hz. (Note that, because of the logarithmic ordinate, PSD increases much more in the low-frequency range even where the PSD curve slopes are similar or decrease with decreasing pressure recovery.)

Particularly conspicuous is the very sharp rise in the low recovery PSD curve at low frequencies for the inboard probe (figure 80).

Power spectral density variation with circumferential angle.- PSD plots for eight engine face total pressure probes, at a constant radius, 6.946 inches (2.741 inches from the hub), are shown in figure 84. The data are for high recovery operation at Mach 3.0. PSD plots for the same probes at low recovery operation are shown in figure 85.

The circumferential variations in PSD at Mach 2.6 were similar to those at Mach 3.0, except that they showed greater axisymmetry.

Power spectral density variation with radius.- PSD plots for the five engine face total pressure probes on the 225-degree rake are shown in figures 86 and 87 for high and low recovery operation at Mach 3.0. Similar radial

variations were observed for the other engine face rakes. The curves confirm previous observations that the turbulent energy is lowest in the flow adjacent to the inner and outer duct walls. Further, turbulence is lowest near the inner wall at high recovery and lowest near the outer wall at low recovery.

Power spectral density variation with angle of attack.- Figures 88 through 93 compare PSD's of the inboard, midstream, and outboard probes of the 225- and 315-degree engine face rakes for angles of attack of 0, 4, and 8 degrees. Comparisons are made at as similar pressure recoveries as possible.

As might be expected, angle of attack effects differ depending on the probe location, from top to bottom, and from centerbody to outer wall.

Resonance peaks are much more evident at the 4- and 8-degree angles of attack than at zero degrees.

Power spectral density variation with station.- The change in PSD's proceeding down the duct is illustrated in figures 94 through 97.

Figure 94 shows total pressure PSD curves at MS 47.30, MS 66.70, and MS 78.95 for approximately the same stream tube. The terminal shock was near MS 39 for this Mach 3.0 test point. It can be seen that there is an appreciable reduction in the PSD levels with increasing distance aft of the shock; the maximum attenuation is at the high frequencies.

Figure 95 presents data similar to figure 94 but for a low recovery point with the terminal shock aft of the upstream rake. The same reduction in PSD levels with distance downstream of the terminal shock is observed. However, the PSD level for the upstream rake, in supersonic flow, is appreciably lower.

Similar trends can be observed in the static pressure PSD curves of figures 96 and 97. That is, the level decreases with distance downstream of the terminal shock and is lower in the supersonic flow. Static pressure PSD is somewhat lower in the engine face annulus area than at the centerbody wall, as previously indicated by the RMS turbulence measurements.

Power spectral density variation at a rake station.- PSD curves for a wall static tap and two total probes at MS 47.30 are compared in figure 98 for a Mach 3.0 high recovery point, and in figure 99 for a Mach 3.0 low recovery point. Although the nominal shock position is slightly aft of MS 47.30, the appreciable turbulence, particularly for the inboard probe, suggests boundary layer instability in the supersonic flow portion of the inlet. This could be triggered either by pressure transmission from the terminal shock system through the subsonic boundary layer, or from the rake strut shock system near the wall.

Effect of the disturbance vane on the external flow field power spectral density. - External flow field PSD's with simulated clear air turbulence are compared to those measured with the disturbance vane installed but stationary in figures 100 through 102. Data are shown for three external probes at a Mach 3.0 operating condition. PSD without the disturbance vane installed in the tunnel is also shown in figure 100. The figures show (1) the flow field generated by the disturbance vane is not uniform, and (2) the clear air turbulence most influences the PSD curves in the lower frequency range as was intended.

Figures 103 through 105 compare PSD's at the engine face for the same runs for which external flow field data are presented in figures 100 through 102. The figures show that, with the possible exception of frequencies below 20 Hz, the external flow field turbulence has negligible effect on the engine face turbulence.

The rather surprising fact that engine PSD's are slightly higher without the disturbance vane installed is believed to be the result of a stronger inlet terminal shock system. Although the total pressure recoveries were similar for the three runs, part of the total pressure loss with the disturbance vane installed was caused by the vane. Consequently, the inlet terminal shock loss was greater by 3 percent or more in the run without the disturbance vane.

The primary observation to be made is that turbulence in the external flow field is not amplified by the inlet, and the inlet terminal shock strength has greater influence on the engine face turbulence level than external flow field turbulence. The relative contribution of the external flow turbulence will, of course, increase as inlet total pressure recovery increases.

Sinusoidal external disturbance effects are described in the section on the inlet control. In summary, the sinusoidal disturbances affected the PSD curves primarily at the disturbance frequencies and their harmonics.

Coherence Characteristics

Coherence is a measure of the degree of interdependence between two time histories at specific frequencies. Perfect coherence has the measure unity while lack of coherence (complete independence) has the measure zero. It is to be noted that the coherence function is not a function of the signal amplitudes but only a measure of the degree of interdependence of two signals, regardless of amplitudes. A general discussion of coherence is given in reference 5.

Engine face coherence.- Coherence functions calculated for 16 pairs of engine face probes during steady-state operation at high and low recovery levels at Mach 3.0 are shown in figure 106. Figure 107 presents similar data for Mach 2.6. The detailed calculations, listed in Appendix E, illustrates the relative magnitude of the four terms entering the coherence function calculation and the limited accuracy with which they could be read from X-Y analog plots.

Coherence between various pairs of engine face total pressure probes provides a measure of the "scale" of turbulence, that is, the portion of the annulus area that will undergo the same pressure change at a given frequency. Inspection of the coherence values in figures 106 and 107 shows that coherence increases as recovery decreases. Coherence was relatively high for adjacent probes. Fairly high coherence was observed between midradius probes 90 degrees apart in the top sector. However, coherence was negligible between (1) inboard probes in the top sector, (2) outboard probes in the top sector, and (3) mid-radius probes in the bottom sector.

A more revealing presentation of the foregoing data is given in figure 108. Coherence is plotted versus frequency, coherence being the numerical average of the coherence functions for each of 13 probe pairs. The fact that the low recovery data is significantly more coherent is readily apparent. Of even greater interest is the peaking at or near 80 Hz. The estimated organ pipe frequency, assuming the terminal shock and the choked exit to act as closed ends, is between 70 and 80 Hz.

A typical coherence function for adjacent probes on the same rake is shown in figure 109. The low recovery resonance indications at the duct organ pipe frequency are strong at both Mach 3.0 and 2.6.

Figure 110 shows high coherence, particularly at the organ pipe frequency, for probes P872 and P887 on adjacent rakes. This high coherence was not observed for any of the other limited checks of coherence between probes on adjacent rakes. For example, the mirror-image pair of probes, P877 and P882, showed negligible coherence.

An unusual condition is shown in figure 111 wherein the adjacent inboard probes on the 215-degree rake show more coherence at high recovery than low recovery. The more outboard probe pair, P882 and P883, had the typically low coherence at high recovery. The reason for this high recovery, high coherence phenomena is not clear. It may be due to some localized disturbance caused by the duct operating in an off-design condition.

Coherence for probes at different stations.- Coherence functions determined for various pairs of probes located in-line but at different inlet stations are listed in table V. Data are tabulated for a high and low recovery

condition at Mach 3.0. The most significant observation is that with one exception, there is negligible coherence between duct stations over the frequency range analyzed.

Coherence between static and rake total pressures.- Table VI lists coherence functions for pairs of wall static and rake total pressures for MS 47.30 and MS 66.70. Coherence values are relatively high at low recovery. Although coherence varies appreciably with frequency, a consistent pattern is not apparent.

Coherence as a function of frequency is shown in figure 112 for pairs of adjacent total and static probes at the engine face station. Maximum coherence peaks exist at low frequencies and at 100 to 120 Hz.

Coherence between static pressures.- Coherence between static pressure taps on opposite sides of the duct is shown as a function of frequency in figure 113.

Coherence between external flow field and engine face total pressure.- Clear air turbulence as simulated by the external disturbance vane affected the engine face turbulence primarily in the low-frequency region. This is shown in figures 103, 104, and 105 which compare PSD curves at similar inlet recovery levels with and without simulated clear air turbulence.

Coherence between an external rake probe and an engine face probe is shown as a function of frequency in figure 114. Coherence is high as might be expected at frequencies below 20 Hz. At higher frequencies, both the low clear air turbulence amplitudes and the attenuating effect of the duct apparently eliminate any coherence.

TERMINAL SHOCK CONTROL SYSTEM TESTS

The terminal shock position control system was evaluated with both internal and external disturbances at a tunnel Mach number of 3.0. The evaluation consisted of comparing such inlet parameters as shock excursion, power spectral densities, and RMS turbulence levels with and without the shock control system in operation. The mechanization and characteristics of the control system were as described in Appendix A except that the integral gain, K_I , was reduced from 100 to 80.

Shock Excursion Comparisons

Sinusoidal exit area disturbances.- Shock travel excursions with and without the control system are listed in table VII for various disturbances. Shock travel was determined from the shock position parameter, PR, which varies with shock position as shown in figure 137 of Appendix B.

The effectiveness of the control system in reducing shock travel caused by sinusoidal exit area disturbances is shown in figure 115. Performance predictions based on the linear analysis and the "hardware tie-in simulation" of Appendix B are also presented for comparison with the test performance.

The reduction in shock excursion for disturbance frequencies below 6 cps and the amplification for disturbance frequencies from 6 to approximately 17 cps, shown by the test data of figure 115, are in good agreement with the hardware tie-in simulation predictions. However, agreement with the linear analysis was poor, indicating the importance of the bypass actuator and servo valve rate limits which were not included in the linear analysis.

The validity of the inlet dynamics representation used in the control system analysis and simulation was obscured by the rate restrictions of the bypass actuator and servo valve hardware. A limited investigation of shock response to sinusoidal exit area disturbances is summarized in Appendix F.

External sinusoidal disturbances.- The ineffectiveness of the control in reducing shock excursions caused by sinusoidal external vane angle disturbances is apparent in figure 116. Except for disturbance frequencies of 1 Hz and less, the control system amplifies the shock excursion.

As would be expected, the control performance with external disturbances was not in agreement with the analytical predictions shown in figure 115. One reason is that the inlet dynamics representation used (from reference 3) is not valid for external disturbances. A second reason is that the shock position parameter, PR, was nondimensionalized by the use of tunnel total pressure, P_{t0} . P_{t0} does not reflect the disturbance vane-induced changes in flow total pressure, Mach number, and direction at the inlet face. The scope of the shock position control portion of the program was too limited to investigate control concepts and modifications to improve the external disturbance characteristics. A more sophisticated shock position parameter wherein the reference pressure varied with flow angle and Mach number would have been of help. However, sensing and logic capable of distinguishing between external (upstream) and internal (downstream) disturbances may well be required for high-performance inlet operation.

Control System Effects on Turbulence

RMS turbulence.- The effects of the control system on overall turbulence levels (as indicated by the RMS pressure level) are shown in figure 117 for sinusoidal exit area disturbances and in figure 118 for sinusoidal external disturbances. The trends shown are in good agreement with those indicated in figures 115 and 116. That is, the control system attenuates the shock travel and its contribution to RMS turbulence for disturbance frequencies below 6 cps, and amplifies them at frequencies from approximately 6 to 17 Hz. The control amplifies the shock travel and turbulence levels for external disturbances in most of the frequency range. The test data indicate that the control system affects turbulence only as it effects shock position.

Power spectral densities.- Three engine face total pressure PSD curves are compared in figure 119. One was recorded with no disturbance input, one with a 2 Hz exit area disturbance, and one with a 14 Hz exit area disturbance. All were run at Mach 3.0 and an initial condition (midpoint) recovery of 0.846. Most of the differences are at the disturbance frequency and, in some instances, the first harmonic of the disturbance frequency. (The cutoff in the PSD curves at 5 Hz is due to the analysis equipment limitations with a 5 Hz bandwidth filter.)

Figures 120 through 122 show the effect of the control on engine face total pressure PSD values for sinusoidal exit area disturbances of 2, 10, and 14 Hz. Except for the reductions or increases at the disturbance frequency (corresponding to the previously noted reductions or increases in shock excursions), the control had no discernible effect on the power spectral density curves. Of interest is the apparent first harmonic for the 10 Hz disturbance present both with and without the controller operating.

PSD comparisons for P830, an inlet throat static pressure tap downstream of the terminal shock, showed the same trends as those described previously for an engine face total pressure probe.

PSD curves with both sinusoidal external disturbances and with simulated clear air turbulence show no discernible difference due to control operation down to 5 Hz.

CONCLUSIONS AND RECOMMENDATIONS

Test Procedures and Equipment

The use of prerecorded magnetic tapes in conjunction with analog computers and servo control system permits a reduction in wind tunnel occupancy time.

Equally important, test conditions such as simulated engine transients or external flow disturbances can be repeated precisely to permit comparison tests.

Dynamic test inlet models should have a sonic point flow control valve at or near the simulated engine face station inasmuch as the inlet dynamic characteristics are influenced by the acoustic characteristics of the total ducting system aft to a sonic point.

Use of a two-dimensional wedge to simulate external flow disturbances leaves much to be desired. The flow field over the inlet face was not uniform. Further, the interrelationships between such flow parameters as Mach number, flow direction, total pressure, and density are not representative of those that would be encountered by an airplane flying through turbulent air.

Miniature pressure transducers exposed directly to the airstream provided good dynamic response characteristics. However, screens or baffles protecting the transducer diaphragms from particles in the airstream were found to be essential.

Turbulence in the NASA Ames 8 x 7 Unitary Wind Tunnel was found to be well below the levels of interest in inlet turbulence investigations.

Data Recording and Analysis Techniques

The large number of parameters which must be recorded and time-correlated in an inlet dynamics test makes it highly desirable to record all data on a single multiplexing tape recorder rather than on a number of tape recorders.

A major problem in recording, playback, and analysis of test data is minimizing noise, particularly the noise associated with 60-cycle electric current. Eliminating the steady-state component of the measured pressures either by regulation of the transducer reference pressures or by biasing the signal electrically aids in obtaining satisfactory signal-to-noise ratios.

The quantity of dynamic data which can be generated in an inlet dynamics test is enormous. Techniques must be developed for rapid scanning and editing of the data if the data analysis efforts are not to be lost in the sheer bulk of material. Experience to date suggests that digital techniques have greater potential for speedup and automation of the data analyses than do analog techniques. Digital techniques should also provide greater accuracy, particularly for those analyses where multiple processing, plotting, and reading of the data is now required using analog techniques. An example of such an analysis is the highly useful coherence function where four parameters must be processed,

plotted, read from the plots, and used in a final calculation. Digital data analysis techniques are also expected to have fewer limitations for analyses in the low-frequency spectrum.

Steady-State Dynamic Distortion

Inlet-induced turbulence contains both random and nonrandom pressure oscillations. As inlet operation becomes increasingly supercritical, both turbulence amplitude and the nonrandom component of turbulence increase. The nonrandom turbulence strongly favors the acoustic frequencies of the inlet duct, particularly the organ-pipe frequencies wherein the terminal shock and the choked (sonic) exit act as acoustically closed ends.

Instantaneous spatial distortions at the engine face station appreciably exceed those which would be measured by conventional steady-state instrumentation. During highly supercritical inlet operation, large changes in engine face pressure patterns occur within a millisecond. The instantaneous pressure recoveries, averaged over the engine face, also vary appreciably with time but at frequencies generally lower than those for the distortion pattern oscillations.

At a given operating condition, regions of maximum turbulence corresponded generally to the regions of maximum pressure recovery; the largest and most conspicuous excursions in pressure are towards the high-pressure side.

Turbulence values at a given inlet operating condition vary appreciably with location in the engine face plane. Variations are typically twofold at high recovery conditions and as much as fourfold at low recovery conditions.

Dynamic Distortion with Internal and External Disturbances

During inlet unstarts, instantaneous distortion values approached 100 percent, more because of the large drop in instantaneous average pressure than because of increased differences between pressures at various locations.

Two types of buzz oscillations were observed, one corresponding to the fully developed "empty-fill" buzz cycle, the other being a shorter cycle corresponding in frequency to the inlet duct organ-pipe frequency.

Exit area disturbances changed the inlet turbulence characteristics only as consistent with steady-state operation over the range of terminal shock positions. Power spectral density changes were limited to frequencies below 150 Hz, the major portion of the change being at the input disturbance frequency.

Simulated clear air turbulence was appreciably attenuated by the inlet.

Sinusoidal external flow disturbances did not noticeably change the power spectral density curve except at the input disturbance frequency.

The shock control system was effective in reducing the terminal shock excursions for simulated engine transients and for exit area disturbances at frequencies up to 6 Hz. Performance was in reasonable agreement with the control system simulation with the exit area disturbances.

The control system increased terminal shock excursions induced by external disturbance inputs at most frequencies. A considerably more sophisticated control would be required to effectively reduce shock travel for both downstream (engine) disturbances and external flow disturbances.

The control system had no effect on the inlet turbulence characteristics other than as it affected the terminal shock position.

Recommendations

The data analysis program was essentially exploratory in nature, and only a portion of the test data recorded have been analyzed. It is recommended that further analyses be made with emphasis on steady-state operation runs at intermediate recovery, and on digitized data coherence studies.

Los Angeles Division
North American Rockwell Corporation
Los Angeles, California July 31, 1969

Appendix A

SERVO CONTROL SYSTEM AND DISTURBANCES MECHANIZATION

Component Positioning Control System

The variable components of the model, cowl, bypass, aft sleeve (plug valve), and the external disturbance vane were positioned by a hydraulically powered servo control system which was capable of accepting manual or programmed (from a magnetic tape recorder) commands. The system included a closed-loop shock position control.

Figure 123 is a diagram of the interfaces between the components employed in the control system. Two PACE TR-10 analog computers were used to implement the computing portion of the control system. A control panel was used to provide manual control inputs to the position control system. A magnetic tape playback machine transferred programmed inputs to the control system. A sine-wave generator was used as a backup for the magnetic tape.

The shock position control system employed four pressure transducers in the throat region to determine the shock position. The transducer outputs were amplified by a CEC 20,000 Hz carrier amplifier. The performance of the system was monitored on an oscilloscope and an eight-channel pen recorder.

Components of the control system were:

- (1) Computing component (PACE TR-10 analog computer)
- (2) Control panel (manual inputs)
- (3) Magnetic tape playback machine (programed inputs)
- (4) Servovalves and hydraulic actuators

Computing component.- The computing component, mechanized on the TR-10A analog computer (figure 124) provided servovalve current based on the feedback potentiometer output and the manual or programed position command. Each actuator loop employed three amplifiers, thereby providing easy monitoring of the system performance and actuator positions. The outputs of the amplifiers, as a function of the actuator position, are shown in figure 125.

The loop gains of the position control system were obtained during bench tests at the contractor's facility. The loop gains were increased until the

system became unstable, then reduced to approximately one-half the instability value for the wind tunnel tests. Gain of the vane control system was lowered from 30 to 24.9 during the wind tunnel test. The gain change was required because of the load added to the actuators by the vane, not part of the bench test setup.

Because high response was not required, the cowl rate was limited to 6 inches per second by a limiter in the cowl servo loop.

Two rates were provided for the aft sleeve (plug valve): a high rate for simulating engine disturbances and a lower rate for restarts.

Control panel.- Manual control inputs were made by means of bias potentiometers in the control panel. The control panel also contained two restart switches (switches 2 and 3 of figure 126) which returned the cowl and sleeve to pre-selected positions which insured restarting the inlet.

Magnetic tape playback.- Preprogramed inputs were obtained from a tape playback machine. The tape outputs are patched directly into the TR-10A computer. The tape inputs were activated by function switches on the computer.

Actuators.- The interfaces between the TR-10A and the hydraulic actuators for the cowl, bypass, sleeve (plug valve), and external vane are shown in figures 127 and 128.

Internal Disturbances

The internal disturbances consisted of sinusoidal exit area variations and engine transients. These disturbances were generated by varying the plug exit area. The sinusoid variations were taped so that the input command increased with frequency to compensate for the attenuation associated with the actuator system. These normalized tape amplitudes were then adjusted by potentiometer 13 of figure 124 to obtain the desired amplitude for each run (or the maximum amplitude attainable within the system capabilities).

External Disturbances

The inlet was subjected to two types of external flow disturbances: sinusoidal disturbances and simulated clear air turbulence (CAT). Both types were generated by a disturbance vane mounted ahead and above the inlet. The vane is discussed in detail in reference 2.

Flow field properties versus vane angle are shown in figure 129 and 130 for Mach 2.6 and 3.0. The curves presented are from reference 2 and are based

on two-dimensional flow in the near flow field. Flow direction variation with time was selected as the most meaningful inlet disturbance.

Because of their similarity, the solid line curve in figure 131 was used to represent both the Mach 2.6 and Mach 3.0 variation of flow angle with wedge angle.

Sinusoidal disturbances.- Two sinusoidal disturbance tapes were generated using the setup illustrated in figure 132 - one giving flow angle sinusoids and the other giving vane angle sinusoids. For the tape-generating flow angle commands, the output of the sine generator was shaped by the inverse of the flow angle versus vane angle curve. For both tapes, the gain, K_X , was adjusted at each frequency to compensate for the actuator dynamics. For flexibility, vane midposition and sinusoid amplitude were set manually for the vane sinusoids.

Preliminary flow surveys using the conical flow direction probes showed appreciable variations, both from the theoretical calculations and with height above and below the inlet centerline. Consequently, the vane angle tape was used for the test program because vane angle could be directly measured and monitored.

Clear air turbulence.- The CAT taped inputs consisted of white noise filtered so that the statistical properties of a CAT model were matched. During selection of the filter to be used, three CAT models were considered. The power spectrum density (PSD) equations for each of the models were:

$$\frac{\phi(\Omega)}{\sigma_{\omega}^2} = \frac{L}{\pi} \frac{(1+3 \Omega^2 L^2)}{(1+\Omega^2 L^2)^2} \quad (1)$$

$$\frac{\phi(\Omega)}{\sigma_{\omega}^2} = \frac{L}{\pi} \frac{[1+ 8/3 (1.339 \Omega L)^2]}{[1+ (1.339 \Omega L)^2]^{11/6}} \quad (\text{Von Karman}) \quad (2)$$

$$\frac{\phi(\Omega)}{\sigma_{\omega}^2} = \frac{L}{\pi} \frac{1}{(1 + 1/3 \Omega^2 L^2)} \quad (3)$$

The CAT power spectrums are dependent on the "scale of turbulence" and the aircraft speed. These parameters are determined by the aircraft operating conditions. For the assumed altitude of 40,000 feet and Mach numbers of 3.0 and 2.6

$$L = 2,500 \text{ ft}$$

$$U = 2,525 \text{ ft/sec } (M_0 = 2.6)$$

$$U = 2,913 \text{ ft/sec } (M_0 = 3.0)$$

To determine the required filter on the white noise to obtain the desired CAT spectrum, the following property of power spectra was used. The power spectrum, $\phi_y(\omega)$, of a linear system with system function $G(j\omega)$ is

$$\phi_y(\omega) = |G(j\omega)|^2 \phi_x(\omega)$$

where $\phi_x(\omega)$ is the power spectrum of the input. Thus, if white noise [$\phi_x(\omega) = 1$] is used as the input,

$$\phi_y(\omega) = |G(j\omega)|^2$$

The required filters for each spectrum are presented in table VIII. The PSD plots are shown in figures 133 and 134.

The Von Karman spectrum was considered the most accurate CAT model. However, the filter required to match its PSD did not lend itself to easy analog computer mechanization. The other two spectra approximate the Von Karman spectrum well at frequencies below 20 rad/sec. The errors occur primarily at frequencies which are attenuated by 20 db or more, thus spectrum 3 was selected due to its simplicity.

From figures 133 and 134, it can be seen that the power spectra are very similar for Mach 3.0 and 2.6. Thus, one filter was used for shaping the white noise. The setup used in taping the CAT inputs is shown in figure 135.

Prior to taping the CAT inputs, a preliminary recording of the CAT and the actuator output was made. PSD plots were obtained for the input and output of the actuator. The actuator did not alter the PSD at frequencies below 35 Hz; thus the filter was not changed to accommodate the actuator dynamics. These PSD's were obtained with actuator alone; i.e., the wedge was not installed.

Appendix B

SHOCK POSITION CONTROL SYSTEM

The closed-loop shock position control system is shown schematically in figure 136. Shock position, as indicated by selected throat static pressure taps, was controlled by actuating the bypass using proportional plus integral compensation. For simplicity, the control was designed for Mach 3.0 operation at zero-degrees angle of attack and yaw. Inlet pressure distributions and the "downstream disturbance duct dynamics" representation used in the control design were obtained from reference 2.

Shock Position Sensing Parameter

Shock position was sensed by four static pressure probes in the inlet throat region. The shock position sensing parameter, PR, was obtained by averaging the output of the four transducers and dividing by free-stream (tunnel) total pressure to make the signal independent of absolute pressure level. Figure 137 is a curve of the shock position parameter, PR, versus shock position as determined from the data of reference 2. The constant slope of $-0.094 \Delta PR/\text{inch}$ of shock travel shown in figure 137 was assumed for the control mechanization.

The advantages of the selected shock sensing parameter include:

- (1) Simple mechanization
- (2) Simple interface with the control system
- (3) Increased range and linearity relative to a single-point pressure signal

Disadvantages of the parameter include the following:

- (1) An a priori knowledge of the pressure distribution is required
- (2) The parameter is not valid for other throat geometries or other upstream flow conditions.

Alternate shock position parameters were considered which utilize the characteristic jump in pressure across the shock. Either pressure differences or pressure ratios are sensed for each adjacent pair in a line of

static pressure taps to determine shock position. Advantages of this type of shock position parameter are that a priori and accurate pressure distributions are not required. Disadvantages include more difficult mechanization, sensitivity to boundary layer separation, and a noncontinuous shock position indication (only the fact that the shock is between two probes is indicated). The latter characteristic would probably result in a limit cycle for the closed-loop control.

Control System Analysis

The control system analysis was conducted in two phases. The first phase consisted of a linear analysis. During this phase, the inlet duct and bypass characteristics were obtained from reference 2, and a preliminary control system was defined. The second phase consisted of a "hardware tie-in" simulation. The simulation was performed on a PACE TR-10 computer.

The block diagram of the control system used in the linear analysis is shown in figure 138. The bypass actuator dynamics used in this phase of the analysis were based on the manufacturer's estimate of the servo valve dynamics. The bypass gain (-0.006 unit engine face total pressure ratio change per square inch of bypass area change) approximates the average of the values determined in the tests of reference 2. The diffuser gain (-41.67) inches of shock travel per unit of engine face total pressure ratio) was similarly obtained from the test data of reference 2. The diffuser dynamics, $e^{-.0071S}$ were approximated by a second-order polynomial which is quite accurate up to 200 radians per second.

The hardware tie-in simulation is shown in figure 139. The simulation included the bypass actuator and the nonlinearities of the controller (limits). Because of its small value and because of analog equipment limitations, the diffuser dynamics term was deleted from the hardware tie-in simulation.

System gains, $K_S = 2.0$ and $K_I = 100$, were determined with the hardware tie-in. The limit on the integral path was included for two reasons. The first was to prevent the integrator amplifier from saturating. The second was to effectively remove the integrator output during large transients, thereby providing faster system response.

The system response to step shock position changes is shown in figure 140 for various system gains. As expected, an increase in gain results in lower damping ratio. Also, if the integral gain is lowered, the response is slower. A complete analysis to determine the effects of varying the gains was not performed. The gains were determined by trial and error during the simulation.

The system response to sinusoidal inputs is shown in figure 141.

Appendix C

TOTAL PRESSURE PROBE TRANSDUCER FAILURES AND PROTECTIVE CONFIGURATIONS

Within minutes of the first air-on operation, 30 of the 32 Kulite transducers mounted in total pressure probed failed. This appendix describes the failures and the alternate probe configurations developed to protect the transducers.

Original Probe Configuration

The transducers which failed were Kulite Model CPL-125-25 differential pressure transducers having a face diameter of 0.125 inch and a rated pressure range of ± 25 psid. This type of transducer, shown in figure 142, has a flush-mounted silicon diaphragm of 1.5 mils thickness. The silicon diaphragm and diffusion bonded semiconductor strain gage network form a mechanically homogeneous silicon wafer.

Two types of total pressure probes were used. One, shown in figure 143, was used in the engine face rakes. The cap served to minimize yaw sensitivity and provide mechanical protection for the transducers during model installation. The alternate configuration, figure 144, had the transducer diaphragm flush with the end of the probe. This configuration had a smaller cross section and was used in the more area-critical portions of the inlet. In both configurations, the transducer diaphragm could "see" the oncoming airstream.

Transducer failures.- All the initial failures were associated with fractures of the silicon diaphragms, the fractures varying from pinholes barely visible to the naked eye to an almost complete loss of the diaphragm material. Figure 144 is a photograph of the centerbody rakes following the initial air-on operation. Figures 145 and 146 are magnified views of two diaphragm failures, one barely visible, the other most obvious.

A number of factors indicated that the failures were caused by small particles in the airstream impacting the silicon diaphragms. These included the following items:

- (1) Thirty of the 32 Kulite transducers having the diaphragms exposed to particle impact were destroyed within minutes. In contrast, none of the 10 Kulite transducers mounted so that the diaphragms were protected against direct impact (static pressure probes and wall static pressure taps) were damaged.

- (2) In a successive test wherein screens or shields were used to protect the transducers from direct particle impingement, no failures occurred. The transducers were located in the same probes where failures had originally been encountered; consequently, they were subjected to the same airflow pressure fluctuations and probe mechanical vibrations.
- (3) The microphotographs suggest impact failures.
- (4) Oil film in the duct metering section had collected a quantity of grit-like and metallic particles. (Welding operations on the tunnel intercooler and model rework and installation prior to the initial air-on operation probably resulted in an exceptionally large amount of debris in the tunnel stream.)

Protective configurations.- A diaphragm failure not only made the transducer inoperative, but also introduced a leak in the reference pressure system. Consequently, the first change made was to provide individual rather than manifold lines from the reference pressure tank to the transducers.

Three basic protective configurations were fabricated and run in the tunnel. These are shown in figure 147. One had two opposing baffles, one had three baffles displaced by 120 degrees, and one had a porous material screen in front of the diaphragm. Several versions of the latter configuration were investigated. In addition, tests were run with silastic rubber coating on the diaphragms to increase impact resistance.

All the protective configurations were successful in preventing impact damage to the diaphragms. Frequency response checks were conducted at the NASA Edwards Flight Research Center and, following the test program, at the Propulsion Wind Tunnel Facility of the Arnold Engineering Development Center. The NASA test apparatus, a piston/cylinder pneumatic signal generator, was limited to 1000 Hz. Within the accuracy of the test setup, the test data showed essentially no effect of the protective devices on frequency response, and no superiority of one configuration over another. The AEDC frequency response test results are presented in figure 148. In these tests, a horn driver was used to generate the pneumatic signal.

Inasmuch as all the configurations appeared satisfactory, the screen configuration was selected for ease of manufacturing. Two versions were used in the wind tunnel tests. The engine face total pressure probes had a Millipore screen installed in the cap approximately 0.015 inch forward of the diaphragm face. The centerbody probes had integrally screened transducers as supplied by the manufacturer. The Millipore screen was epoxy bonded to a 0.015-inch

spacer ring. The spacer ring was fastened to the diaphragm case with contact cement. The Millipore screen has 27-percent open area, with hole diameters of 0.0055 inch.

The screen-protected engine face and centerbody probes functioned satisfactorily when the test program was resumed.

Appendix D

DYNAMIC DISTORTION TEST RUN SUMMARY, TEST 87-255

The following run summary lists all the test runs made, including a number of runs for which limited or no data analyses have been made as of this report date.

During the runs where engine transients were to be simulated, the polarity of the amplifier converting the tape input signal to the desired amplitude was inadvertently reversed, an error not discovered until after the tests were completed. Consequently, the simulated lights listed in the run summary more nearly represented blowouts, and the blowouts more nearly represented lights.

For consistency with the steady-state data printouts, the position data for the cowl, bypass, and exit area sleeve are presented in Beckman counts. These counts can be converted to physical dimensions by the following equations:

Cowl position, model station = $22.7 + 0.001207$ (counts)

Bypass exit area, square feet = $0.05027 + 0.00001828$ (counts)

Exit area, square feet = $0 + 0.001414$ (counts)

Vane angle, degrees = $0 + 0.00566$ (counts)

DYNAMIC DISTORTION TEST RUN SUMMARY, TEST 87-255

FIXED GEOMETRY OPERATION

Run No.	Correlation No.	Mach No.	Angle of Attack, Deg	Total Pressure Recovery	Boundary Layer Config	Cowl Position	Bypass Position	Sleeve Position	Comments
						In Counts			
3	54	3.0	0.0	0.794	Prelim	39.0	0.0	425.0	} All total pressure probes capped
↓	55	↓	↓	.749	↓	39.0	↓	450.0	
↓	56	↓	↓	.720	↓	38.0	↓	475.0	
↓	57	↓	↓	.649	↓	38.0	↓	525.0	
↓	58	↓	↓	.572	↓	57.0	↓	600.0	
↓	59	↓	↓	.515	↓	38.0	↓	675.0	
3	60	↓	↓	.834	Prelim	28.0	↓	393.0	
10	134	↓	↓	.864	A'	15.0	↓	371.5	
↓	135	↓	↓	.814	↓	↓	↓	412.0	
↓	136	↓	↓	.766	↓	↓	↓	437.0	
↓	137	↓	↓	.727	↓	↓	↓	464.0	
↓	138	↓	↓	.644	↓	↓	↓	526.0	
10	139	↓	↓	.563	↓	15.0	↓	600.0	
11	140	↓	↓	.551	↓	60.0	↓	648.0	
↓	141	↓	↓	.622	↓	↓	↓	548.0	
↓	142	↓	↓	.826	↓	↓	↓	384.0	
↓	149	↓	↓	.789	↓	↓	↓	419.0	
↓	150	↓	↓	.742	↓	↓	↓	453.0	
11	151	↓	0.0	.694	↓	60.0	↓	487.0	
12	152	↓	4.0	.808	↓	35.0	↓	397.0	
↓	153	↓	↓	.780	↓	↓	↓	421.0	
↓	154	↓	↓	.727	↓	↓	↓	449.0	
↓	155	↓	↓	.695	↓	↓	↓	477.0	
↓	156	↓	↓	.608	↓	↓	↓	541.0	
12	157	↓	4.0	.529	↓	35.0	↓	626.0	
13	158	↓	8.0	.625	↓	275.0	↓	480.0	
↓	159	↓	↓	.591	↓	↓	↓	503.0	
13	160	3.0	8.0	.565	A'	↓	0.0	529.0	

DYNAMIC DISTORTION TEST RUN SUMMARY, TEST 87-255

FIXED GEOMETRY OPERATION (CONTINUED)

Run No.	Correlation No.	Mach No.	Angle of Attack, Deg	Total Pressure Recovery	Boundary Layer Config	Cowl Position	Bypass Position	Sleeve Position	Comments
						In Counts			
13	161	3.0	8.0	0.533	A'	275.0	0.0	574.0	
▼	162	↓	▼	.443	↓	▼	↓	641.0	
13	163	↓	8.0	.469	↓	275.0	↓	738.0	
21	209	↓	0.0	.877	↓	0.0	↓	366.0	
↓	210	↓	↓	.824	↓	↓	↓	411.0	
↓	211	↓	↓	.779	↓	↓	↓	436.0	
↓	212	↓	↓	.732	↓	↓	↓	462.0	
▼	213	↓	↓	.651	↓	▼	↓	524.0	
21	214	↓	↓	.565	↓	0.0	↓	598.0	
22	215	↓	↓	.573	↓	15.0	▼	598.0	
22	216	↓	↓	.869	↓	15.0	0.0	369.0	
23	224	↓	↓	.878	↓	0.0	825.0	320.5	
↓	225	↓	↓	.878	↓	↓	725.0	326.0	
↓	226	↓	↓	.877	↓	↓	650.0	330.5	
↓	227	↓	↓	.877	↓	↓	525.0	341.5	
▼	228	↓	↓	.876	▼	400.0	400.0	354.5	
23	229	↓	↓	.874	A'	↓	0.0	369.5	
25	237	↓	↓	.872	B	↓	↓	371.0	
↓	238	↓	↓	.872	C	↓	↓	374.5	
↓	239	↓	↓	.868	D	↓	↓	379.0	
↓	240	↓	↓	.844	D	↓	↓	402.0	
▼	241	▼	↓	.843	C	▼	↓	401.0	
25	242	3.0	↓	.842	B	0.0	↓	400.0	
27	250	2.6	↓	.918	A'	119.0	↓	444.5	
↓	251	↓	↓	.900	↓	↓	↓	467.0	
↓	252	↓	↓	.867	↓	↓	↓	490.0	
↓	253	↓	↓	.774	↓	↓	↓	556.0	
▼	254	▼	▼	.705	▼	▼	▼	604.0	
27	255	2.6	0.0	.642	A'	119.0	0.0	675.0	

DYNAMIC DISTORTION TEST RUN SUMMARY, TEST 87-255

SINUSOIDAL EXIT AREA VARIATIONS

Run No.	Correlation No.	Mach No.	Angle of Attack, Deg	Total Pressure Recovery	Boundary Layer Config	Cowl Position	Bypass Position	Sleeve Center Position	Sine Amplitude	Comments
						In Counts			2 IN.	
19	195	3.0	0.0	0.797	A'	15.0	0.0	410.0	±4.5	Control and no control Control and no control
20	205	↓	↓	.841	↓	0.0	↓	403.0	±4.5	
20	206	↓	↓	.838	↓	↓	↓	403.0	±2.0	
30	268	↓	↓	.735	↓	↓	↓	462.0	±4.5	
31	270	↓	↓	.789	↓	↓	0.0	432.0	±2.0	
46	305	↓	↓	.845	↓	↓	553.0	370.0	±2.0	
	306	↓	↓	.846	↓	↓	550.0	370.0	±4.0	

DYNAMIC DISTORTION TEST RUN SUMMARY, TEST 87-255

ENGINE TRANSIENTS*

Run No.	Correlation No.	Mach No.	Angle of Attack, Deg	Total Pressure Recovery	Boundary Layer Config	Cowl Position	Bypass Position	Sleeve Position	Comments
						In Counts			
29	262	3.0	0.0	0.842	A'	0.0	0.0	400.0	Augmentor light, turbojet and turbofan
	263	↓	↓	.842	↓	↓	↓	↓	Augmentor light, turbojet and turbofan
	264	↓	↓	.841	↓	↓	↓	↓	Augmentor blowout, turbojet
	266	↓	↓	.843	↓	↓	↓	↓	Augmentor blowout, turbojet
29	267	3.0	0.0	.849	A'	0.0	0.0	400.0	All engine transients
46	307	3.0	0.0	.843	A'	0.0	560.0	370.0	All engine transients, control and no control

*Amplifier polarity inadvertently reversed for engine transients

DYNAMIC DISTORTION TEST RUN SUMMARY, TEST 87-255

INLET TRANSIENTS

Run No.	Correlation No.	Mach No.	Angle of Attack, Deg	Total Pressure Recovery	Boundary Layer Config	Cowl Position	Bypass Position	Sleeve Position	Restart Rate	Unstart With	Comments
						In Counts					
28	257	2.6	0.0	0.918	A'	118.5	0.0	446.5	Fast	Plug	Start, unstart, buzz, restart
	258			.918		119.0		446.5	Slow	Plug	Start, unstart, buzz, restart
	260			.917		118.5		447.0	Fast	Cowl	Start, unstart, restart
28	261	2.6		.917		119.0		446.5	Slow	Cowl	Start, unstart, restart
43	297	3.0		.864		12.0		379.0	Fast	Plug	Start, unstart, buzz, restart
43	298	3.0				12.0		379.0	Slow	Plug	Start, unstart, buzz, restart
44	300	2.9		.873		13.0		412.0	Fast	Cowl	Start, unstart, buzz
44	301			.872				412.0	Slow	Cowl	Start, unstart, buzz
45	302			.741				495.0	Fast	Cowl	Start, unstart, restart
45	303	2.9	0.0	.743	A'	13.0	0.0	495.0	Slow	Cowl	Start, unstart, restart

DYNAMIC DISTORTION TEST RUN SUMMARY, TEST 87-255

EXTERNAL DISTURBANCES

Run No.	Correlation No.	Mach No.	Angle of Attack, Deg	Total Pressure Recovery	Boundary Layer Config	Cowl Position	Bypass Position	Sleeve Position	Vane Center Position	Sine Amplitude	Comments
							In Counts			Deg	
57	444	3.0	0.0	--	A'	30.0	0.0	435.0	Var		Calibration of external flow field during step changes in vane angle
57	445			0.785					175.0	±7.5	
58	447			.783					175.0	±3.5	
	448			.785					177.0	±7.5	
	449			.785			0.0	435.0	176.0	CAT.	
58	451			.783			507.0	412.0	175.0	CAT.	
60	452			.782			514.0	412.0	175.0	±3.5	
60	453	3.0	0.0	.778	A'	30.0	530.0	412.0	175.0	±7.5	
											Control and no control

APPENDIX E

COHERENCE CALCULATIONS

Corr No. 209 $M_o = 3.0$ Frequency = 20 Hz
 $\bar{P}_{t2}/P_{t0} = 0.877$

Column Number									
1	2	3*	4*	5*	6*	7*	8	9	10
Probe 1	Probe 2	PSD 1	PSD 2	Co CPSD	Quad CPSD	K Factor	K^2	③ X ④	γ^2
		$\times 10^{-7}$	$\times 10^{-7}$			$\times 10^{-7}$	$\times 10^{-14}$	$\times 10^{-14}$	
870	880	1.1	1.3	0.1	0.1	2.46	6.05	1.43	0.08
874	884	1.0	1.6	.1	.1	4.77	22.8	1.6	.29
874	889	1.0	1.3	.1	0	2.79	7.78	1.3	.06
876	877	1.2	1.7	.3	.1	1.88	3.53	2.04	.17
877	878	1.7	2.2	1.5	.1	.66	.436	3.74	.26
877	882	1.7	.85	.2	.2	.493	.243	1.45	.02
882	880	.85	1.3	.1	0	1.28	1.64	1.11	.01
882	881	.85	2.1	1.4	.6	.503	.253	1.79	.33
882	883	.85	1.8	.9	.5	.352	.124	1.53	.09
886	887	1.7	.75	.35	.1	.853	.728	1.28	.08
887	888	.75	1.3	.2	0	1.03	1.06	.975	.04
887	872	.75	1.4	0	.3	.248	.062	1.05	.01
872	873	1.4	1.8	.5	.3	.868	.753	2.52	.10
870	872	1.1	1.4	0	.5	.556	.309	1.54	.05
871	872	1.9	1.4	.3	1.0	.396	.157	2.66	.06
870	885	1.1	1.2	.1	0	1.91	3.05	1.32	.03

* Observed data from analog plots

$$\gamma^2 = \frac{[C_o^2 + Quad^2] K^2}{PSD_1 \cdot PSD_2} = \text{coherence function}$$

K = X - Y plotter scaling factor

COHERENCE CALCULATIONS

Corr No. 209
 $\overline{P}_{t2}/P_{t0} = 0.877$

$M_0 = 3.0$ Frequency = 40 Hz

Column Number									
1	2	3*	4*	5*	6*	7*	8	9	10
Probe 1	Probe 2	PSD 1	PSD 2	Co CPSD	Quad CPSD	K Factor	K ²	③ x ④	γ^2
		X 10 ⁻⁷	X 10 ⁻⁷			X 10 ⁻⁷	X 10 ⁻¹⁴	X 10 ⁻¹⁴	
870	880	0.76	1.0	0.03	0.05	2.46	6.05	0.76	0.04
874	884	1.0	1.0	.05	0	4.77	22.8	1.0	.06
874	889	1.0	1.0	.1	0	2.79	7.78	1.0	.08
876	877	1.2	1.2	.1	.15	1.88	3.53	1.44	.08
877	878	1.2	1.8	1.1	0	.66	.436	2.16	.24
877	882	1.2	.85	.2	.2	.493	.243	1.02	.02
882	880	.85	1.0	0	.15	1.28	1.64	.85	.04
882	881	.85	2.1	1.3	.3	.503	.253	1.79	.25
882	883	.85	1.7	.6	.7	.352	.124	1.45	.07
886	887	1.6	.80	.35	.1	.853	.728	1.28	.08
887	888	.80	1.2	.30	.1	1.03	1.06	.96	.11
887	872	.80	1.2	.8	.8	.248	.062	.96	.08
872	873	1.2	1.8	.4	0.	.868	.753	2.16	.06
870	872	.76	1.2	0	.3	.556	.309	.912	.03
871	872	1.3	1.2	.8	.3	.396	.157	1.56	.07
870	885	.76	1.1	0	0	1.91	3.0	.836	0

* Observed data from analog plots

$$\gamma^2 = \frac{[C_0^2 + Quad^2] K^2}{PSD_1 \cdot PSD_2}$$

COHERENCE CALCULATIONS

Corr No. 209
 $\overline{P}_{t2}/P_{t0} = 0.877$

$M_0 = 3.0$ Frequency = 80 Hz

Column Number									
1	2	3*	4*	5*	6*	7*	8	9	10
Probe 1	Probe 2	PSD 1	PSD 2	Co CPSD	Quad CPSD	K Factor	K^2	③ X ④	γ^2
		$\times 10^{-7}$	$\times 10^{-7}$			$\times 10^{-7}$	$\times 10^{-14}$	$\times 10^{-14}$	
870	880	1.1	1.0	0.1	0.1	2.46	6.05	1.1	0.11
874	884	.80	1.1	0	0	4.77	22.8	.88	0
874	889	.80	1.1	0	.1	2.79	7.78	.88	.09
876	877	1.0	1.5	.2	0	1.88	3.53	1.5	.09
877	878	1.5	1.3	1.0	0	.66	.436	1.95	.22
877	882	1.5	.75	.1	.1	.493	.243	.113	.004
882	880	.75	1.0	0	0	1.28	1.69	.75	0
882	881	.75	1.8	1.3	.7	.503	.253	1.35	.41
882	883	.75	1.6	.7	.3	.352	.124	1.20	.06
886	887	1.5	1.0	.30	.05	.853	.728	1.5	.05
887	888	1.0	1.6	.6	.1	1.03	1.06	1.6	.25
887	872	1.0	1.2	.6	.7	.248	.062	1.2	.04
872	873	1.2	2.0	.5	.1	.868	.753	2.4	.08
870	872	1.1	1.2	.2	.1	.556	.309	1.32	.01
871	872	1.6	1.2	1.0	.3	.396	.157	1.92	.09
870	885	1.1	1.1	0	0	1.91	3.65	1.21	0

*Observed data from analog plots

$$\gamma^2 = \frac{[C_o^2 + Quad^2] K^2}{PSD_1 \cdot PSD_2}$$

COHERENCE CALCULATIONS

Corr No. 209
 $\overline{P}_{t2}/P_{t0} = 0.877$

$M_o = 3.0$ Frequency = 100 Hz

Column Number									
1	2	3 *	4 *	5 *	6 *	7 *	8	9	10
Probe 1	Probe 2	PSD 1	PSD 2	Co CPSD	Quad CPSD	K Factor	K^2	③ x ④	γ^2
		$\times 10^{-7}$	$\times 10^{-7}$			$\times 10^{-7}$	$\times 10^{-14}$	$\times 10^{-14}$	
870	880	0.80	1.3	0	0	2.40	6.05	1.4	0
874	884	.72	1.2	0	0	4.77	22.8	.864	0
874	889	.72	1.1	0	0	2.79	7.78	.792	0
876	877	1.3	1.2	.1	.1	1.88	3.53	1.56	.05
877	878	1.2	1.9	1.4	0	.66	.436	2.28	.37
877	882	1.2	.90	0	.3	.493	.243	1.08	.02
882	880	.90	1.3	.1	.1	1.28	1.64	1.17	.03
882	881	.90	1.8	.7	.5	.503	.253	1.62	.12
882	883	.90	1.4	1.1	.3	.352	.124	1.26	.13
886	887	1.3	.80	.3	.1	.853	.728	1.04	.07
887	888	.80	1.3	.4	.1	1.03	1.06	1.04	.17
887	872	.80	2.3	0	.5	.248	.062	1.04	.02
872	873	1.3	2.1	.7	0	.868	.753	2.73	.14
870	872	.80	1.3	0	0	.556	.309	1.04	.0
871	872	1.4	1.3	.2	.6	.396	.157	1.82	.03
870	885	.80	1.0	0	0	1.91	3.65	.80	0

* Observed data from analog plots

$$\gamma^2 = \frac{[C_o^2 + Quad^2] K^2}{PSD_1 \cdot PSD_2}$$

COHERENCE CALCULATIONS

Corr No. 209
 $\frac{P_{t2}}{P_{t0}} = 0.877$

$M_o = 3.0$ Frequency = 200 Hz

Column Number									
1	2	3*	4*	5*	6*	7*	8	9	10
Probe 1	Probe 2	PSD 1	PSD 2	Co CPSD	Quad CPSD	K Factor	K ²	③ x ④	γ ²
		X 10 ⁻⁷	X 10 ⁻⁷			X 10 ⁻⁷	X 10 ⁻¹⁴	X 10 ⁻¹⁴	
870	880	0.70	0.65	0	0	2.46	6.05	0.455	0
874	884	.70	.80	0	0	4.77	22.8	.560	0
874	889	.70	.90	0	0	2.79	7.78	.630	0
876	877	.90	1.3	.1	0	1.88	3.53	1.17	.03
877	878	1.3	1.5	1.0	0	.66	.436	1.95	.22
877	882	1.3	.80	0	.2	.493	24.3	1.04	.01
882	880	.80	.65	.1	0	1.28	1.64	.520	.03
882	881	.80	1.6	.8	.3	.503	.253	1.28	.14
882	883	.80	1.3	1.0	1.0	.352	.124	1.04	.24
886	887	1.3	.80	.1	.2	.853	72.8	1.04	.04
887	888	.80	1.5	.5	.1	1.03	1.06	1.20	.23
887	872	.80	1.1	.2	.3	.248	.062	.88	.01
872	873	1.1	1.8	.5	0	.868	.753	1.98	.10
870	872	.70	1.1	.3	.3	.556	.309	.77	.07
871	872	1.5	1.1	.8	.5	.396	.157	1.65	.08
870	885	.70	.80	0	0	1.91	3.65	.56	0

*Observed data from analog plots

$$\gamma^2 = \frac{[C_o^2 + Quad^2] K^2}{PSD_1 \cdot PSD_2}$$

COHERENCE CALCULATIONS

Corr No. 214
 $\overline{P}_{t2}/P_{t0} = 0.565$

$M_o = 3.0$

Frequency = 20 Hz

Column Number									
1	2	3*	4*	5*	6*	7*	8	9	10
Probe 1	Probe 2	PSD 1	PSD 2	Co CPSD	Quad CPSD	K Factor	K ²	③ x ④	γ^2
		X 10 ⁻⁵	X 10 ⁻⁵			X 10 ⁻⁵	X 10 ⁻¹⁰	X 10 ⁻¹⁰	
870	874	0.6	0.35	0.1	0	1.36	1.85	0.21	0.09
872	887	1.6	1.4	.15	.1	5.93	35.2	2.29	.51
887	886	1.4	3.8	1.1	0	2.06	4.24	5.32	.96
870	885	.60	4.0	0	.1	2.71	7.34	2.4	.03
872	873	1.6	1.2	.45	0	1.99	3.97	1.92	.42
872	871	1.6	1.2	.16	0	3.14	9.86	1.92	.13
872	870	1.6	.60	.1	0	3.14	9.86	.96	.10
887	888	1.4	.65	.5	0	1.78	3.17	.91	.87
870	880	.60	1.2	.1	0	1.06	1.12	.72	.02
880	884	1.2	.50	.4	.1	.816	.666	.60	.19
874	884	.35	.50	.05	.05	.988	.977	.175	.01
874	889	.35	.40	.1	.05	.575	.331	.140	.03
877	876	5.0	10.	1.2	.1	5.2	27.0	50.	.78
877	878	5.0	1.5	2.7	.1	.86	.740	7.5	.72
877	882	5.0	4.5	0	.3	7.18	51.6	22.5	.21

* Observed data from analog plots

$$\gamma^2 = \frac{[C_o^2 + Quad^2] K^2}{PSD_1 \cdot PSD_2}$$

COHERENCE CALCULATIONS

Corr No. 214
 $\overline{P}_{t2}/P_{t0} = 0.565$

$M_0 = 3.0$ Frequency = 40 Hz

Column Number									
1	2	3*	4*	5*	6*	7*	8	9	10
Probe 1	Probe 2	PSD 1	PSD 2	Co CPSD	Quad CPSD	K Factor	K ²	③ × ④	γ^2
		X 10 ⁻⁵	X 10 ⁻⁵			X 10 ⁻⁵	X 10 ⁻¹⁰	X 10 ⁻¹⁰	
870	874	0.50	0.36	0	0	1.36	1.85	0.180	0
872	887	1.5	1.4	.1	.1	5.93	35.2	2.10	.35
887	886	1.4	4.0	.8	.15	2.06	4.24	5.6	.50
870	885	.50	4.0	0	.05	2.71	7.34	2.0	.09
872	873	1.5	1.1	.5	0	1.99	3.92	1.65	.60
872	871	1.5	1.5	.3	0	3.14	9.86	2.25	.40
872	870	1.5	.50	.1	0	3.14	9.86	.75	.13
887	888	1.4	.70	.5	0	1.78	3.17	.98	.81
870	880	.50	1.3	0	0	1.06	1.12	.65	0
880	884	1.3	.52	.3	.1	.816	.666	.676	.10
874	884	.36	.52	0	0	.988	.977	.187	0
874	889	.36	.37	0	0	.575	.331	.133	0
877	876	2.0	3.5	.4	.05	5.2	27.0	7.0	.63
877	878	2.0	.72	1.3	.1	.86	.740	1.44	.87
877	882	2.0	3.0	.05	.05	7.18	51.6	6.0	.04

* Observed data from analog plots

$$\gamma^2 = \frac{[C_0^2 + Quad^2] K^2}{PSD_1 \cdot PSD_2}$$

COHERENCE CALCULATIONS

Corr No. 214
 $\overline{P}_{t2}/P_{t0} = 0.565$

$M_o = 3.0$ Frequency = 80 Hz

Column Number									
1	2	3 *	4 *	5 *	6 *	7 *	8	9	10
Probe 1	Probe 2	PSD 1	PSD 2	Co CPSD	Quad CPSD	K Factor	K ²	③ X ④	γ^2
		X 10 ⁻⁵	X 10 ⁻⁵			X 10 ⁻⁵	X 10 ⁻¹⁰	X 10 ⁻¹⁰	
870	874	0.45	0.30	0.02	0	1.36	1.85	0.135	0
872	887	1.0	1.1	.1	.1	5.93	35.2	1.1	.64
887	886	1.1	2.3	.7	.1	2.06	4.24	2.54	.83
870	885	.45	3.3	.1	.1	2.71	7.34	1.49	.10
872	873	1.0	1.0	.5	0	1.99	3.97	1.0	.96
872	871	1.0	1.2	.3	0	3.14	9.86	1.2	.70
872	870	1.0	.45	.05	0	3.14	9.86	.45	.05
887	888	1.1	.60	.5	0	1.78	3.17	.66	1.0
870	880	.45	1.3	.1	0	1.06	1.12	.585	.02
880	884	1.3	.52	.5	.1	.816	.666	.676	.26
874	884	.30	.52	.1	0	.988	.977	.156	.06
874	889	.30	.40	.05	.1	.575	.331	.120	.03
877	876	1.6	2.5	.3	0	5.2	27.0	4.0	.61
877	878	1.6	.64	1.0	0	.86	.74	1.02	.72
877	882	1.6	3.8	.1	0	7.18	51.6	6.06	.08

* Observed data from analog plots

$$\gamma^2 = \frac{[C_o^2 + Quad^2] K^2}{PSD_1 \cdot PSD_2}$$

COHERENCE CALCULATIONS

Corr No. 214 $M_o = 3.0$ Frequency = 100 Hz
 $\bar{P}_{t2}/P_{t0} = 0.565$

Column Number									
1	2	3*	4*	5*	6*	7*	8	9	10
Probe 1	Probe 2	PSD 1	PSD 2	Co CPSD	Quad CPSD	K Factor	K ²	③ × ④	γ^2
		X 10 ⁻⁵	X 10 ⁻⁵			X 10 ⁻⁵	X 10 ⁻¹⁰	X 10 ⁻¹⁰	
870	874	0.40	0.25	0.1	0	1.36	1.85	0.100	0.18
872	887	1.2	1.2	0	.1	5.93	35.2	1.44	.24
887	886	1.2	2.0	.7	.15	2.06	4.24	2.4	.90
870	885	.40	2.5	.1	.1	2.71	7.34	1.00	.15
872	873	1.2	.85	.45	0	1.99	3.97	1.02	.80
872	871	1.2	1.1	.25	0	3.14	9.86	1.32	.47
872	870	1.2	.40	0	0	3.14	9.86	.48	0
887	888	1.2	.60	.5	0	1.78	3.17	.72	1.0
870	880	.40	1.5	.1	0	1.06	1.12	.60	.02
880	884	1.5	.52	.5	.2	.816	.666	.78	.25
874	884	.25	.52	.1	.1	.988	.977	.130	.15
874	889	.25	.40	.1	0	.575	.331	.100	.03
877	876	1.2	2.0	.25	0	5.2	27.0	2.4	.70
877	878	1.2	.40	.7	.05	.86	.74	.48	.76
877	882	1.2	4.0	0	0	7.18	51.6	4.8	0

* Observed data from analog plots

$$\gamma^2 = \frac{[C_o^2 + Quad^2] K^2}{PSD_1 \cdot PSD_2}$$

COHERENCE CALCULATIONS

Corr No. 214 $M_o = 3.0$ Frequency = 200 Hz
 $\overline{P}_{t2}/P_{t0} = 0.565$

Column Number									
1	2	3*	4*	5*	6*	7*	8	9	10
Probe 1	Probe 2	PSD 1	PSD 2	Co CPSD	Quad CPSD	K Factor	K ²	③ × ④	γ^2
		X 10 ⁻⁵	X 10 ⁻⁵			X 10 ⁻⁵	X 10 ⁻¹⁰	X 10 ⁻¹⁰	
870	874	0.38	0.23	0	0	1.36	1.85	0.087	0
872	887	1.1	.70	0	0	5.93	35.2	.77	0
887	886	.70	1.0	.3	0	2.06	4.24	.70	.55
870	885	.38	1.0	0	0	2.71	7.34	.38	0
872	873	1.1	.70	.2	0	1.99	3.97	.77	.21
872	871	1.1	.90	.15	0	3.14	9.86	.99	.22
872	870	1.1	.38	0	0	3.14	9.86	.418	0
887	888	.70	.32	.2	0	1.78	3.17	.224	.57
870	880	.38	1.1	0	0	1.06	1.12	.418	0
880	884	1.1	.40	.3	0	.816	.666	.44	.13
874	884	.23	.40	0	.1	.988	.977	.092	.10
874	889	.23	.30	.08	0	.575	.331	.069	.03
877	876	.54	.90	.1	0	5.2	27.0	.486	.57
877	878	.54	.22	.35	0	.86	.740	.119	.76
877	882	.54	3.0	0	0	7.18	51.6	1.62	0

* Observed data from analog plots

$$\gamma^2 = \frac{[C_o^2 + Quad^2] K^2}{PSD_1 \cdot PSD_2}$$

COHERENCE CALCULATIONS

Corr No. 250 $M_o = 2.6$ Frequency = 20 Hz
 $\overline{P}_{t2}/P_{t0} = 0.918$

Column Number									
1	2	3*	4*	5*	6*	7*	8	9	10
Probe 1	Probe 2	PSD 1	PSD 2	Co CPSD	Quad CPSD	K Factor	K^2	③ x ④	γ^2
		$\times 10^{-7}$	$\times 10^{-7}$			$\times 10^{-7}$	$\times 10^{-14}$	$\times 10^{-14}$	
872	871	0.28	2.0	0.30	0	0.915	0.841	0.56	0.14
872	870	.28	.90	.10	.1	.656	.430	.252	.03
887	886	4.0	3.5	1.4	.15	1.20	1.44	14.0	.20
887	888	4.0	3.2	3.5	.1	.707	.500	12.8	.48
872	887	.28	4.0	.5	.3	.353	.125	1.12	.04
885	870	1.2	.90	0	0	2.84	8.07	1.08	0
877	876	4.5	4.8	.5	.05	5.41	29.3	21.6	.34
877	878	4.5	1.1	.05	0	5.37	28.8	4.95	.01
877	882	4.5	11.0	.15	.1	9.0	81.0	49.5	.05
882	881	11.0	6.0	.9	.1	7.12	50.7	66.0	.63
882	883	11.0	1.57	1.0	.2	1.42	2.02	16.5	.12
882	880	11.0	1.2	.30	.1	6.50	42.3	13.2	.32
870	880	.90	1.2	0	0	3.70	13.7	1.08	0
874	884	.60	2.2	0	0	.173	.0299	1.32	0
874	889	.60	1.2	0	0	1.44	2.07	.72	0

* Observed data from analog plots

$$\gamma^2 = \frac{[C_o^2 + Quad^2] K^2}{PSD_1 \cdot PSD_2}$$

COHERENCE CALCULATIONS

Corr No. 250 $M_o = 2.6$ Frequency = 40 Hz
 $\frac{P_{t2}}{P_{t0}} = 0.918$

Column Number									
1	2	3*	4*	5*	6*	7*	8	9	10
Probe 1	Probe 2	PSD 1	PSD 2	Co CPSD	Quad CPSD	K Factor	K^2	③ x ④	γ^2
		$\times 10^{-7}$	$\times 10^{-7}$			$\times 10^{-7}$	$\times 10^{-14}$	$\times 10^{-14}$	
872	871	0.28	1.6	0.10	0	0.917	0.841	0.488	0.02
872	870	.28	.88	.10	.05	.656	.430	.246	.02
887	886	3.2	3.0	1.3	.10	1.20	1.44	9.6	.26
887	888	3.2	2.8	2.5	.20	.107	.50	8.96	.35
872	887	.28	3.2	.1	.5	.353	.125	.896	.04
885	870	1.3	.88	0	0	2.84	8.07	1.14	0
877	876	5.0	4.0	.5	.05	5.41	29.3	20.0	.37
877	878	5.0	1.2	.1	0	5.37	28.8	6.0	.05
877	882	5.0	7.2	.05	.1	9.0	81.0	36.0	.03
882	881	7.2	6.2	.9	.3	7.12	50.7	44.6	1.0
882	883	7.2	1.2	.85	.1	1.42	2.02	8.64	.17
882	880	7.2	1.3	.30	.1	6.50	42.3	9.36	.45
870	880	.88	1.3	0	0	3.70	13.7	1.14	0
874	884	.66	1.5	0	0	.173	.030	.99	0
874	889	.66	1.2	0	0	1.44	2.07	.792	0

* Observed data from analog plots

$$\gamma^2 = \frac{[C_o^2 + Quad^2] K^2}{PSD_1 \cdot PSD_2}$$

COHERENCE CALCULATIONS

Corr No. 250
 $\overline{P}_{t2}/P_{t0} = 0.918$

$M_0 = 2.6$

Frequency = 80 Hz

Column Number									
1	2	3*	4*	5*	6*	7*	8	9	10
Probe 1	Probe 2	PSD 1	PSD 2	Co CPSD	Quad CPSD	K Factor	K ²	③ x ④	γ^2
		X 10 ⁻⁷	X 10 ⁻⁷			X 10 ⁻⁷	X 10 ⁻¹⁴	X 10 ⁻¹⁴	
872	871	0.26	1.35	0.20	0	0.917	0.841	0.351	0.10
872	870	.216	.75	-.1	0	.656	.430	.195	.02
887	886	3.8	3.0	1.5	-.2	1.20	1.44	11.4	.29
887	888	3.8	2.6	1.9	-.4	.707	.50	9.88	.19
872	887	.26	3.8	-.5	-.1	.353	.125	.988	.03
885	870	1.1	.75	0	0	2.84	8.07	.825	0
877	876	3.6	4.0	.4	0	5.41	29.3	14.4	.33
877	878	3.6	1.0	.1	.1	5.37	28.8	3.6	.16
877	882	3.6	4.5	0	-.05	9.0	81.0	16.2	.01
882	881	4.5	3.5	.5	-.1	7.12	50.7	15.8	.83
882	883	4.5	.82	.2	0	1.42	2.02	3.69	.02
882	880	4.5	.85	.1	-.1	6.50	42.3	3.83	.23
870	880	.75	.85	0	0	3.70	13.7	.63	0
874	884	.80	1.5	0	0	.173	.030	1.20	0
874	889	.80	1.15	0	0	1.44	2.07	.92	0

* Observed data from analog plots

$$\gamma^2 = \frac{[C_0^2 + Quad^2] K^2}{PSD_1 \cdot PSD_2}$$

COHERENCE CALCULATIONS

Corr No. 250
 $\overline{P_{t2}/P_{t0}} = 0.918$

$M_0 = 2.6$

Frequency = 100 Hz

Column Number									
1	2	3*	4*	5*	6*	7*	8	9	10
Probe 1	Probe 2	PSD 1	PSD 2	Co CPSD	Quad CPSD	K Factor	K ²	③ X ④	γ^2
		X 10 ⁻⁷	X 10 ⁻⁷			X 10 ⁻⁷	X 10 ⁻¹⁴	X 10 ⁻¹⁴	
872	871	0.28	1.8	0.25	0	0.917	0.84	.504	0.10
872	870	.28	.85	0	-.1	.656	.43	.23	.02
887	886	3.0	3.0	1.3	-.50	1.20	1.44	9.0	.31
887	888	3.0	2.0	2.0	0	.707	.500	6.0	.33
872	887	.28	3.0	-.3	0	.353	.12	.84	.13
885	870	1.1	.85	0	0	2.84	8.07	.935	0
877	876	2.7	3.0	.3	0	5.41	29.3	8.1	.33
877	878	2.7	.80	.1	.1	5.37	28.8	2.16	.27
877	882	2.7	4.0	0	-.05	9.0	81.0	1.18	.17
882	881	4.0	3.0	.3	-.1	7.12	50.7	12.0	.42
882	883	4.0	.80	-.1	.1	1.42	2.02	3.20	.01
882	880	4.0	.75	0	-.05	6.50	42.3	3.00	.03
870	880	.85	.75	0	0	3.70	13.7	.638	0
874	884	.75	1.1	0	0	.173	.030	.825	0
874	889	.75	1.2	0	0	1.44	2.07	.90	0

* Observed data from analog plots

$$\gamma^2 = \frac{[C_o^2 + Quad^2] K^2}{PSD_1 \cdot PSD_2}$$

COHERENCE CALCULATIONS

Corr No. 250
 $\overline{P}_{t2}/P_{t0} = 0.918$

$M_0 = 2.6$

Frequency = 200 Hz

Column Number									
1	2	3	4*	5*	6*	7*	8	9	10
Probe 1	Probe 2	PSD 1	PSD 2	Co CPSD	Quad CPSD	K Factor	K ²	③ × ④	γ ²
		X 10 ⁻⁷	X 10 ⁻⁷			X 10 ⁻⁷	X 10 ⁻¹⁴	X 10 ⁻¹⁴	
872	871	0.25	1.5	0.13	0	0.917	0.841	0.375	0.04
872	870	.25	.70	0	0	.656	.430	.175	0
887	886	2.57	2.57	.80	-.6	1.20	1.44	6.25	.23
887	888	2.57	1.3	1.3	0	.707	.500	3.25	.26
872	887	.25	2.57	-.35	0	.353	.125	.625	.025
885	870	.80	.70	0	0	2.84	8.07	.56	0
877	876	2.9	2.4	.2	0	5.41	29.3	6.96	.17
877	878	2.9	1.4	0	.08	5.37	28.8	4.06	.05
877	882	2.9	3.0	0	-.05	9.0	81.0	8.7	.02
882	881	3.0	3.0	.2	-.1	7.12	50.7	9.0	.28
882	883	3.0	.60	-.1	0	1.42	2.02	1.8	.01
882	880	3.0	.45	0	0	6.50	42.3	1.35	0
870	880	.70	.45	0	0	3.70	13.7	.318	0
874	884	.60	1.3	0	0	.173	.030	.78	0
874	889	.60	1.5	0	0	1.44	2.07	.90	0

* Observed data from analog plots

$$\gamma^2 = \frac{[C_o^2 + Quad^2] K^2}{PSD_1 \cdot PSD_2}$$

COHERENCE CALCULATIONS

Corr No. 255 $M_o = 2.6$ Frequency = 20 Hz
 $\bar{P}_{t2}/P_{t0} = 0.642$

Column Number									
1	2	3*	4*	5*	6*	7*	8	9	10
Probe 1	Probe 2	PSD 1	PSD 2	Co CPSD	Quad CPSD	K Factor	K^2	③ x ④	γ^2
		10^{-5}	$\times 10^{-5}$			$\times 10^{-5}$	$\times 10^{-10}$	$\times 10^{-10}$	
877	876	2.8	7.2	1.0	0	4.02	16.2	20.2	0.8
877	878	2.8	1.3	2.2	-.2	.662	.438	3.64	.59
877	882	2.8	4.5	.1	-.1	3.32	11.0	12.6	.02
882	881	4.5	3.2	.75	-.25	2.64	6.97	14.4	.30
882	883	4.5	1.6	.7	.1	2.64	6.97	7.2	.48
882	880	4.5	2.0	.05	-.15	2.4	5.76	9.0	.02
887	886	2.8	5.0	1.2	-.3	2.64	6.97	14.0	.76
887	888	2.8	1.2	1.2	0	1.53	2.34	3.36	1.0
887	872	2.8	2.2	-.05	.05	3.05	9.3	6.16	.004
872	871	2.2	3.5	1.0	-.4	1.61	2.59	7.7	.39
872	873	2.2	2.1	.6	.15	2.3	5.29	4.62	.44
872	870	2.2	.65	.4	.1	1.61	2.59	1.43	.31
870	874	.65	1.1	0	.35	.90	.81	.715	.14
870	885	.65	3.0	.1	0	1.4	1.96	1.95	.01
870	880	.65	2.0	0	0	1.83	3.35	1.30	0
880	884	2.0	1.5	-.2	.1	3.2	10.2	3.0	.17

*Observed data from analog plots

$$\gamma^2 = \frac{[C_o^2 + Quad^2] K^2}{PSD_1 \cdot PSD_2}$$

COHERENCE CALCULATIONS

Corr No. 255
 $\bar{P}_{t2}/P_{t0} = 0.642$

$M_0 = 2.6$

Frequency = 40 Hz

Column Number									
1	2	3*	4*	5*	6*	7*	8	9	10
Probe 1	Probe 2	PSD 1	PSD 2	Co CPSD	Quad CPSD	K Factor	K ²	③ × ④	γ ²
		X 10 ⁻⁵	X 10 ⁻⁵			X 10 ⁻⁵	X 10 ⁻¹⁰	X 10 ⁻¹⁰	
877	876	2.5	5.4	0.75	0	4.02	16.2	13.5	0.68
877	878	2.5	1.3	2.0	-.1	.662	.438	3.25	.54
877	882	2.5	3.5	.2	-.1	3.32	11.0	8.75	.06
882	881	3.5	2.3	.80	.05	2.64	6.97	8.05	.56
882	883	3.5	1.5	.70	-.1	2.64	6.97	5.25	.66
882	880	3.5	.80	.05	0	2.4	5.76	2.8	.005
887	886	4.6	7.0	1.7	-.2	2.64	6.97	32.2	.63
887	888	4.6	1.6	1.4	0	1.53	2.34	7.36	.62
887	872	4.6	2.1	-.1	-.05	3.05	9.3	9.66	.01
872	871	2.1	2.8	1.0	-.50	1.61	2.59	5.88	.55
872	873	2.1	1.7	.6	.15	2.3	5.29	3.57	.57
872	870	2.1	.56	.4	.1	1.61	2.59	1.18	.04
870	874	.56	1.0	.2	0	.90	.810	.56	.06
870	885	.56	2.3	0	-.3	1.4	1.96	1.24	.08
870	880	.56	.80	-.05	0	1.83	3.35	.448	.02
880	884	.80	1.1	-.1	0	3.2	10.2	.88	.12

* Observed data from analog plots

$$\gamma^2 = \frac{[C_o^2 + Quad^2] K^2}{PSD_1 \cdot PSD_2}$$

COHERENCE CALCULATIONS

Corr No. 255 $M_0 = 2.6$ Frequency = 80 Hz
 $\overline{P}_{t2}/P_{t0} = 0.642$

Column Number									
1	2	3*	4*	5*	6*	7*	8	9	10
Probe 1	Probe 2	PSD 1	PSD 2	Co CPSD	Quad CPSD	K Factor	K^2	③ × ④	γ^2
		$\times 10^{-5}$	$\times 10^{-5}$			$\times 10^{-5}$	$\times 10^{-10}$	$\times 10^{-10}$	
877	876	1.5	3.5	0.5	0	4.02	16.2	5.25	0.77
877	878	1.5	.70	1.25	-.2	.662	.438	1.05	.67
877	882	1.5	2.9	.1	0	3.32	11.0	4.35	.03
882	881	2.9	1.4	.40	.1	2.64	6.97	4.06	.29
882	883	2.9	1.3	.60	0	2.64	6.97	3.77	.67
882	880	2.9	1.2	0	.15	2.4	5.76	3.48	.04
887	886	3.3	5.0	1.1	-.2	2.64	6.97	16.5	.53
887	888	3.5	1.4	1.0	-.1	1.53	2.34	4.62	.51
887	872	3.3	2.0	0	-.15	3.05	9.3	6.6	.03
872	871	2.0	1.5	.75	-.1	1.61	2.59	3.0	.49
872	873	2.0	1.6	.7	-.1	2.3	5.29	3.2	.83
872	870	2.0	.68	.3	0	1.61	2.59	1.36	.17
870	874	.68	.80	.4	-.15	.90	.810	.544	.27
870	885	.68	2.3	-.3	.1	1.4	1.96	1.56	.13
870	880	.68	1.2	0	0	1.83	3.35	.816	0
880	884	1.2	.95	0	-.08	3.2	10.2	1.14	.06

* Observed data from analog plots

$$\gamma^2 = \frac{[C_o^2 + Quad^2] K^2}{PSD_1 \cdot PSD_2}$$

COHERENCE CALCULATIONS

Corr No. 255 $M_0 = 2.6$ Frequency = 100 Hz
 $\bar{P}_{t2}/P_{t0} = 0.642$

Column Number									
1	2	3*	4*	5*	6*	7*	8	9	10
Probe 1	Probe 2	PSD 1	PSD 2	Co CPSD	Quad CPSD	K Factor	K ²	③ x ④	γ^2
		X 10 ⁻⁵	X 10 ⁻⁵			X 10 ⁻⁵	X 10 ⁻¹⁰	X 10 ⁻¹⁰	
877	876	1.2	2.6	0.3	0	4.02	16.2	3.12	0.47
877	878	1.2	.70	.9	-.1	.662	.438	.84	.43
877	882	1.2	2.5	0	-.1	3.32	11.0	3.0	.04
882	881	2.5	1.8	.30	0	2.64	6.97	4.5	.14
882	883	2.5	1.0	.50	0	2.64	6.95	2.5	.70
882	880	2.5	1.0	0	.1	2.4	5.76	2.5	.02
887	886	2.0	4.0	.75	-.2	2.64	6.97	8.0	.52
887	888	2.0	.70	.75	0	1.53	2.34	1.40	.94
887	872	2.0	1.6	0	-.1	3.05	9.3	3.2	.03
872	871	1.6	1.1	.5	-.1	1.61	2.59	1.76	.38
872	873	1.6	1.3	.5	0	2.3	5.29	2.08	.64
872	870	1.6	.74	.4	0	1.61	2.59	1.18	.35
870	874	.74	.80	.5	-.1	.90	.810	.592	.36
870	885	.74	1.5	-.3	0	1.4	1.96	1.11	.16
870	880	.74	1.0	0	0	1.83	3.35	.74	0
880	884	1.0	.80	0	-.08	3.2	10.2	.80	.08

* Observed data from analog plots

$$\gamma^2 = \frac{[C_o^2 + Quad^2] K^2}{PSD_1 \cdot PSD_2}$$

COHERENCE CALCULATIONS

Corr No. 255
 $\overline{P}_{t2}/P_{t0} = 0.642$

$M_0 = 2.6$

Frequency = 200 Hz

Column Number									
1	2	3*	4*	5*	6*	7*	8	9	10
Probe 1	Probe 2	PSD 1	PSD 2	Co CPSD	Quad CPSD	K Factor	K ²	③ × ④	γ ²
		X 10 ⁻⁵	X 10 ⁻⁵			X 10 ⁻⁵	X 10 ⁻¹⁰	X 10 ⁻¹⁰	
877	876	0.90	1.5	0.2	0	4.02	16.2	1.3	0.48
877	878	.90	.50	.7	0	.62	.438	.450	.48
877	882	.90	1.4	0	0	3.32	11.0	1.26	0
882	881	1.4	1.0	.2	0	2.64	6.97	1.4	.20
882	883	1.4	.65	.2	0	2.64	6.97	.91	.31
882	880	1.4	.74	-.06	0	2.4	5.76	1.04	.02
887	886	1.0	1.9	.3	-.1	2.64	6.97	1.9	.37
887	888	1.0	.46	.3	0	1.53	2.34	.46	.46
887	872	1.0	.85	0	0	3.05	9.3	.85	0
872	871	.85	.70	.1	-.1	1.61	2.59	.595	.09
872	873	.85	.65	.2	0	2.3	5.29	.553	.38
872	870	.85	.35	0	0	1.61	2.59	.298	0
870	874	.35	.45	.1	-.1	.90	.810	.158	.10
870	885	.35	1.0	0	-.05	1.4	1.96	.35	.01
870	880	.35	.74	0	0	1.83	3.35	.259	0
880	884	.74	.42	0	-.05	3.2	10.2	.311	.08

* Observed data from analog plots

$$\gamma^2 = \frac{[C_o^2 + Quad^2] K^2}{PSD_1 \cdot PSD_2}$$

Appendix F

DETERMINATION OF TRANSFER FUNCTIONS FROM STATISTICAL PARAMETERS

Analog computations of statistical parameters were used to obtain shock position response to sinusoidal exit area disturbances. The method used, the inputs required, and the results are presented in this appendix. The calculation uses a number of analog-computed parameters which must be read from X-Y plots. The possible errors (introduced by the input parameters, departure of the exit disturbance from a true sinusoid, nonlinearity of the shock position pressure parameter versus shock position, etc) make the accuracy of the results questionable. They are presented, however, for illustrative purposes.

The transfer function, $H(f)$, relating shock position with exit area disturbance, can be found from the following statistical relations:

$$\left| H_T(f) \right|^2 = \gamma^2(f) \frac{\text{PSD}(X_S, f)}{\text{PSD}(X_P, f)} \quad (\text{F-1})$$

$$\phi(f) = \tan^{-1} \frac{Q_U(X_S, X_P, f)}{C_O(X_S, X_P, f)} \quad (\text{F-2})$$

where $\gamma^2(f)$ is the coherence function between X_P and X_S

PSD (f) is the power spectral density function

$\phi(f)$ is the phase relationship between X_P and X_S

$C_O(f)$ is the coherent component of the cross power spectral density function

$Q_U(f)$ is the quadrature component of the cross power spectral density function

The calculations are provided in table IX. The typical PSD and cross PSD data reduction plots which were used for these calculations are given for the 10 Hz excitation in figures 149 through 151. The PSD curve for the shock position parameter was obtained in terms of the pressure variable by a summation of the four pressure sensors as discussed in Appendix B. The PSD curve for the exit area parameter was obtained in terms of voltage. Both the shock position pressure parameter and the exit area voltage are assumed to be linear functions of the shock position and exit area.

Although the intent during the course of the test was to hold the plug displacement constant as a function of frequency, the data revealed that the plug position actually decreased significantly with frequency. However, if the linear system analogy is valid, this is not meaningful in terms of the amplitude ratio presented in column 12 of table IX. It should be noted, however, that the units are not the same as the units represented by equation F-1 but differ by a constant. For the actual calculations

$$\left| H(f) \right|^2 = \gamma^2(f) \frac{\text{PSD (pressure, f)}}{\text{PSD (volts, f)}} \quad (\text{F-3})$$

where

$$\text{pressure} = K_1 X_S$$

$$\text{volts} = K_2 X_p$$

$$\begin{aligned} \left| H(f) \right|^2 &= \gamma^2(f) \frac{\text{PSD (pressure, f)}}{\text{PSD (volts, f)}} = \left(\frac{K_1}{K_2} \right)^2 \gamma^2(f) \frac{\text{PSD}(X_S, f)}{\text{PSD}(X_p, f)} \\ &= \left(\frac{K_1}{K_2} \right)^2 \left| H_T(f) \right|^2 \end{aligned} \quad (\text{F-4})$$

The transfer function can be nondimensionalized by determining a value for $H(0)$. Since

$$\left| H(0) \right|^2 = \left(\frac{K_1}{K_2} \right)^2 \left| H_T(0) \right|^2$$

$$\text{then} \quad \left| \frac{H(f)}{H(0)} \right| = \left| \frac{H_T(f)}{H_T(0)} \right| = G(f) \quad (\text{F-5})$$

and the transfer function becomes independent of the units used. This transfer function can then be interpreted as the amplitude ratio of the shock position at the excited frequency, f , to the shock position response at zero frequency.

The value of $H(0)$ was found from an extrapolation of the transfer function as plotted on a linear frequency scale (figure 152). From the curve of figure 152, the value of $H(0) = 2.0$ was selected. The normalized transfer function is shown in figure 153.

REFERENCES

1. Mantz, K. L.; and King, R. W.: Proposed Investigation of the Dynamic Response of a Supersonic Inlet when Exposed to Internal and External Disturbances in the Ames 8 x 7 Foot Unitary Wind Tunnel. Tech. Report LFL N-44P (NASA Contract NAS2-2363), Lockheed Aircraft Corporation, California Division, January 1965.
2. Benson, J. L., et al: Investigation of Supersonic Transport Engine Inlet Configurations, Final Report. Tech. Report No. 19014 (NASA Contract NAS2-2363), Lockheed Aircraft Corporation, September 1965.
3. Anon.: Pretest Information for Wind Tunnel Tests to Investigate Dynamic Distortion of an Axisymmetric Mixed Compression Inlet in the Ames 8 x 7 Foot Unitary Wind Tunnel. Tech. Report No. NA-68-262 (NASA Contract NAS2-4667), North American Rockwell Corporation, Los Angeles Division, March 1968.
4. Bellman, R.: Adaptive Control Processes. Princeton University Press, 1961.
5. Bendat, J. S.; and Piersol, A. G.: Design Considerations and Use of Analog Power Spectral Density Analyzers. Report by Measurements Analysis Corporation, Los Angeles, California, Printed and Distributed by Honeywell, Incorporated, Denver Division.

TABLE I.- RMS/ P_{t0} MEASUREMENTS FOR DIFFERENT SECTIONS OF A

5-SECOND INTERVAL, $M_0 = 3.0$, $\bar{P}_{t2}/P_{t0} = 0.877$

Probe	0.00-0.05 Second	0.05-0.10 Second	0.10-0.15 Second	0.15-0.20 Second	0.00-0.20 Second	0.00-5.0 Seconds
870	0.0059	0.0053	0.0063	0.0061	0.0059	0.00592
871	0.0102	0.0099	0.0096	0.0094	0.0098	0.00966
872	0.0091	0.0097	0.0089	0.0090	0.0092	0.00884
873	0.0107	0.0105	0.0094	0.0091	0.0100	0.01030
874	0.0072	0.0062	0.0064	0.0068	0.0067	0.00694
875	0.0068	0.0076	0.0074	0.0088	0.0077	0.00728
876	0.0087	0.0098	0.0098	0.0099	0.0096	0.00966
877	0.0088	0.0094	0.0092	0.0094	0.0092	0.00864
*878						
*879						
880	0.0073	0.0067	0.0064	0.0057	0.0066	0.00605
881	0.0088	0.0091	0.0089	0.0083	0.0088	0.00946
882	0.0094	0.0084	0.0092	0.0090	0.0090	0.00878
*883						
*884						
885	0.0076	0.0069	0.0070	0.0063	0.0070	0.00599
886	0.0086	0.0080	0.0078	0.0090	0.0084	0.00830
887	0.0081	0.0091	0.0081	0.0082	0.0084	0.00789
888	0.0072	0.0088	0.0082	0.0085	0.0082	0.00783
889	0.0053	0.0068	0.0062	0.0067	0.0063	0.00605

*Probe data questionable for these runs.

TABLE II.- RMS/ P_{t0} MEASUREMENTS FOR THREE 5-SECOND
 INTERVALS IN A 7-MINUTE RUN, $M_0 = 3.0$, $\bar{P}_{t2}/P_{t0} = 0.877$

Interval Probe	1 Minute Into Run	3 Minutes Into Run	5 Minutes Into Run
870	0.0060	0.0060	0.0057
873	0.0103	0.0103	0.0103
874	0.0072	0.0072	0.0072

TABLE III.- RMS/ P_{t0} MEASUREMENTS FOR DIFFERENT SECTIONS

OF A 5-SECOND INTERVAL, $M_o = 3.0$, $\bar{P}_{t2}/P_{t0} = 0.565$

Probe	0.00-0.05 Second	0.05-0.10 Second	0.10-0.15 Second	0.15-0.20 Second	0.00-0.20 Second	0.0-5.0 Seconds
870	0.0344	0.0319	0.0312	0.0292	0.0317	0.0358
871	0.0494	0.0392	0.0386	0.0466	0.0437	0.0520
872	0.0441	0.0427	0.0362	0.0463	0.0425	0.0506
873	0.0286	0.0323	0.0257	0.0311	0.0296	0.0365
874	0.0192	0.0244	0.0171	0.0169	0.0196	0.0220
875	0.0644	0.0521	0.0524	0.0489	0.0547	0.0593
876	0.0656	0.0547	0.0728	0.0485	0.0611	0.0636
877	0.0572	0.0350	0.0574	0.0399	0.0484	0.0433
*878						
*879						
880	0.0510	0.0491	0.0555	0.0503	0.0515	0.0539
881	0.0723	0.0748	0.0635	0.0710	0.0705	0.0773
882	0.0776	0.0801	0.0738	0.0770	0.0772	0.0803
883	0.0522	0.0549	0.0392	0.0457	0.0484	0.0270
884	0.0338	0.0286	0.0203	0.0232	0.0270	0.0295
885	0.0525	0.0422	0.0439	0.0450	0.0461	0.0539
886	0.0532	0.0398	0.0505	0.0489	0.0483	0.0549
887	0.0433	0.0352	0.0403	0.0416	0.0402	0.0402
888	0.0358	0.0403	0.0222	0.0422	0.0350	0.0277
889	0.0182	0.0236	0.0181	0.0244	0.0213	0.0196

*Probe data questionable for these runs.

TABLE IV.- RMS/ P_{t0} MEASUREMENTS FOR THREE 5-SECOND
 INTERVALS IN A 7-MINUTE RUN, $M_o = 3.0$, $\bar{P}_{t2}/P_{t0} = 0.565$

Interval Probe	1 Minute Into Run	3 Minutes Into Run	5 Minutes Into Run
870	0.0368	0.0358	0.0358
873	0.0370	0.0370	0.0370
874	0.0220	0.0220	0.0220

TABLE V.- COHERENCE FUNCTIONS FOR PAIRS OF IN-LINE PROBES

$$M_0 = 3.0$$

		Coherence						
$\frac{\overline{P}_{t2}}{P_{t0}}$	Probe Pair	20 Hz	40 Hz	80 Hz	100 Hz	140 Hz	160 Hz	200 Hz
0.877	831-870	0.0815	0.1560	0.0000	0.0027	0	0.0096	0
	833-874	0.252	0.0266	0.0062	0.0296	0.0515	0.0032	0.0105
	833-839	0.0960	0.0900	0.0013	0.0451	0.0017	0.0150	0.0460
	839-871	0.0275	0.0684	0.0549	0.0216	0.0320	0.0291	0.0163
0.565	831-870	0.0327	0.0133	0	0.0007	0	0	0
	833-874	0.0138	0.0407	0.0519	0.0685	0.0445	0	0.0814
	833-839	0	0.0031	0.0066	0.0353	0.0069	0.0149	0.0139
	839-871	0.0052	0.0011	0.0041	0.0026	0.0035	0.0026	0.0003

TABLE VI.- COHERENCE FUNCTIONS FOR PAIRS OF STATIC AND TOTAL PRESSURES AT MS47.30 AND MS66.70

		Coherence						
$\frac{\overline{P}_{t2}}{P_{t0}}$	Probe Pair	20 Hz	40 Hz	80 Hz	100 Hz	140 Hz	160 Hz	200 Hz
0.877	830-831	0.0028	0.0444	0.1625	0.0378	0.0151	0.0550	0.0032
	830-833	0.0286	0.0370	0.0006	0.0305	0.0004	0.0123	0.0295
	836-839	0.0489	0.0470	0.0278	0.0560	0.0003	0.0021	0.0725
0.565	830-831	0.278	0.525	0	0	0	0	0
	830-833	1.0	0.216	0.473	0.182	0.3560	0.0437	0.728
	836-839	0.552	0.0894	0.0815	0.1122	0.0394	0.0738	0.0593

TABLE VII.- CONTROL SYSTEM TEST SUMMARY OF SHOCK TRAVEL

Input Freq. (Hz)	Shock Travel - ΔX_S (inches)							
	Control	No Control	Control	No Control	Control	No Control	Control	No Control
Input Amp1	Plug ± 2 in. ²	Plug ± 2 in. ²	Plug ± 4 in. ²	Plug ± 4 in. ²	Wedge $\pm 3.5^\circ$	Wedge $\pm 3.5^\circ$	Wedge $\pm 7.5^\circ$	Wedge $\pm 7.5^\circ$
\bar{P}_{t2}/P_{t0}	0.845	0.845	0.846	0.846	0.782	0.782	0.778	0.778
Corr	305	305	306	306	452	452	453	453
0.5	0.340	1.064	0.340	1.702	0.319	0.426	0.426	0.638
1	0.426	1.064	0.808	1.702	0.372	0.426	0.745	0.745
2	0.511	1.064	1.106	1.702	0.532	0.426	1.170	0.745
4	0.511	0.638	1.489	1.702	0.851	0.426		
6	0.766	0.808	1.277	1.277	0.958	0.426	1.490	0.745
8	0.851	0.681	1.362	1.064	0.851	0.426	1.702	1.064
10	0.766	0.638	1.362	1.064	0.851	0.532	1.649	1.064
12	0.681	0.596	1.191	0.936	0.904	0.585	1.649	1.17
14	0.596	0.511	1.064	0.851	0.904	0.532	1.490	1.064
16	0.426	0.426			0.851	0.585	1.436	1.064
18	0.340	0.383			0.851	0.638	1.33	1.011
20	0.298	0.340			0.851	0.745	1.33	1.064
22					0.904	0.745	1.43	1.064
24					1.064	0.745	1.49	1.17
26					1.117	0.851	1.49	1.17
28					1.117	0.851	1.543	1.117
30					1.064	1.064	1.49	1.17

$X_0 \approx 40.0$ inches aft of inlet spike

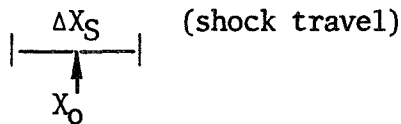
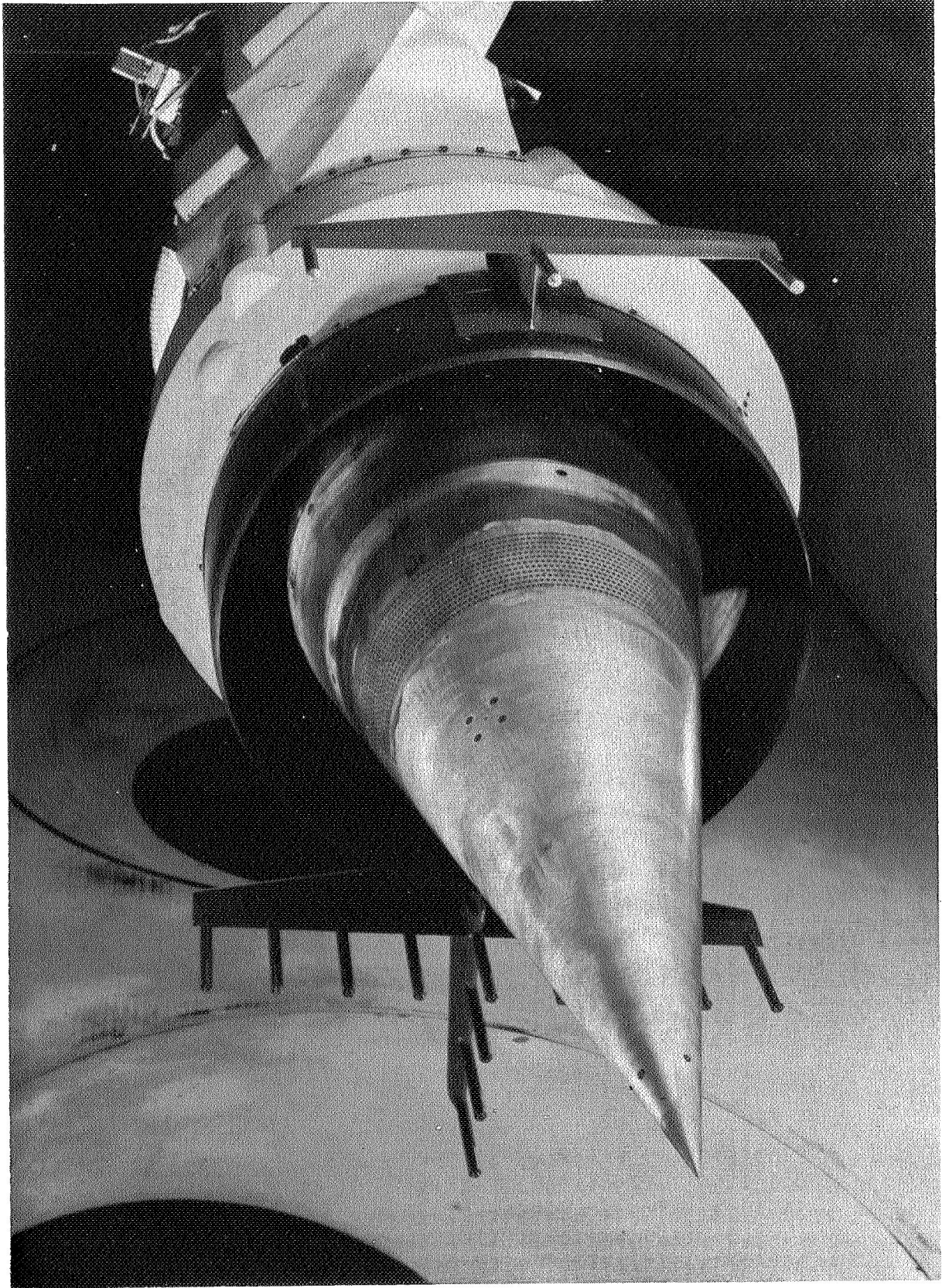


TABLE VIII.- CAT FILTER TRANSFER FUNCTIONS

Spectrum	$\frac{G(S)}{\sigma_\omega}, M_0 = 2.6$	$\frac{G(S)}{\sigma_\omega}, M_0 = 3.0$
1	$\frac{.979(S + .577)}{(S + 1)^2}$	$\frac{1.058(S + .671)}{(S + 1.165)^2}$
2	$\frac{.690(S + .458)}{(S + .745)^{1.883}}$	$\frac{.7425(S + .532)}{(S + 1.165)^{1.883}}$
3	$\frac{.979}{(S + 1.732)}$	$\frac{1.055}{(S + 2.01)}$
	L = 2,500 ft h = 40,000 ft	



A-41156

Figure 1.- Inlet and external rakes

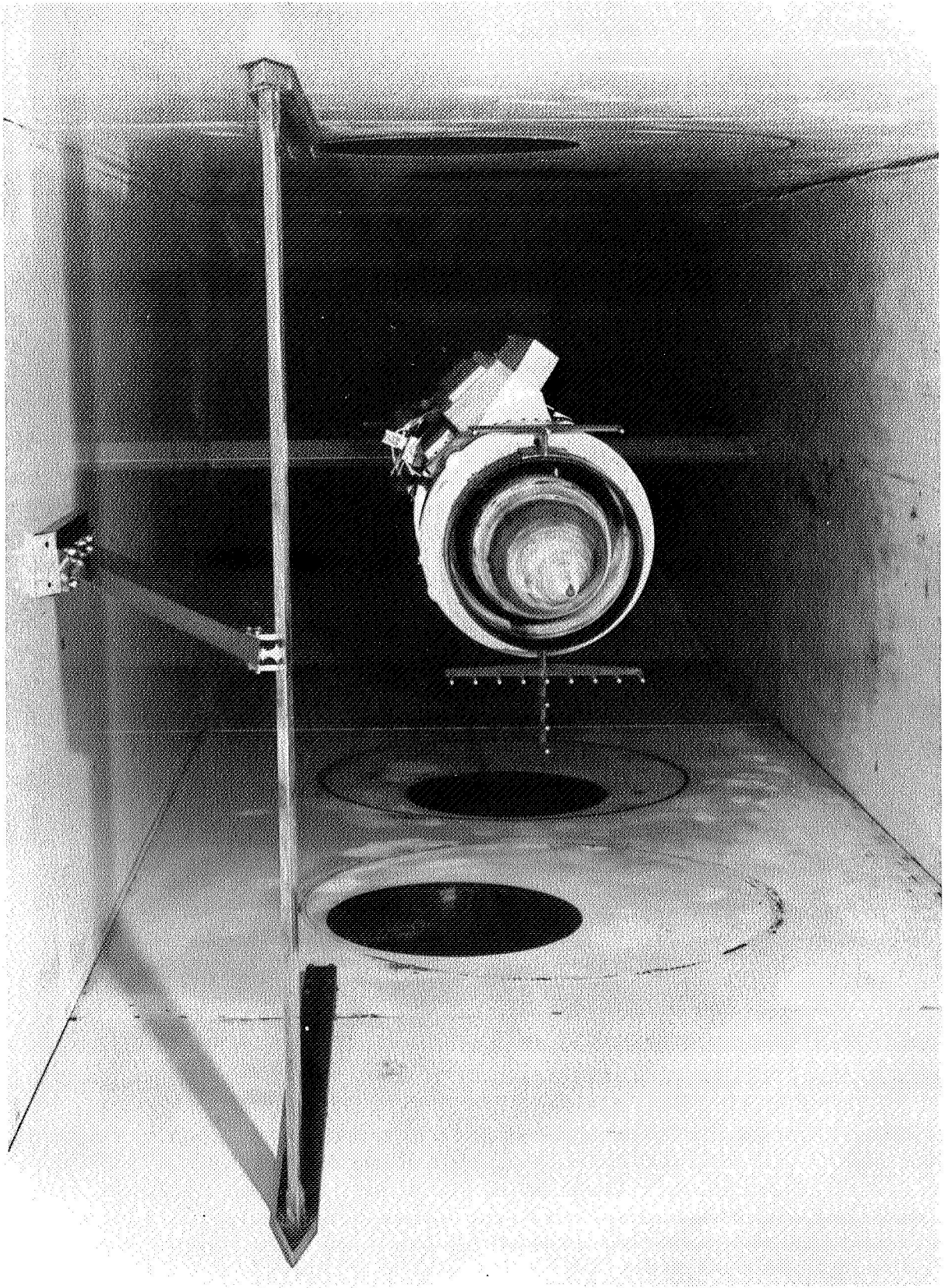


Figure 2.- Inlet and external disturbance vane.

A-41165

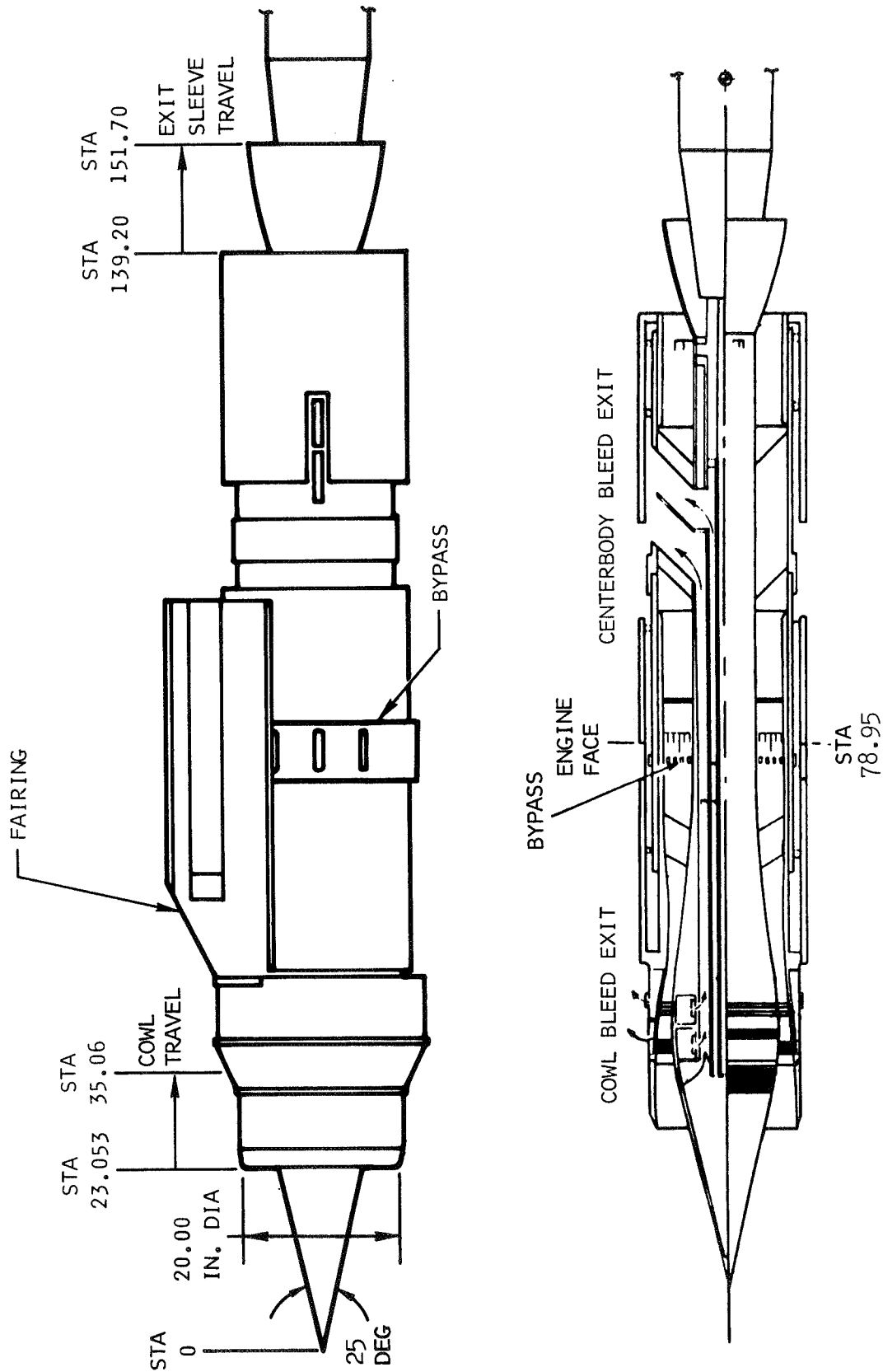


Figure 3.- Supersonic inlet configuration.

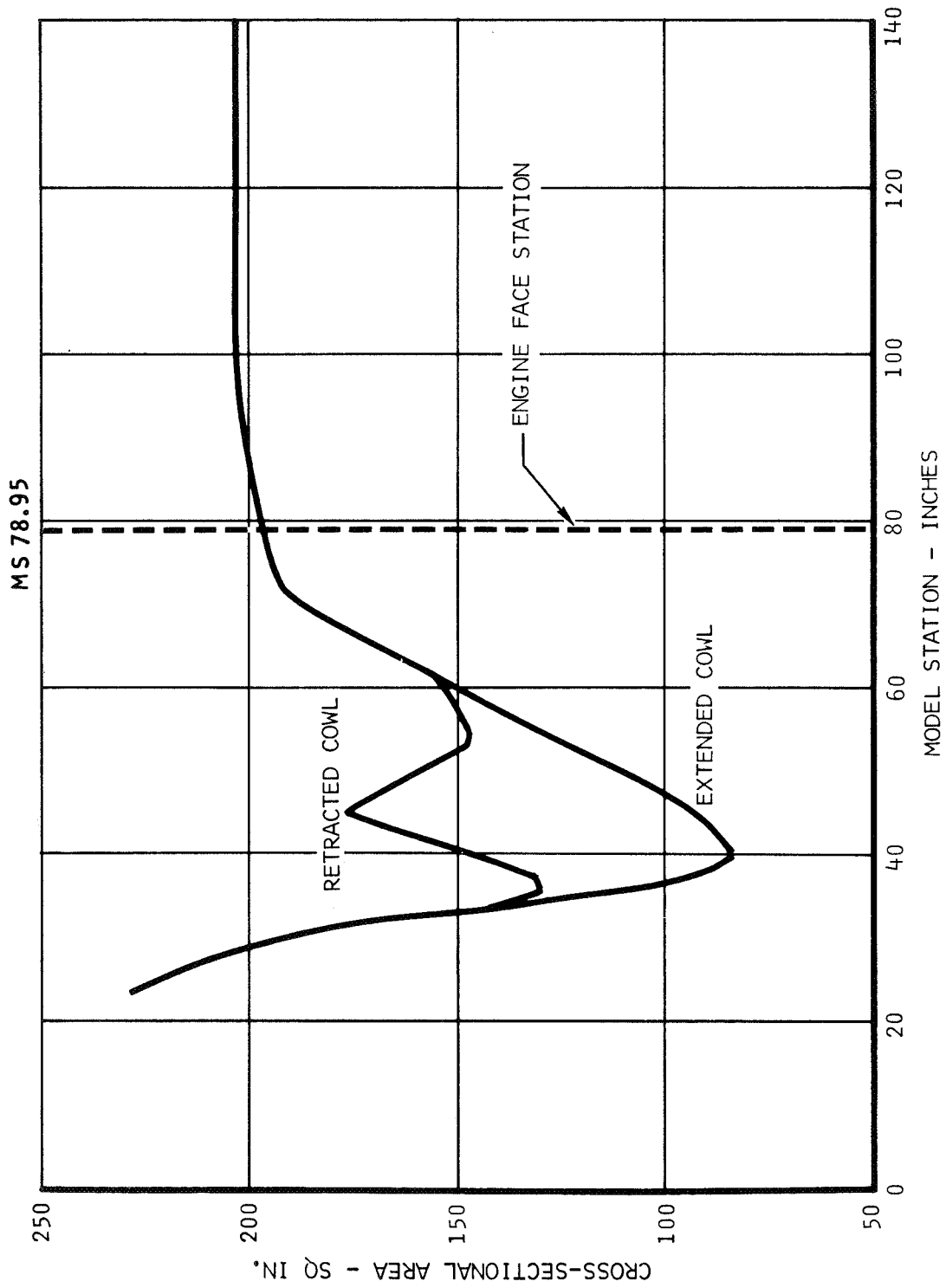


Figure 4.- Inlet cross-sectional area variation - NASA Ames axisymmetric inlet.

BLEED NO.	POROSITY	HOLE DIA
1	41%	0.067
2	41%	0.102 & 0.125
3		0.125
4	41%	0.043
5		0.125

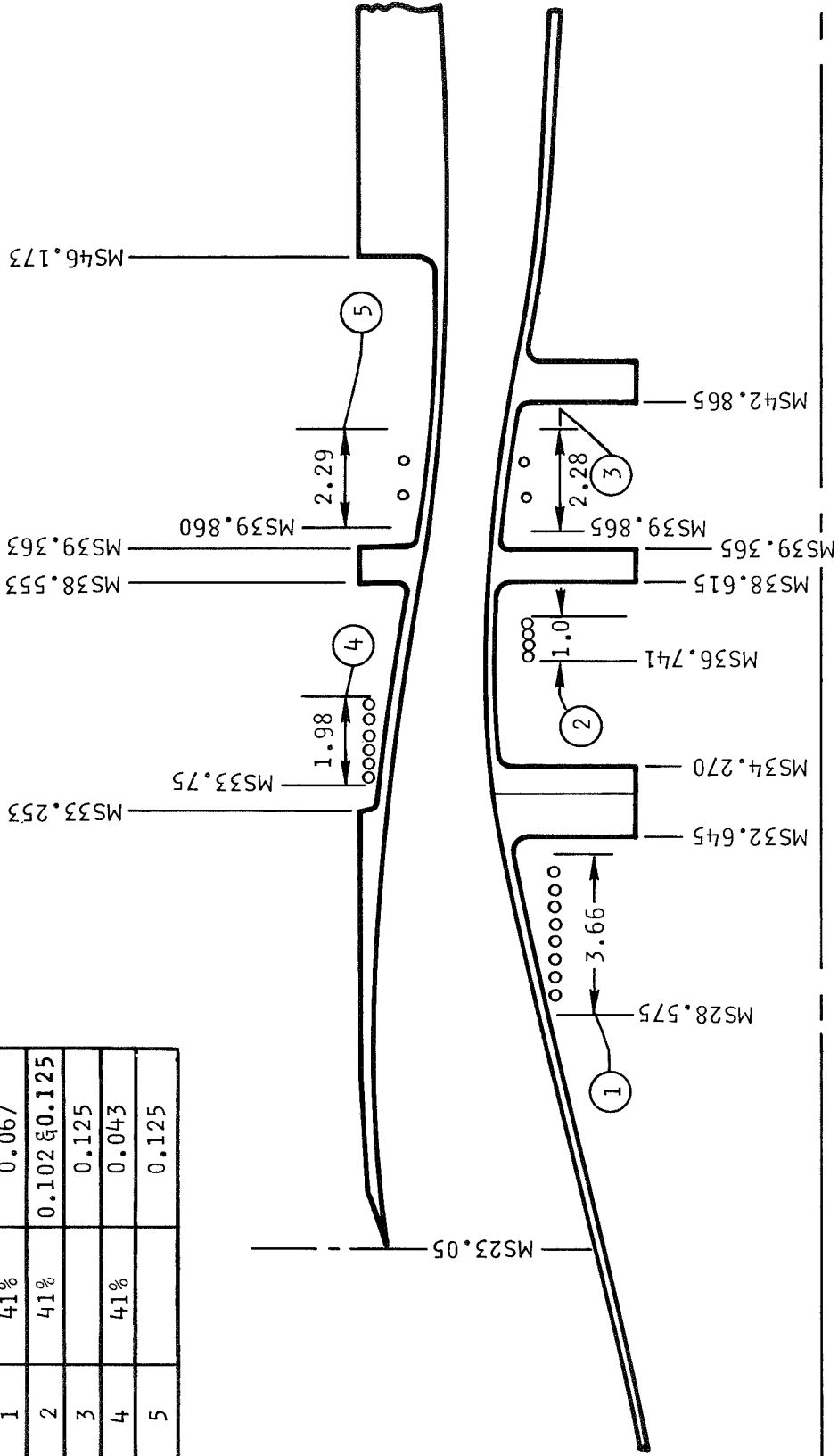


Figure 5. - Bleed configuration.

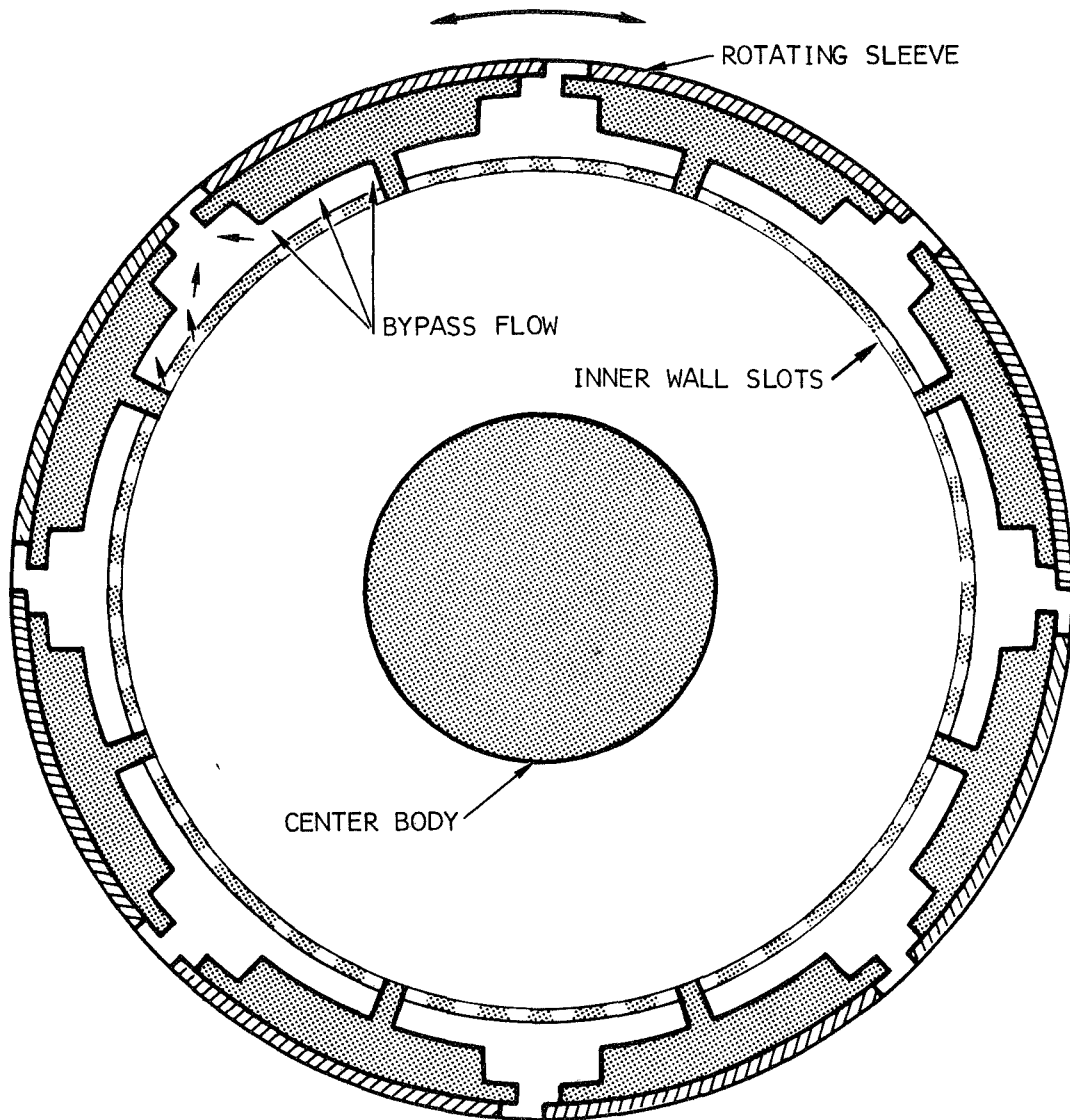


Figure 6.- Bypass valve schematic

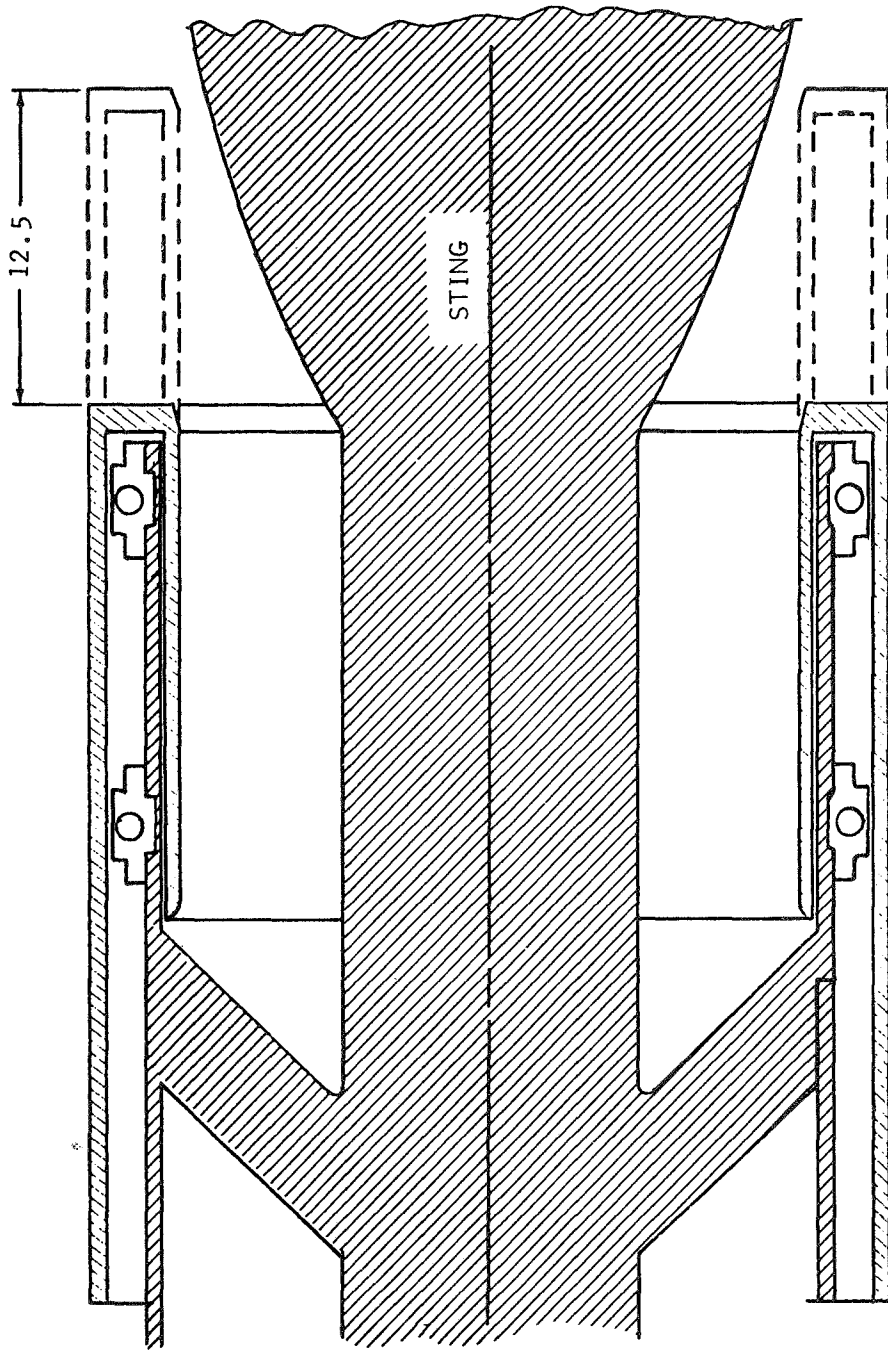


Figure 7.- Translating sleeve / plug valve

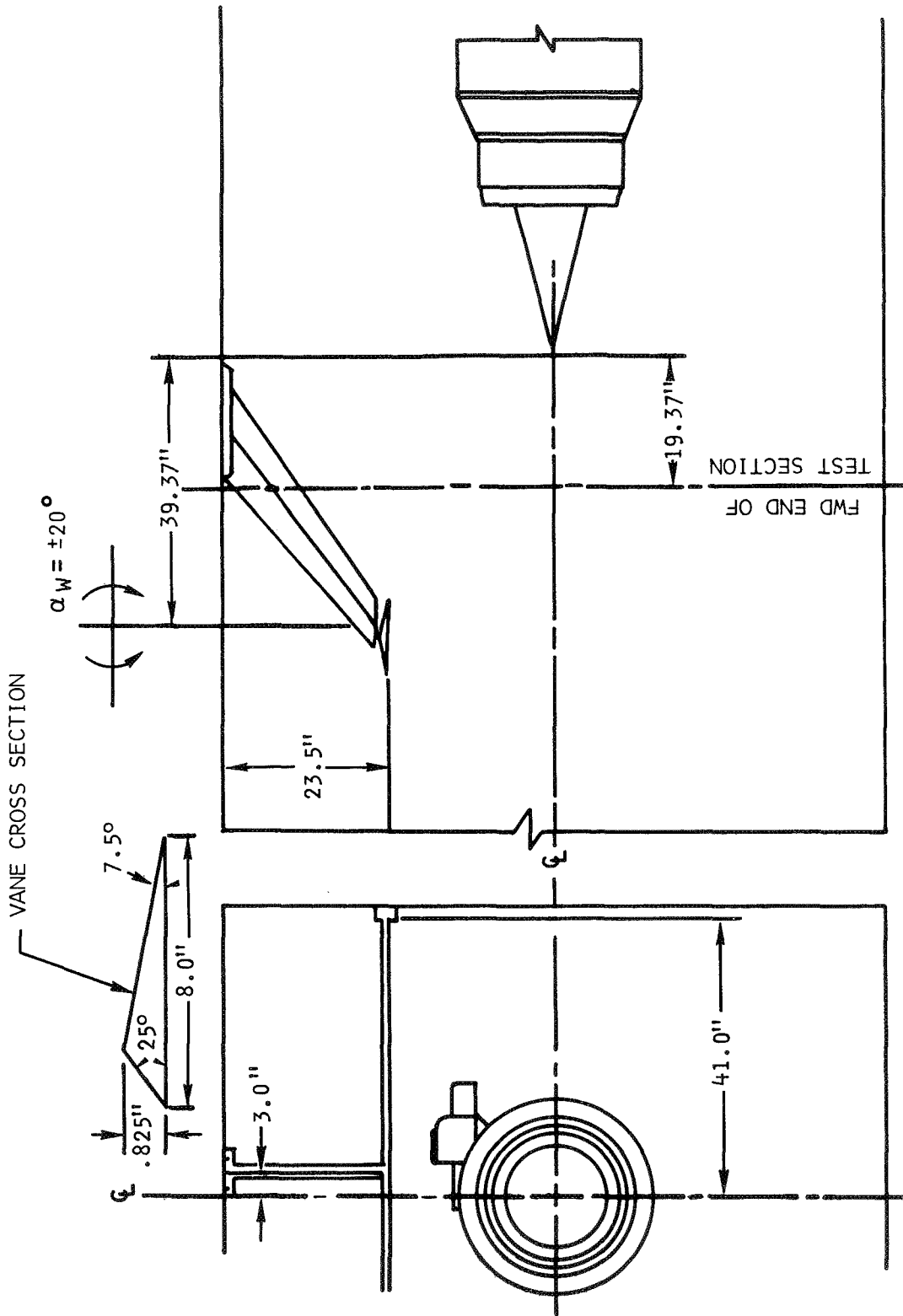


Figure 8.- External disturbance vane.

SEE FIGURE 15
 FOR STEADY-STATE
 CONICAL PROBE DETAILS

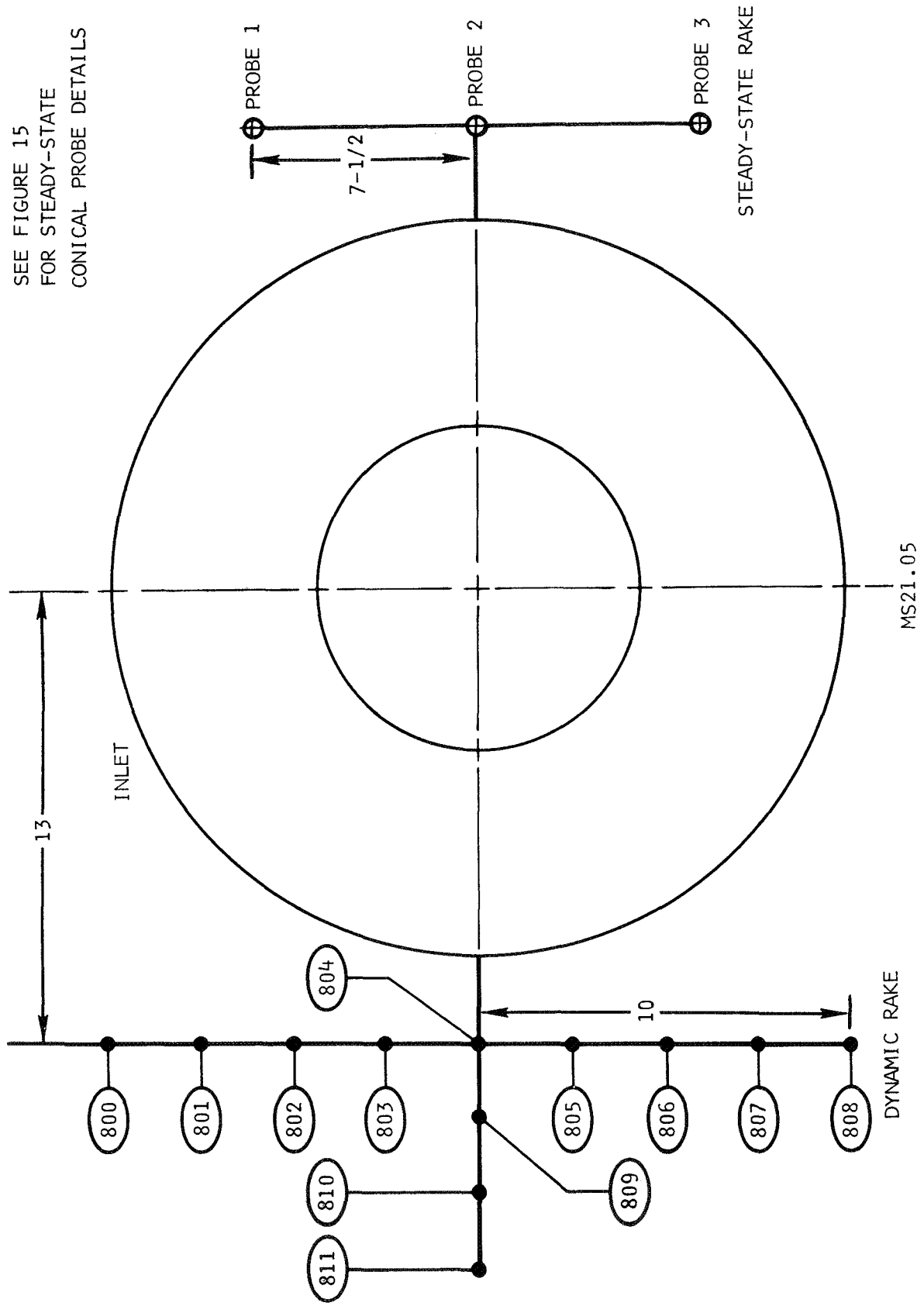


Figure 9.- External flow field rake.

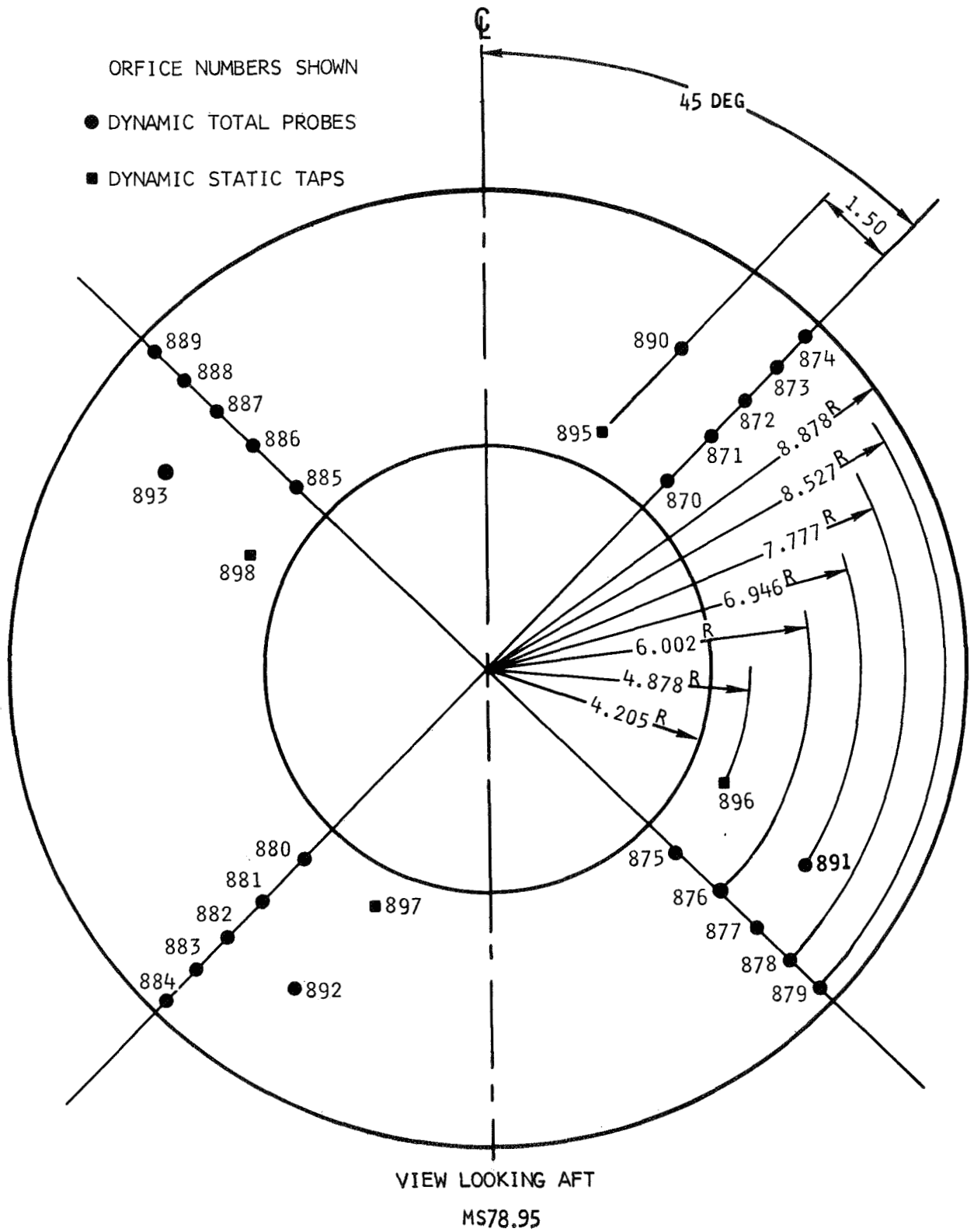


Figure 10. Engine face dynamic pressure instrumentation.

LEGEND

○

● DYNAMIC TOTAL PRESSURE PROBE

◐ DYNAMIC TOTAL PRESSURE TAP

⊙(XXX) ORIFICE NUMBER AT ANGULAR POSITION

● ⊙(821) 315 DEG

STA
0.0

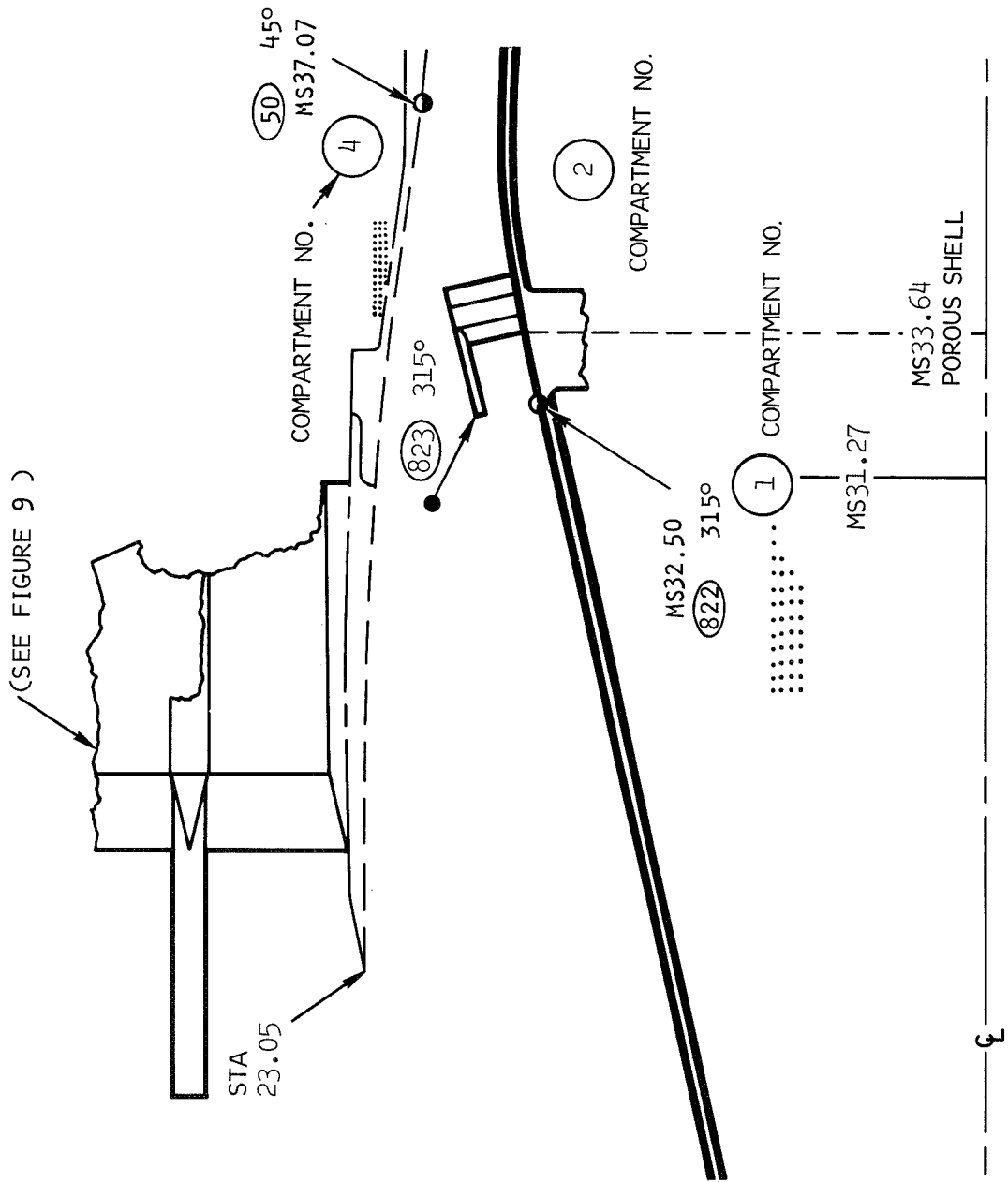
MS14.00

⊙(820) 315 DEG

ξ

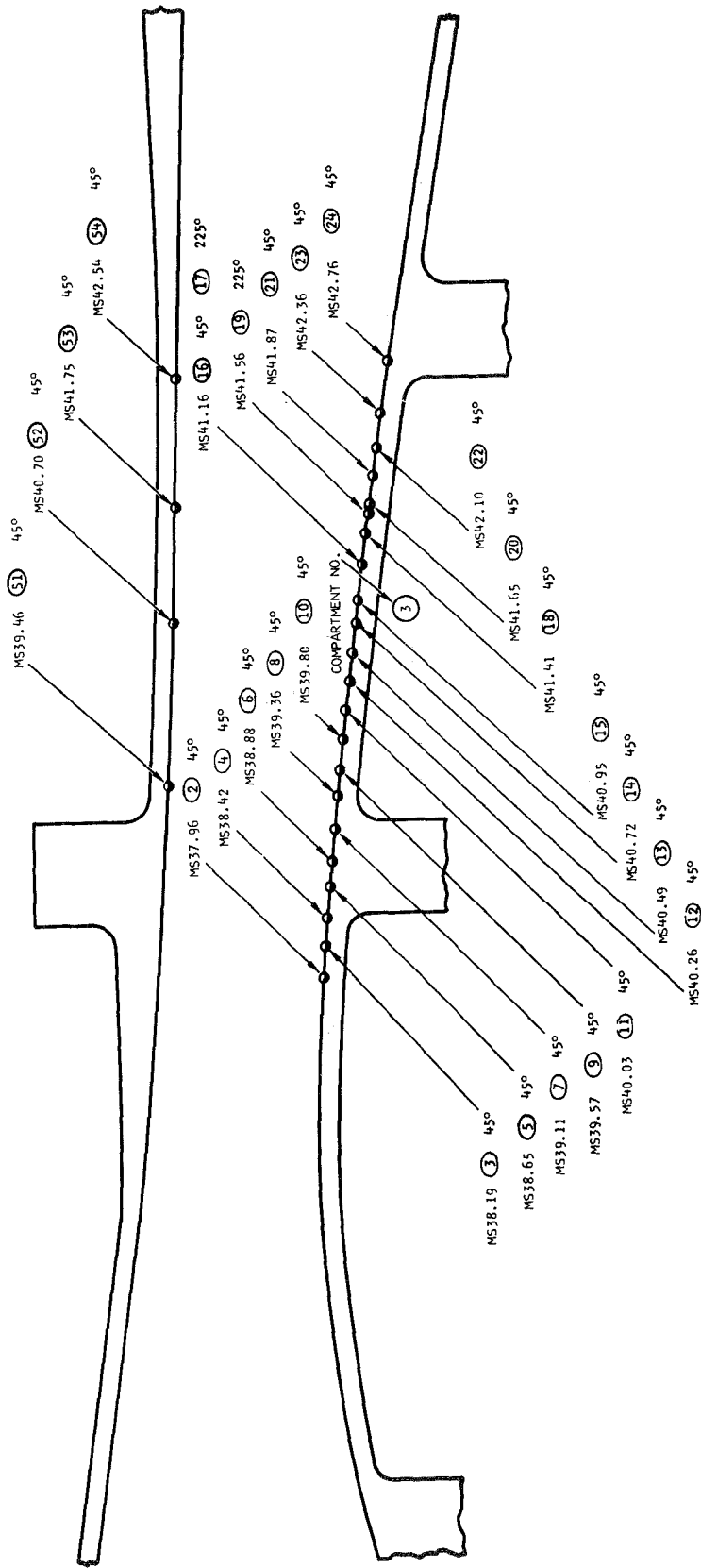
(a)

Figure 11.- Inlet duct dynamic instrumentation.

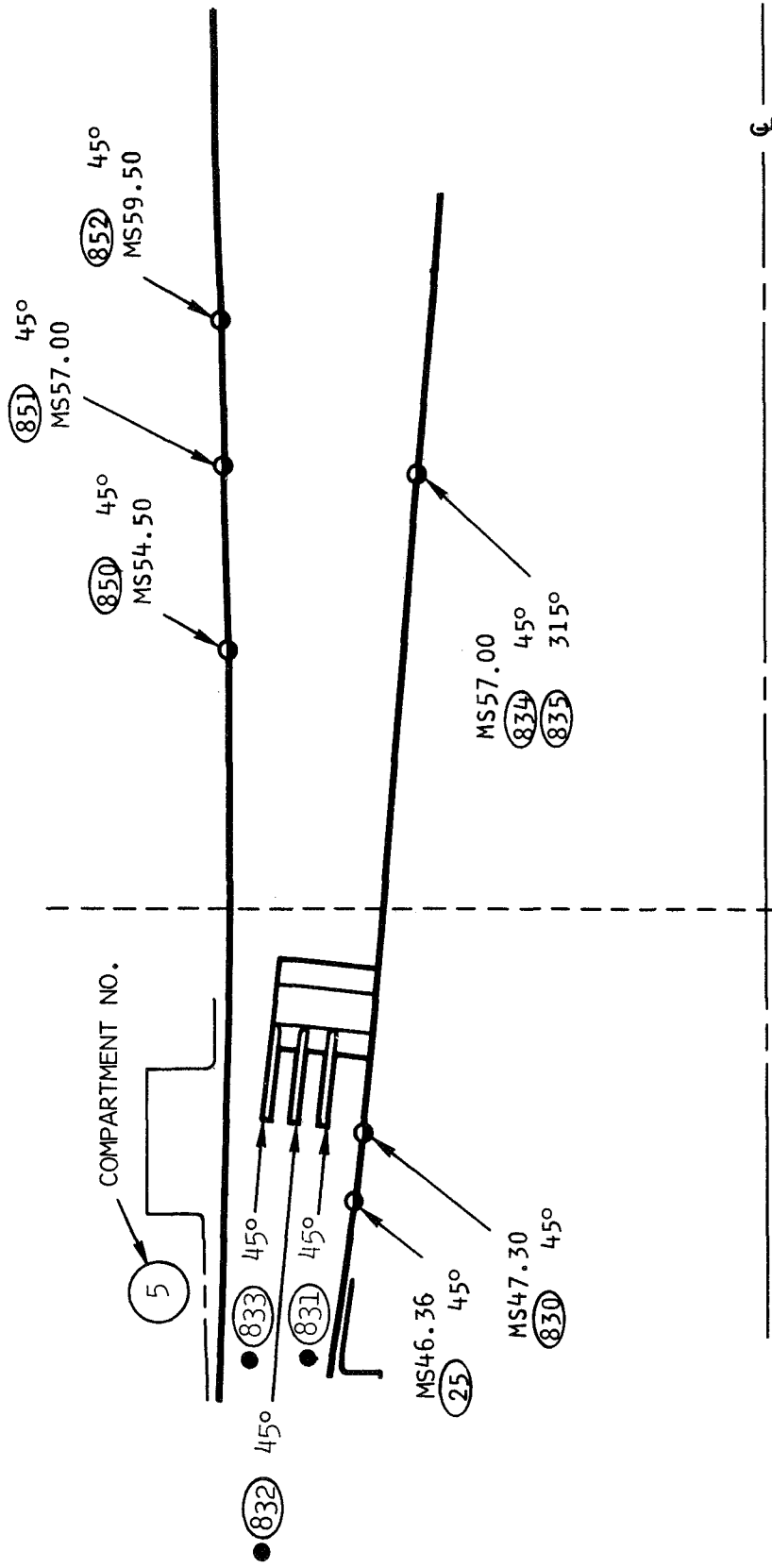


(b)

Figure 11.- Continued.

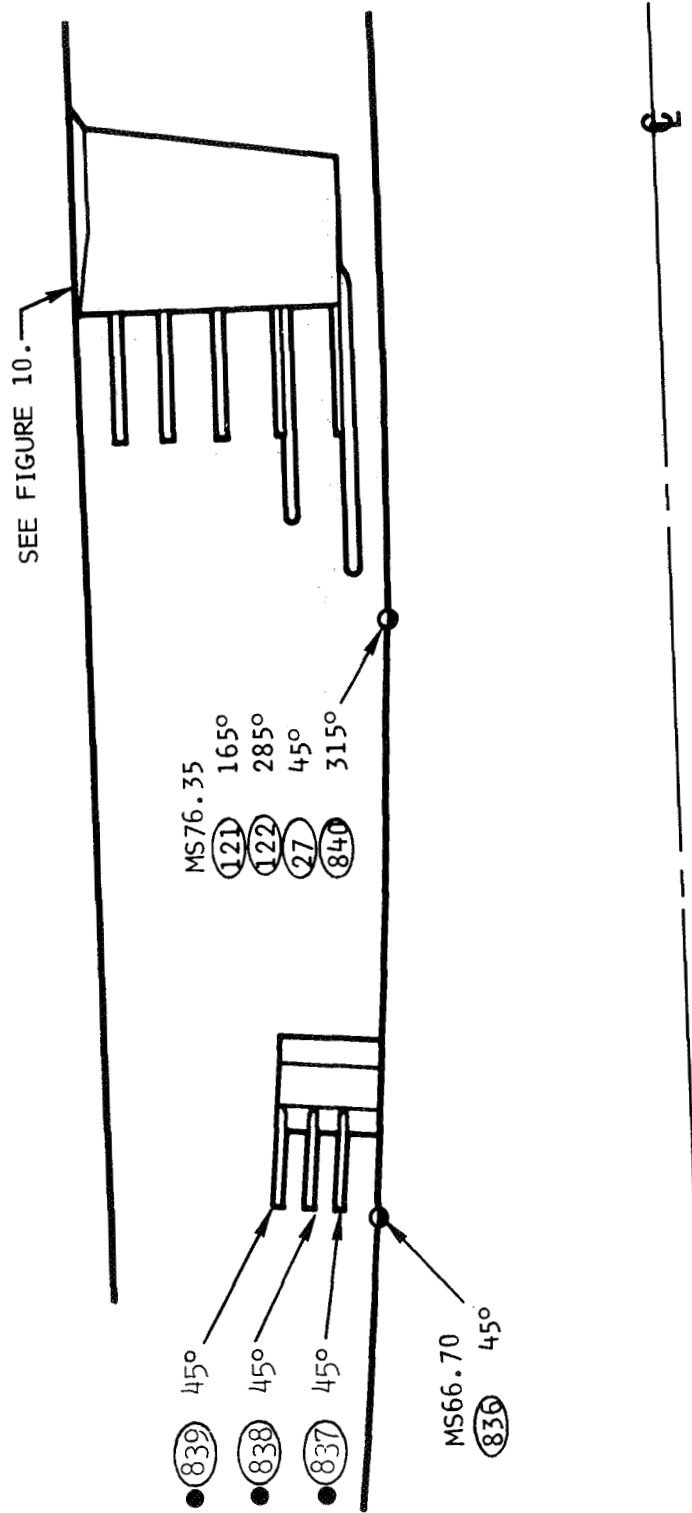


(c)
Figure 11.- Continued.



(d)
Figure 11.- Continued.

(SEE FIGURE 17 FOR EXIT NOZZLE DYNAMIC PROBE LOCATION)



(e)
Figure 11.- Concluded.

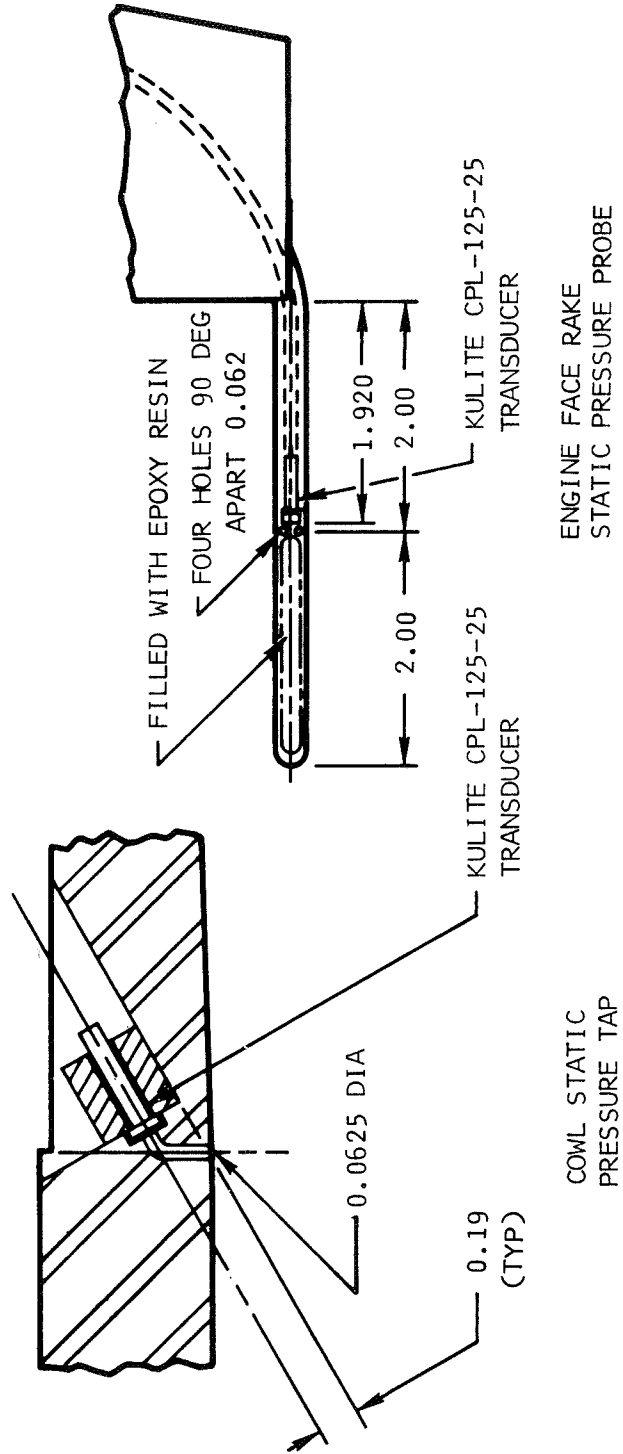


Figure 12.- Typical installations of dynamic static pressure instrumentation.

CHANNEL NO.	RECORDER NUMBER								
	1	2	3	4	5	6	7	8	9
1	VOICE	VOICE	VOICE	VOICE	VOICE	VOICE	VOICE	VOICE	VOICE
2	TIME	TIME	TIME	TIME	TIME	TIME	TIME	TIME	TIME
3	870 ²	VANE	VANE	885 ²	870 ²	870 ²	VANE	VANE	VANE
4	875 ²	884 ²	880 ²	886 ²	871 ²	884 ²	BYPASS	BYPASS	872 ²
5	880 ²	885 ²	881 ²	887 ²	873 ²	885 ²	872 ²	872 ²	890 ²
6	885 ²	886 ²	882 ²	888 ²	874 ²	24 ¹	6 ¹	23 ¹	14 ¹
7	874 ²	887 ²	883 ²	889 ²	830 ³	54 ¹	7 ¹	—	20 ¹
8	879 ²	888 ²	884 ²	802 ³	831 ³	834 ³	8 ¹	3 ¹	21 ¹
9	884 ²	889 ²	892 ²	820 ³	832 ³	835 ³	10 ¹	4 ¹	22 ¹
10	889 ²	893 ²	804 ²	804 ³	833 ³	850 ³	13 ¹	5 ¹	23 ¹
11	895 ³	800 ³	805 ³	822 ³	836 ³	851 ³	15 ¹	9 ¹	804 ³
12	896 ³	801 ³	806 ³	900 ³	837 ³	852 ³	16 ¹	10 ¹	809 ³
13	897 ³	802 ³	807 ³	835 ³	838 ³	27 ³	18 ¹	11 ¹	810 ³
14	898 ³	803 ³	808 ³	840 ³	839 ³	840 ³	51 ¹	12 ¹	811 ³

NOTES

1. ABSOLUTE PRESSURE
2. ABSOLUTE PRESSURE MINUS VARIABLE REFERENCE PRESSURE
3. AC COMPONENT WITH MAXIMUM DC SUPPRESSION (ELECTRICAL BIAS)

Figure 13.- Tape recorder channel listings - vane installed.

CHANNEL NO.	RECORDER NUMBER								
	1	2	3	4	5	6	7	8	9
1	VOICE	VOICE	VOICE	VOICE	VOICE	VOICE	VOICE	VOICE	VOICE
2	TIME	TIME	TIME	TIME	TIME	TIME	TIME	TIME	TIME
3	870 2	890 2	875 2	885 2	870 2	870 2	PLUG SLEEVE	PLUG SLEEVE	870 2
4	875 2	872 2	876 2	886 2	871 2	874 2	BYPASS	BYPASS	871 2
5	880 2	891 2	877 2	887 2	873 2	885 2	872 2	872 2	872 2
6	885 2	877 2	878 2	888 2	874 2	24 1	6 1	23 1	873 2
7	874 2	892 2	879 2	889 2	830 2	54 1	7 1	—	874 2
8	879 2	882 2	880 2	802 3	831 3	834 3	8 1	3 1	885 2
9	884 2	893 2	881 2	820 3	832 3	835 3	10 1	4 1	886 2
10	889 2	887 2	882 2	821 3	833 3	850 3	13 1	5 1	887 2
11	895 3	900 1	883 2	822 3	836 3	851 3	15 1	9 1	888 2
12	896 3	21 1	884 2	823 3	837 3	852 3	16 1	10 1	889 2
13	897 3	14 1	891 1	835 3	838 3	27 3	18 1	11 1	890 1
14	898 3	52 1	892 1	840 3	839 3	840 3	20 1	12 1	893 1

NOTES

1. ABSOLUTE PRESSURE
2. ABSOLUTE PRESSURE MINUS VARIABLE REFERENCE PRESSURE
3. AC COMPONENT WITH MAXIMUM DC SUPPRESSION (ELECTRICAL BIAS)

Figure 14.- Tape recorder channel listings - no vane.

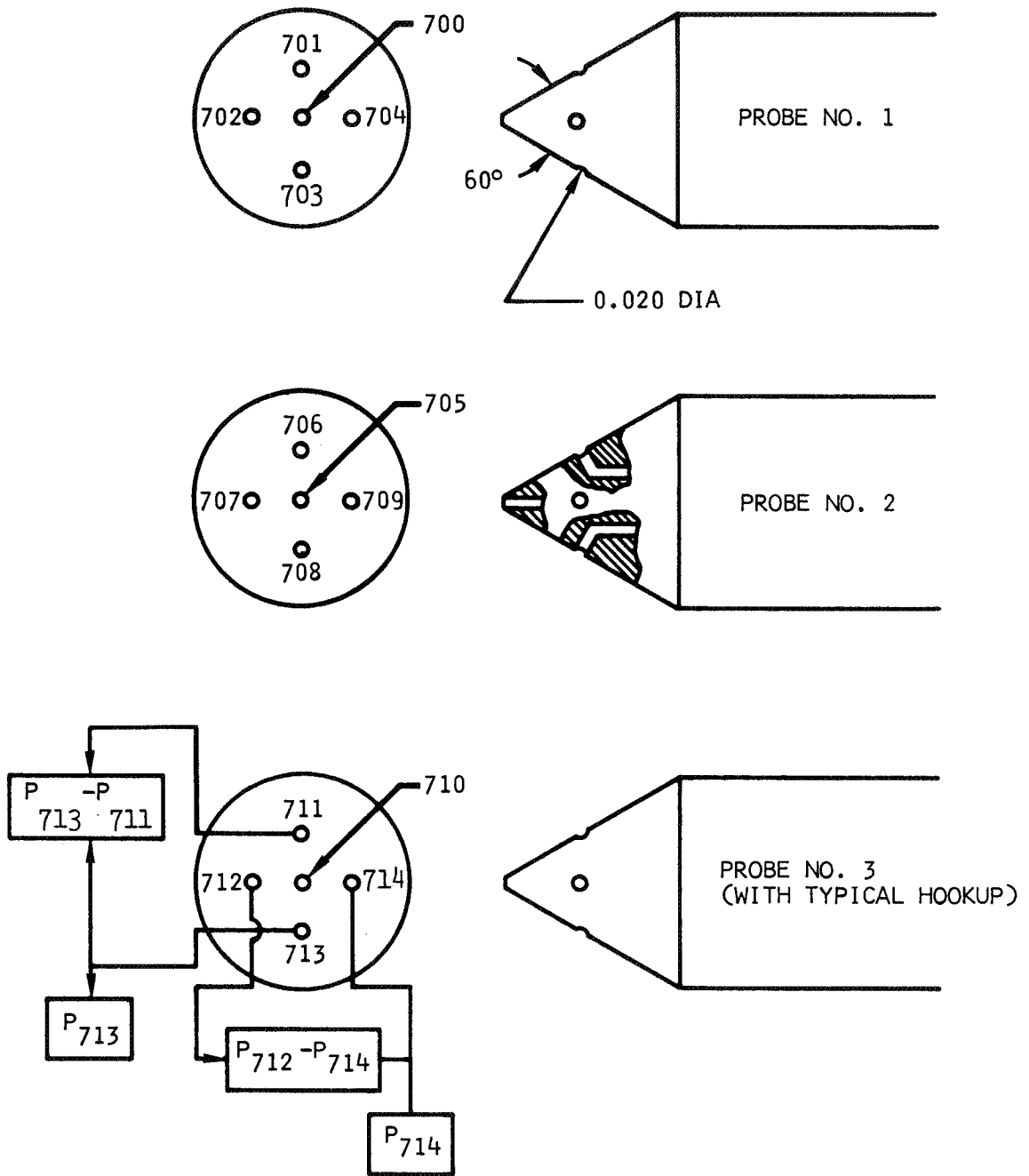
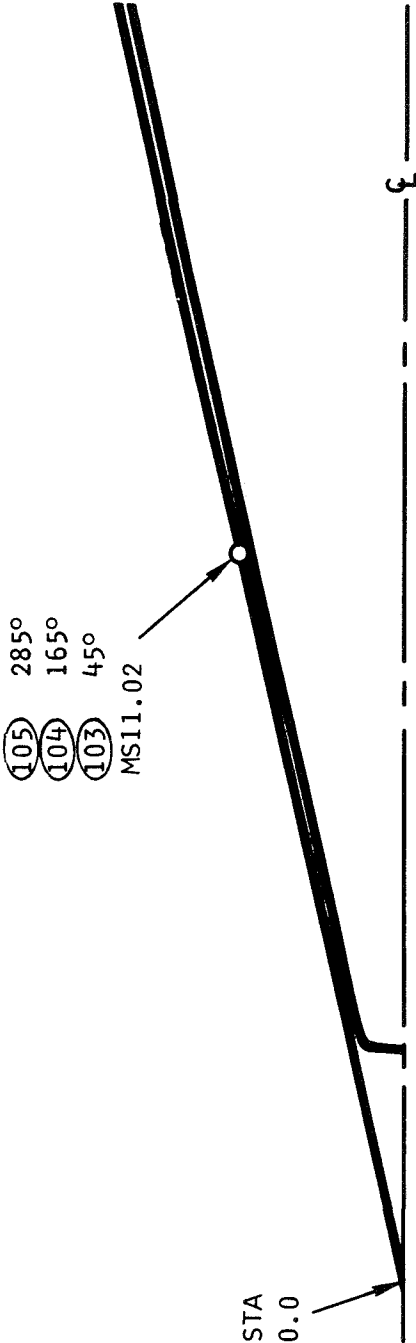


Figure 15.- Conical probe configuration.



(a)

Figure 16. - Inlet duct steady-state instrumentation.

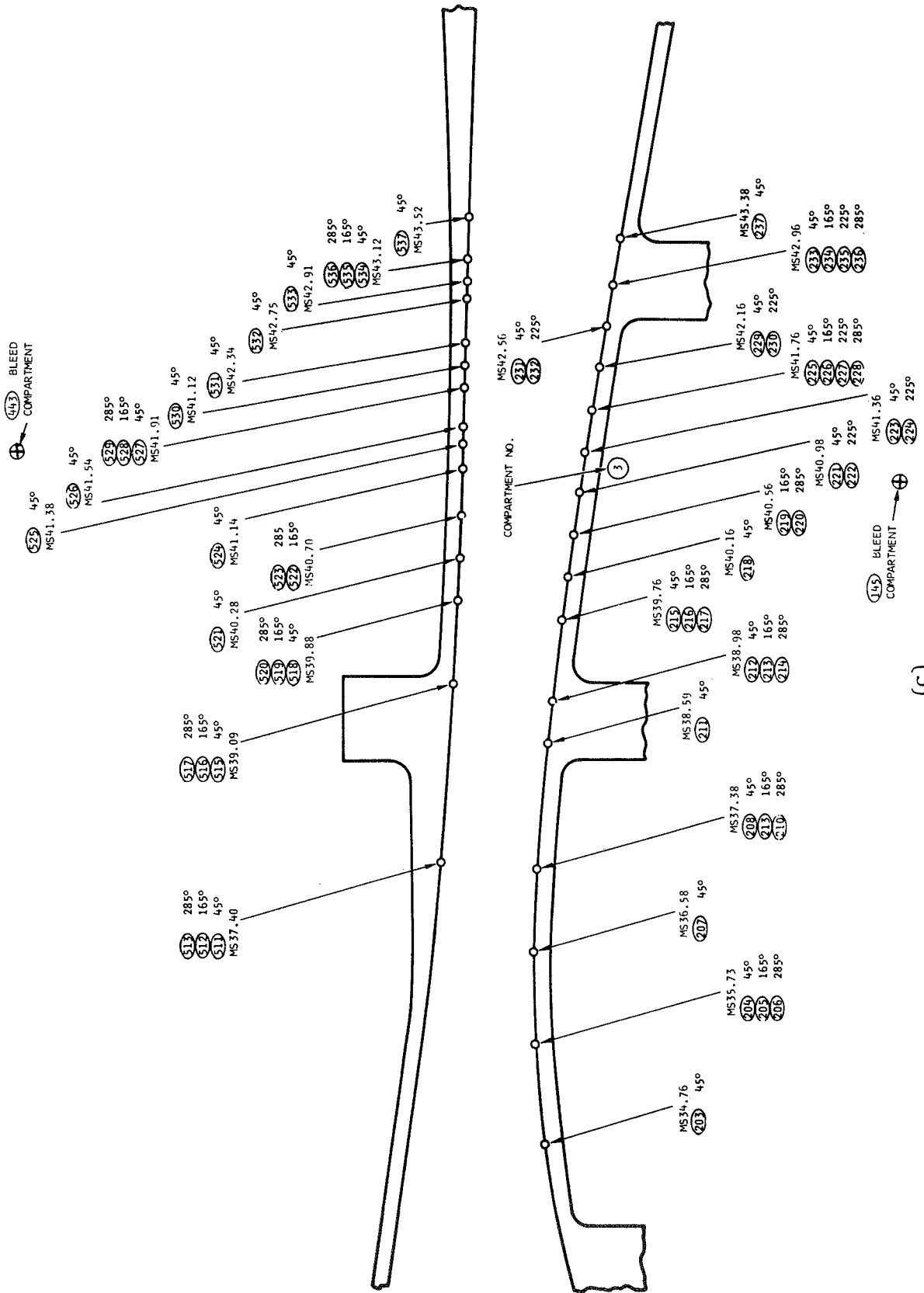
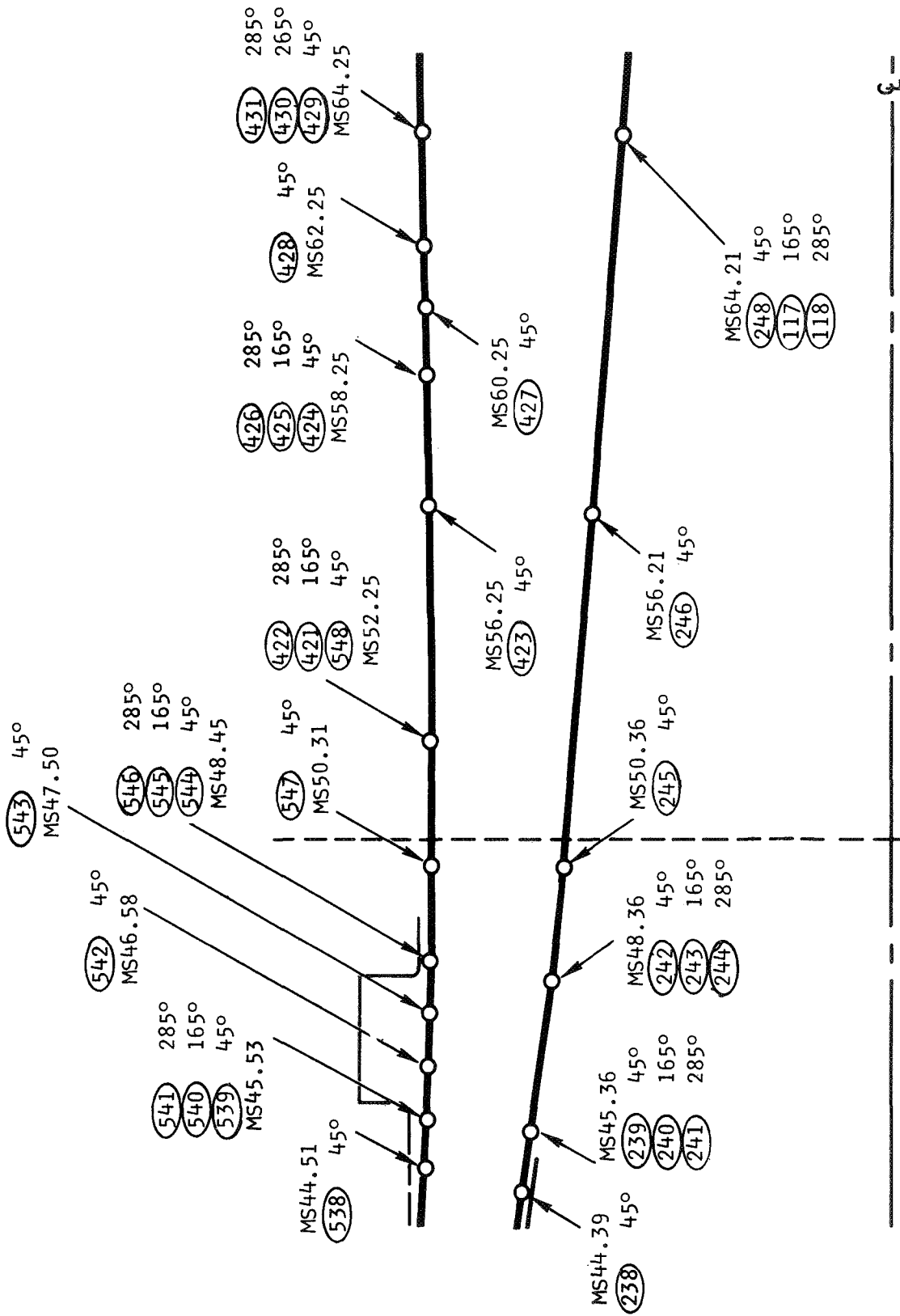


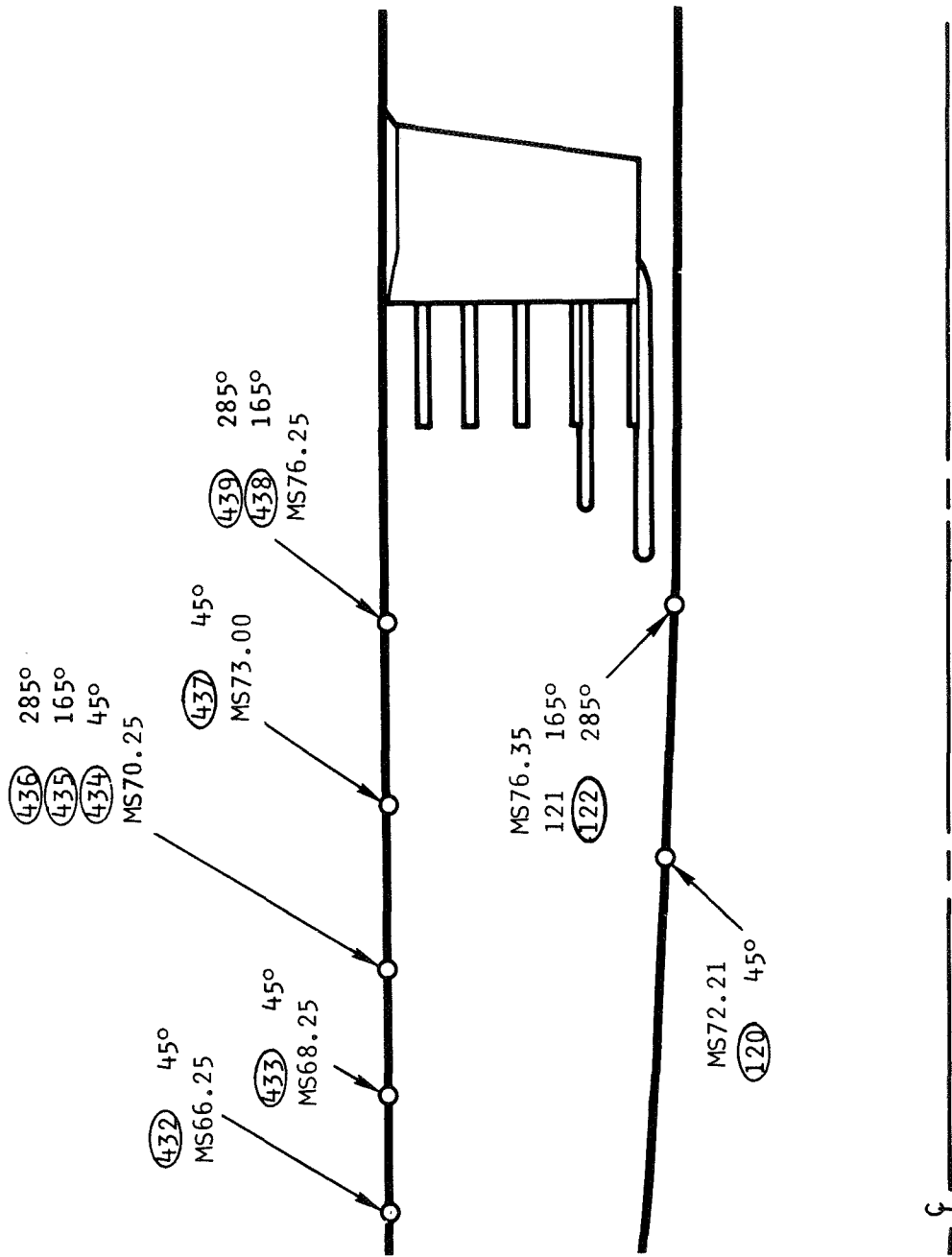
Figure 16.- Continued.

(c)

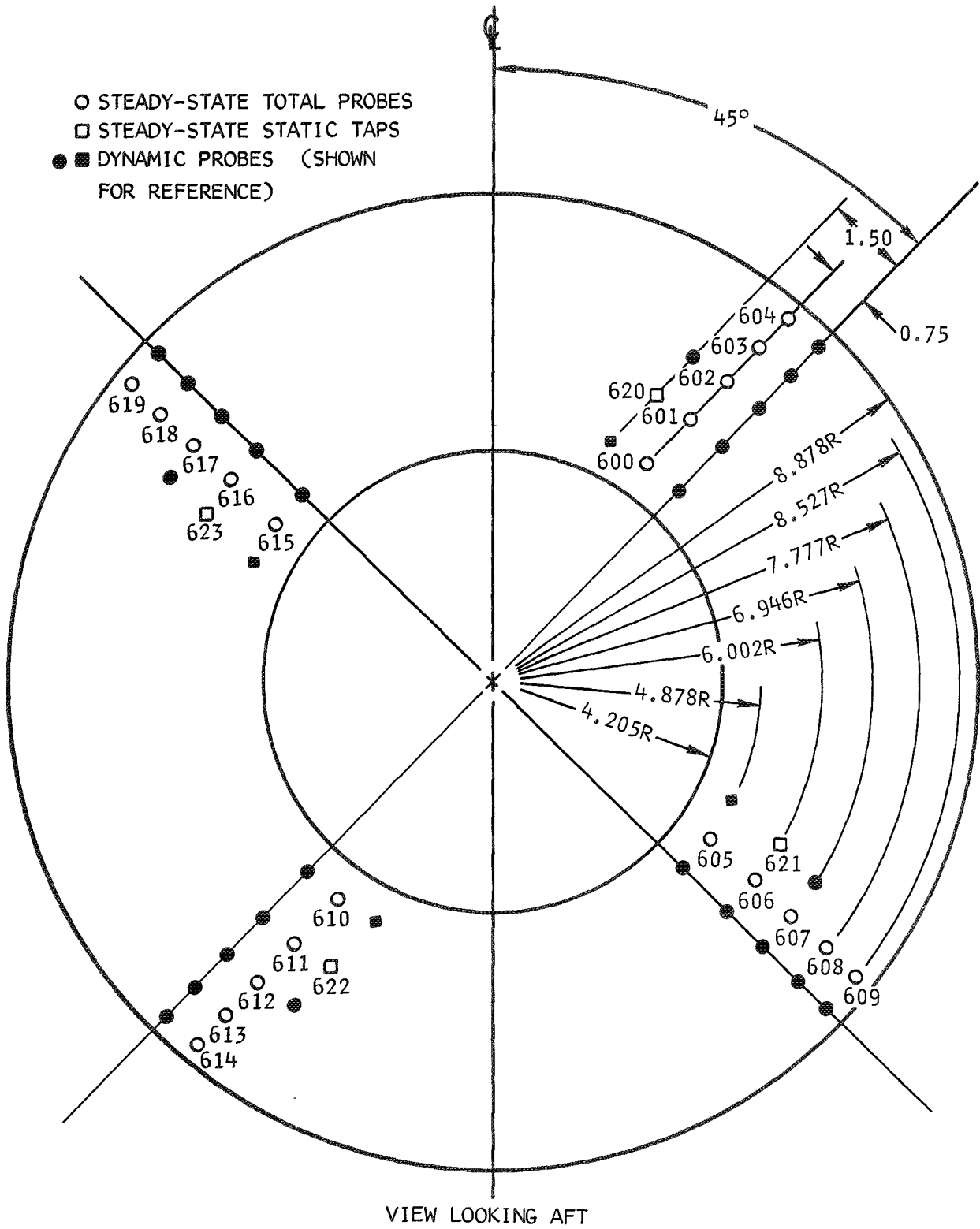


(d)

Figure 16. - Continued.



(e)
Figure 16.- Continued.



(f)

Figure 16.- Concluded.

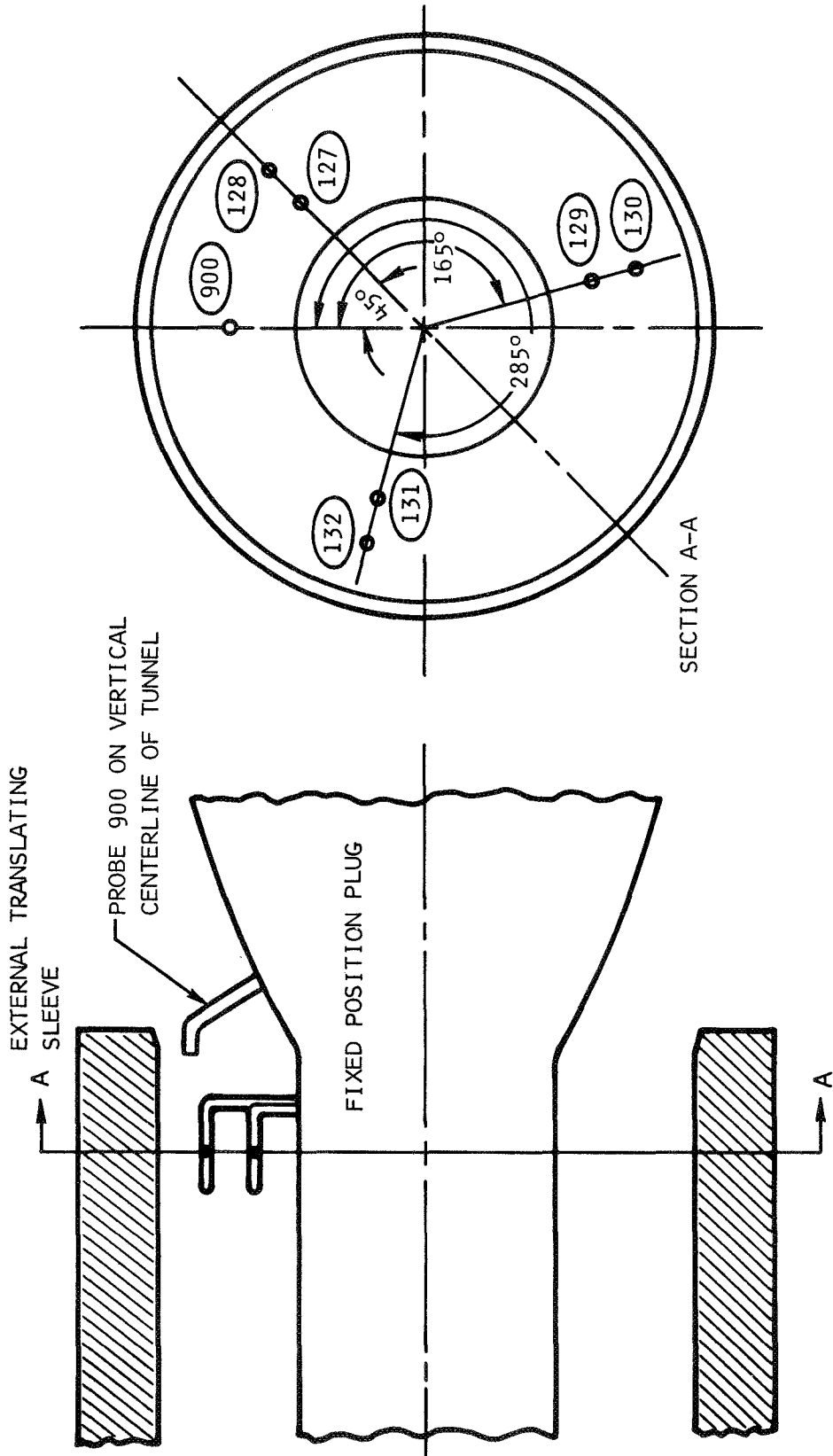


Figure 17. Metering nozzle and instrumentation.

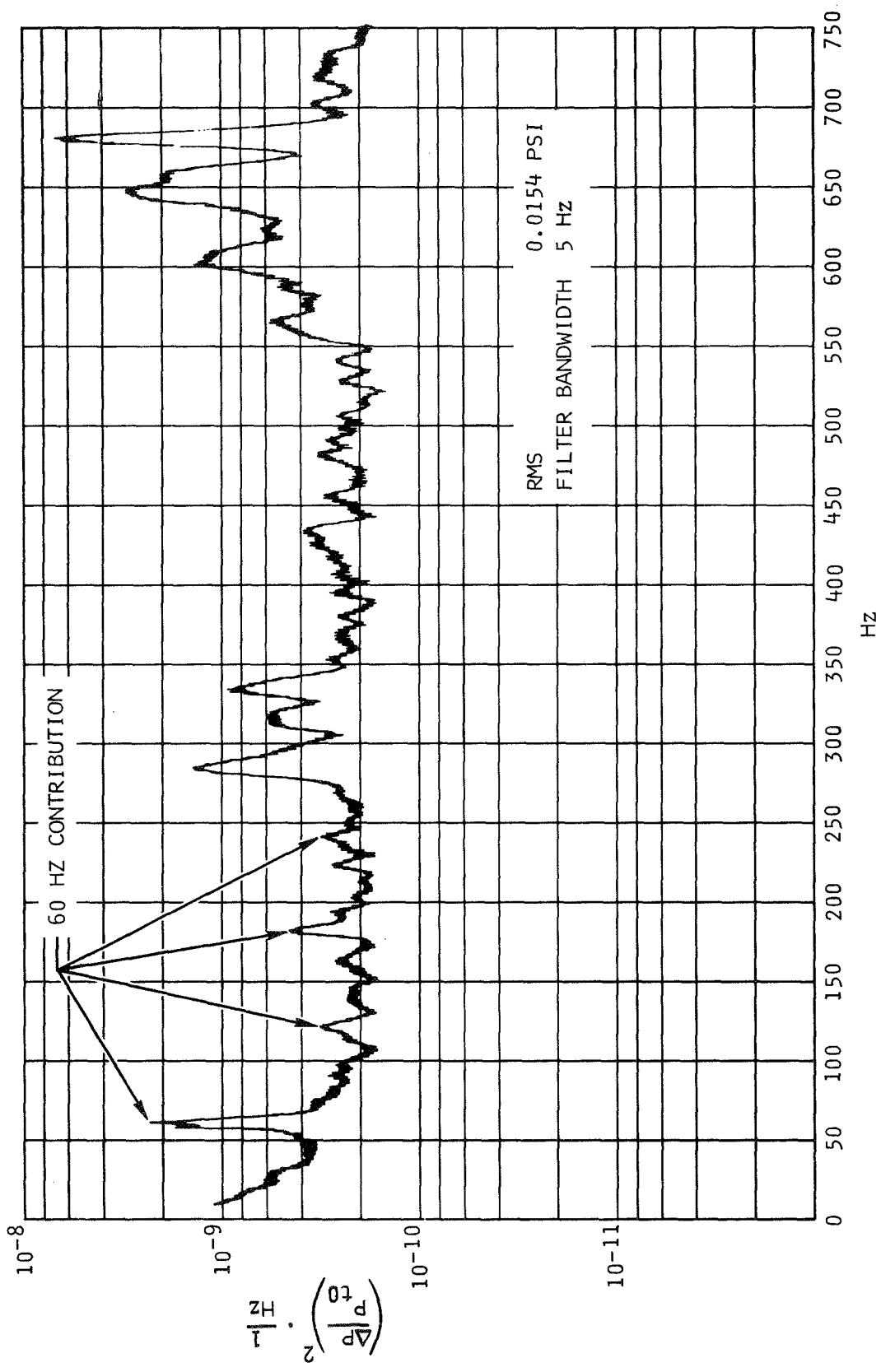


Figure 18.- Tunnel flow power spectral density, probe 802, $M_0 = 2.6$, $\overline{P_{t2}}/P_{t0} = 0.918$

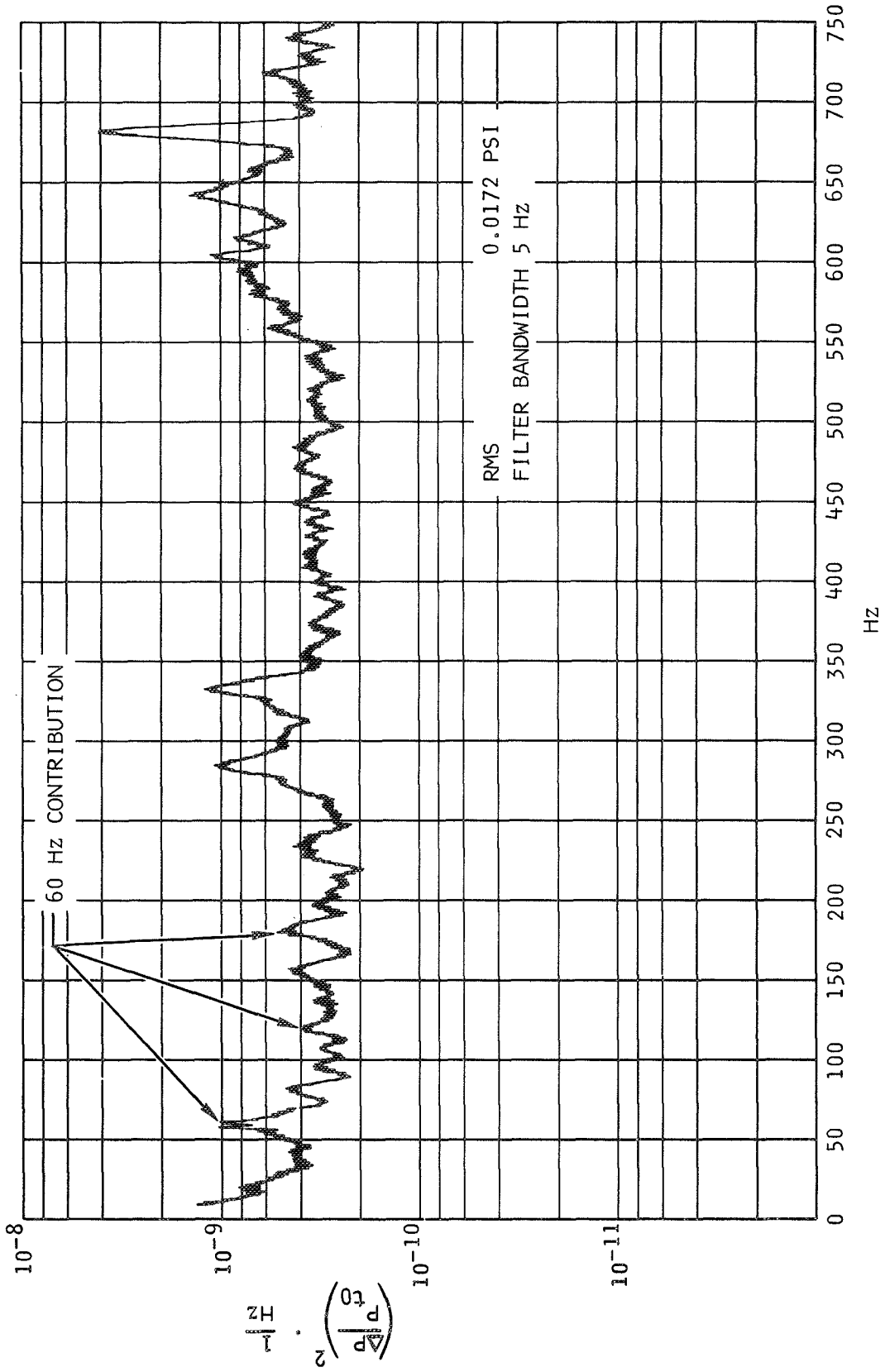


Figure 19.- Tunnel flow power spectral density, probe 802, $M_0 = 3.0$, $\overline{P_{t2}/P_{t0}} = 0.877$

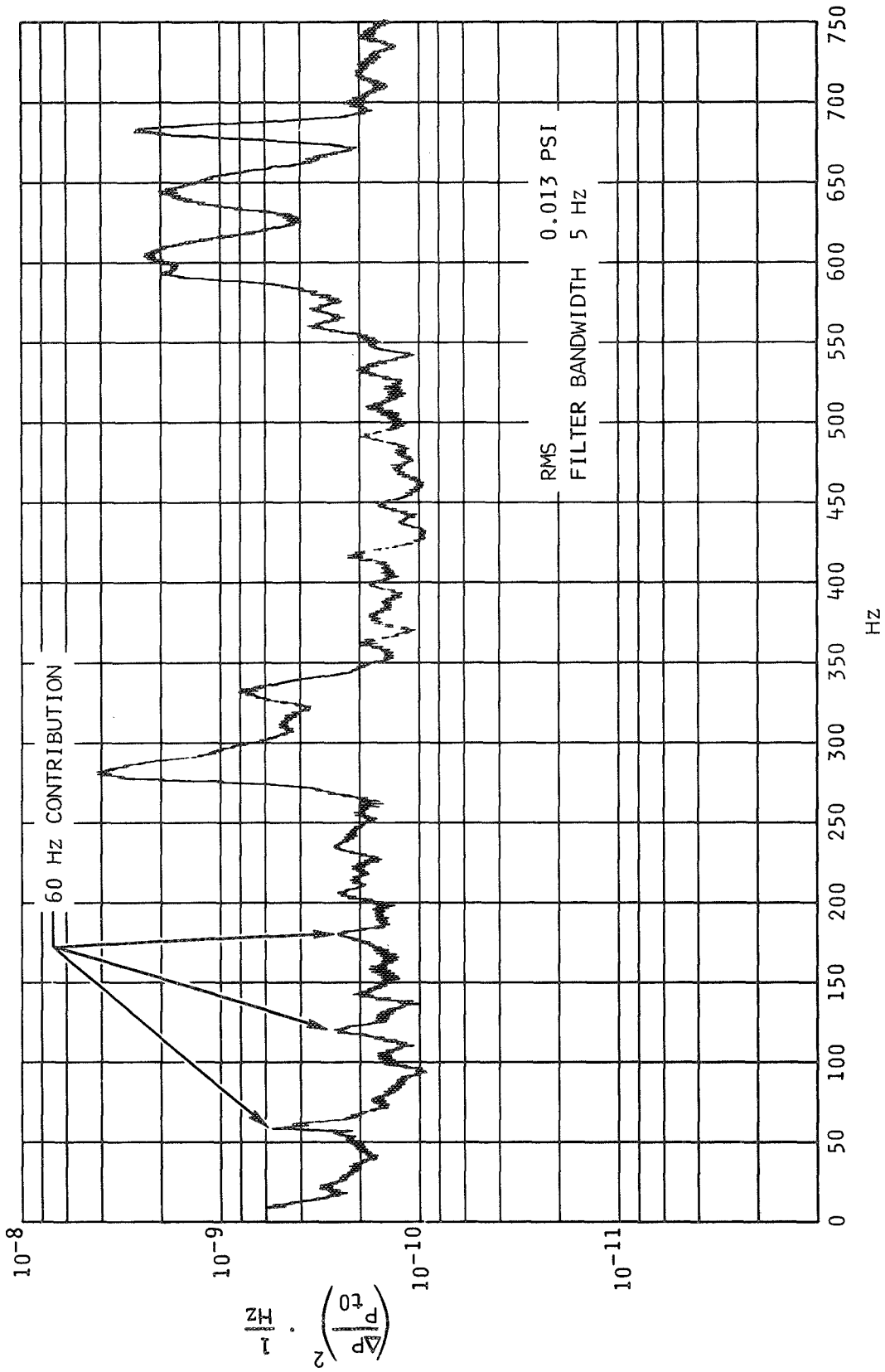


Figure 20.- Tunnel flow power spectral density, probe 802, $M_0 = 3.0$, $\overline{P_{t2}}/P_{t0} = 0.565$.

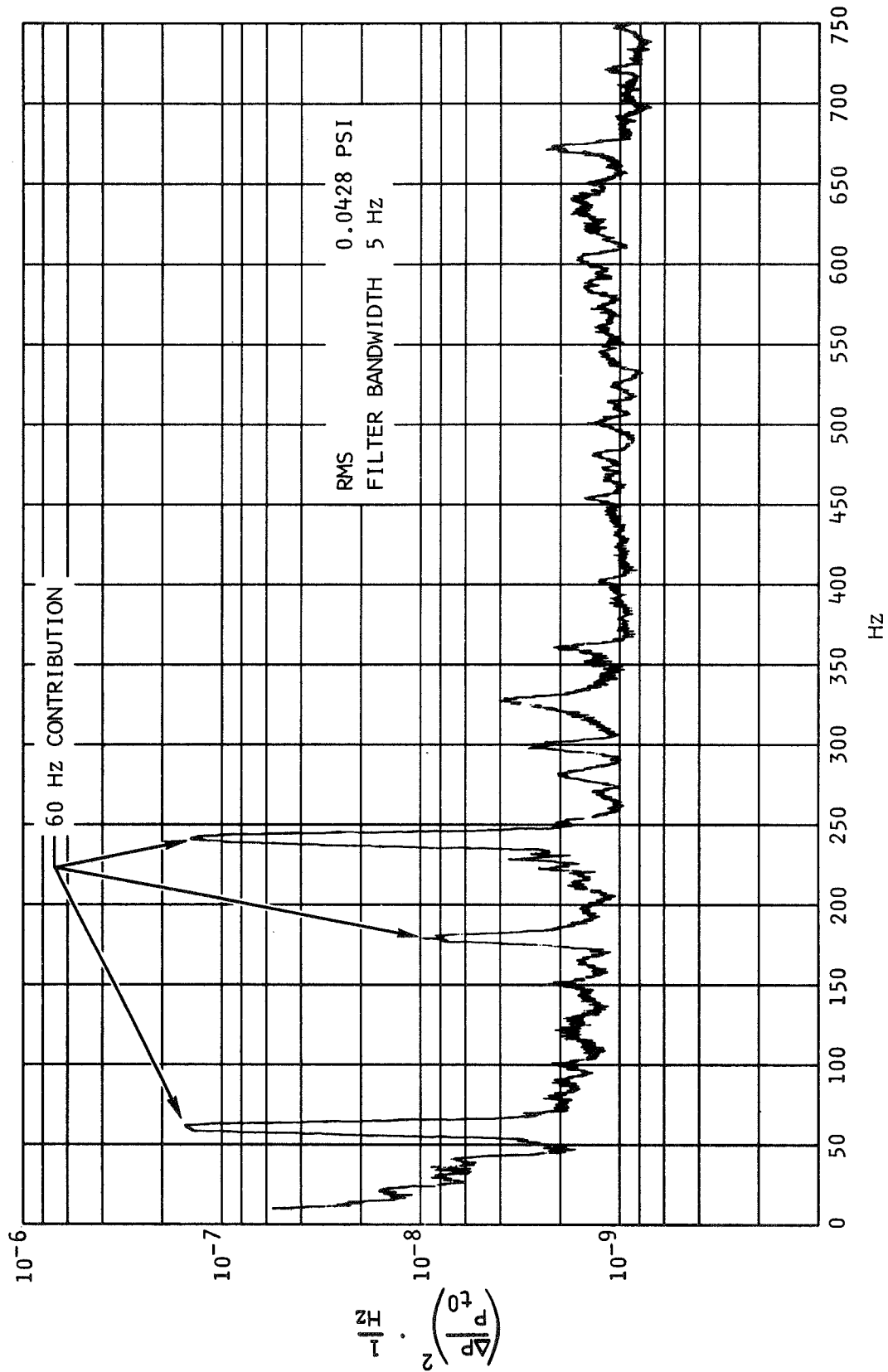


Figure 21.- Tunnel flow power spectral density with vane installed, probe 802, $M_0 = 3.0$, $\bar{P}_{t2}/P_{t0} = 0.785$

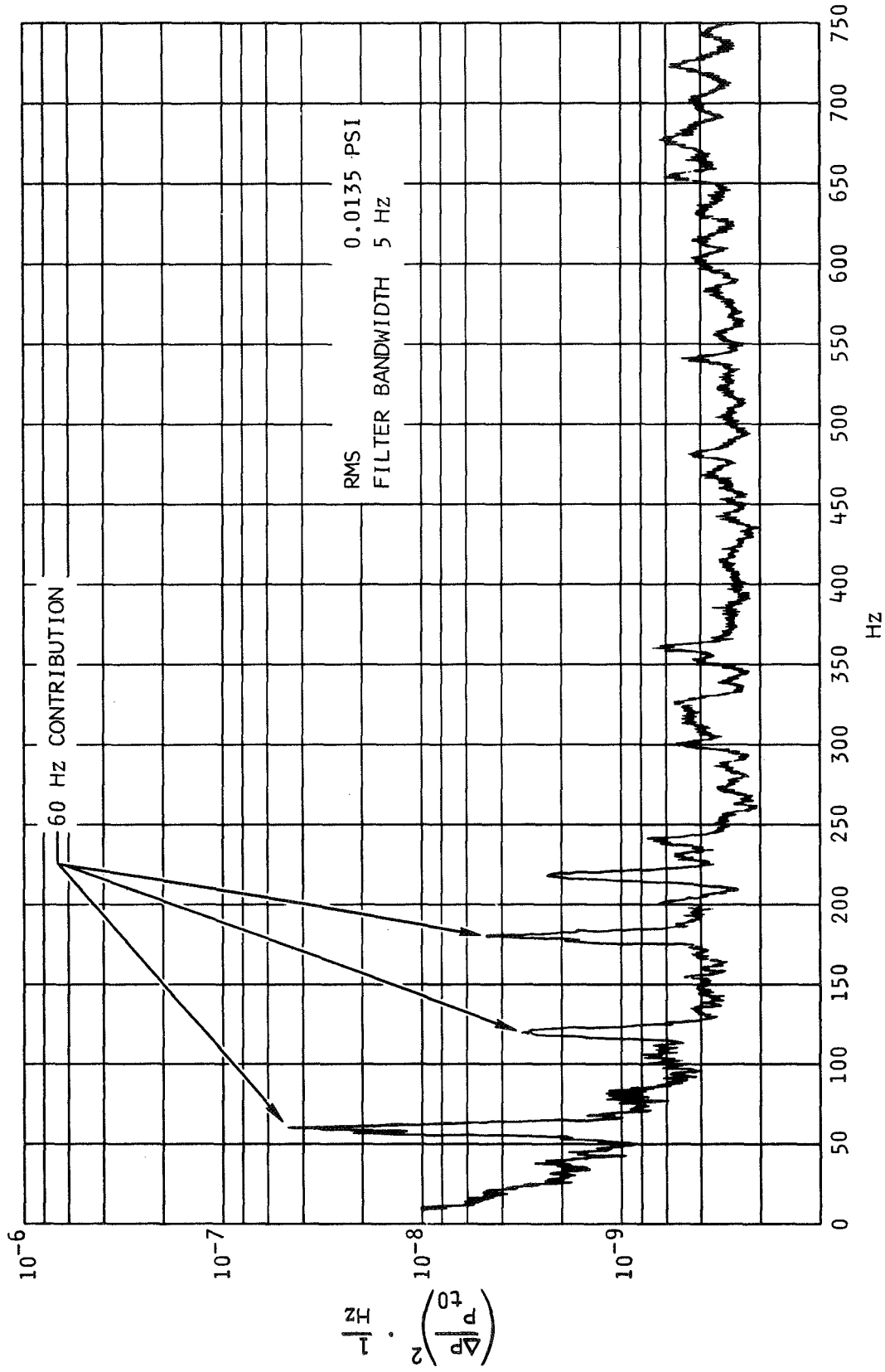


Figure 22.- Tunnel flow power spectral density with vane installed, probe 804,

$$M_o = 3.0, \bar{P}_{t2}/P_{to} = 0.785$$

$M_0 = 3.0$
 VANE ANGLE = 0°

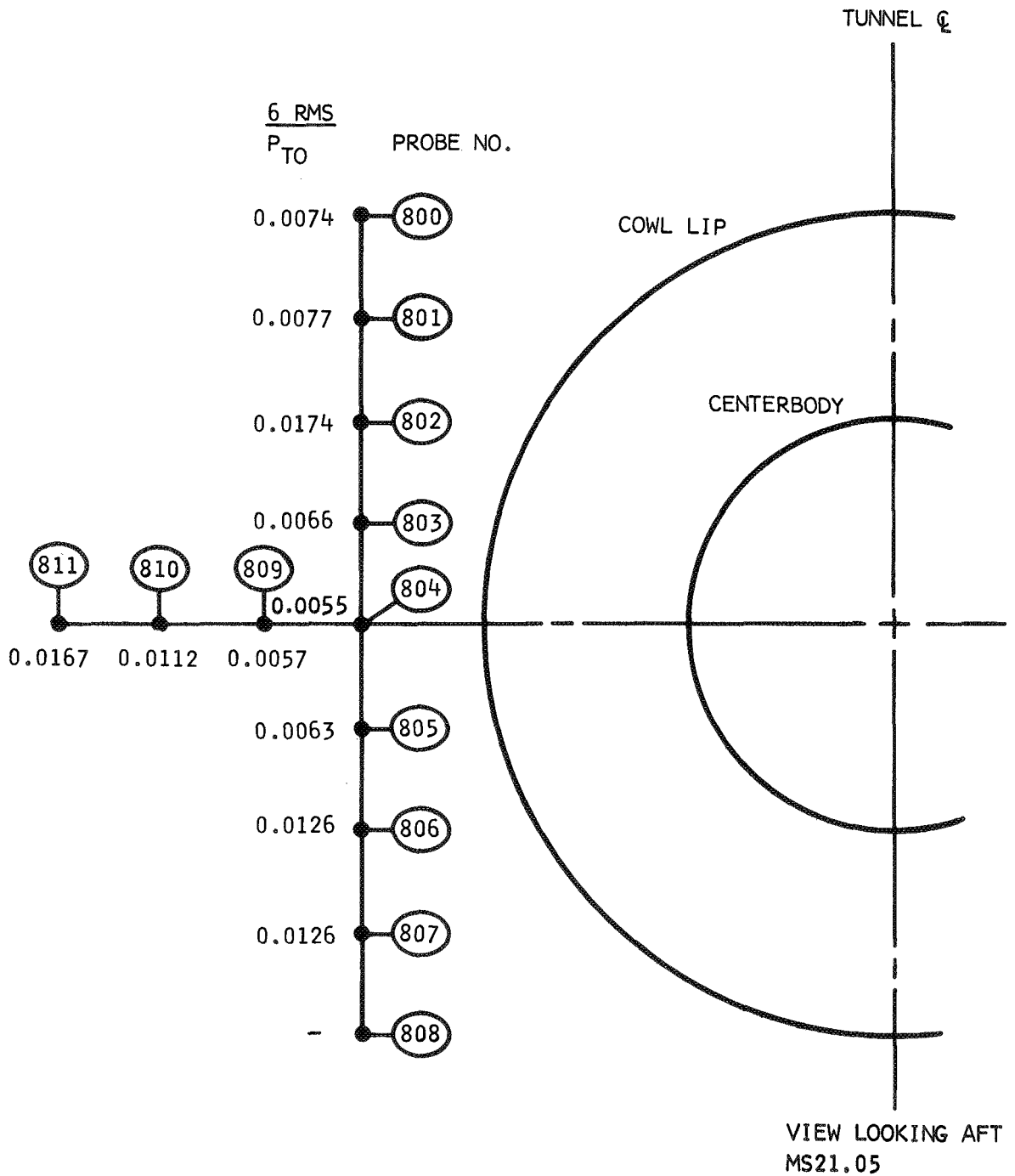


Figure 23.- Typical turbulence values, external rake pressure probes.

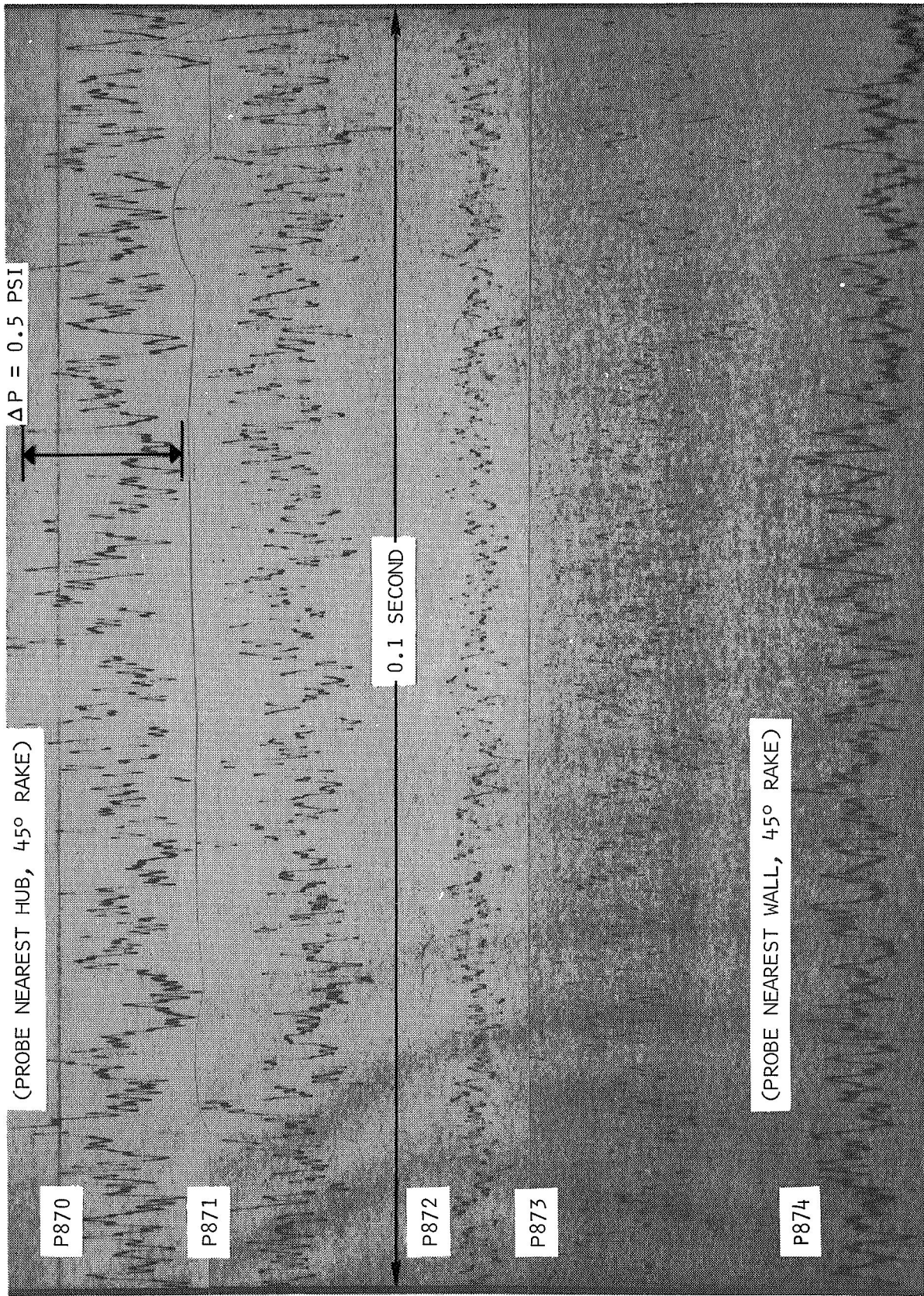


Figure 24.- Engine face total pressures vs time, $M_0 = 3.0$, $\bar{P}_{t2}/P_{t0} = 0.877$.

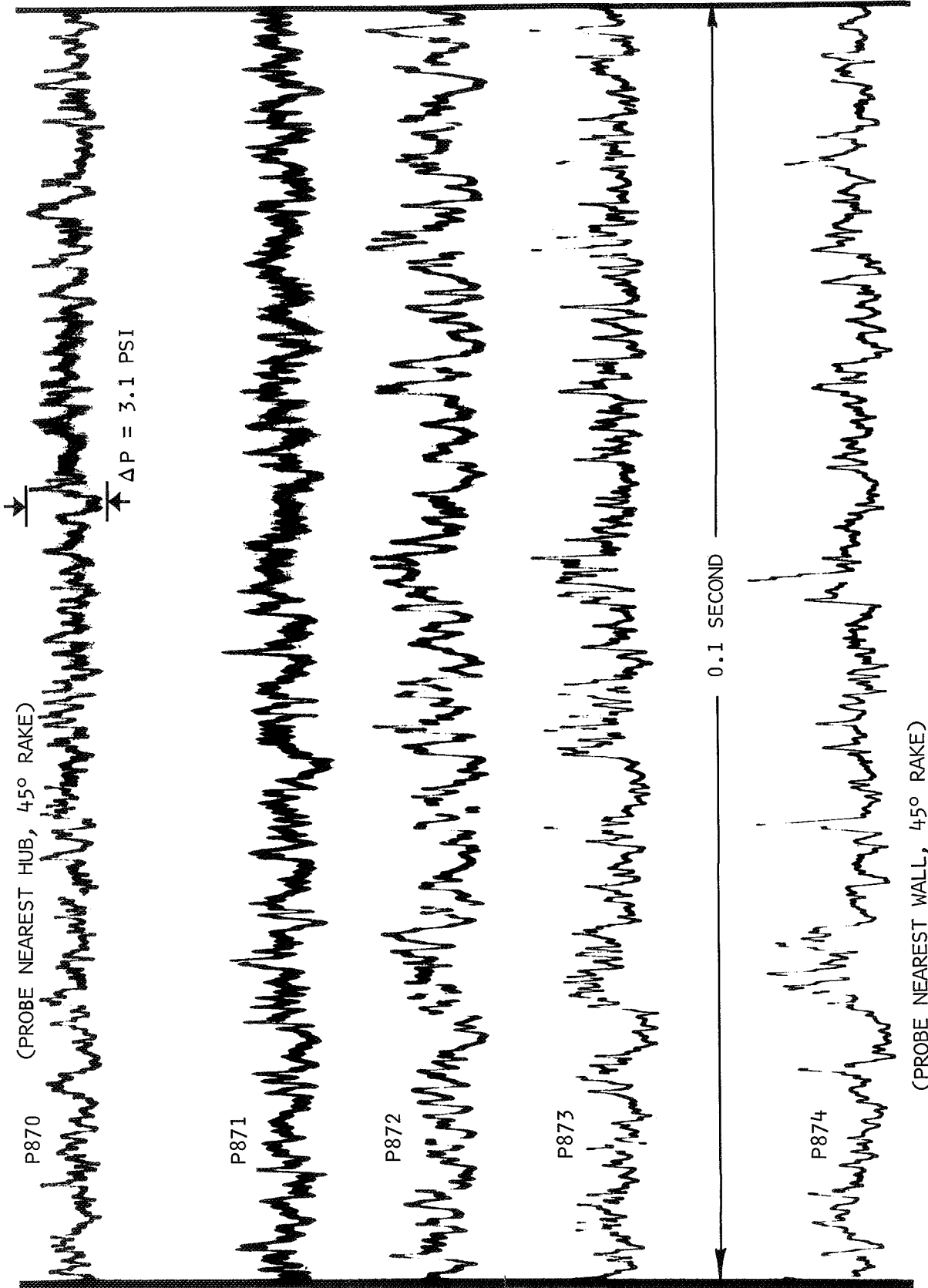
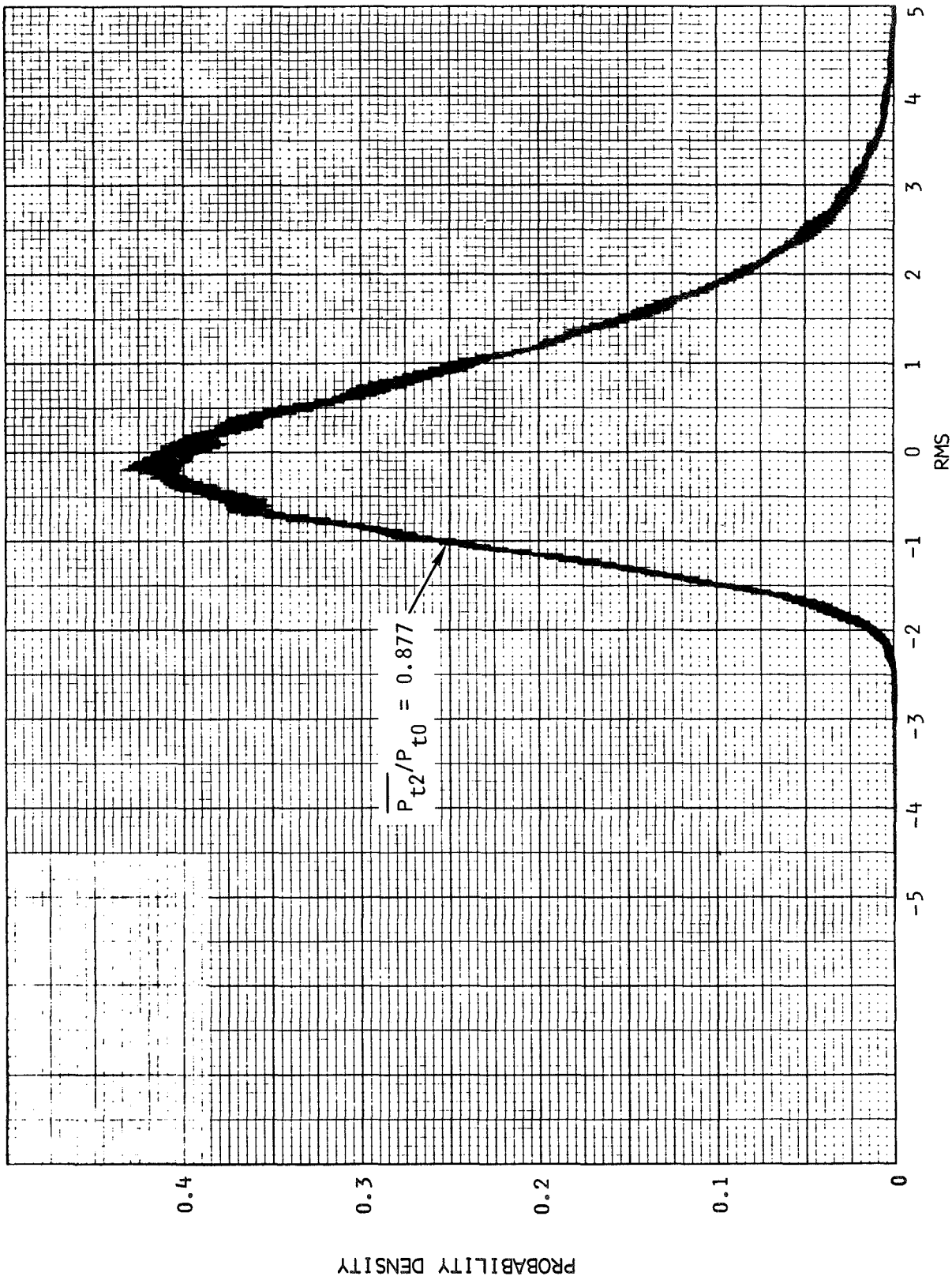
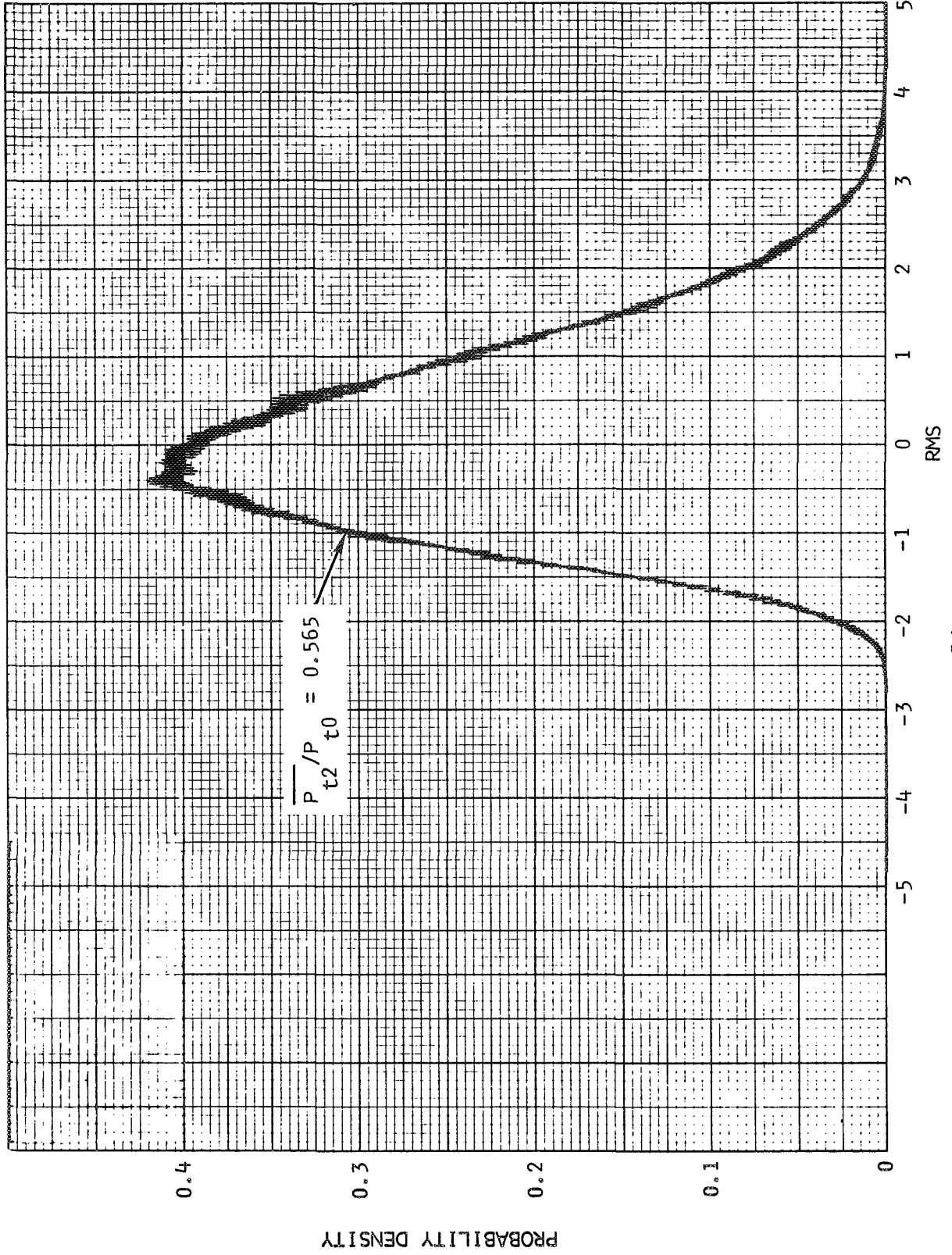


Figure 25.- Engine face total pressures vs time, $M_0 = 3.0$, $\overline{P_{t2}/P_{t0}} = 0.565$.

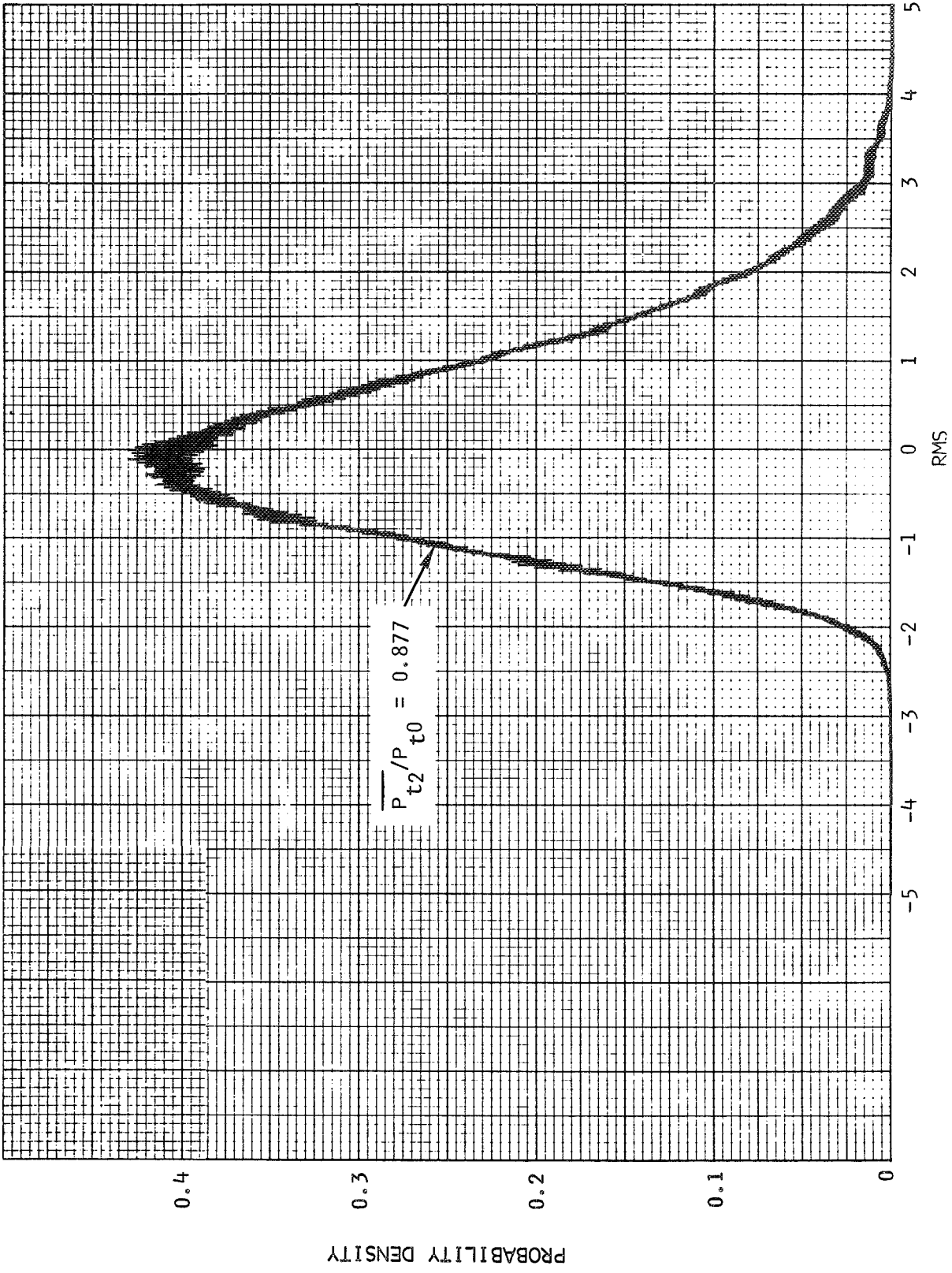


(a)

Figure 26.- Probability density, probe P870, $M_0 = 3.0$.

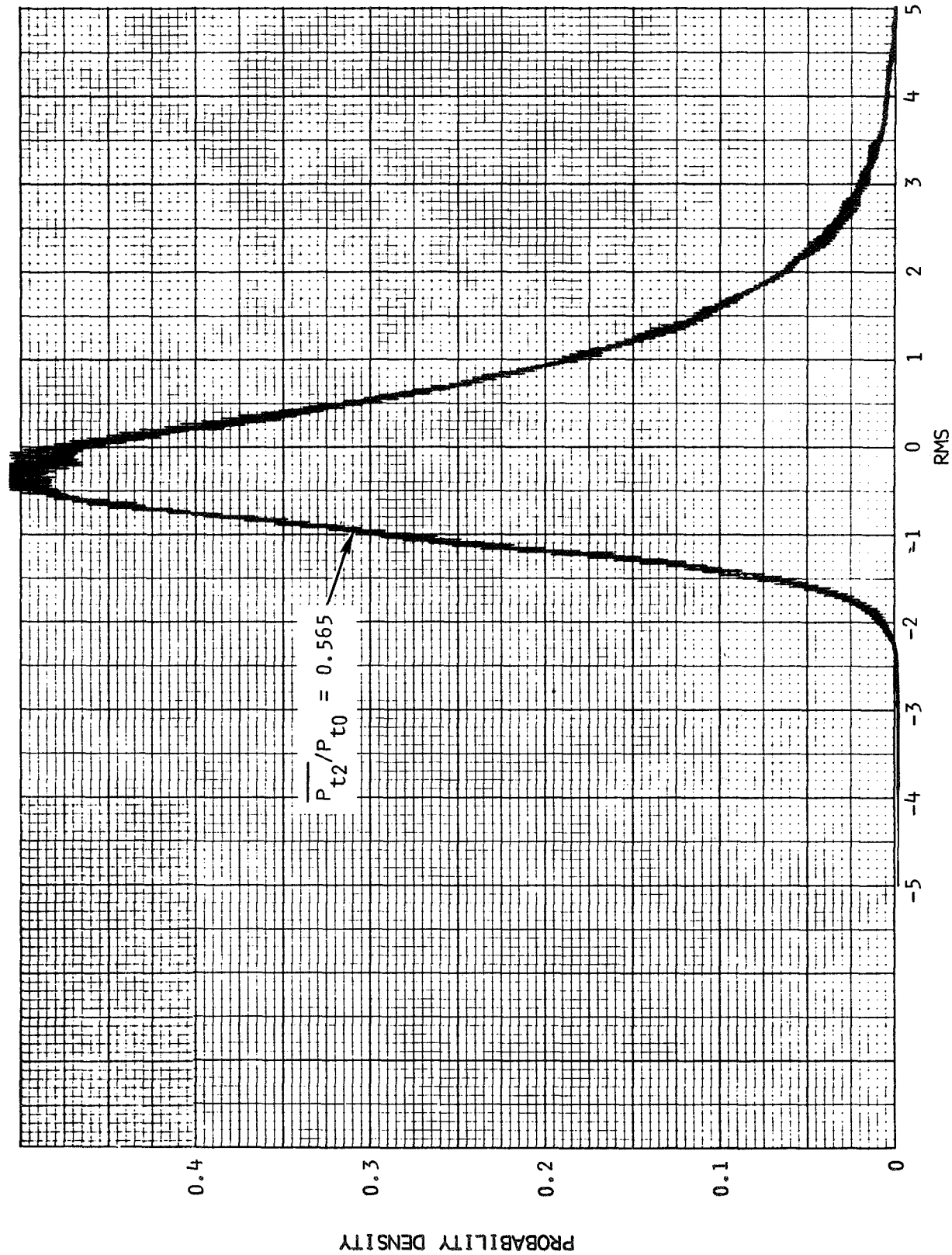


(b)
Figure 26.- Concluded.



(a)

Figure 27.- Probability density, probe P874, $M_O = 3.0$.



(b)
Figure 27.- Concluded

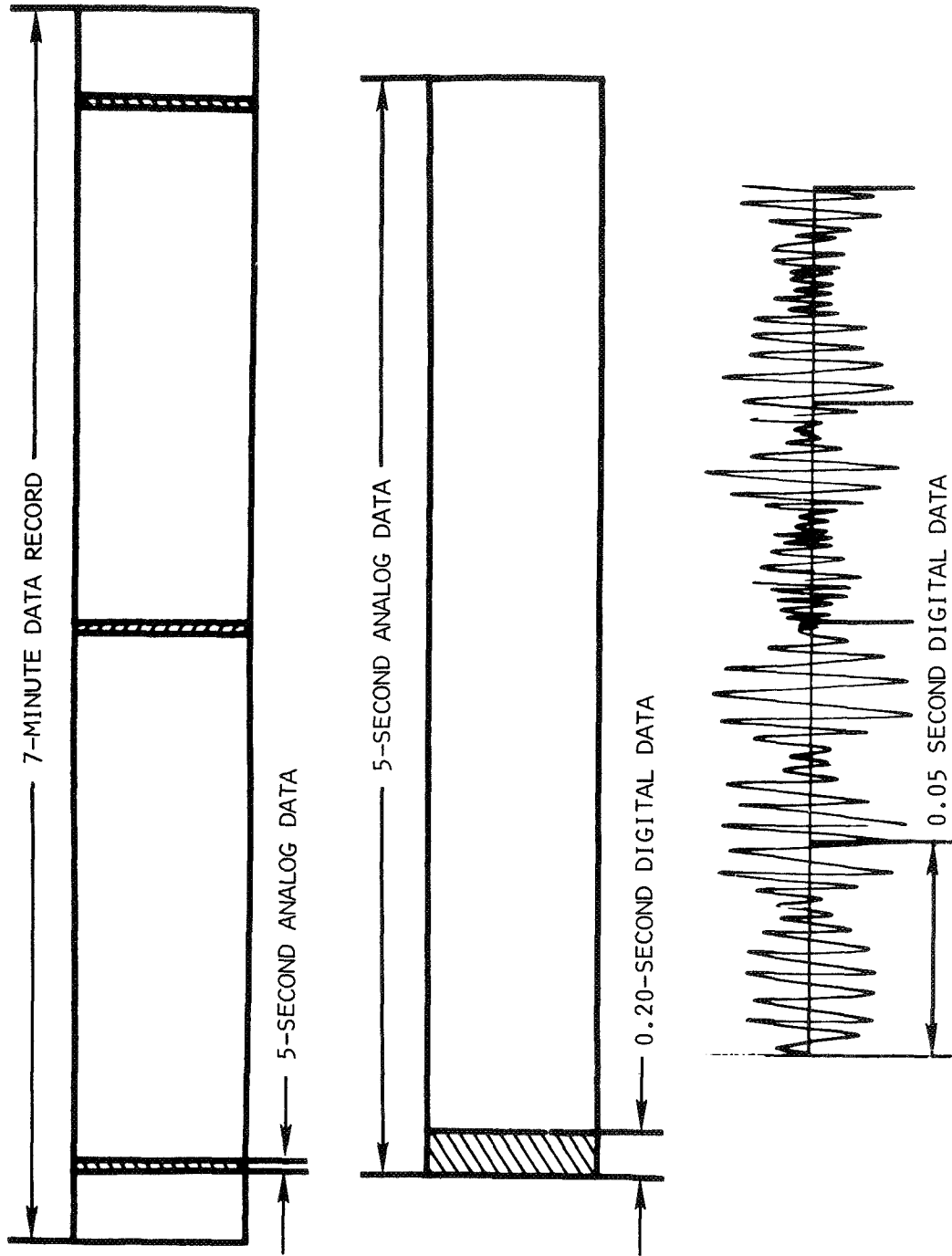
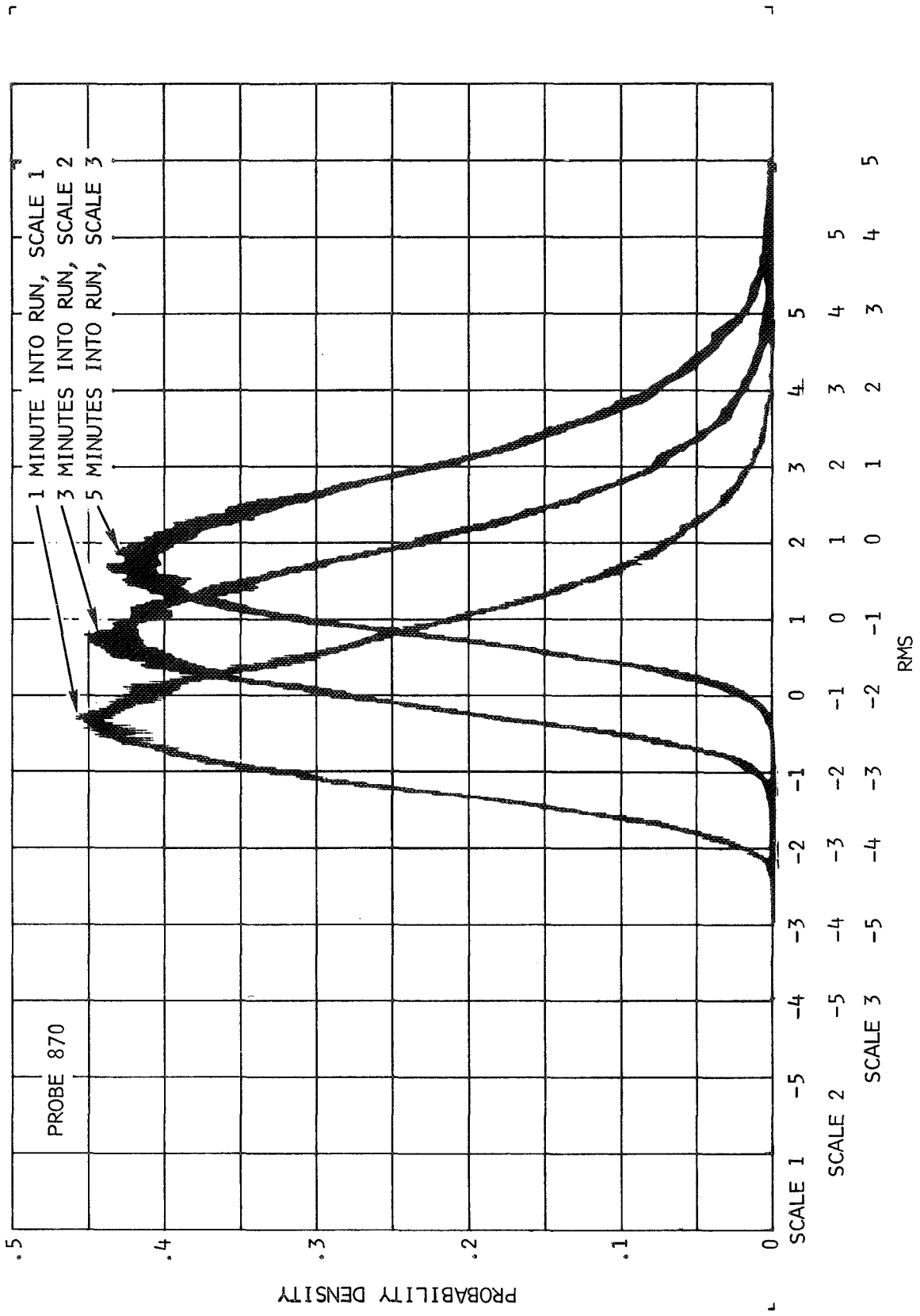
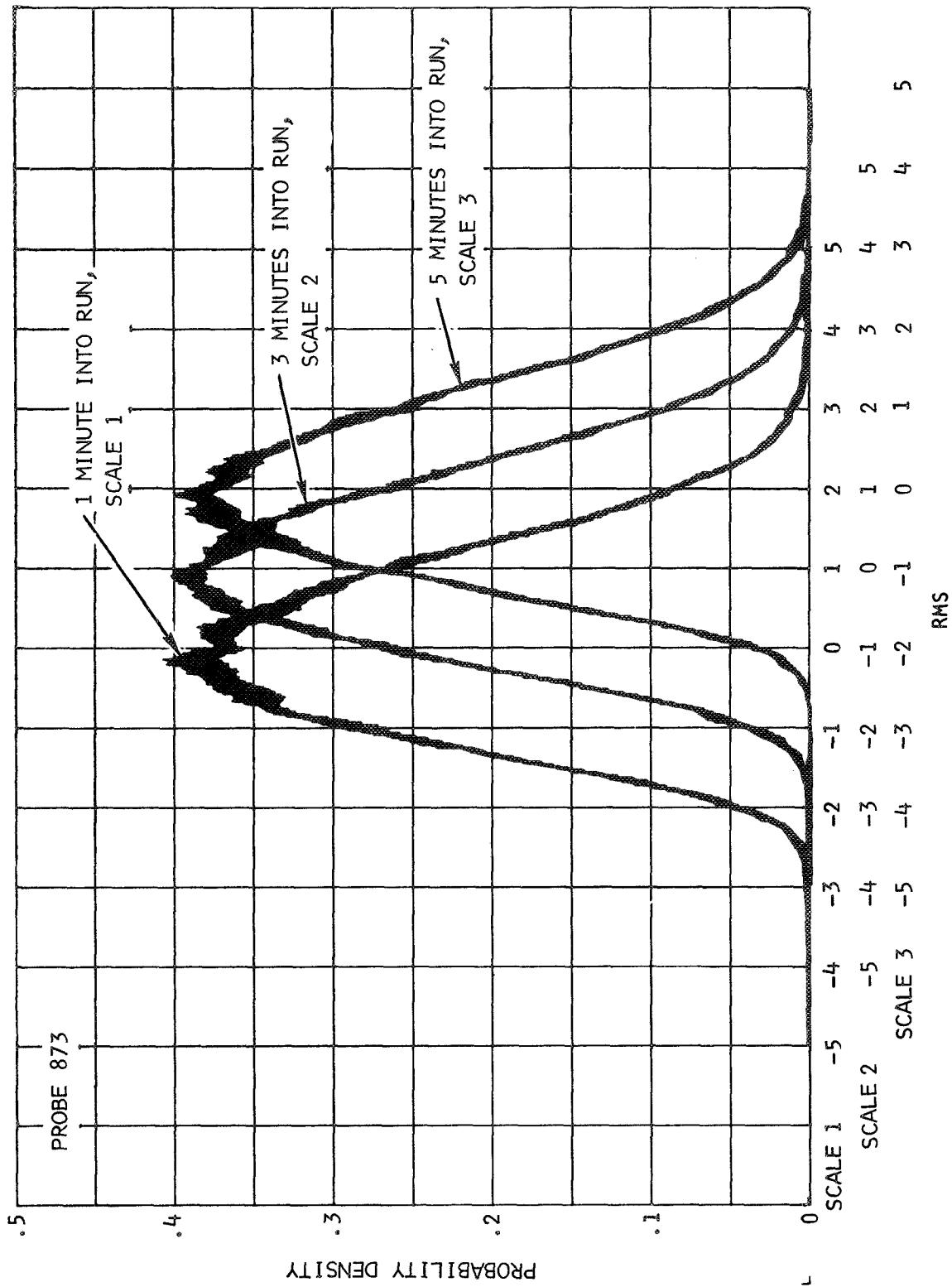


Figure 28.- Statistical data intervals.



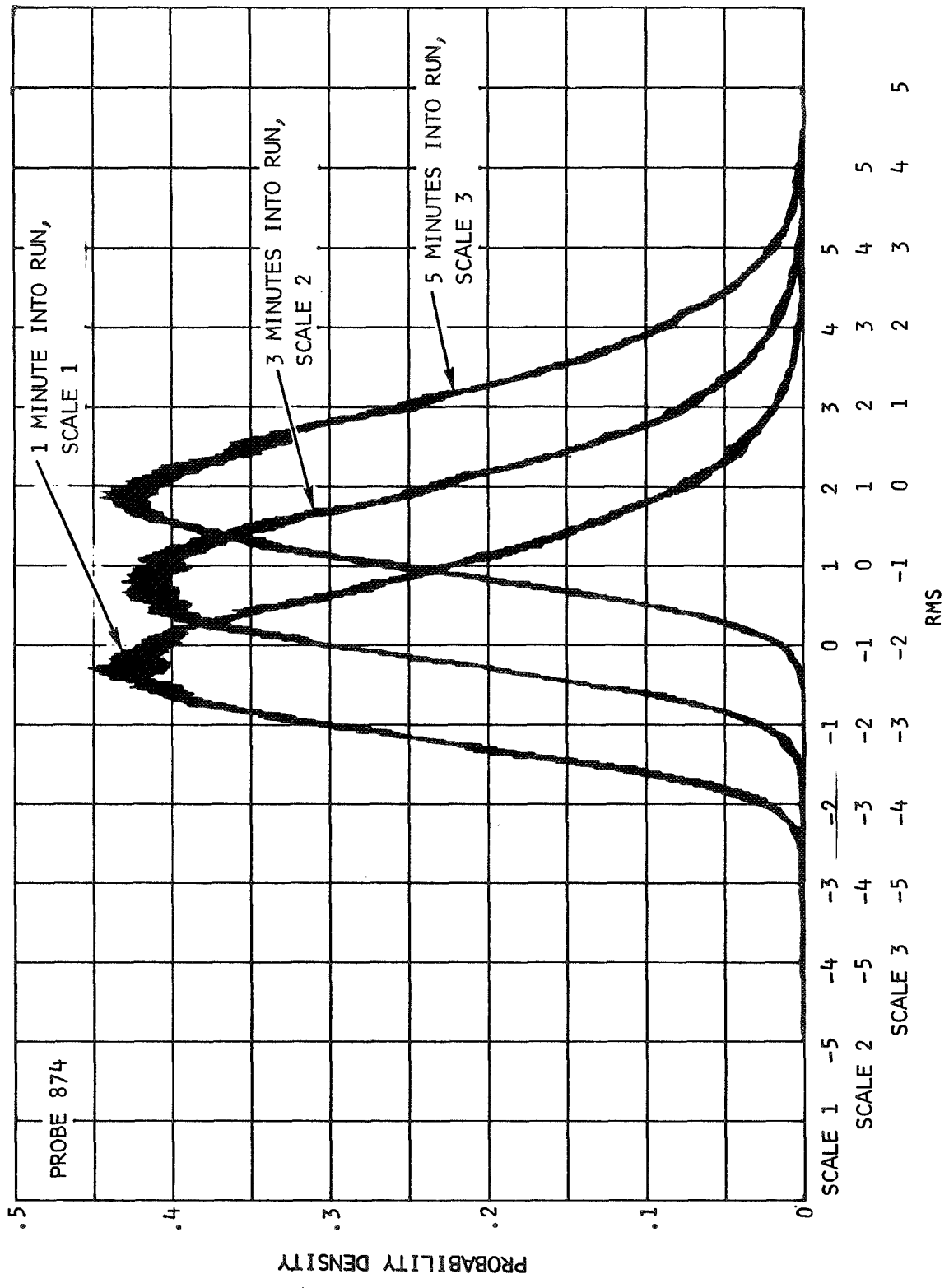
(a)

Figure 29.- Probability density functions for different 5-second intervals, $M_0 = 3.0$, $\bar{P}_{t_2}/P_{t_0} = 0.877$.



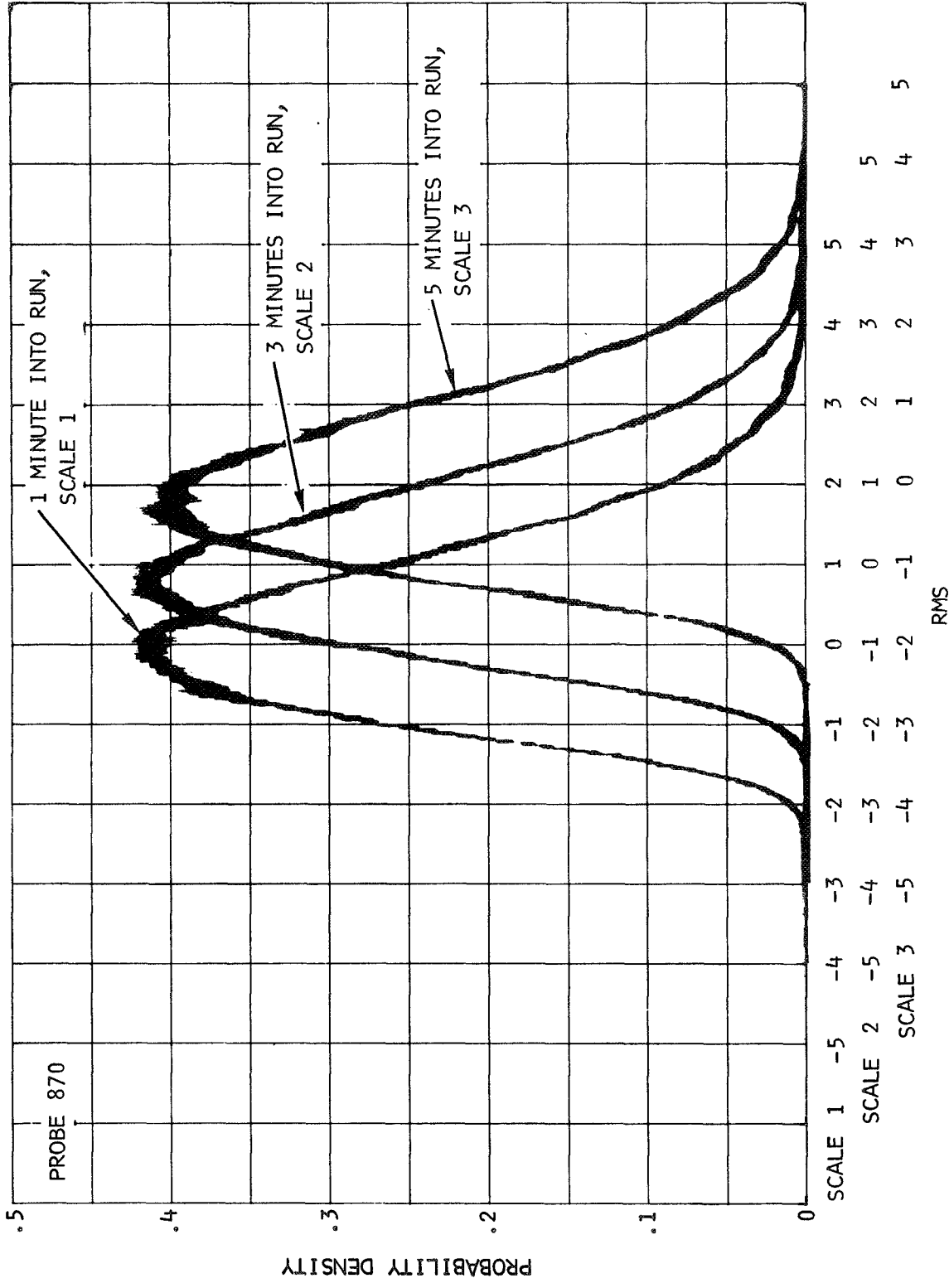
(b)

Figure 29.- Continued.



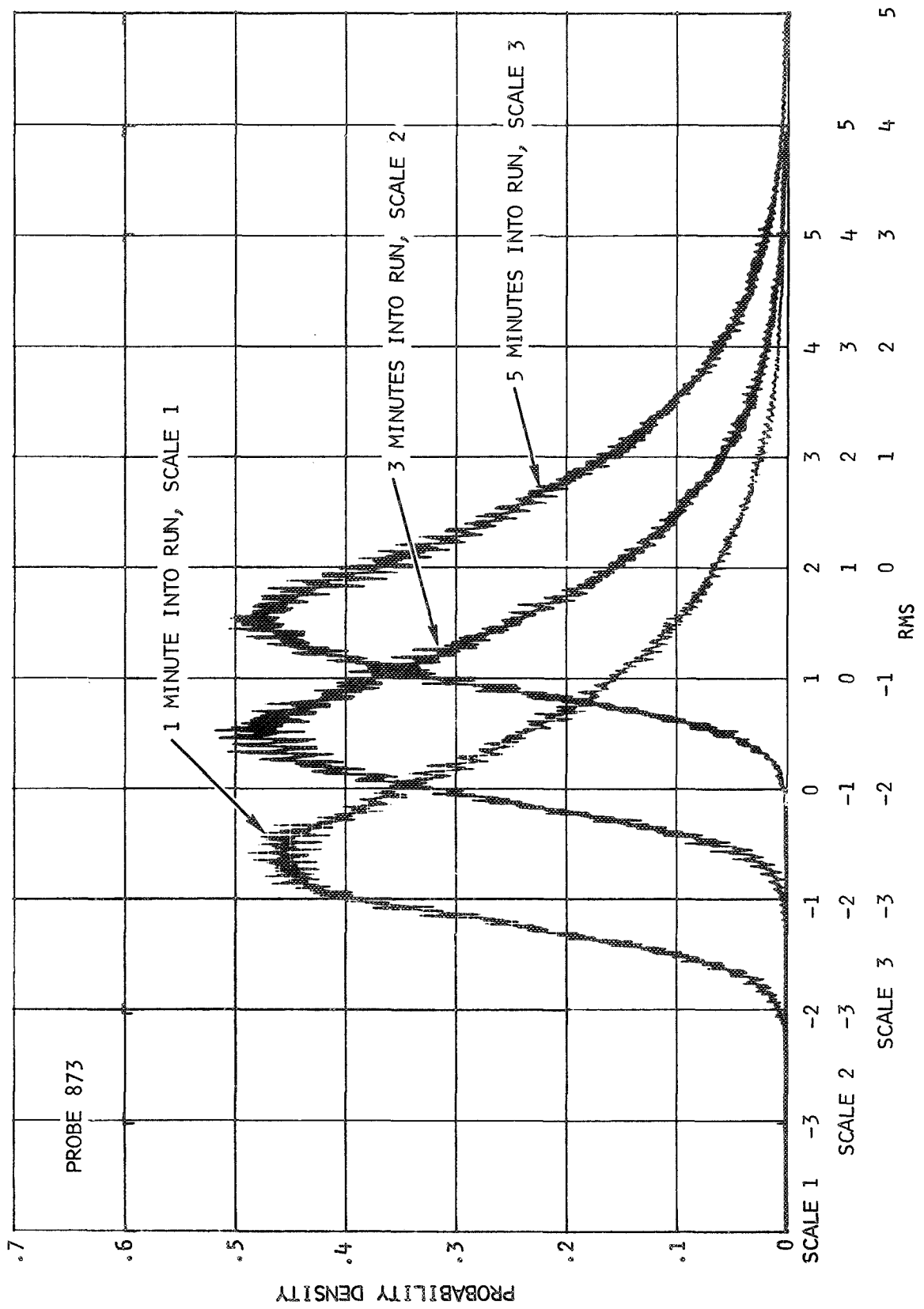
(c)

Figure 29.- Concluded.

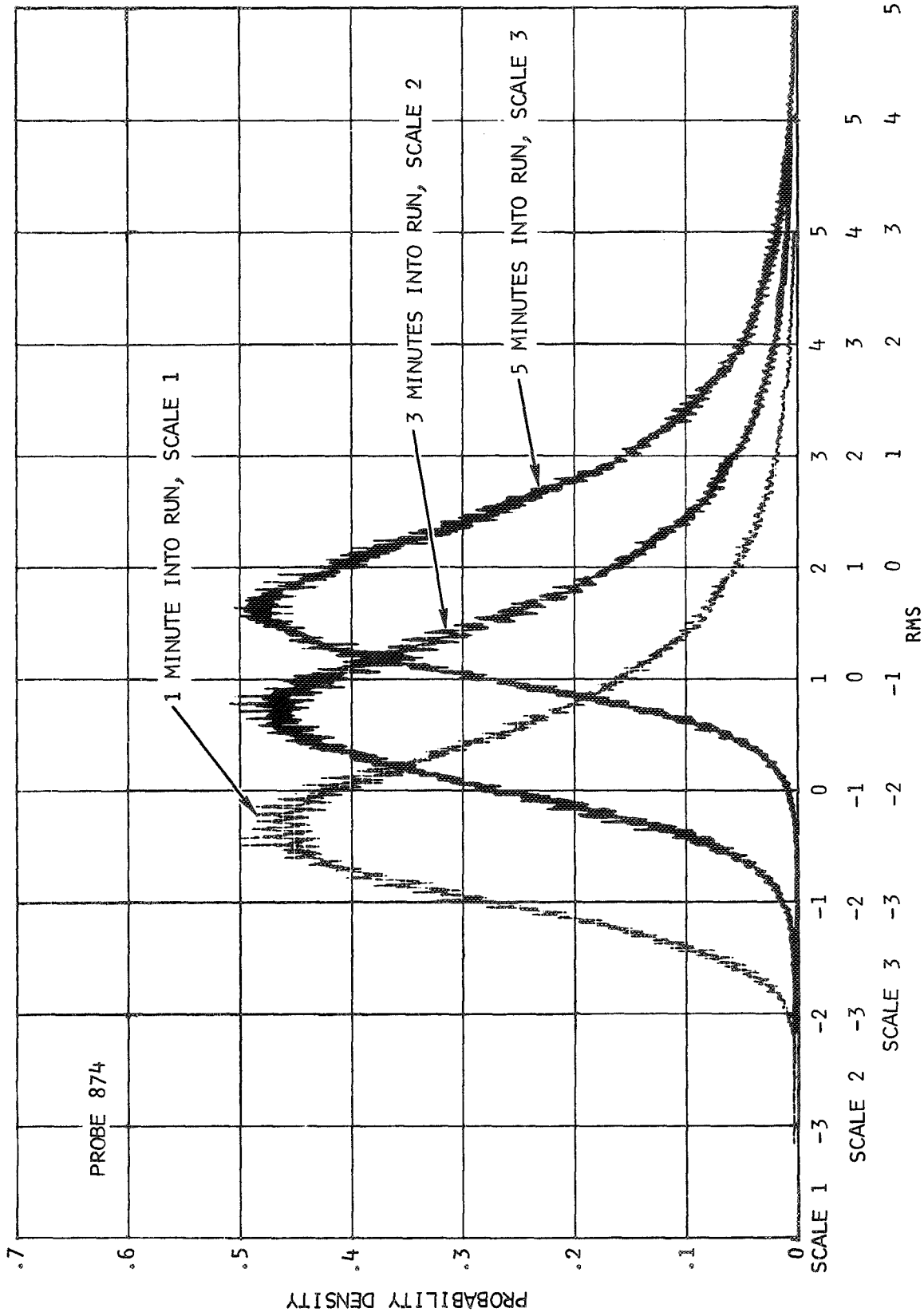


(a)

Figure 30.- Probability density functions for different 5-second intervals, $M_0 = 3.0$, $\bar{P}_{t2}/P_{t0} = 0.565$.

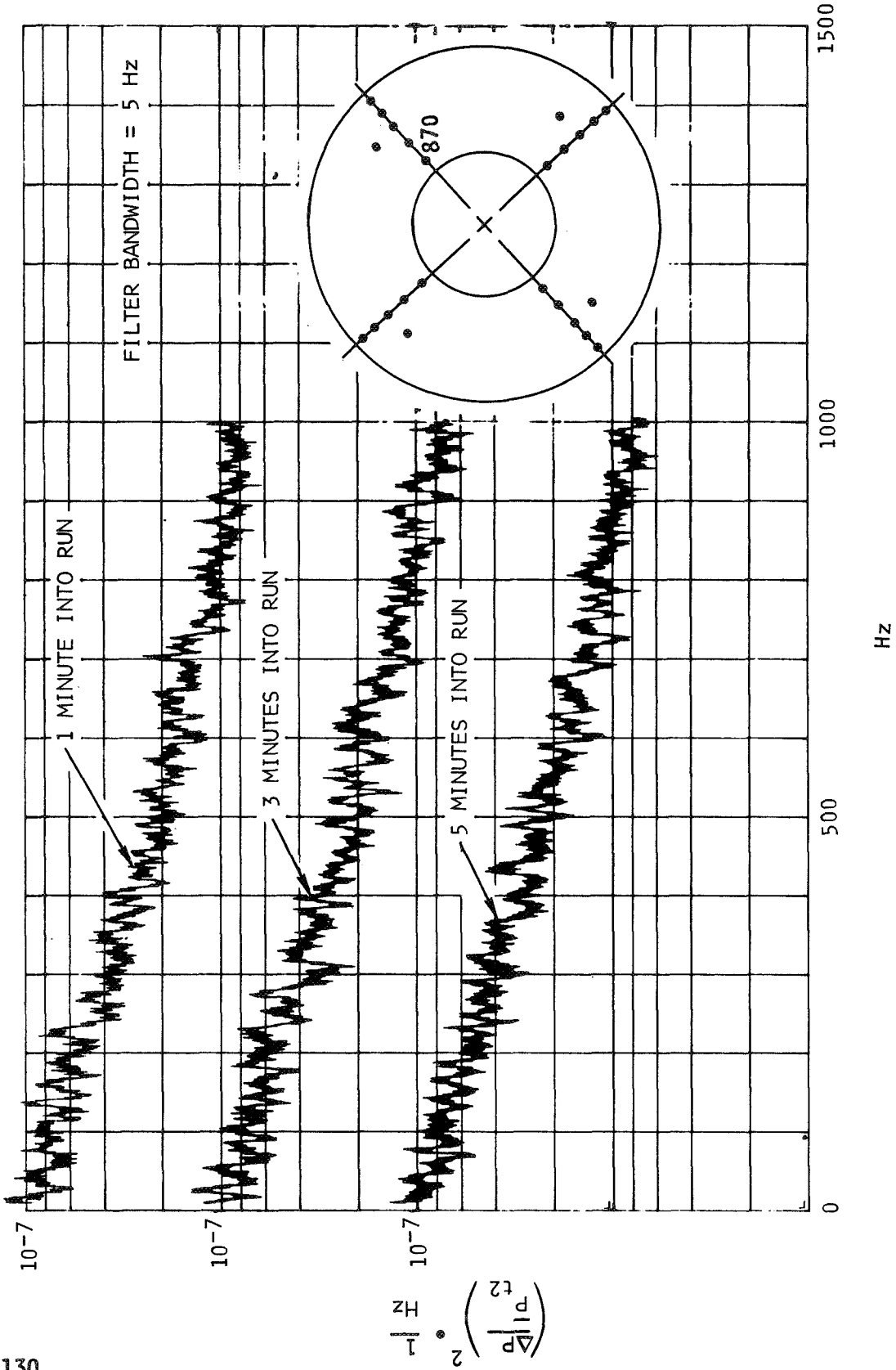


(b)
Figure 30.- Continued.



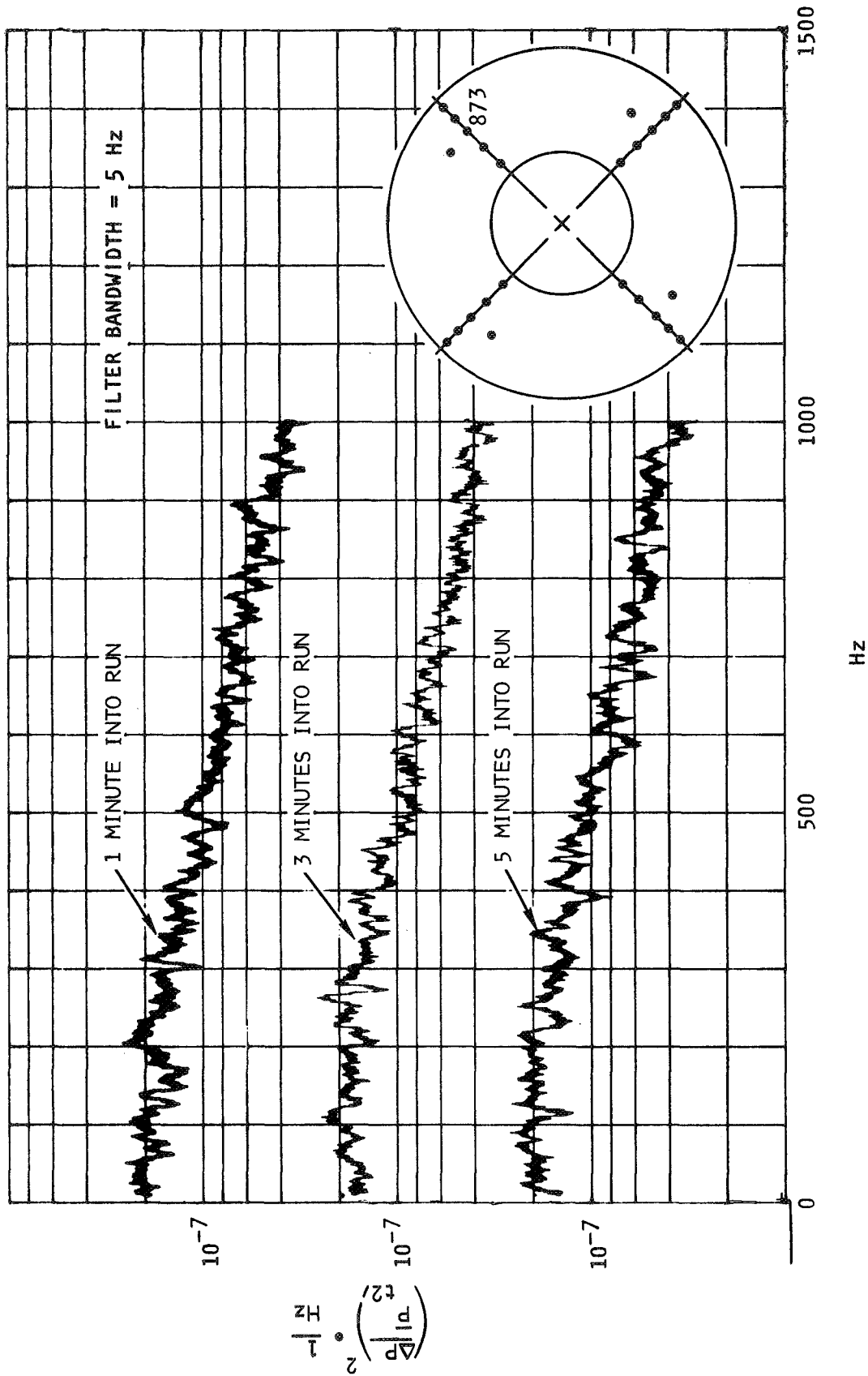
(c)

Figure 30.- Concluded.



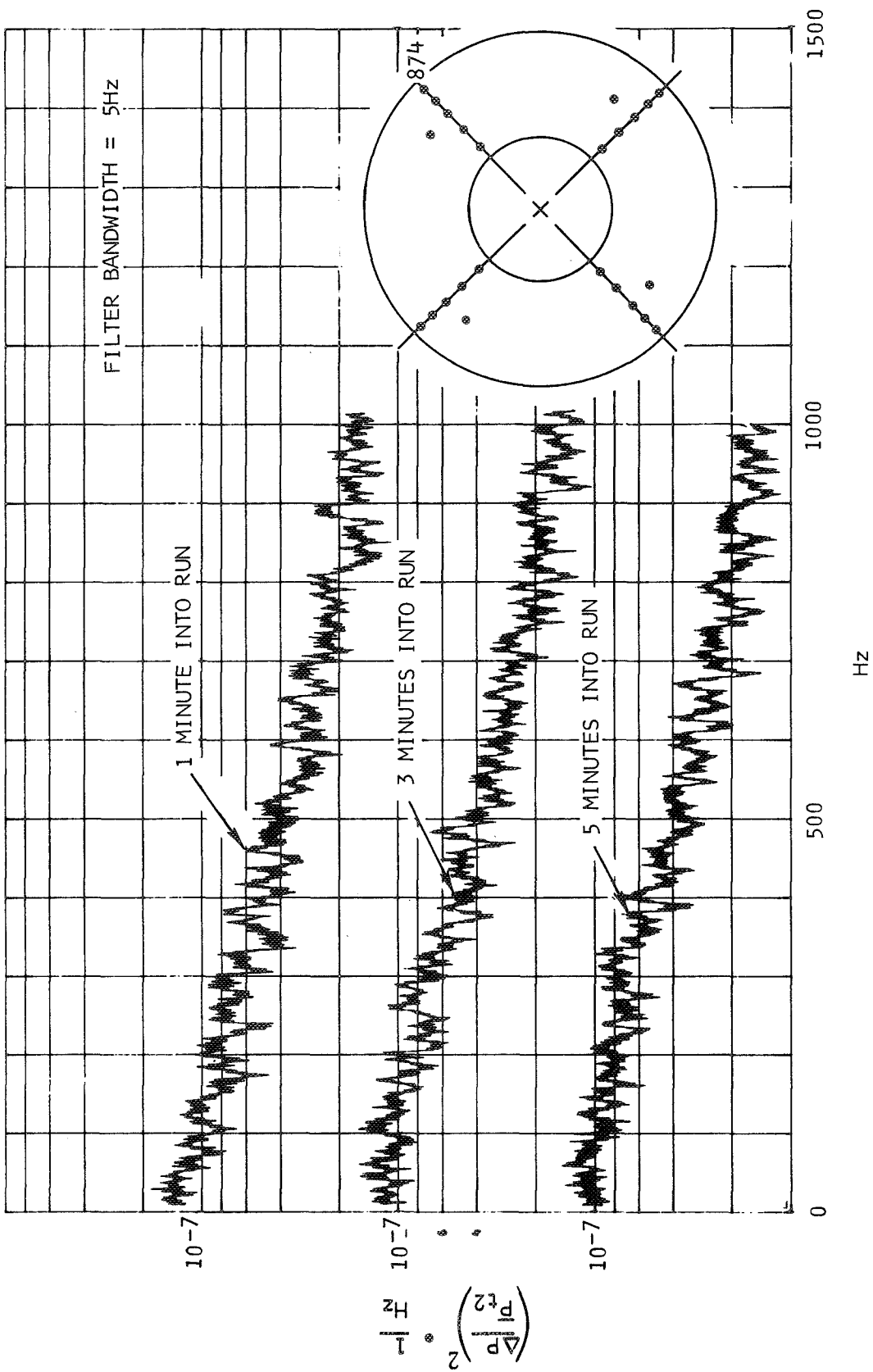
(a)

Figure 31.- Power spectral density at different 5-second intervals, $M_0 = 3.0$, $\bar{P}_{t_2}/P_{t_0} = 0.877$.



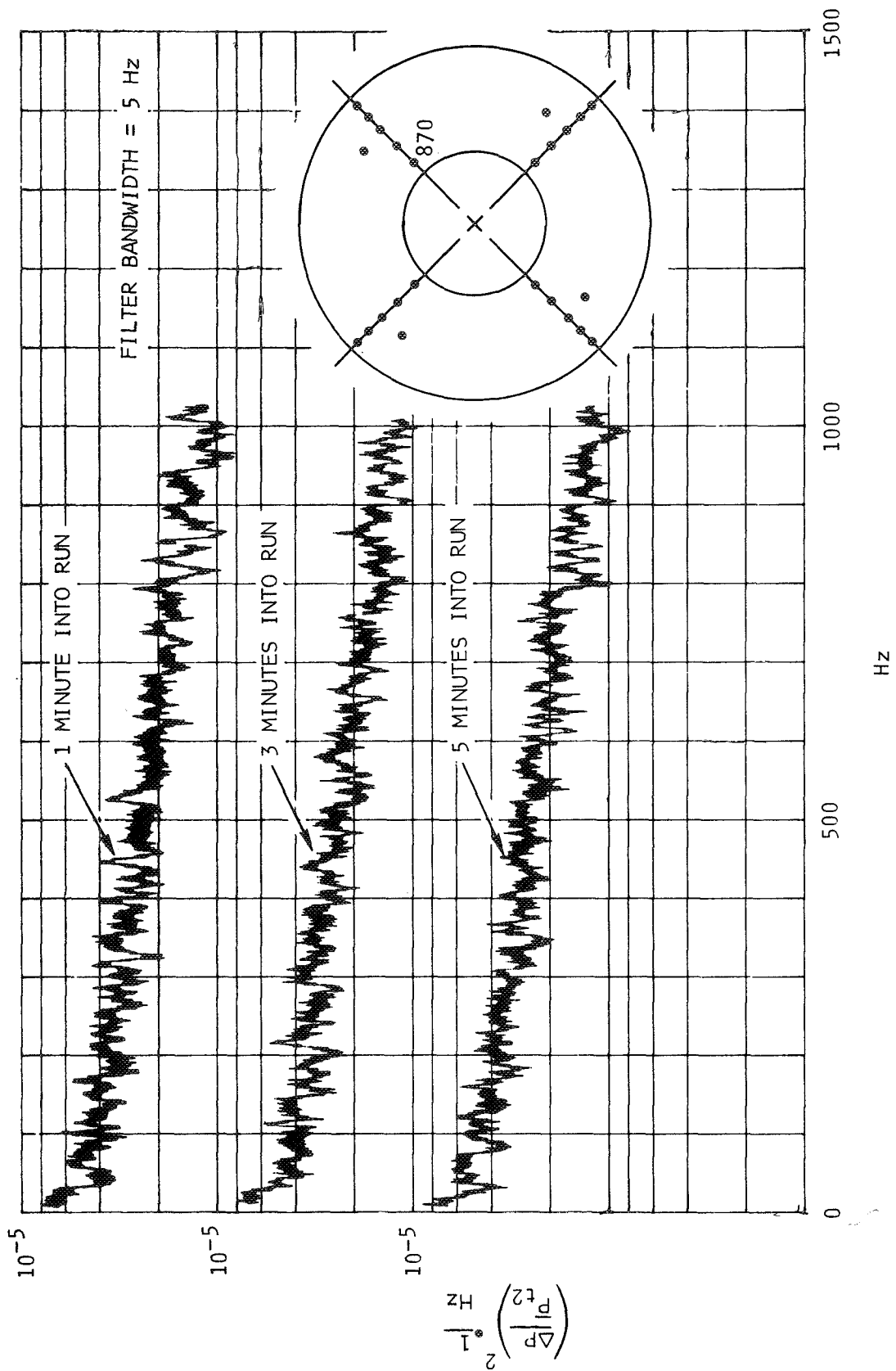
(b)

Figure 31.- Continued



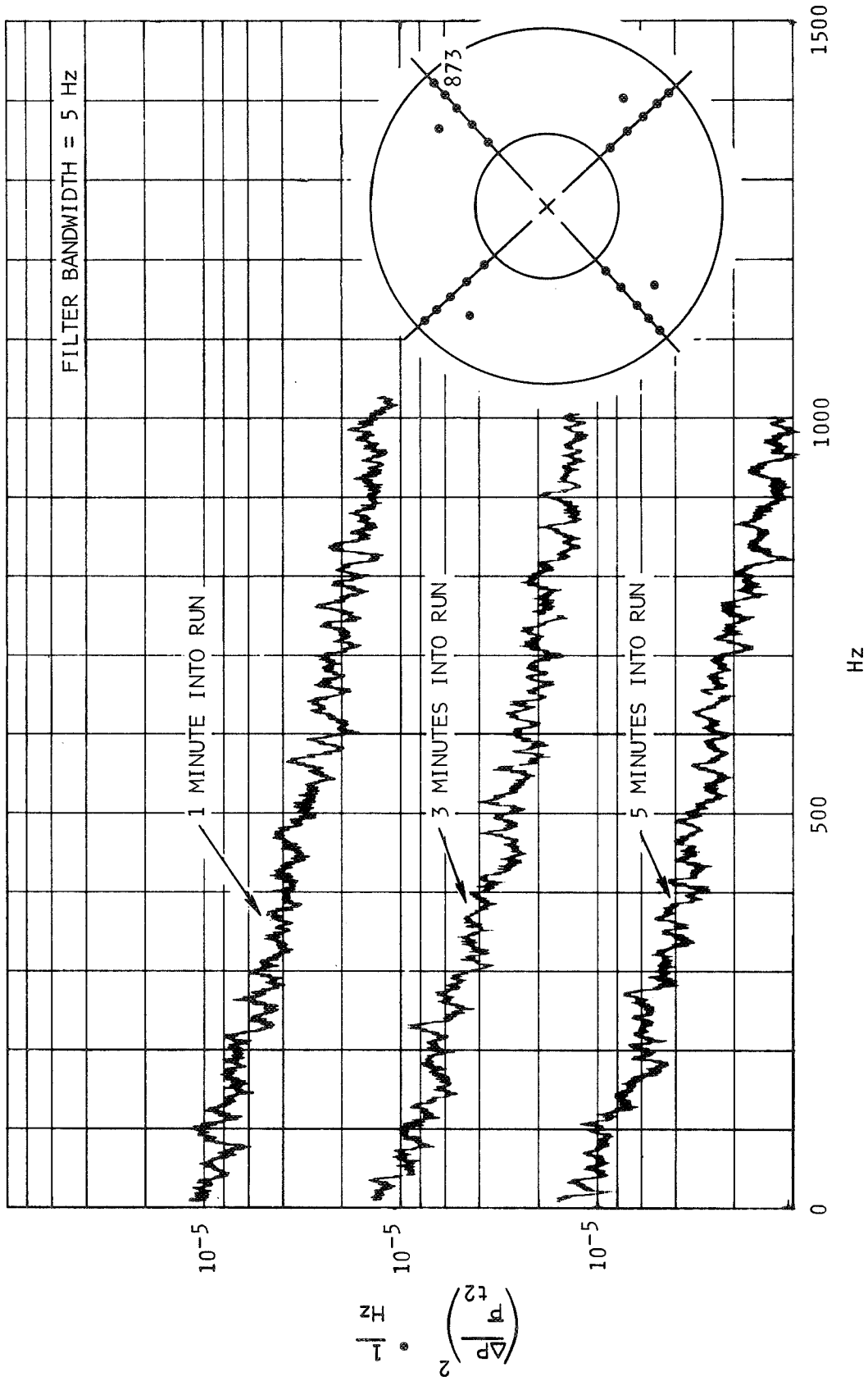
(c)

Figure 31.- Concluded.



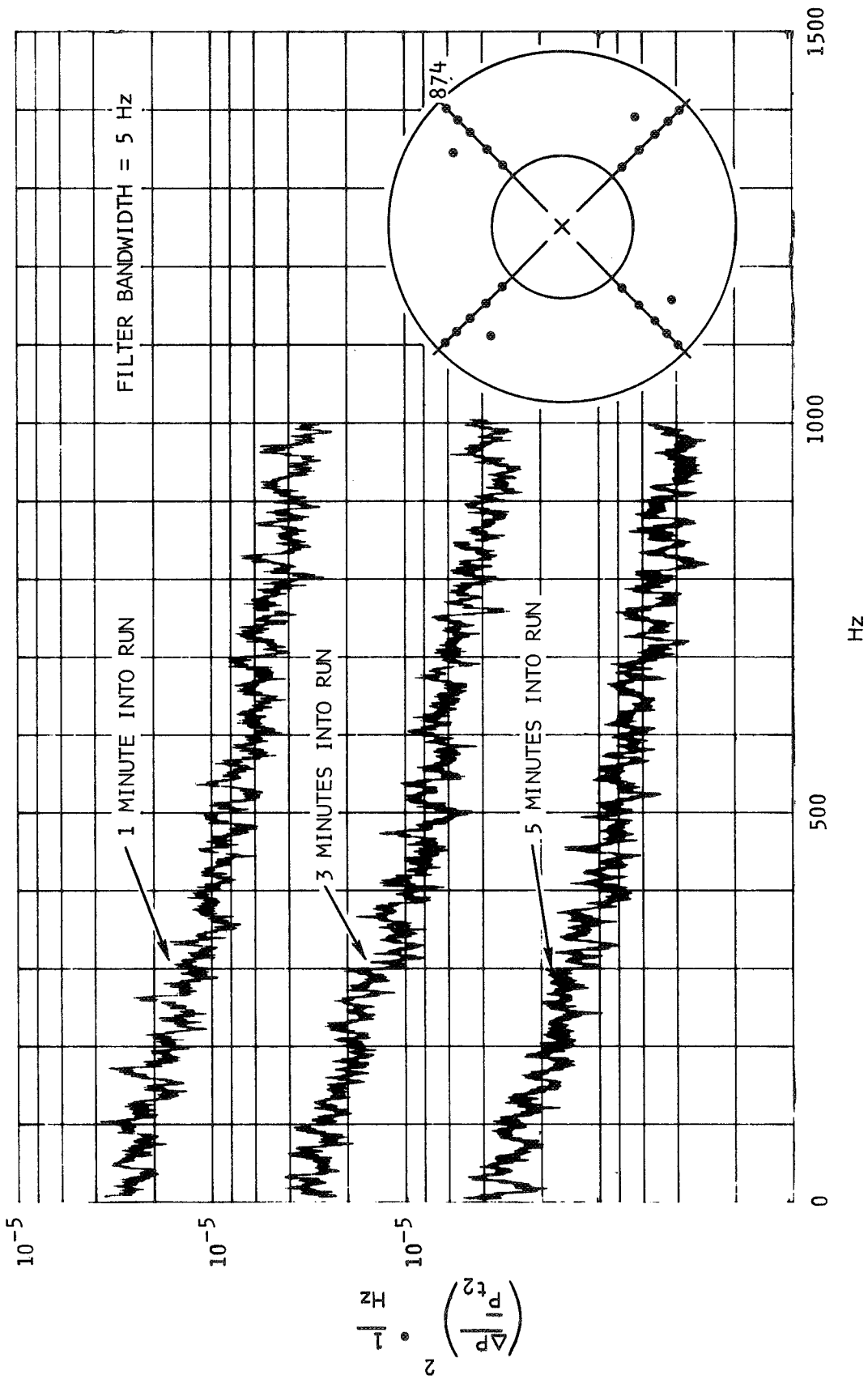
(a)

Figure 32.- Power spectral density at different 5-second intervals, $M_0 = 3.0$, $\bar{P}_{t_2}/P_{t_0} = 0.565$.



(b)

Figure 32.- Continued.



(c)

Figure 32.- Concluded.

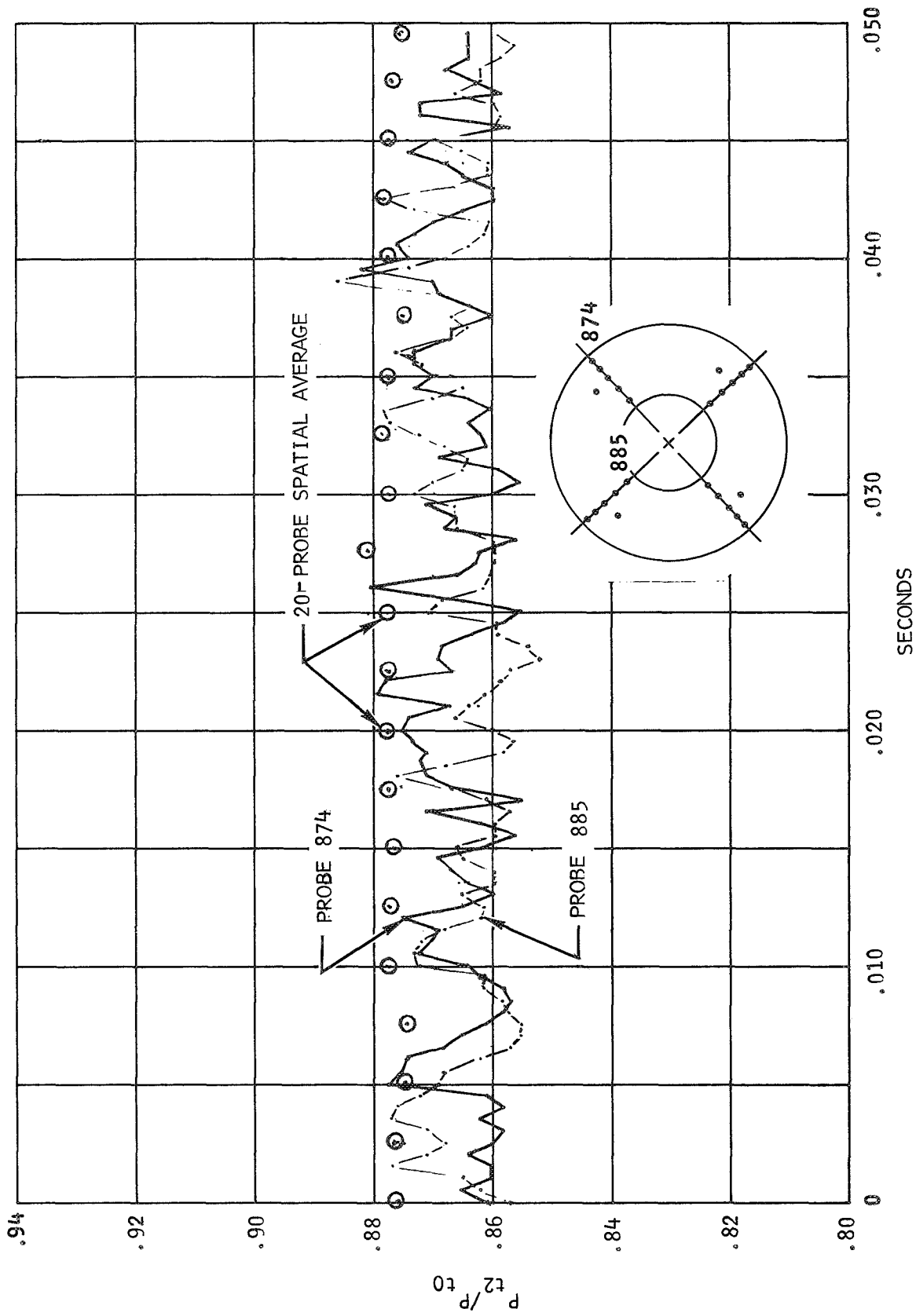


Figure 33.- Instantaneous average and individual engine face total pressure comparisons,
 $M_0 = 3.0, \bar{P}_{t2}/P_{t0} = 0.877.$

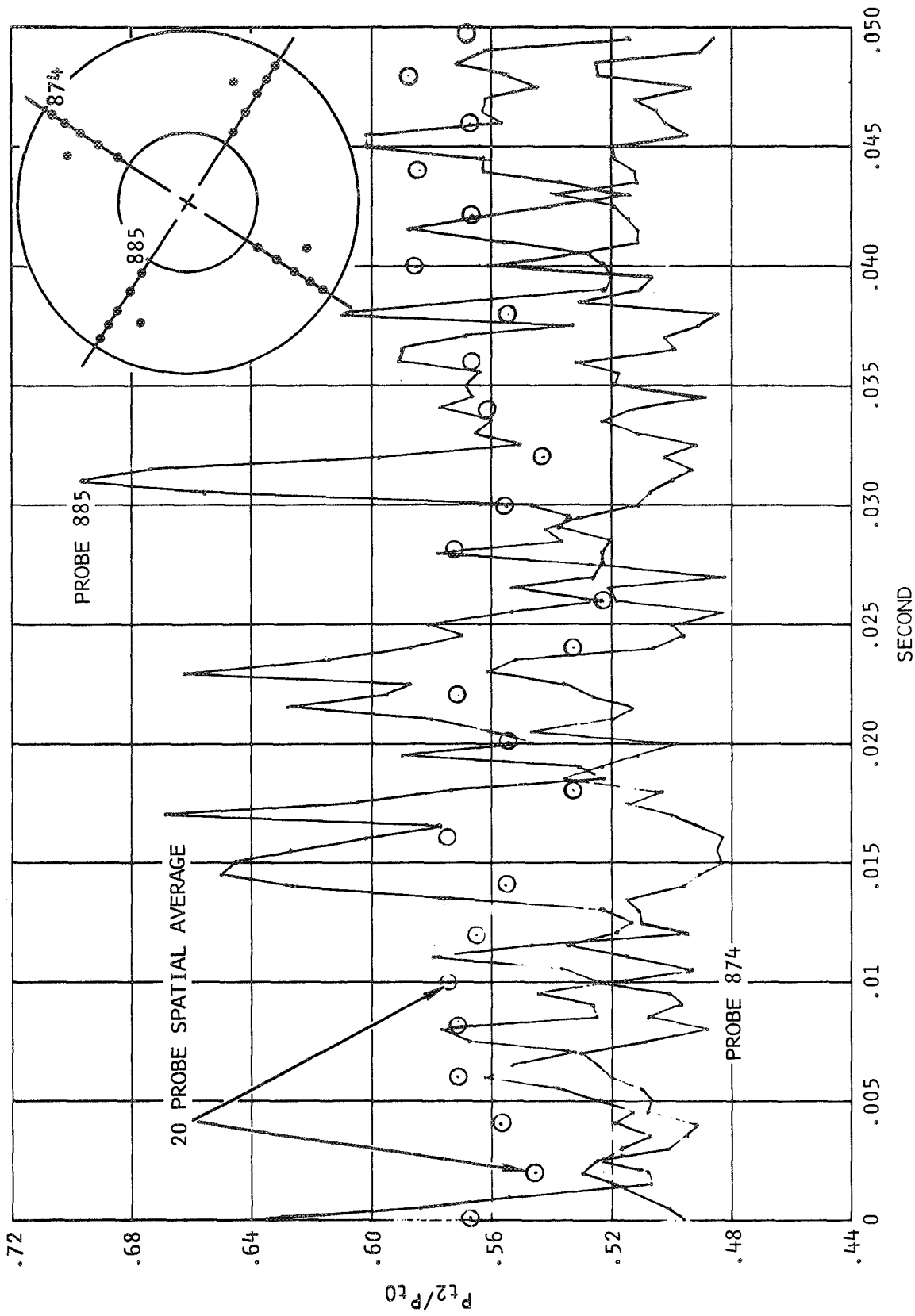


Figure 34.- Instantaneous average and individual engine face total pressure comparisons,
 $M_0 = 3.0$, $\bar{P}_{t2}/P_{t0} = 0.565$.

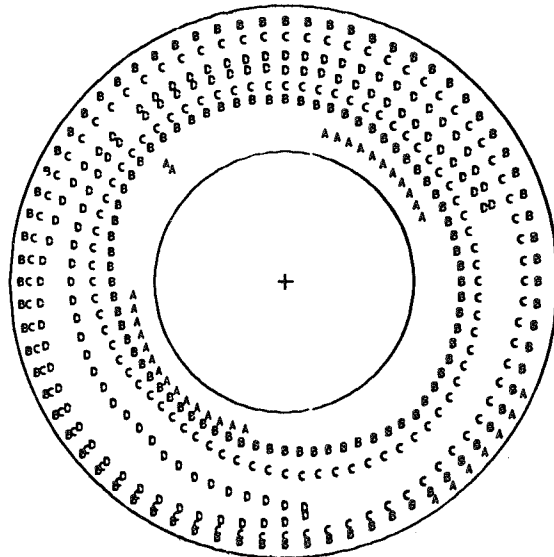
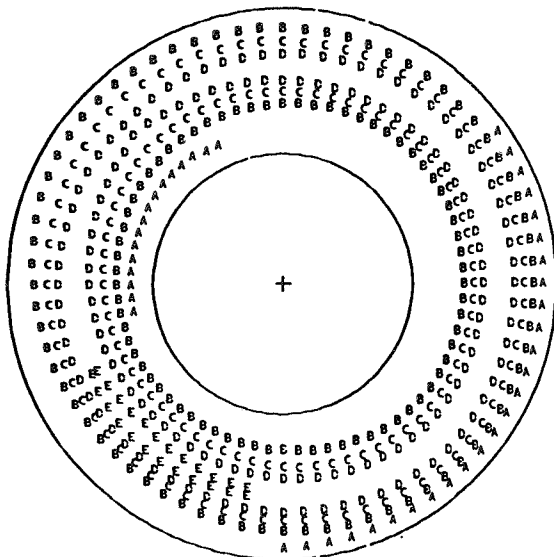
TIME IS SHOWN IN HOURS, MINUTES, AND SECONDS.

RUN 21.209
 TIME 8 26 0.0000

$\frac{PT2AVG}{PT0}$ = 0.8760	$\frac{PTMAX-PTMIN}{PT2AVG}$ = 0.0573
MINIMUM = 0.8505	INCREMENT = 0.010
MAXIMUM = 0.9007	INCREASING A.B.C.....E

RUN 21.209
 TIME 8 26 0.0005

$\frac{PT2AVG}{PT0}$ = 0.8753	$\frac{PTMAX-PTMIN}{PT2AVG}$ = 0.0484
MINIMUM = 0.8572	INCREMENT = 0.010
MAXIMUM = 0.8997	INCREASING A.B.C.....D

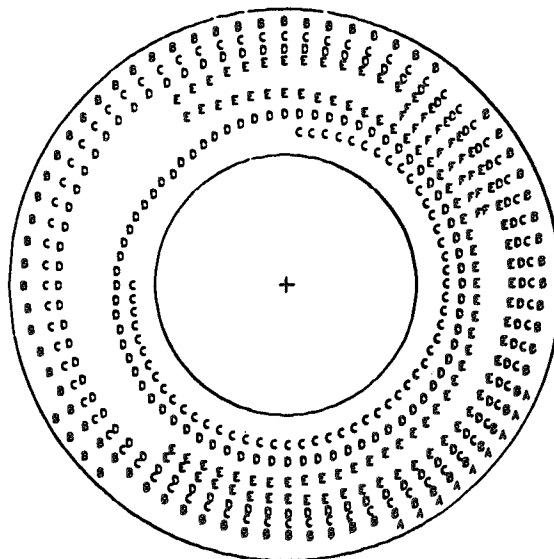
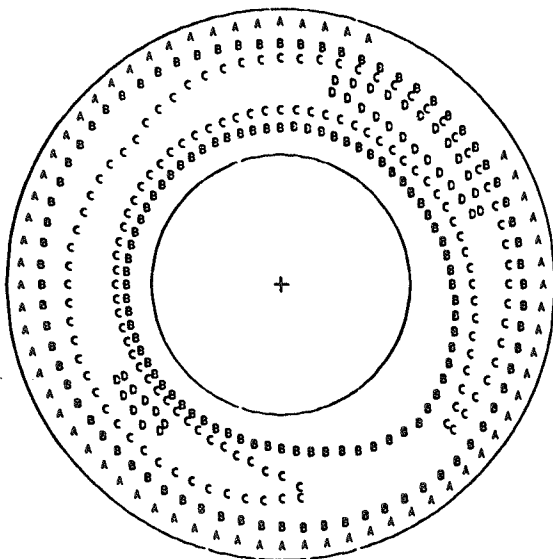


RUN 21.209
 TIME 8 26 0.0010

$\frac{PT2AVG}{PT0}$ = 0.8713	$\frac{PTMAX-PTMIN}{PT2AVG}$ = 0.0445
MINIMUM = 0.8553	INCREMENT = 0.010
MAXIMUM = 0.8941	INCREASING A.B.C.....D

RUN 21.209
 TIME 8 26 0.0015

$\frac{PT2AVG}{PT0}$ = 0.8747	$\frac{PTMAX-PTMIN}{PT2AVG}$ = 0.0631
MINIMUM = 0.8466	INCREMENT = 0.010
MAXIMUM = 0.9018	INCREASING A.B.C.....F

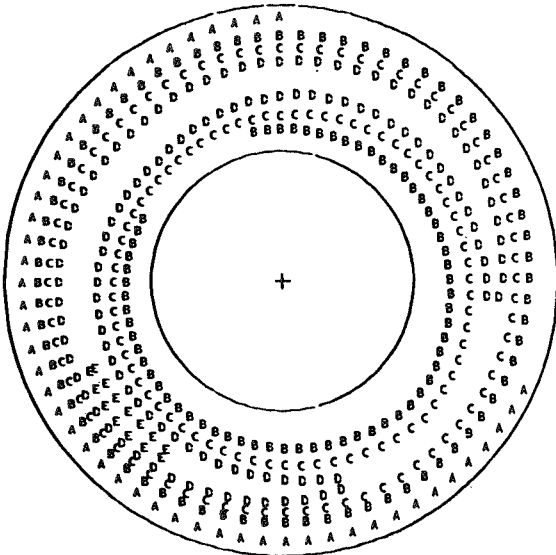


(a)

Figure 35.- Instantaneous total pressure ratio contours,
 $M_0 = 3.0$, $\bar{P}_{t2}/P_{t0} = 0.877$.

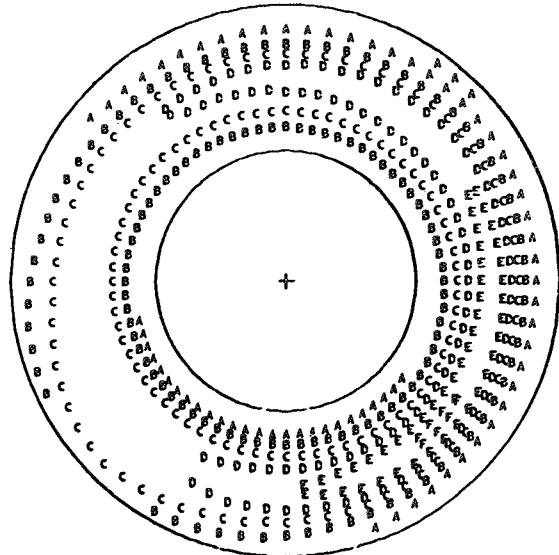
RUN 21.209
 TIME 8 26 0.0020

<u>PT2AVG</u>	= 0.8752	<u>PTMAX-PTMIN</u>	= 0.0531
<u>PT0</u>		<u>PT2AVG</u>	
MINIMUM	= 0.8553	INCREMENT	= 0.010
MAXIMUM	= 0.9018	INCREASING A,B,C.....E	



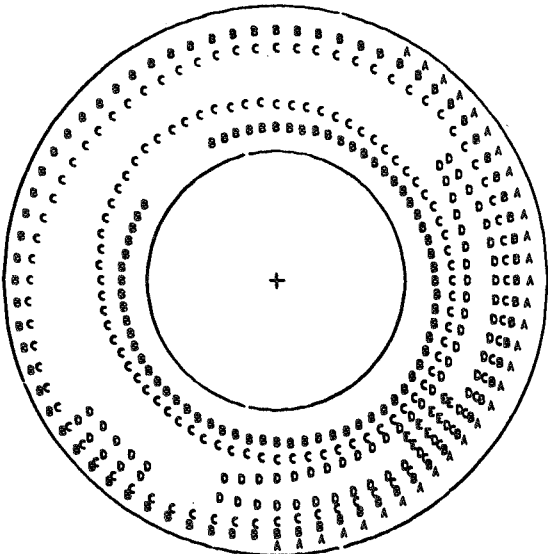
RUN 21.209
 TIME 8 26 0.0025

<u>PT2AVG</u>	= 0.8760	<u>PTMAX-PTMIN</u>	= 0.0649
<u>PT0</u>		<u>PT2AVG</u>	
MINIMUM	= 0.8539	INCREMENT	= 0.010
MAXIMUM	= 0.9108	INCREASING A,B,C.....F	



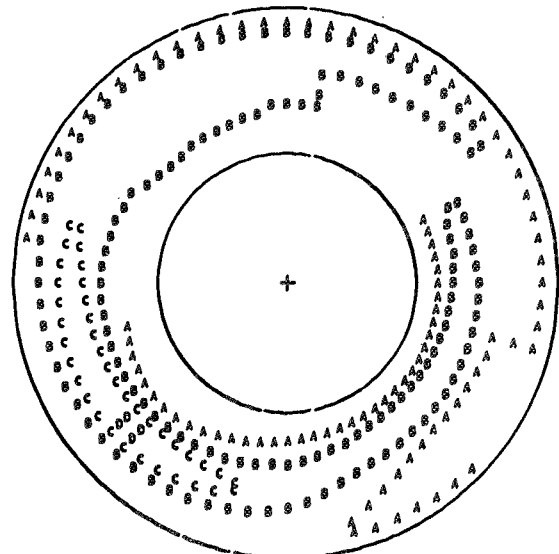
RUN 21.209
 TIME 8 26 0.0030

<u>PT2AVG</u>	= 0.8758	<u>PTMAX-PTMIN</u>	= 0.0559
<u>PT0</u>		<u>PT2AVG</u>	
MINIMUM	= 0.8522	INCREMENT	= 0.010
MAXIMUM	= 0.9012	INCREASING A,B,C.....E	



RUN 21.209
 TIME 8 26 0.0035

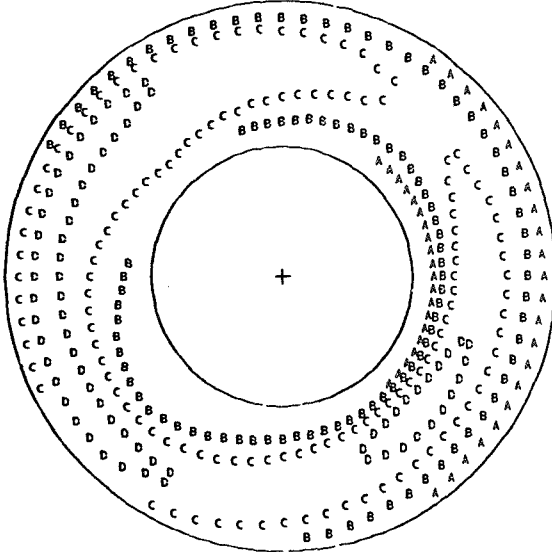
<u>PT2AVG</u>	= 0.8762	<u>PTMAX-PTMIN</u>	= 0.0456
<u>PT0</u>		<u>PT2AVG</u>	
MINIMUM	= 0.8623	INCREMENT	= 0.010
MAXIMUM	= 0.9022	INCREASING A,B,C.....D	



(b)
 Figure 35.- Continued.

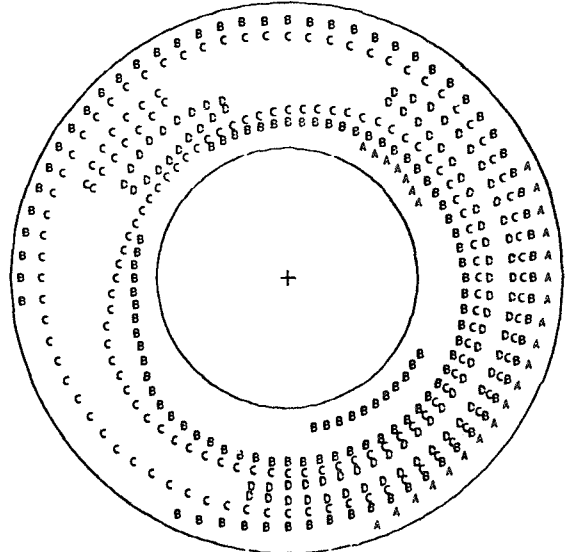
RUN 21.209
 TIME 8 26 0.0040

$\frac{PT2AVG}{PT0} = 0.8761$	$\frac{PTMAX-PTMIN}{PT2AVG} = 0.0439$
MINIMUM = 0.8565	INCREMENT = 0.010
MAXIMUM = 0.8950	INCREASING A.B.C.....D



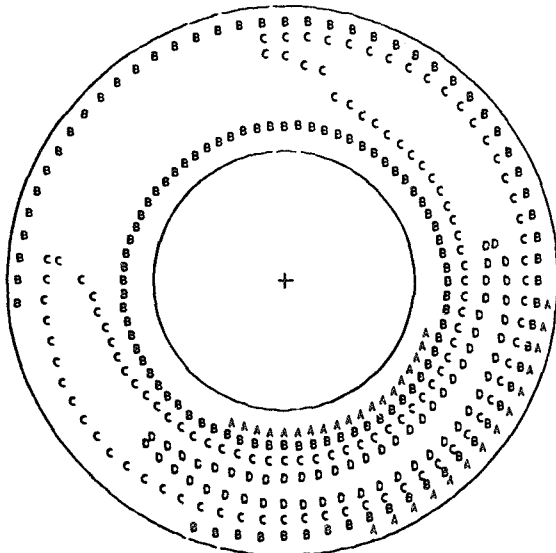
RUN 21.209
 TIME 8 26 0.0045

$\frac{PT2AVG}{PT0} = 0.8753$	$\frac{PTMAX-PTMIN}{PT2AVG} = 0.0494$
MINIMUM = 0.8541	INCREMENT = 0.010
MAXIMUM = 0.8974	INCREASING A.B.C.....D



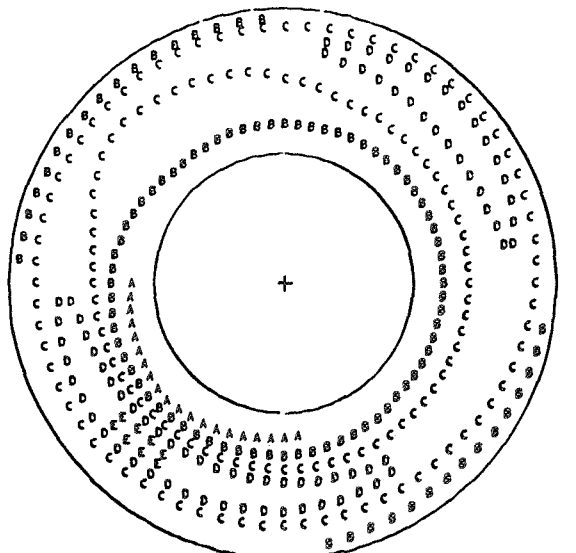
RUN 21.209
 TIME 8 26 0.0050

$\frac{PT2AVG}{PT0} = 0.8749$	$\frac{PTMAX-PTMIN}{PT2AVG} = 0.0493$
MINIMUM = 0.8533	INCREMENT = 0.010
MAXIMUM = 0.8364	INCREASING A.B.C.....D



RUN 21.209
 TIME 8 26 0.0055

$\frac{PT2AVG}{PT0} = 0.8771$	$\frac{PTMAX-PTMIN}{PT2AVG} = 0.0586$
MINIMUM = 0.8513	INCREMENT = 0.010
MAXIMUM = 0.9027	INCREASING A.B.C.....E



(c)

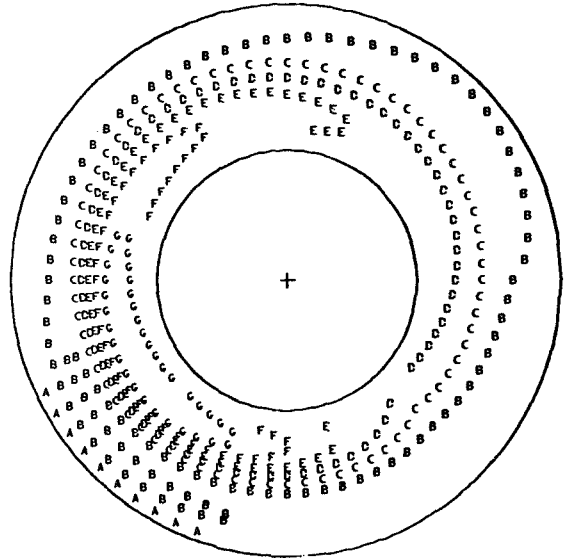
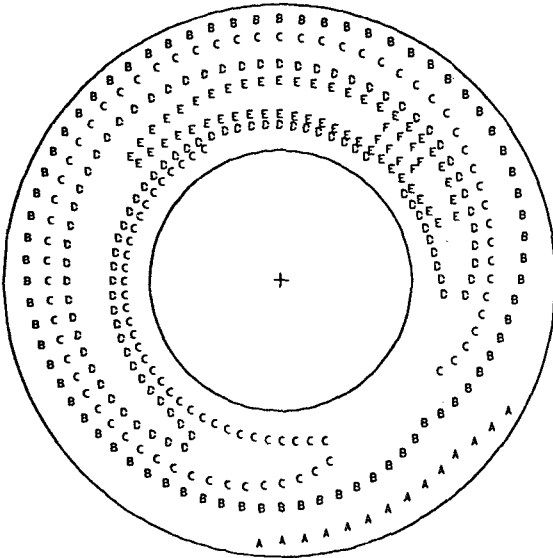
Figure 35.- Concluded.

RUN 21.214
 TIME 9 49 42.0300

$\frac{PT2AVG}{PT0}$	= 0.5267	$\frac{PTMAX-PTMIN}{PT2AVG}$	= 0.3252
MINIMUM	= 0.4610	INCREMENT	= 0.040
MAXIMUM	= 0.6323	INCREASING A.B.C.....E	

RUN 21.214
 TIME 9 49 42.0305

$\frac{PT2AVG}{PT0}$	= 0.5299	$\frac{PTMAX-PTMIN}{PT2AVG}$	= 0.5501
MINIMUM	= 0.4350	INCREMENT	= 0.040
MAXIMUM	= 0.7265	INCREASING A.B.C.....H	

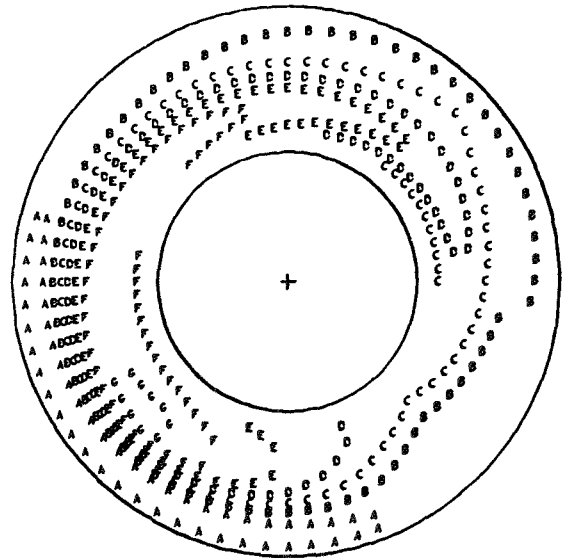
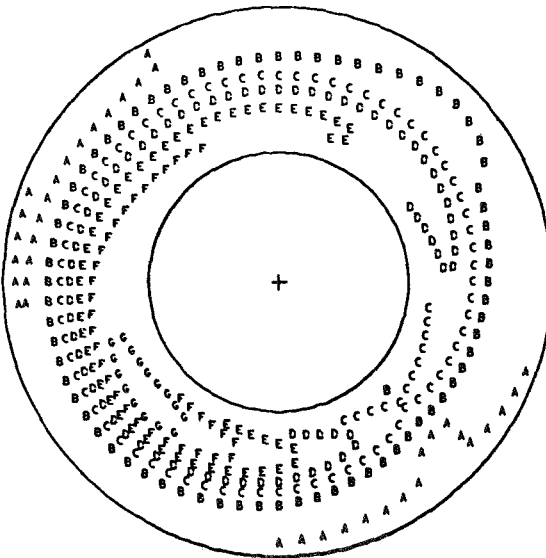


RUN 21.214
 TIME 9 49 42.0310

$\frac{PT2AVG}{PT0}$	= 0.5567	$\frac{PTMAX-PTMIN}{PT2AVG}$	= 0.4773
MINIMUM	= 0.4706	INCREMENT	= 0.040
MAXIMUM	= 0.7364	INCREASING A.B.C.....G	

RUN 21.214
 TIME 9 49 42.0315

$\frac{PT2AVG}{PT0}$	= 0.5587	$\frac{PTMAX-PTMIN}{PT2AVG}$	= 0.4546
MINIMUM	= 0.4665	INCREMENT	= 0.040
MAXIMUM	= 0.7206	INCREASING A.B.C.....G	

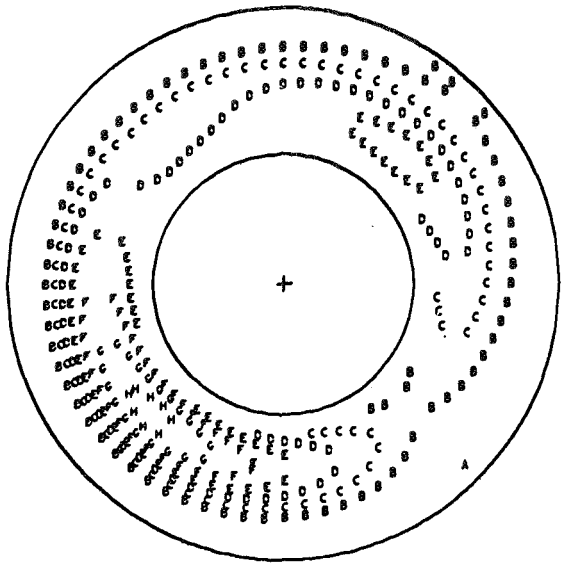


(a)

Figure 36.- Instantaneous total pressure ratio contours, $M_0 = 3.0$, $\bar{P}_{t2}/P_{t0} = 0.565$.

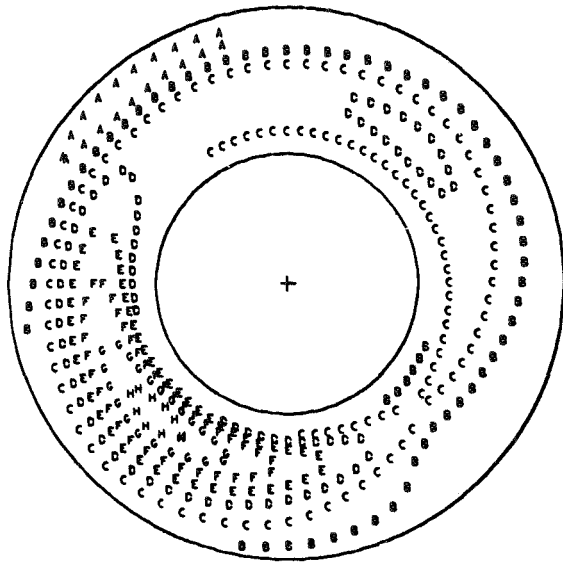
RUN 21.214
 TIME 9 49 42.0320

$\frac{PT2AVG}{PT0}$	= 0.5433	$\frac{PTMAX-PTMIN}{PT2AVG}$	= 0.5648
MINIMUM	= 0.4583	INCREMENT	= 0.040
MAXIMUM	= 0.7652	INCREASING A.B.C.....H	



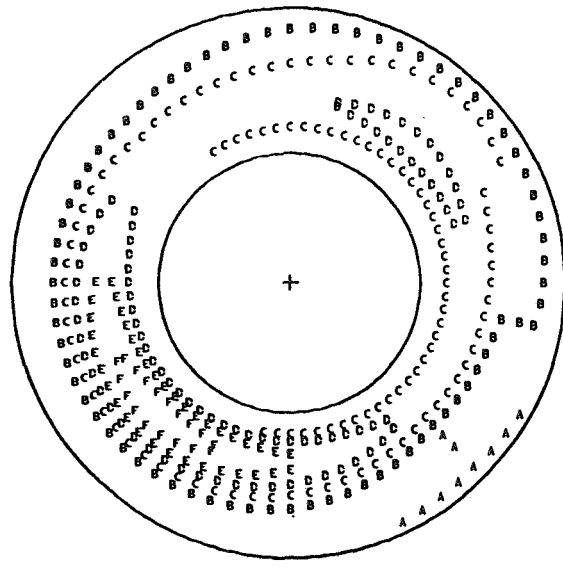
RUN 21.214
 TIME 9 49 42.0325

$\frac{PT2AVG}{PT0}$	= 0.5520	$\frac{PTMAX-PTMIN}{PT2AVG}$	= 0.5687
MINIMUM	= 0.4617	INCREMENT	= 0.040
MAXIMUM	= 0.7757	INCREASING A.B.C.....H	



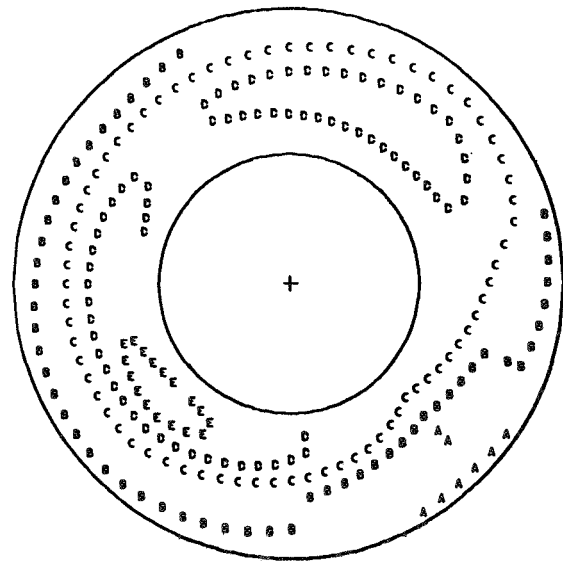
RUN 21.214
 TIME 9 49 42.0330

$\frac{PT2AVG}{PT0}$	= 0.5481	$\frac{PTMAX-PTMIN}{PT2AVG}$	= 0.4369
MINIMUM	= 0.4719	INCREMENT	= 0.040
MAXIMUM	= 0.7114	INCREASING A.B.C.....F	



RUN 21.214
 TIME 9 49 42.0335

$\frac{PT2AVG}{PT0}$	= 0.5388	$\frac{PTMAX-PTMIN}{PT2AVG}$	= 0.3220
MINIMUM	= 0.4514	INCREMENT	= 0.040
MAXIMUM	= 0.6249	INCREASING A.B.C.....E	

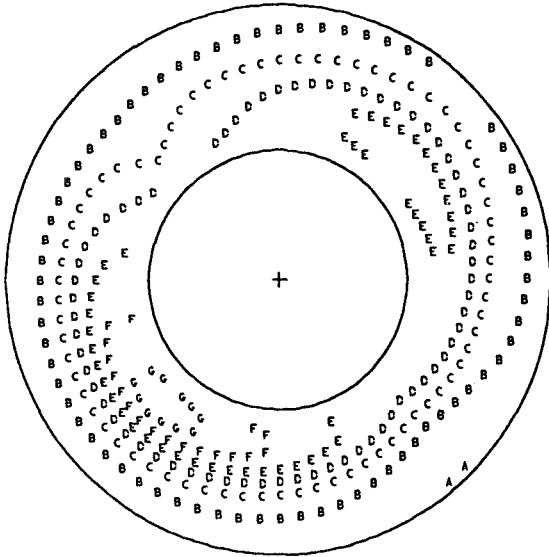


(b)

Figure 36.- Continued.

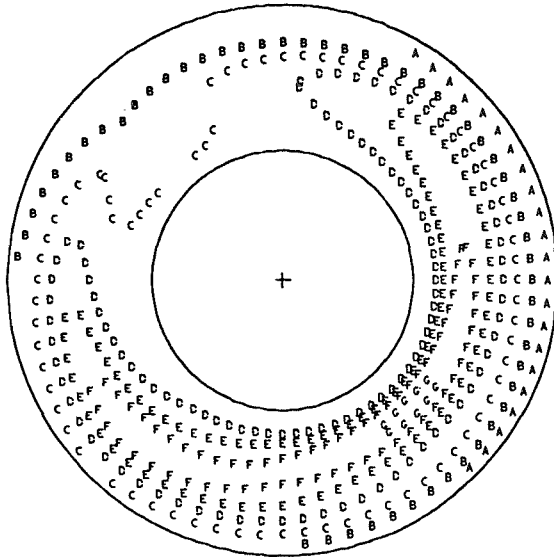
RUN 21.214
 TIME 9 49 42.0340

$\frac{PT2AVG}{PT0}$	= 0.5609	$\frac{PTMAX-PTMIN}{PT2AVG}$	= 0.4390
MINIMUM	= 0.4688	INCREMENT	= 0.040
MAXIMUM	= 0.7151	INCREASING A,B,C.....G	



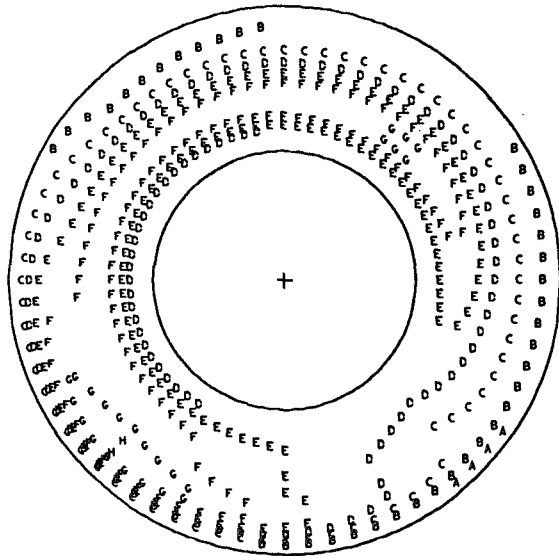
RUN 21.214
 TIME 9 49 42.0345

$\frac{PT2AVG}{PT0}$	= 0.5897	$\frac{PTMAX-PTMIN}{PT2AVG}$	= 0.4248
MINIMUM	= 0.4880	INCREMENT	= 0.040
MAXIMUM	= 0.7385	INCREASING A,B,C.....G	



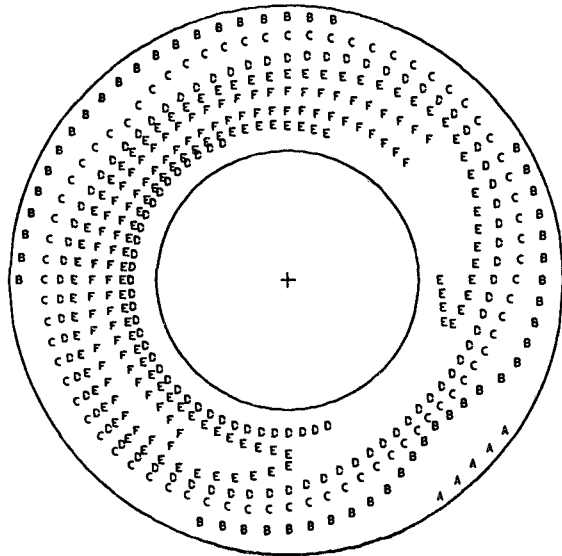
RUN 21.214
 TIME 9 49 42.0350

$\frac{PT2AVG}{PT0}$	= 0.5958	$\frac{PTMAX-PTMIN}{PT2AVG}$	= 0.4987
MINIMUM	= 0.4624	INCREMENT	= 0.040
MAXIMUM	= 0.7596	INCREASING A,B,C.....H	



RUN 21.214
 TIME 9 49 42.0355

$\frac{PT2AVG}{PT0}$	= 0.5766	$\frac{PTMAX-PTMIN}{PT2AVG}$	= 0.3778
MINIMUM	= 0.4608	INCREMENT	= 0.040
MAXIMUM	= 0.6787	INCREASING A,B,C.....F	

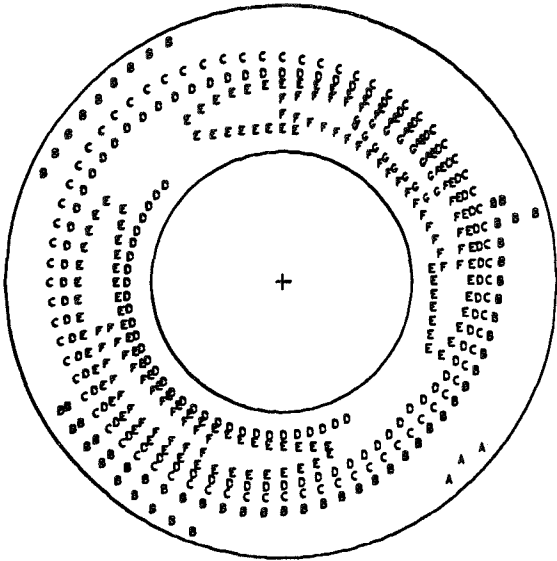


(c)

Figure 36.- Continued.

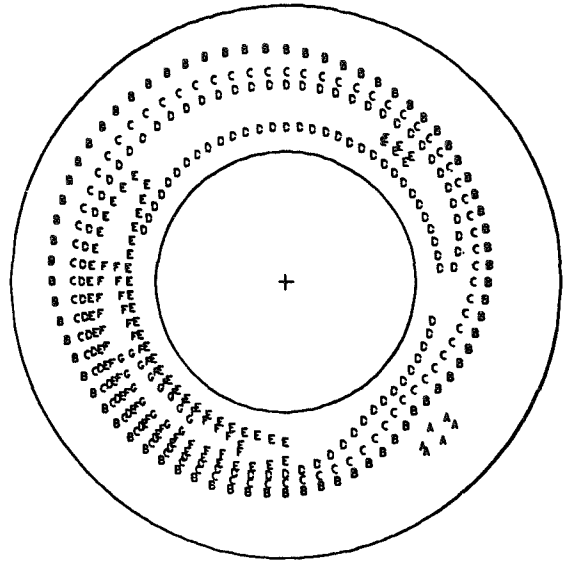
RUN 21.214
 TIME 9 49 42.0360

<u>PT2AVG</u>	= 0.5660	<u>PTMAX-PTMIN</u>	= 0.4398
<u>PT0</u>		<u>PT2AVG</u>	
MINIMUM	= 0.4632	INCREMENT	= 0.040
MAXIMUM	= 0.7122	INCREASING A.B.C.....G	



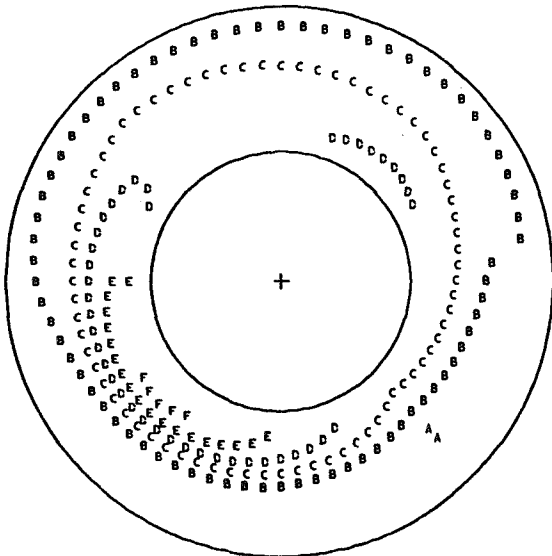
RUN 21.214
 TIME 9 49 42.0365

<u>PT2AVG</u>	= 0.5506	<u>PTMAX-PTMIN</u>	= 0.4597
<u>PT0</u>		<u>PT2AVG</u>	
MINIMUM	= 0.4764	INCREMENT	= 0.040
MAXIMUM	= 0.7295	INCREASING A.B.C.....G	



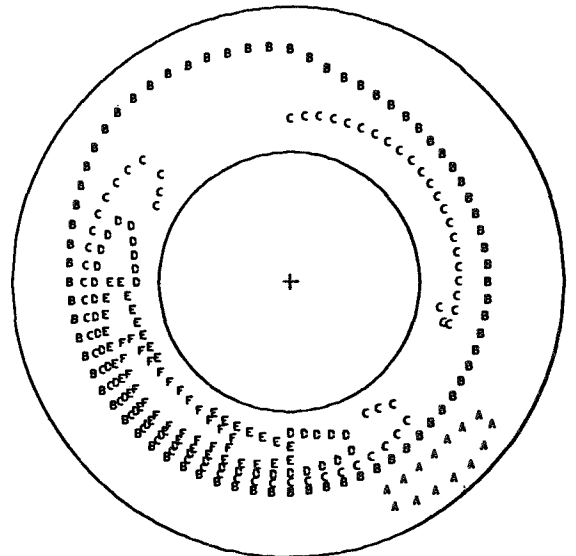
RUN 21.214
 TIME 9 49 42.0370

<u>PT2AVG</u>	= 0.5402	<u>PTMAX-PTMIN</u>	= 0.4105
<u>PT0</u>		<u>PT2AVG</u>	
MINIMUM	= 0.4676	INCREMENT	= 0.040
MAXIMUM	= 0.6894	INCREASING A.B.C.....F	



RUN 21.214
 TIME 9 49 42.0375

<u>PT2AVG</u>	= 0.5341	<u>PTMAX-PTMIN</u>	= 0.4188
<u>PT0</u>		<u>PT2AVG</u>	
MINIMUM	= 0.4745	INCREMENT	= 0.040
MAXIMUM	= 0.6982	INCREASING A.B.C.....F	

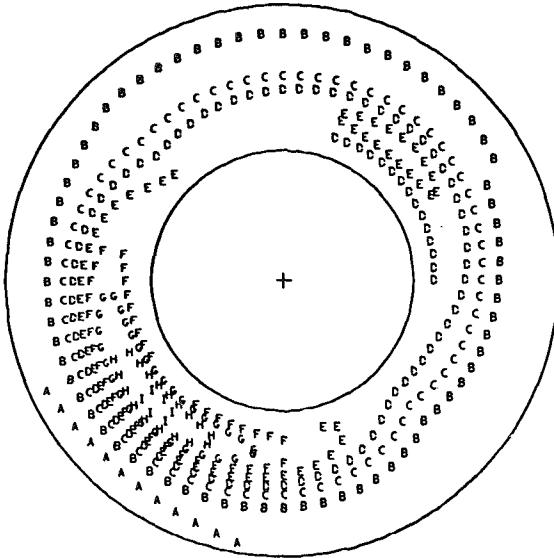


(d)

Figure 36.- Continued.

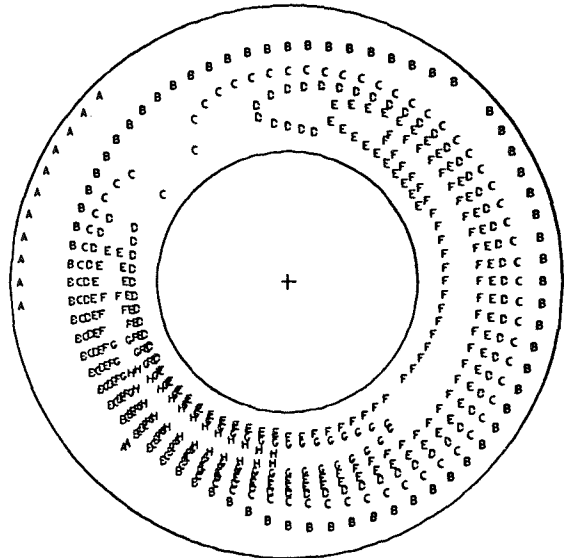
RUN 21.214
TIME 9 49 0380

$\frac{PT2AVG}{PT0}$	= 0.5541	$\frac{PTMAX-PTMIN}{PT2AVG}$	= 0.5948
MINIMUM	= 0.4621	INCREMENT	= 0.040
MAXIMUM	= 0.7917	INCREASING A,B,C.....I	



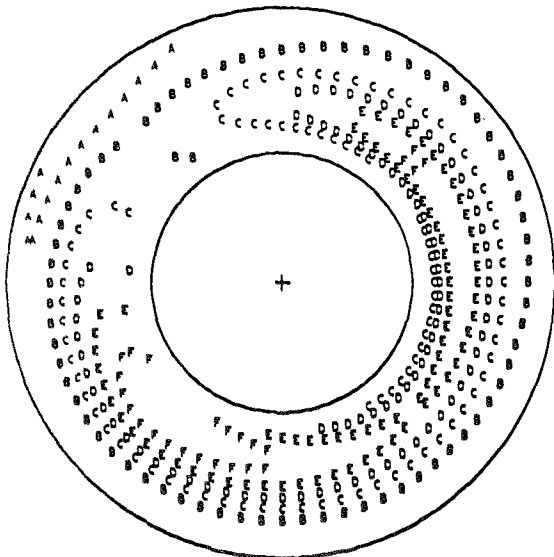
RUN 21.214
TIME 9 49 42.0385

$\frac{PT2AVG}{PT0}$	= 0.5837	$\frac{PTMAX-PTMIN}{PT2AVG}$	= 0.5167
MINIMUM	= 0.4894	INCREMENT	= 0.040
MAXIMUM	= 0.7910	INCREASING A,B,C.....H	



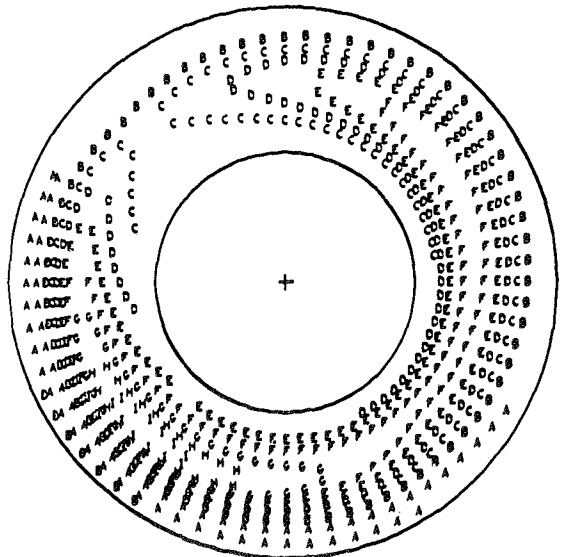
RUN 21.214
TIME 9 49 42.0390

$\frac{PT2AVG}{PT0}$	= 0.5694	$\frac{PTMAX-PTMIN}{PT2AVG}$	= 0.4277
MINIMUM	= 0.4820	INCREMENT	= 0.040
MAXIMUM	= 0.7257	INCREASING A,B,C.....F	



RUN 21.214
TIME 9 49 42.0395

$\frac{PT2AVG}{PT0}$	= 0.5843	$\frac{PTMAX-PTMIN}{PT2AVG}$	= 0.5806
MINIMUM	= 0.4733	INCREMENT	= 0.040
MAXIMUM	= 0.8125	INCREASING A,B,C.....I	

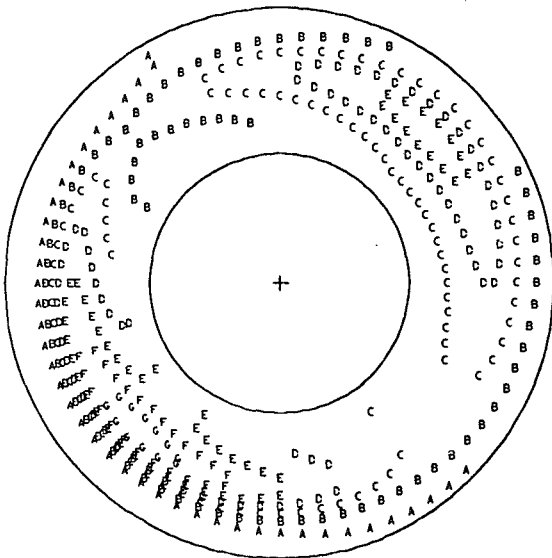


(e)

Figure 36.- Continued.

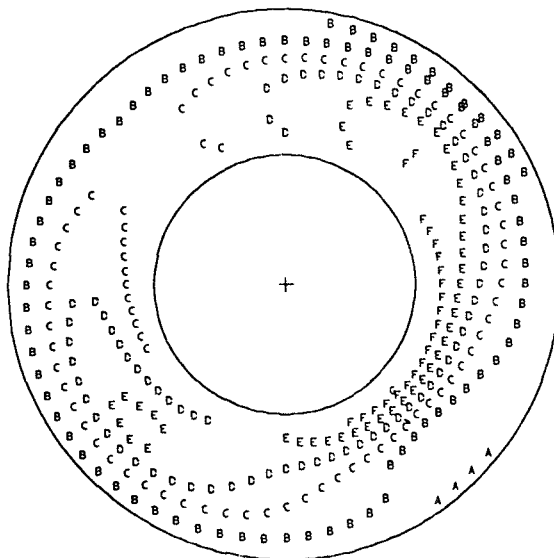
RUN 21.214
 TIME 9 49 42.0400

$\frac{PT2AVG}{PT0}$	= 0.5855	$\frac{PTMAX-PTMIN}{PT2AVG}$	= 0.4514
MINIMUM	= 0.5018	INCREMENT	= 0.040
MAXIMUM	= 0.7661	INCREASING A.B.C.....G	



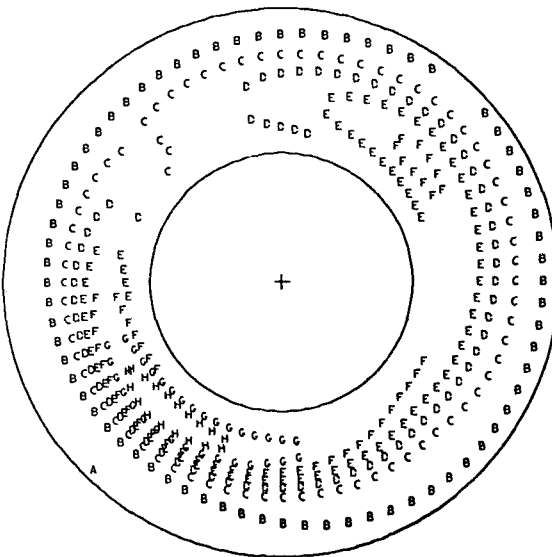
RUN 21.214
 TIME 9 49 42.0405

$\frac{PT2AVG}{PT0}$	= 0.5685	$\frac{PTMAX-PTMIN}{PT2AVG}$	= 0.4338
MINIMUM	= 0.4748	INCREMENT	= 0.040
MAXIMUM	= 0.7214	INCREASING A.B.C.....G	



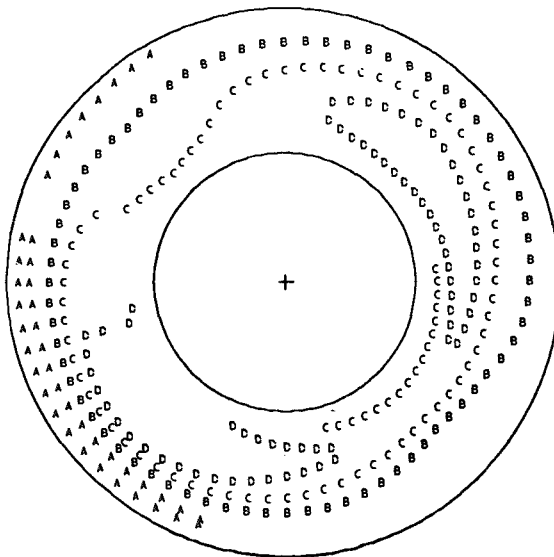
RUN 21.214
 TIME 9 49 42.0410

$\frac{PT2AVG}{PT0}$	= 0.5722	$\frac{PTMAX-PTMIN}{PT2AVG}$	= 0.5133
MINIMUM	= 0.4697	INCREMENT	= 0.040
MAXIMUM	= 0.7634	INCREASING A.B.C.....H	



RUN 21.214
 TIME 9 49 42.0415

$\frac{PT2AVG}{PT0}$	= 0.5660	$\frac{PTMAX-PTMIN}{PT2AVG}$	= 0.2773
MINIMUM	= 0.4975	INCREMENT	= 0.040
MAXIMUM	= 0.6545	INCREASING A.B.C.....D	

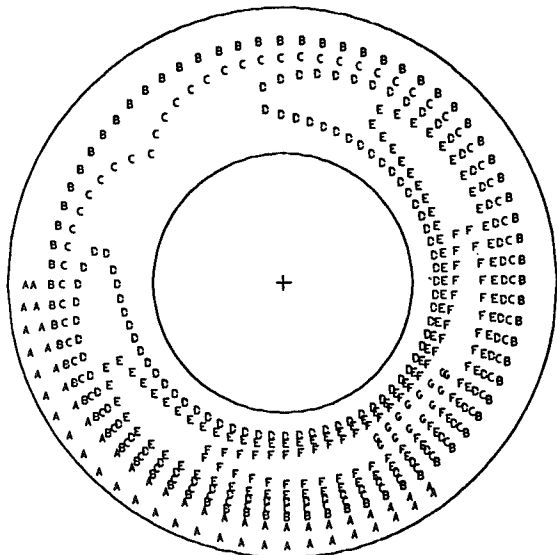


(f)

Figure 36.- Continued.

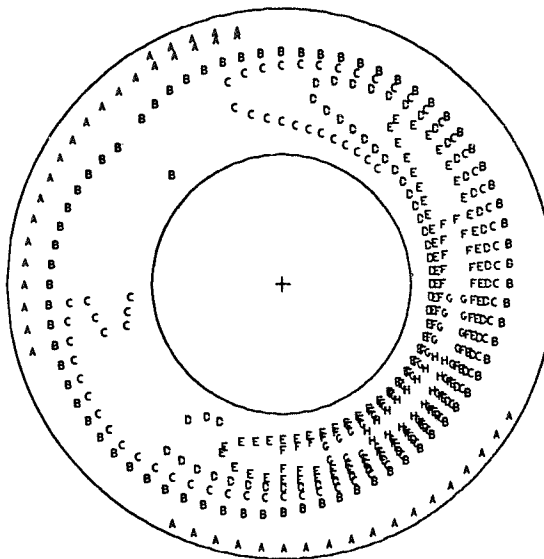
RUN 21.214
TIME 9 49 42.0420

$\frac{PT2AVG}{PT0} = 0.5684$ $\frac{PTMAX-PTMIN}{PT2AVG} = 0.4549$
 MINIMUM = 0.4742 INCREMENT = 0.040
 MAXIMUM = 0.7328 INCREASING A,B,C.....G



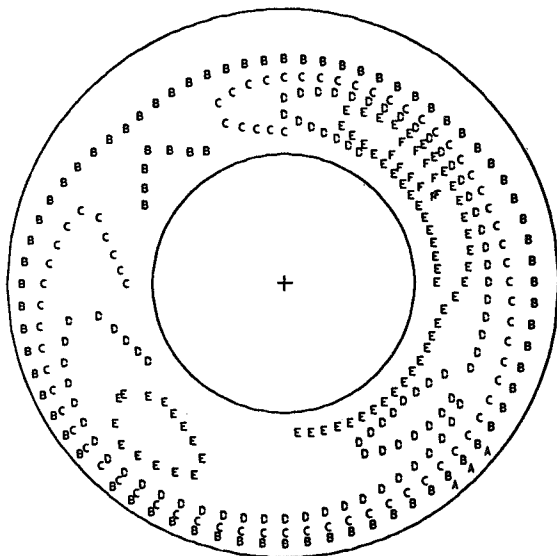
RUN 21.214
TIME 9 49 42.0425

$\frac{PT2AVG}{PT0} = 0.5703$ $\frac{PTMAX-PTMIN}{PT2AVG} = 0.5253$
 MINIMUM = 0.4947 INCREMENT = 0.040
 MAXIMUM = 0.7943 INCREASING A,B,C.....H



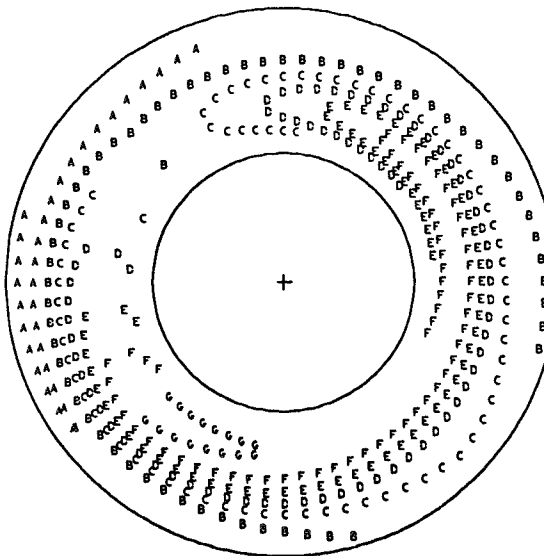
RUN 21.214
TIME 9 49 42.0430

$\frac{PT2AVG}{PT0} = 0.5874$ $\frac{PTMAX-PTMIN}{PT2AVG} = 0.3571$
 MINIMUM = 0.4952 INCREMENT = 0.040
 MAXIMUM = 0.7050 INCREASING A,B,C.....F



RUN 21.214
TIME 9 49 42.0435

$\frac{PT2AVG}{PT0} = 0.5871$ $\frac{PTMAX-PTMIN}{PT2AVG} = 0.4441$
 MINIMUM = 0.4801 INCREMENT = 0.040
 MAXIMUM = 0.7409 INCREASING A,B,C.....G

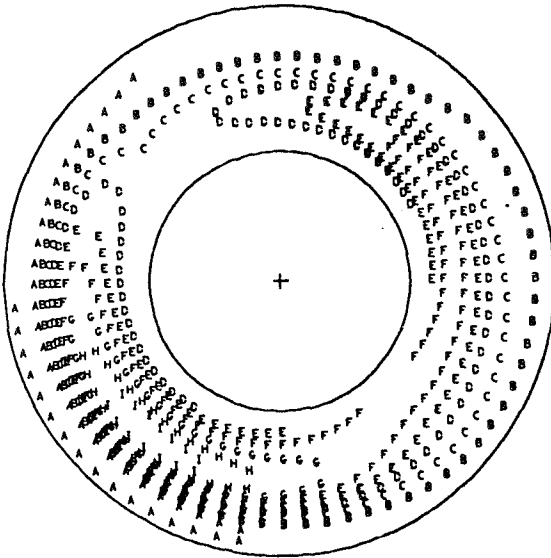


(g)

Figure 36.- Continued.

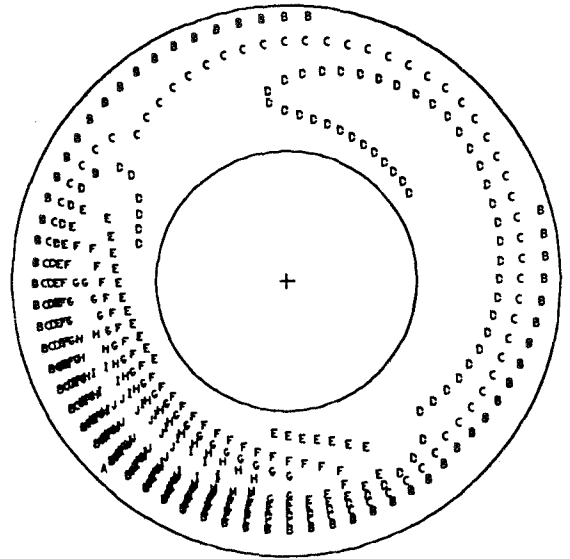
RUN 21.214
 TIME 9 49 42.0440

<u>PT2AVG</u>	= 0.5841	<u>PTMAX-PTMIN</u>	= 0.5858
<u>PT0</u>		<u>PT2AVG</u>	
MINIMUM	= 0.4745	INCREMENT	= 0.040
MAXIMUM	= 0.8168	INCREASING A.B.C.....I	



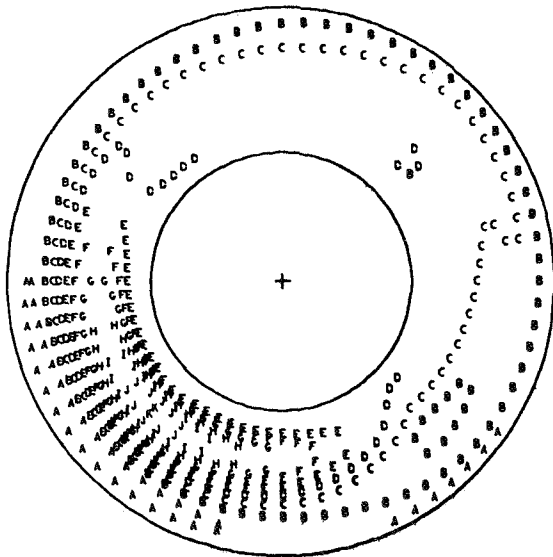
RUN 21.214
 TIME 9 49 42.0445

<u>PT2AVG</u>	= 0.5851	<u>PTMAX-PTMIN</u>	= 0.6645
<u>PT0</u>		<u>PT2AVG</u>	
MINIMUM	= 0.4691	INCREMENT	= 0.040
MAXIMUM	= 0.8579	INCREASING A.B.C.....J	



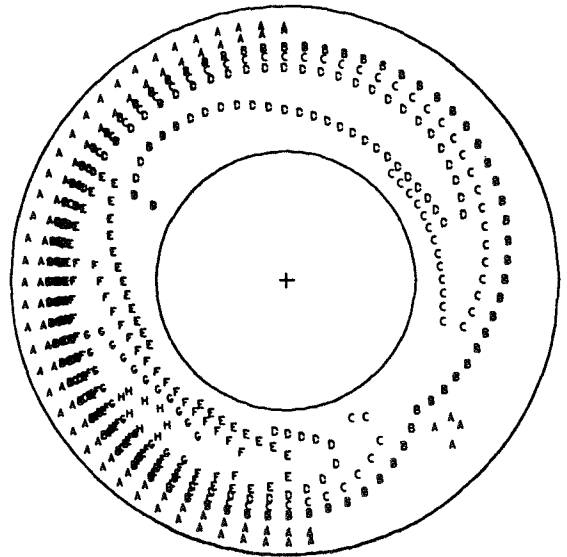
RUN 21.214
 TIME 9 49 42.0450

<u>PT2AVG</u>	= 0.5760	<u>PTMAX-PTMIN</u>	= 0.7088
<u>PT0</u>		<u>PT2AVG</u>	
MINIMUM	= 0.4731	INCREMENT	= 0.040
MAXIMUM	= 0.8814	INCREASING A.B.C.....K	



RUN 21.214
 TIME 9 49 42.0455

<u>PT2AVG</u>	= 0.5702	<u>PTMAX-PTMIN</u>	= 0.5200
<u>PT0</u>		<u>PT2AVG</u>	
MINIMUM	= 0.4842	INCREMENT	= 0.040
MAXIMUM	= 0.7807	INCREASING A.B.C.....H	

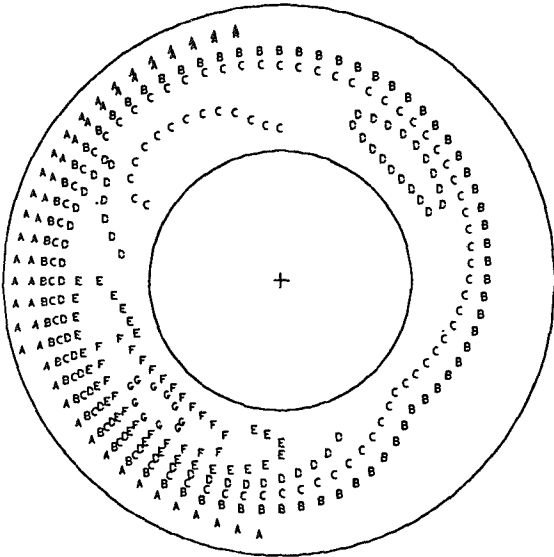


(h)

Figure 36.- Continued.

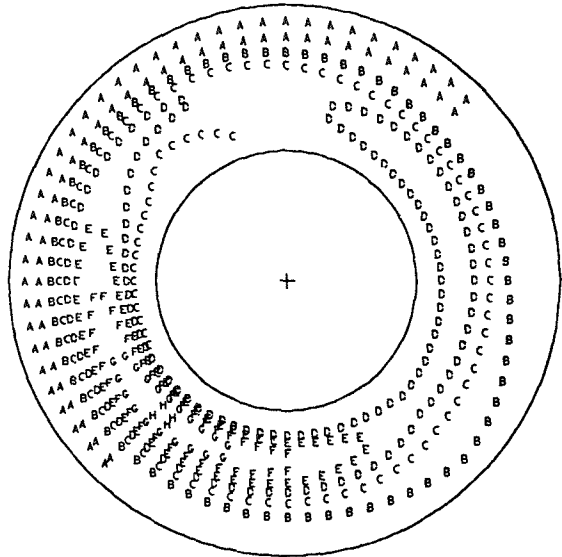
RUN 21.214
 TIME 9 49 42.0460

$\frac{PT2AVG}{PT0} = 0.5668$	$\frac{PTMAX-PTMIN}{PT2AVG} = 0.4709$
MINIMUM = 0.4910	INCREMENT = 0.040
MAXIMUM = 0.7579	INCREASING A,B,C.....G



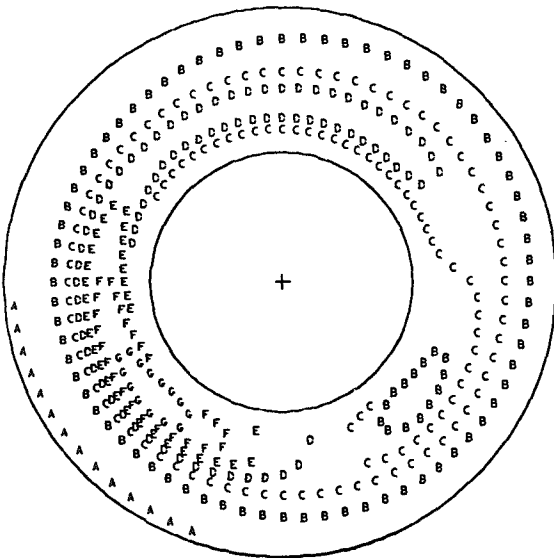
RUN 21.214
 TIME 9 49 42.0465

$\frac{PT2AVG}{PT0} = 0.5756$	$\frac{PTMAX-PTMIN}{PT2AVG} = 0.5047$
MINIMUM = 0.4994	INCREMENT = 0.040
MAXIMUM = 0.7899	INCREASING A,B,C.....H



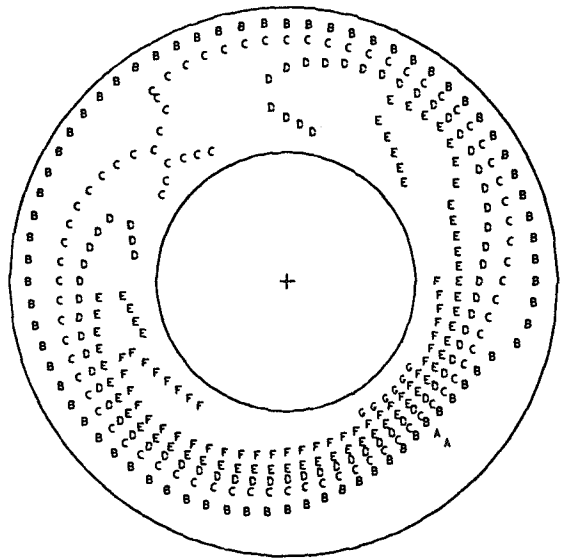
RUN 21.214
 TIME 9 49 42.0470

$\frac{PT2AVG}{PT0} = 0.5716$	$\frac{PTMAX-PTMIN}{PT2AVG} = 0.4351$
MINIMUM = 0.4946	INCREMENT = 0.040
MAXIMUM = 0.7434	INCREASING A,B,C.....G



RUN 21.214
 TIME 9 49 42.0475

$\frac{PT2AVG}{PT0} = 0.5771$	$\frac{PTMAX-PTMIN}{PT2AVG} = 0.4380$
MINIMUM = 0.4793	INCREMENT = 0.040
MAXIMUM = 0.7322	INCREASING A,B,C.....G

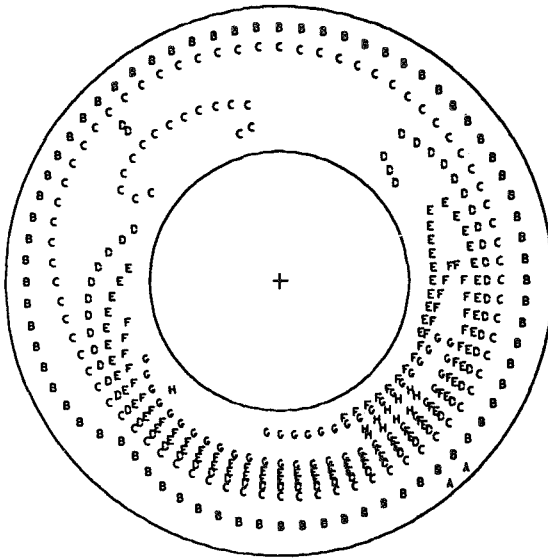


(i)

Figure 36.- Continued.

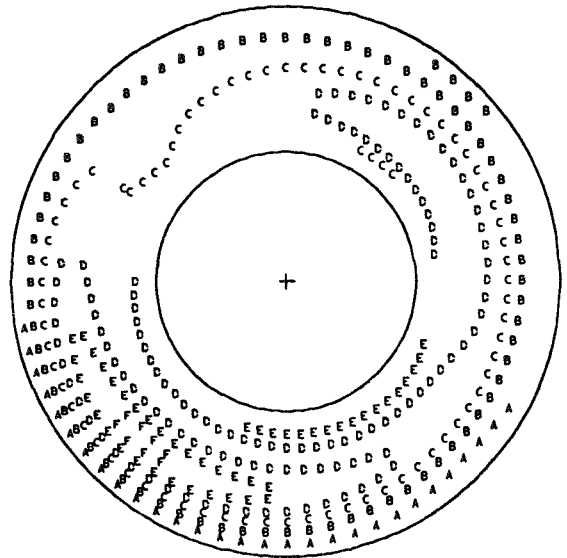
RUN 21.214
 TIME 9 49 42.0480

<u>PT2AVG</u>	= 0.5875	<u>PTMAX-PTMIN</u>	= 0.4823
<u>PT0</u>		<u>PT2AVG</u>	
MINIMUM	= 0.4882	INCREMENT	= 0.040
MAXIMUM	= 0.7716	INCREASING A,B,C.....H	



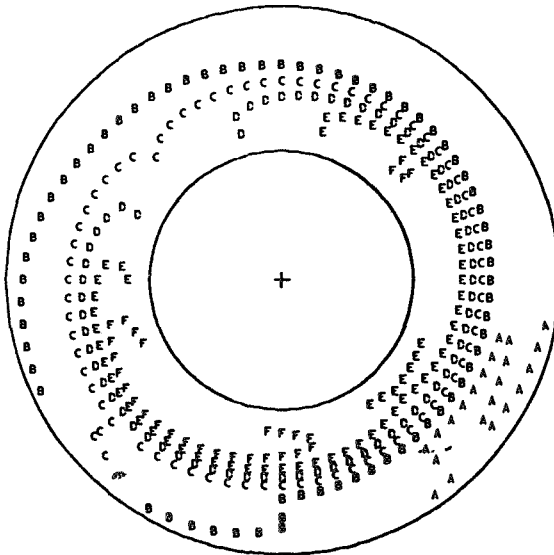
RUN 21.214
 TIME 9 49 42.0485

<u>PT2AVG</u>	= 0.5657	<u>PTMAX-PTMIN</u>	= 0.4007
<u>PT0</u>		<u>PT2AVG</u>	
MINIMUM	= 0.4702	INCREMENT	= 0.040
MAXIMUM	= 0.6970	INCREASING A,B,C.....F	



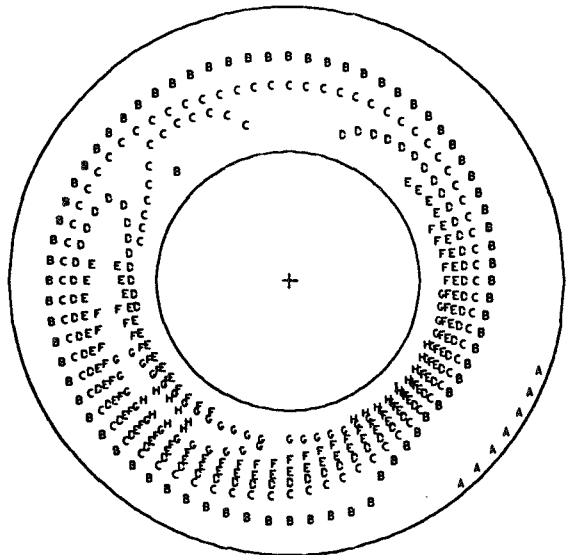
RUN 21.214
 TIME 9 49 42.0490

<u>PT2AVG</u>	= 0.5601	<u>PTMAX-PTMIN</u>	= 0.4291
<u>PT0</u>		<u>PT2AVG</u>	
MINIMUM	= 0.4723	INCREMENT	= 0.040
MAXIMUM	= 0.7127	INCREASING A,B,C.....F	



RUN 21.214
 TIME 9 49 42.0495

<u>PT2AVG</u>	= 0.5621	<u>PTMAX-PTMIN</u>	= 0.5763
<u>PT0</u>		<u>PT2AVG</u>	
MINIMUM	= 0.4770	INCREMENT	= 0.040
MAXIMUM	= 0.8010	INCREASING A,B,C.....I	

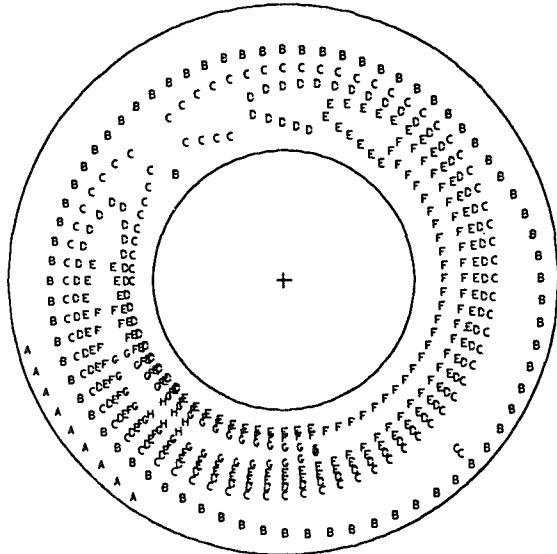


(j)

Figure 36.- Continued.

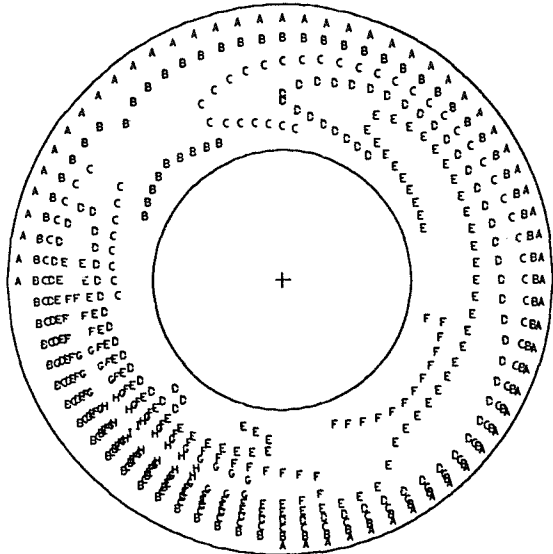
RUN 21.214
TIME 9 49 42.0500

<u>PT2AVG</u>	= 0.5680	<u>PTMAX-PTMIN</u>	= 0.5221
<u>PT0</u>		<u>PT2AVG</u>	
MINIMUM	= 0.4738	INCREMENT	= 0.040
MAXIMUM	= 0.7704	INCREASING A.B.C.....H	



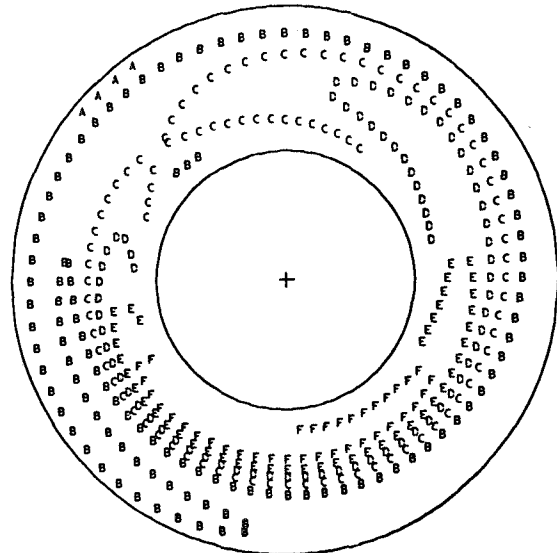
RUN 21.214
TIME 9 49 42.0505

<u>PT2AVG</u>	= 0.6018	<u>PTMAX-PTMIN</u>	= 0.5575
<u>PT0</u>		<u>PT2AVG</u>	
MINIMUM	= 0.4905	INCREMENT	= 0.040
MAXIMUM	= 0.8261	INCREASING A.B.C.....I	



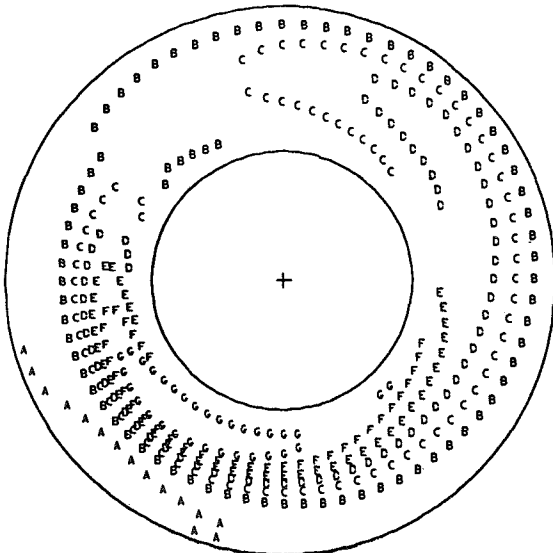
RUN 21.214
TIME 9 49 42.0510

<u>PT2AVG</u>	= 0.5810	<u>PTMAX-PTMIN</u>	= 0.3847
<u>PT0</u>		<u>PT2AVG</u>	
MINIMUM	= 0.4975	INCREMENT	= 0.040
MAXIMUM	= 0.7211	INCREASING A.B.C.....F	



RUN 21.214
TIME 9 49 42.0515

<u>PT2AVG</u>	= 0.5844	<u>PTMAX-PTMIN</u>	= 0.4620
<u>PT0</u>		<u>PT2AVG</u>	
MINIMUM	= 0.4937	INCREMENT	= 0.040
MAXIMUM	= 0.7637	INCREASING A.B.C.....G	

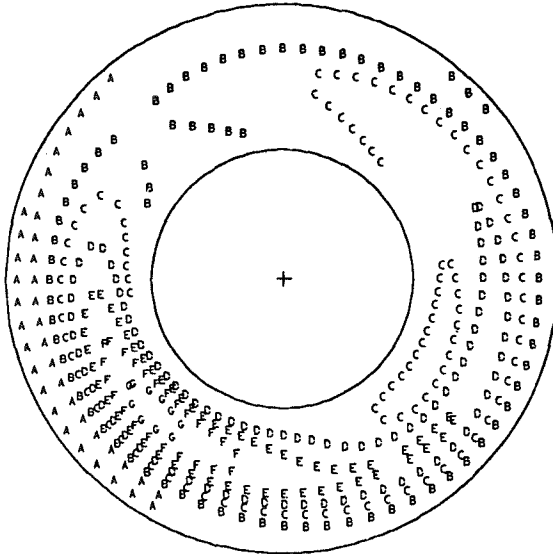


(k)

Figure 36.- Continued.

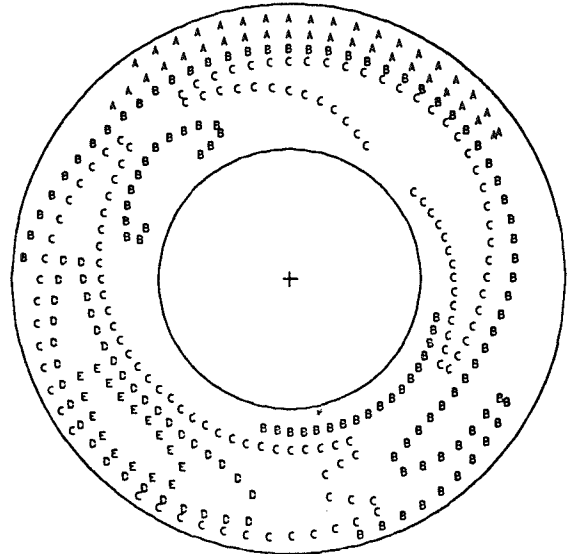
RUN 21.214
 TIME 9 49 42.0520

$\frac{PT2AVG}{PT0} = 0.5738$	$\frac{PTMAX-PTMIN}{PT2AVG} = 0.4715$
MINIMUM = 0.4961	INCREMENT = 0.040
MAXIMUM = 0.7667	INCREASING A,B,C.....G



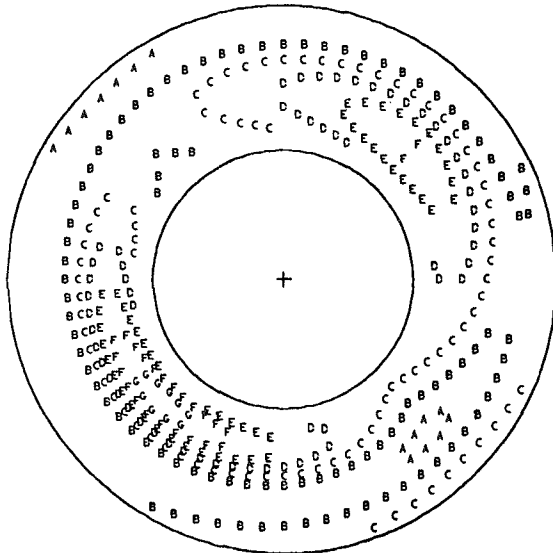
RUN 21.214
 TIME 9 49 42.0525

$\frac{PT2AVG}{PT0} = 0.5725$	$\frac{PTMAX-PTMIN}{PT2AVG} = 0.3349$
MINIMUM = 0.5083	INCREMENT = 0.040
MAXIMUM = 0.7001	INCREASING A,B,C.....E



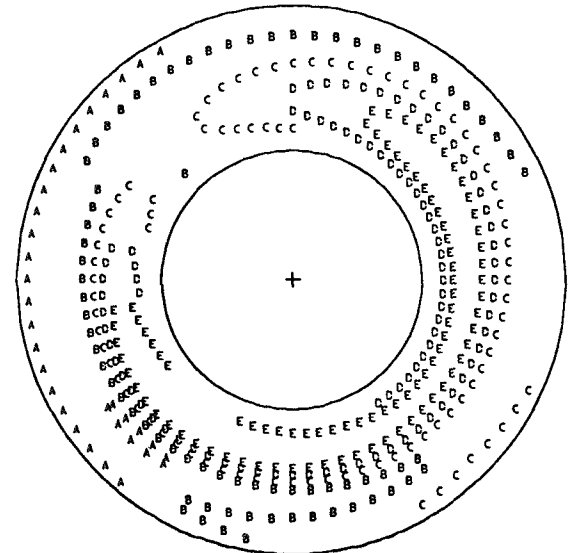
RUN 21.214
 TIME 9 49 42.0530

$\frac{PT2AVG}{PT0} = 0.5708$	$\frac{PTMAX-PTMIN}{PT2AVG} = 0.4370$
MINIMUM = 0.4906	INCREMENT = 0.040
MAXIMUM = 0.7401	INCREASING A,B,C.....G



RUN 21.214
 TIME 9 49 42.0535

$\frac{PT2AVG}{PT0} = 0.5778$	$\frac{PTMAX-PTMIN}{PT2AVG} = 0.3529$
MINIMUM = 0.4935	INCREMENT = 0.040
MAXIMUM = 0.6975	INCREASING A,B,C.....E

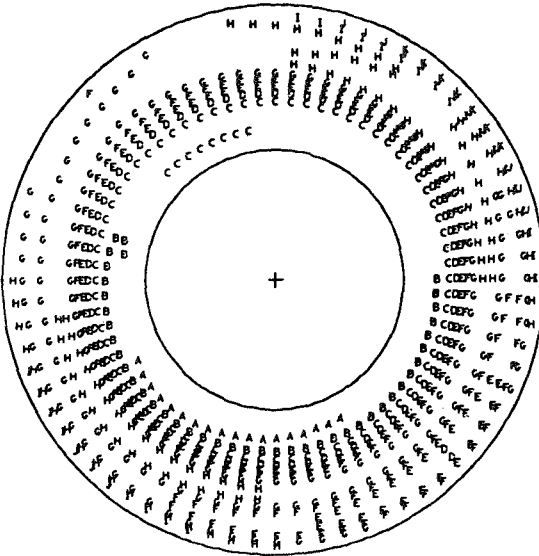


(1)

Figure 36.- Concluded.

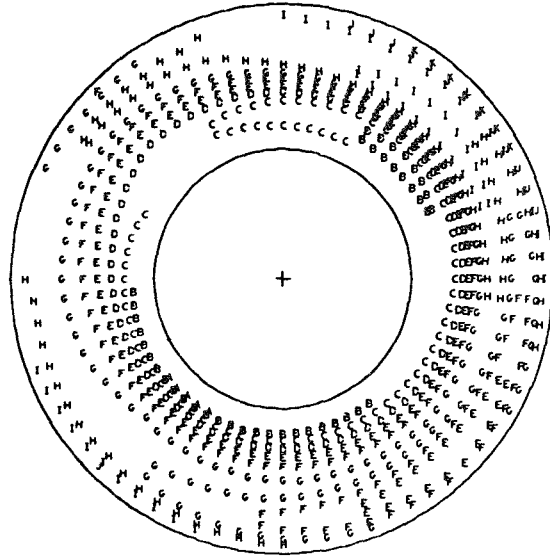
RUN 27.250
 TIME 6 57 0.0400

$\frac{PT2AVG}{PT0}$	= 0.9077	$\frac{PTMAX-PTMIN}{PT2AVG}$	= 0.1271
MINIMUM	= 0.8555	INCREMENT	= 0.010
MAXIMUM	= 0.9709	INCREASING A,B,C.....L	



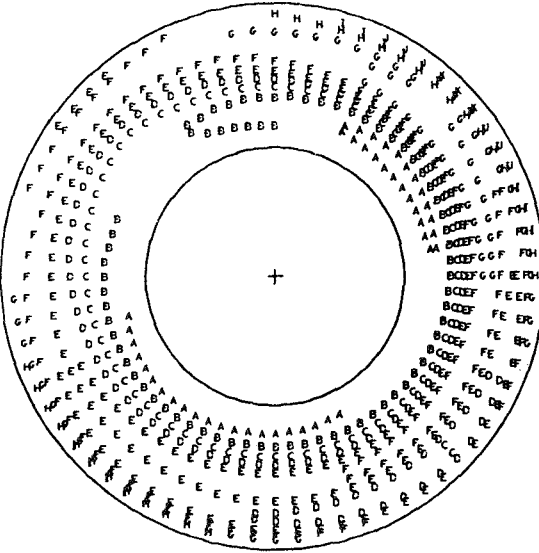
RUN 27.250
 TIME 6 57 0.0405

$\frac{PT2AVG}{PT0}$	= 0.9103	$\frac{PTMAX-PTMIN}{PT2AVG}$	= 0.1268
MINIMUM	= 0.8574	INCREMENT	= 0.010
MAXIMUM	= 0.9729	INCREASING A,B,C.....L	



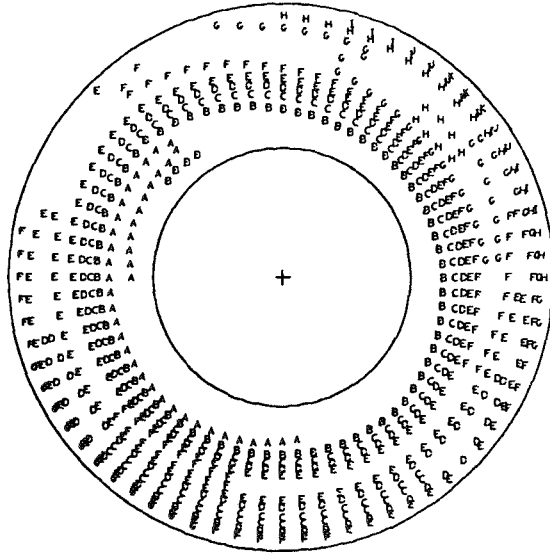
RUN 27.250
 TIME 6 57 0.0410

$\frac{PT2AVG}{PT0}$	= 0.9063	$\frac{PTMAX-PTMIN}{PT2AVG}$	= 0.1281
MINIMUM	= 0.8613	INCREMENT	= 0.010
MAXIMUM	= 0.9774	INCREASING A,B,C.....K	



RUN 27.250
 TIME 6 57 0.0415

$\frac{PT2AVG}{PT0}$	= 0.9053	$\frac{PTMAX-PTMIN}{PT2AVG}$	= 0.1251
MINIMUM	= 0.8604	INCREMENT	= 0.010
MAXIMUM	= 0.9736	INCREASING A,B,C.....K	

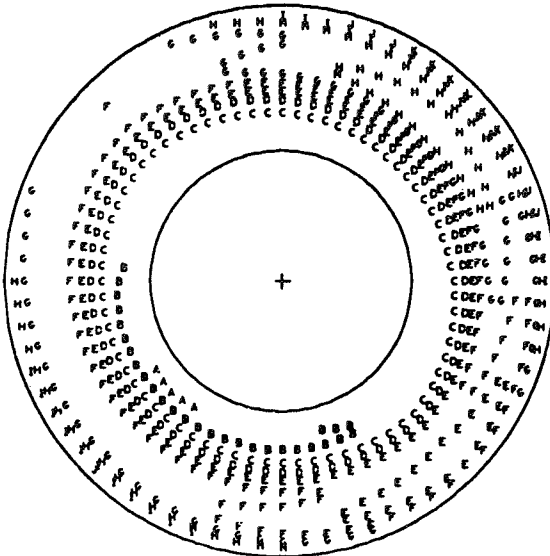


(a)

Figure 37.- Instantaneous total pressure ratio contours, $M_0 = 2.6$, $\bar{P}_{t2}/P_{t0} = 0.918$.

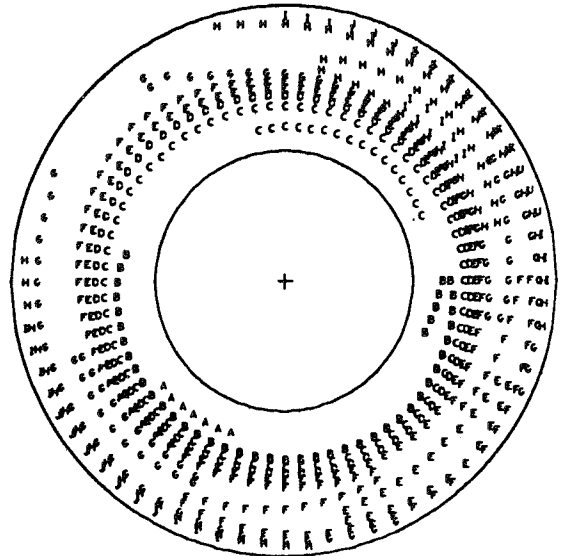
RUN 27.250
 TIME 6 57 0.0420

<u>PT2AVG</u>	= 0.9055	<u>PTMAX-PTMIN</u>	= 0.1271
<u>PT0</u>		<u>PT2AVG</u>	
MINIMUM	= 0.8573	INCREMENT	= 0.010
MAXIMUM	= 0.9725	INCREASING A.B.C.....L	



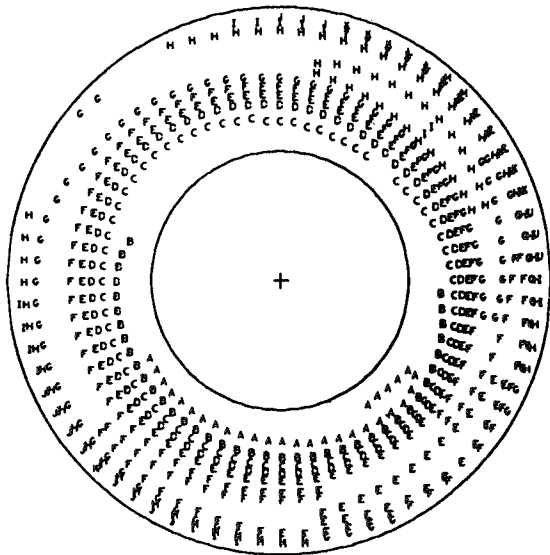
RUN 27.250
 TIME 6 57 0.0425

<u>PT2AVG</u>	= 0.9056	<u>PTMAX-PTMIN</u>	= 0.1244
<u>PT0</u>		<u>PT2AVG</u>	
MINIMUM	= 0.8582	INCREMENT	= 0.010
MAXIMUM	= 0.9708	INCREASING A.B.C.....L	



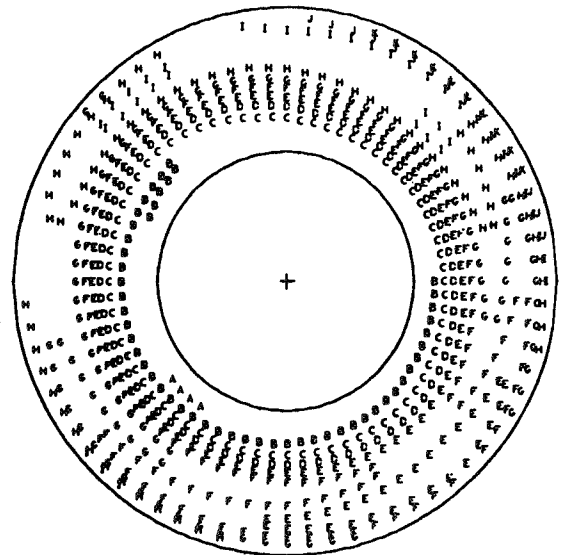
RUN 27.250
 TIME 6 57 0.0430

<u>PT2AVG</u>	= 0.9064	<u>PTMAX-PTMIN</u>	= 0.1410
<u>PT0</u>		<u>PT2AVG</u>	
MINIMUM	= 0.8560	INCREMENT	= 0.010
MAXIMUM	= 0.9839	INCREASING A.B.C.....M	



RUN 27.250
 TIME 6 57 0.0435

<u>PT2AVG</u>	= 0.9083	<u>PTMAX-PTMIN</u>	= 0.1290
<u>PT0</u>		<u>PT2AVG</u>	
MINIMUM	= 0.8590	INCREMENT	= 0.010
MAXIMUM	= 0.9762	INCREASING A.B.C.....L	

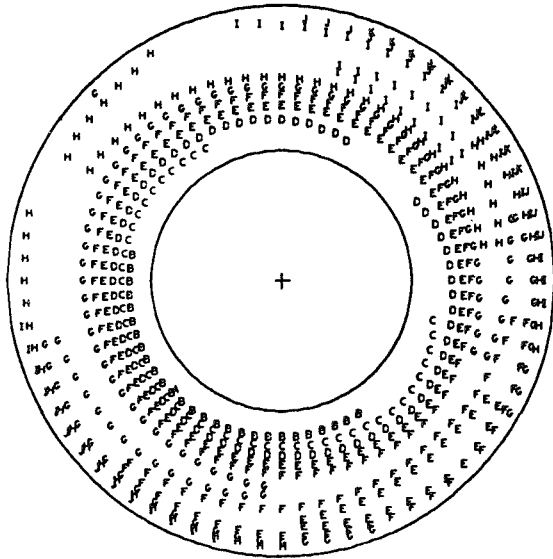


(b)

Figure 37.- Continued.

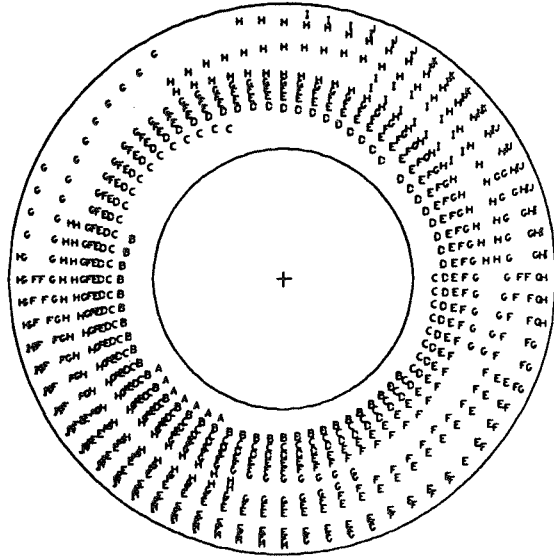
RUN 27.250
 TIME 6 57 0.0440

<u>PT2AVG</u>	= 0.9135	<u>PTMAX-PTMIN</u>	= 0.1310
<u>PT0</u>		<u>PT2AVG</u>	
MINIMUM	= 0.8593	INCREMENT	= 0.010
MAXIMUM	= 0.9790	INCREASING A,B,C.....L	



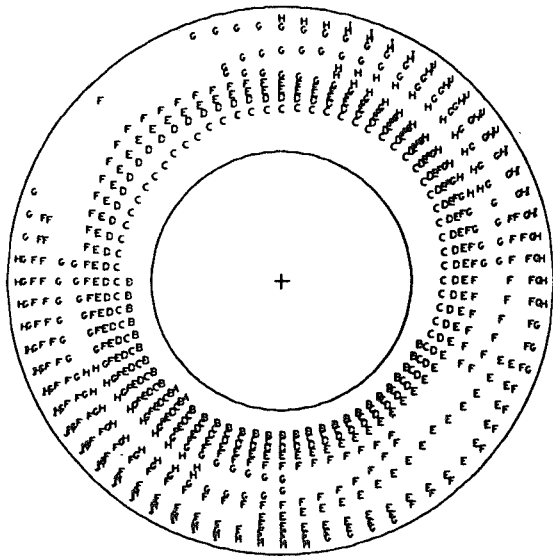
RUN 27.250
 TIME 6 57 0.0445

<u>PT2AVG</u>	= 0.9103	<u>PTMAX-PTMIN</u>	= 0.1198
<u>PT0</u>		<u>PT2AVG</u>	
MINIMUM	= 0.8571	INCREMENT	= 0.010
MAXIMUM	= 0.9662	INCREASING A,B,C.....K	



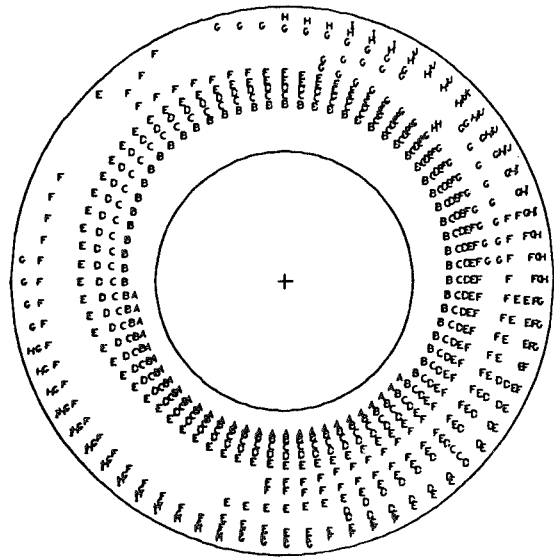
RUN 27.250
 TIME 6 57 0.0450

<u>PT2AVG</u>	= 0.9067	<u>PTMAX-PTMIN</u>	= 0.1089
<u>PT0</u>		<u>PT2AVG</u>	
MINIMUM	= 0.8594	INCREMENT	= 0.010
MAXIMUM	= 0.9582	INCREASING A,B,C.....J	



RUN 27.250
 TIME 6 57 0.0455

<u>PT2AVG</u>	= 0.9091	<u>PTMAX-PTMIN</u>	= 0.1171
<u>PT0</u>		<u>PT2AVG</u>	
MINIMUM	= 0.8657	INCREMENT	= 0.010
MAXIMUM	= 0.9722	INCREASING A,B,C.....K	



(c)

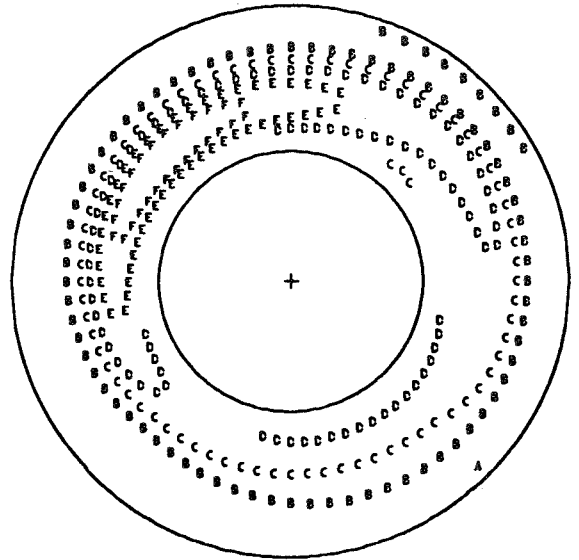
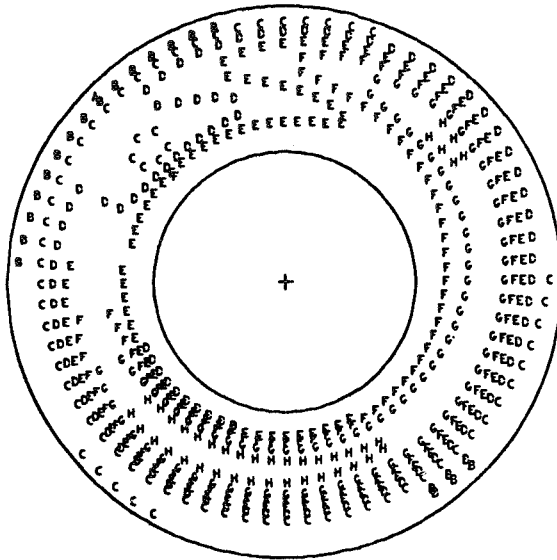
Figure 37.- Concluded.

RUN 27.255
 TIME 8 27 0.0280

<u>PT2AVG</u>	= 0.6420	<u>PTMAX-PTMIN</u>	= 0.4763
<u>PT0</u>		<u>PT2AVG</u>	
MINIMUM	= 0.4891	INCREMENT	= 0.040
MAXIMUM	= 0.7949	INCREASING A.B.C.....H	

RUN 27.255
 TIME 8 27 0.0285

<u>PT2AVG</u>	= 0.6160	<u>PTMAX-PTMIN</u>	= 0.3821
<u>PT0</u>		<u>PT2AVG</u>	
MINIMUM	= 0.5389	INCREMENT	= 0.040
MAXIMUM	= 0.7743	INCREASING A.B.C.....F	

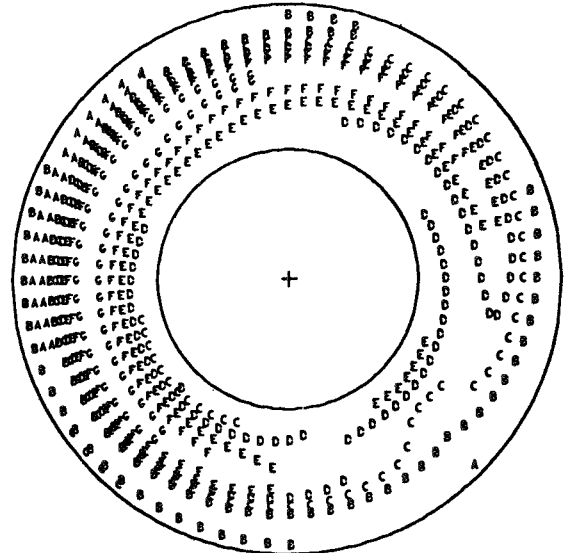
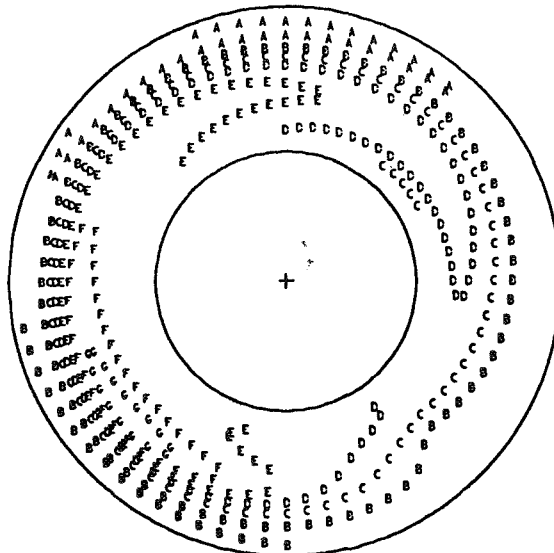


RUN 27.255
 TIME 8 27 0.0290

<u>PT2AVG</u>	= 0.6262	<u>PTMAX-PTMIN</u>	= 0.4181
<u>PT0</u>		<u>PT2AVG</u>	
MINIMUM	= 0.5233	INCREMENT	= 0.040
MAXIMUM	= 0.7852	INCREASING A.B.C.....G	

RUN 27.255
 TIME 8 27 0.0295

<u>PT2AVG</u>	= 0.6504	<u>PTMAX-PTMIN</u>	= 0.3807
<u>PT0</u>		<u>PT2AVG</u>	
MINIMUM	= 0.5389	INCREMENT	= 0.040
MAXIMUM	= 0.7865	INCREASING A.B.C.....G	

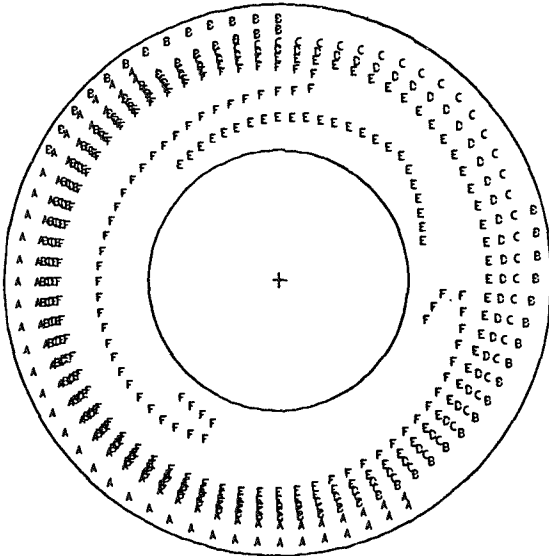


(a)

Figure 38.- Instantaneous total pressure ratio contours, $M_0 = 2.6$, $\bar{P}_{t2}/P_{t0} = 0.642$.

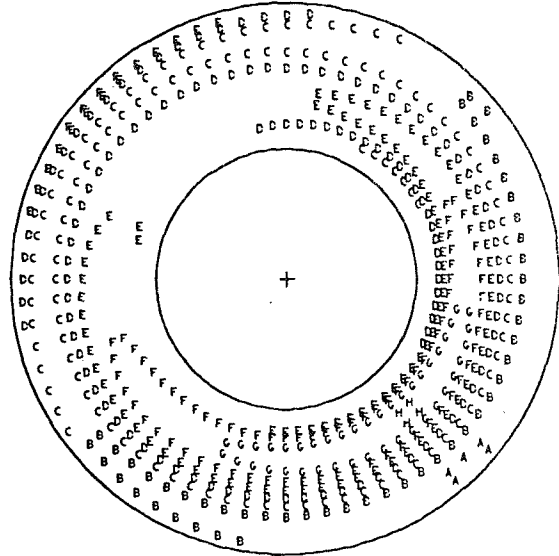
RUN 27.255
TIME 8 27 0.0300

$\frac{PT2AVG}{PT0}$	= 0.6595	$\frac{PTMAX-PTMIN}{PT2AVG}$	= 0.3635
MINIMUM	= 0.5206	INCREMENT	= 0.040
MAXIMUM	= 0.7603	INCREASING A.B.C.....F	



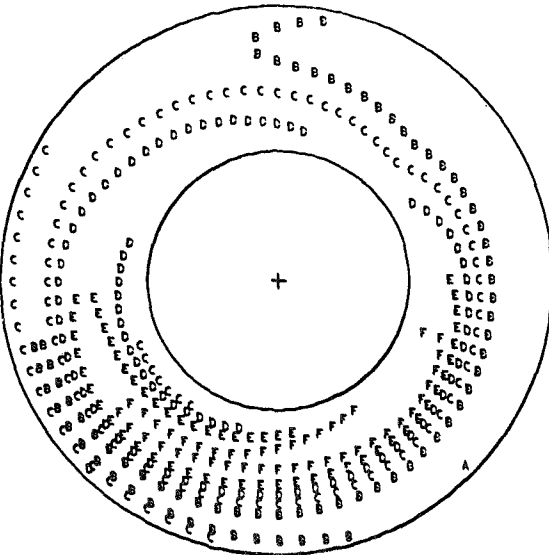
RUN 27.255
TIME 8 27 0.0305

$\frac{PT2AVG}{PT0}$	= 0.6577	$\frac{PTMAX-PTMIN}{PT2AVG}$	= 0.4343
MINIMUM	= 0.5389	INCREMENT	= 0.040
MAXIMUM	= 0.8245	INCREASING A.B.C.....H	



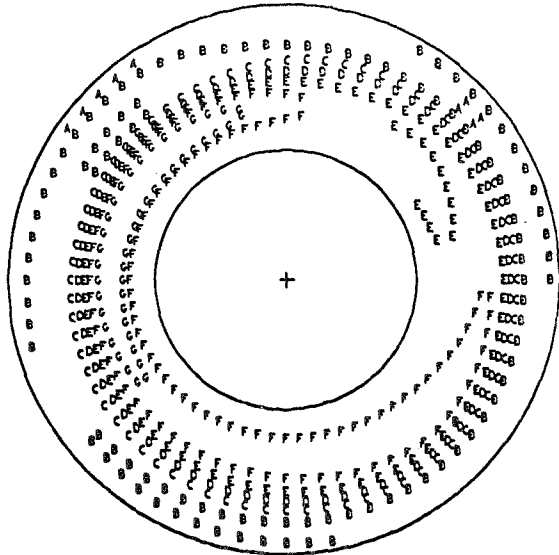
RUN 27.255
TIME 8 27 0.0310

$\frac{PT2AVG}{PT0}$	= 0.6287	$\frac{PTMAX-PTMIN}{PT2AVG}$	= 0.3641
MINIMUM	= 0.5389	INCREMENT	= 0.040
MAXIMUM	= 0.7678	INCREASING A.B.C.....F	



RUN 27.255
TIME 8 27 0.0315

$\frac{PT2AVG}{PT0}$	= 0.6258	$\frac{PTMAX-PTMIN}{PT2AVG}$	= 0.4247
MINIMUM	= 0.5000	INCREMENT	= 0.040
MAXIMUM	= 0.7658	INCREASING A.B.C.....G	

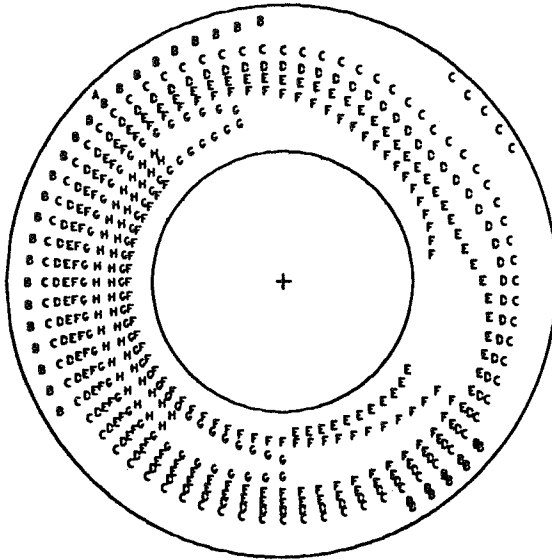


(b)

Figure 38.- Continued.

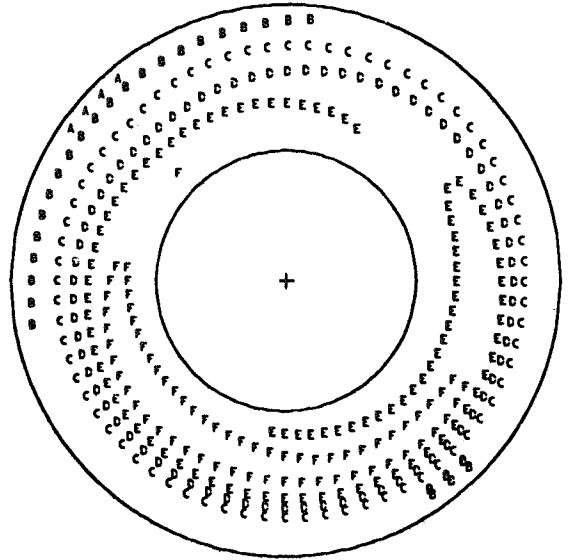
RUN 27.255
 TIME 8 27 0.0320

<u>PT2AVG</u>	= 0.6252	<u>PTMAX-PTMIN</u>	= 0.4636
<u>PT0</u>		<u>PT2AVG</u>	
MINIMUM	= 0.4875	INCREMENT	= 0.040
MAXIMUM	= 0.7774	INCREASING A.B.C.....H	



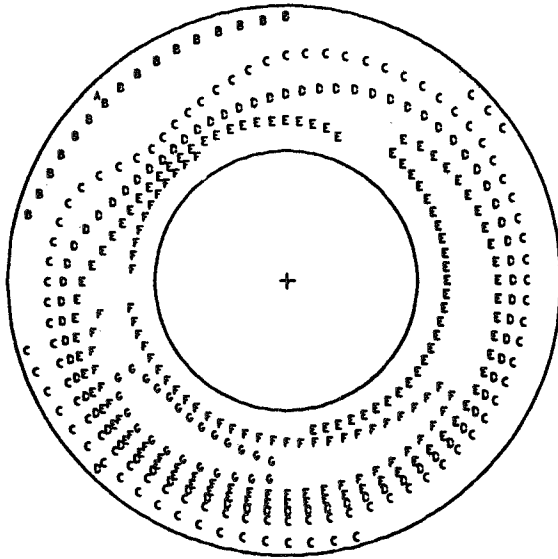
RUN 27.255
 TIME 8 27 0.0325

<u>PT2AVG</u>	= 0.6090	<u>PTMAX-PTMIN</u>	= 0.3754
<u>PT0</u>		<u>PT2AVG</u>	
MINIMUM	= 0.4812	INCREMENT	= 0.040
MAXIMUM	= 0.7099	INCREASING A.B.C.....F	



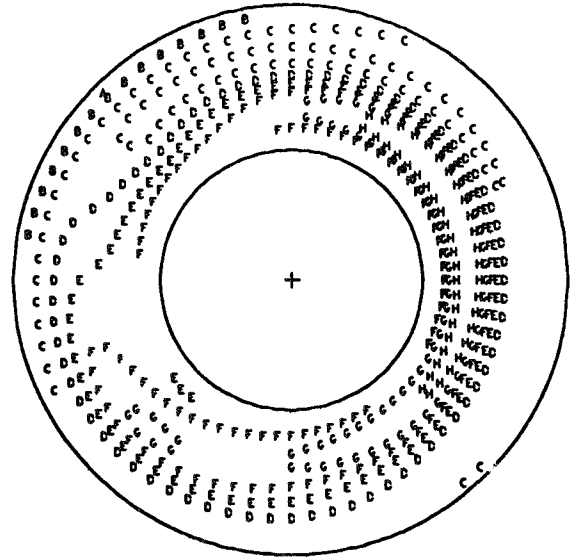
RUN 27.255
 TIME 8 27 0.0330

<u>PT2AVG</u>	= 0.6065	<u>PTMAX-PTMIN</u>	= 0.4617
<u>PT0</u>		<u>PT2AVG</u>	
MINIMUM	= 0.4752	INCREMENT	= 0.040
MAXIMUM	= 0.7553	INCREASING A.B.C.....G	



RUN 27.255
 TIME 8 27 0.0335

<u>PT2AVG</u>	= 0.6029	<u>PTMAX-PTMIN</u>	= 0.5156
<u>PT0</u>		<u>PT2AVG</u>	
MINIMUM	= 0.4594	INCREMENT	= 0.040
MAXIMUM	= 0.7704	INCREASING A.B.C.....H	

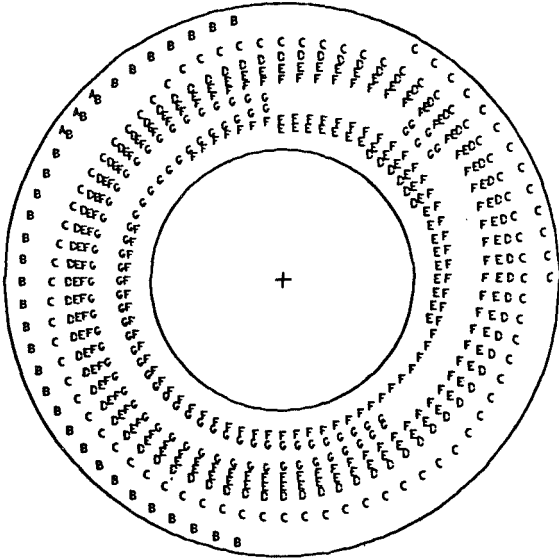


(c)

Figure 38.- Continued.

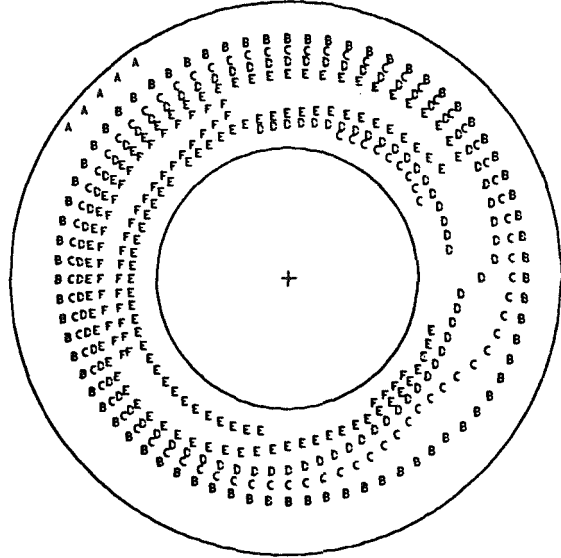
RUN 27.255
 TIME 8 27 0.0340

<u>PT2AVG</u>	= 0.6114	<u>PTMAX-PTMIN</u>	= 0.4337
<u>PT0</u>		<u>PT2AVG</u>	
MINIMUM	= 0.4750	INCREMENT	= 0.040
MAXIMUM	= 0.7401	INCREASING A,B,C.....G	



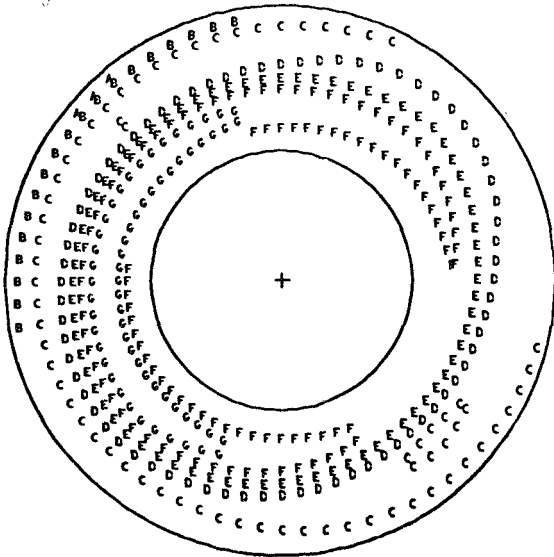
RUN 27.255
 TIME 8 27 0.0345

<u>PT2AVG</u>	= 0.6150	<u>PTMAX-PTMIN</u>	= 0.3534
<u>PT0</u>		<u>PT2AVG</u>	
MINIMUM	= 0.5253	INCREMENT	= 0.040
MAXIMUM	= 0.7427	INCREASING A,B,C.....F	



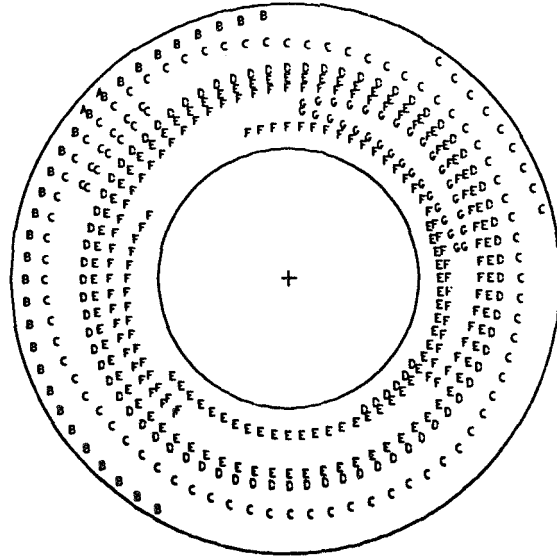
RUN 27.255
 TIME 8 27 0.0350

<u>PT2AVG</u>	= 0.6040	<u>PTMAX-PTMIN</u>	= 0.4537
<u>PT0</u>		<u>PT2AVG</u>	
MINIMUM	= 0.4626	INCREMENT	= 0.040
MAXIMUM	= 0.7367	INCREASING A,B,C.....G	



RUN 27.255
 TIME 8 27 0.0355

<u>PT2AVG</u>	= 0.5984	<u>PTMAX-PTMIN</u>	= 0.4405
<u>PT0</u>		<u>PT2AVG</u>	
MINIMUM	= 0.4775	INCREMENT	= 0.040
MAXIMUM	= 0.7411	INCREASING A,B,C.....G	

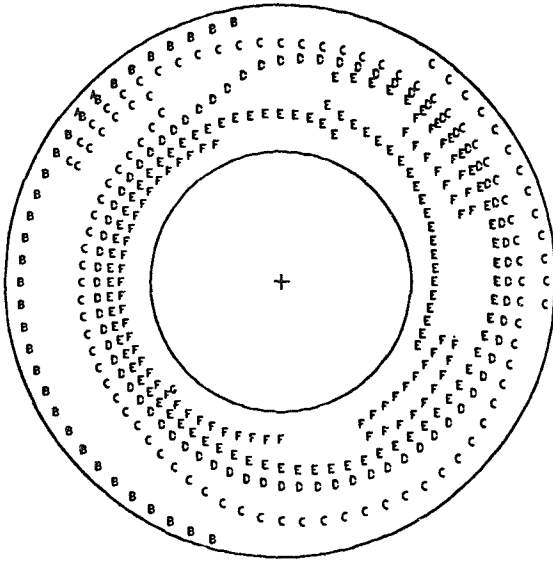


(d)

Figure 38.- Continued.

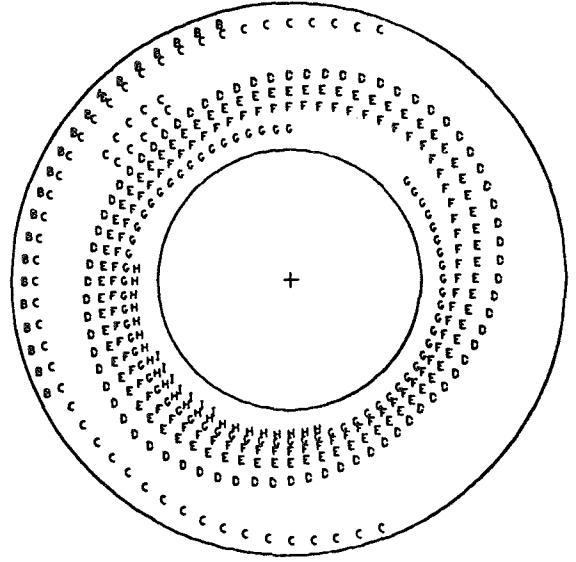
RUN 27.255
 TIME 8 27 0.0360

<u>PT2AVG</u>	= 0.5868	<u>PTMAX-PTMIN</u>	= 0.4121
<u>PT0</u>		<u>PT2AVG</u>	
MINIMUM	= 0.4682	INCREMENT	= 0.040
MAXIMUM	= 0.7101	INCREASING A,B,C.....G	



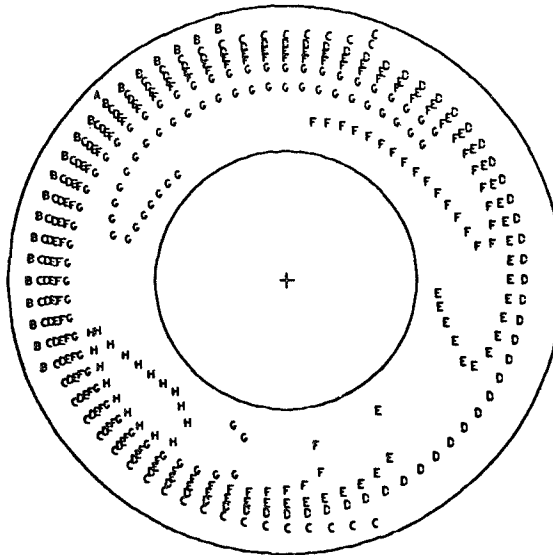
RUN 27.255
 TIME 8 27 0.0365

<u>PT2AVG</u>	= 0.5884	<u>PTMAX-PTMIN</u>	= 0.5725
<u>PT0</u>		<u>PT2AVG</u>	
MINIMUM	= 0.4492	INCREMENT	= 0.040
MAXIMUM	= 0.7860	INCREASING A,B,C.....I	



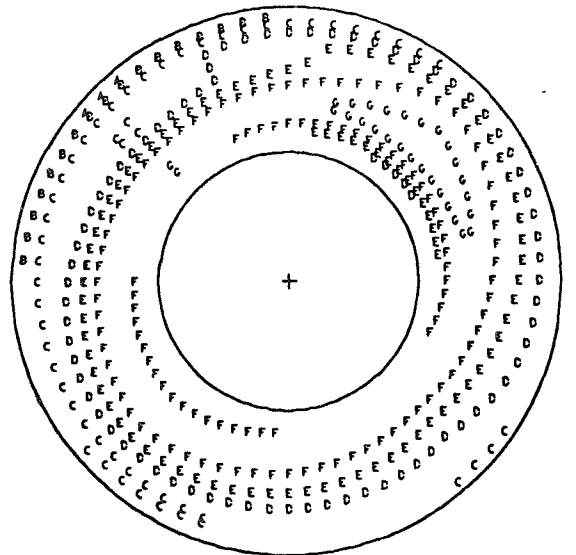
RUN 27.255
 TIME 8 27 0.0370

<u>PT2AVG</u>	= 0.6124	<u>PTMAX-PTMIN</u>	= 0.4978
<u>PT0</u>		<u>PT2AVG</u>	
MINIMUM	= 0.4480	INCREMENT	= 0.040
MAXIMUM	= 0.7529	INCREASING A,B,C.....H	



RUN 27.255
 TIME 8 27 0.0375

<u>PT2AVG</u>	= 0.6080	<u>PTMAX-PTMIN</u>	= 0.4444
<u>PT0</u>		<u>PT2AVG</u>	
MINIMUM	= 0.4535	INCREMENT	= 0.040
MAXIMUM	= 0.7237	INCREASING A,B,C.....G	

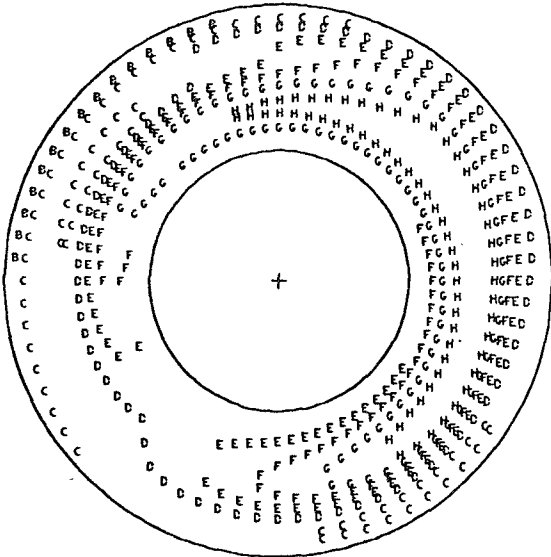


(e)

Figure 38.- Continued.

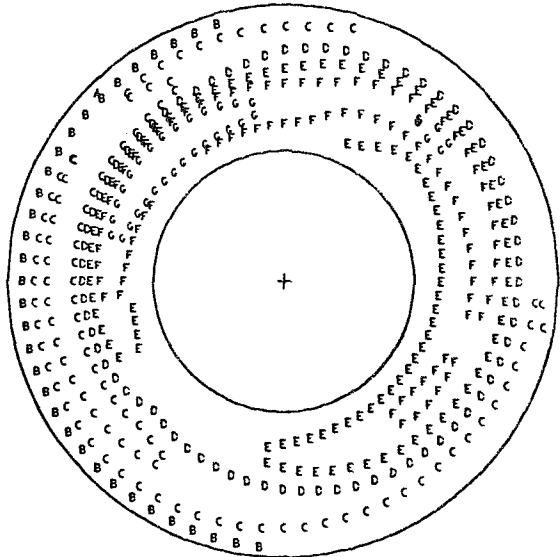
RUN 27.255
 TIME 8 27 0.0380

$\frac{PT2AVG}{PT0}$ = 0.6122	$\frac{PTMAX-PTMIN}{PT2AVG}$ = 0.5090
MINIMUM = 0.4500	INCREMENT = 0.040
MAXIMUM = 0.7616	INCREASING A,B,C.....H



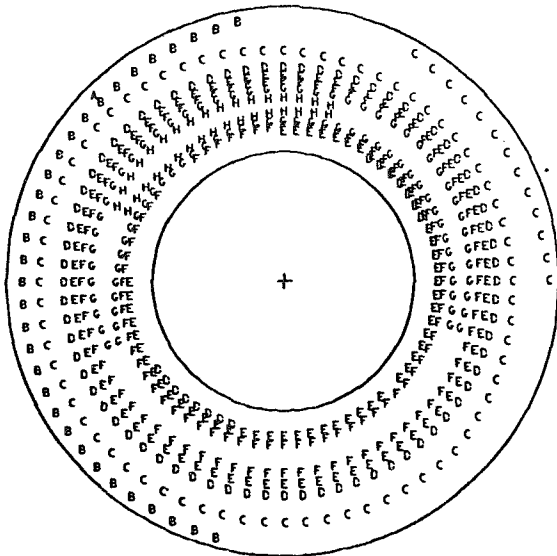
RUN 27.255
 TIME 8 27 0.0385

$\frac{PT2AVG}{PT0}$ = 0.6045	$\frac{PTMAX-PTMIN}{PT2AVG}$ = 0.4338
MINIMUM = 0.4790	INCREMENT = 0.040
MAXIMUM = 0.7413	INCREASING A,B,C.....G



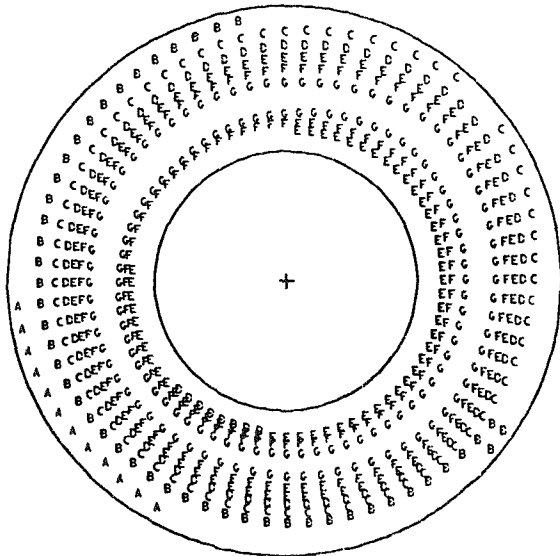
RUN 27.255
 TIME 8 27 0.0390

$\frac{PT2AVG}{PT0}$ = 0.6070	$\frac{PTMAX-PTMIN}{PT2AVG}$ = 0.4687
MINIMUM = 0.4797	INCREMENT = 0.040
MAXIMUM = 0.7642	INCREASING A,B,C.....H



RUN 27.255
 TIME 8 27 0.0395

$\frac{PT2AVG}{PT0}$ = 0.6358	$\frac{PTMAX-PTMIN}{PT2AVG}$ = 0.4507
MINIMUM = 0.4900	INCREMENT = 0.040
MAXIMUM = 0.7766	INCREASING A,B,C.....G

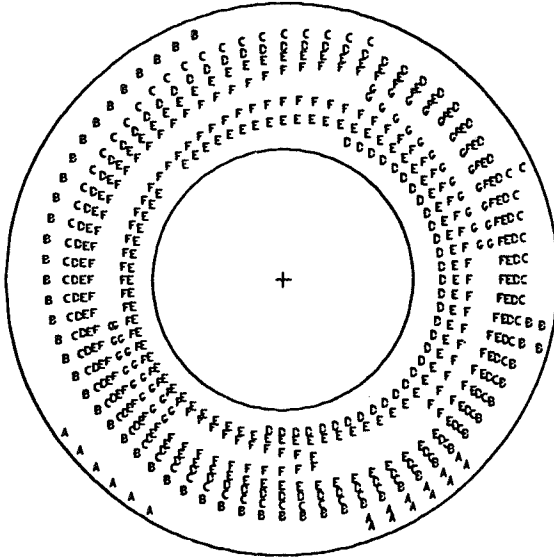


(f)

Figure 38.- Continued.

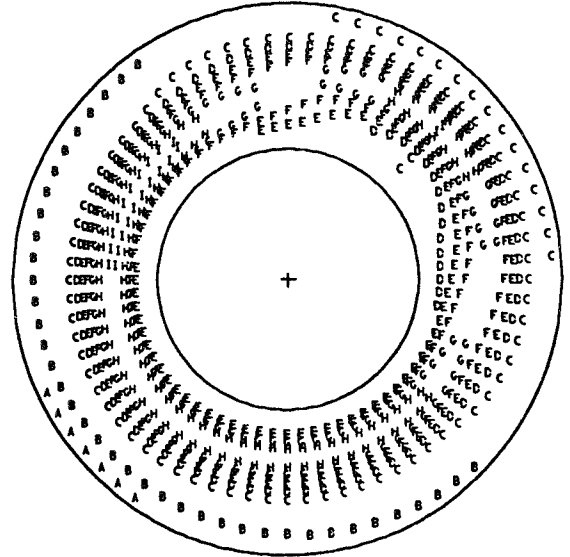
RUN 27.255
 TIME 8 27 0.0400

<u>PT2AVG</u>	= 0.6448	<u>PTMAX-PTMIN</u>	= 0.4210
<u>PT0</u>		<u>PT2AVG</u>	
MINIMUM	= 0.5279	INCREMENT	= 0.040
MAXIMUM	= 0.7994	INCREASING A.B.C.....G	



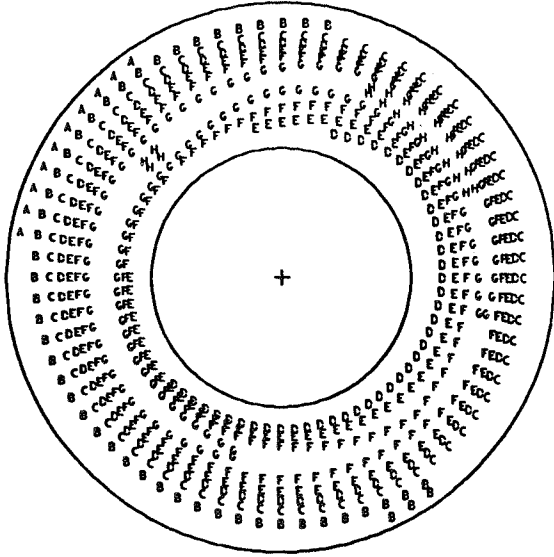
RUN 27.255
 TIME 8 27 0.0405

<u>PT2AVG</u>	= 0.6318	<u>PTMAX-PTMIN</u>	= 0.5272
<u>PT0</u>		<u>PT2AVG</u>	
MINIMUM	= 0.4926	INCREMENT	= 0.040
MAXIMUM	= 0.8257	INCREASING A.B.C.....I	



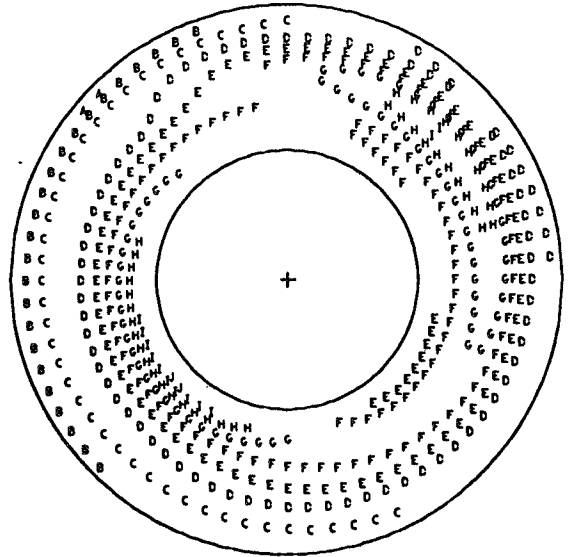
RUN 27.255
 TIME 8 27 0.0410

<u>PT2AVG</u>	= 0.6209	<u>PTMAX-PTMIN</u>	= 0.5072
<u>PT0</u>		<u>PT2AVG</u>	
MINIMUM	= 0.4804	INCREMENT	= 0.040
MAXIMUM	= 0.7954	INCREASING A.B.C.....H	



RUN 27.255
 TIME 8 27 0.0415

<u>PT2AVG</u>	= 0.6096	<u>PTMAX-PTMIN</u>	= 0.6100
<u>PT0</u>		<u>PT2AVG</u>	
MINIMUM	= 0.4451	INCREMENT	= 0.040
MAXIMUM	= 0.8170	INCREASING A.B.C.....J	

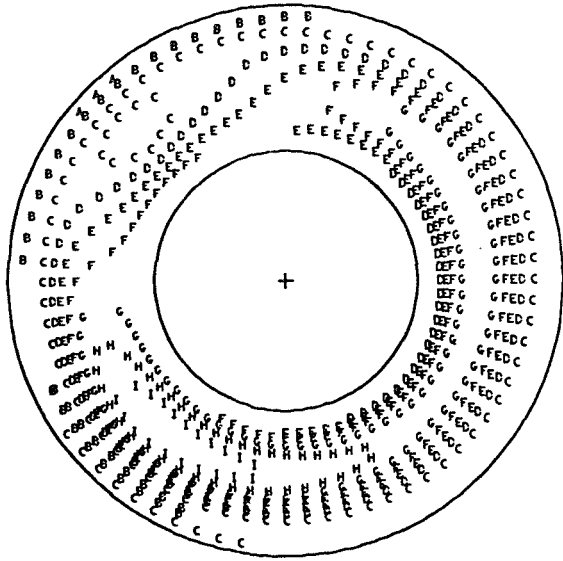


(g)

Figure 38.- Continued.

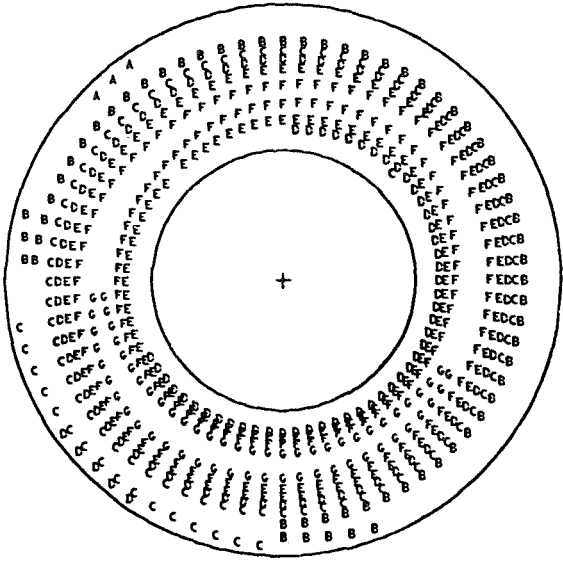
RUN 27.255
 TIME 8 27 0.0420

$\frac{PT2AVG}{PT0} = 0.6282$	$\frac{PTMAX-PTMIN}{PT2AVG} = 0.5782$
MINIMUM = 0.4727	INCREMENT = 0.040
MAXIMUM = 0.8361	INCREASING A,B,C.....I



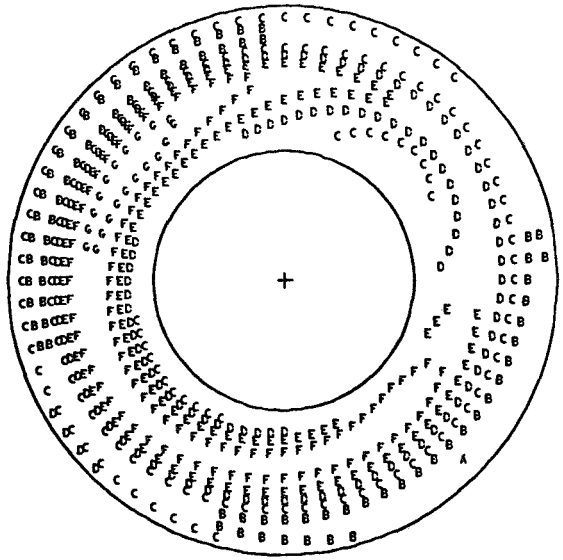
RUN 27.255
 TIME 8 27 0.0425

$\frac{PT2AVG}{PT0} = 0.6481$	$\frac{PTMAX-PTMIN}{PT2AVG} = 0.4228$
MINIMUM = 0.5256	INCREMENT = 0.040
MAXIMUM = 0.7996	INCREASING A,B,C.....G



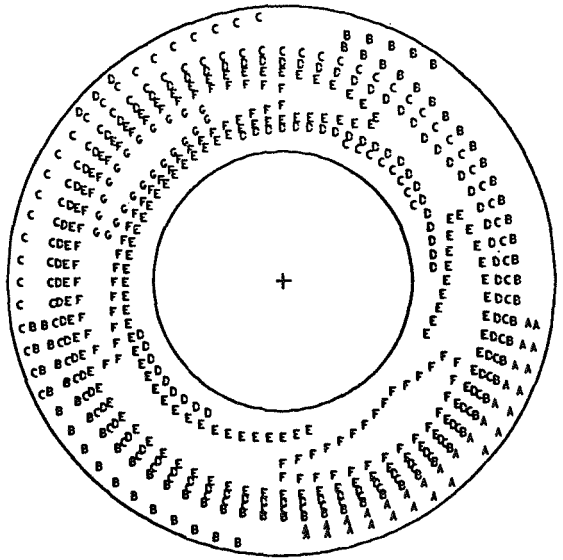
RUN 27.255
 TIME 8 27 0.0430

$\frac{PT2AVG}{PT0} = 0.6558$	$\frac{PTMAX-PTMIN}{PT2AVG} = 0.3885$
MINIMUM = 0.5389	INCREMENT = 0.040
MAXIMUM = 0.7937	INCREASING A,B,C.....G



RUN 27.255
 TIME 8 27 0.0435

$\frac{PT2AVG}{PT0} = 0.6535$	$\frac{PTMAX-PTMIN}{PT2AVG} = 0.4188$
MINIMUM = 0.5389	INCREMENT = 0.040
MAXIMUM = 0.8126	INCREASING A,B,C.....G

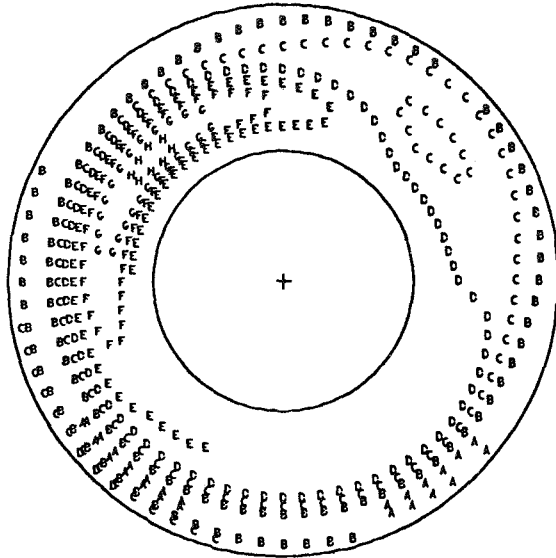


(h)

Figure 38.- Continued.

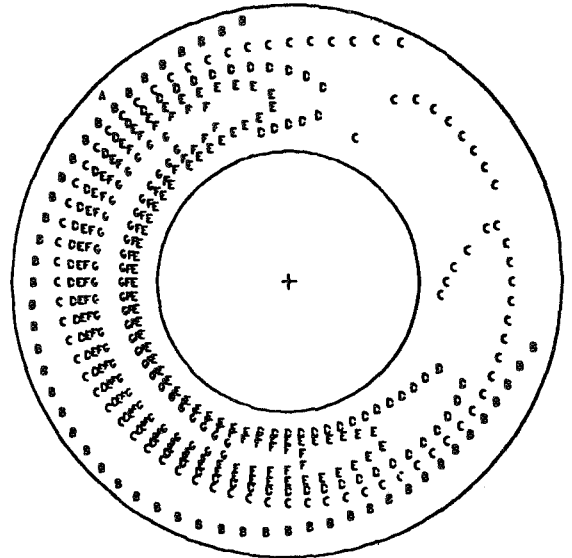
RUN 27.255
 TIME 8 27 0.0440

<u>PT2AVG</u>	= 0.6447	<u>PTMAX-PTMIN</u>	= 0.4617
<u>PT0</u>		<u>PT2AVG</u>	
MINIMUM	= 0.5363	INCREMENT	= 0.040
MAXIMUM	= 0.8340	INCREASING A.B.C.....H	



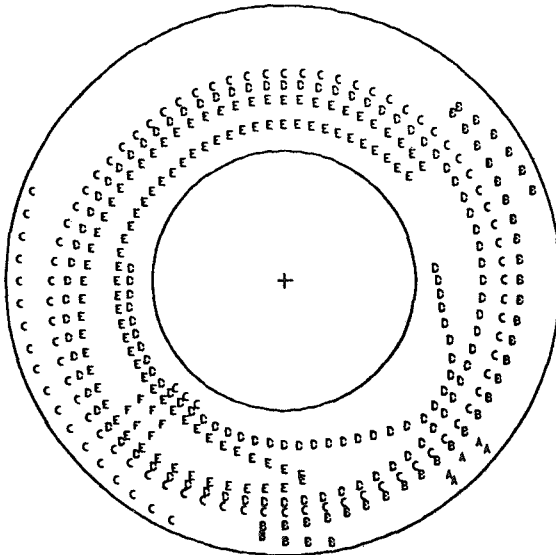
RUN 27.255
 TIME 8 27 0.0445

<u>PT2AVG</u>	= 0.6283	<u>PTMAX-PTMIN</u>	= 0.4311
<u>PT0</u>		<u>PT2AVG</u>	
MINIMUM	= 0.5285	INCREMENT	= 0.040
MAXIMUM	= 0.7994	INCREASING A.B.C.....G	



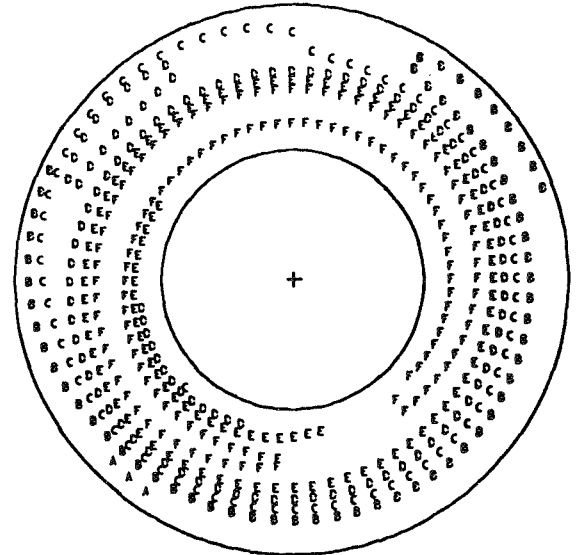
RUN 27.255
 TIME 8 27 0.0450

<u>PT2AVG</u>	= 0.6359	<u>PTMAX-PTMIN</u>	= 0.3225
<u>PT0</u>		<u>PT2AVG</u>	
MINIMUM	= 0.5389	INCREMENT	= 0.040
MAXIMUM	= 0.7440	INCREASING A.B.C.....F	



RUN 27.255
 TIME 8 27 0.0455

<u>PT2AVG</u>	= 0.6348	<u>PTMAX-PTMIN</u>	= 0.3680
<u>PT0</u>		<u>PT2AVG</u>	
MINIMUM	= 0.5174	INCREMENT	= 0.040
MAXIMUM	= 0.7511	INCREASING A.B.C.....F	

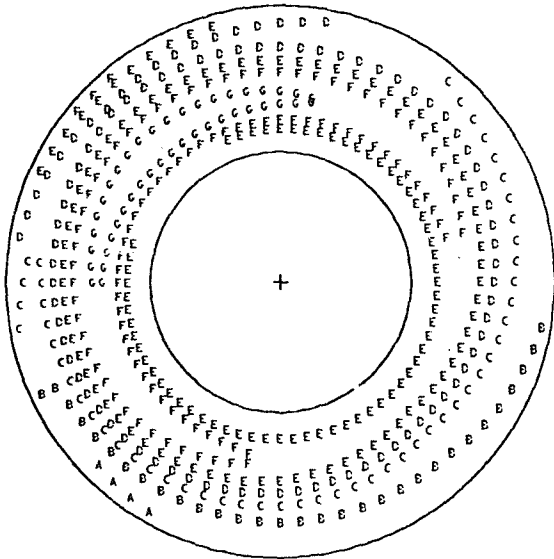


(i)

Figure 38.- Continued.

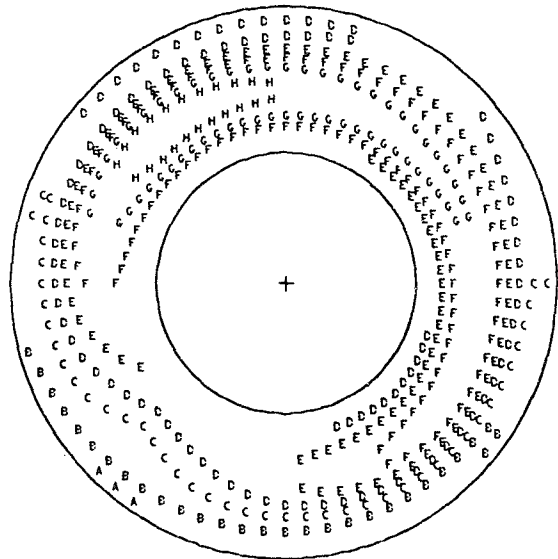
RUN 27.255
 TIME 8 27 0.0460

<u>PT2AVG</u>	= 0.6500	<u>PTMAX-PTMIN</u>	= 0.4025
<u>PT0</u>		<u>PT2AVG</u>	
MINIMUM	= 0.5160	INCREMENT	= 0.040
MAXIMUM	= 0.7777	INCREASING A,B,C.....G	



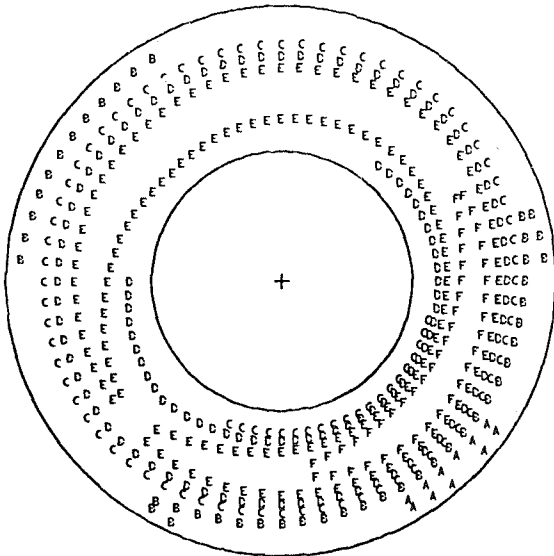
RUN 27.255
 TIME 8 27 0.0465

<u>PT2AVG</u>	= 0.6449	<u>PTMAX-PTMIN</u>	= 0.4811
<u>PT0</u>		<u>PT2AVG</u>	
MINIMUM	= 0.4928	INCREMENT	= 0.040
MAXIMUM	= 0.8031	INCREASING A,B,C.....H	



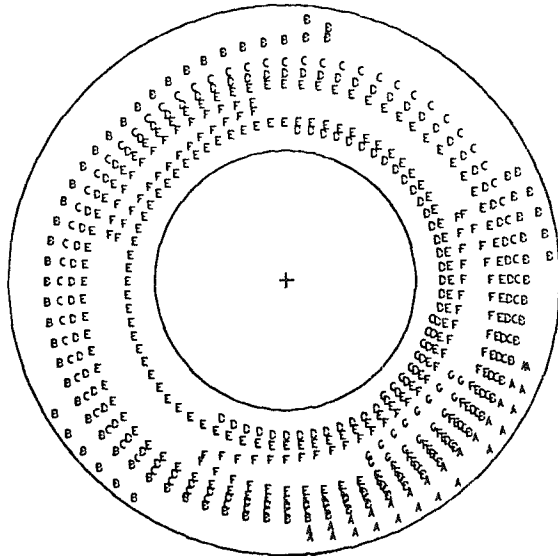
RUN 27.255
 TIME 8 27 0.0470

<u>PT2AVG</u>	= 0.6496	<u>PTMAX-PTMIN</u>	= 0.3622
<u>PT0</u>		<u>PT2AVG</u>	
MINIMUM	= 0.5389	INCREMENT	= 0.040
MAXIMUM	= 0.7742	INCREASING A,B,C.....F	



RUN 27.255
 TIME 8 27 0.0475

<u>PT2AVG</u>	= 0.6433	<u>PTMAX-PTMIN</u>	= 0.3758
<u>PT0</u>		<u>PT2AVG</u>	
MINIMUM	= 0.5389	INCREMENT	= 0.040
MAXIMUM	= 0.7807	INCREASING A,B,C.....G	

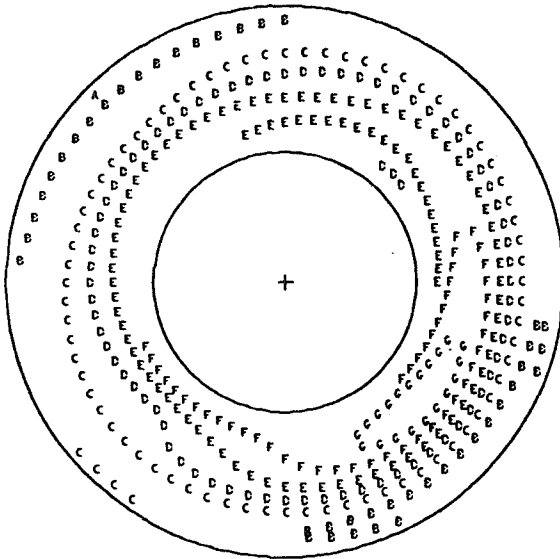


(j)

Figure 38.- Continued.

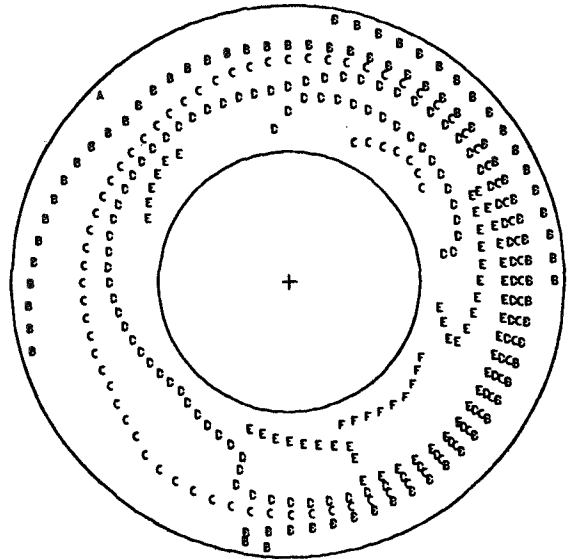
RUN 27.255
 TIME 8 27 0.0480

<u>PT2AVG</u>	= 0.6246	<u>PTMAX-PTMIN</u>	= 0.4340
<u>PT0</u>		<u>PT2AVG</u>	
MINIMUM	= 0.5093	INCREMENT	= 0.040
MAXIMUM	= 0.7804	INCREASING A.B.C.....G	



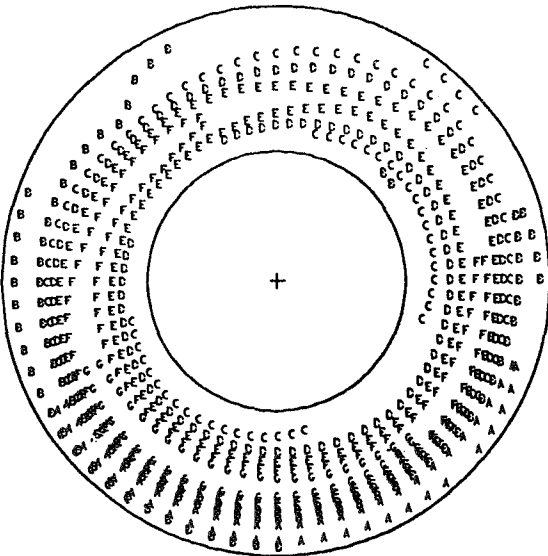
RUN 27.255
 TIME 8 27 0.0485

<u>PT2AVG</u>	= 0.6134	<u>PTMAX-PTMIN</u>	= 0.3802
<u>PT0</u>		<u>PT2AVG</u>	
MINIMUM	= 0.5199	INCREMENT	= 0.040
MAXIMUM	= 0.7531	INCREASING A.B.C.....F	



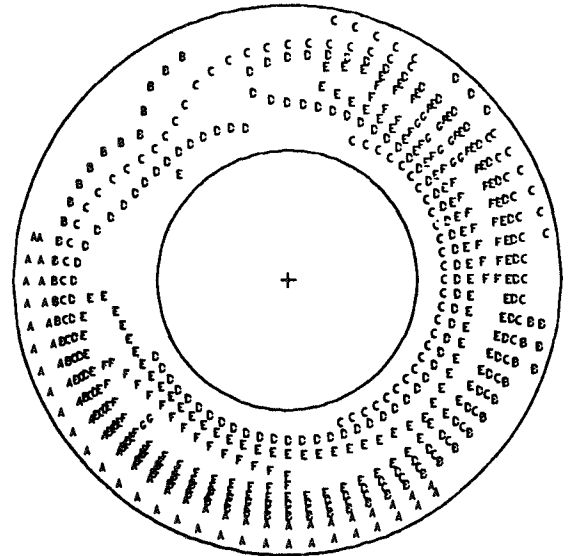
RUN 27.255
 TIME 8 27 0.0490

<u>PT2AVG</u>	= 0.6461	<u>PTMAX-PTMIN</u>	= 0.4150
<u>PT0</u>		<u>PT2AVG</u>	
MINIMUM	= 0.5389	INCREMENT	= 0.040
MAXIMUM	= 0.8071	INCREASING A.B.C.....G	



RUN 27.255
 TIME 8 27 0.0495

<u>PT2AVG</u>	= 0.6283	<u>PTMAX-PTMIN</u>	= 0.4054
<u>PT0</u>		<u>PT2AVG</u>	
MINIMUM	= 0.5258	INCREMENT	= 0.040
MAXIMUM	= 0.7806	INCREASING A.B.C.....G	



(k)

Figure 38.- Concluded.

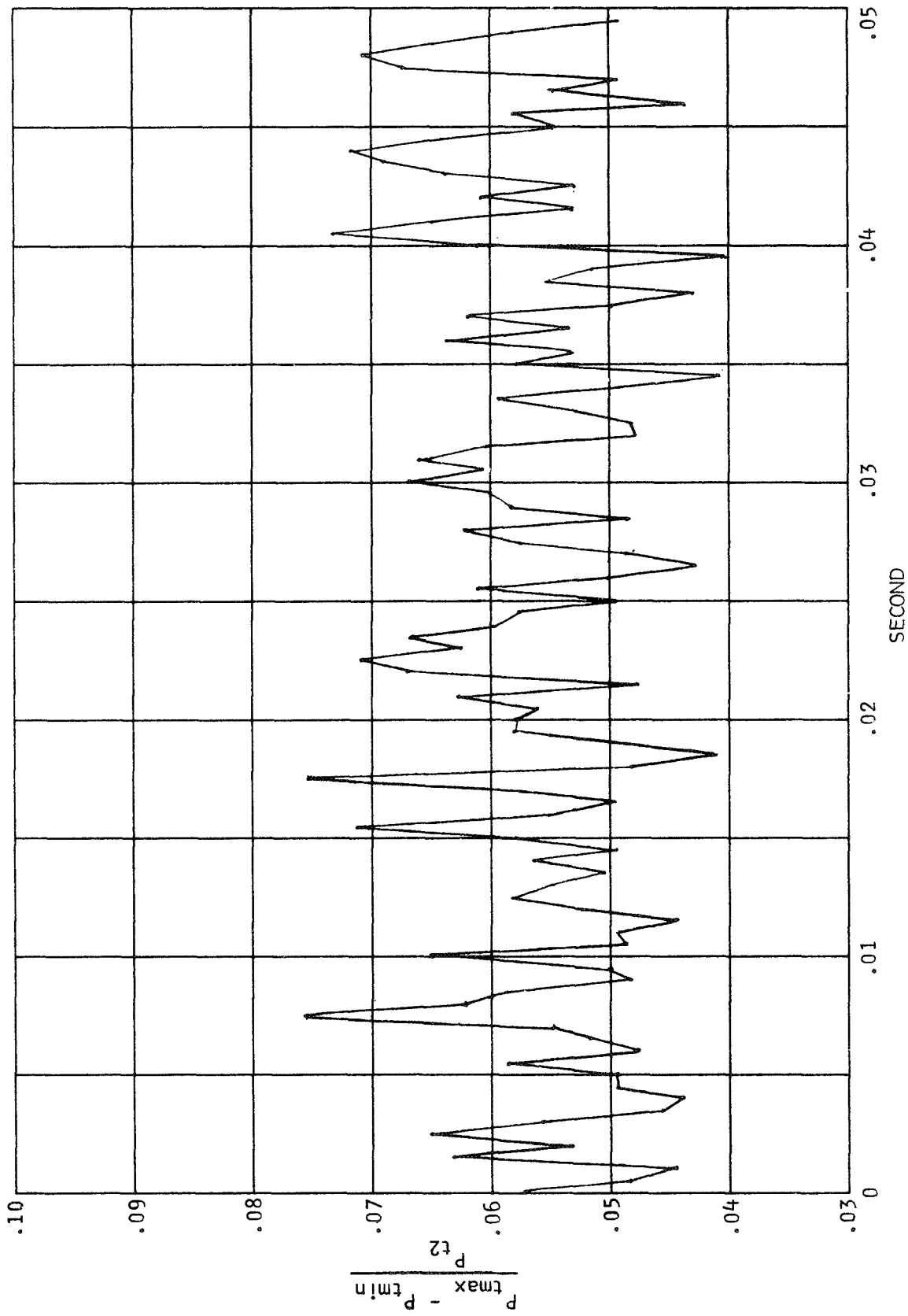


Figure 39.- Instantaneous spatial distortion versus time, $M_0 = 3.0$, $\bar{P}_{t2} / P_{t0} = 0.877$.

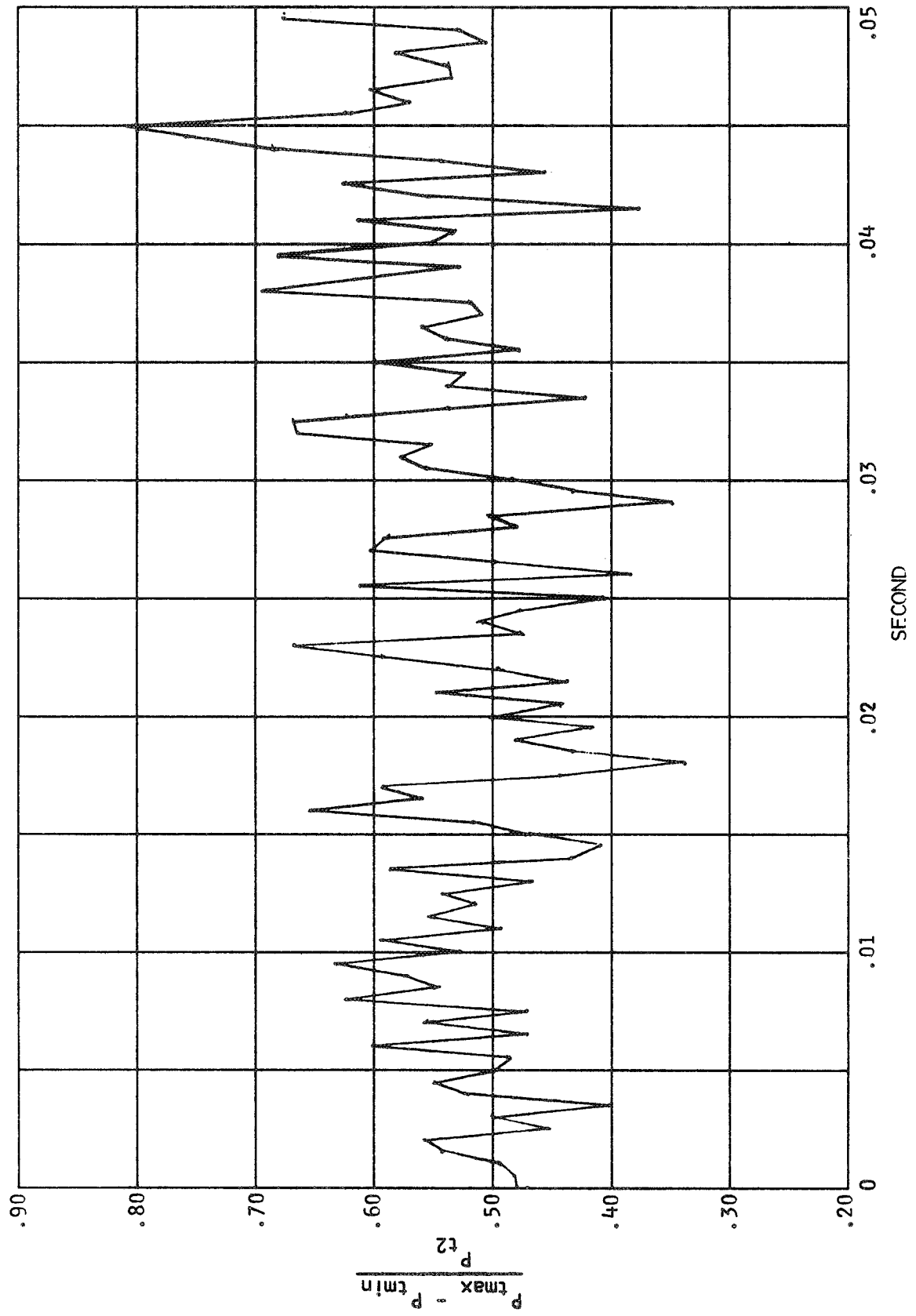


Figure 40.- Instantaneous spatial distortion versus time, $M_0 = 3.0$, $\bar{P}_{t_2}/P_{t_0} = 0.565$.

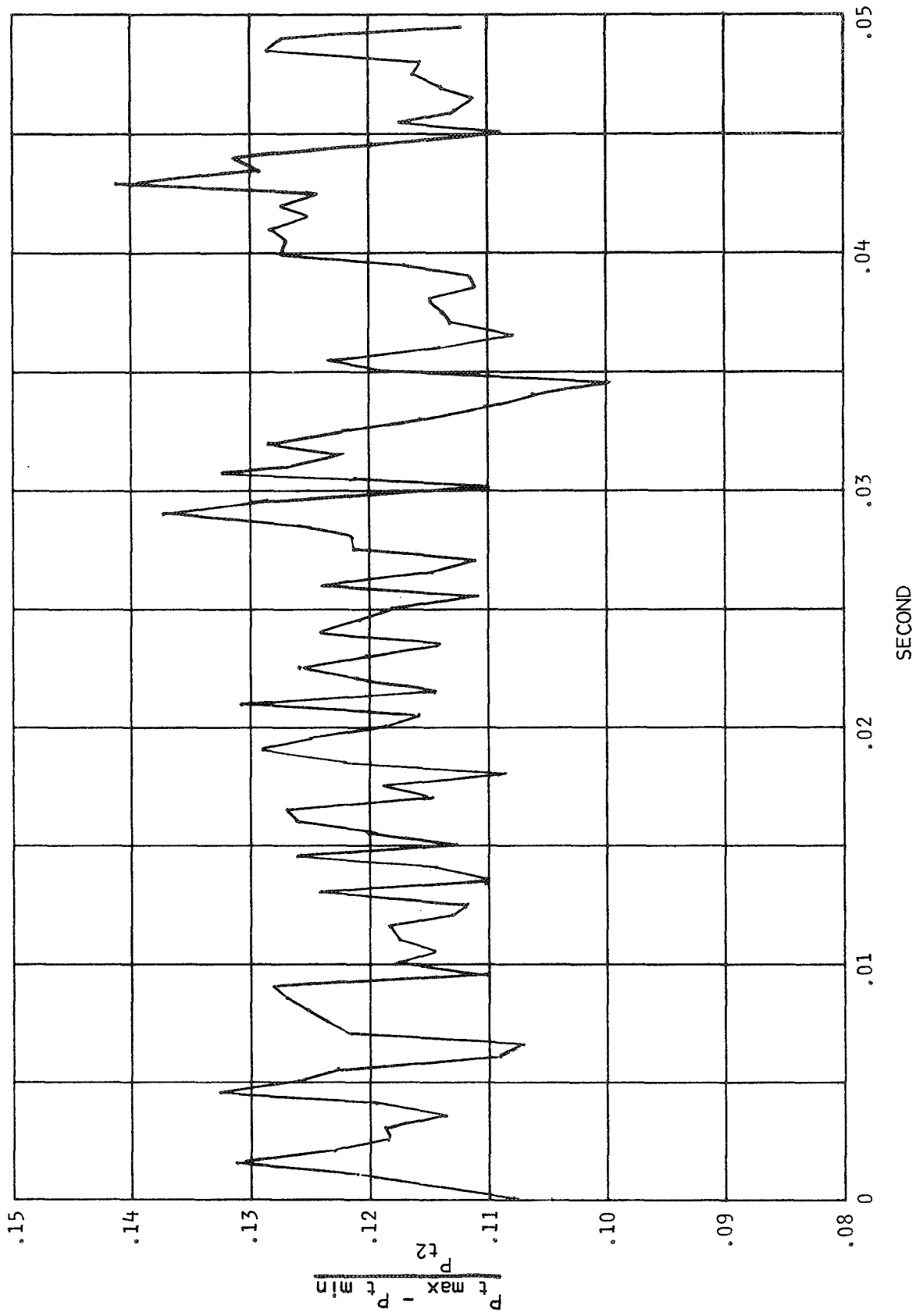


Figure 41.- Instantaneous spatial distortion versus time, $M_0 = 2.6, \bar{P}_{t2}/P_{t0} = 0.918$.

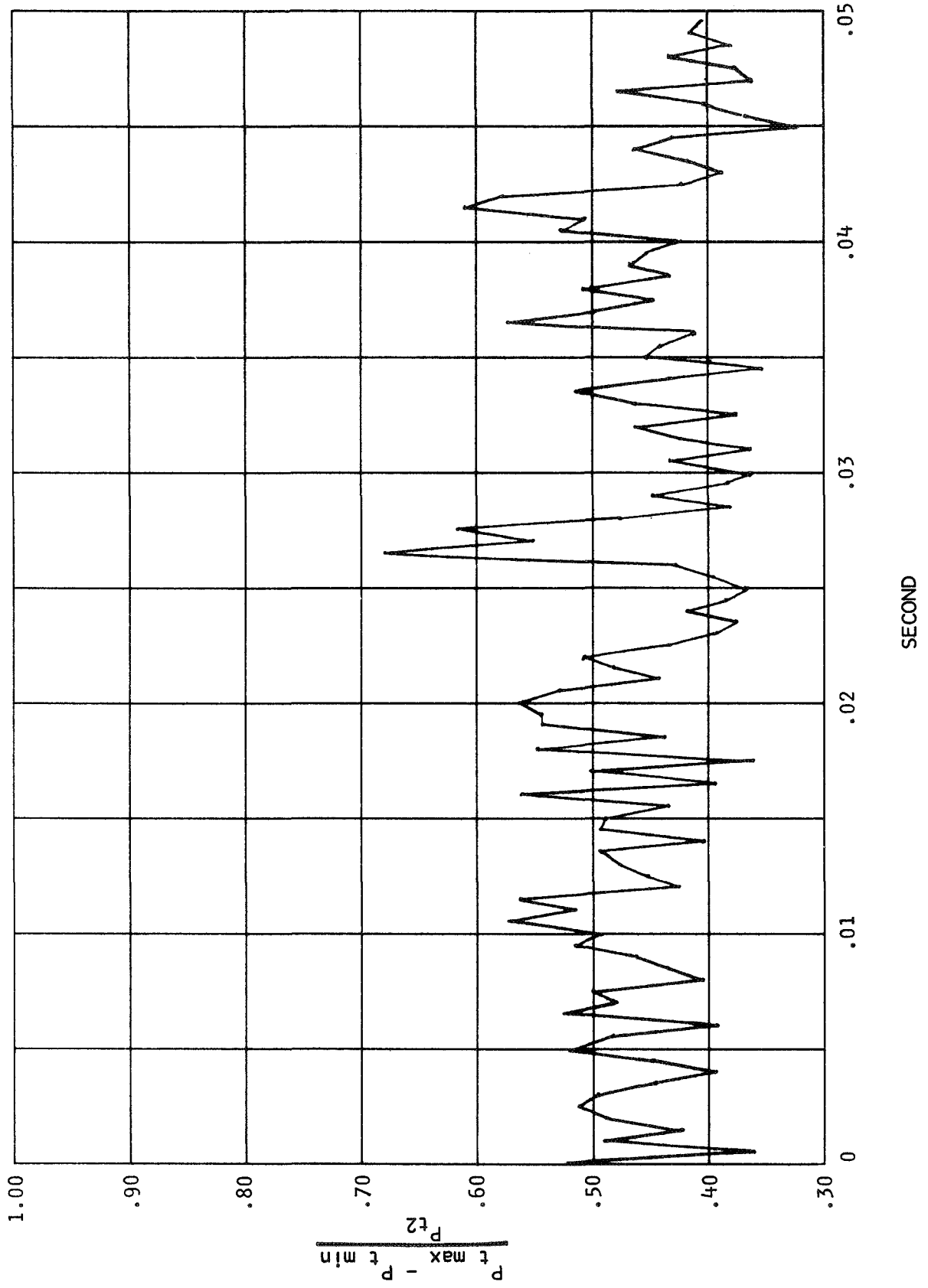


Figure 42.- Instantaneous spatial distortion versus time, $M_0 = 2.6$, $\bar{P}_{t2}/P_{t0} = 0.642$.

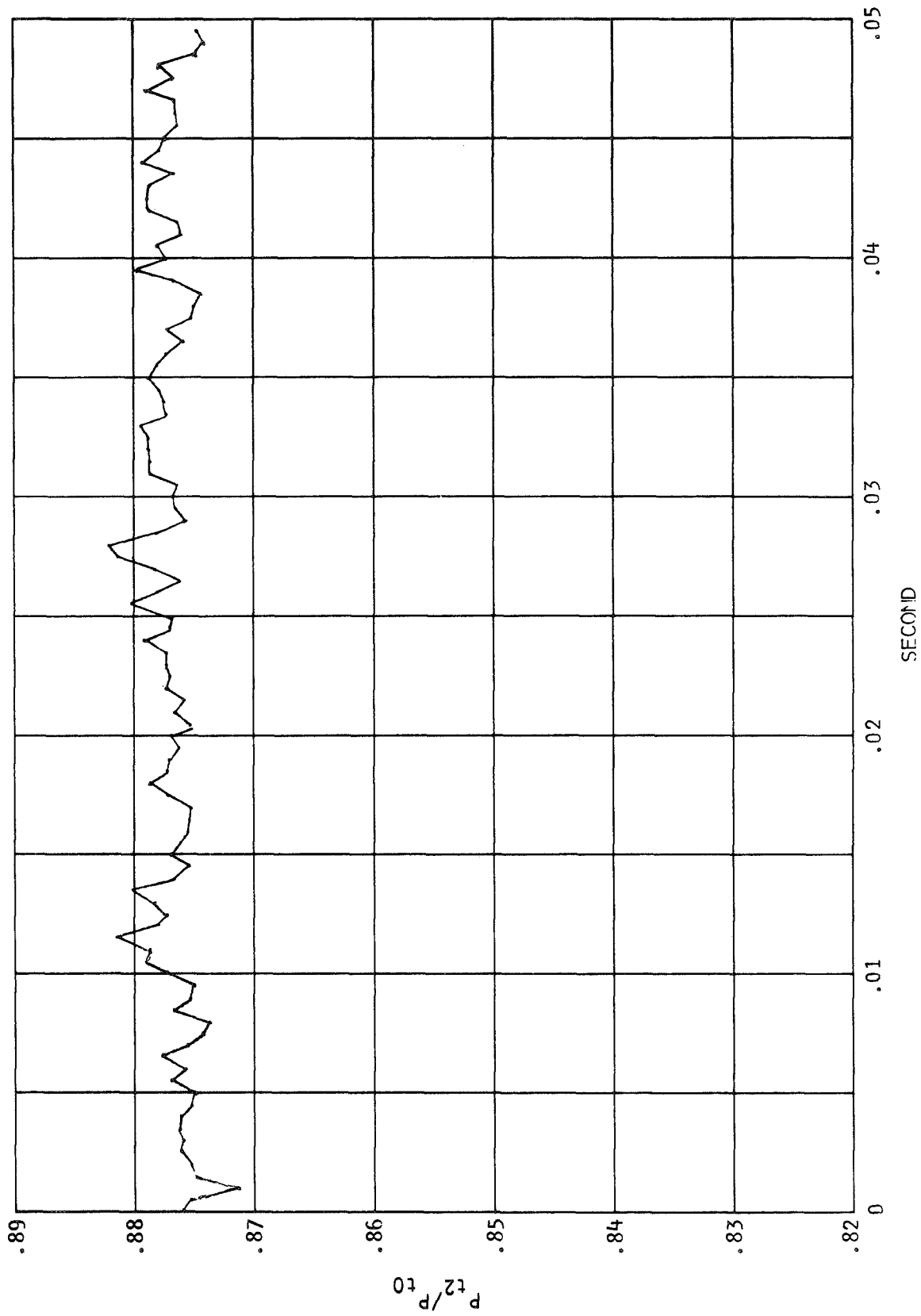


Figure 43.- Instantaneous average pressure recovery versus time, $M_0 = 3.0$, $\bar{P}_{t2}/P_{t0} = 0.877$.

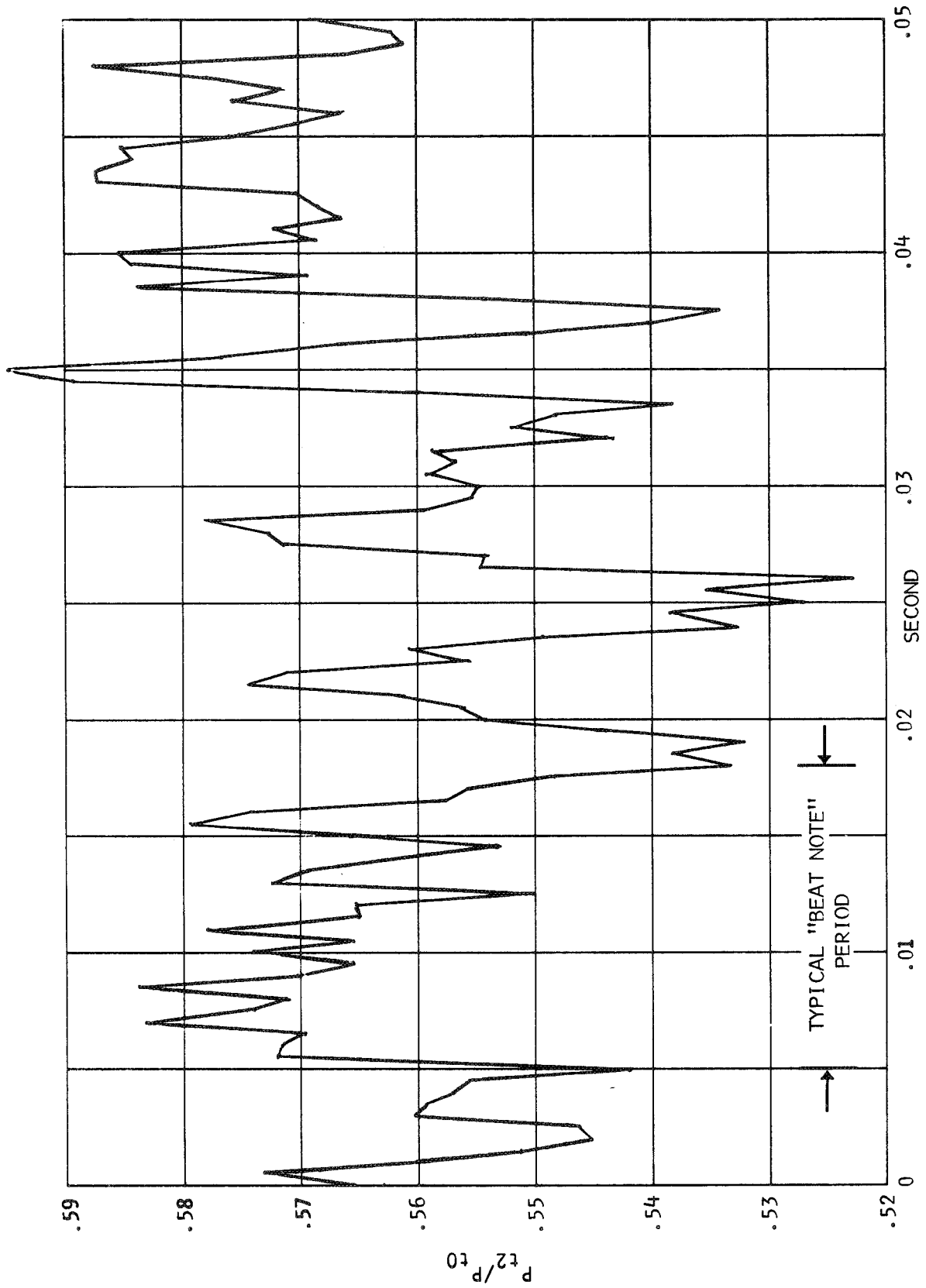
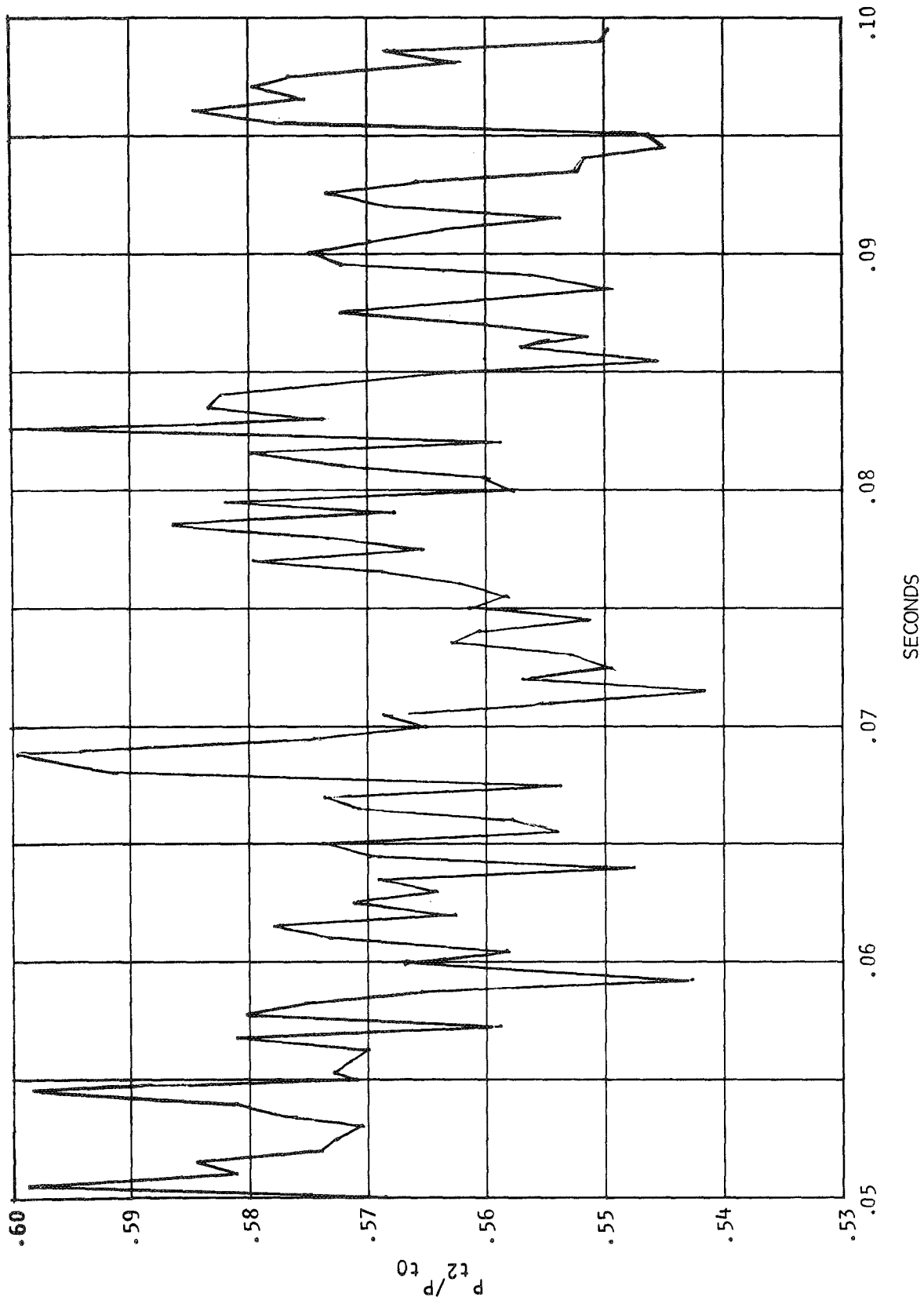


Figure 44.- Instantaneous average pressure recovery versus time, $M_0 = 3.0$, $\bar{P}_{t2}/P_{t0} = 0.565$.
(a)



(b)
Figure 44.- Concluded.

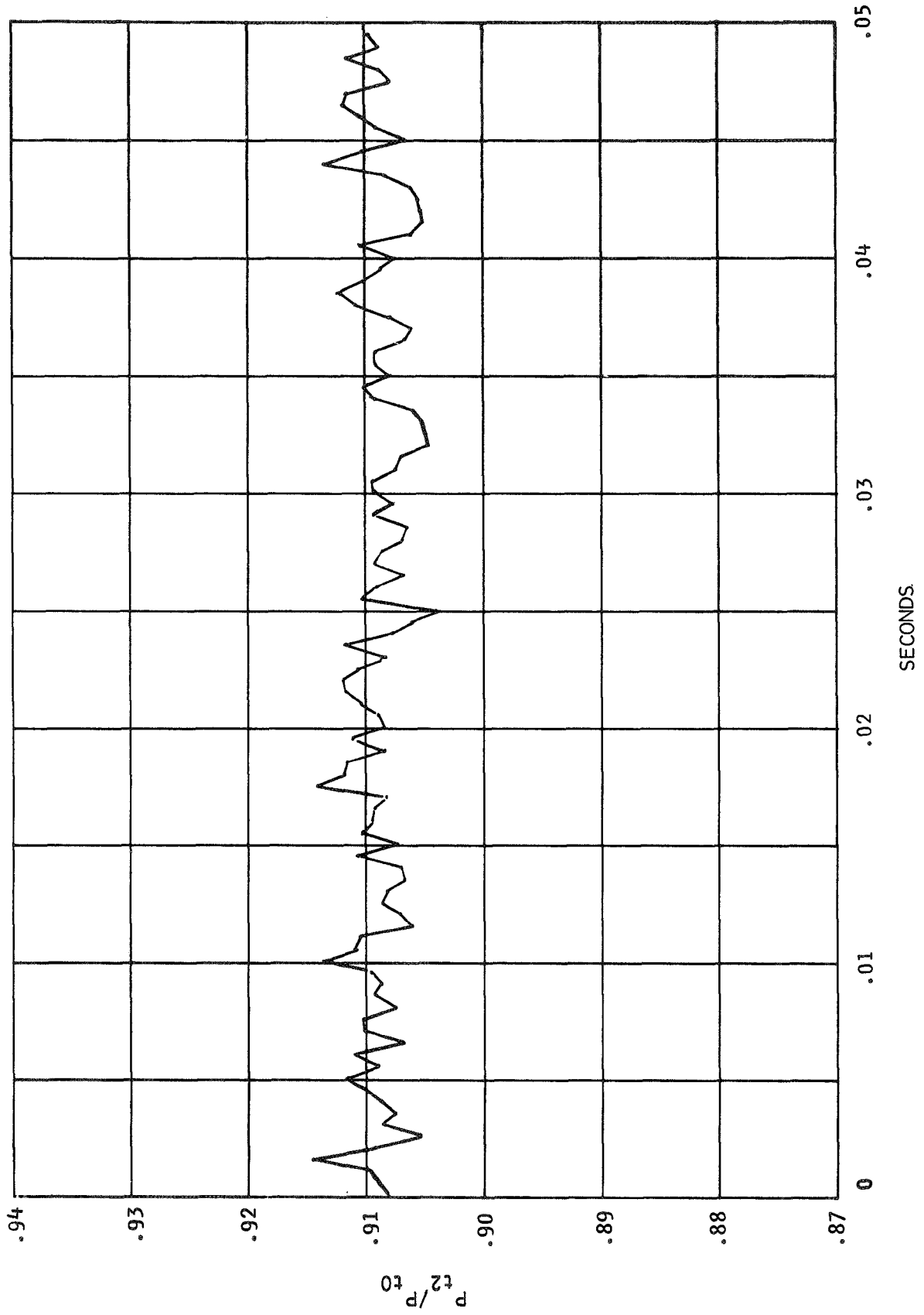


Figure 45.- Instantaneous average pressure recovery versus time, $M_0 = 2.6$, $\bar{P}_{t2}/P_{t0} = 0.918$.

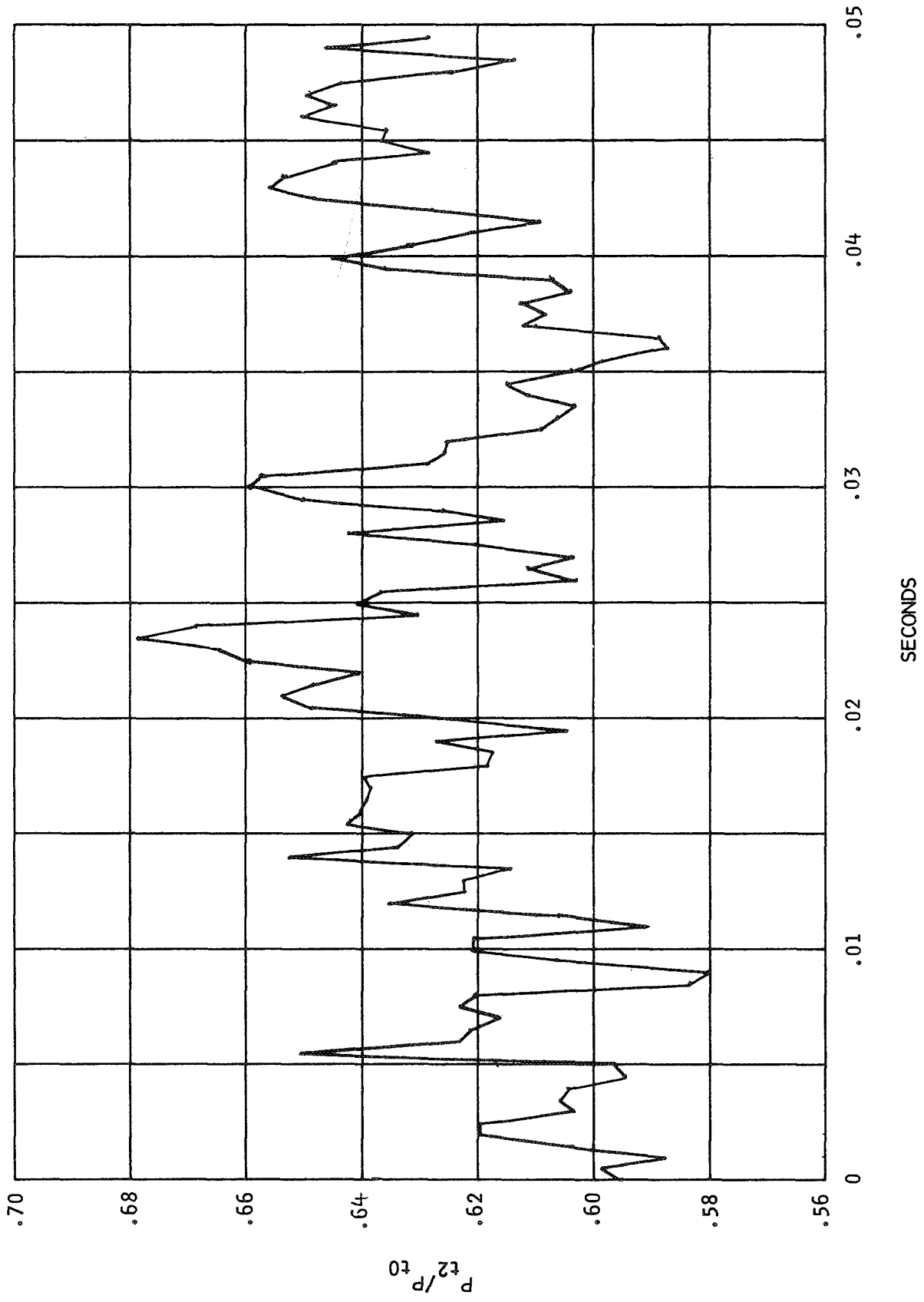
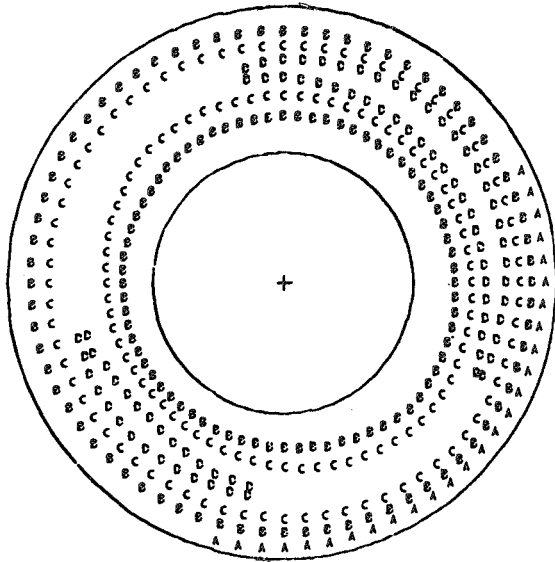


Figure 46.- Instantaneous average pressure recovery versus time, $M_0 = 2.6$, $\bar{P}_{t2}/P_{t0} = 0.642$.

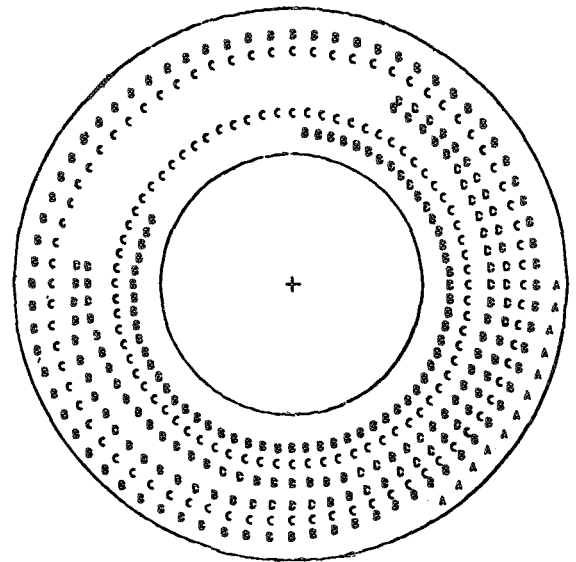
RUN 21.209
 TIME 8 26 0.0000

$\frac{P_{T2AVG}}{P_{T0}}$	= 0.8743	$\frac{P_{TMAX}-P_{TMIN}}{P_{T2AVG}}$	= 0.0503
MINIMUM	= 0.8532	INCREMENT	= 0.010
MAXIMUM	= 0.8973	INCREASING A.B.C.....D	



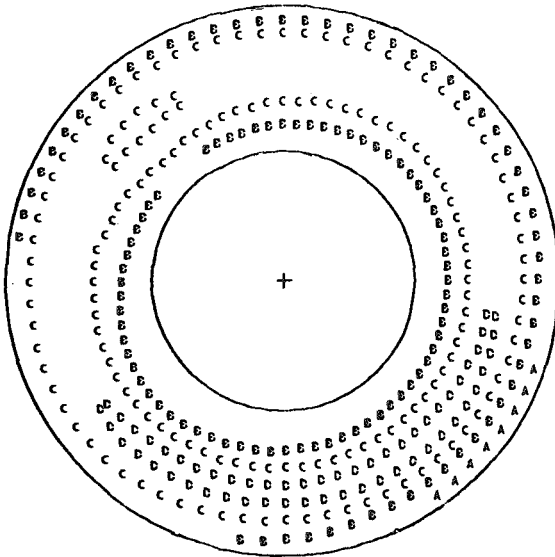
RUN 21.209
 TIME 8 26 0.0020

$\frac{P_{T2AVG}}{P_{T0}}$	= 0.8758	$\frac{P_{TMAX}-P_{TMIN}}{P_{T2AVG}}$	= 0.0397
MINIMUM	= 0.8587	INCREMENT	= 0.010
MAXIMUM	= 0.8936	INCREASING A.B.C.....D	



RUN 21.209
 TIME 8 26 0.0040

$\frac{P_{T2AVG}}{P_{T0}}$	= 0.8758	$\frac{P_{TMAX}-P_{TMIN}}{P_{T2AVG}}$	= 0.0399
MINIMUM	= 0.8574	INCREMENT	= 0.010
MAXIMUM	= 0.8924	INCREASING A.B.C.....D	



RUN 21.209
 TIME 8 26 0.0060

$\frac{P_{T2AVG}}{P_{T0}}$	= 0.8759	$\frac{P_{TMAX}-P_{TMIN}}{P_{T2AVG}}$	= 0.0481
MINIMUM	= 0.8569	INCREMENT	= 0.010
MAXIMUM	= 0.8991	INCREASING A.B.C.....D	

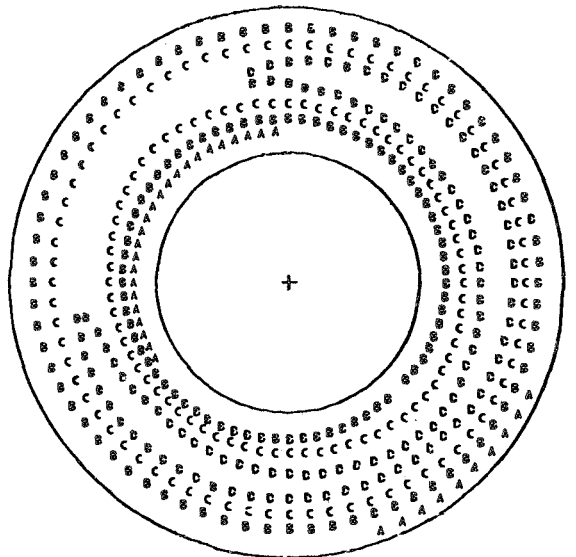
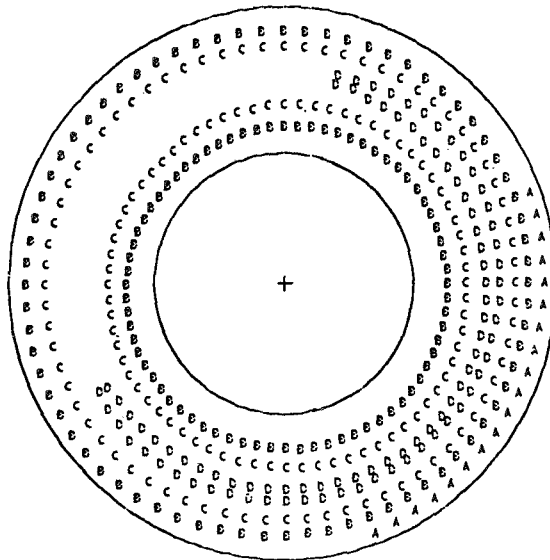


Figure 47.- Time-averaged total pressure ratio contours, 0.002-second span, $M_0 = 3.0$, $\bar{P}_{t2}/P_{t0} = 0.877$.

RUN 21.209
 TIME 8 2G 0.0000

$\frac{P_{T2AVG}}{P_{T0}}$	= 0.8752	$\frac{P_{TMAX}-P_{TMIN}}{P_{T2AVG}}$	= 0.0412
MINIMUM	= 0.8558	INCREMENT	= 0.010
MAXIMUM	= 0.8919	INCREASING A,B,C.....D	



RUN 21.209
 TIME 8 2G 0.0050

$\frac{P_{T2AVG}}{P_{T0}}$	= 0.8756	$\frac{P_{TMAX}-P_{TMIN}}{P_{T2AVG}}$	= 0.0439
MINIMUM	= 0.8577	INCREMENT	= 0.010
MAXIMUM	= 0.8962	INCREASING A,B,C.....D	

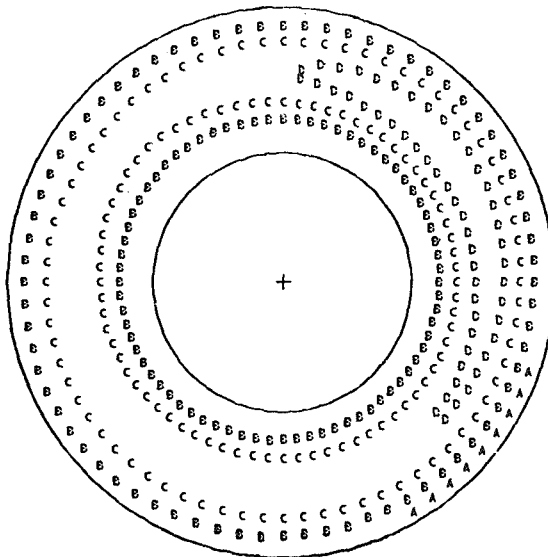
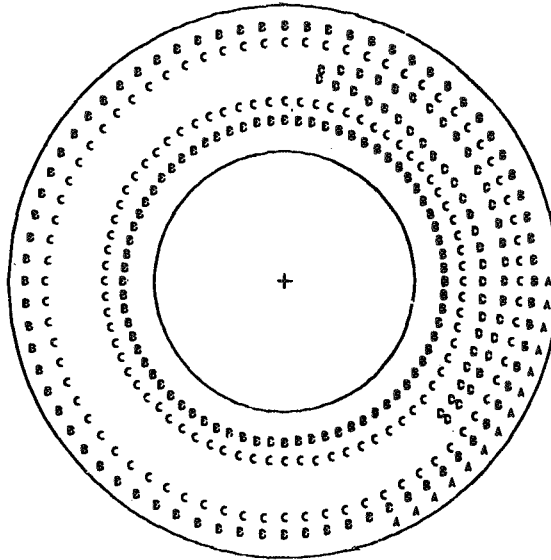


Figure 48.- Time-averaged total pressure ratio contours, 0.005-second span, $M_0 = 3.0$, $\bar{P}_{t2}/P_{t0} = 0.877$.

RUN 21.209
TIME 8 26 0.0000

<u>PT2AVG</u> PT0 = 0.8754	<u>PTMAX-PTMIN</u> PT2AVG = 0.0425
MINIMUM = 0.8568	INCREMENT = 0.010
MAXIMUM = 0.8941	INCREASING A.B.C....D



RUN 21.209
TIME 8 26 0.0100

<u>PT2AVG</u> PT0 = 0.8774	<u>PTMAX-PTMIN</u> PT2AVG = 0.0460
MINIMUM = 0.8592	INCREMENT = 0.010
MAXIMUM = 0.8996	INCREASING A.B.C....D

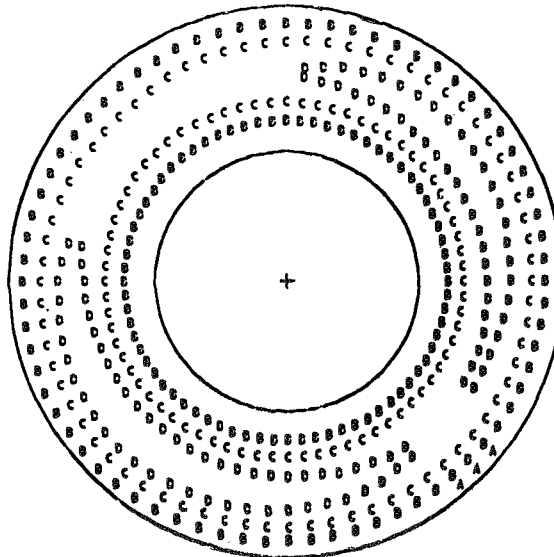
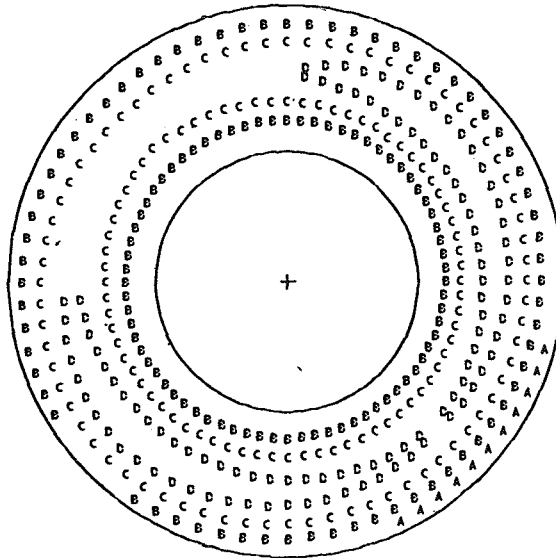


Figure 49.- Time-averaged total pressure ratio contours, 0.010-second span, $M_0 = 3.0$, $\bar{P}_{t2}/P_{t0} = 0.877$.

RUN 21.209
TIME 8 26 0.0000

<u>PT2AVG</u> = 0.8770	<u>PTMAX-PTMIN</u> = 0.0443
<u>PT0</u>	<u>PT2AVG</u>
MINIMUM = 0.8565	INCREMENT = 0.010
MAXIMUM = 0.8954	INCREASING A,B,C,...,D



RUN 21.209
TIME 8 26 0.0400

<u>PT2AVG</u> = 0.8766	<u>PTMAX-PTMIN</u> = 0.0487
<u>PT0</u>	<u>PT2AVG</u>
MINIMUM = 0.8540	INCREMENT = 0.010
MAXIMUM = 0.8968	INCREASING A,B,C,...,D

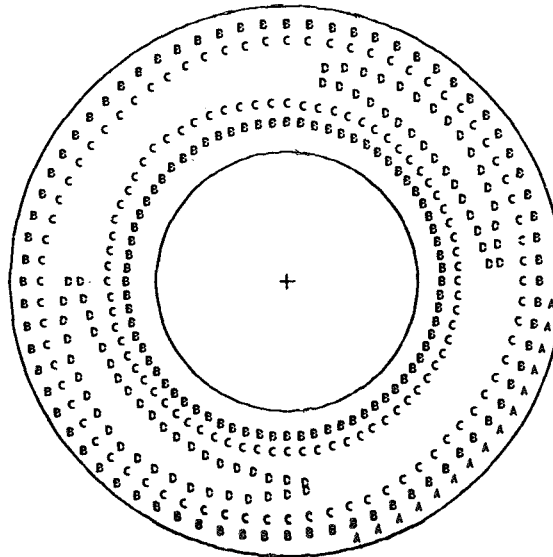


Figure 50. Time-averaged total pressure ratio contours, 0.040-second span, $M_0 = 3.0$, $\bar{P}_{t2}/P_{t0} = 0.877$

RUN 21.209

$\frac{PT2AVG}{PT0}$	= 0.8768	$\frac{PTMAX-PTMIN}{PT2AVG}$	= 0.0474
MINIMUM	= 0.8551	INCREMENT	= 0.010
MAXIMUM	= 0.8967	INCREASING A.B.C.....D	

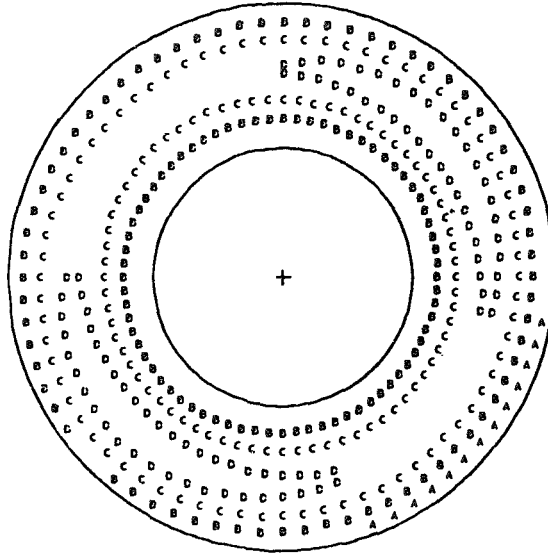
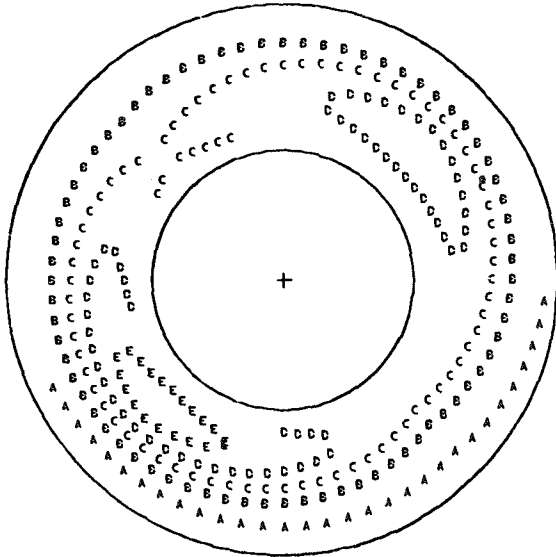
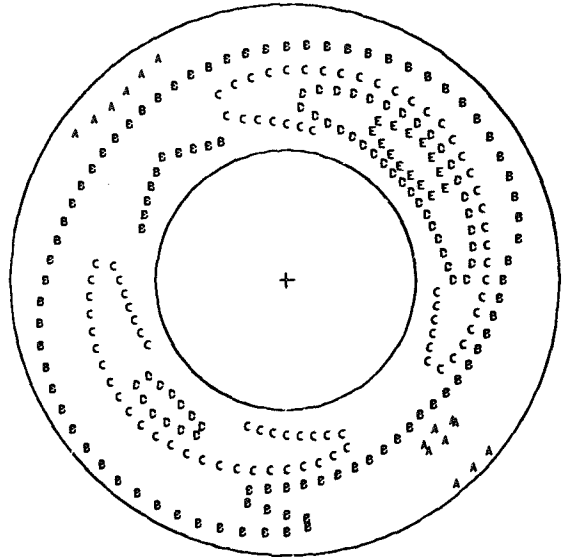


Figure 51.- Steady-state total pressure ratio contours, $M_0 = 3.0$,
 $\bar{P}_{t2}/P_{t0} = 0.877$.

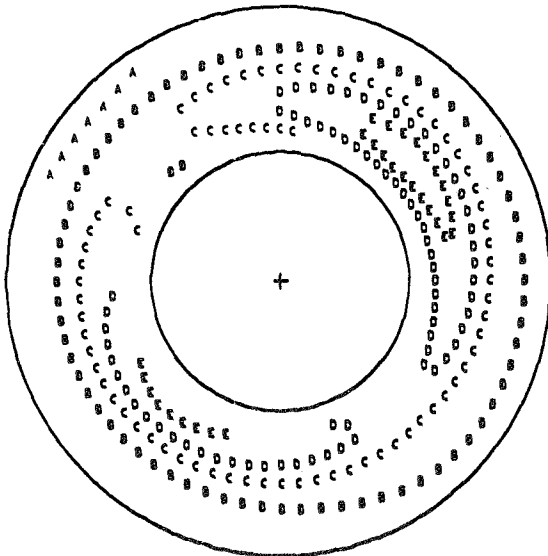
RUN 21.214
 TIME 9 49 42.0000
 $\frac{PT2AVG}{PT0} = 0.5626$ $\frac{PTMAX-PTMIN}{PT2AVG} = 0.3306$
 MINIMUM = 0.4932 INCREMENT = 0.040
 MAXIMUM = 0.6792 INCREASING A,B,C.....E



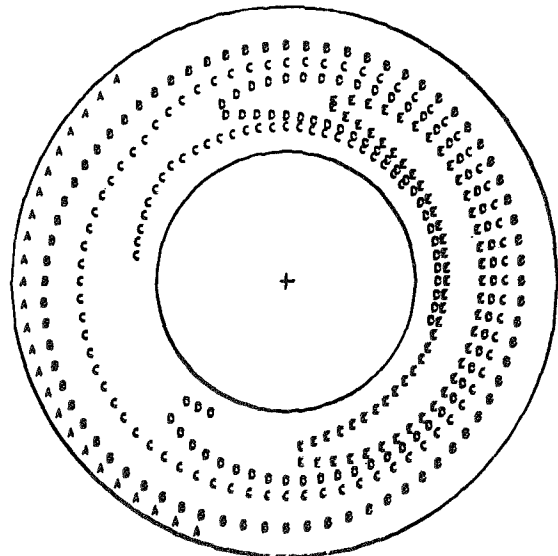
RUN 21.214
 TIME 9 49 42.0020
 $\frac{PT2AVG}{PT0} = 0.5527$ $\frac{PTMAX-PTMIN}{PT2AVG} = 0.3323$
 MINIMUM = 0.4956 INCREMENT = 0.040
 MAXIMUM = 0.6793 INCREASING A,B,C.....E



RUN 21.214
 TIME 9 49 42.0040
 $\frac{PT2AVG}{PT0} = 0.5567$ $\frac{PTMAX-PTMIN}{PT2AVG} = 0.3554$
 MINIMUM = 0.4872 INCREMENT = 0.040
 MAXIMUM = 0.6851 INCREASING A,B,C.....E



RUN 21.214
 TIME 9 49 42.0060
 $\frac{PT2AVG}{PT0} = 0.5746$ $\frac{PTMAX-PTMIN}{PT2AVG} = 0.3528$
 MINIMUM = 0.4913 INCREMENT = 0.040
 MAXIMUM = 0.6940 INCREASING A,B,C.....E

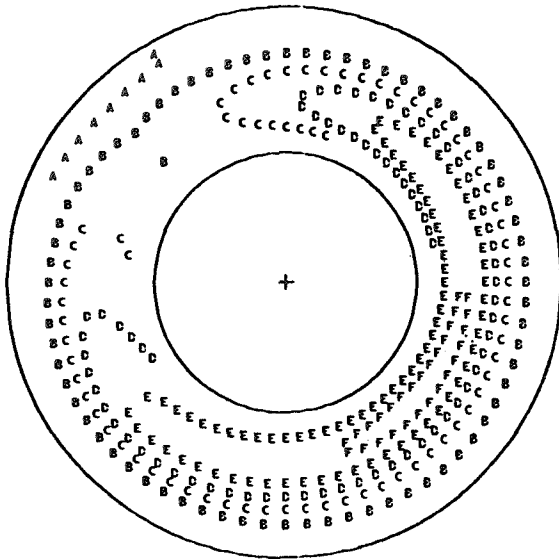


(a)

Figure 52.- Time-averaged total pressure ratio contours, 0.002-second span, $M_0 = 3.0$, $\bar{P}_{t2}/P_{t0} = 0.565$.

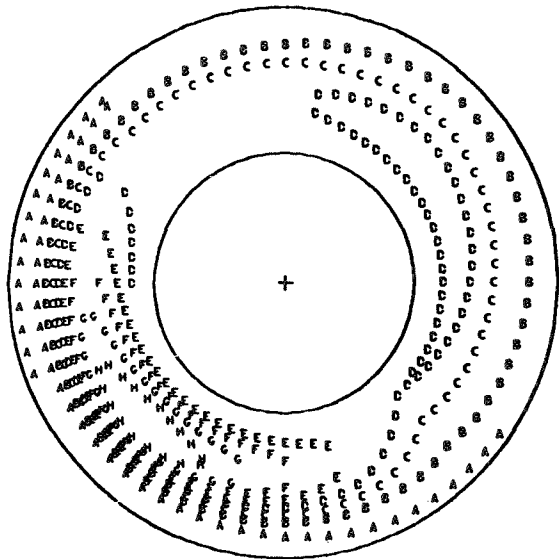
RUN 21.214
 TIME 9 49 42.0420

<u>PT2AVG</u>	= 0.5783	<u>PTMAX-PTMIN</u>	= 0.3595
<u>PT0</u>		<u>PT2AVG</u>	
MINIMUM	= 0.4970	INCREMENT	= 0.040
MAXIMUM	= 0.7050	INCREASING A,B,C....F	



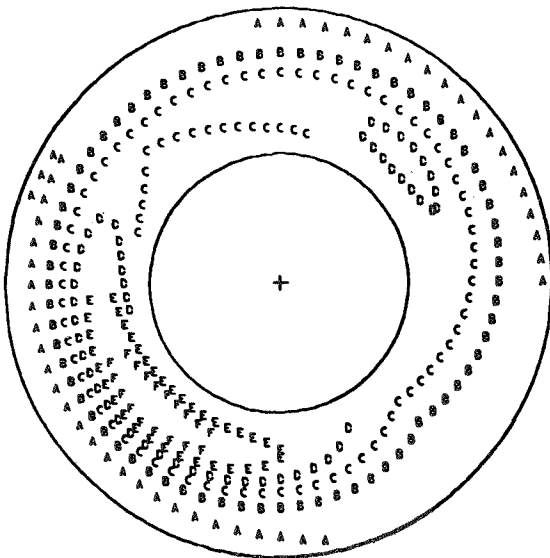
RUN 21.214
 TIME 9 49 42.0440

<u>PT2AVG</u>	= 0.5789	<u>PTMAX-PTMIN</u>	= 0.5543
<u>PT0</u>		<u>PT2AVG</u>	
MINIMUM	= 0.4867	INCREMENT	= 0.040
MAXIMUM	= 0.8076	INCREASING A,B,C....H	



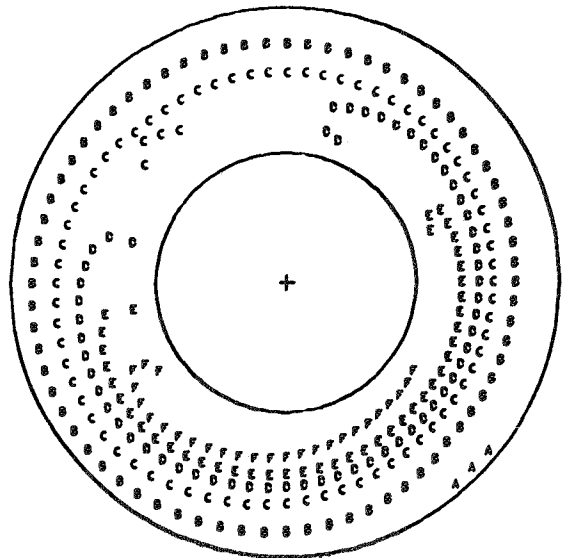
RUN 21.214
 TIME 9 49 42.0460

<u>PT2AVG</u>	= 0.5728	<u>PTMAX-PTMIN</u>	= 0.4347
<u>PT0</u>		<u>PT2AVG</u>	
MINIMUM	= 0.5004	INCREMENT	= 0.040
MAXIMUM	= 0.7494	INCREASING A,B,C....F	



RUN 21.214
 TIME 9 49 42.0480

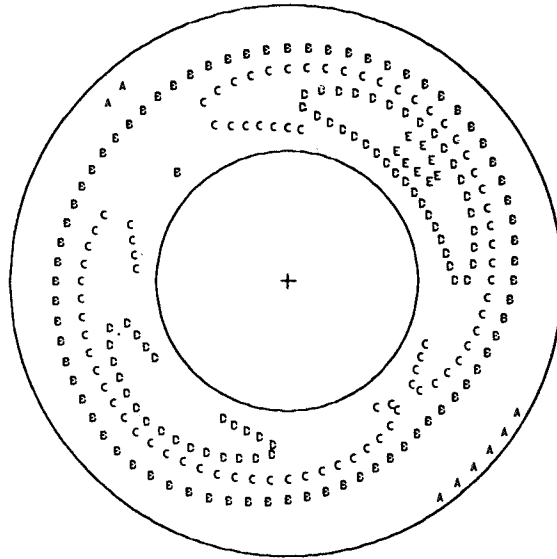
<u>PT2AVG</u>	= 0.5688	<u>PTMAX-PTMIN</u>	= 0.3770
<u>PT0</u>		<u>PT2AVG</u>	
MINIMUM	= 0.4769	INCREMENT	= 0.040
MAXIMUM	= 0.6914	INCREASING A,B,C....F	



(b)
 Figure 52.- Concluded.

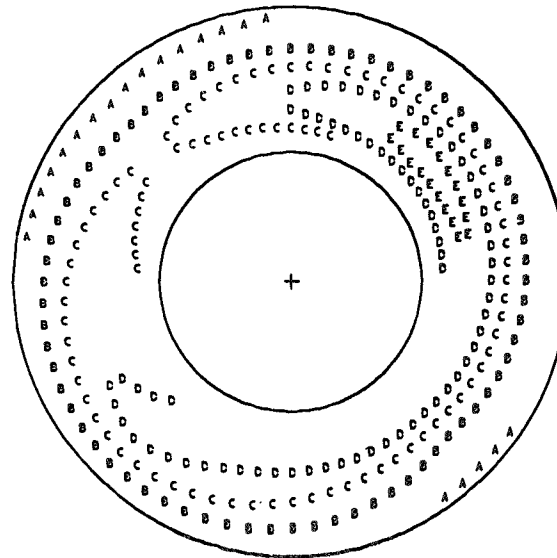
RUN 21.214
TIME 9 49 42.0000

<u>PT2AVG</u>	<u>PTMAX-PTMIN</u>
<u>PT0</u> = 0.5574	<u>PT2AVG</u> = 0.3071
MINIMUM = 0.4981	INCREMENT = 0.040
MAXIMUM = 0.6693	INCREASING A,B,C,....E



RUN 21.214
TIME 9 49 42.0050

<u>PT2AVG</u>	<u>PTMAX-PTMIN</u>
<u>PT0</u> = 0.5703	<u>PT2AVG</u> = 0.3195
MINIMUM = 0.4916	INCREMENT = 0.040
MAXIMUM = 0.6738	INCREASING A,B,C,....E

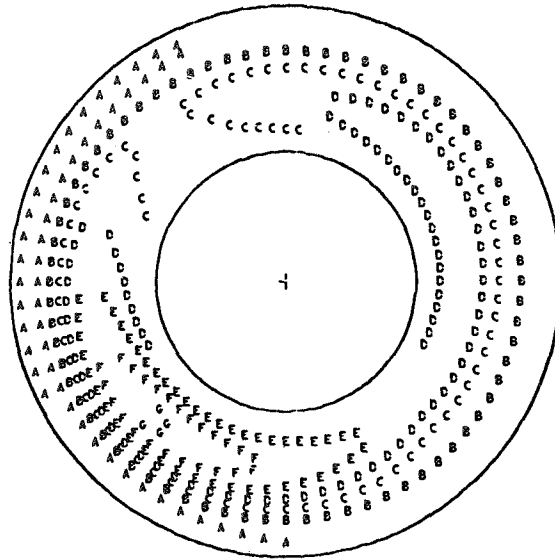


(a)

Figure 53.- Time-averaged total pressure ratio contours, 0.005-second span, $M_0 = 3.0$, $\bar{P}_{t2}/P_{t0} = 0.565$.

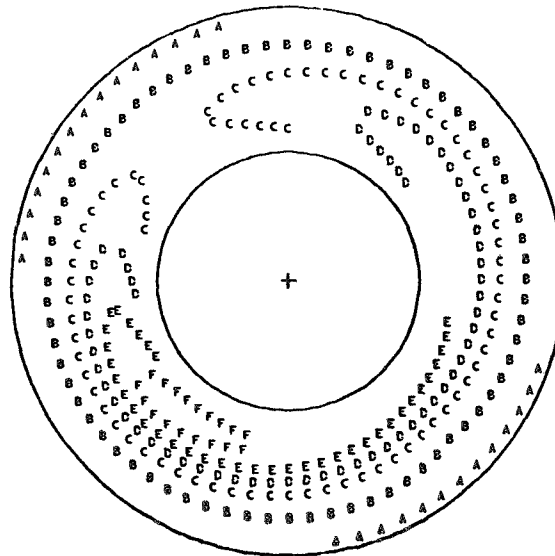
RUN 21.214
TIME 9 49 42.0420

<u>PT2AVG</u>	<u>PTMAX-PTMIN</u>
<u>PT0</u> = 0.5771	<u>PT2AVG</u> = 0.4272
MINIMUM = 0.4995	INCREMENT = 0.040
MAXIMUM = 0.7461	INCREASING A.B.C....G



RUN 21.214
TIME 9 49 42.0470

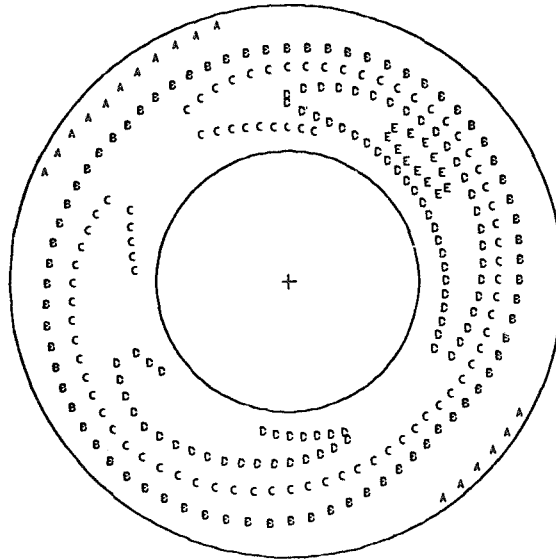
<u>PT2AVG</u>	<u>PTMAX-PTMIN</u>
<u>PT0</u> = 0.5759	<u>PT2AVG</u> = 0.3722
MINIMUM = 0.4966	INCREMENT = 0.040
MAXIMUM = 0.7110	INCREASING A.B.C....F



(b)
Figure 53.- Concluded.

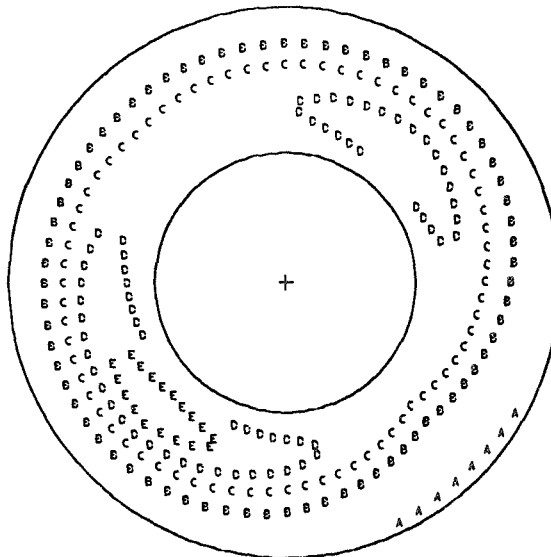
RUN 21.214
TIME 9 49 42.0000

$\frac{PT2AVG}{PT0} = 0.5639$	$\frac{PTMAX-PTMIN}{PT2AVG} = 0.3123$
MINIMUM = 0.4954	INCREMENT = 0.040
MAXIMUM = 0.6716	INCREASING A,B,C.....E



RUN 21.214
TIME 9 49 42.0100

$\frac{PT2AVG}{PT0} = 0.5589$	$\frac{PTMAX-PTMIN}{PT2AVG} = 0.3379$
MINIMUM = 0.4838	INCREMENT = 0.040
MAXIMUM = 0.6727	INCREASING A,B,C.....E

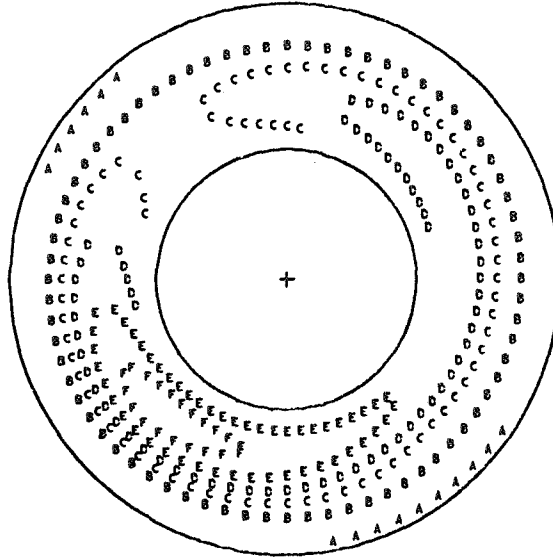


(a)

Figure 54.- Time-averaged total pressure ratio contours, 0.010-second span, $M_0 = 3.0$, $\bar{P}_{t2}/P_{t0} = 0.565$.

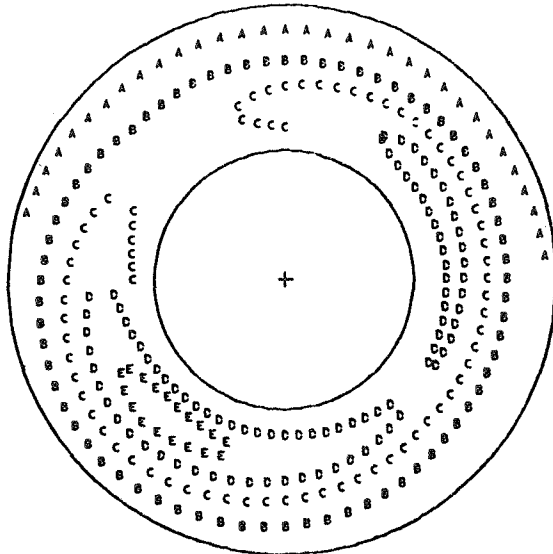
RUN 21.214
TIME 9 49 42.0420

<u>PT2AVG</u>	<u>PTMAX-PTMIN</u>
<u>PT0</u> = 0.5765	<u>PT2AVG</u> = 0.3986
MINIMUM = 0.4987	INCREMENT = 0.040
MAXIMUM = 0.7285	INCREASING A,B,C.....F



RUN 21.214
TIME 9 49 42.0520

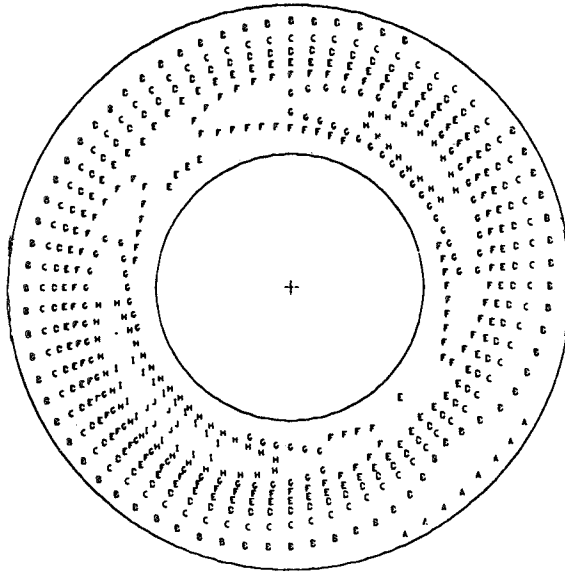
<u>PT2AVG</u>	<u>PTMAX-PTMIN</u>
<u>PT0</u> = 0.5720	<u>PT2AVG</u> = 0.3344
MINIMUM = 0.5001	INCREMENT = 0.040
MAXIMUM = 0.6914	INCREASING A,B,C.....E



(b)
Figure 54.- Concluded.

RUN 21.214
TIME 9 49 42.0000

<u>PT2AVG</u>	<u>PTMAX-PTMIN</u>
<u>PT0</u> = 0.5594	<u>PT2AVG</u> = 0.3347
MINIMUM = 0.4840	INCREMENT = 0.020
MAXIMUM = 0.6713	INCREASING A,B,C.....J



RUN 21.214
TIME 9 49 42.0400

<u>PT2AVG</u>	<u>PTMAX-PTMIN</u>
<u>PT0</u> = 0.5708	<u>PT2AVG</u> = 0.3670
MINIMUM = 0.4979	INCREMENT = 0.020
MAXIMUM = 0.7074	INCREASING A,B,C.....K

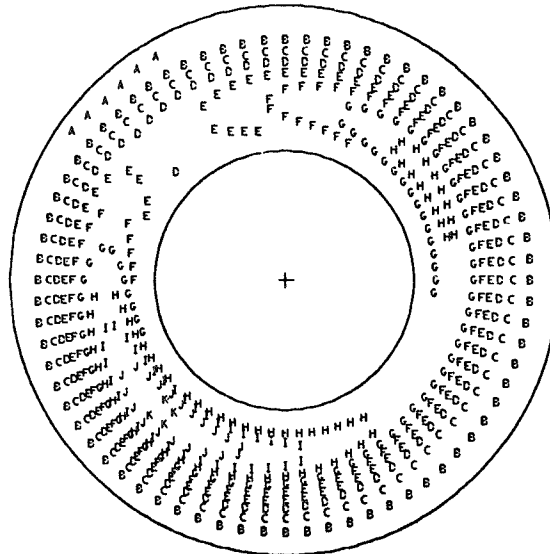


Figure 55. Time-averaged total pressure ratio contours, 0.040-second span, $M_0 = 3.0$, $\bar{P}_{t2}/P_{t0} = 0.565$.

RUN 21.214

<u>PT2AVG</u>	<u>PTMAX-PTMIN</u>
<u>PTD</u> = 0.5645	<u>PT2AVG</u> = 0.3464
MINIMUM = 0.4917	INCREMENT = 0.020
MAXIMUM = 0.6873	INCREASING A,B,C.....J

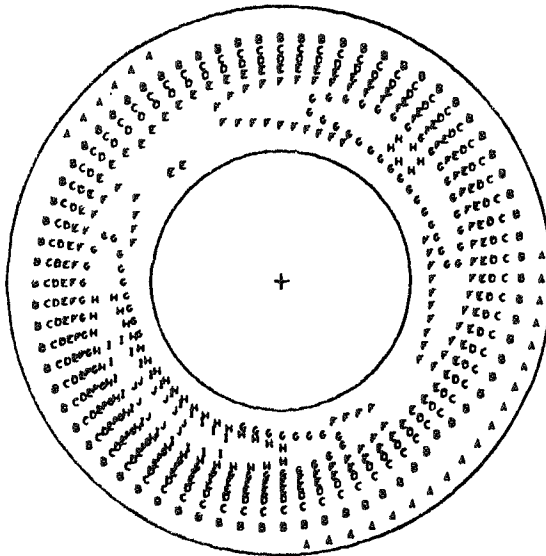
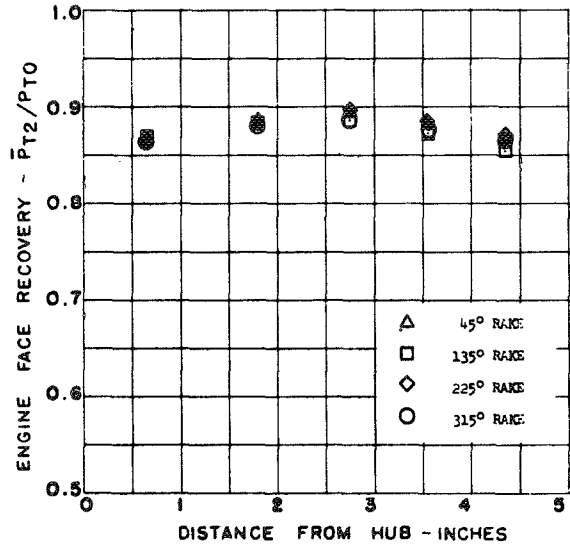
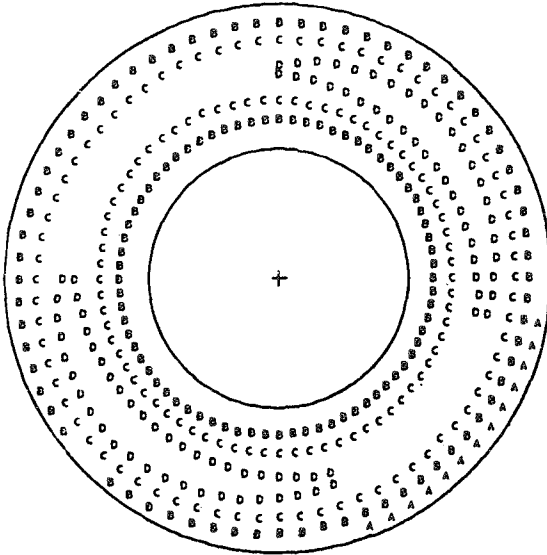


Figure 56.- Steady-state total pressure ratio contour, $M_0 = 3.0$,
 $\bar{P}_{t2}/P_{t0} = 0.565$.

RUN 21.209

$\frac{PT2AVG}{PT0} = 0.8768$ $\frac{PTMAX-PTMIN}{PT2AVG} = 0.0474$
 MINIMUM = 0.8551 INCREMENT = 0.010
 MAXIMUM = 0.8967 INCREASING A.B.C.....D

MACH 3.0



RUN 21.214

$\frac{PT2AVG}{PT0} = 0.5645$ $\frac{PTMAX-PTMIN}{PT2AVG} = 0.3464$
 MINIMUM = 0.4917 INCREMENT = 0.020
 MAXIMUM = 0.6873 INCREASING A.B.C.....J

MACH 3.0

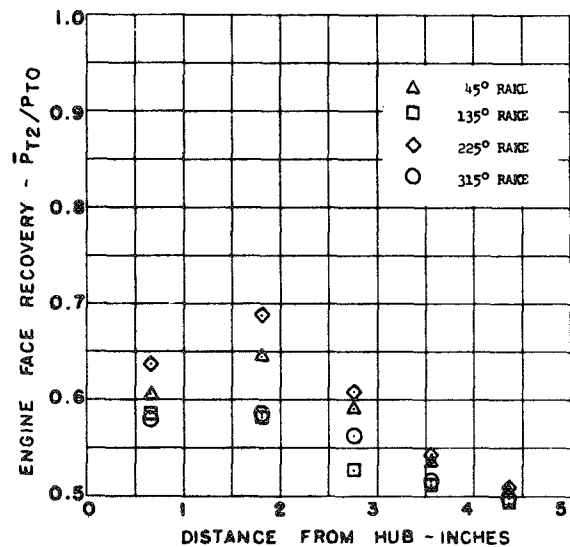
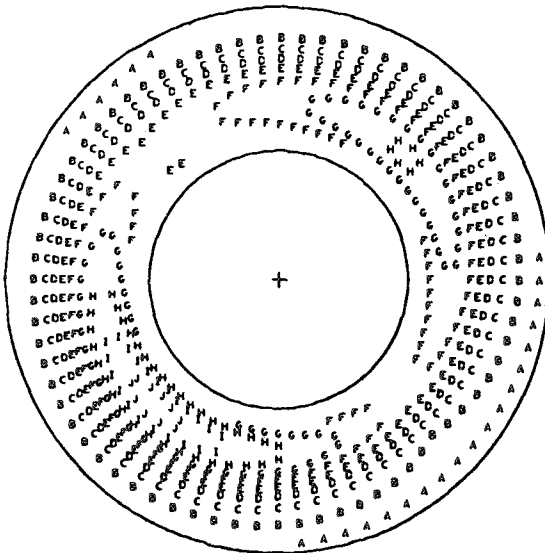
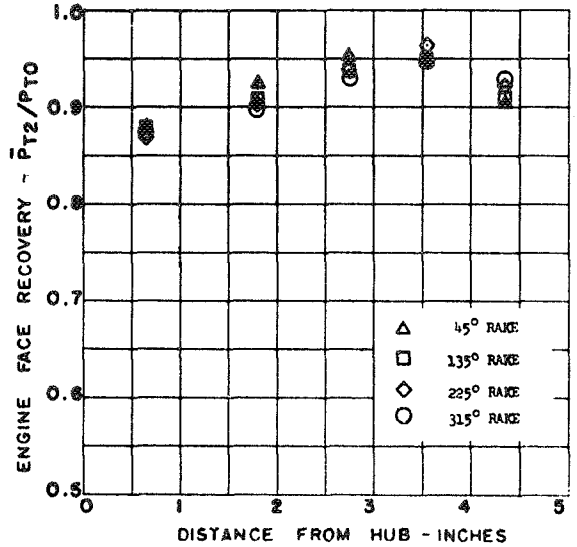
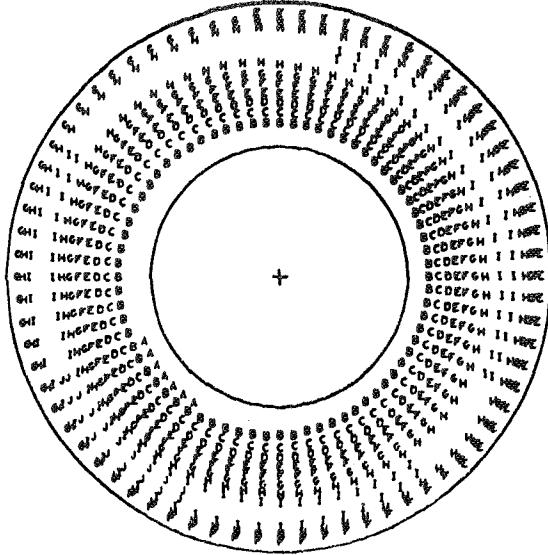


Figure 57.- Typical steady-state total pressure ratio contours and profiles, $M_0 = 3.0$.

RUN 27.250

PT2AVG / PTO = 0.9184 PTHAX-PTMIN / PT2AVG = 0.1045
 MINIMUM = 0.8683 INCREMENT = 0.010
 MAXIMUM = 0.9643 INCREASING A.B.C.....J

MACH 2.6



RUN 27.255

PT2AVG / PTO = 0.6421 PTHAX-PTMIN / PT2AVG = 0.4411
 MINIMUM = 0.5389 INCREMENT = 0.020
 MAXIMUM = 0.8222 INCREASING A.B.C.....@

MACH 2.6

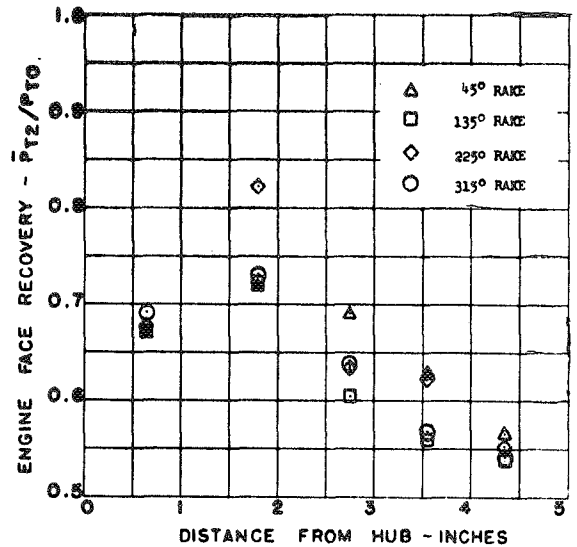
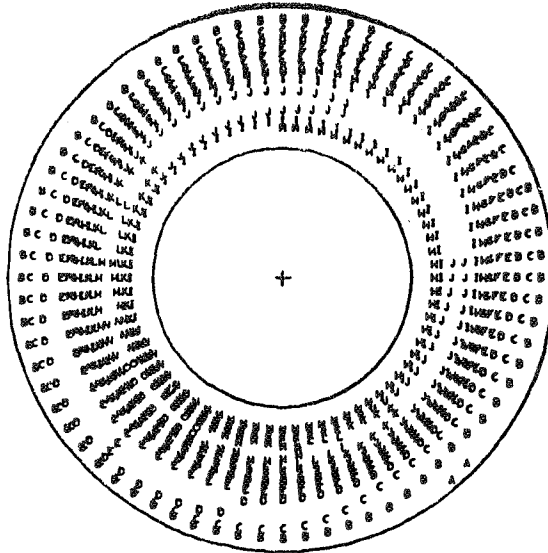


Figure 58.- Typical steady-state total pressure ratio contours and profiles, $M_0 = 2.6$.

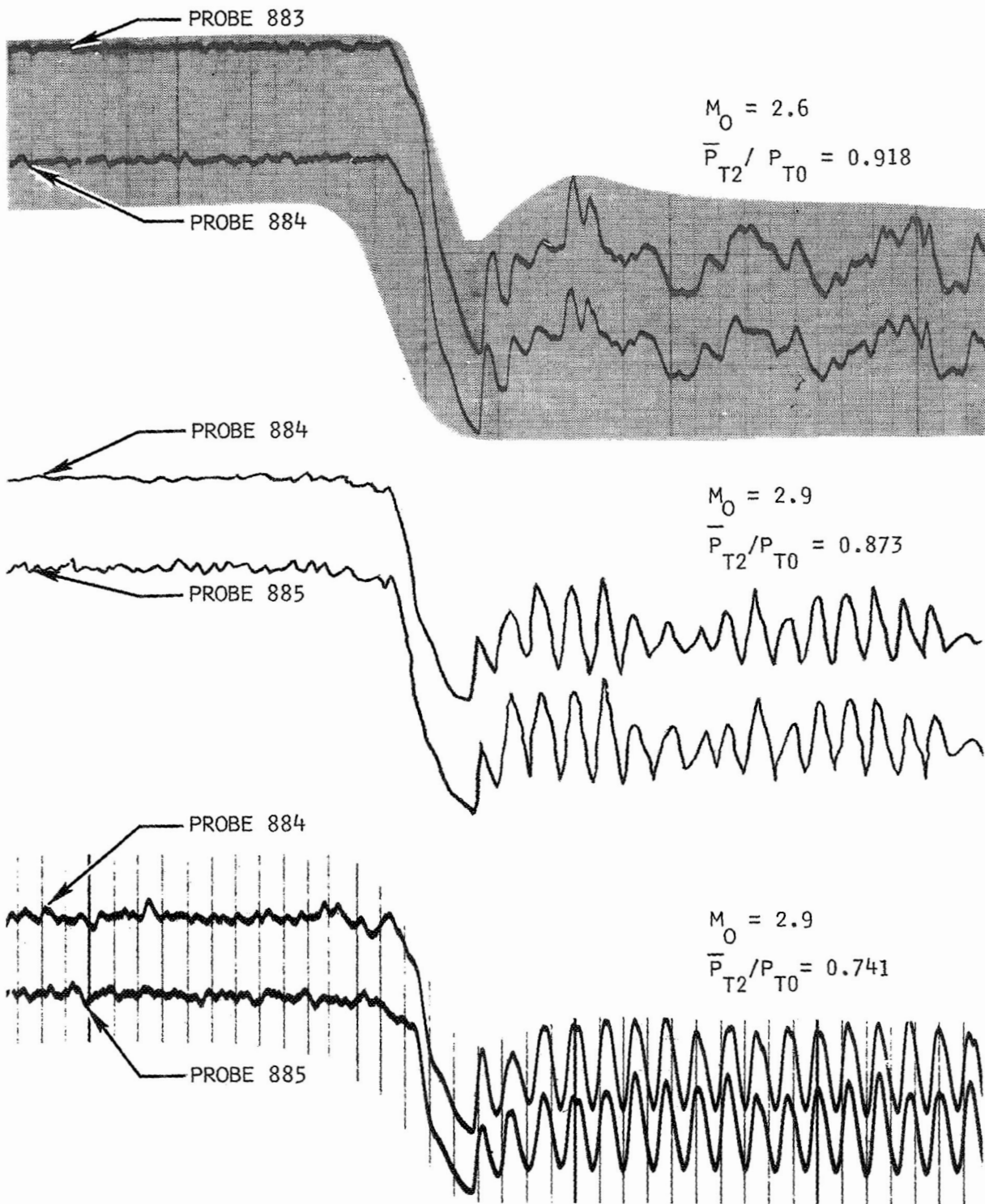
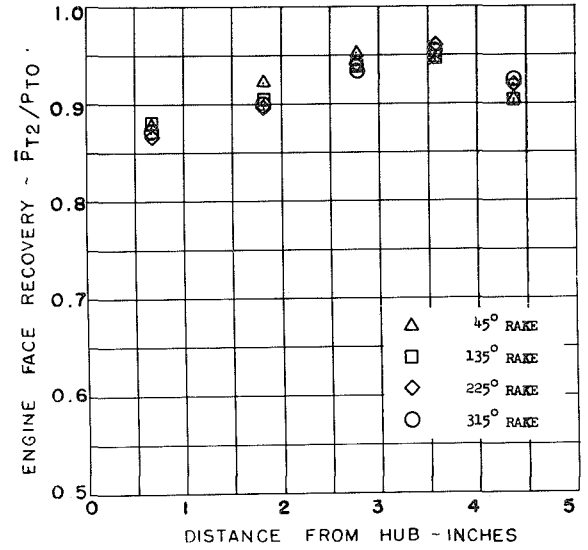
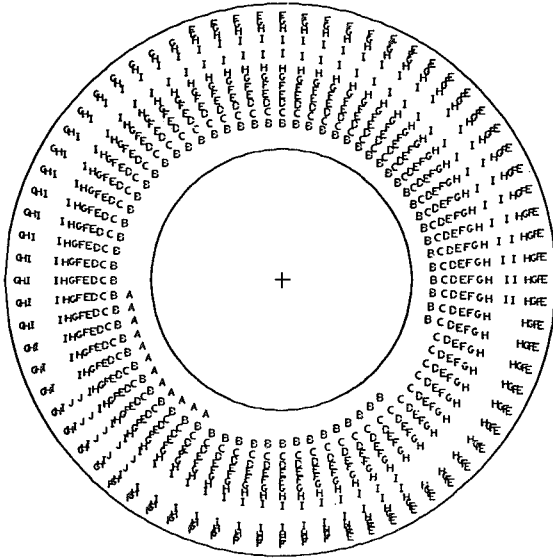


Figure 59.- Engine face total pressure during unstarts.

RUN 28.257

$\frac{PT2AVG}{PT0} = 0.9176$ $\frac{PTMAX-PTMIN}{PT2AVG} = 0.1026$
 MINIMUM = 0.8678 INCREMENT = 0.010
 MAXIMUM = 0.9620 INCREASING A,B,C.....J

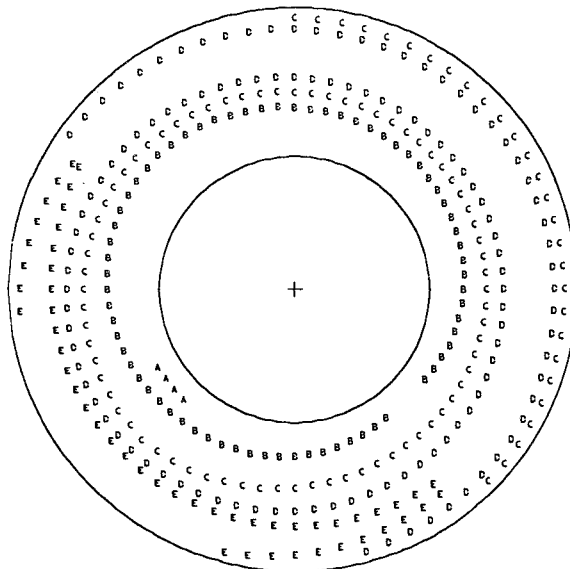
MACH 2.6



STEADY STATE PRIOR TO EXIT AREA REDUCTION

RUN 28.257
TIME 9 1 57.0640

$\frac{PT2AVG}{PT0} = 0.9176$ $\frac{PTMAX-PTMIN}{PT2AVG} = 0.1076$
 MINIMUM = 0.8698 INCREMENT = 0.020
 MAXIMUM = 0.9686 INCREASING A,B,C.....E



(a)

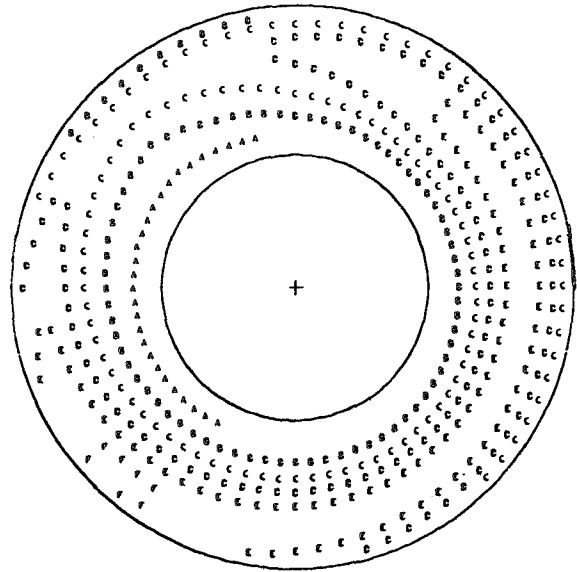
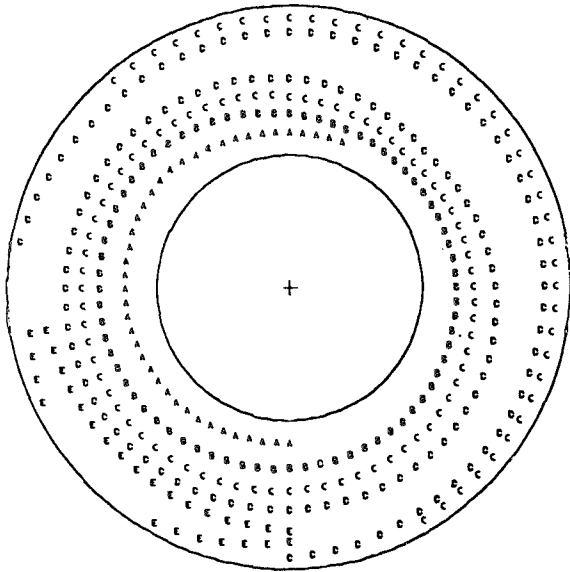
Figure 60. Instantaneous total pressure ratio contours during inlet unstart, $M_0 = 2.6$.

RUN 28.257
 TIME 9 1 57.0740

<u>PT2AVG</u>	= 0.9132	<u>PTMAX-PTMIN</u>	= 0.1029
<u>PT0</u>		<u>PT2AVG</u>	
MINIMUM	= 0.8663	INCREMENT	= 0.020
MAXIMUM	= 0.9602	INCREASING A.B.C.....E	

RUN 28.257
 TIME 9 1 57.0780

<u>PT2AVG</u>	= 0.9065	<u>PTMAX-PTMIN</u>	= 0.1182
<u>PT0</u>		<u>PT2AVG</u>	
MINIMUM	= 0.8553	INCREMENT	= 0.020
MAXIMUM	= 0.9625	INCREASING A.B.C.....F	

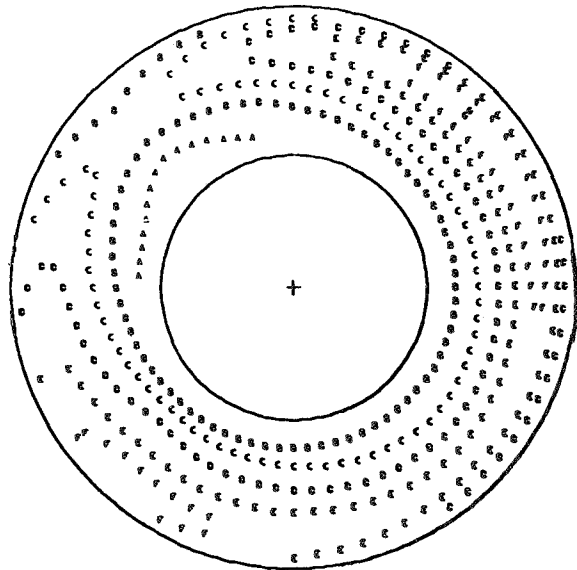
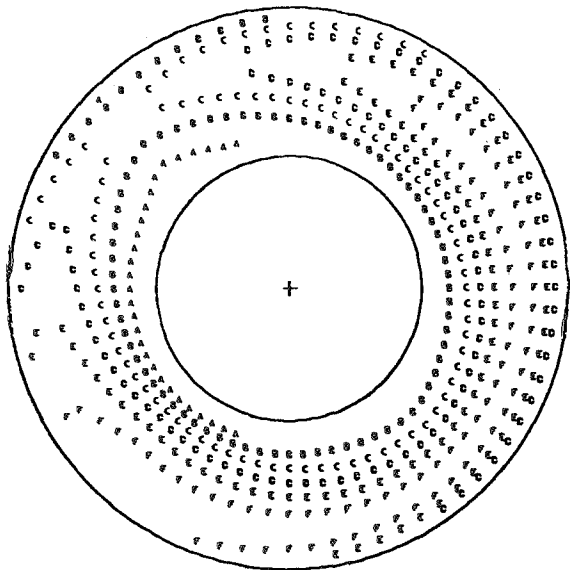


RUN 28.257
 TIME 9 1 57.0800

<u>PT2AVG</u>	= 0.9043	<u>PTMAX-PTMIN</u>	= 0.1327
<u>PT0</u>		<u>PT2AVG</u>	
MINIMUM	= 0.8443	INCREMENT	= 0.020
MAXIMUM	= 0.9644	INCREASING A.B.C.....F	

RUN 28.257
 TIME 9 1 57.0840

<u>PT2AVG</u>	= 0.8803	<u>PTMAX-PTMIN</u>	= 0.1443
<u>PT0</u>		<u>PT2AVG</u>	
MINIMUM	= 0.8244	INCREMENT	= 0.020
MAXIMUM	= 0.9514	INCREASING A.B.C.....G	

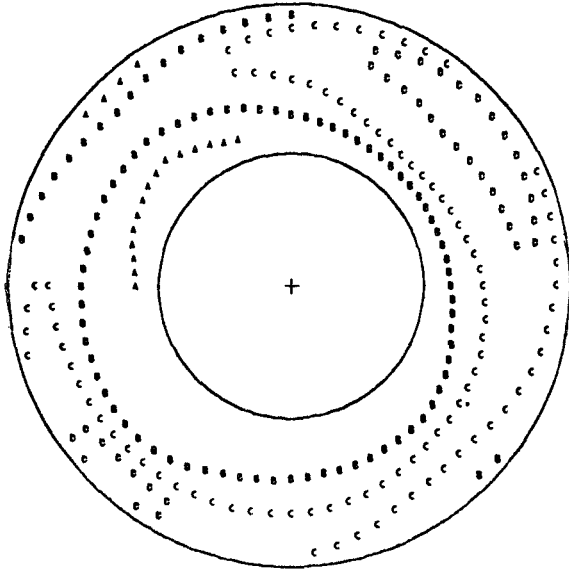


(b)

Figure 60.- Continued.

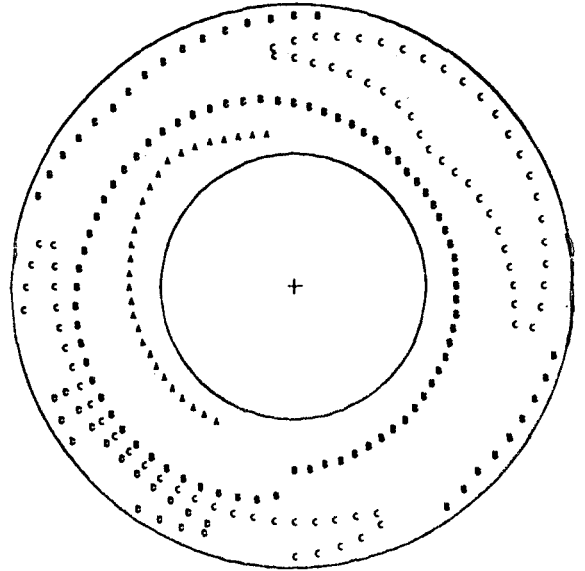
RUN 28.257
 TIME 9 1 57.0880

<u>PT2AVG</u>	= 0.8401	<u>PTMAX-PTMIN</u>	= 0.1022
<u>PT0</u>		<u>PT2AVG</u>	
MINIMUM	= 0.8019	INCREMENT	= 0.020
MAXIMUM	= 0.8878	INCREASING A,B,C.....D	



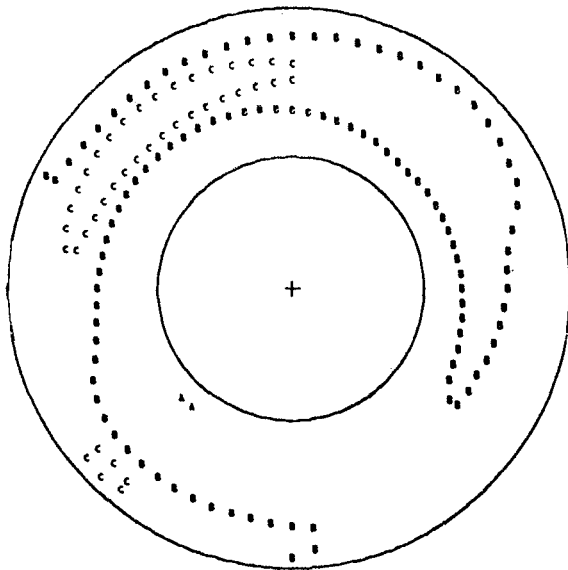
RUN 28.257
 TIME 9 1 57.0900

<u>PT2AVG</u>	= 0.8257	<u>PTMAX-PTMIN</u>	= 0.0885
<u>PT0</u>		<u>PT2AVG</u>	
MINIMUM	= 0.7924	INCREMENT	= 0.020
MAXIMUM	= 0.8655	INCREASING A,B,C.....D	



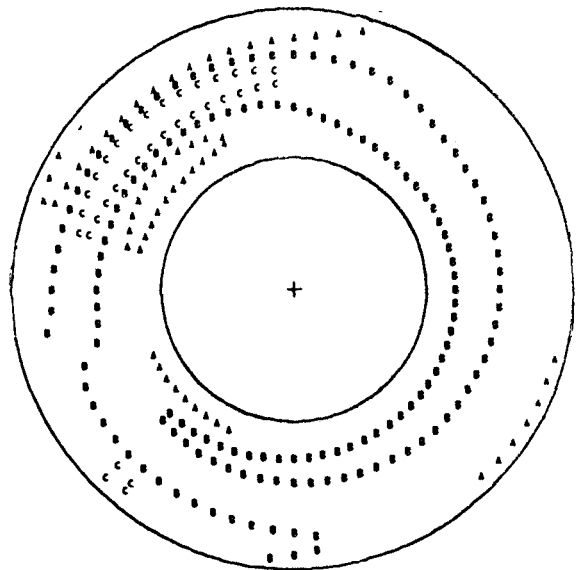
RUN 28.257
 TIME 9 1 57.0960

<u>PT2AVG</u>	= 0.6189	<u>PTMAX-PTMIN</u>	= 0.0985
<u>PT0</u>		<u>PT2AVG</u>	
MINIMUM	= 0.5994	INCREMENT	= 0.020
MAXIMUM	= 0.6603	INCREASING A,B,C.....D	



RUN 28.257
 TIME 9 1 57.1040

<u>PT2AVG</u>	= 0.3140	<u>PTMAX-PTMIN</u>	= 0.2139
<u>PT0</u>		<u>PT2AVG</u>	
MINIMUM	= 0.2929	INCREMENT	= 0.020
MAXIMUM	= 0.3601	INCREASING A,B,C.....D	



(c)

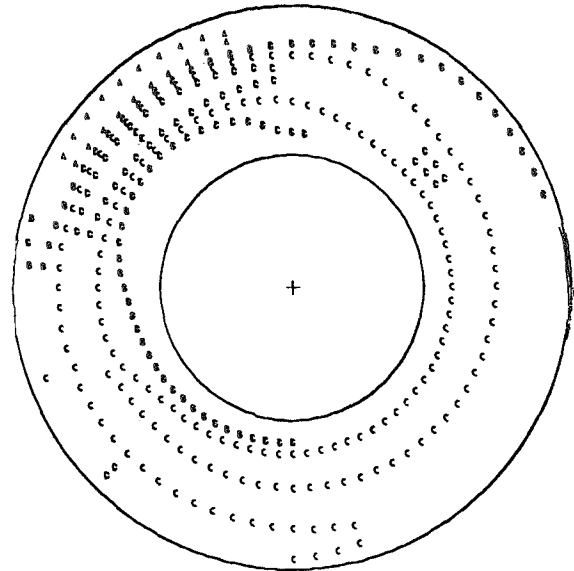
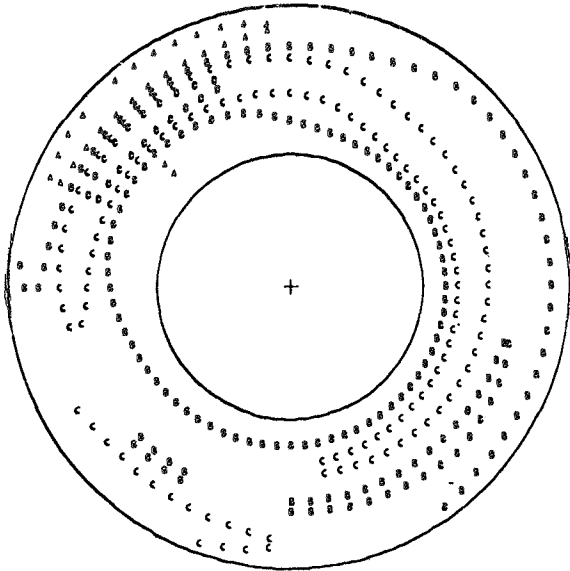
Figure 60.- Continued..

RUN 28.257
 TIME 9 1 57.1120

<u>PT2AVG</u>	= 0.1555	<u>PTMAX-PTMIN</u>	= 0.4987
<u>PT0</u>		<u>PT2AVG</u>	
MINIMUM	= 0.1765	INCREMENT	= 0.020
MAXIMUM	= 0.2041	INCREASING A.B.C.....D	

RUN 28.257
 TIME 9 1 57.1140

<u>PT2AVG</u>	= 0.1325	<u>PTMAX-PTMIN</u>	= 0.6749
<u>PT0</u>		<u>PT2AVG</u>	
MINIMUM	= 0.0979	INCREMENT	= 0.020
MAXIMUM	= 0.1807	INCREASING A.B.C.....E	

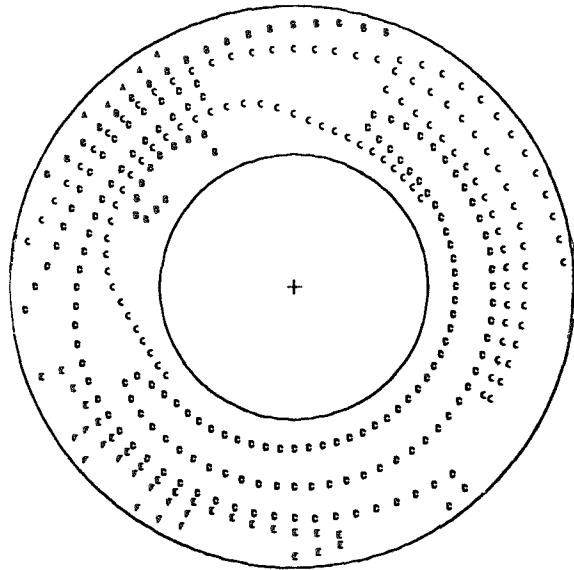
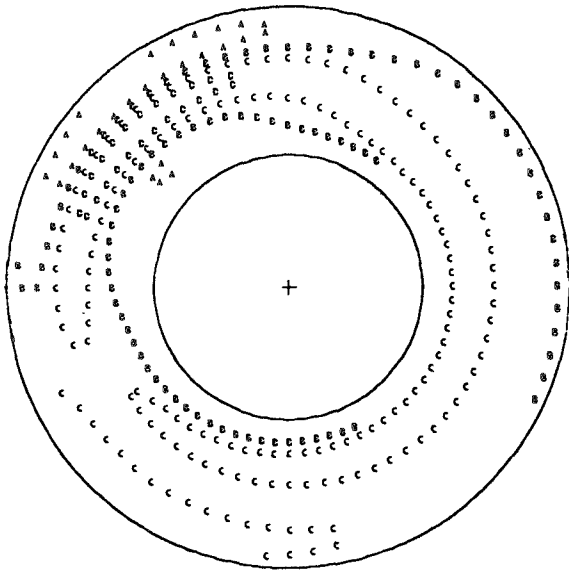


RUN 28.257
 TIME 9 1 57.1160

<u>PT2AVG</u>	= 0.1193	<u>PTMAX-PTMIN</u>	= 0.6906
<u>PT0</u>		<u>PT2AVG</u>	
MINIMUM	= 0.0825	INCREMENT	= 0.020
MAXIMUM	= 0.1649	INCREASING A.B.C.....D	

RUN 28.257
 TIME 9 1 57.1180

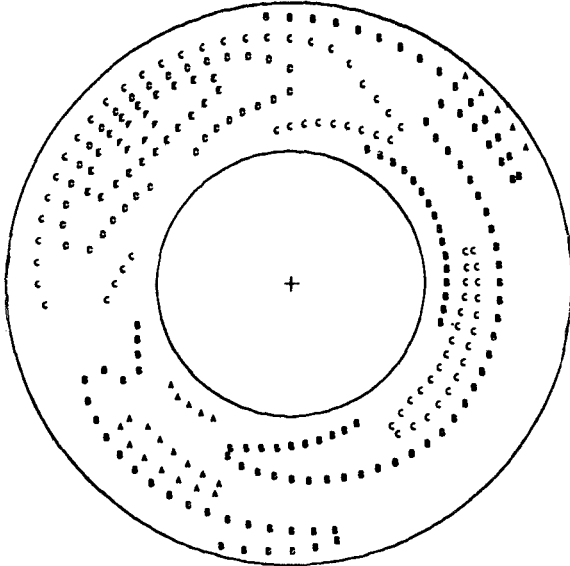
<u>PT2AVG</u>	= 0.2595	<u>PTMAX-PTMIN</u>	= 0.4295
<u>PT0</u>		<u>PT2AVG</u>	
MINIMUM	= 0.2033	INCREMENT	= 0.020
MAXIMUM	= 0.3148	INCREASING A.B.C.....F	



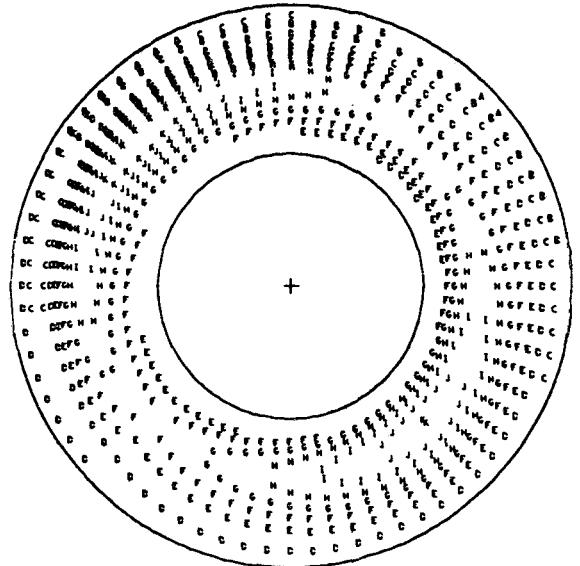
(d)

Figure 60.- Continued.

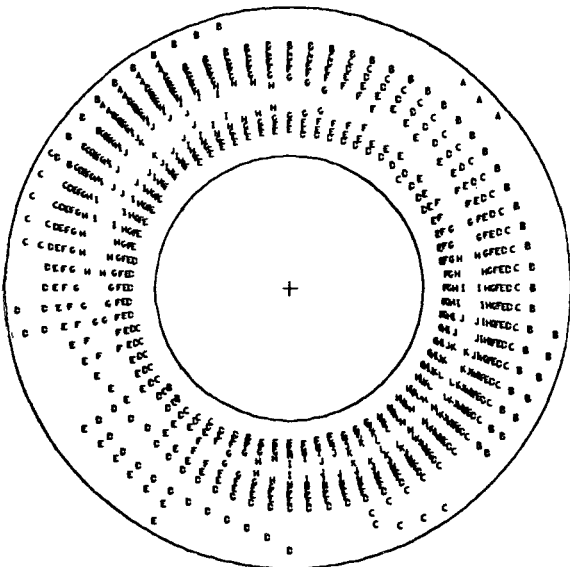
RUN 28.257
 TIME 9 1 57.1200
 $\frac{PT2AVG}{PT0} = 0.3885$ $\frac{PTMAX-PTMIN}{PT2AVG} = 0.2909$
 MINIMUM = 0.3530 INCREMENT = 0.020
 MAXIMUM = 0.4660 INCREASING A.B.C.....F



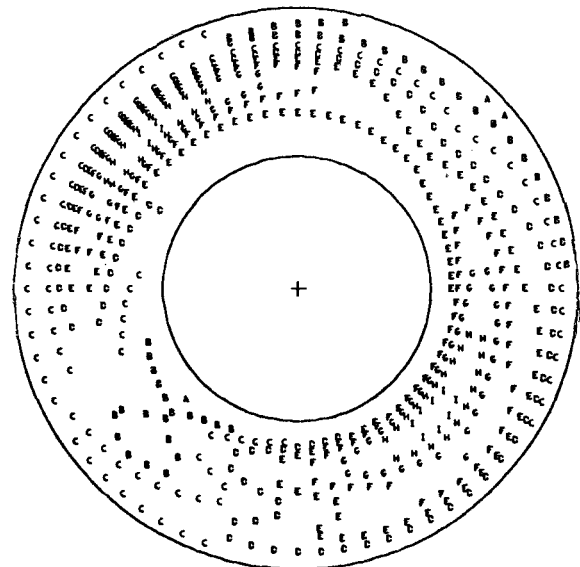
RUN 28.257
 TIME 9 1 57.1240
 $\frac{PT2AVG}{PT0} = 0.3240$ $\frac{PTMAX-PTMIN}{PT2AVG} = 0.6600$
 MINIMUM = 0.2266 INCREMENT = 0.020
 MAXIMUM = 0.4404 INCREASING A.B.C.....K



RUN 28.257
 TIME 9 1 57.1300
 $\frac{PT2AVG}{PT0} = 0.3938$ $\frac{PTMAX-PTMIN}{PT2AVG} = 0.6196$
 MINIMUM = 0.3175 INCREMENT = 0.020
 MAXIMUM = 0.5616 INCREASING A.B.C.....M



RUN 28.257
 TIME 9 1 57.1340
 $\frac{PT2AVG}{PT0} = 0.4251$ $\frac{PTMAX-PTMIN}{PT2AVG} = 0.4159$
 MINIMUM = 0.3568 INCREMENT = 0.020
 MAXIMUM = 0.5337 INCREASING A.B.C.....I



(e)

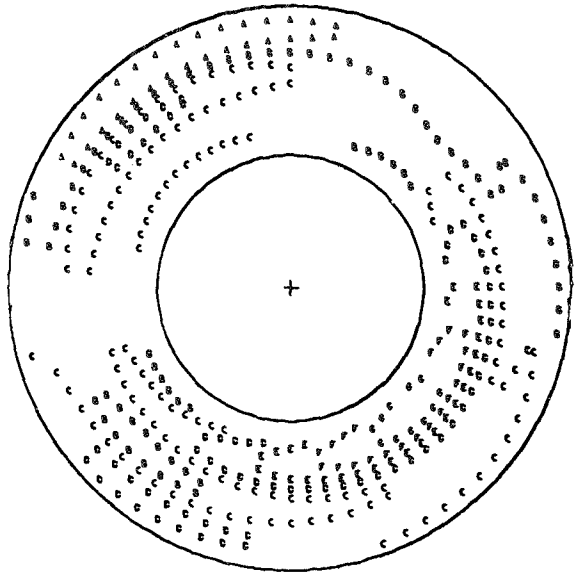
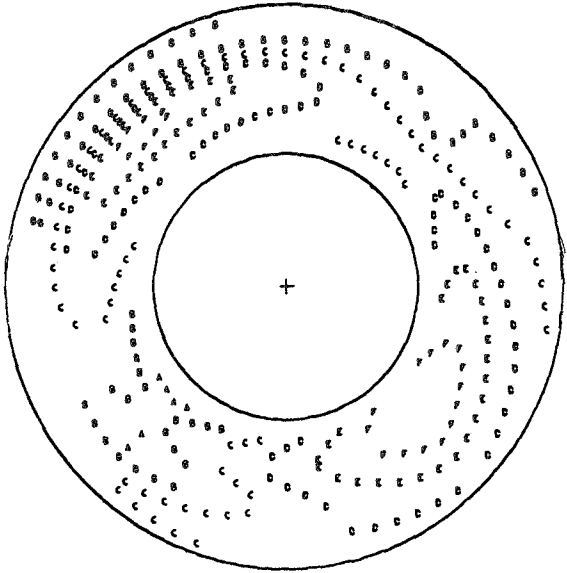
Figure 60.- Continued.

RUN 28.257
 TIME 9 1 57.1360

$\frac{PI2AVG}{PT0}$ = 0.3975	$\frac{PTMAX-PTMIN}{PT2AVG}$ = 0.3247
MINIMUM = 0.3406	INCREMENT = 0.020
MAXIMUM = 0.4698	INCREASING A,B,C.....F

RUN 28.257
 TIME 9 1 57.1400

$\frac{PI2AVG}{PT0}$ = 0.4287	$\frac{PTMAX-PTMIN}{PT2AVG}$ = 0.3112
MINIMUM = 0.3822	INCREMENT = 0.020
MAXIMUM = 0.5157	INCREASING A,B,C.....G

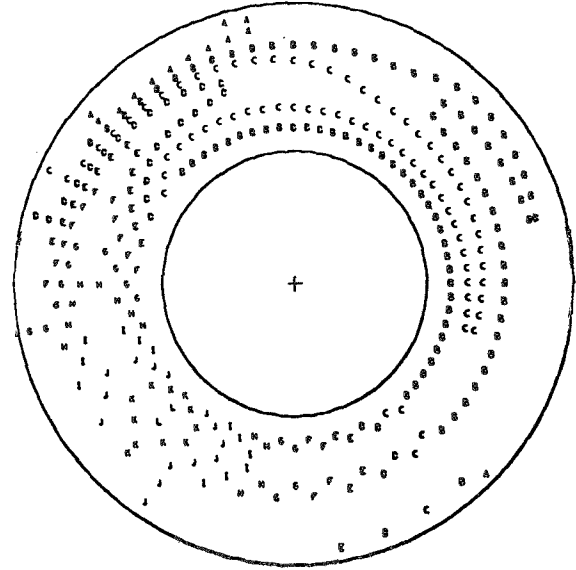
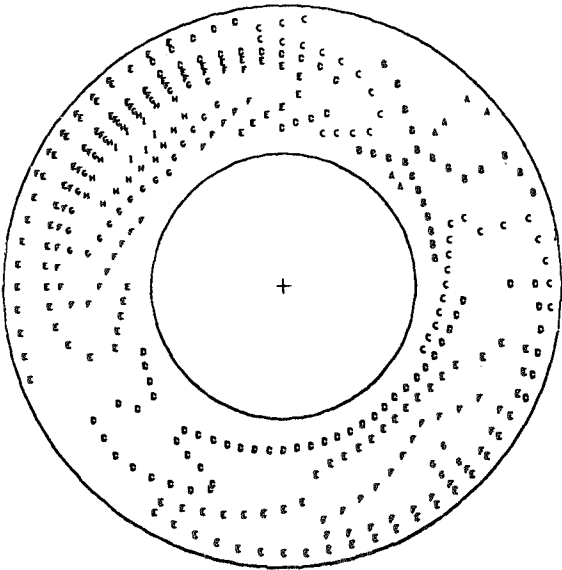


RUN 28.257
 TIME 9 1 57.1460

$\frac{PI2AVG}{PT0}$ = 0.4182	$\frac{PTMAX-PTMIN}{PT2AVG}$ = 0.4084
MINIMUM = 0.3437	INCREMENT = 0.020
MAXIMUM = 0.5146	INCREASING A,B,C.....I

RUN 28.257
 TIME 9 1 57.1600

$\frac{PI2AVG}{PT0}$ = 0.4271	$\frac{PTMAX-PTMIN}{PT2AVG}$ = 0.5307
MINIMUM = 0.3554	INCREMENT = 0.020
MAXIMUM = 0.5821	INCREASING A,B,C.....L



(f)

Figure 60.- Concluded.

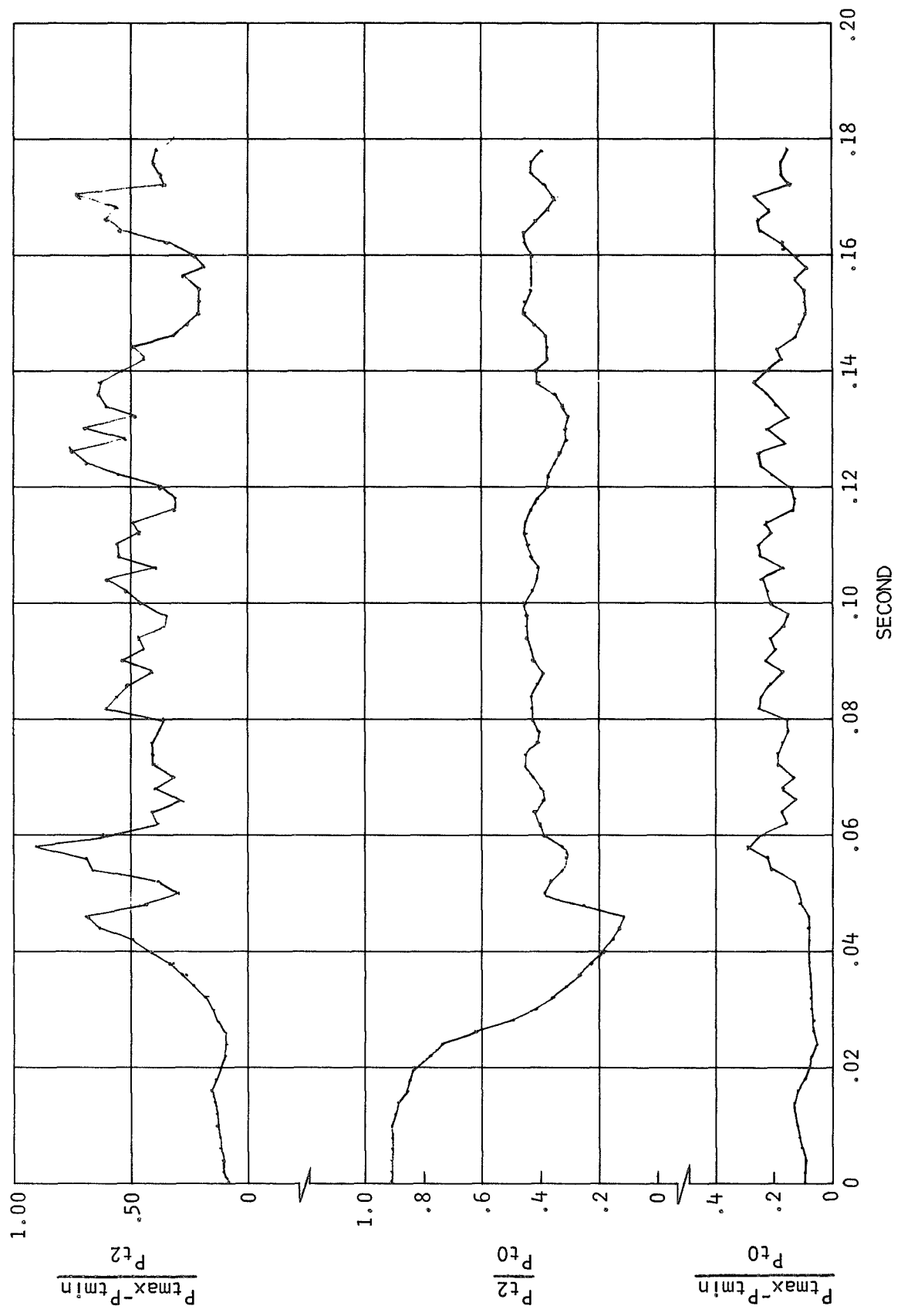


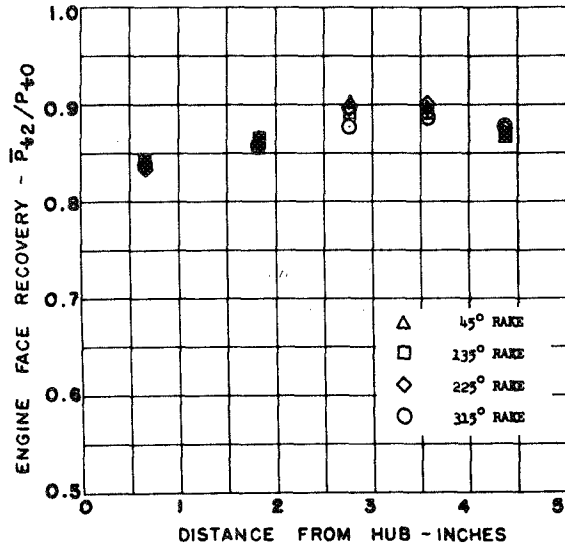
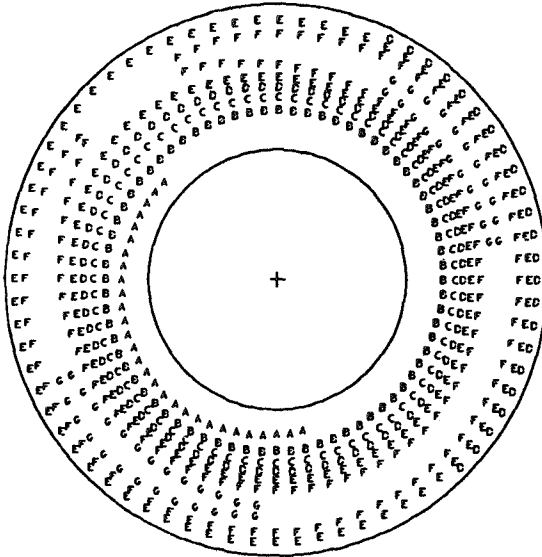
Figure 61.- Exit-induced inlet unstart time history, $M_0 = 2.6$, $\bar{P}_{t2}/P_{t0} = 0.918$.

RUN 44.300

$\frac{PT2AVG}{PT0} = 0.8728$
 MINIMUM = 0.8355
 MAXIMUM = 0.9034

$\frac{PTMAX-PTMIN}{PT2AVG} = 0.0777$
 INCREMENT = 0.010
 INCREASING A,B,C.....G

MACH 2.9

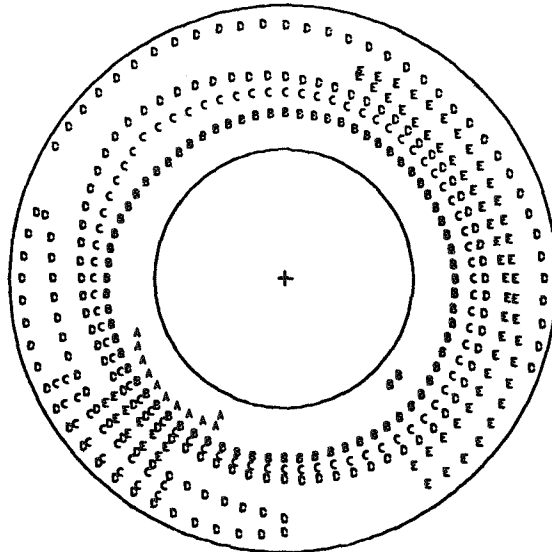


STEADY STATE PRIOR TO COWL TRANSLATION

RUN 44.300
 TIME 3 28 41.0000

$\frac{PT2AVG}{PT0} = 0.8683$
 MINIMUM = 0.8143
 MAXIMUM = 0.9101

$\frac{PTMAX-PTMIN}{PT2AVG} = 0.1103$
 INCREMENT = 0.020
 INCREASING A,B,C.....E

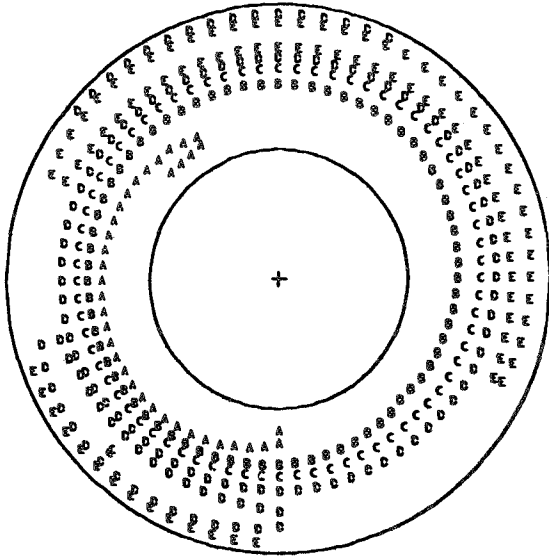


(a)

Figure 62.- Instantaneous total pressure ratio contours during inlet unstart, $M_0 = 2.9, \bar{P}_{t2}/P_{t0} = 0.873$.

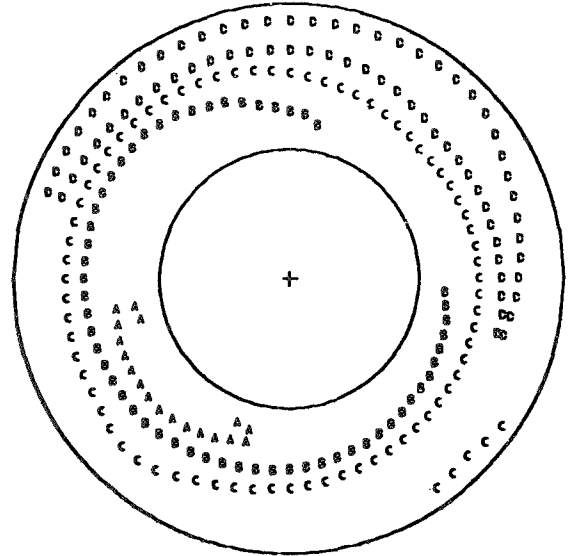
RUN 44.300
 TIME 3 28 41.0120

$\frac{PT2AVG}{PT0}$	= 0.8531	$\frac{PTMAX-PTMIN}{PT2AVG}$	= 0.1214
MINIMUM	= 0.8002	INCREMENT	= 0.020
MAXIMUM	= 0.9038	INCREASING A.B.C.....E	



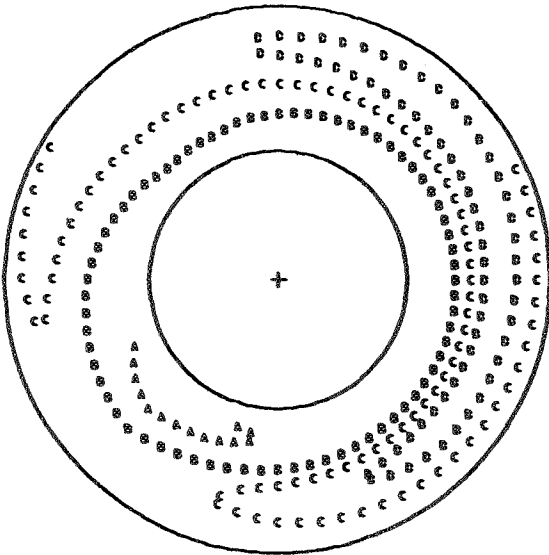
RUN 44.300
 TIME 3 28 41.0200

$\frac{PT2AVG}{PT0}$	= 0.8266	$\frac{PTMAX-PTMIN}{PT2AVG}$	= 0.0893
MINIMUM	= 0.7837	INCREMENT	= 0.020
MAXIMUM	= 0.8575	INCREASING A.B.C.....D	



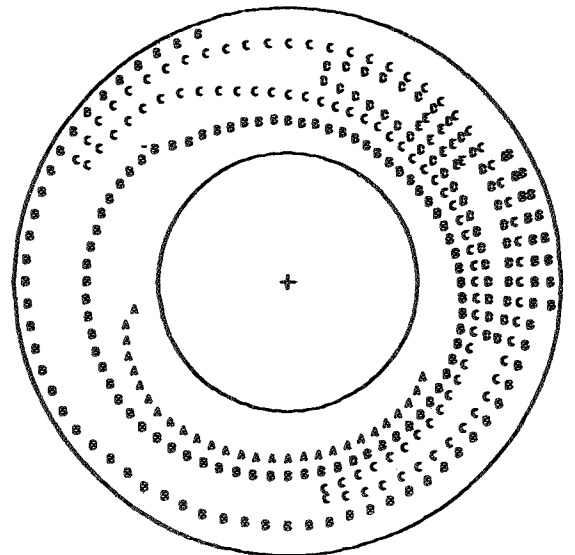
RUN 44.300
 TIME 3 28 41.0220

$\frac{PT2AVG}{PT0}$	= 0.8138	$\frac{PTMAX-PTMIN}{PT2AVG}$	= 0.0933
MINIMUM	= 0.7741	INCREMENT	= 0.020
MAXIMUM	= 0.8501	INCREASING A.B.C.....D	



RUN 44.300
 TIME 3 28 41.0240

$\frac{PT2AVG}{PT0}$	= 0.8149	$\frac{PTMAX-PTMIN}{PT2AVG}$	= 0.1145
MINIMUM	= 0.7800	INCREMENT	= 0.020
MAXIMUM	= 0.8733	INCREASING A.B.C.....E	

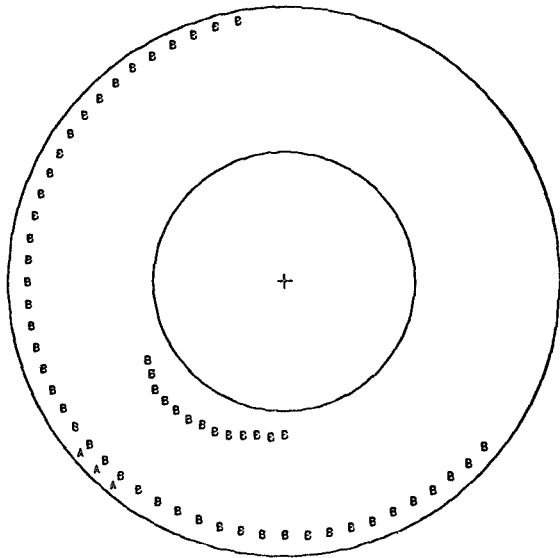


(b)

Figure 62.- Continued.

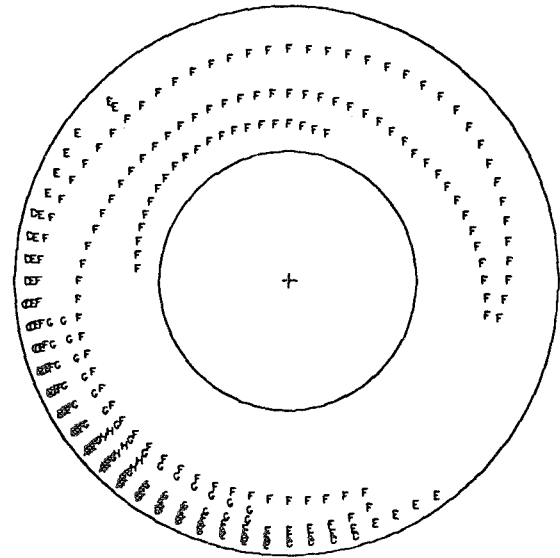
RUN 44.300
 TIME 3 28 41.0280

$\frac{PT2AVG}{PT0}$	= 0.7463	$\frac{PTMAX-PTMIN}{PT2AVG}$	= 0.0553
MINIMUM	= 0.7181	INCREMENT	= 0.020
MAXIMUM	= 0.7594	INCREASING A.B.C.....B	



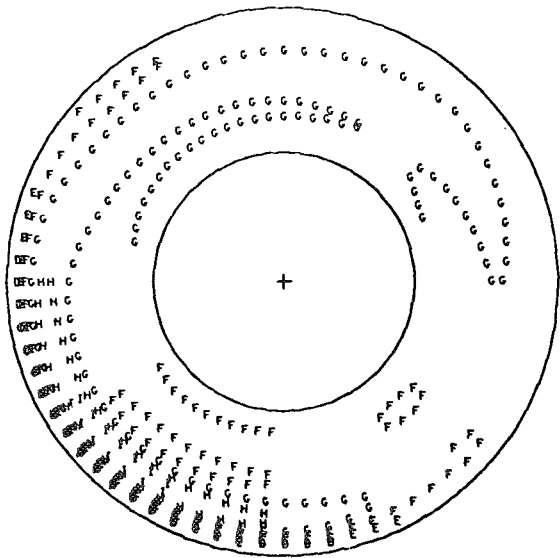
RUN 44.300
 TIME 3 28 41.0360

$\frac{PT2AVG}{PT0}$	= 0.4221	$\frac{PTMAX-PTMIN}{PT2AVG}$	= 0.3639
MINIMUM	= 0.3226	INCREMENT	= 0.020
MAXIMUM	= 0.4763	INCREASING A.B.C.....H	



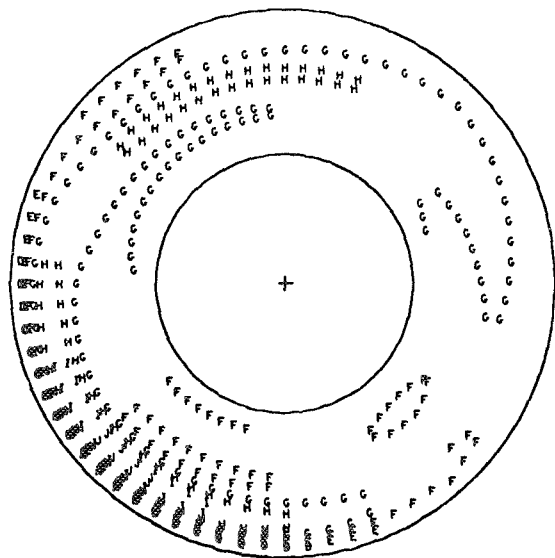
RUN 44.300
 TIME 3 28 41.0400

$\frac{PT2AVG}{PT0}$	= 0.3402	$\frac{PTMAX-PTMIN}{PT2AVG}$	= 0.5490
MINIMUM	= 0.2205	INCREMENT	= 0.020
MAXIMUM	= 0.4073	INCREASING A.B.C.....I	



RUN 44.300
 TIME 3 28 41.0440

$\frac{PT2AVG}{PT0}$	= 0.2529	$\frac{PTMAX-PTMIN}{PT2AVG}$	= 0.7956
MINIMUM	= 0.1309	INCREMENT	= 0.020
MAXIMUM	= 0.3321	INCREASING A.B.C.....J	

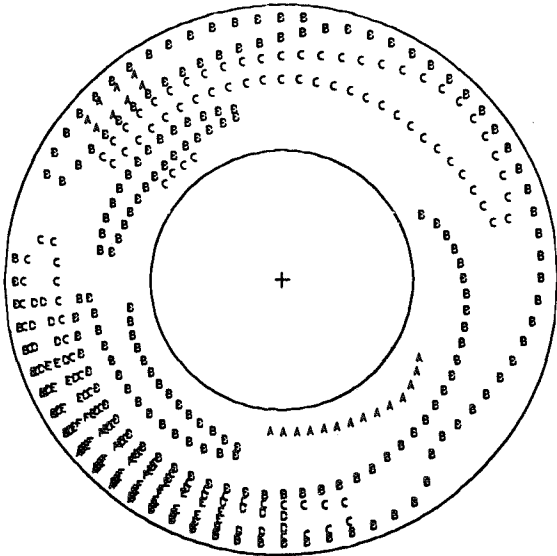


(c)

Figure 62.- Continued.

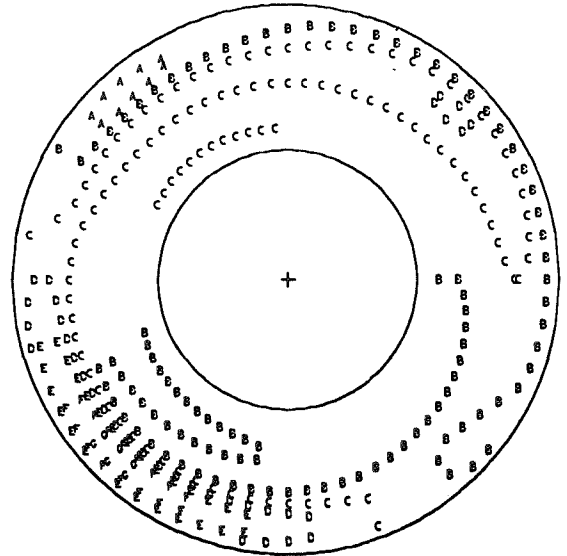
RUN 44.300
 TIME 3 28 41.0520

$\frac{PT2AVG}{PT0}$	= 0.1457	$\frac{PTMAX-PTMIN}{PT2AVG}$	= 0.8630
MINIMUM	= 0.1117	INCREMENT	= 0.020
MAXIMUM	= 0.2375	INCREASING A.B.C.....F	



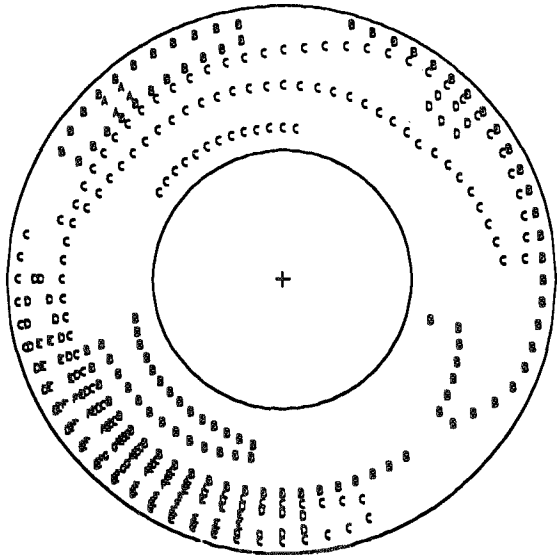
RUN 44.300
 TIME 3 28 41.0560

$\frac{PT2AVG}{PT0}$	= 0.1331	$\frac{PTMAX-PTMIN}{PT2AVG}$	= 0.9739
MINIMUM	= 0.0963	INCREMENT	= 0.020
MAXIMUM	= 0.2259	INCREASING A.B.C.....G	



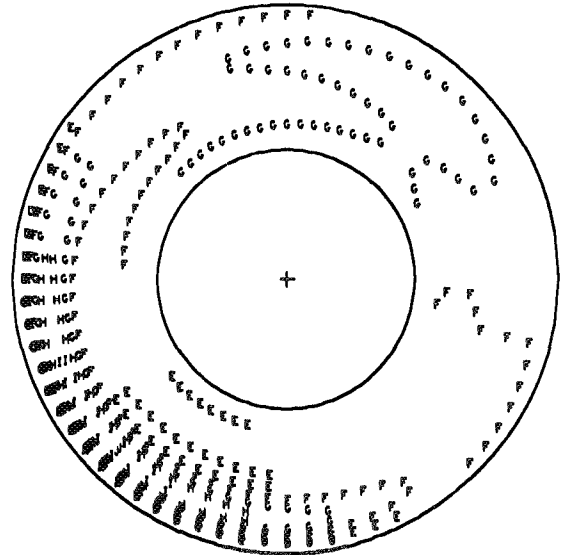
RUN 44.300
 TIME 3 28 41.0580

$\frac{PT2AVG}{PT0}$	= 0.1321	$\frac{PTMAX-PTMIN}{PT2AVG}$	= 0.9701
MINIMUM	= 0.0958	INCREMENT	= 0.020
MAXIMUM	= 0.2239	INCREASING A.B.C.....G	



RUN 44.300
 TIME 3 28 41.0600

$\frac{PT2AVG}{PT0}$	= 0.2708	$\frac{PTMAX-PTMIN}{PT2AVG}$	= 0.6928
MINIMUM	= 0.1637	INCREMENT	= 0.020
MAXIMUM	= 0.3514	INCREASING A.B.C.....J	

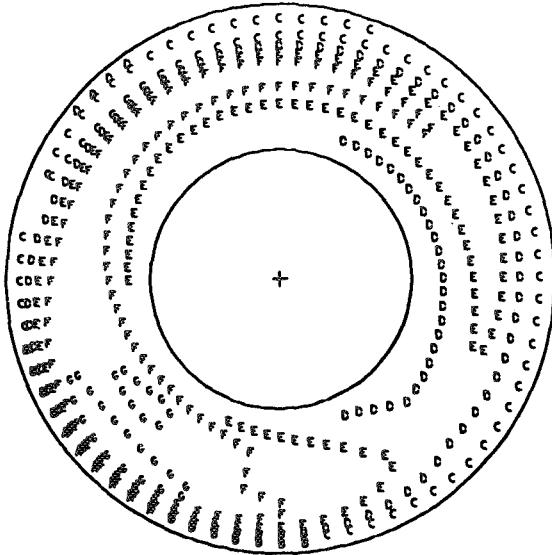


(d)

Figure 62.- Continued.

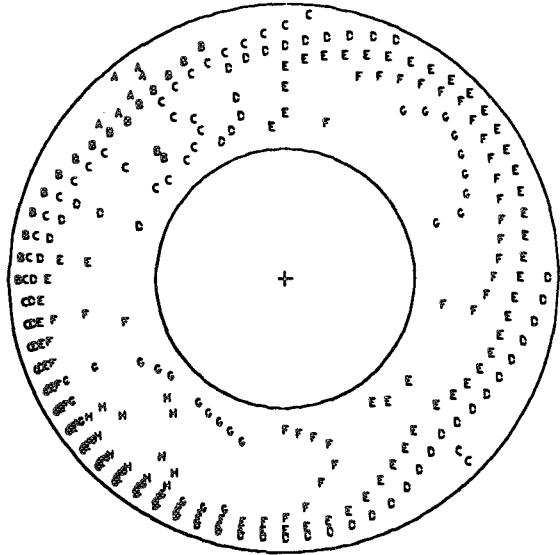
RUN 44.300
 TIME 3 28 41.0640

$\frac{PT2AVG}{PT0}$	= 0.2624	$\frac{PTMAX-PTMIN}{PT2AVG}$	= 0.5555
MINIMUM	= 0.1811	INCREMENT	= 0.020
MAXIMUM	= 0.3269	INCREASING A.B.C.....G	



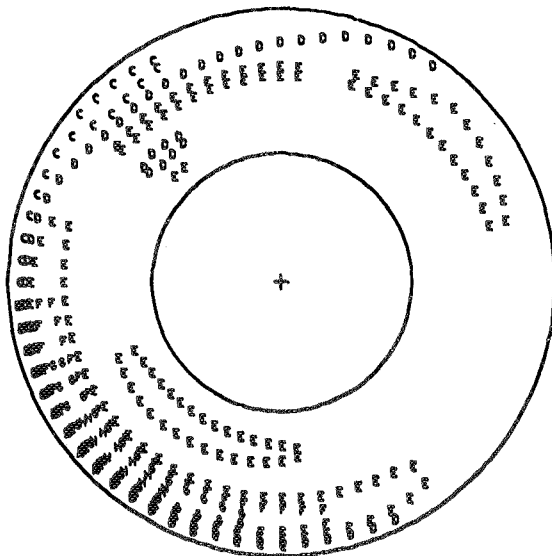
RUN 44.300
 TIME 3 28 41.0760

$\frac{PT2AVG}{PT0}$	= 0.3591	$\frac{PTMAX-PTMIN}{PT2AVG}$	= 0.4553
MINIMUM	= 0.2736	INCREMENT	= 0.020
MAXIMUM	= 0.4372	INCREASING A.B.C.....H	



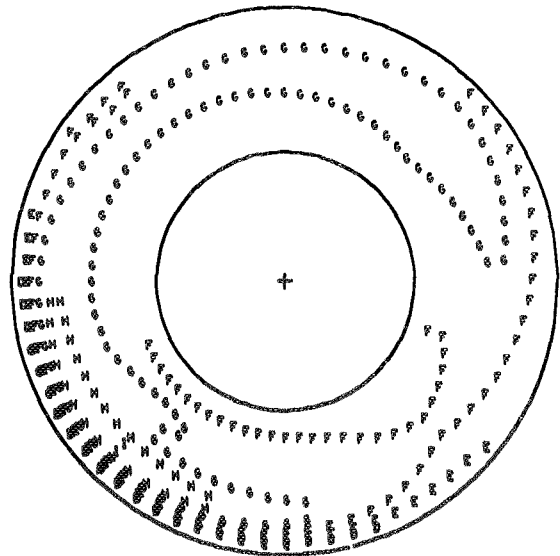
RUN 44.300
 TIME 3 28 41.0820

$\frac{PT2AVG}{PT0}$	= 0.2513	$\frac{PTMAX-PTMIN}{PT2AVG}$	= 0.6287
MINIMUM	= 0.1773	INCREMENT	= 0.020
MAXIMUM	= 0.3353	INCREASING A.B.C.....H	



RUN 44.300
 TIME 3 28 41.0900

$\frac{PT2AVG}{PT0}$	= 0.3571	$\frac{PTMAX-PTMIN}{PT2AVG}$	= 0.4555
MINIMUM	= 0.2494	INCREMENT	= 0.020
MAXIMUM	= 0.4121	INCREASING A.B.C.....I	



(e)

Figure 62.- Concluded.

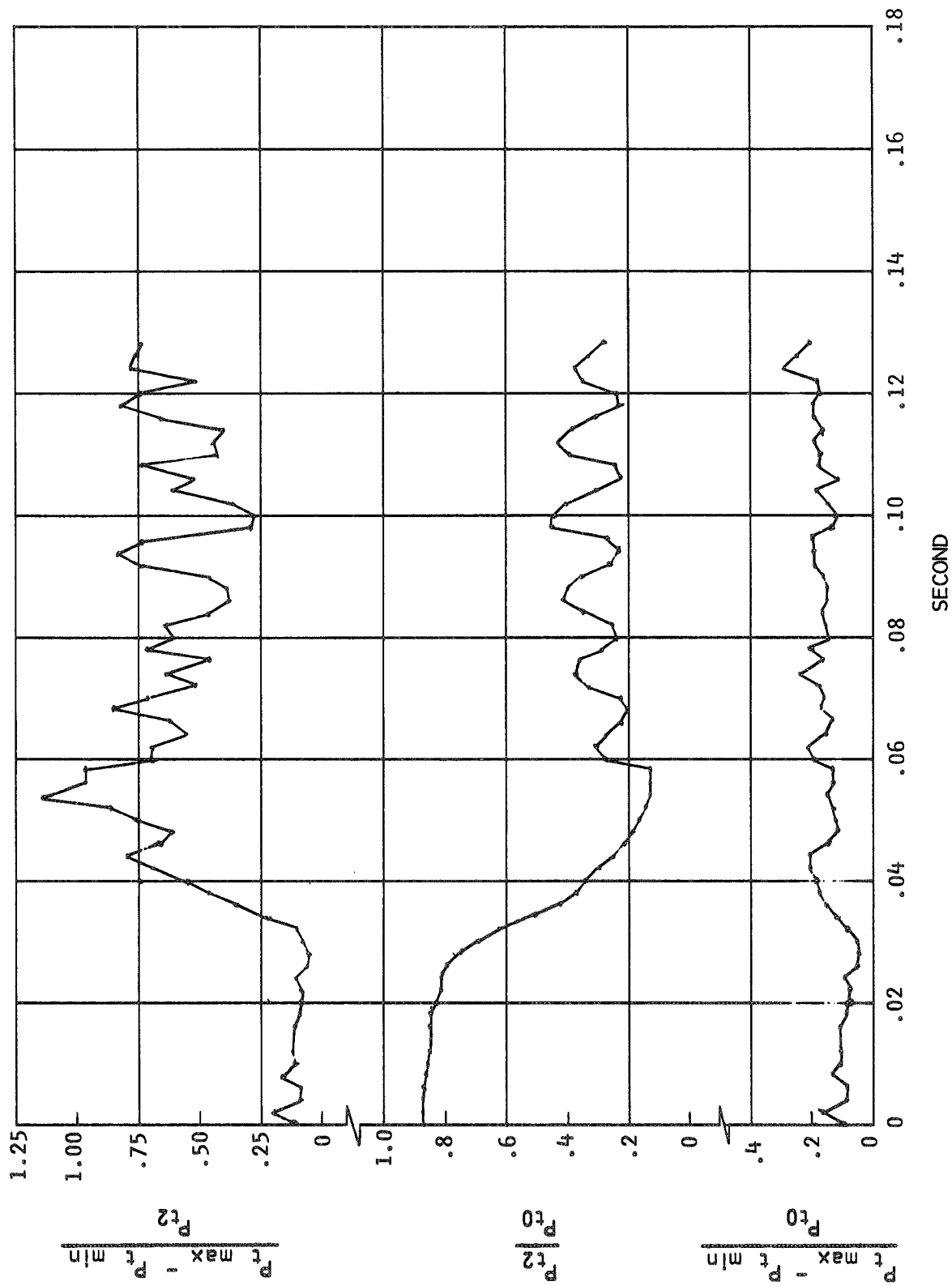
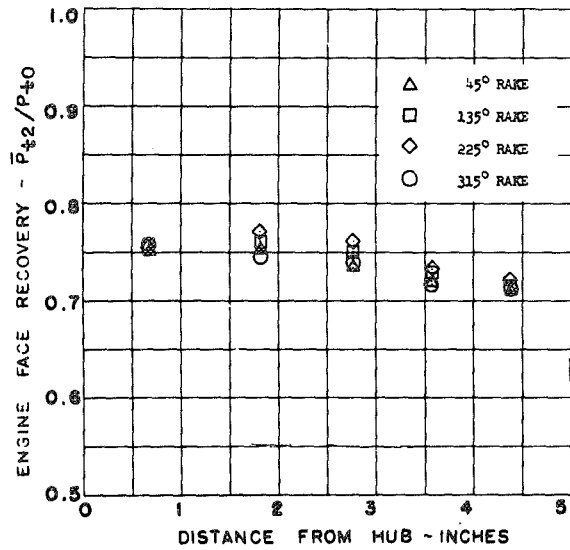
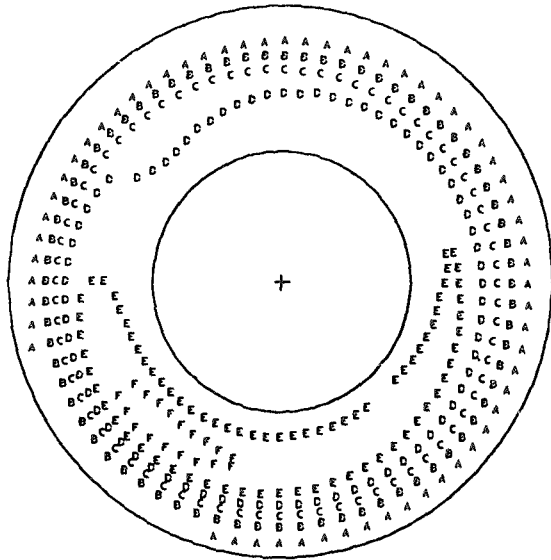


Figure 63. - Cowl-induced inlet unstart time history, $M_0 = 2.9$, $\bar{P}_{t2}/P_{t0} = 0.873$

RUN 45.302

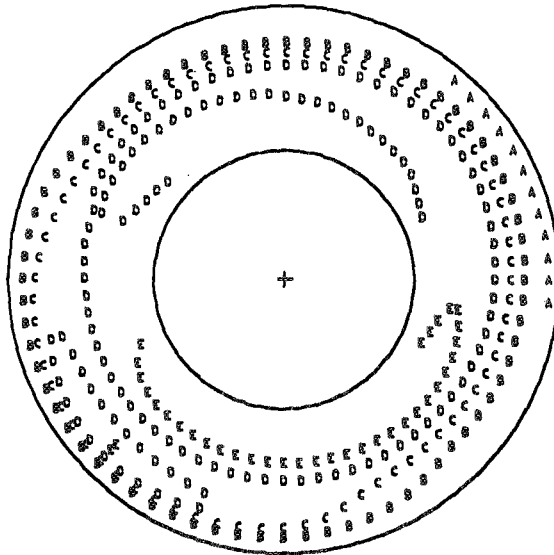
$\frac{PT2AVG}{PT0} = 0.7407$ $\frac{PTMAX-PTMIN}{PT2AVG} = 0.0855$
 MINIMUM = 0.7102 INCREMENT = 0.010
 MAXIMUM = 0.7736 INCREASING A.B.C.....F

MACH 2.9



STEADY STATE PRIOR TO COWL TRANSLATION

RUN 45.302
 TIME 3 46 28.2020
 $\frac{PT2AVG}{PT0} = 0.7467$ $\frac{PTMAX-PTMIN}{PT2AVG} = 0.1198$
 MINIMUM = 0.6983 INCREMENT = 0.020
 MAXIMUM = 0.7878 INCREASING A.B.C.....E

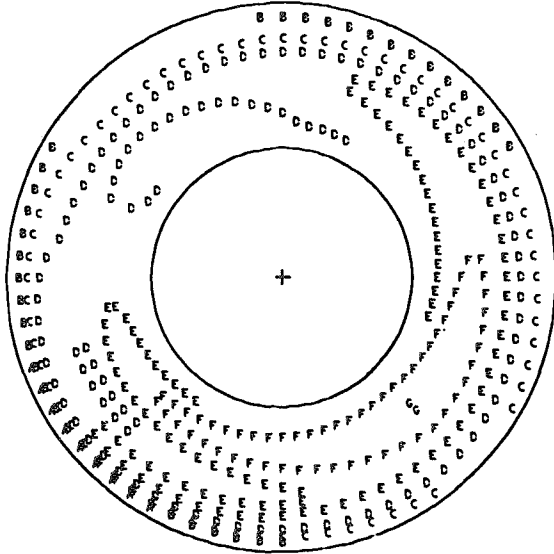


(a)

Figure 64.- Instantaneous total pressure ratio contours during inlet unstart, $M_0 = 2.9$, $\bar{P}_{t2}/P_{t0} = 0.741$.

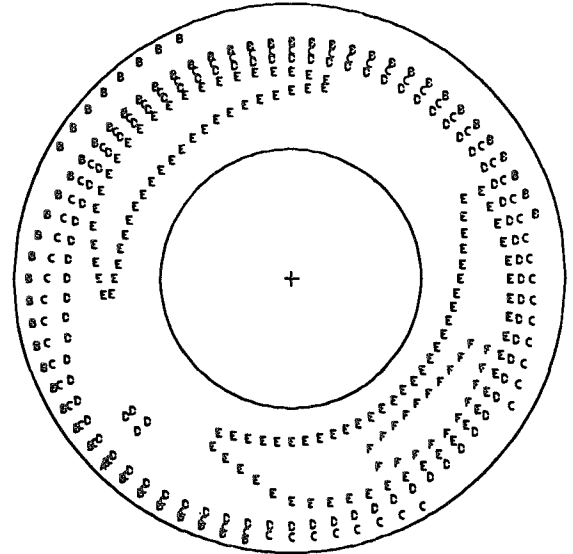
RUN 45.302
 TIME 3 46 28.2200

<u>PT2AVG</u>	= 0.7420	<u>PTMAX-PTMIN</u>	= 0.1755
<u>PT0</u>		<u>PT2AVG</u>	
MINIMUM	= 0.6700	INCREMENT	= 0.020
MAXIMUM	= 0.8003	INCREASING A.B.C.....G	



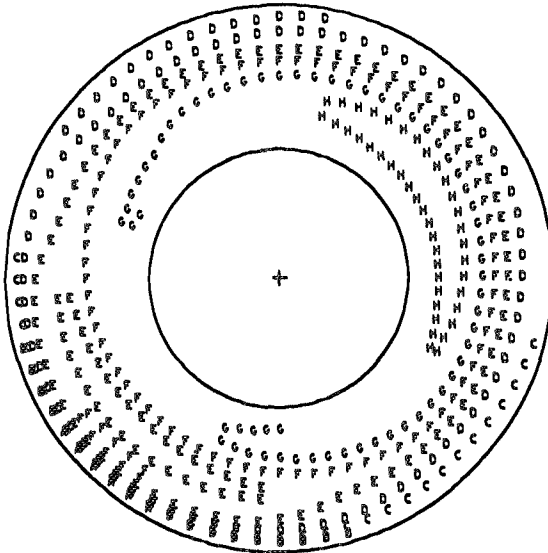
RUN 45.302
 TIME 3 46 28.2220

<u>PT2AVG</u>	= 0.7478	<u>PTMAX-PTMIN</u>	= 0.1438
<u>PT0</u>		<u>PT2AVG</u>	
MINIMUM	= 0.6893	INCREMENT	= 0.020
MAXIMUM	= 0.7968	INCREASING A.B.C.....F	



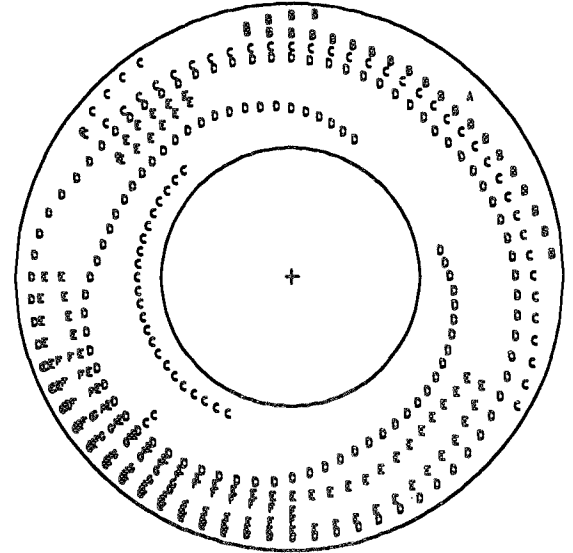
RUN 45.302
 TIME 3 46 28.2280

<u>PT2AVG</u>	= 0.7199	<u>PTMAX-PTMIN</u>	= 0.2205
<u>PT0</u>		<u>PT2AVG</u>	
MINIMUM	= 0.6210	INCREMENT	= 0.020
MAXIMUM	= 0.7798	INCREASING A.B.C.....H	



RUN 45.302
 TIME 3 46 28.2360

<u>PT2AVG</u>	= 0.7147	<u>PTMAX-PTMIN</u>	= 0.1853
<u>PT0</u>		<u>PT2AVG</u>	
MINIMUM	= 0.6577	INCREMENT	= 0.020
MAXIMUM	= 0.7902	INCREASING A.B.C.....G	

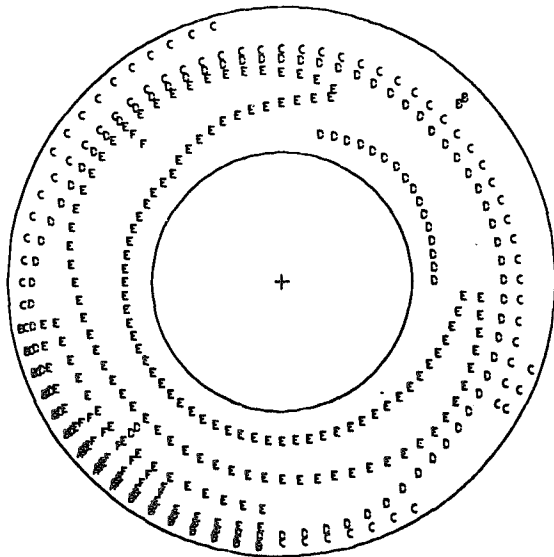


(b)

Figure 64.- Continued.

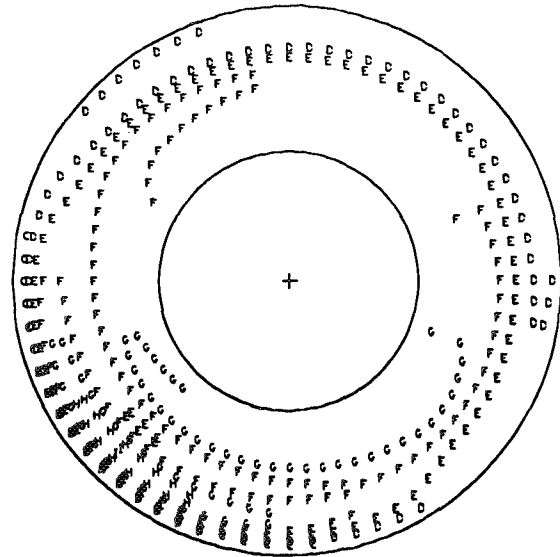
RUN 45.302
TIME 3 46 28.2420

$\frac{PT2AVG}{PT0}$	= 0.6615	$\frac{PTMAX-PTMIN}{PT2AVG}$	= 0.1759
MINIMUM	= 0.5961	INCREMENT	= 0.020
MAXIMUM	= 0.7125	INCREASING A.B.C.....F	



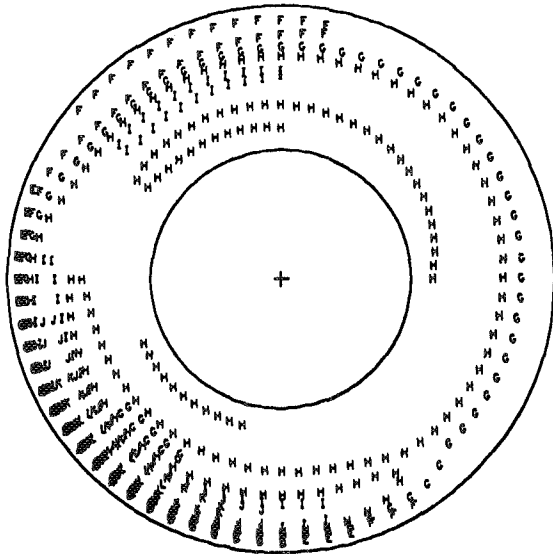
RUN 45.302
TIME 3 46 28.2480

$\frac{PT2AVG}{PT0}$	= 0.5483	$\frac{PTMAX-PTMIN}{PT2AVG}$	= 0.2994
MINIMUM	= 0.4596	INCREMENT	= 0.020
MAXIMUM	= 0.6238	INCREASING A.B.C.....I	



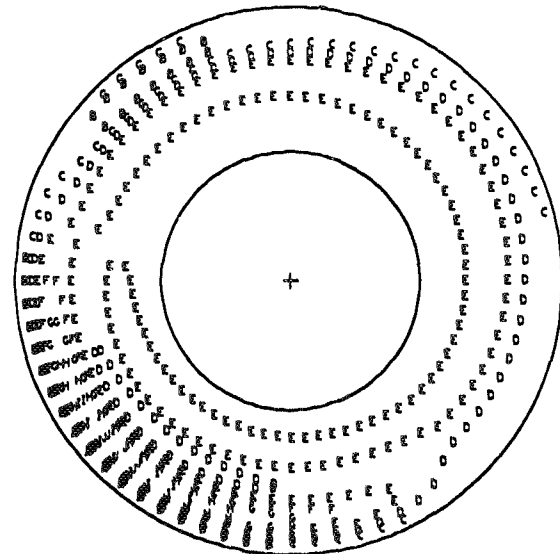
RUN 45.302
TIME 3 46 28.2540

$\frac{PT2AVG}{PT0}$	= 0.3114	$\frac{PTMAX-PTMIN}{PT2AVG}$	= 0.8122
MINIMUM	= 0.1725	INCREMENT	= 0.020
MAXIMUM	= 0.4255	INCREASING A.B.C.....M	



RUN 45.302
TIME 3 46 28.2600

$\frac{PT2AVG}{PT0}$	= 0.2183	$\frac{PTMAX-PTMIN}{PT2AVG}$	= 0.9160
MINIMUM	= 0.1419	INCREMENT	= 0.020
MAXIMUM	= 0.3419	INCREASING A.B.C.....J	

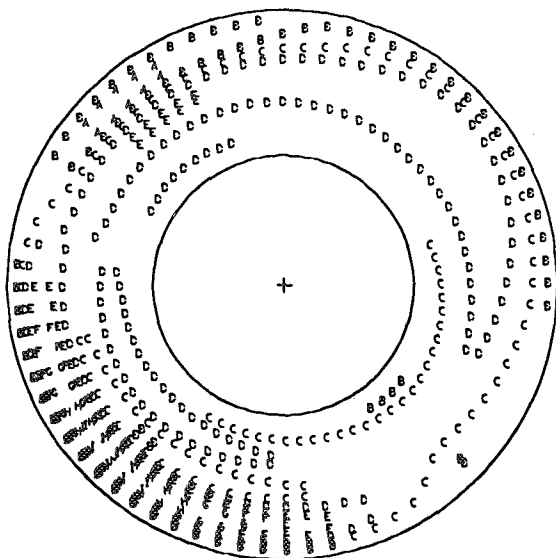


(c)

Figure 64.- Continued.

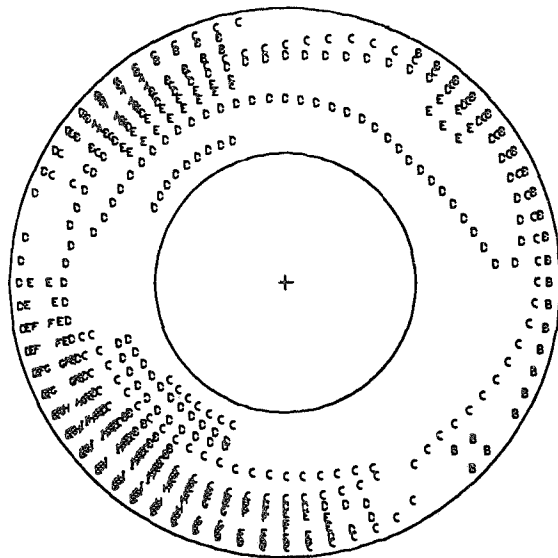
RUN 45.302
 TIME 3 46 28.2660

<u>PT2AVG</u>	= 0.1393	<u>PTMAX-PTMIN</u>	= 1.3642
<u>PT0</u>		<u>PT2AVG</u>	
MINIMUM	= 0.0803	INCREMENT	= 0.020
MAXIMUM	= 0.2704	INCREASING A.B.C.....J	



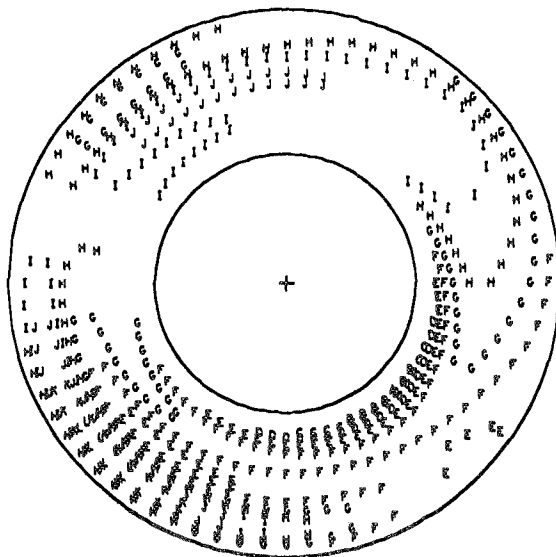
RUN 45.302
 TIME 3 46 28.2680

<u>PT2AVG</u>	= 0.1331	<u>PTMAX-PTMIN</u>	= 1.4168
<u>PT0</u>		<u>PT2AVG</u>	
MINIMUM	= 0.0704	INCREMENT	= 0.020
MAXIMUM	= 0.2591	INCREASING A.B.C.....I	



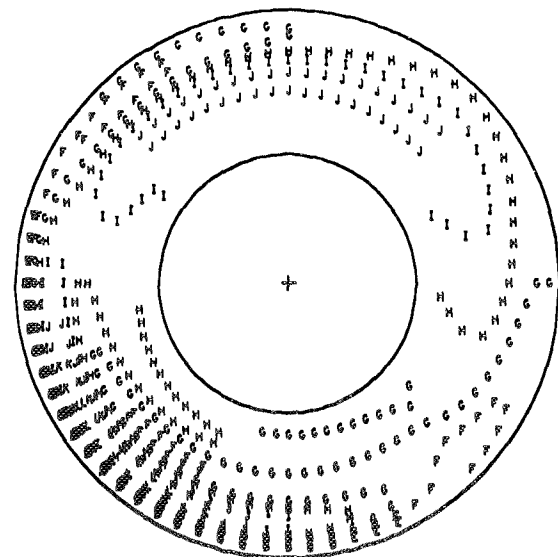
RUN 45.302
 TIME 3 46 28.2700

<u>PT2AVG</u>	= 0.1584	<u>PTMAX-PTMIN</u>	= 1.4751
<u>PT0</u>		<u>PT2AVG</u>	
MINIMUM	= 0.0283	INCREMENT	= 0.020
MAXIMUM	= 0.2620	INCREASING A.B.C.....L	



RUN 45.302
 TIME 3 46 28.2720

<u>PT2AVG</u>	= 0.2949	<u>PTMAX-PTMIN</u>	= 0.8676
<u>PT0</u>		<u>PT2AVG</u>	
MINIMUM	= 0.1529	INCREMENT	= 0.020
MAXIMUM	= 0.4089	INCREASING A.B.C.....H	

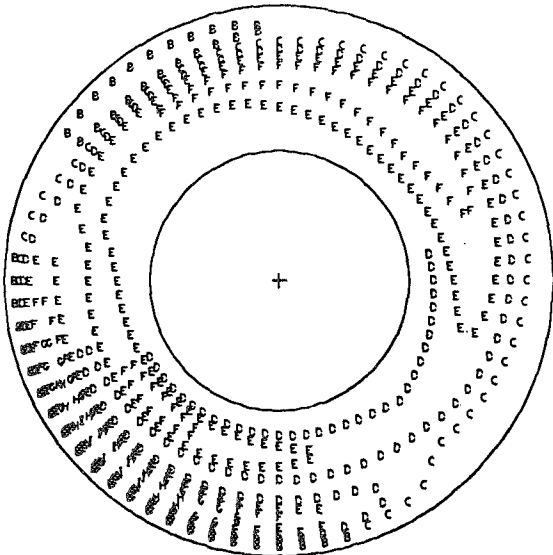


(d)

Figure 64.- Continued.

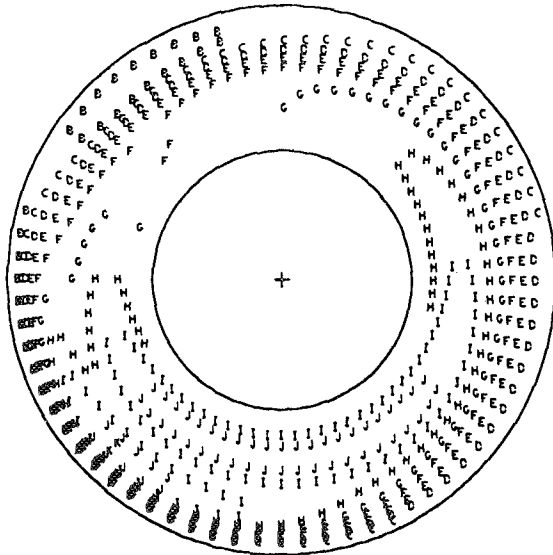
RUN 45.302
TIME 3 46 28.2800

$\frac{PT2AVG}{PT0}$	= 0.1928	$\frac{PTMAX-PTMIN}{PT2AVG}$	= 0.9272
MINIMUM	= 0.1294	INCREMENT	= 0.020
MAXIMUM	= 0.3082	INCREASING A,B,C.....I	



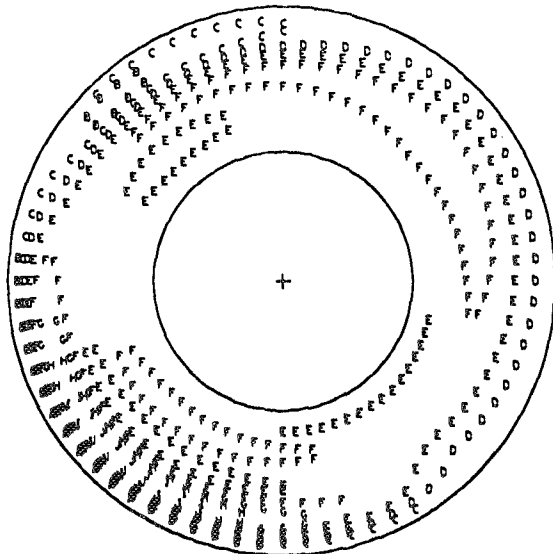
RUN 45.302
TIME 3 46 28.2860

$\frac{PT2AVG}{PT0}$	= 0.3558	$\frac{PTMAX-PTMIN}{PT2AVG}$	= 0.5813
MINIMUM	= 0.2466	INCREMENT	= 0.020
MAXIMUM	= 0.4535	INCREASING A,B,C.....K	



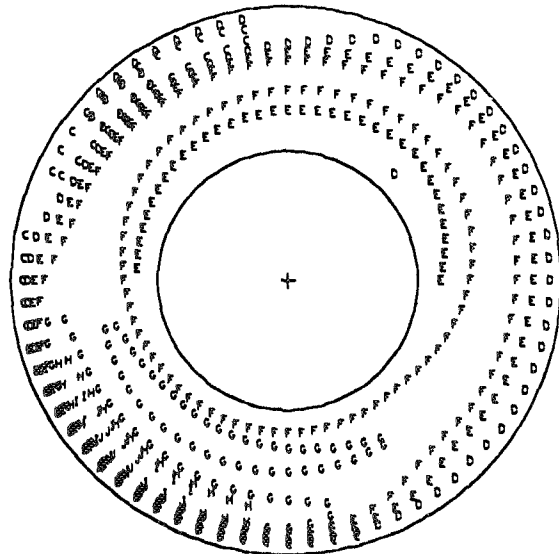
RUN 45.302
TIME 3 46 28.2920

$\frac{PT2AVG}{PT0}$	= 0.2090	$\frac{PTMAX-PTMIN}{PT2AVG}$	= 1.0013
MINIMUM	= 0.1211	INCREMENT	= 0.020
MAXIMUM	= 0.3304	INCREASING A,B,C.....K	



RUN 45.302
TIME 3 46 28.3000

$\frac{PT2AVG}{PT0}$	= 0.3976	$\frac{PTMAX-PTMIN}{PT2AVG}$	= 0.4952
MINIMUM	= 0.3071	INCREMENT	= 0.020
MAXIMUM	= 0.5041	INCREASING A,B,C.....J	

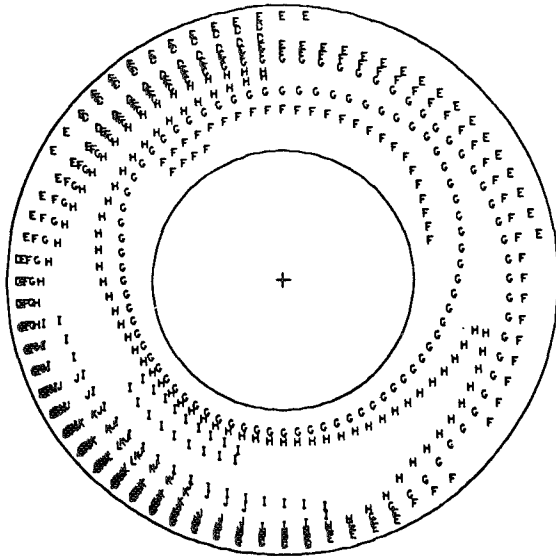


(e)

Figure 64.- Continued.

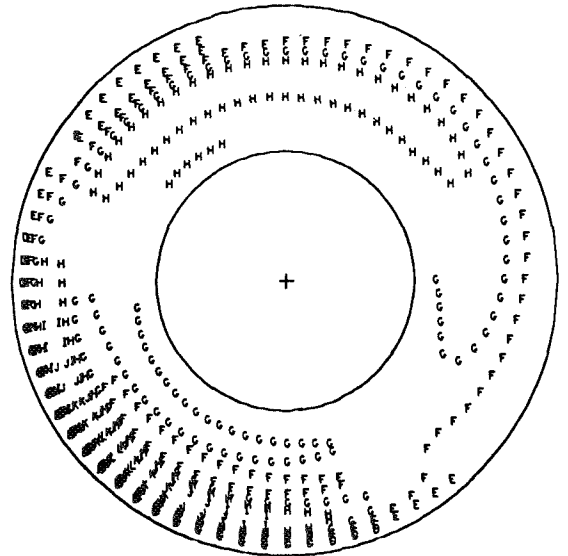
RUN 45.302
 TIME 3 46 28.3020

<u>PT2AVG</u>	=	0.3036	<u>PTMAX-PTMIN</u>	=	0.7889
<u>PT0</u>			<u>PT2AVG</u>		
MINIMUM	=	0.1832	INCREMENT	=	0.020
MAXIMUM	=	0.4227	INCREASING A.B.C.....L		



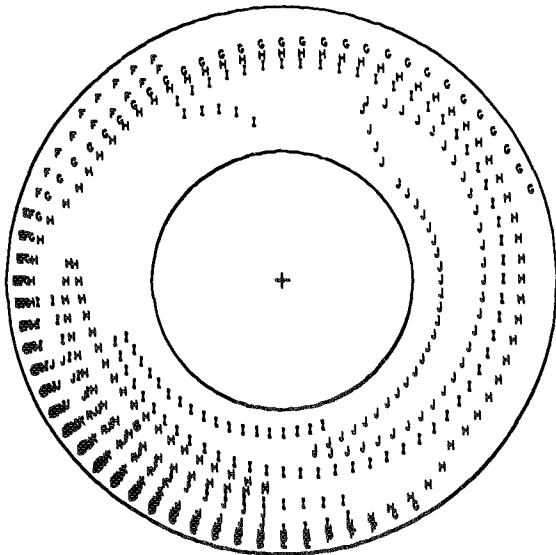
RUN 45.302
 TIME 3 46 28.3060

<u>PT2AVG</u>	=	0.2138	<u>PTMAX-PTMIN</u>	=	1.0806
<u>PT0</u>			<u>PT2AVG</u>		
MINIMUM	=	0.0984	INCREMENT	=	0.020
MAXIMUM	=	0.3295	INCREASING A.B.C.....L		



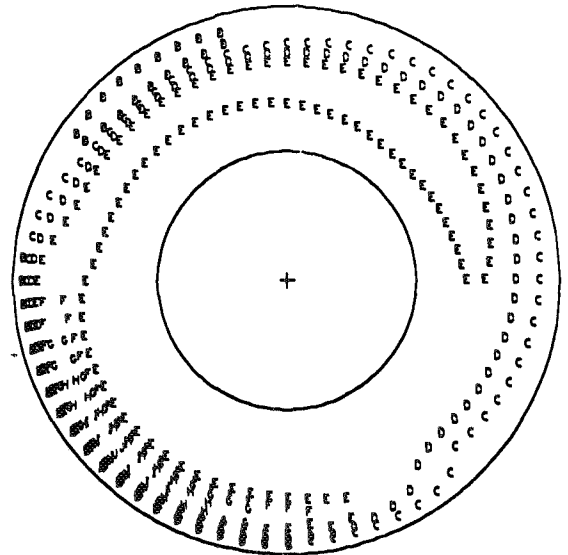
RUN 45.302
 TIME 3 46 28.3100

<u>PT2AVG</u>	=	0.4241	<u>PTMAX-PTMIN</u>	=	0.5269
<u>PT0</u>			<u>PT2AVG</u>		
MINIMUM	=	0.2763	INCREMENT	=	0.020
MAXIMUM	=	0.4998	INCREASING A.B.C.....K		



RUN 45.302
 TIME 3 46 28.3180

<u>PT2AVG</u>	=	0.2058	<u>PTMAX-PTMIN</u>	=	0.9078
<u>PT0</u>			<u>PT2AVG</u>		
MINIMUM	=	0.1392	INCREMENT	=	0.020
MAXIMUM	=	0.3260	INCREASING A.B.C.....J		



(f)

Figure 64.- Concluded.

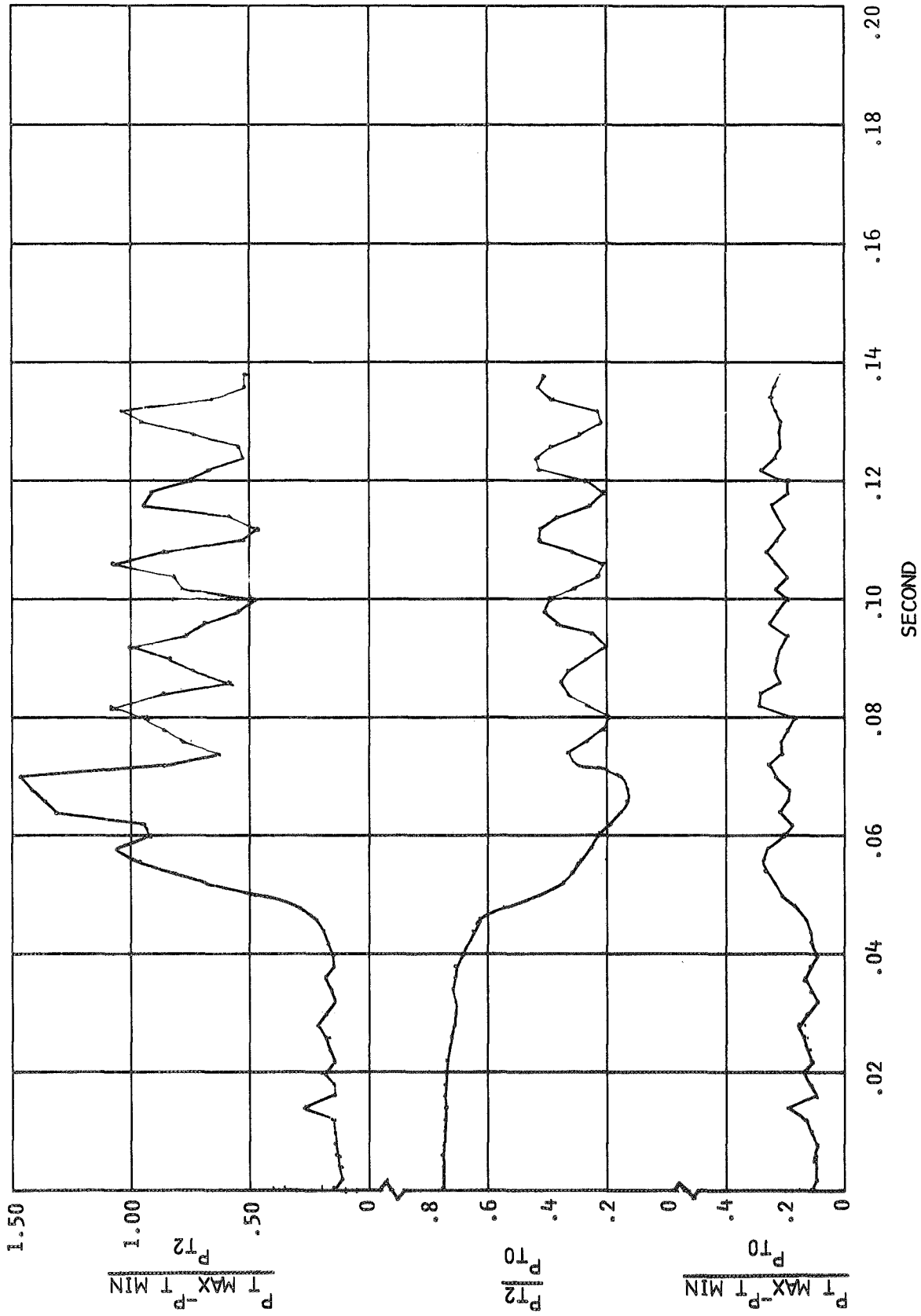


Figure 65. - Cowl-induced inlet unstart time history, $M_0 = 2.9$, $\bar{P}_{t2}/P_{t0} = 0.741$

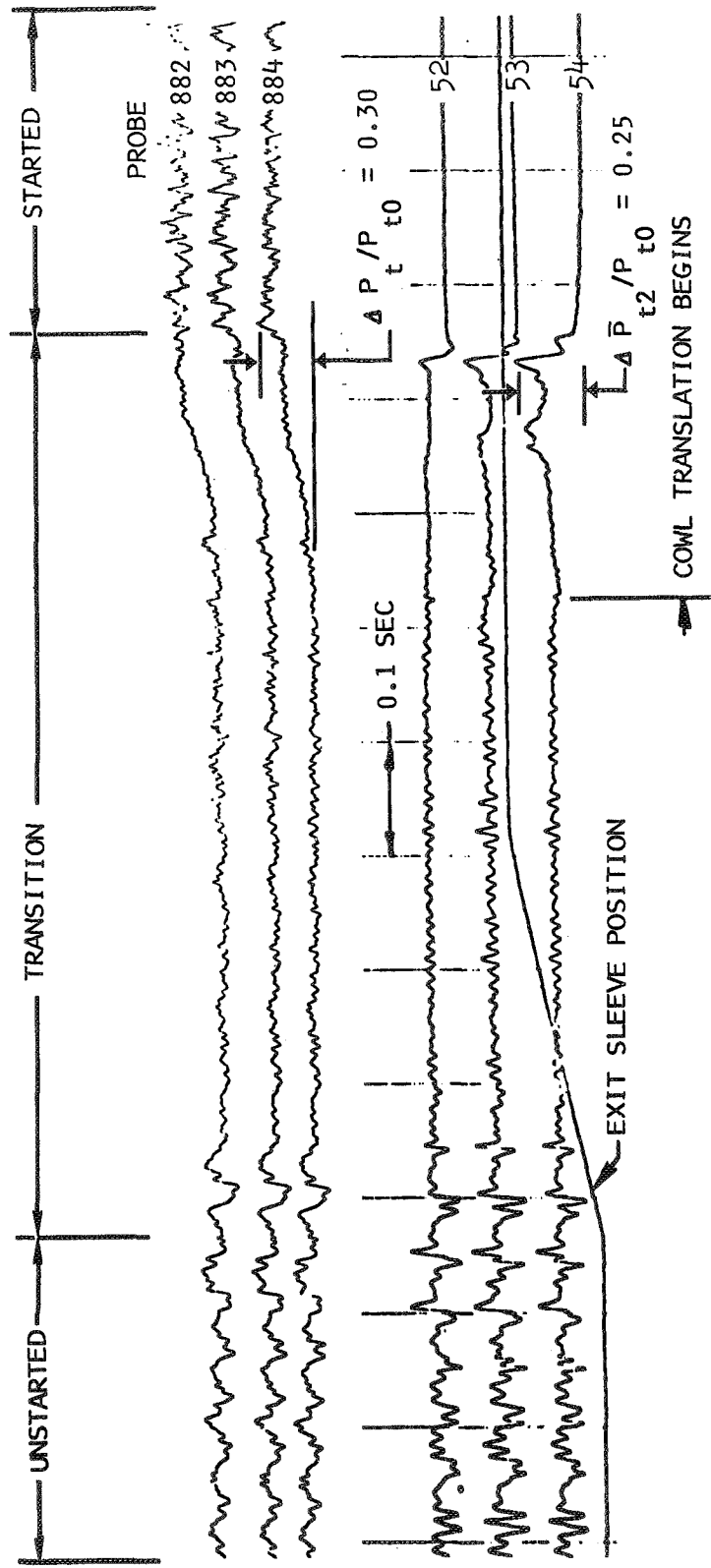
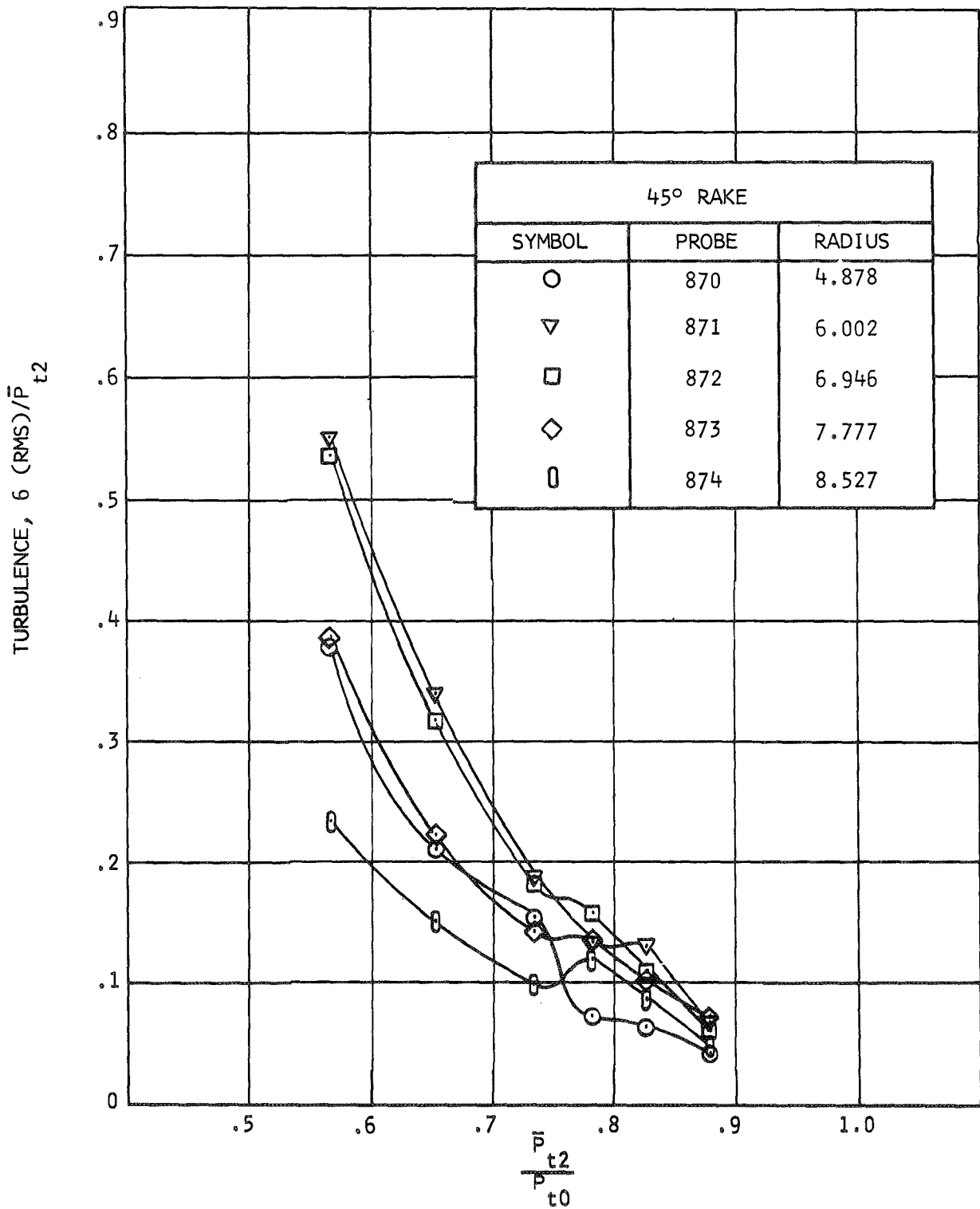
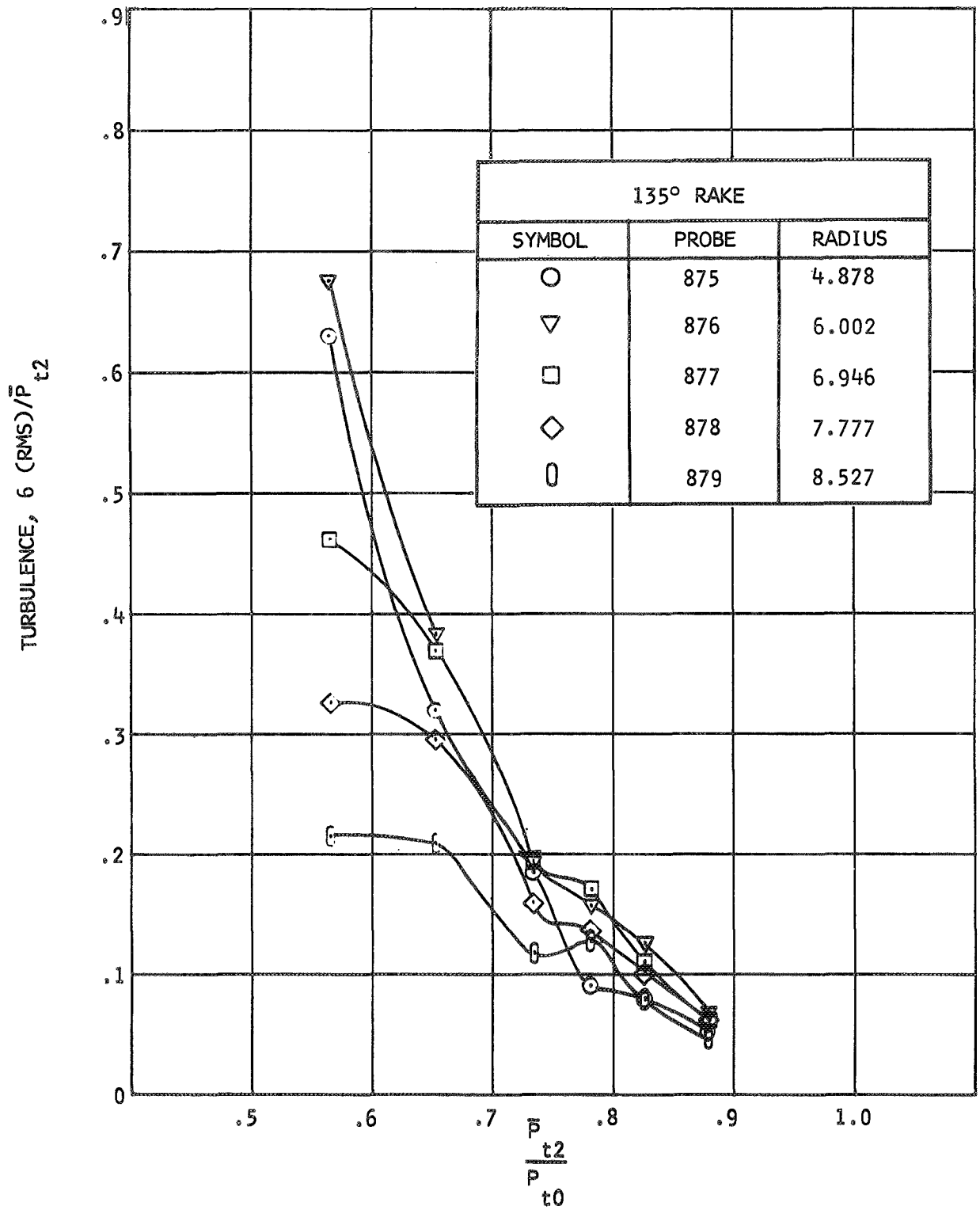


Figure 66. - Duct pressures during inlet restart.



(a)

Figure 67.- Engine face turbulence variation with recovery, $M_0 = 3.0$.



(b)

Figure 67.- Continued.

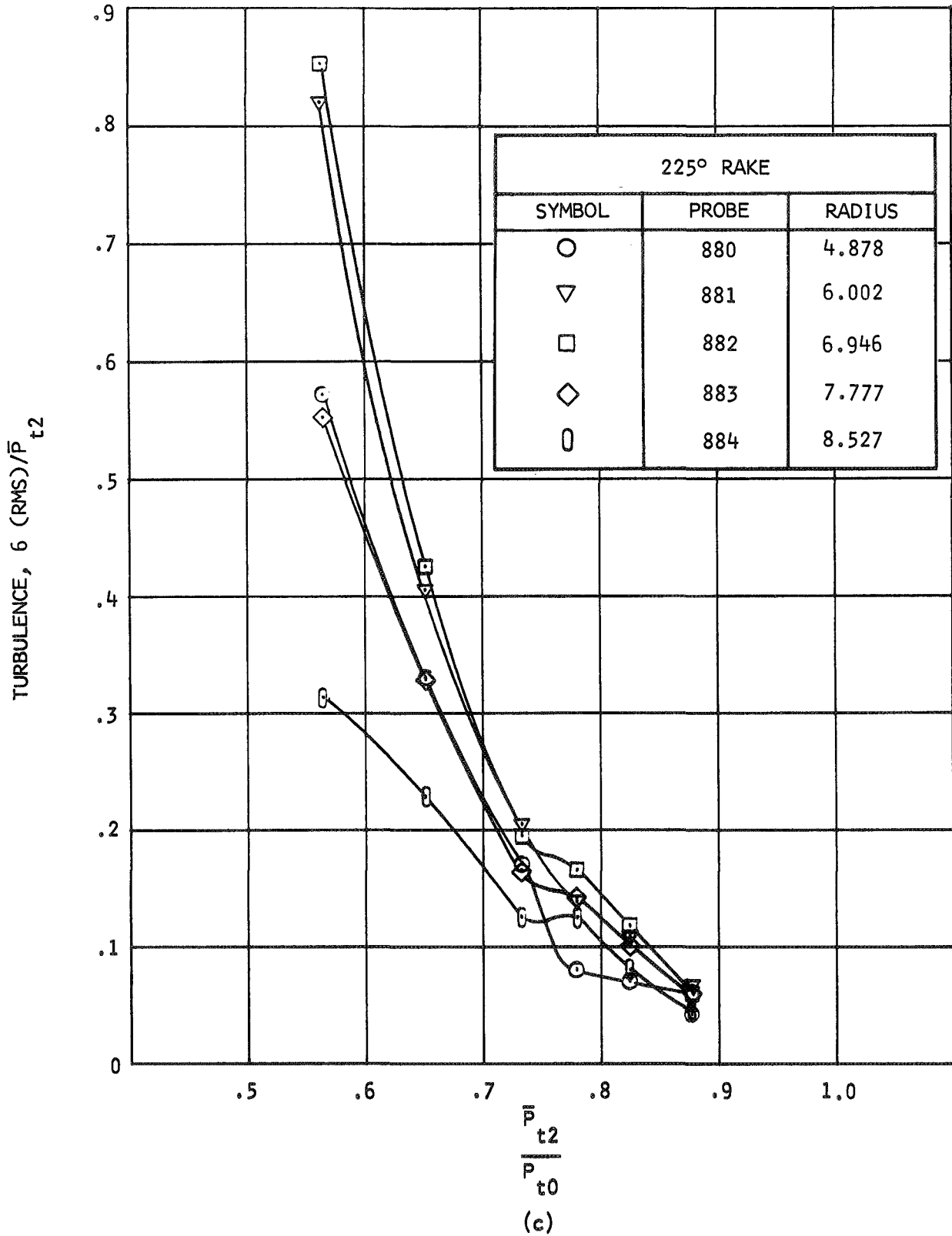
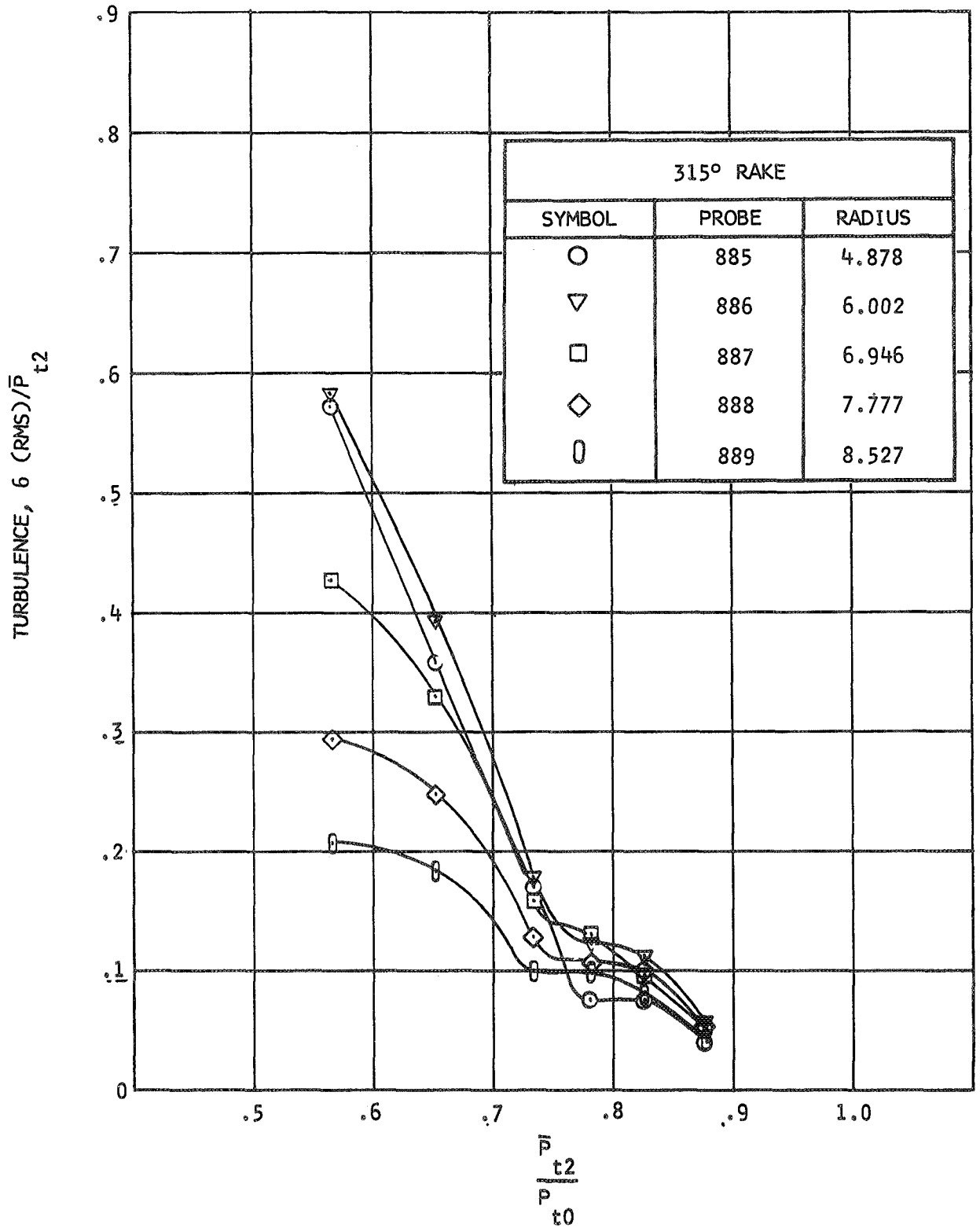


Figure 67.- Continued.



(d)

Figure 67.- Concluded.

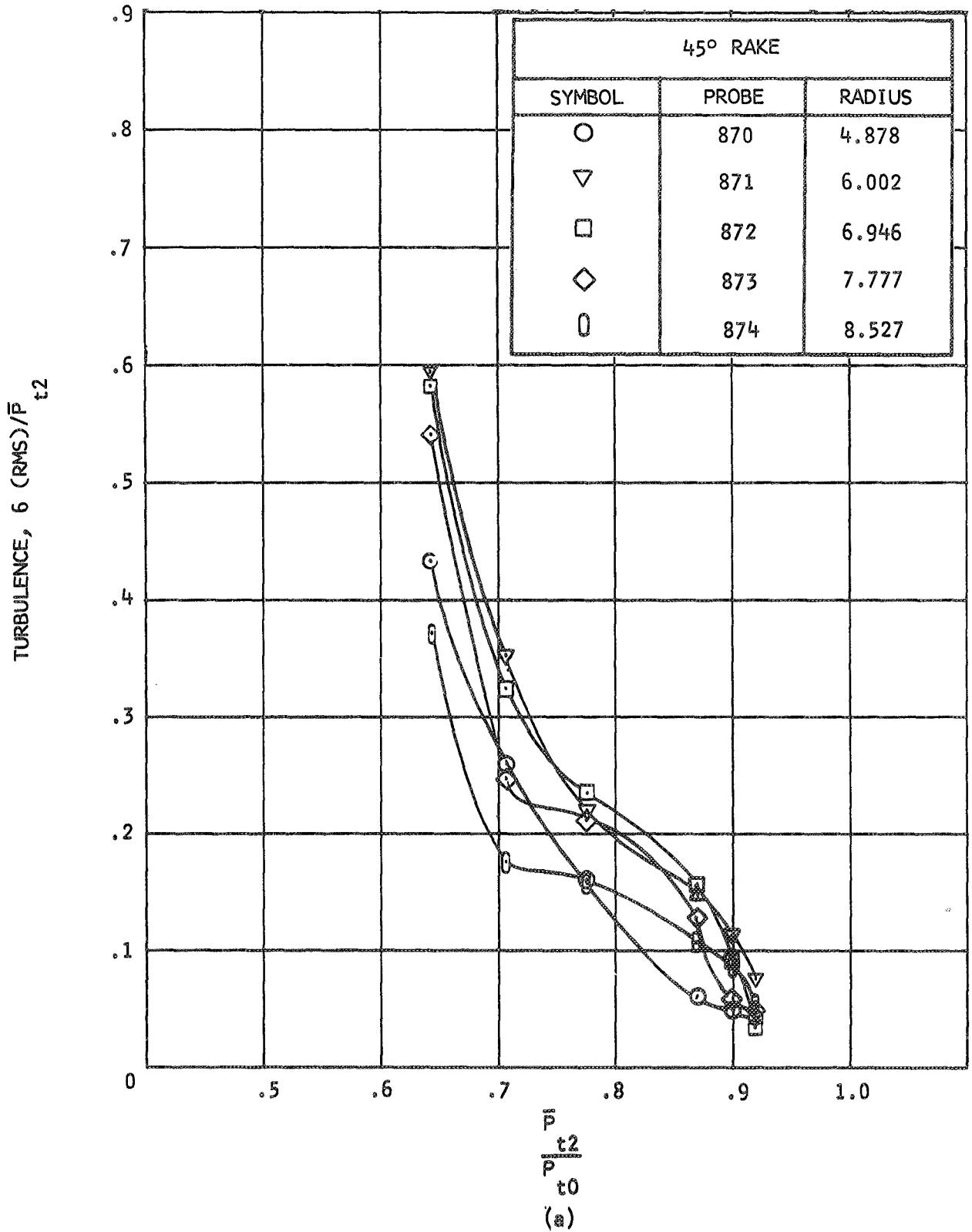
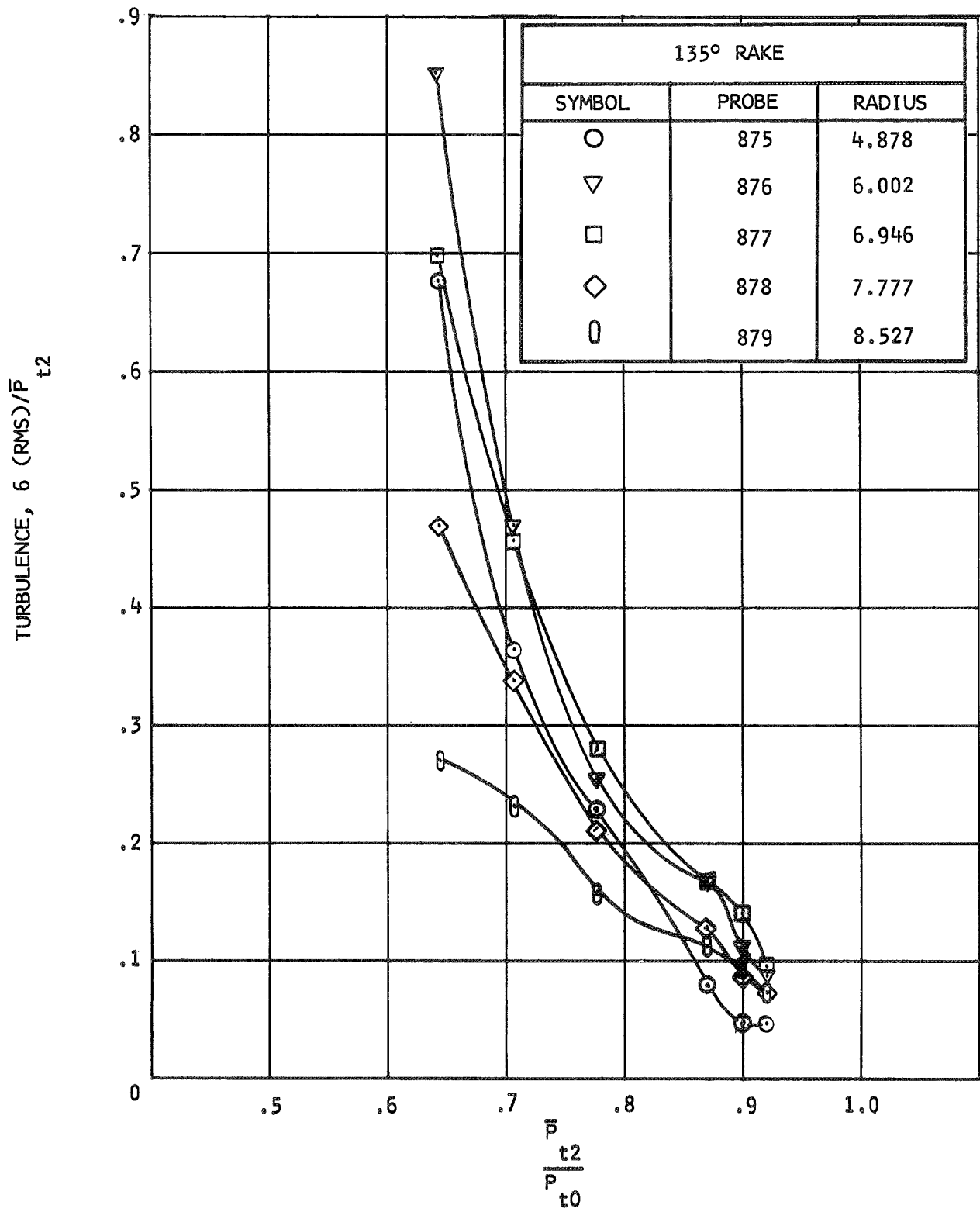


Figure 68.- Engine face turbulence variation with recovery, $M_0 = 2.6$.



(b)

Figure 68.- Continued.

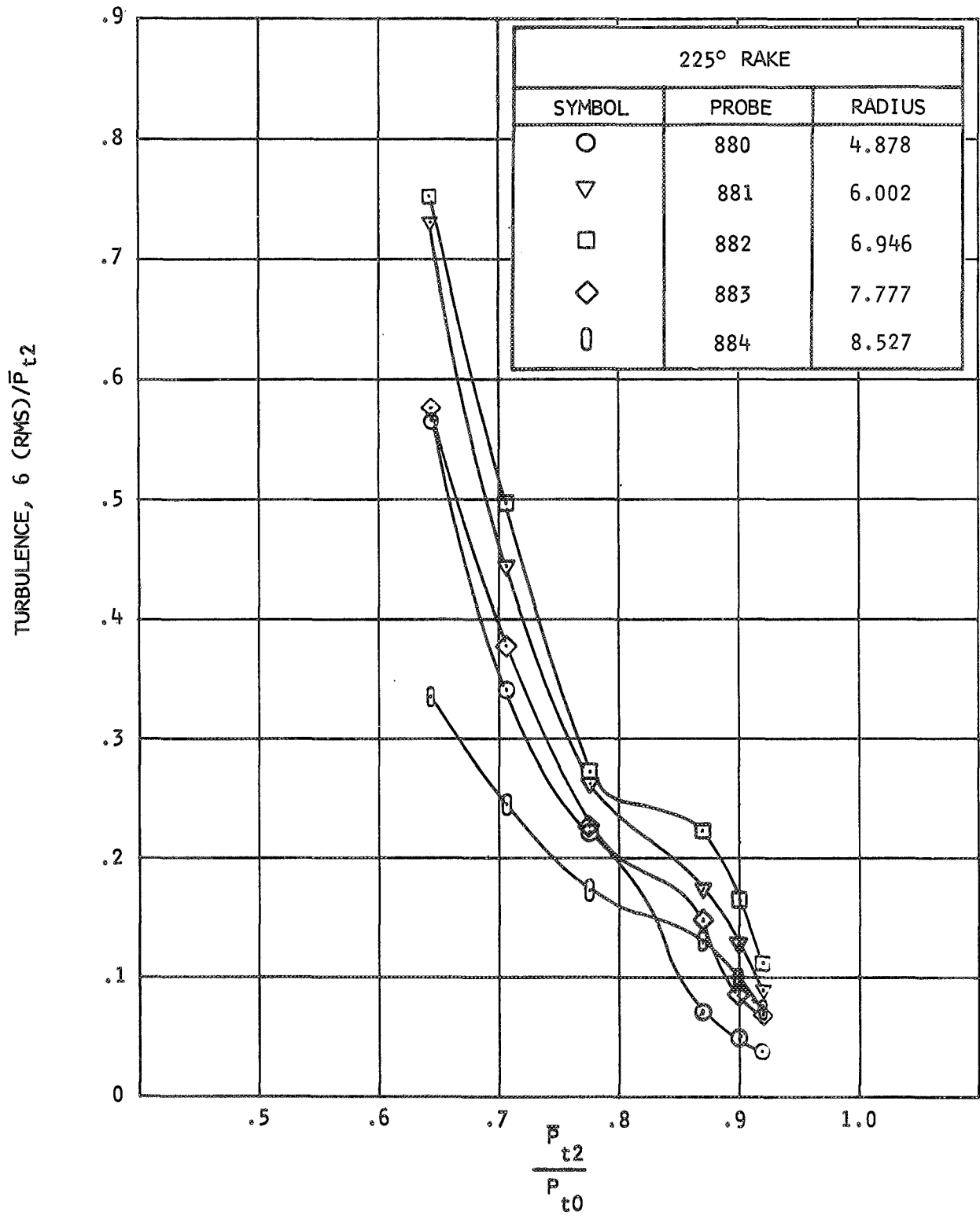


Figure 68.- Continued.

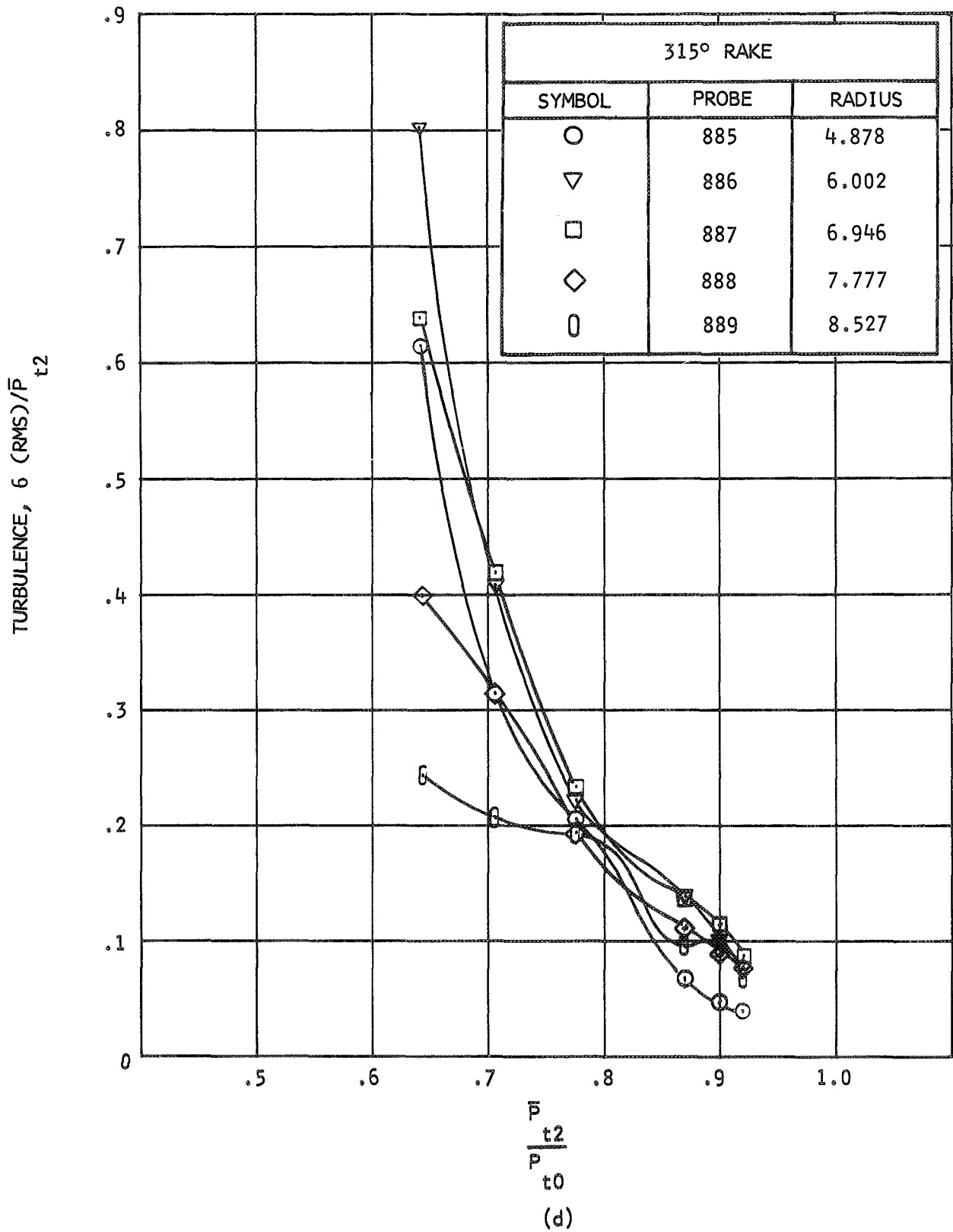


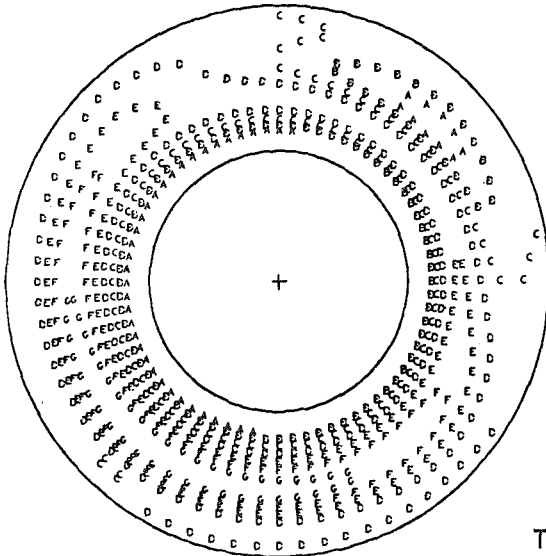
Figure 68.- Concluded.

MACH 2.6

$\frac{PT2AVG}{PT0} = 0.9184$

TURBULENCE AVG = 0.0666

MINIMUM = 0.0326 INCREMENT = 0.010
MAXIMUM = 0.1100 INCREASING A,B,C.....G

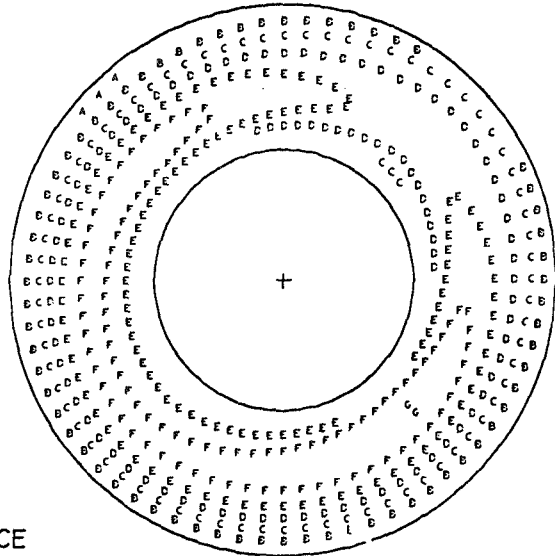


MACH 2.6

$\frac{PT2AVG}{PT0} = 0.6421$

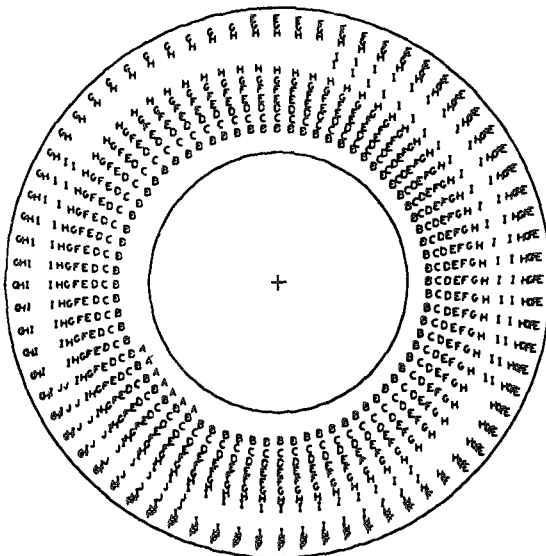
TURBULENCE AVG = 0.5566

MINIMUM = 0.2425 INCREMENT = 0.100
MAXIMUM = 0.8530 INCREASING A,B,C.....G

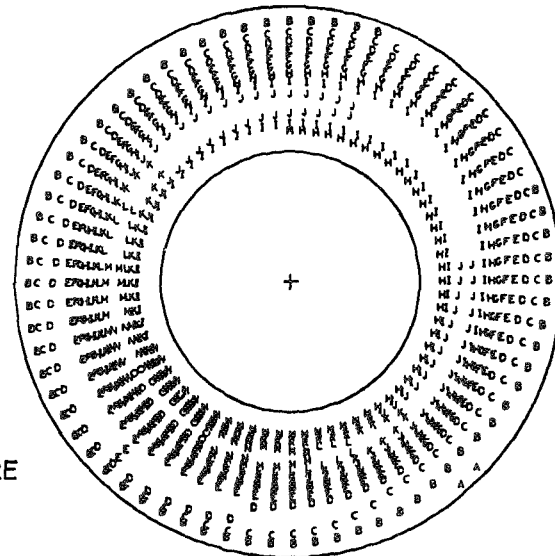


TURBULENCE

$\frac{PT2AVG}{PT0} = 0.9184$ $\frac{PTMAX-PTMIN}{PT2AVG} = 0.1045$
 MINIMUM = 0.8683 INCREMENT = 0.010
 MAXIMUM = 0.9643 INCREASING A,B,C.....J

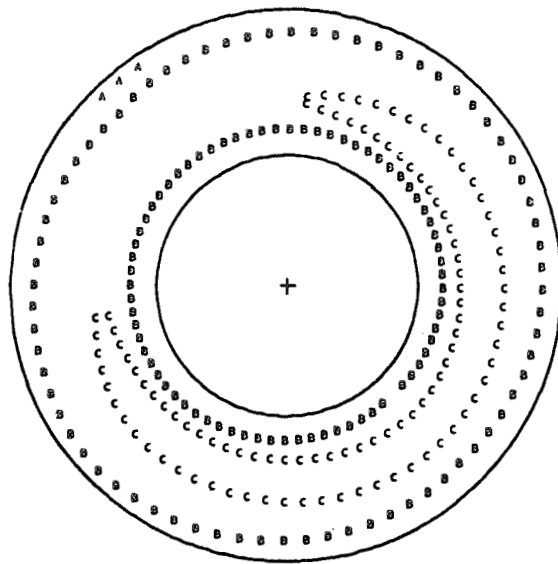


$\frac{PT2AVG}{PT0} = 0.6421$ $\frac{PTMAX-PTMIN}{PT2AVG} = 0.4411$
 MINIMUM = 0.5389 INCREMENT = 0.020
 MAXIMUM = 0.8222 INCREASING A,B,C.....G



PRESSURE RATIO

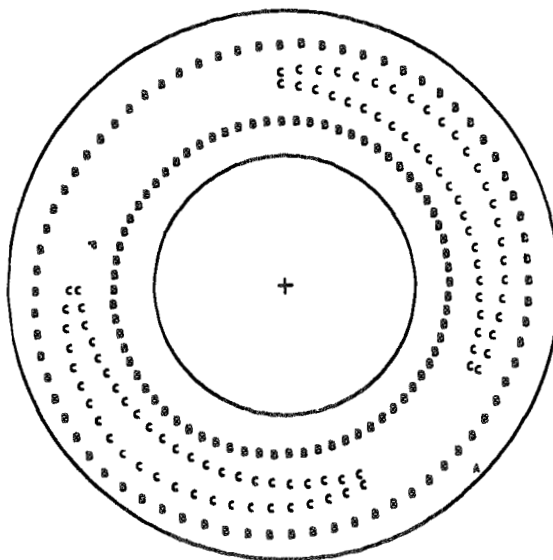
Figure 69.- Engine face turbulence and total pressure ratio contour comparisons.



$$M_o = 3.0$$

$$\bar{P}_{t2}/P_{t0} = 0.842$$

TURBULENCE



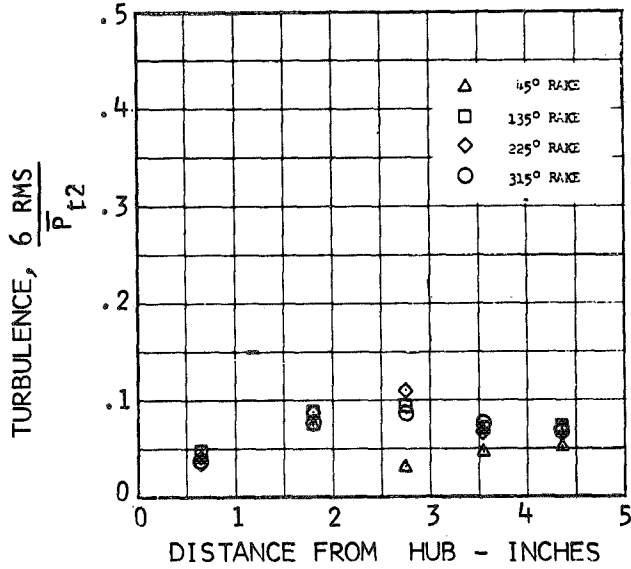
PRESSURE RATIO

(b)

Figure 69.- Concluded.

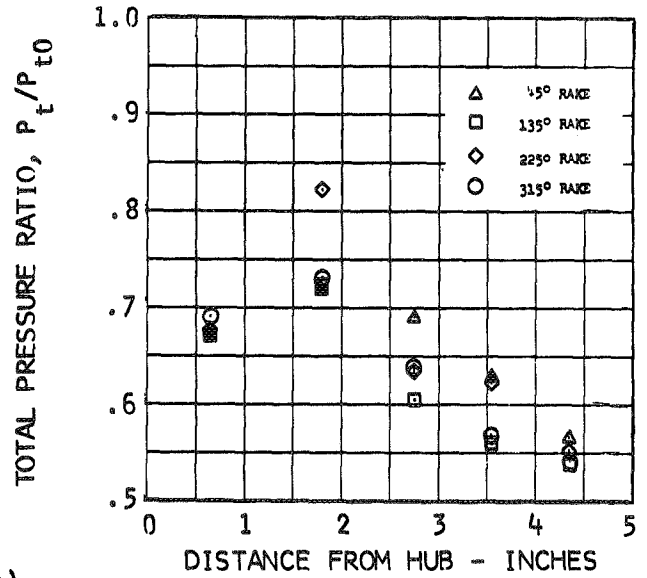
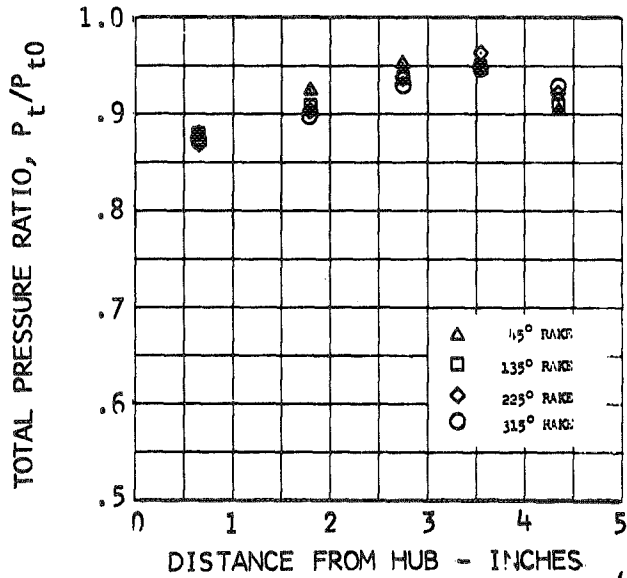
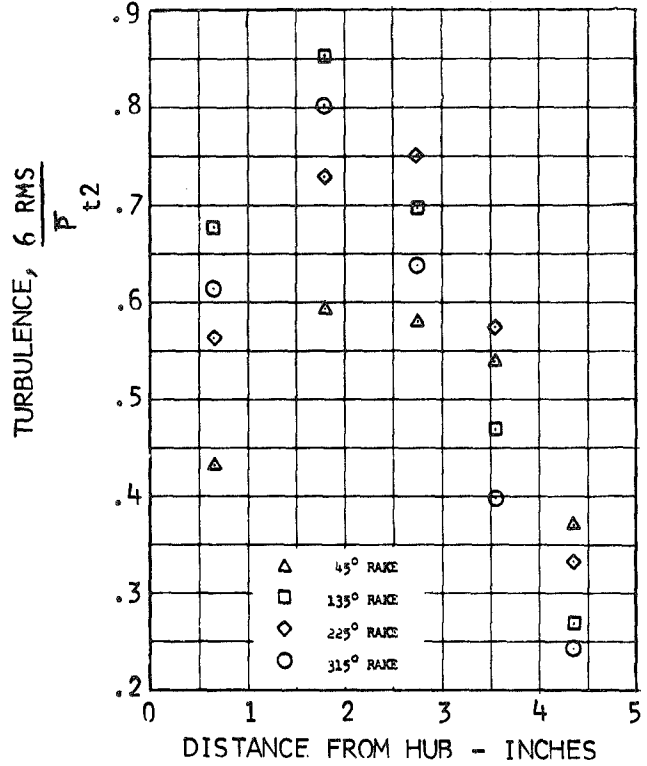
$M_o = 2.6$

$\frac{PT2AVG}{PT0} = 0.9184$



$M_o = 2.6$

$\frac{PT2AVG}{PT0} = 0.6421$

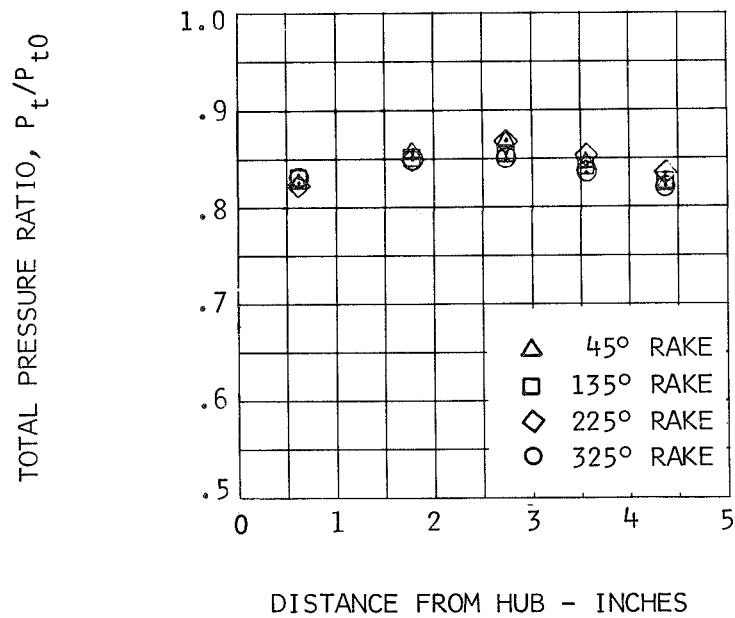
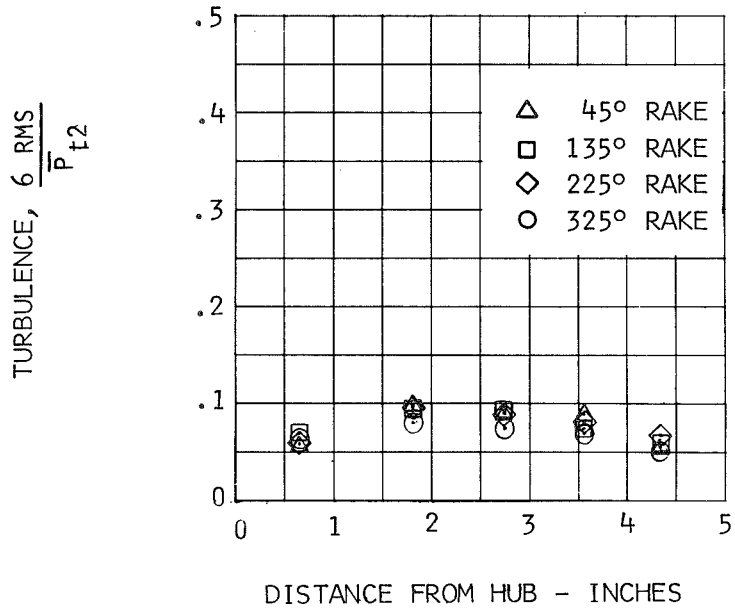


(a)

Figure 70.- Engine face turbulence and total pressure ratio radial profile comparisons.

$$M_0 = 3.0$$

$$\bar{P}_{t2}/P_{t0} = 0.842$$



(b)

Figure 70. - Concluded.

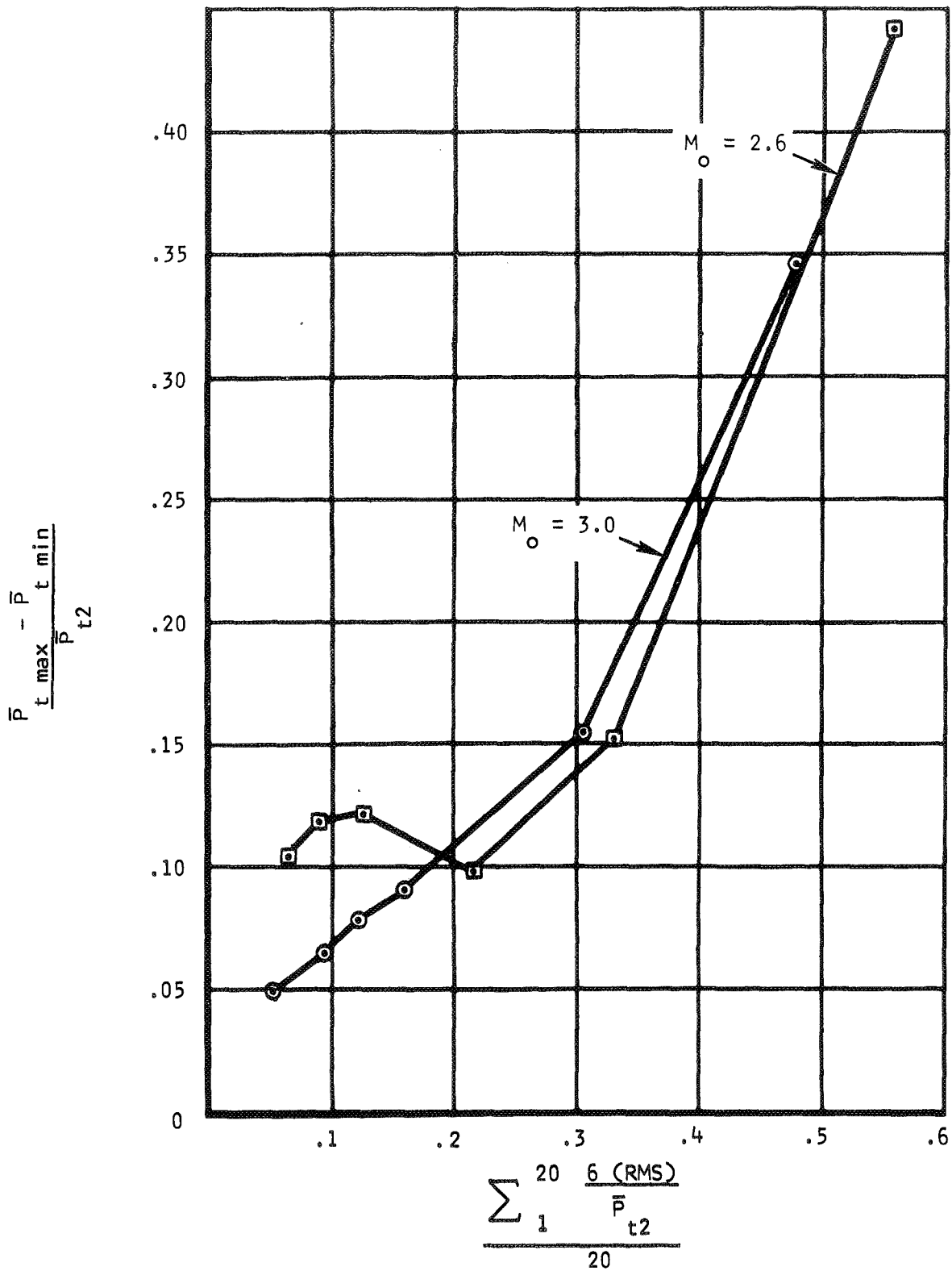


Figure 71.- Steady-state distortion versus average turbulence of individual probes.

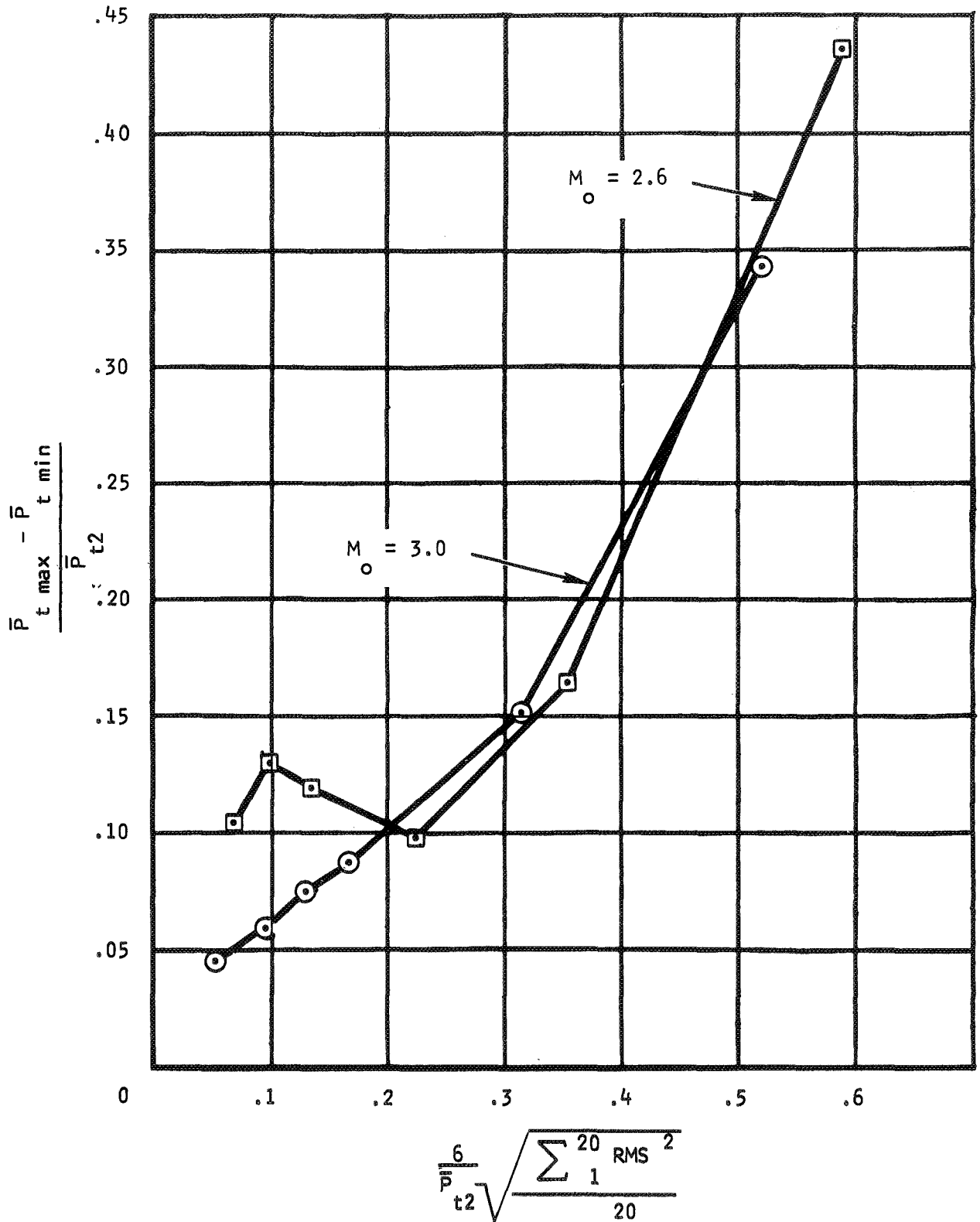
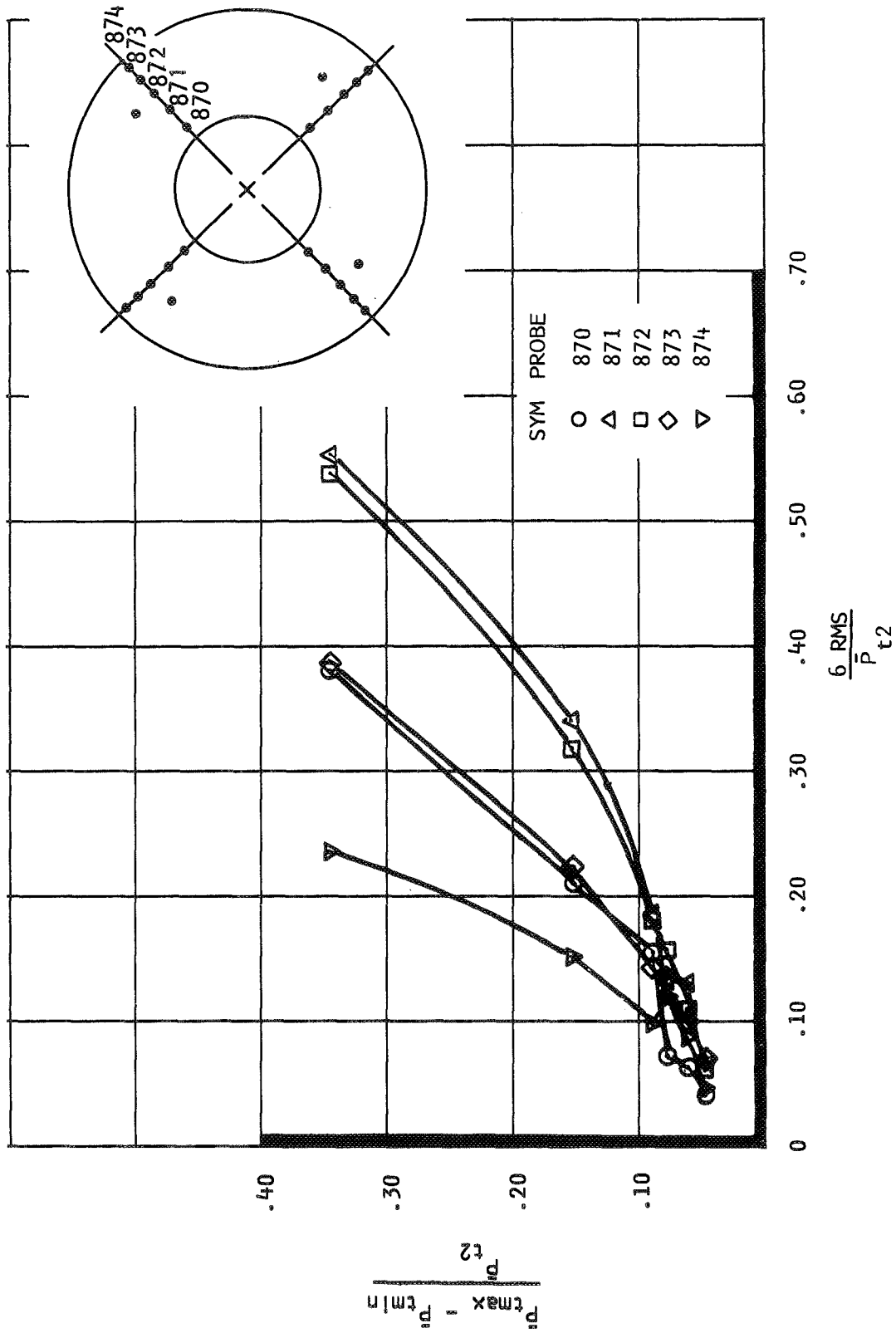
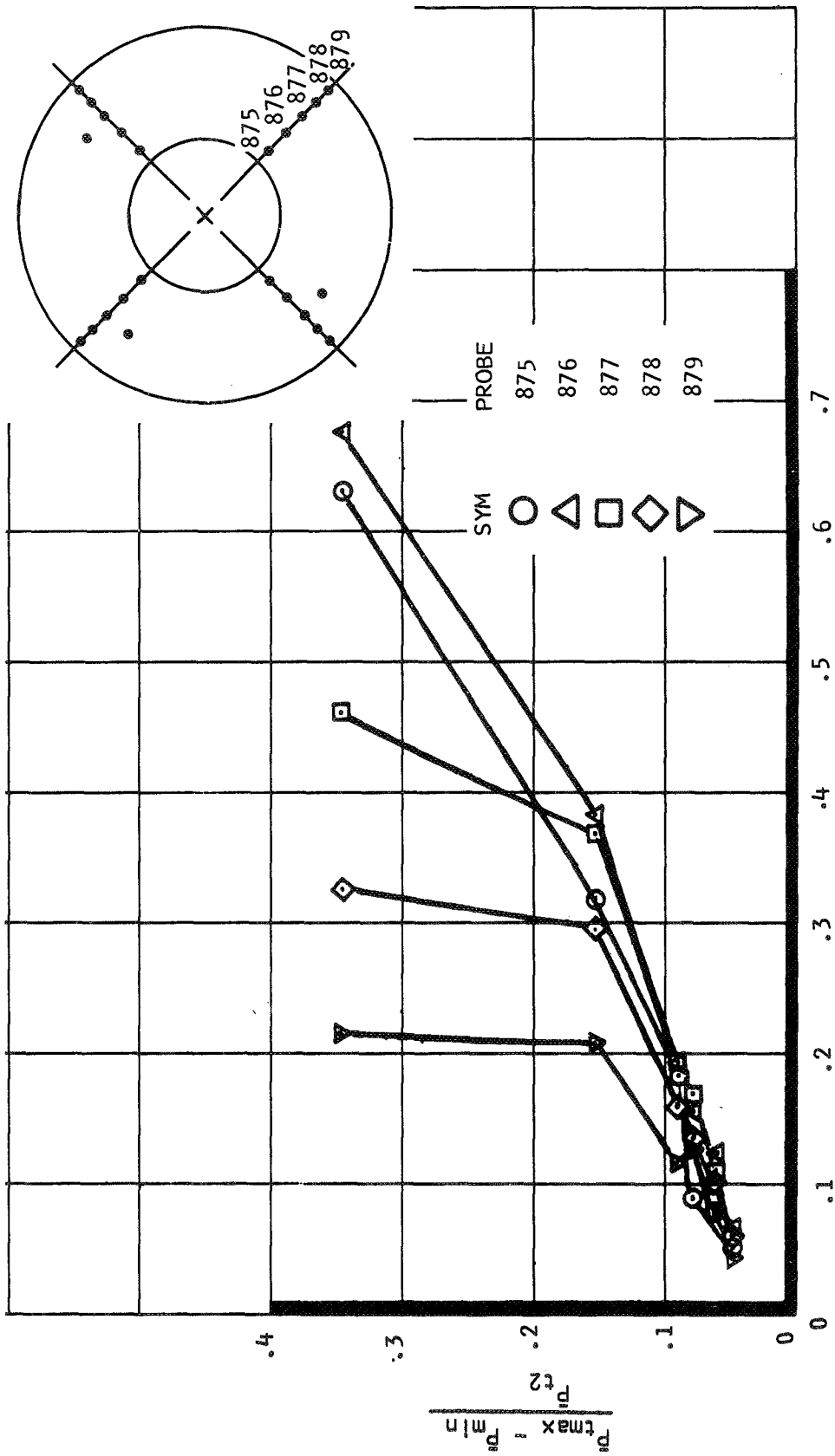


Figure 72.- Steady-state distortion versus average turbulence.

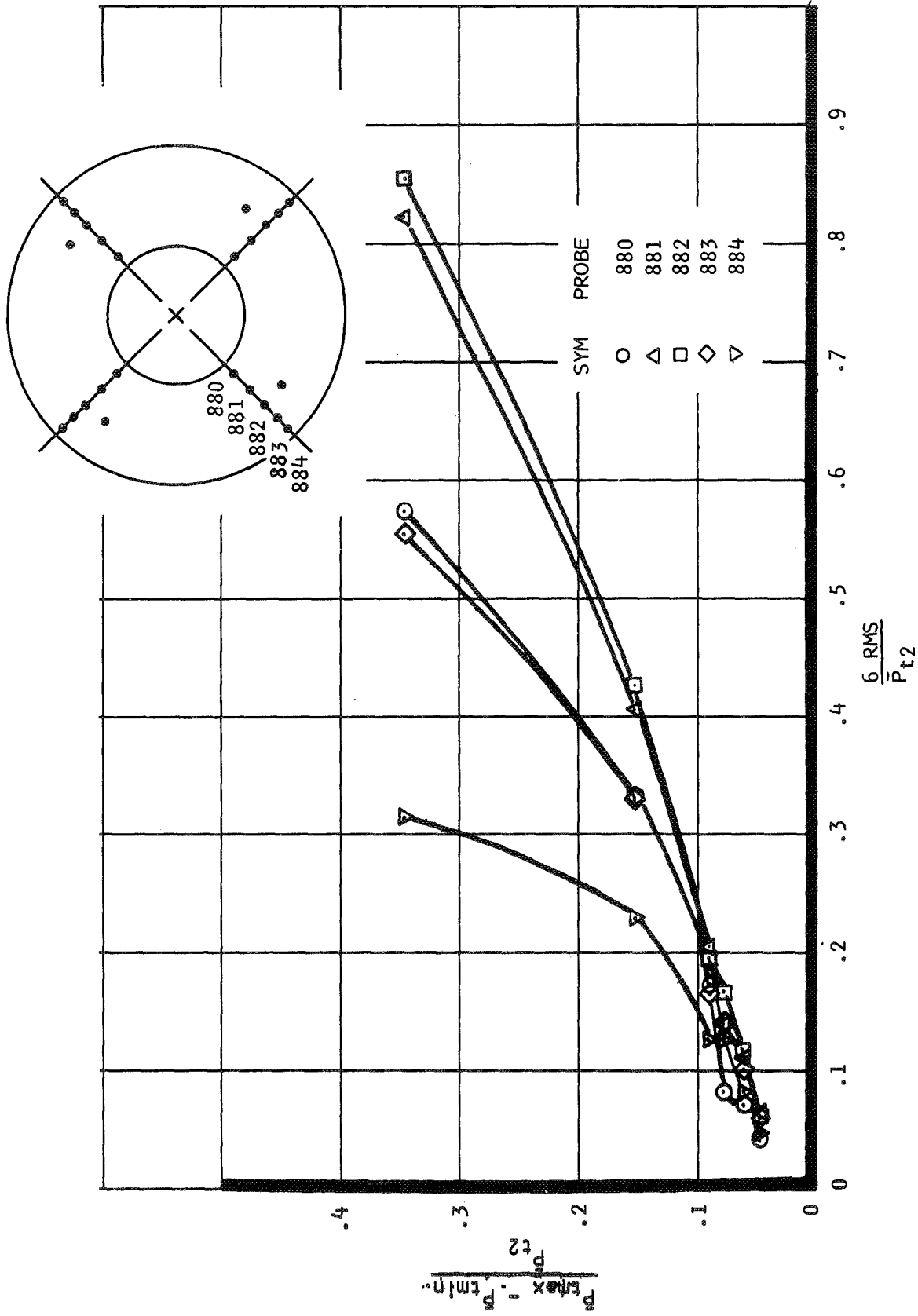


(a) 45° RAKE POSITION

Figure 73.- Turbulence variation with distortion, individual probes, $M_0 = 3.0$

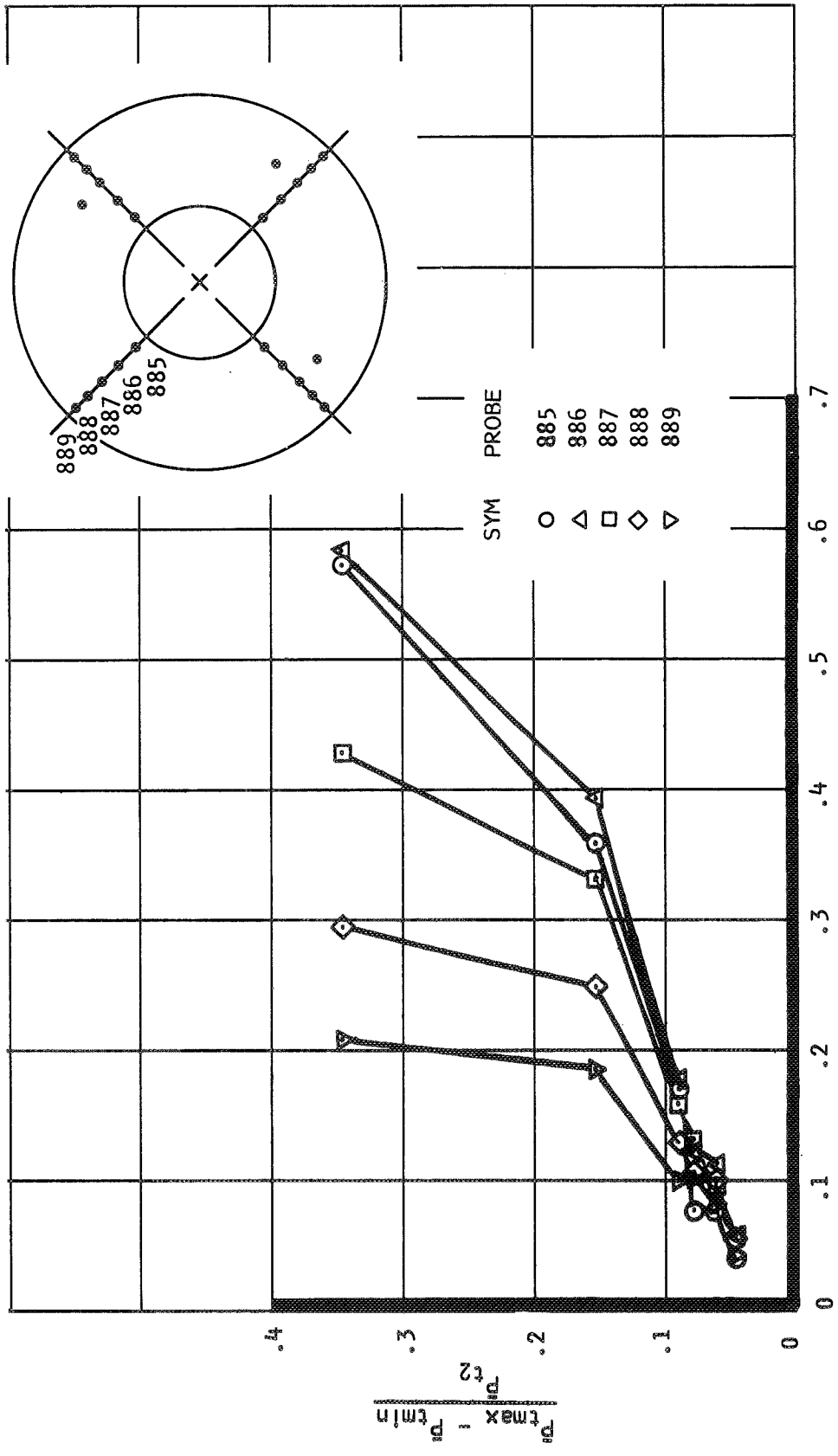


(b) 135° RAKE POSITION
Figure 73.- Continued.

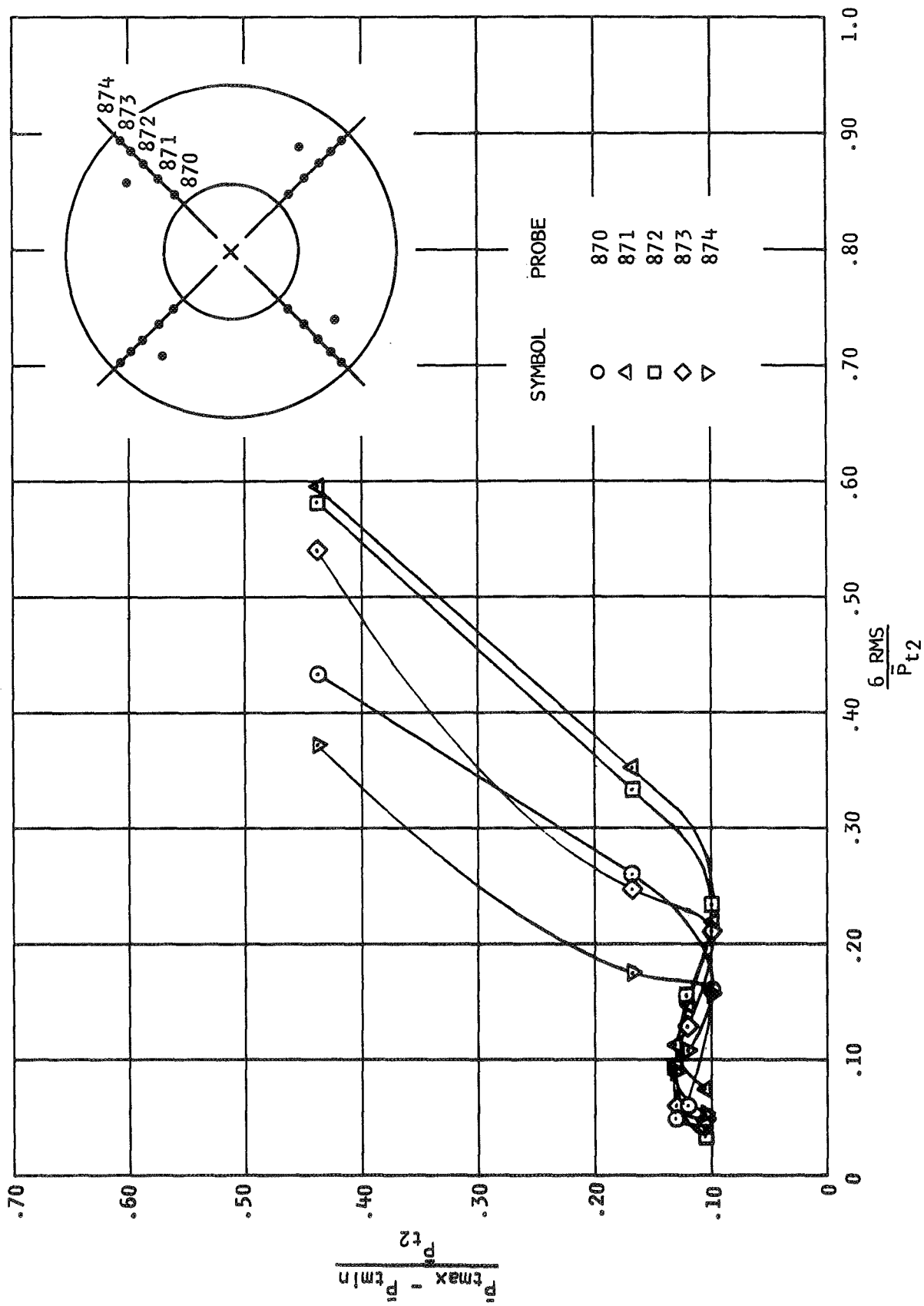


(c) 225° RAKE POSITION.

Figure 73.- Continued.

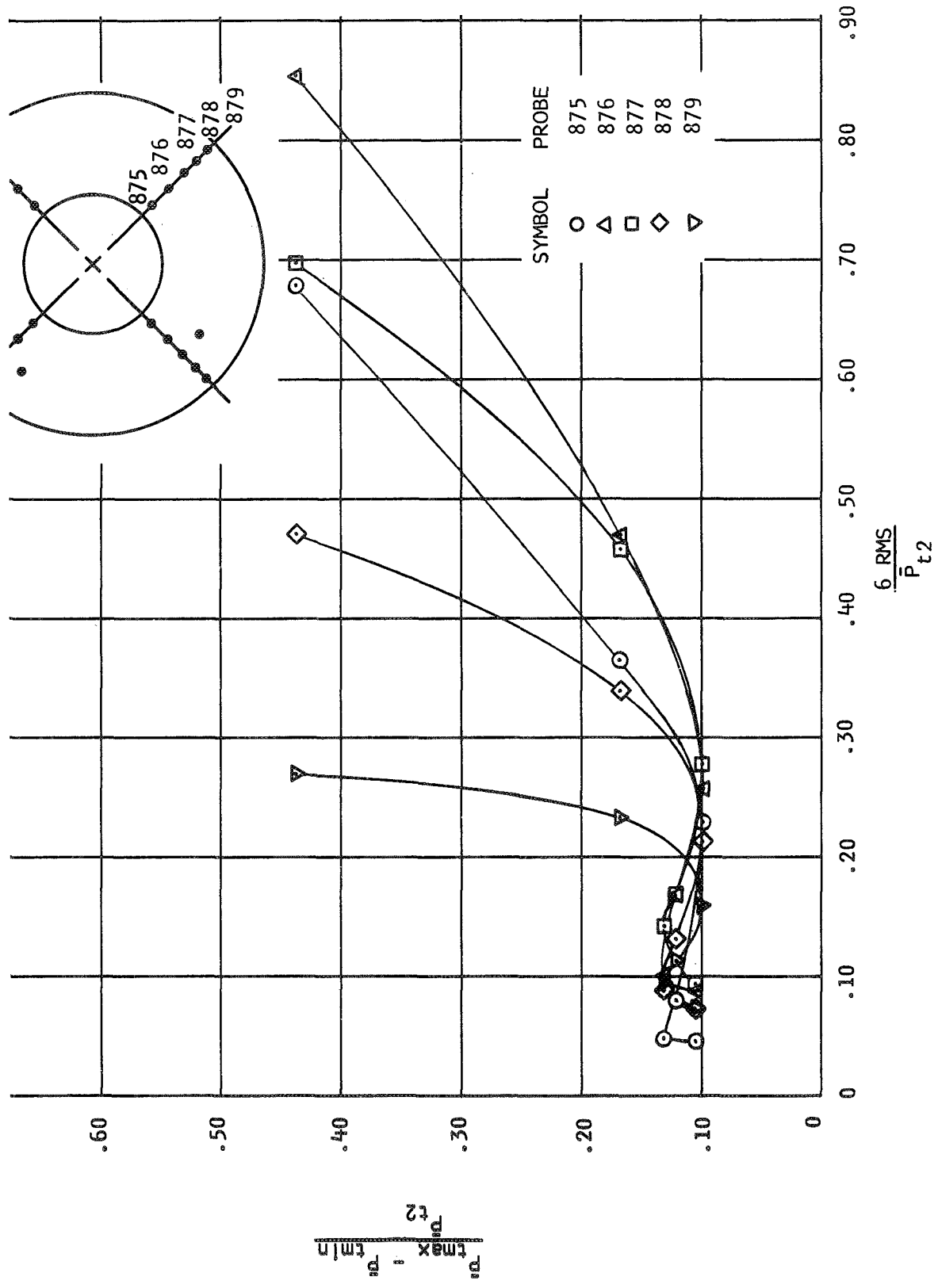


(d) 315° RAKE POSITION
Figure 73.- Concluded.

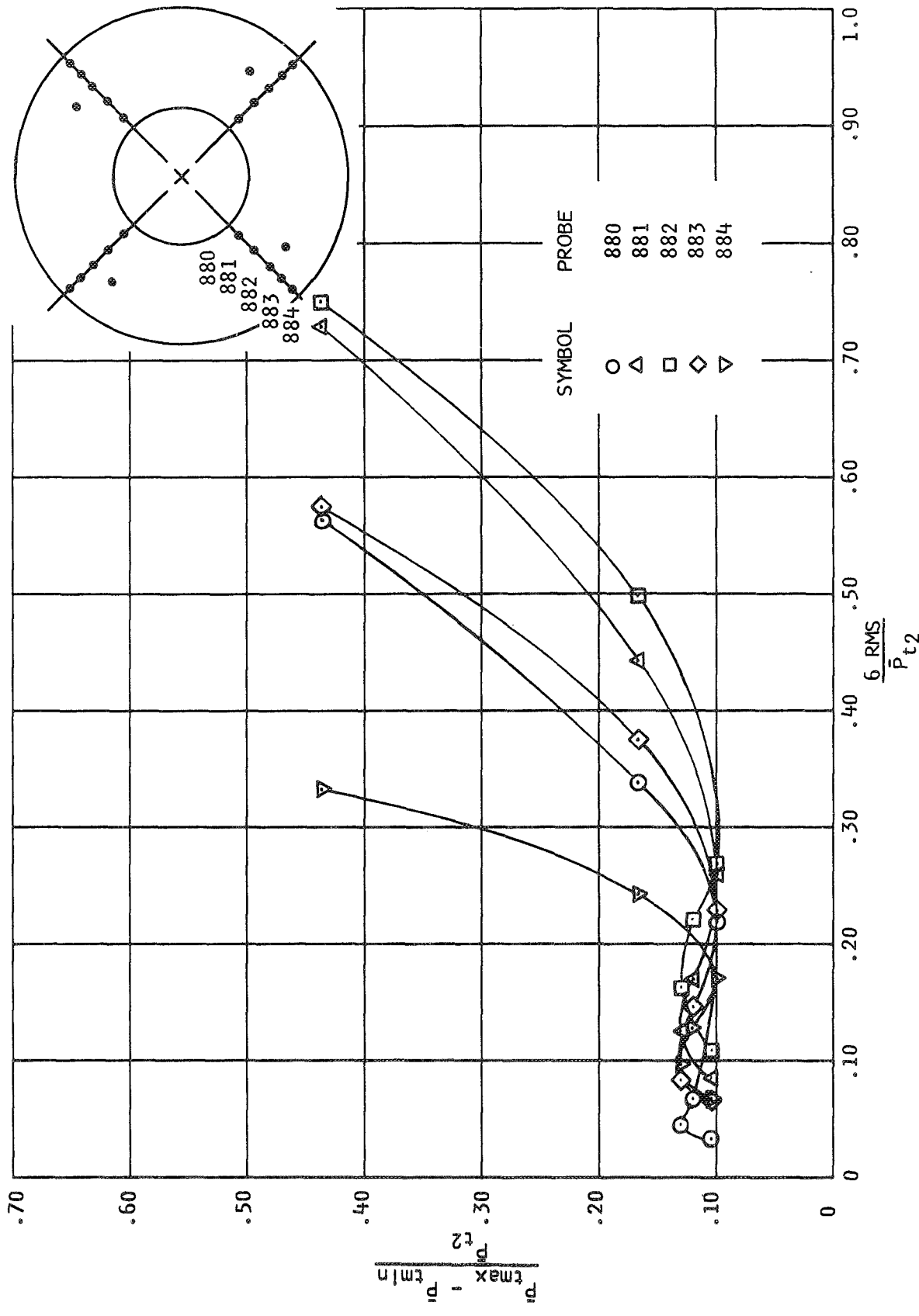


(a) 45° RAKE POSITION

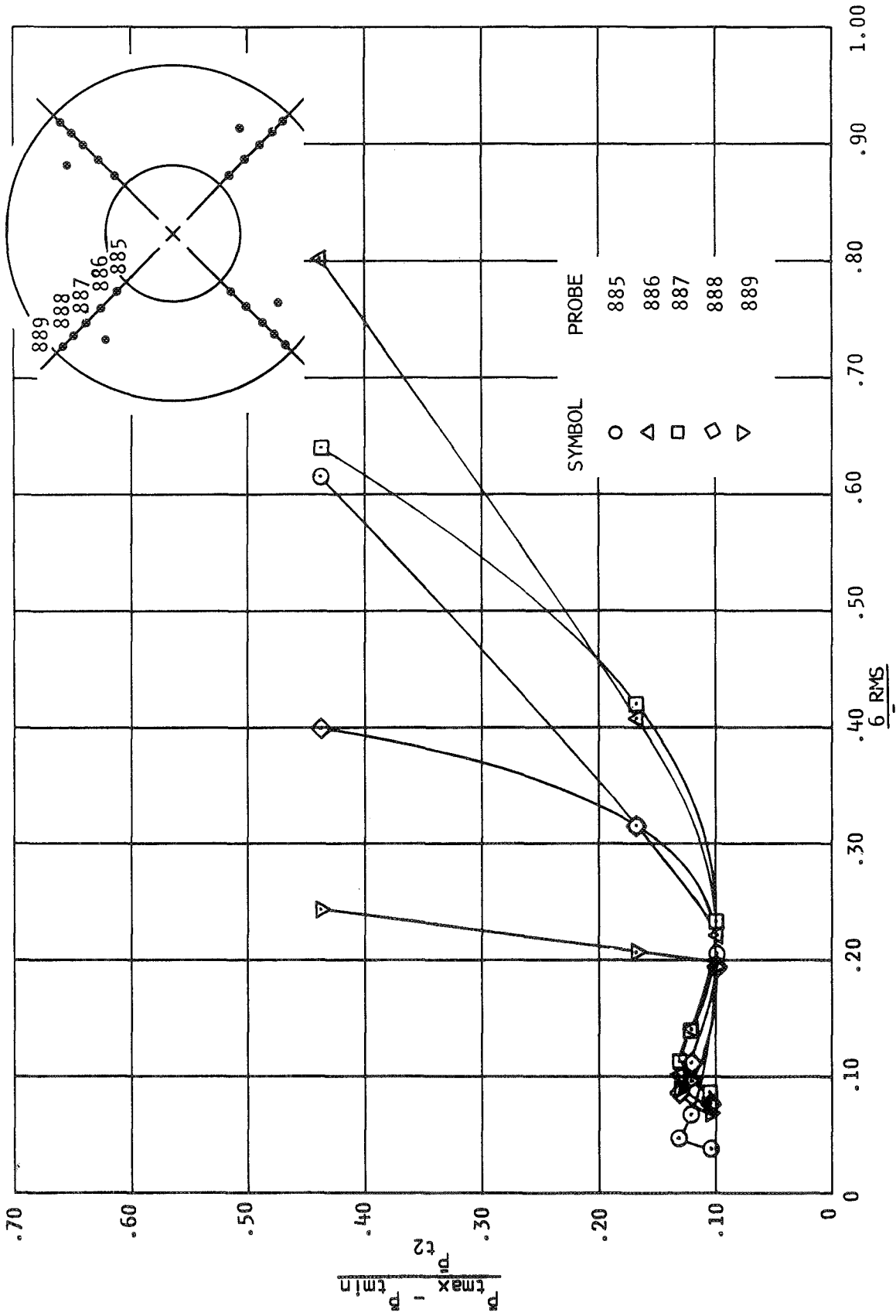
Figure 74.- Turbulence variation with distortion, individual probes, $M_0 = 2.6$.



(b) 135° RAKE POSITION
Figure 74.- Continued.



(c) 225° RAKE POSITION
Figure 74.- Continued.



(d) 315° RAKE POSITION

Figure 74.- Concluded.

CLOSED SYMBOL, UPSTREAM RAKES IN 315-DEGREE PLANE INSTALLED, $\bar{P}_{t2}/P_{t0} = 0.563$

OPEN SYMBOL, UPSTREAM RAKES IN 315-DEGREE PLANE REMOVED, $\bar{P}_{t2}/P_{t0} = 0.565$

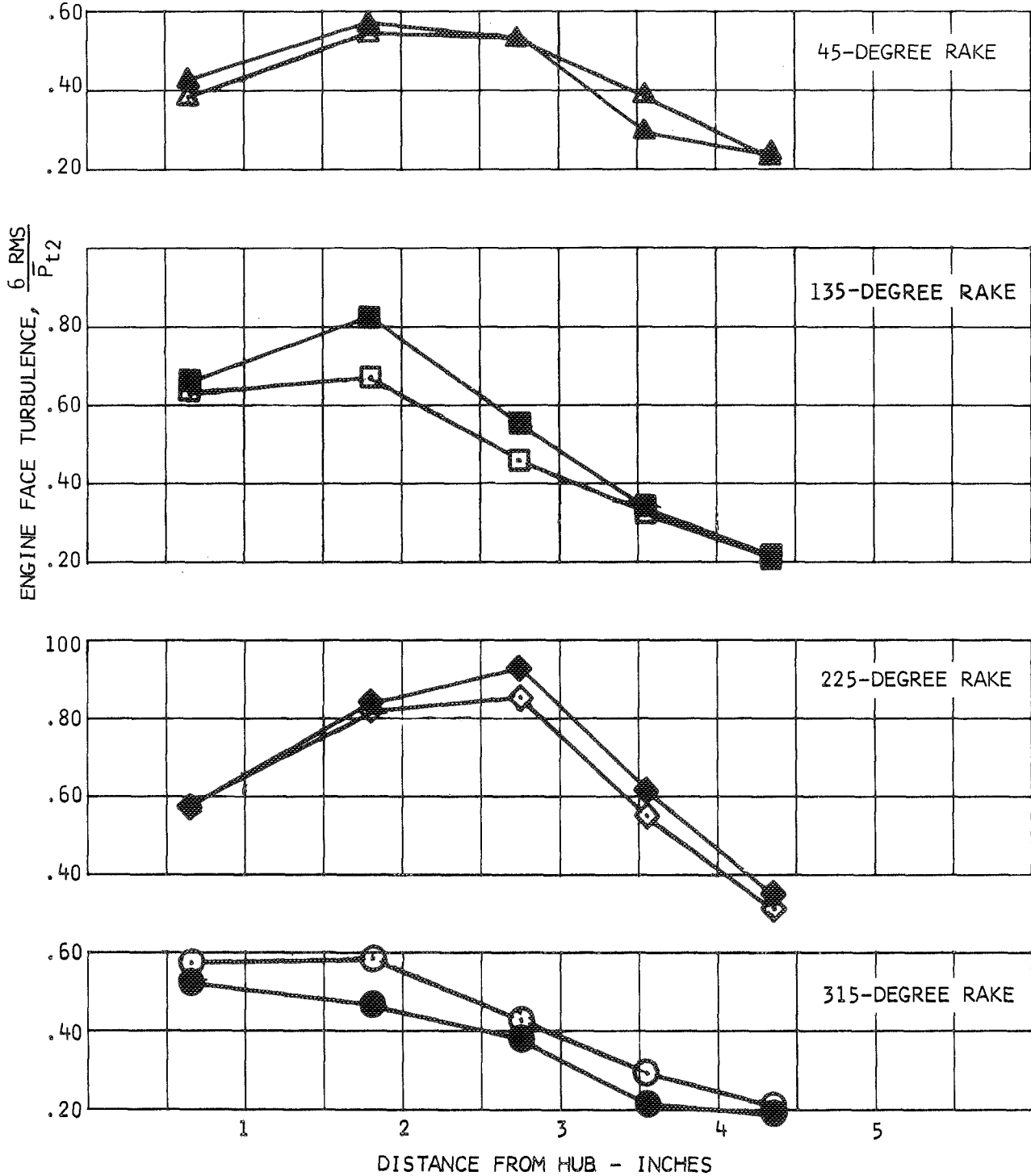


Figure 75.- Upstream rake effect on engine face turbulence, $M_0 = 3.0$.

SYMBOL	α_0	$\frac{\bar{P}_{t2}}{P_{t0}}$
○	0°	0.563
△	4°	0.529
□	8°	0.533

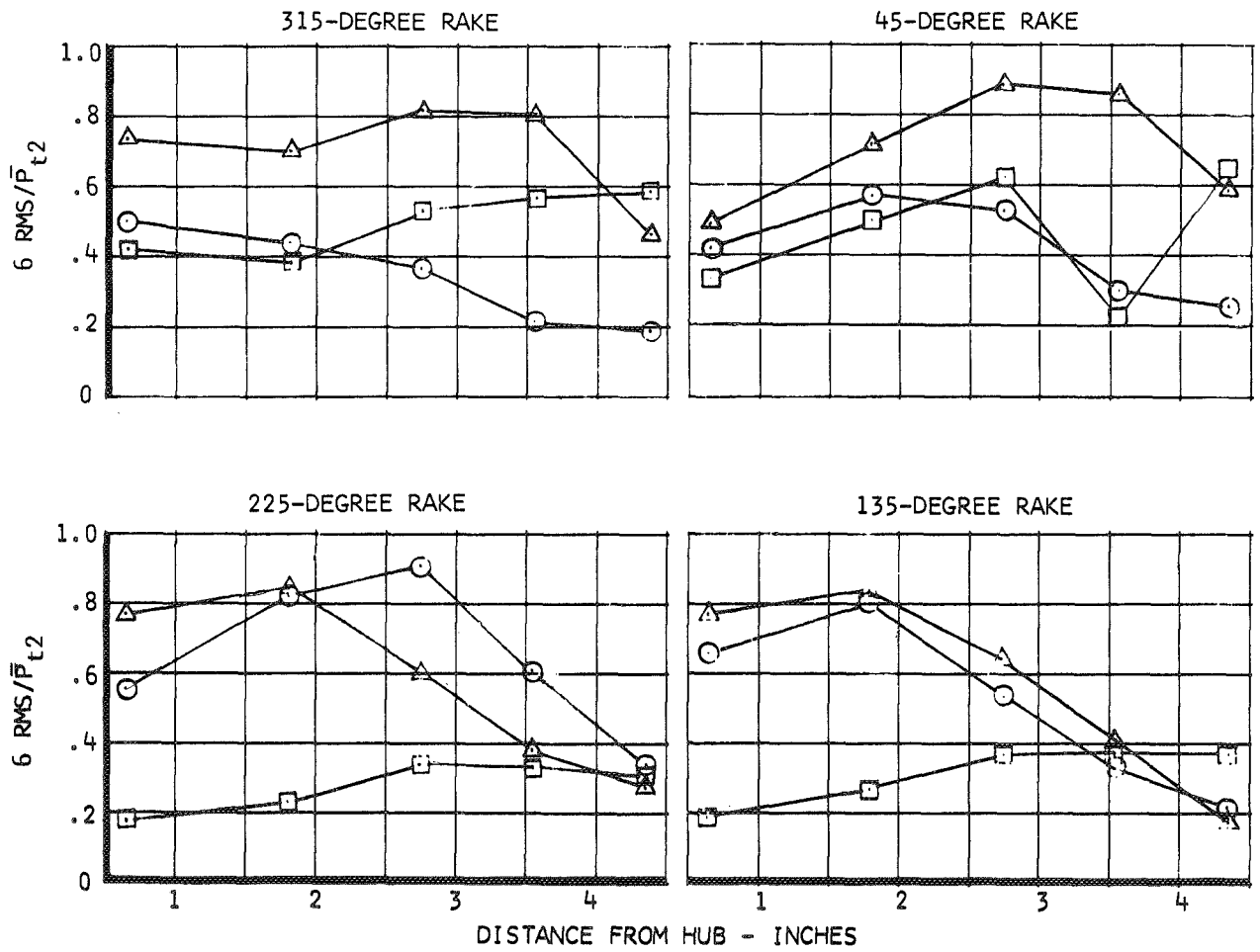
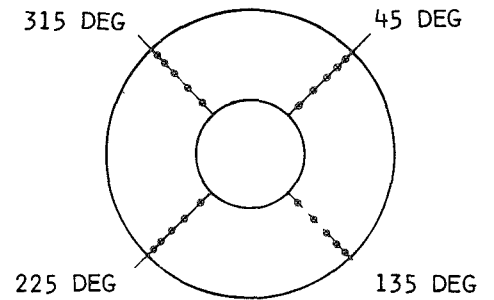
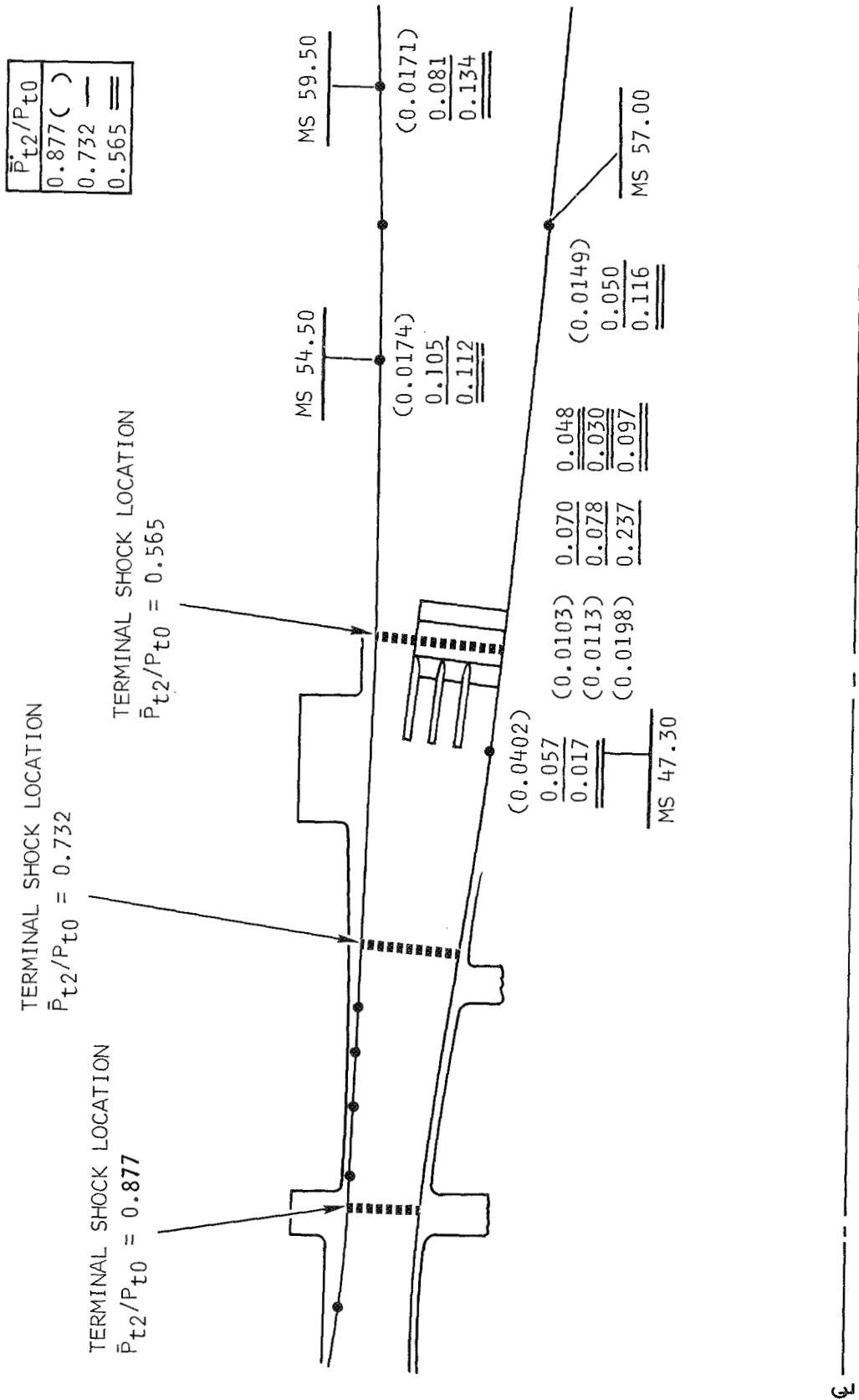


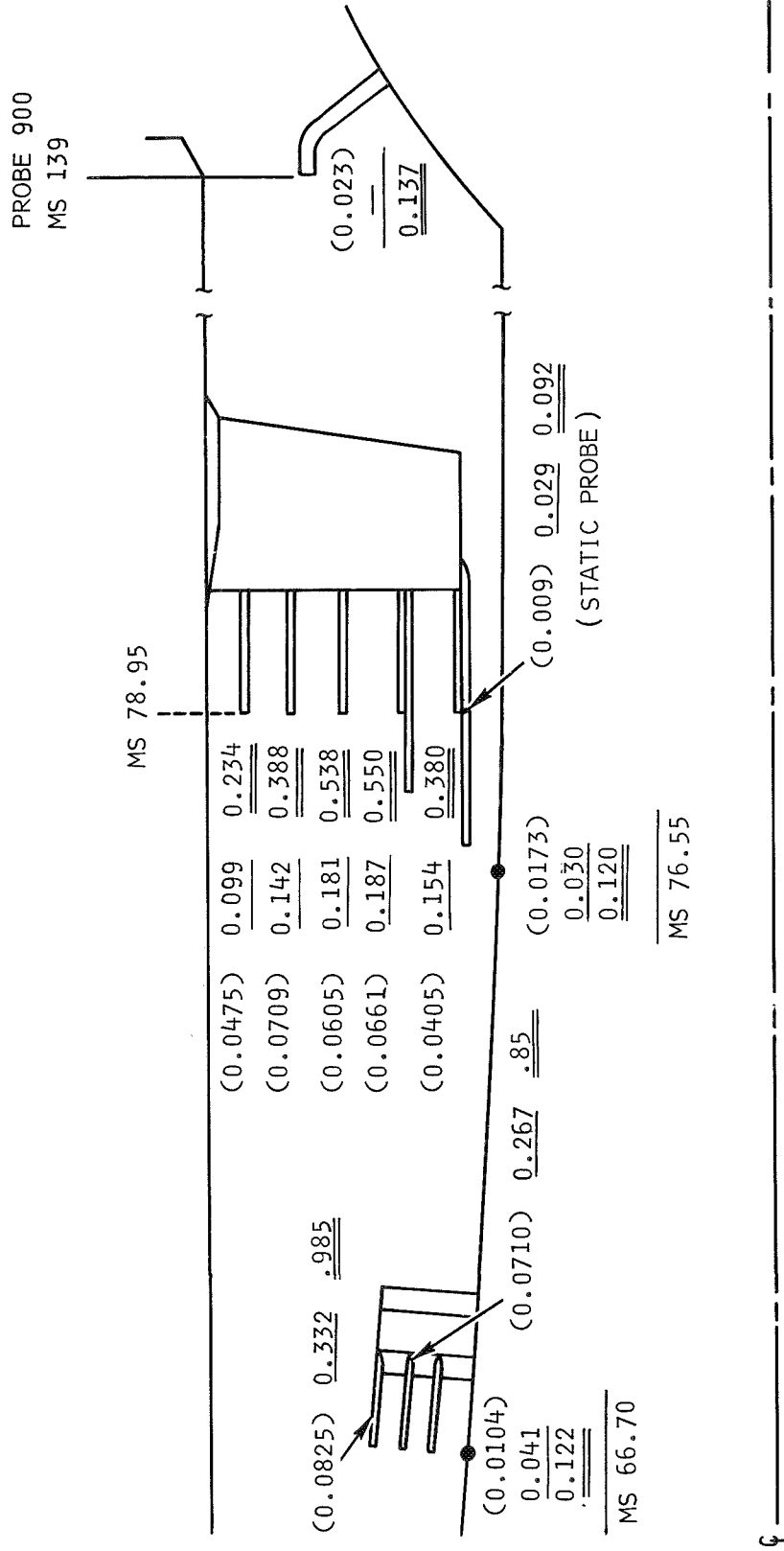
Figure 76.- Engine face turbulence variations with angle of attack, $M_0 = 3.0$.



(a)

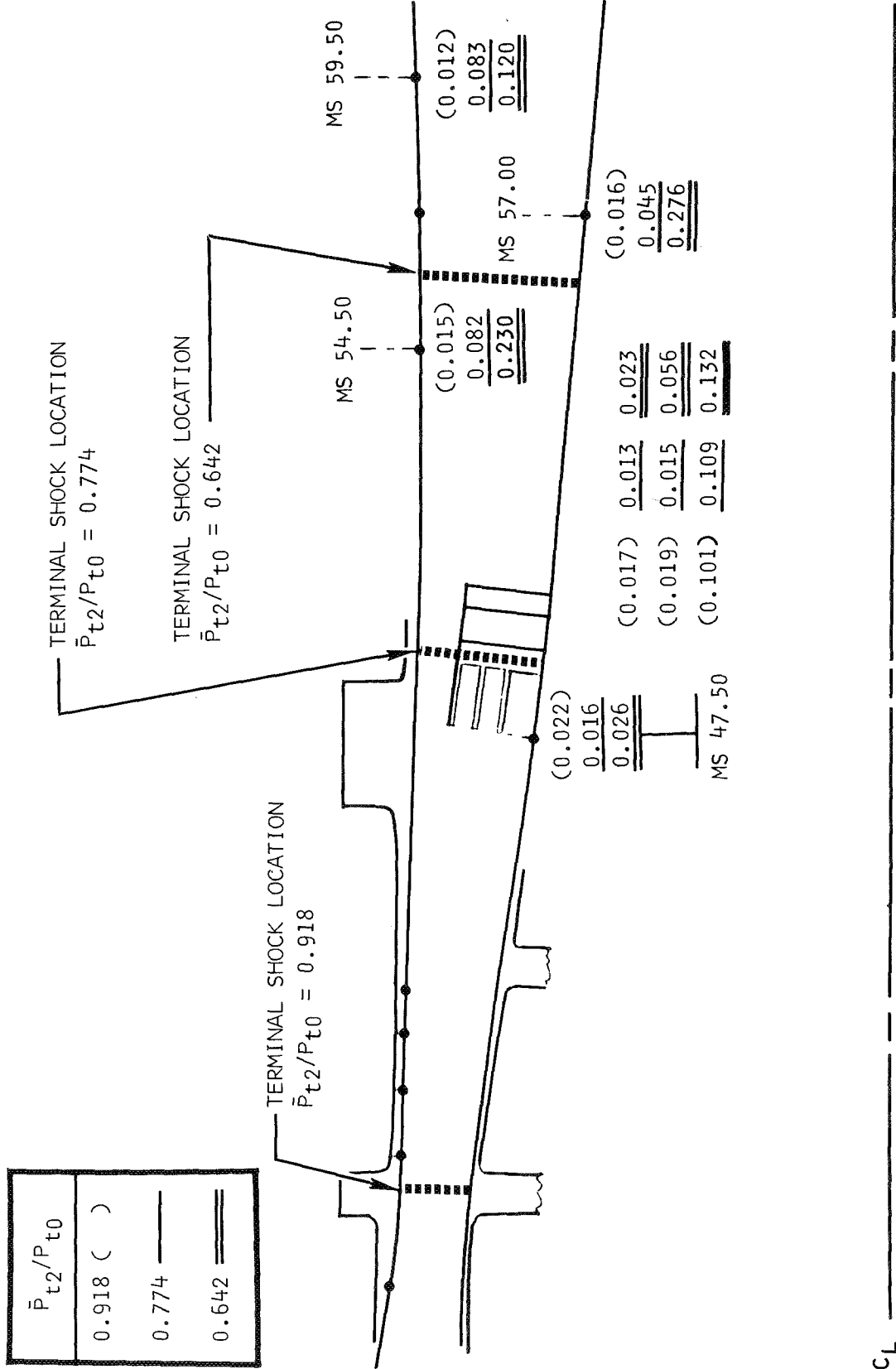
Figure 77.- Turbulence variation with station, $M_0 = 3.0$.

\bar{P}_{t2}/P_{t0}
.877 ()
.732
.565



(b)

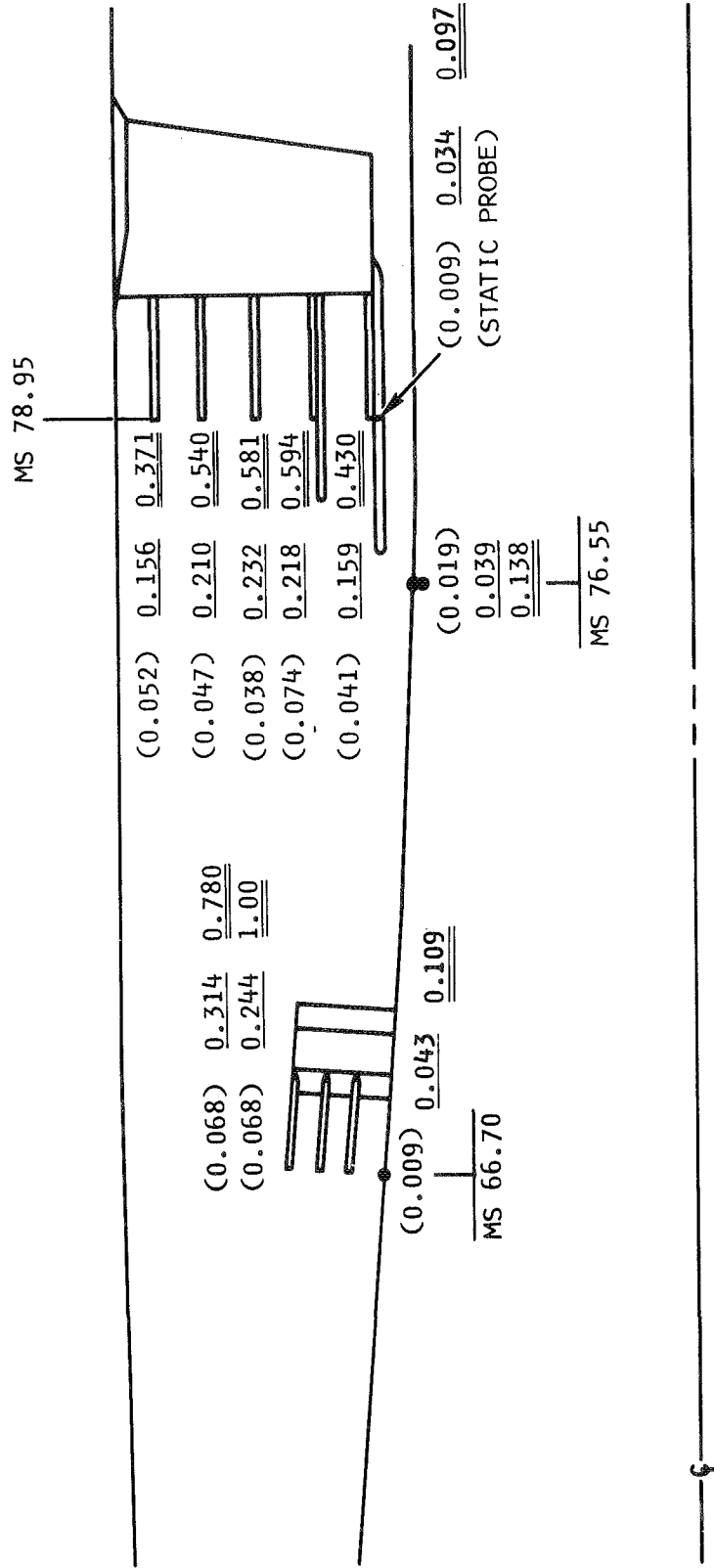
Figure 77. - Concluded.



(a)

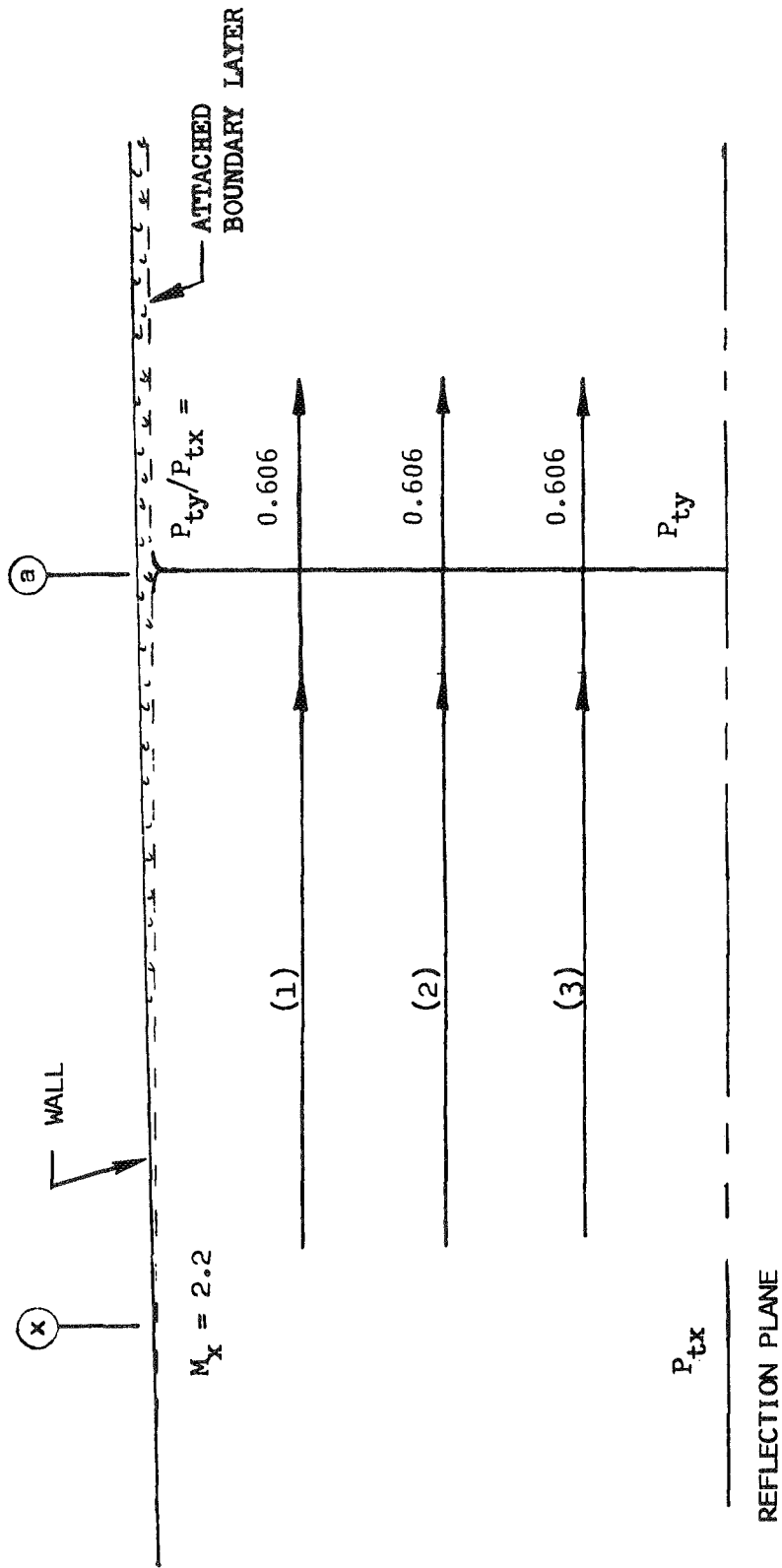
Figure 78.- Turbulence variation with station, $M_0 = 2.6$.

\bar{P}_{t2}/P_{t0}	
0.918	()
0.774	()
0.642	()



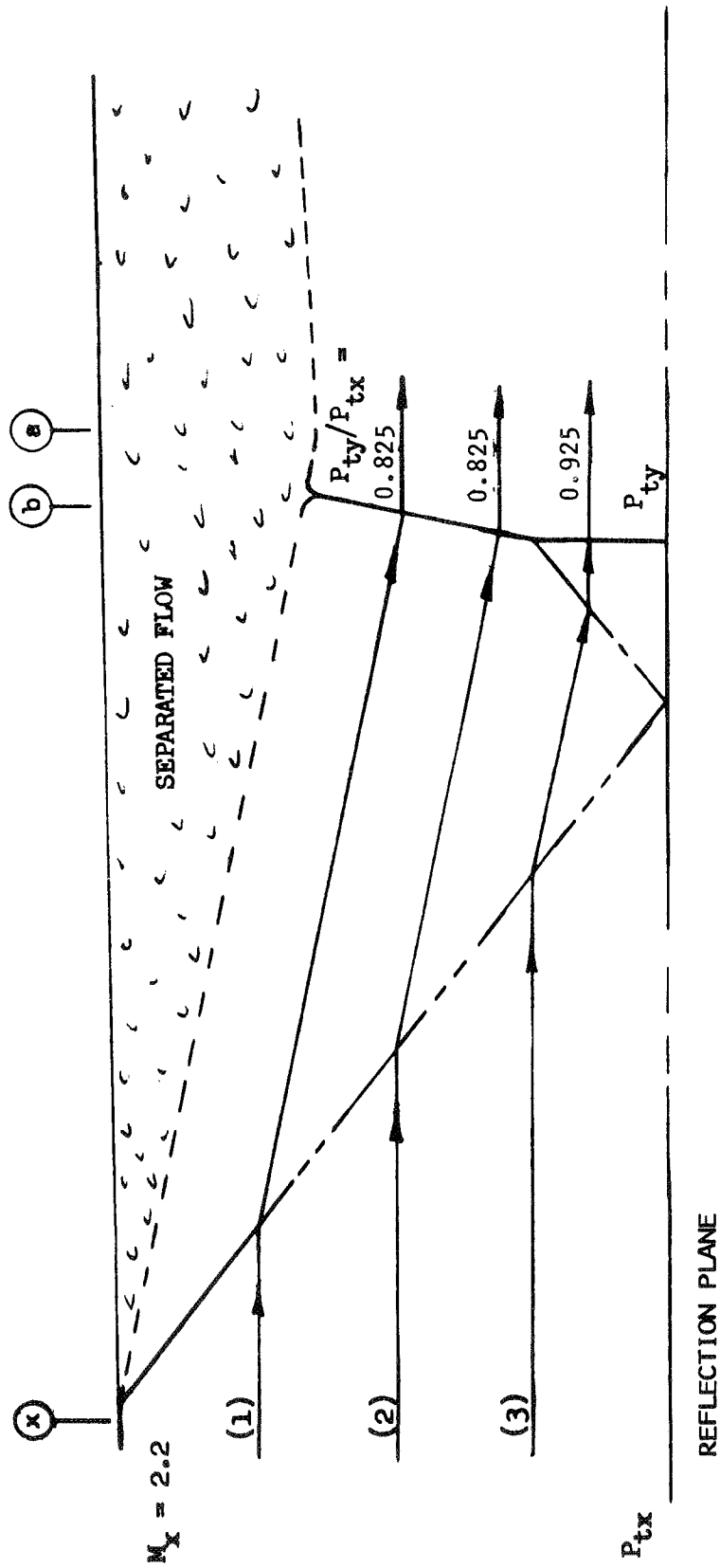
(b)

Figure 78.- Concluded.



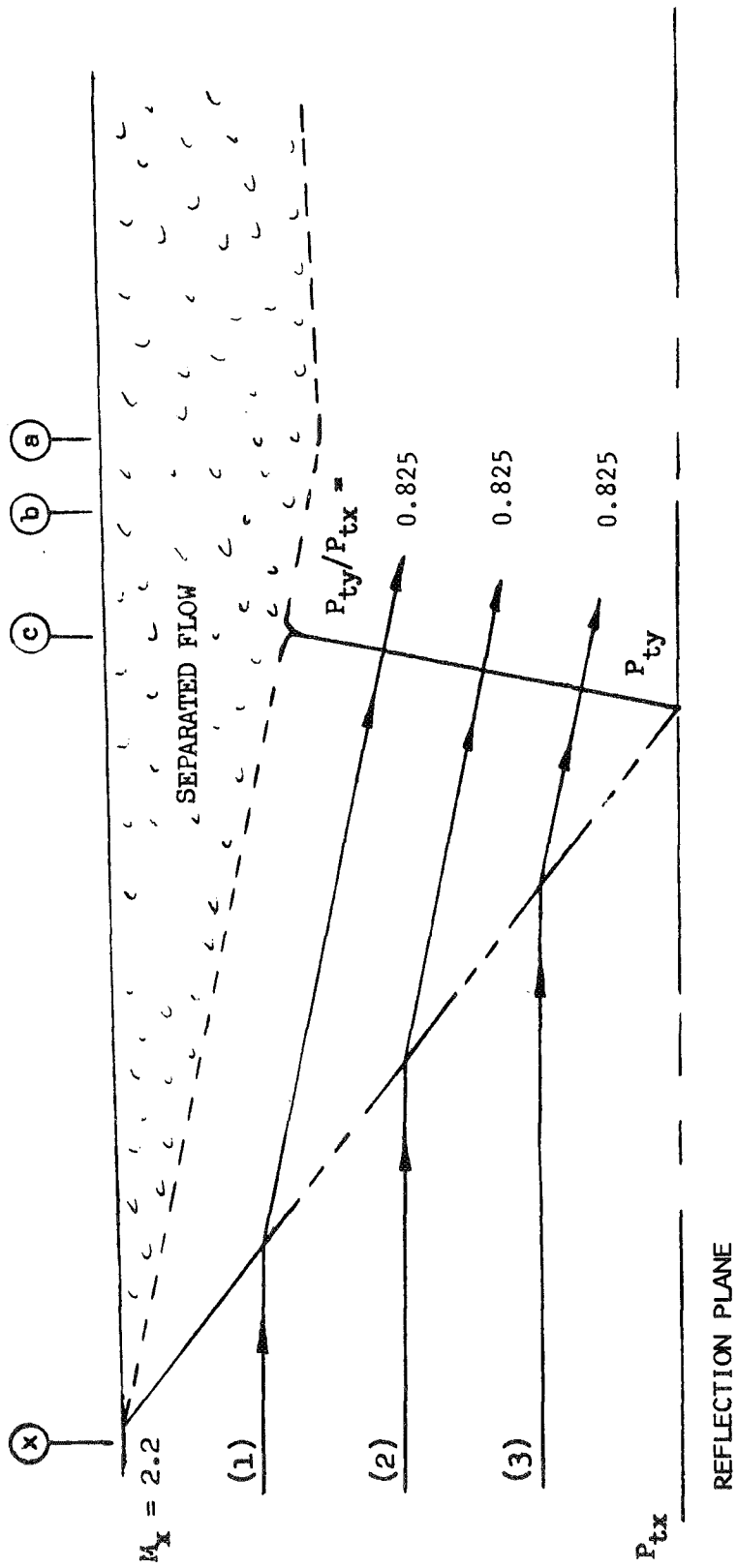
(a)

Figure 79.- Hypothetical model of turbulence.



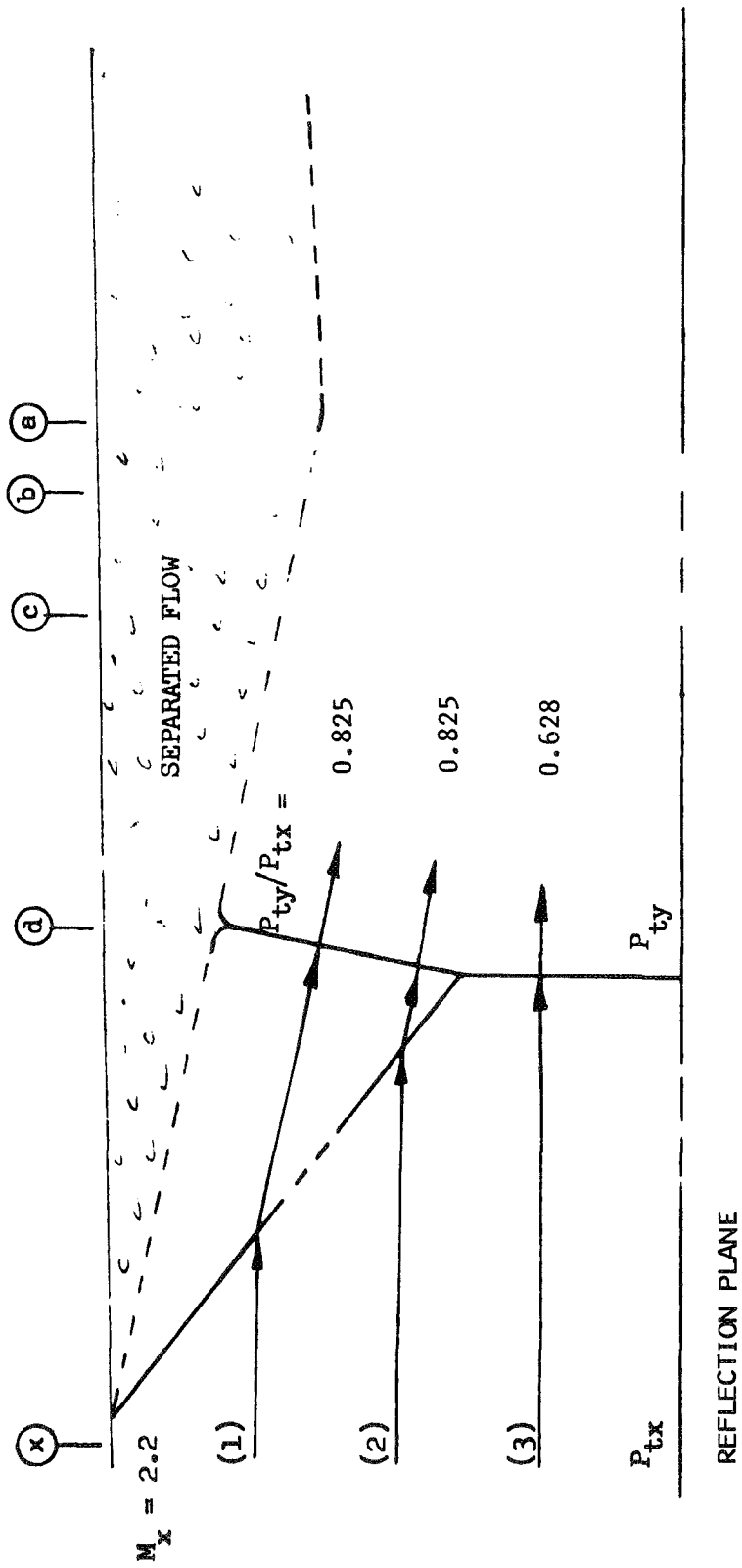
(b)

Figure 79.- Continued.



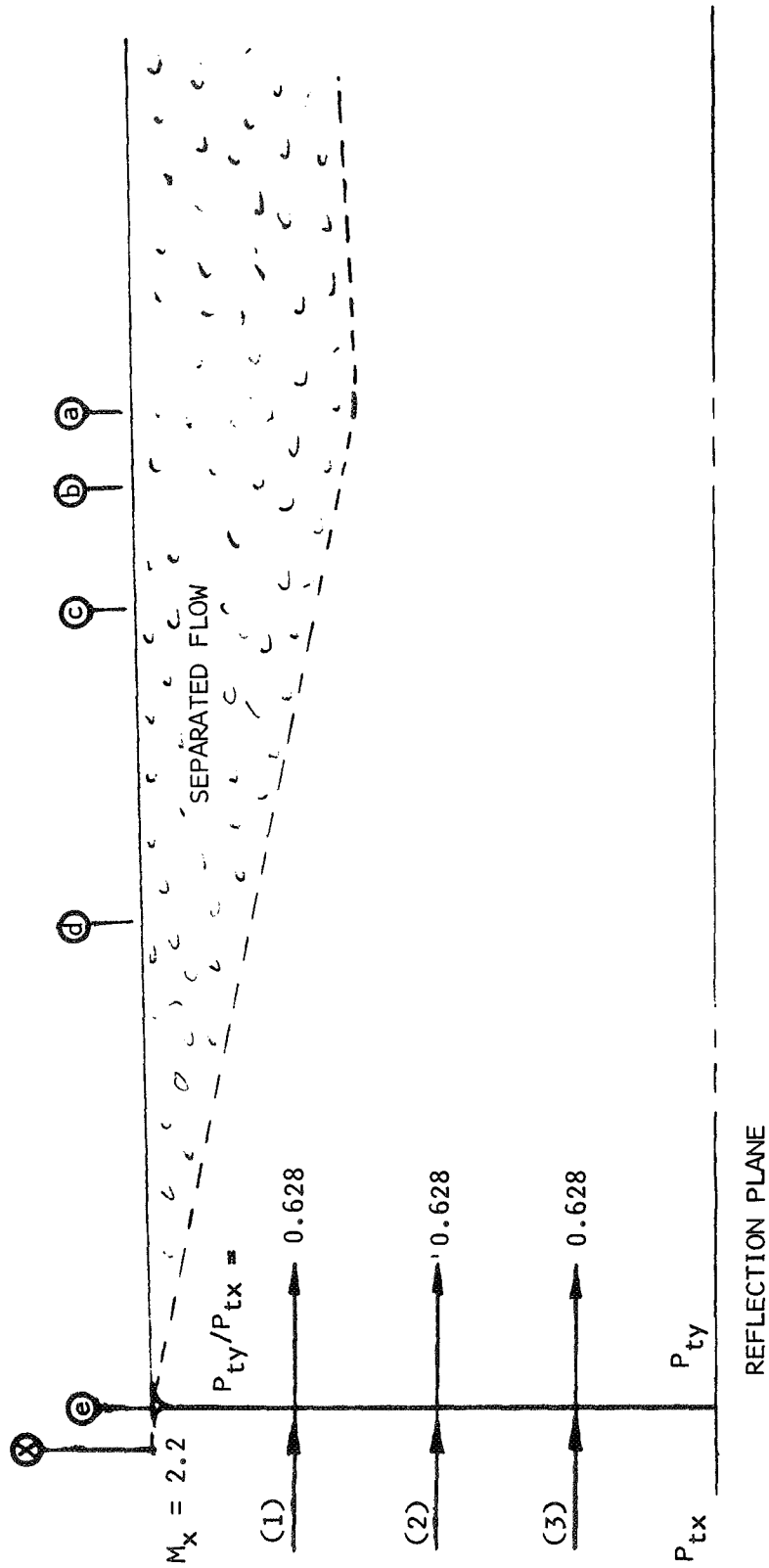
(c)

Figure 79.- Continued.



(d)

Figure 79.- Continued.



(e)

Figure 79.- Concluded.

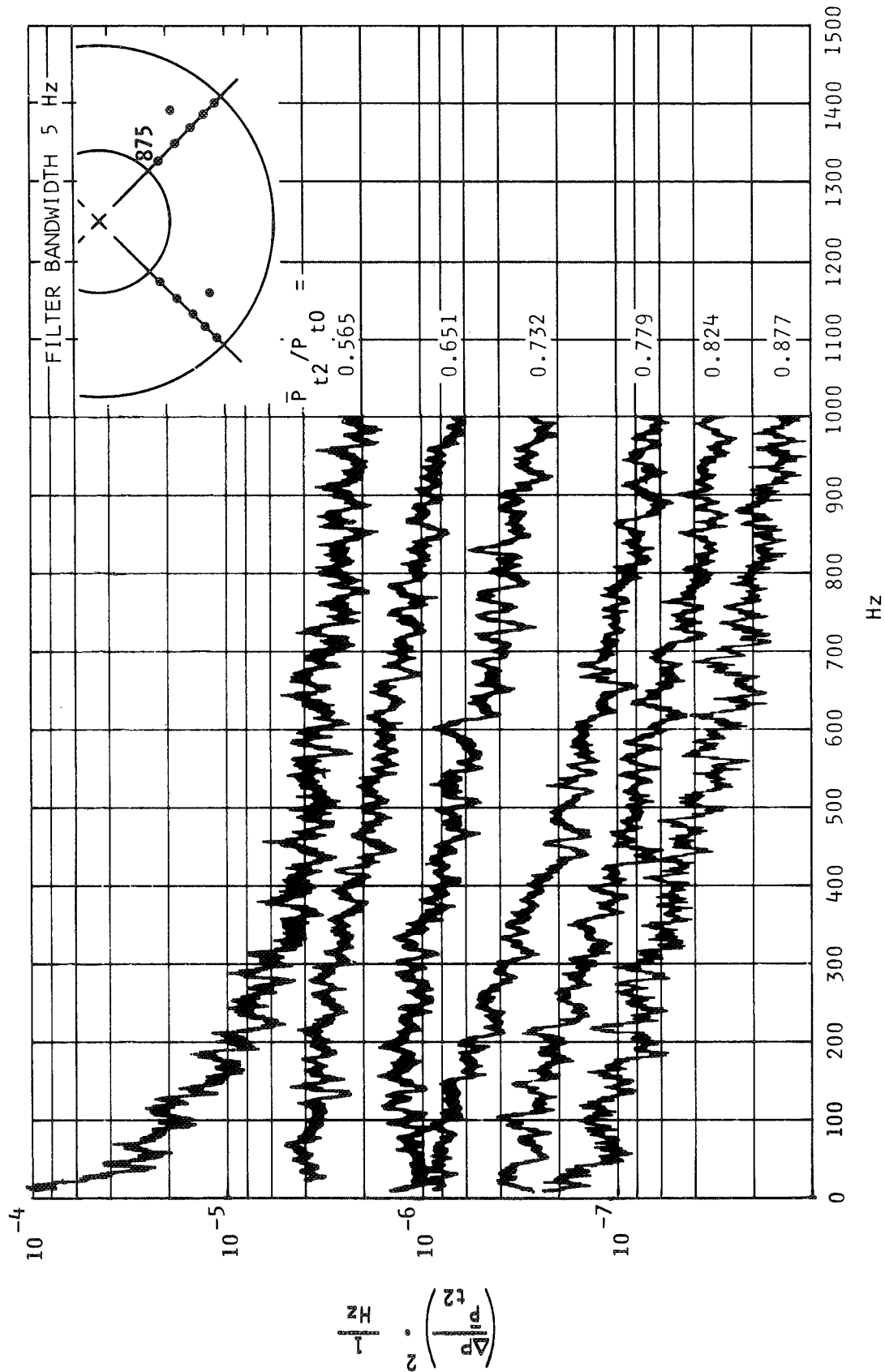


Figure 80. - Power spectral density variation with recovery, $M_0 = 3.0$, $\alpha_0 = 0$ degrees, engine face inboard total pressure probe 875

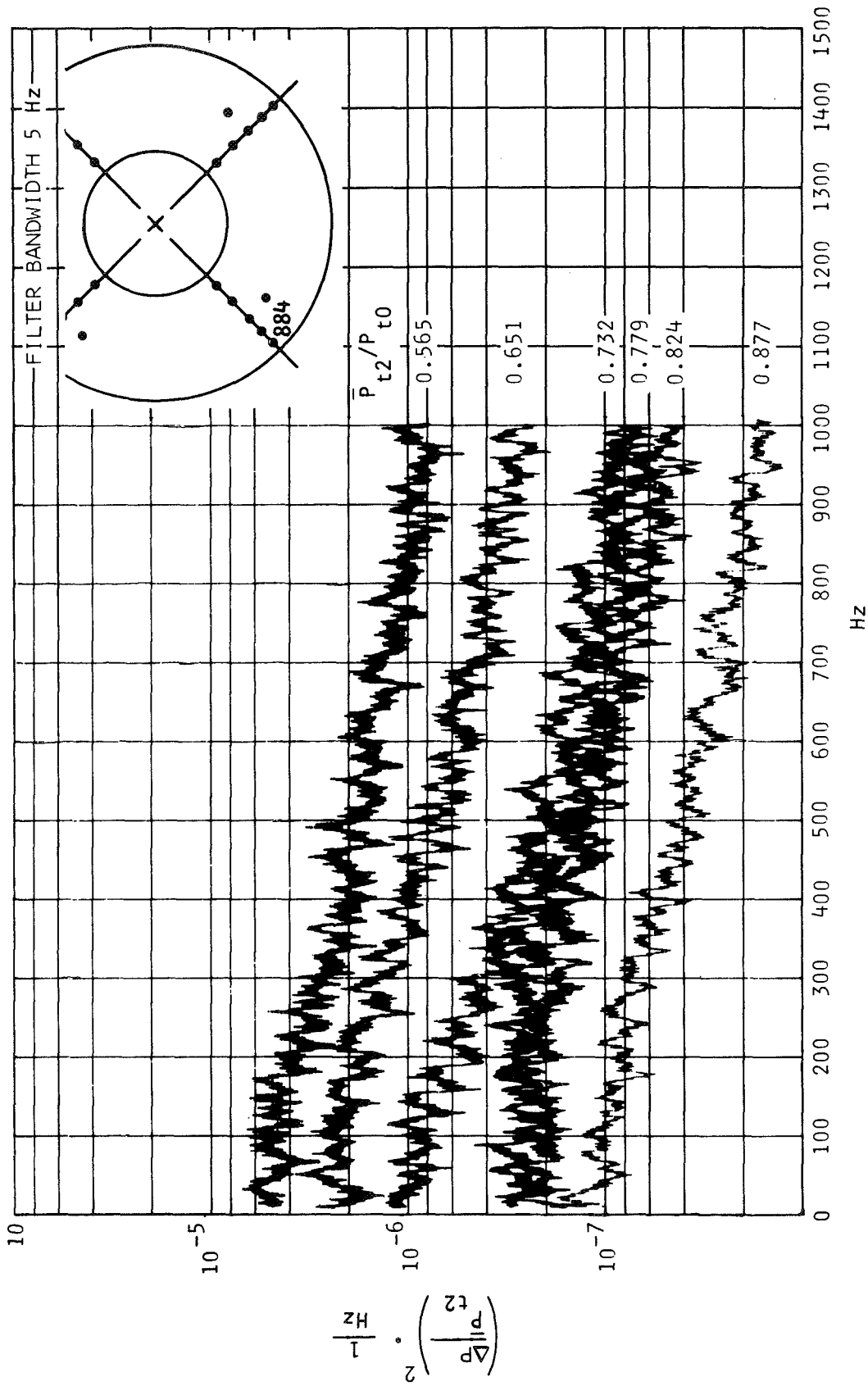


Figure 81. - Power spectral density variation with recovery, $M_0 = 3.0$, $\alpha_0 = 0$ degrees, engine face outboard total pressure probe 884

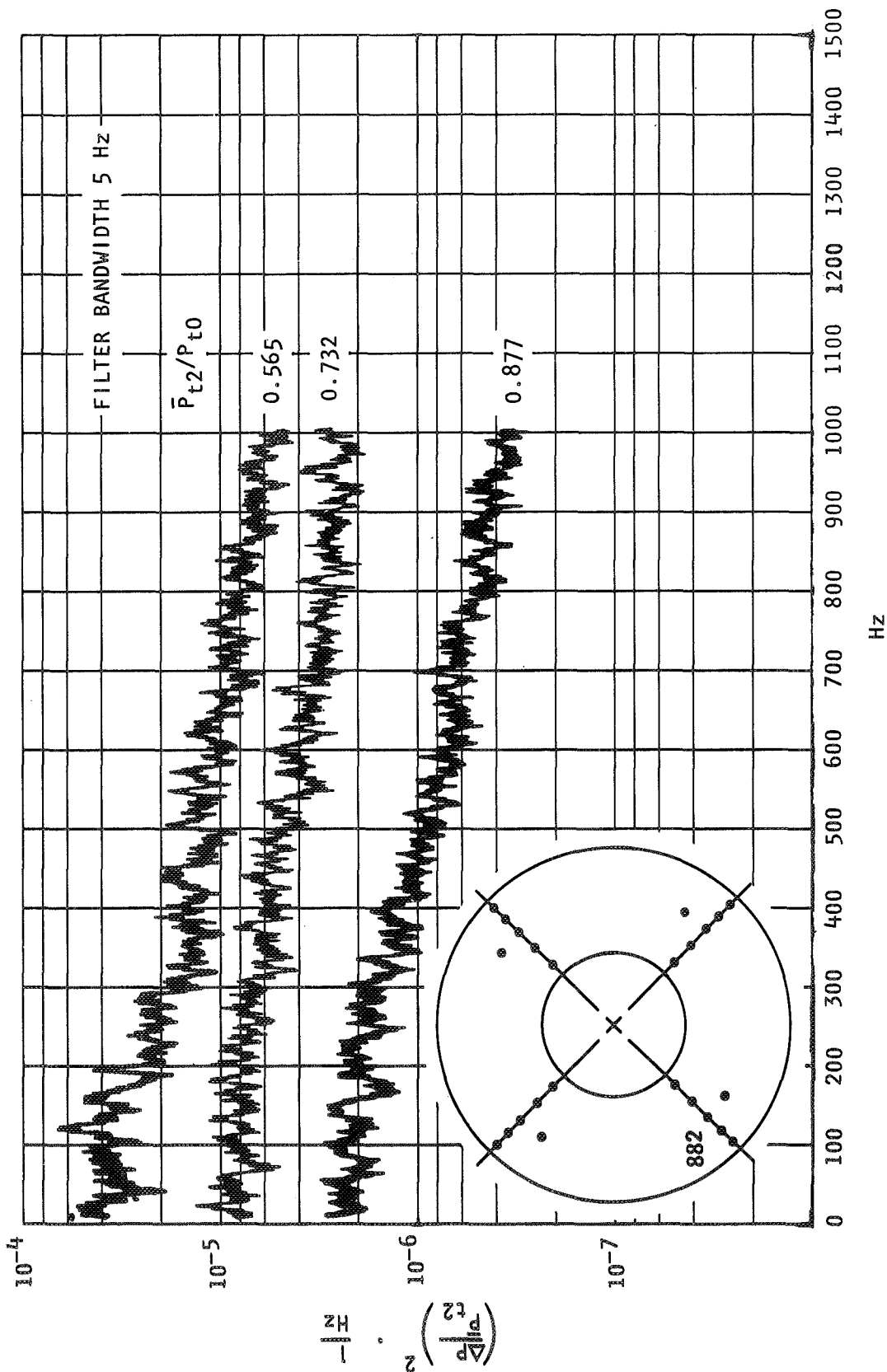


Figure 82.- Power spectral density variation with recovery, $M_0 = 3.0$, engine face annulus center total pressure probe 882.

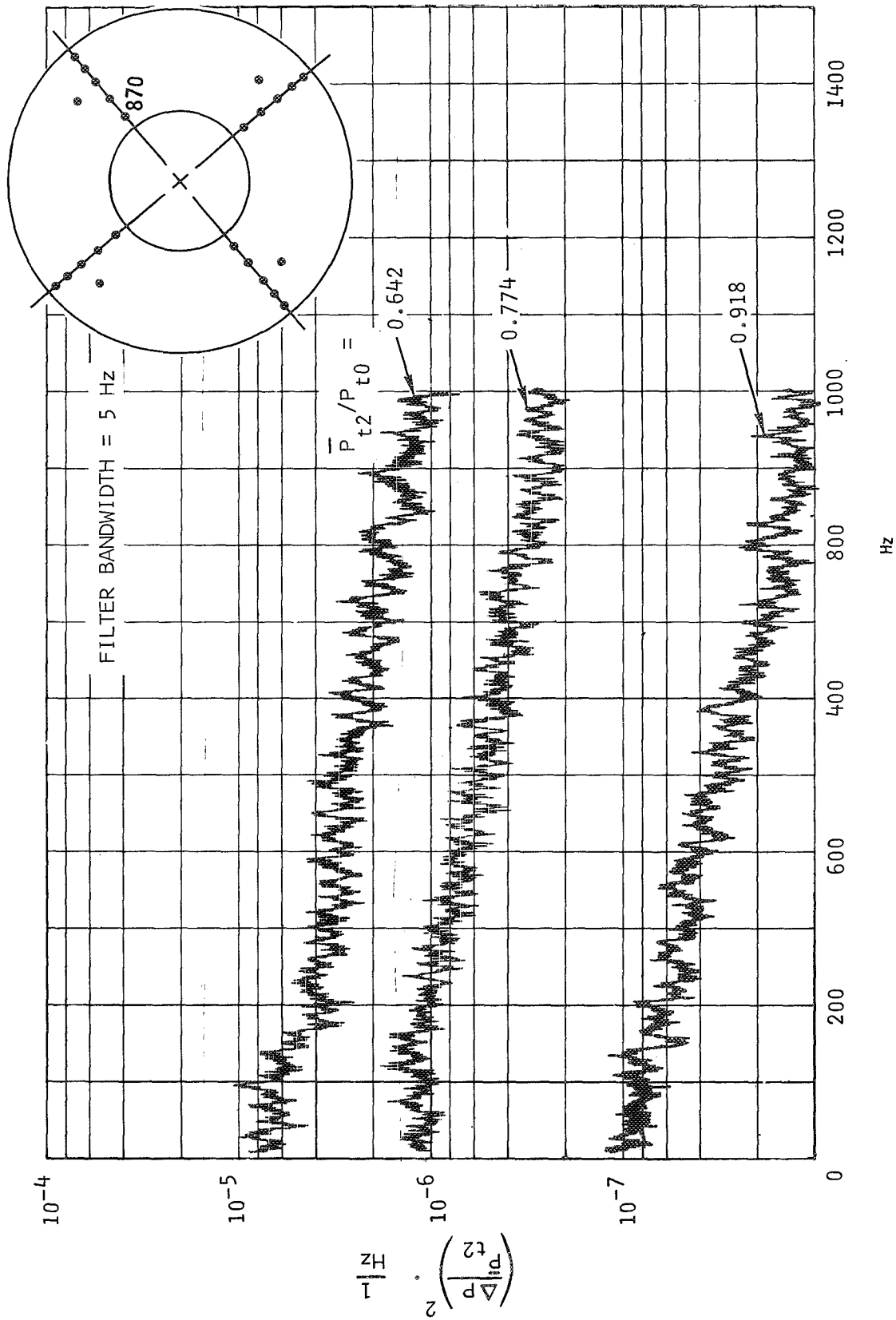


Figure 83. Power spectral density variation with recovery, probe 870, $M_0 = 2.6$.

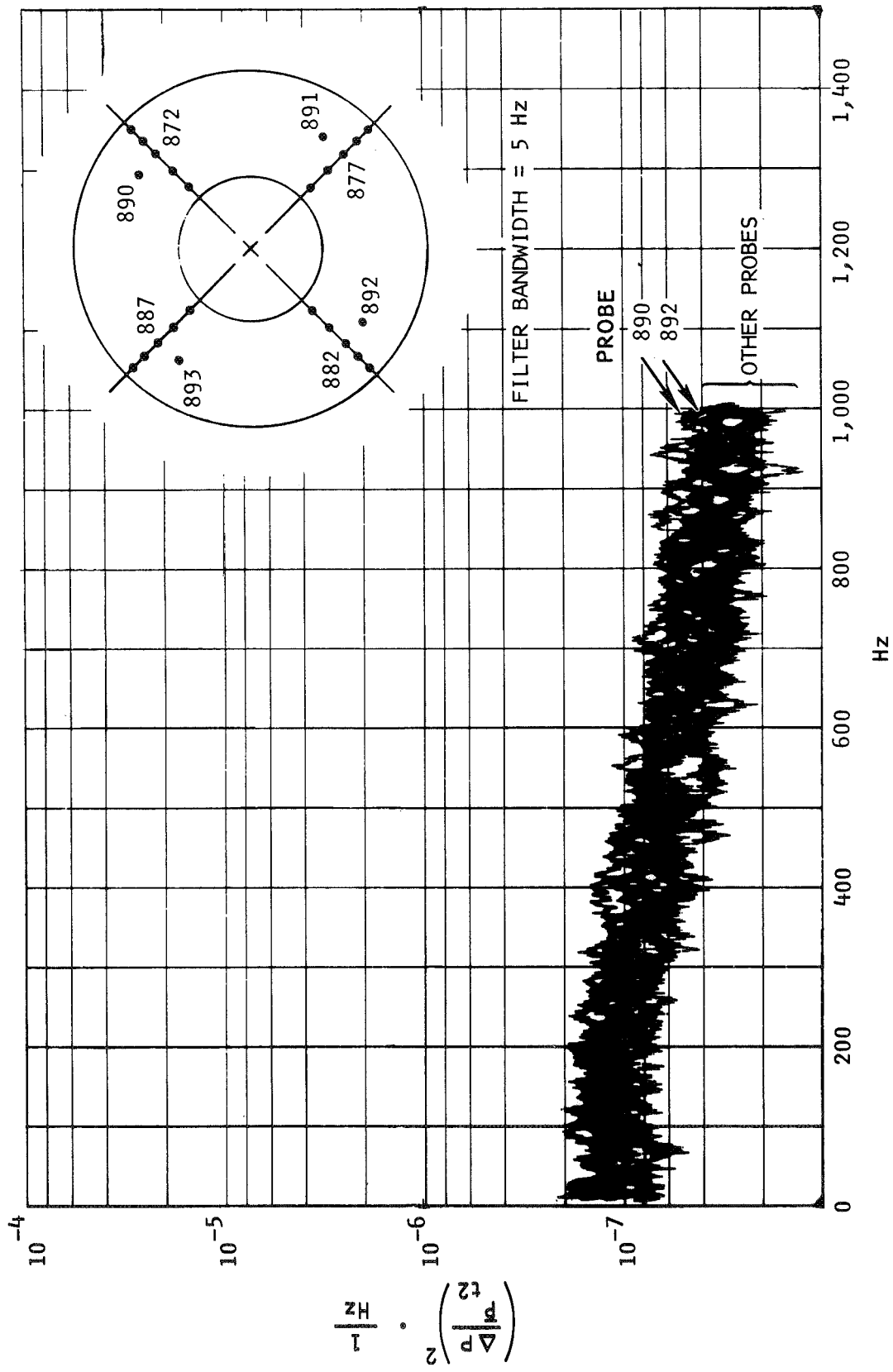


Figure 84. - Power spectral density variation with circumferential angle, $M_0 = 3.0$, $\bar{P}_{t2}/P_{t0} = 0.877$

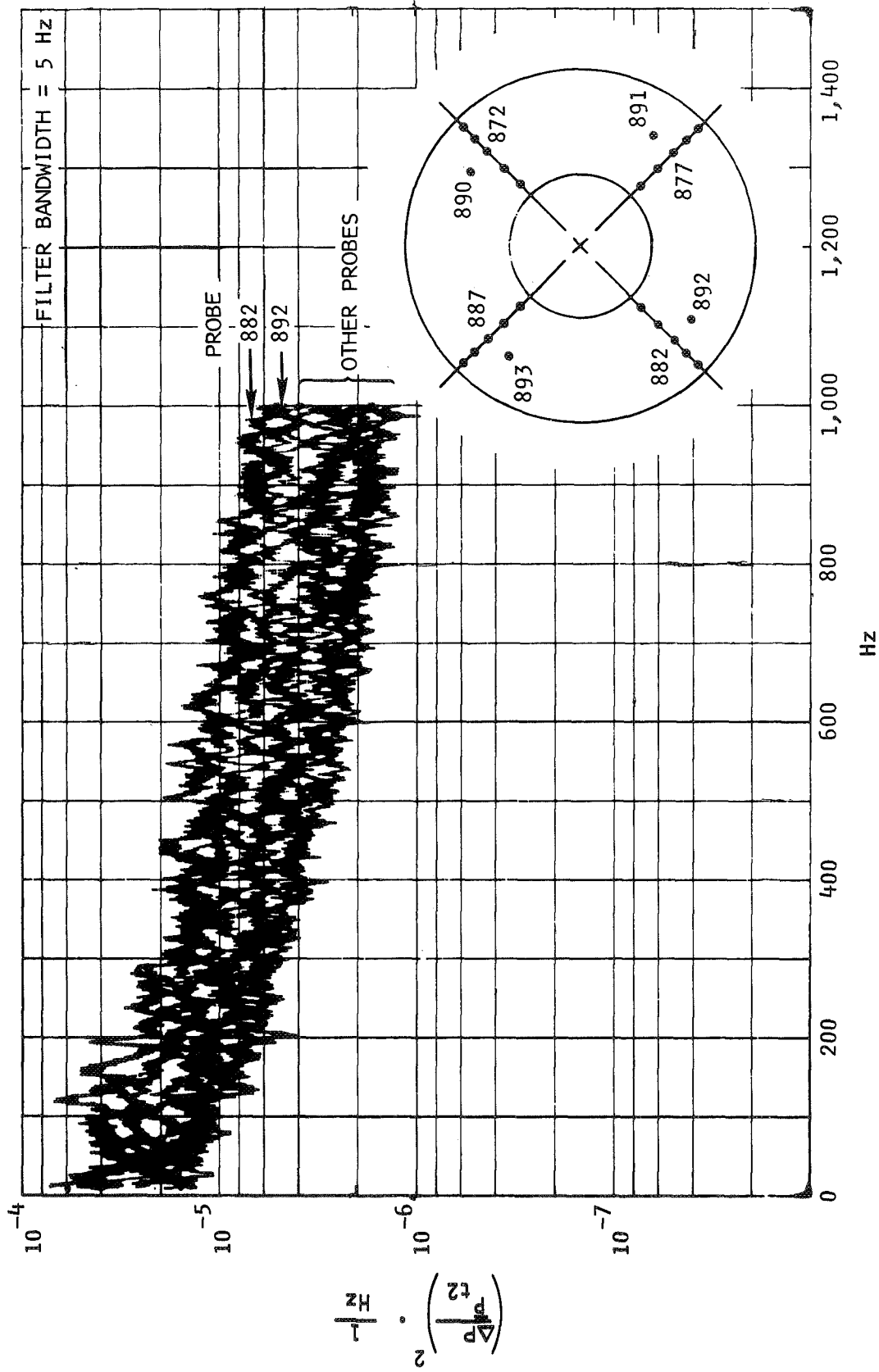


Figure 85. - Power spectral density variation with circumferential angle, $M_0 = 3.0$, $\bar{P}_{t_2}/P_{t_0} = 0.565$

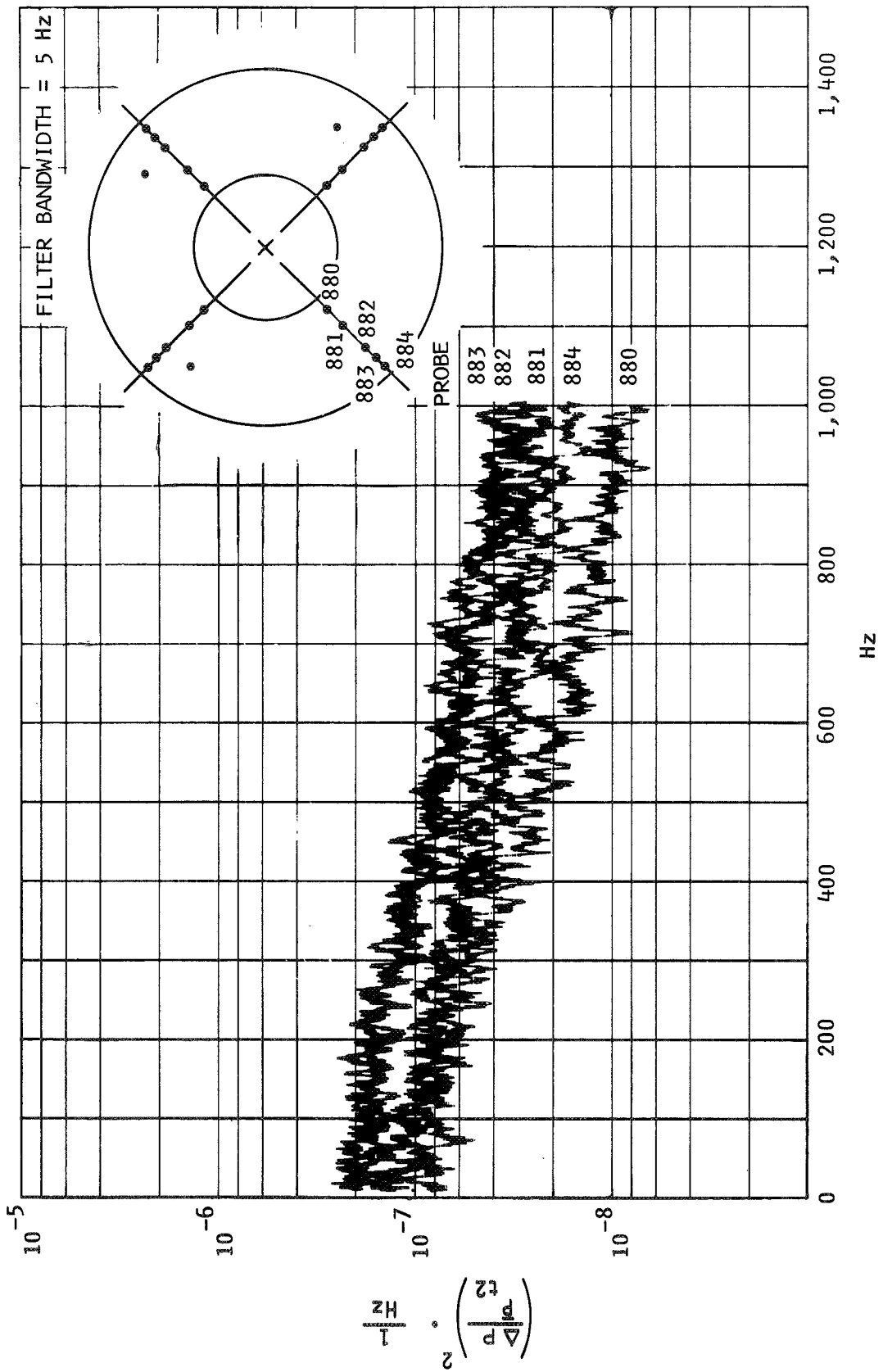


Figure 86. - Power spectral density variation with radius,
 $M_0 = 3.0, \bar{P}_{t2}/P_{t0} = 0.877$

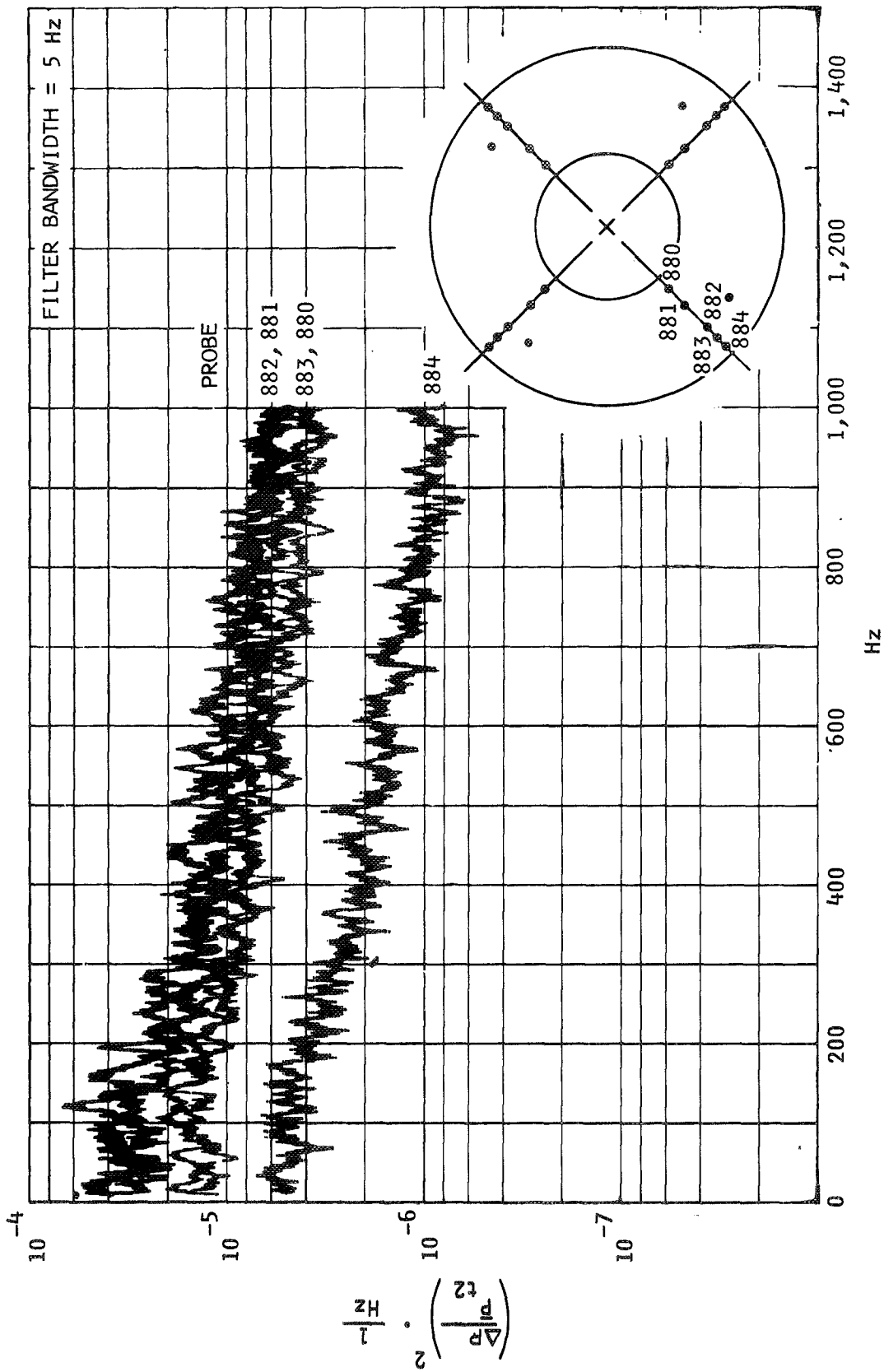


Figure 87. - Power spectral density variation with radius,
 $M_0 = 3.0, \bar{P}_{t2}/P_{t0} = 0.565$

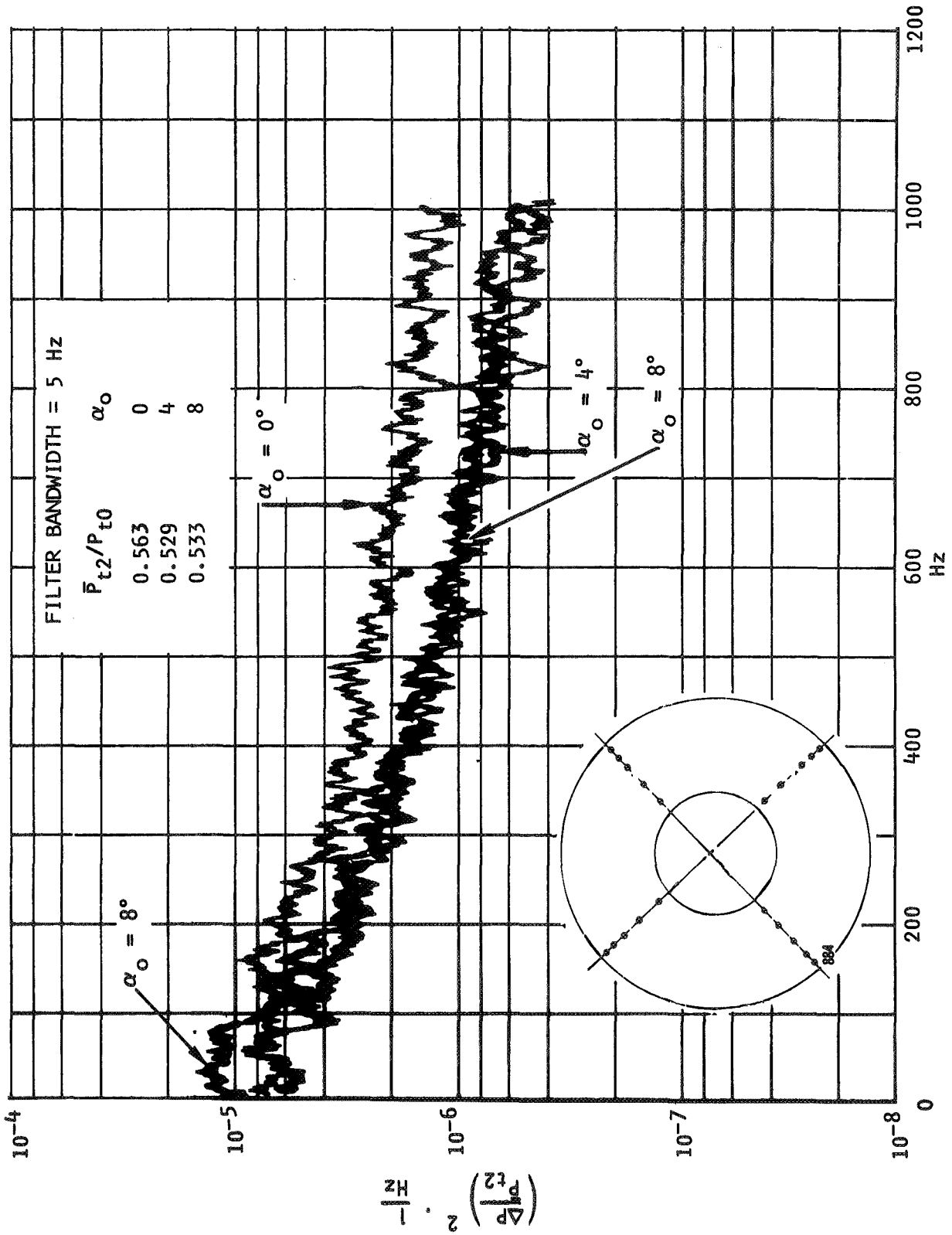


Figure 88.- Power spectral density variation with angle of attack, probe 884, $M_0 = 3.0$.

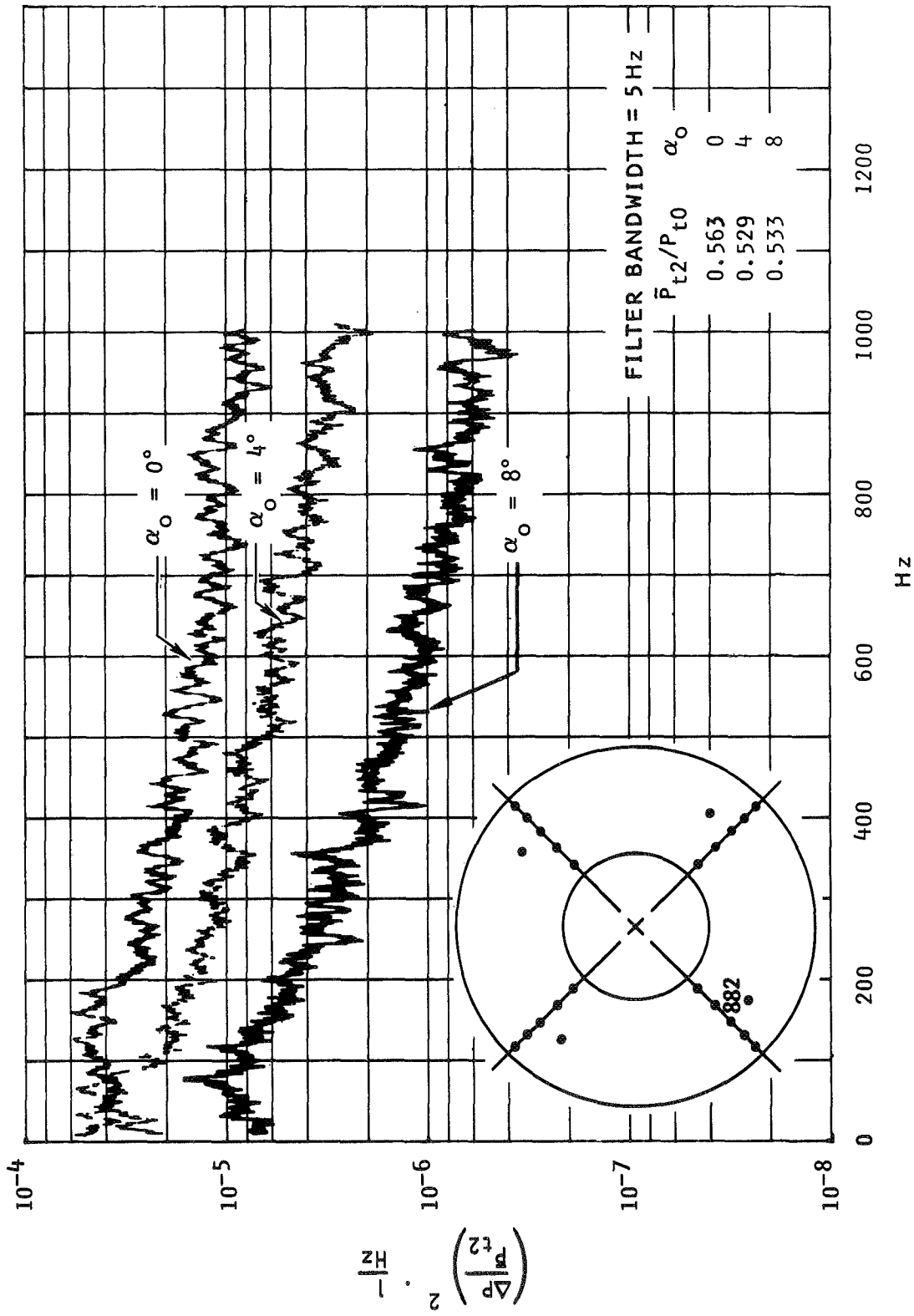


Figure 89.- Power spectral density variation with angle of attack, probe 882, $M_0 = 3.0$.

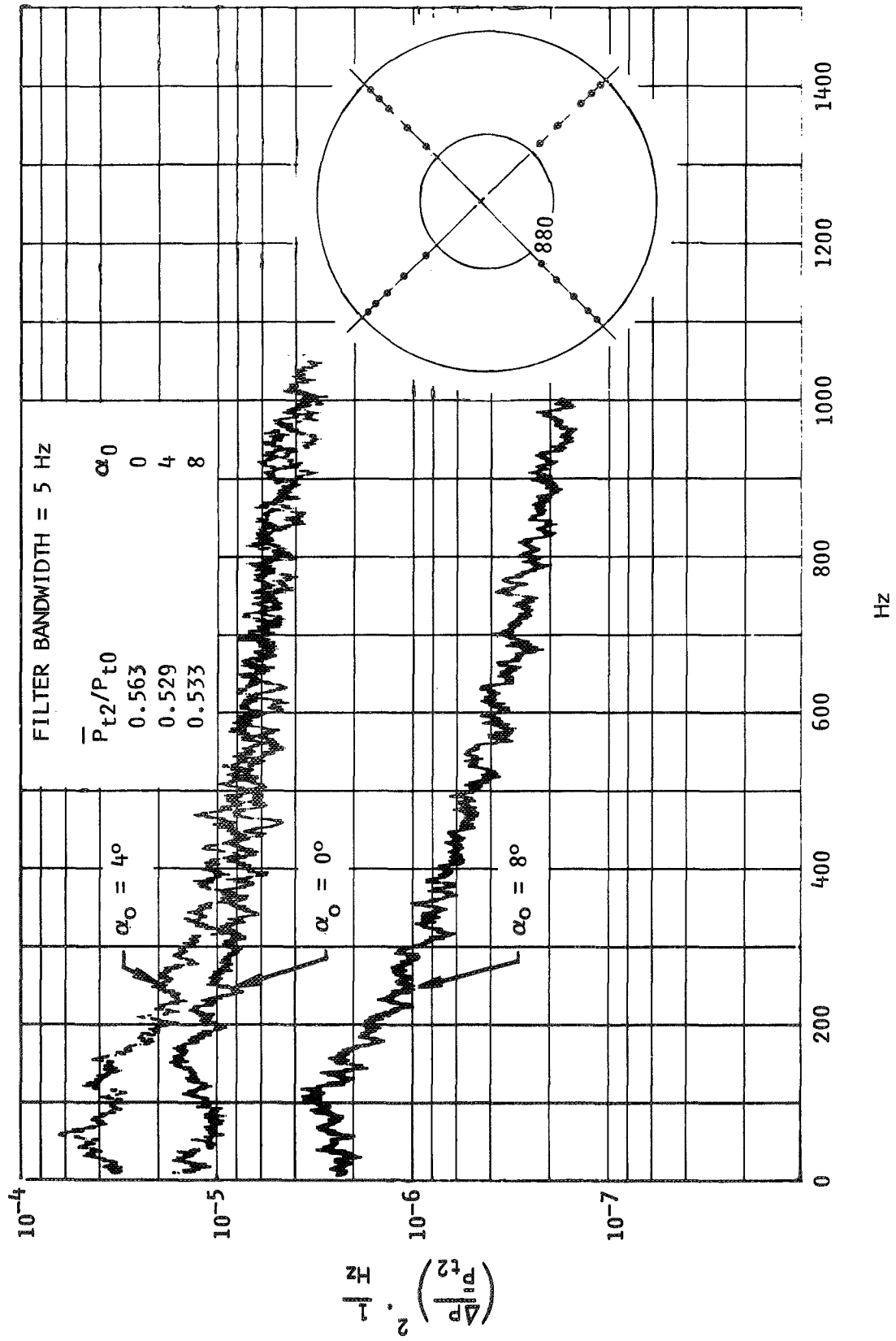


Figure 90.- Power spectral density variation with angle of attack, probe 880, $M_0 = 3.0$.

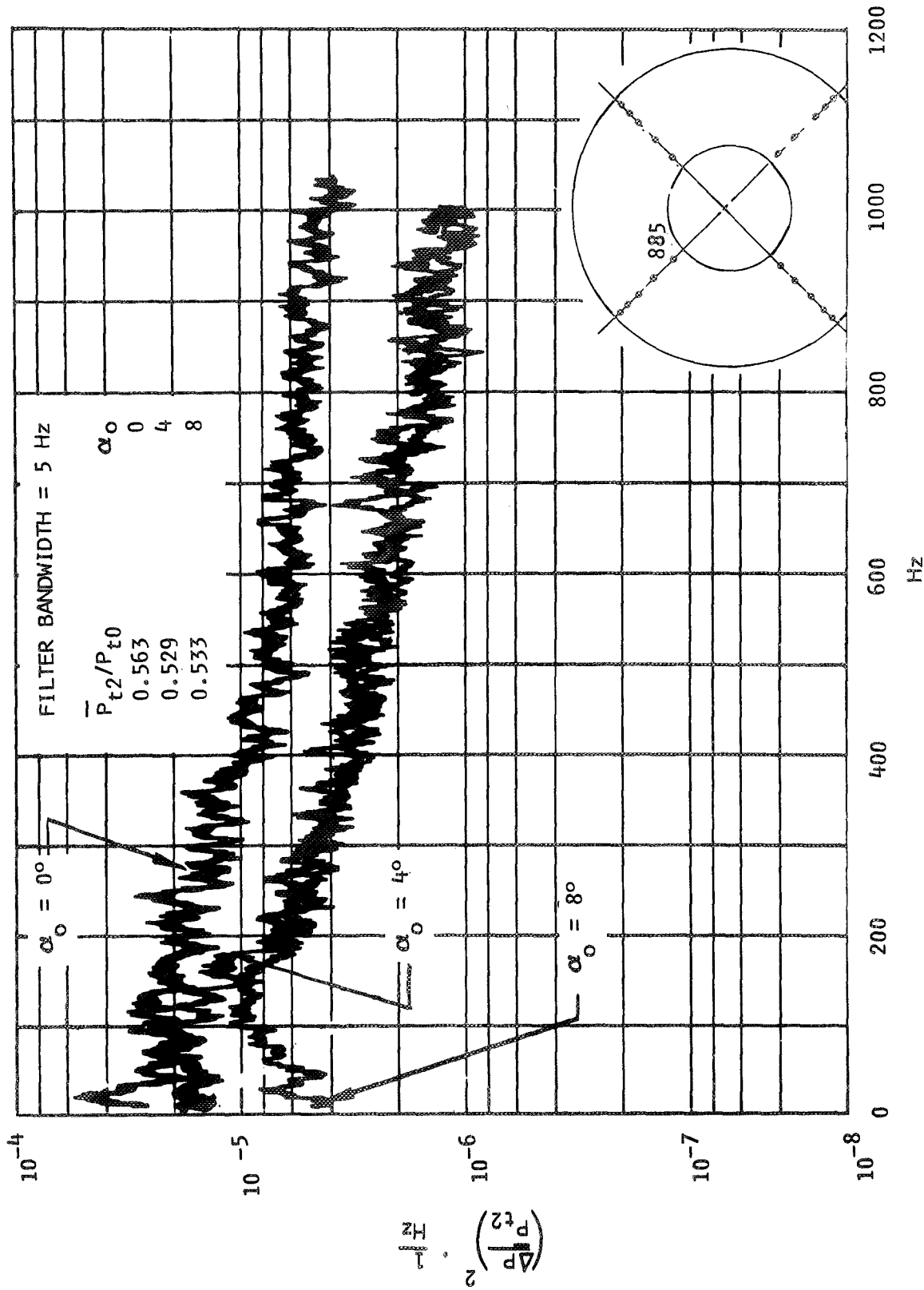


Figure 91.- Power spectral density variation with angle of attack, probe 885, $M_0 = 3.0$.

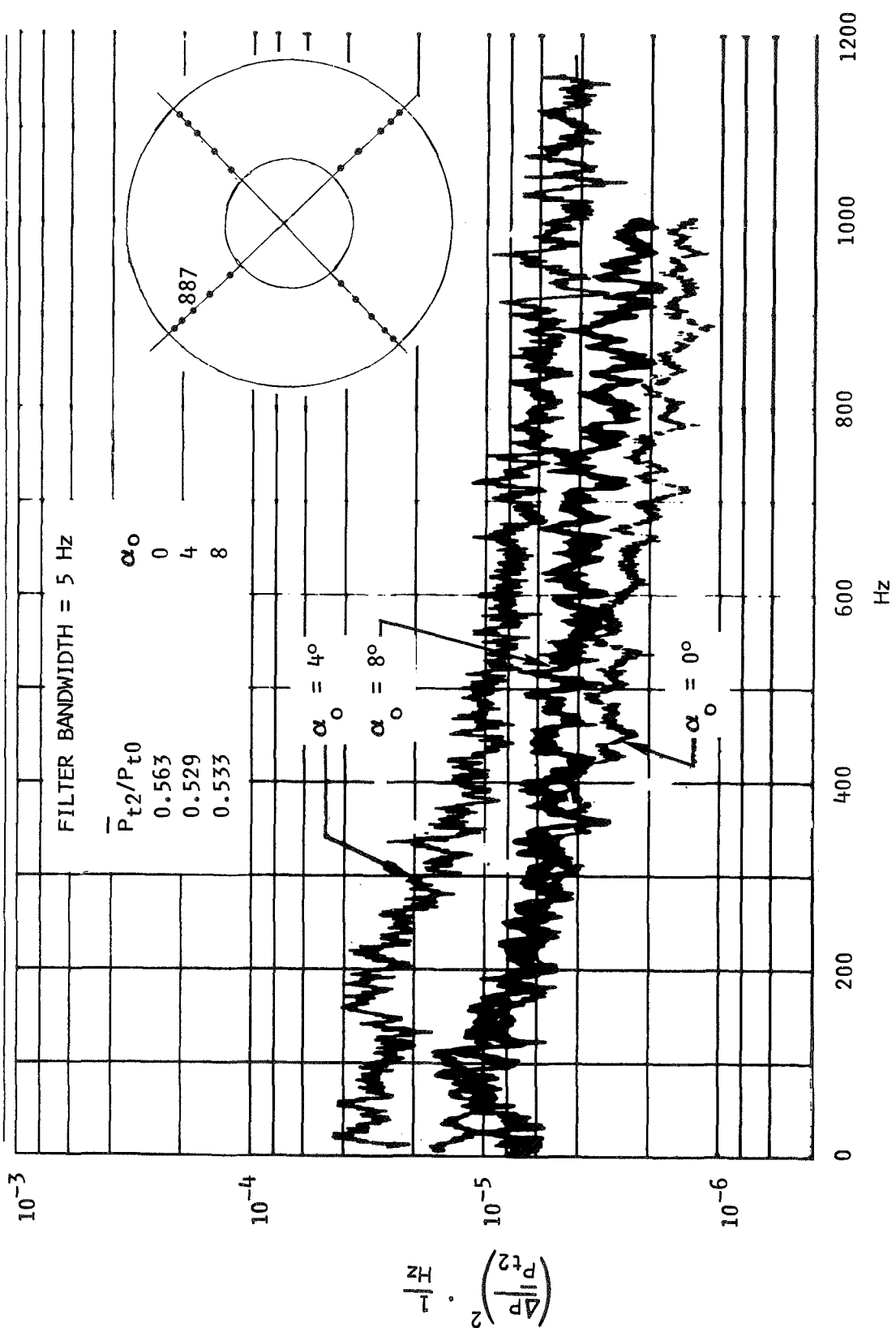


Figure 92.- Power spectral density variation with angle of attack, probe 887, $M_0 = 3.0$.

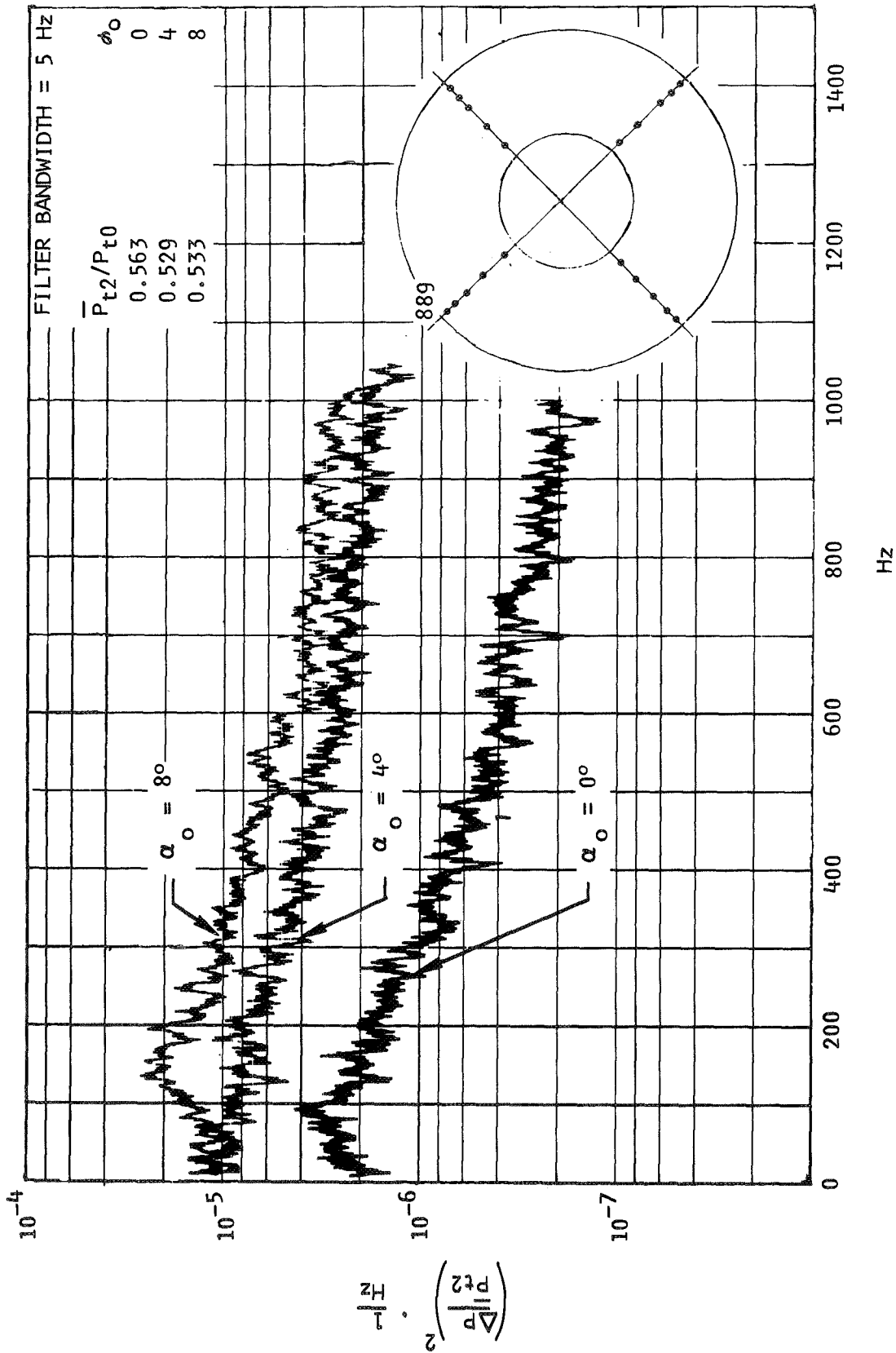


Figure 93.- Power spectral density variation with angle of attack, probe 889, $M_0 = 3.0$.

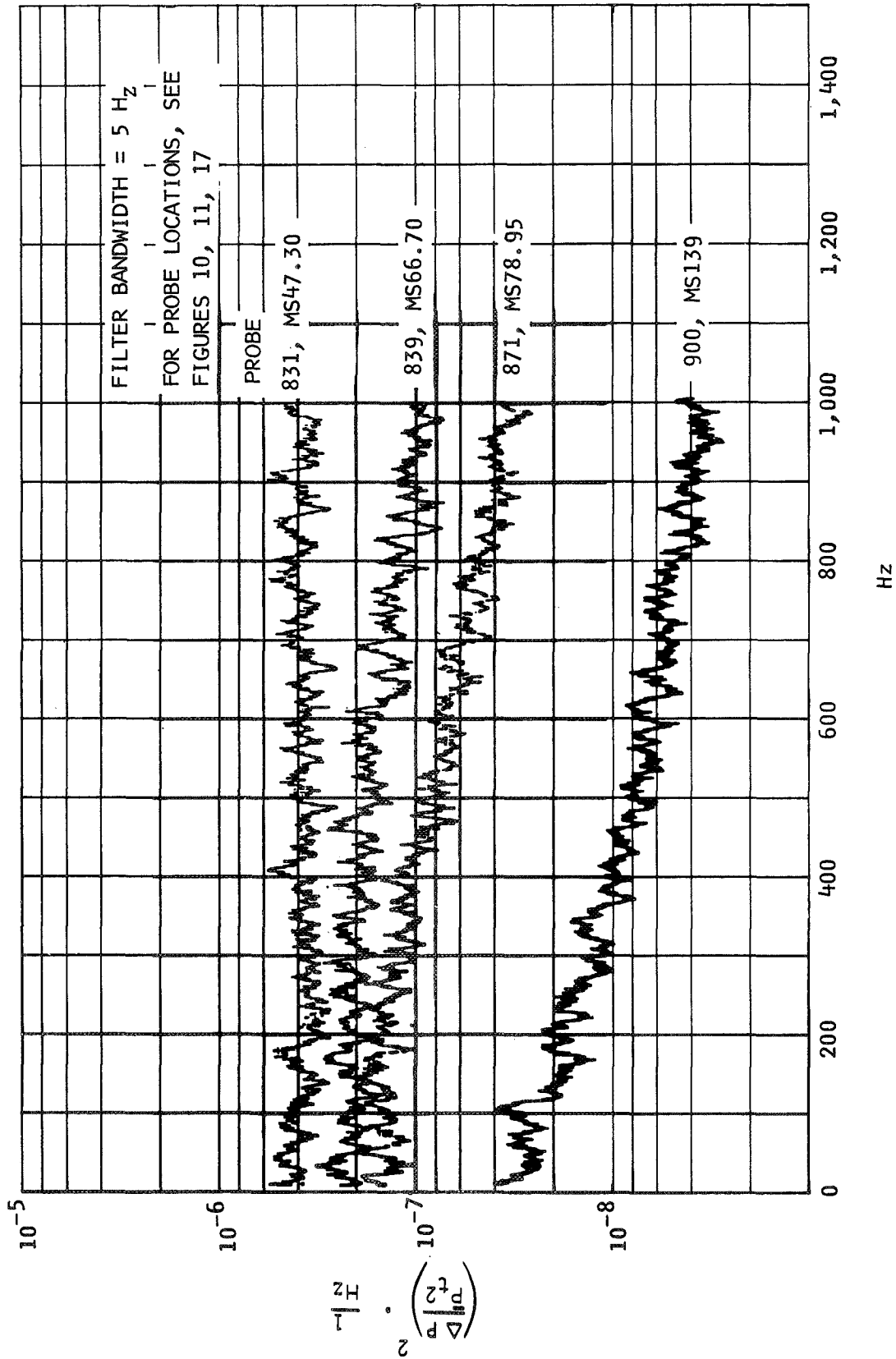


Figure 94.- Total pressure power spectral density variation with station, $M_0 = 3.0$, $\bar{P}_{t2}/P_{t0} = 0.877$.

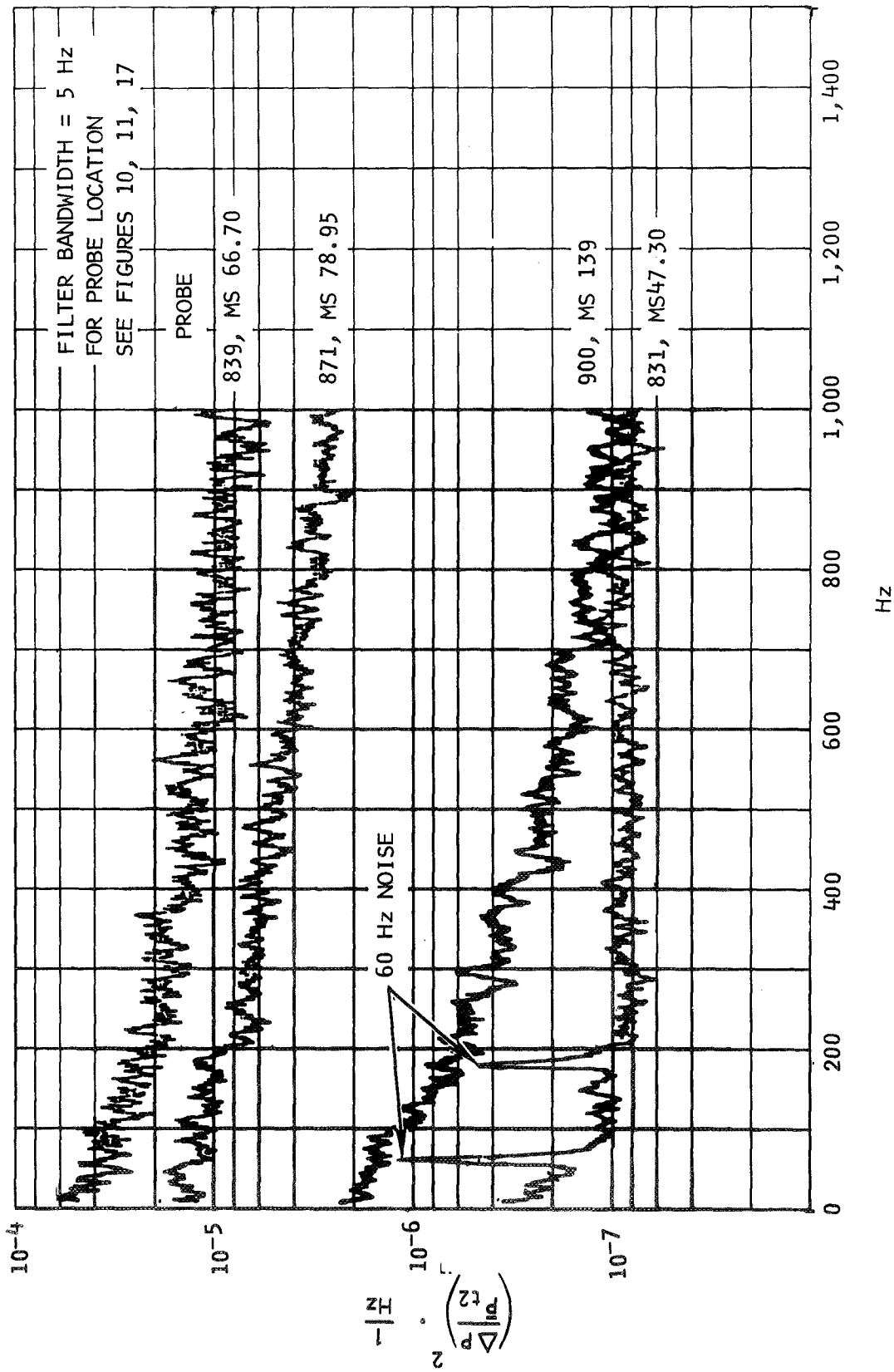


Figure 95. - Total pressure power spectral density variation with station, $M_0 = 3.0$, $\bar{P}_{t2}/P_{t0} = 0.565$.

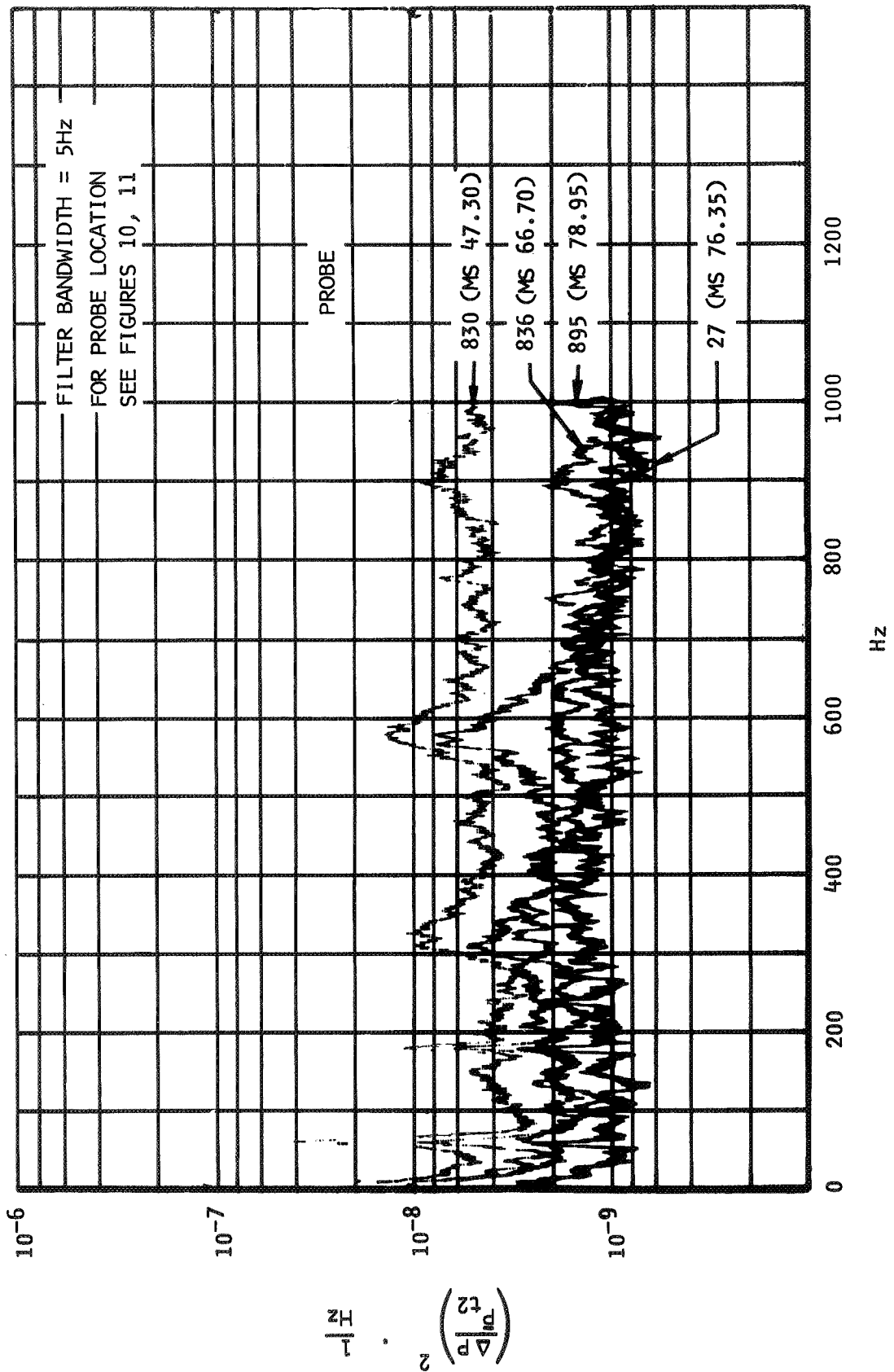


Figure 96.- Static pressure power spectral density variation with station, NASA/Ames axisymmetric inlet, $M_0 = 3.0$, $P_{t2}/P_{t0} = 0.877$.

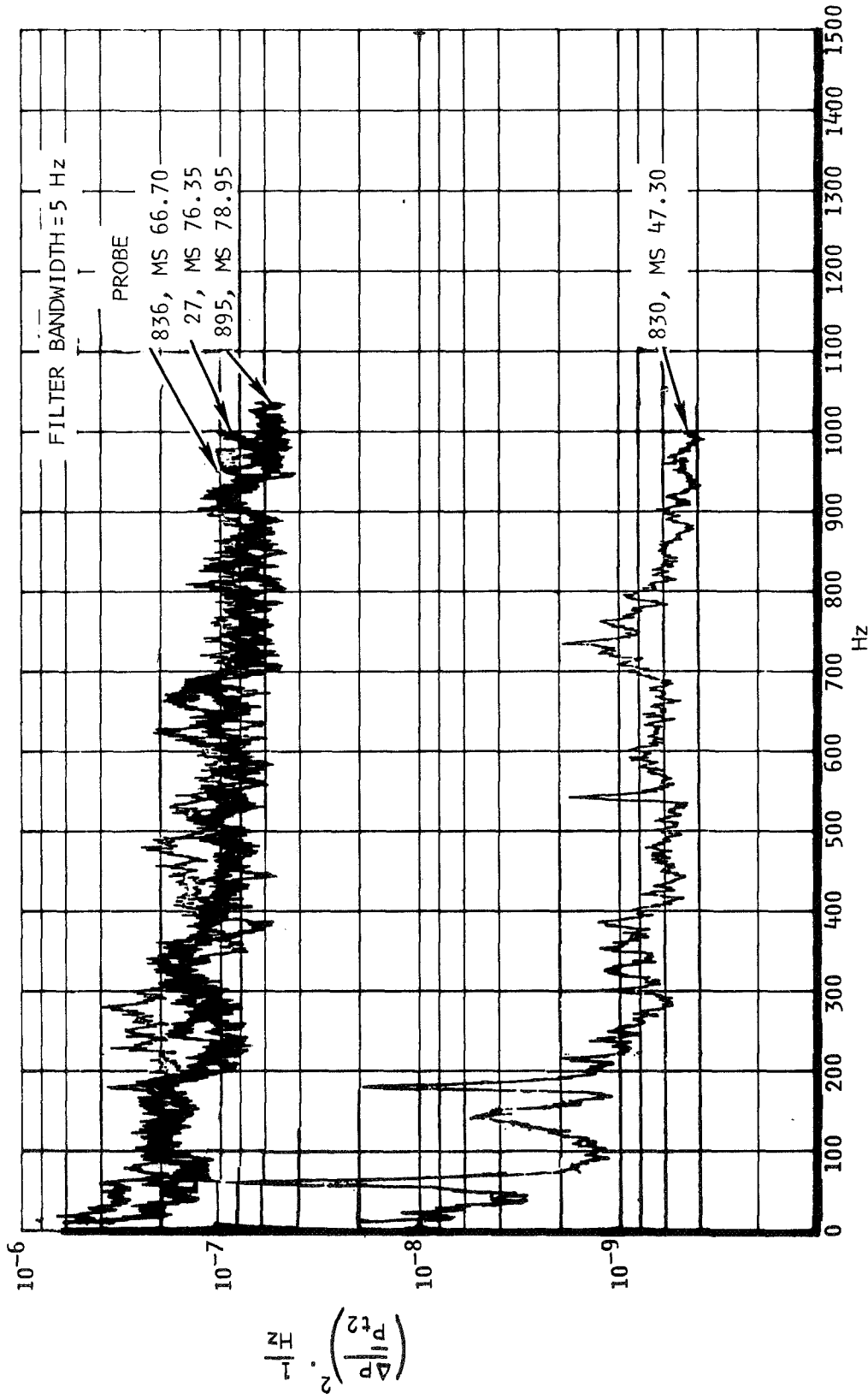


Figure 97.- Static pressure power spectral density variation with station, $M_0 = 3.0$, $\bar{P}_{t2}/P_{t0} = 0.565$.

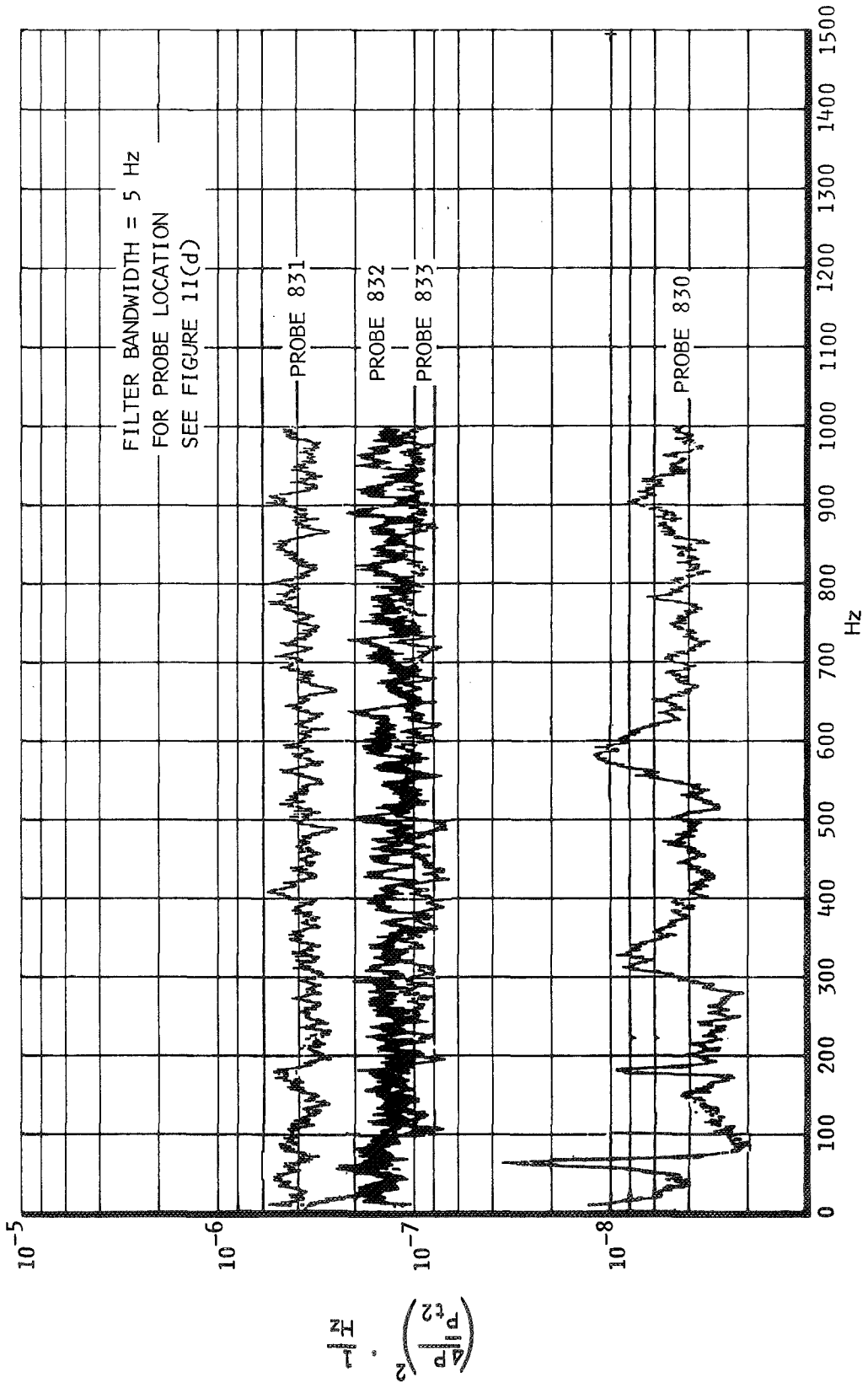


Figure 98.- Power spectral densities at rake MS 47.30, $M_0 = 3.0$, $\bar{P}_{t2}/P_{t0} = 0.877$.

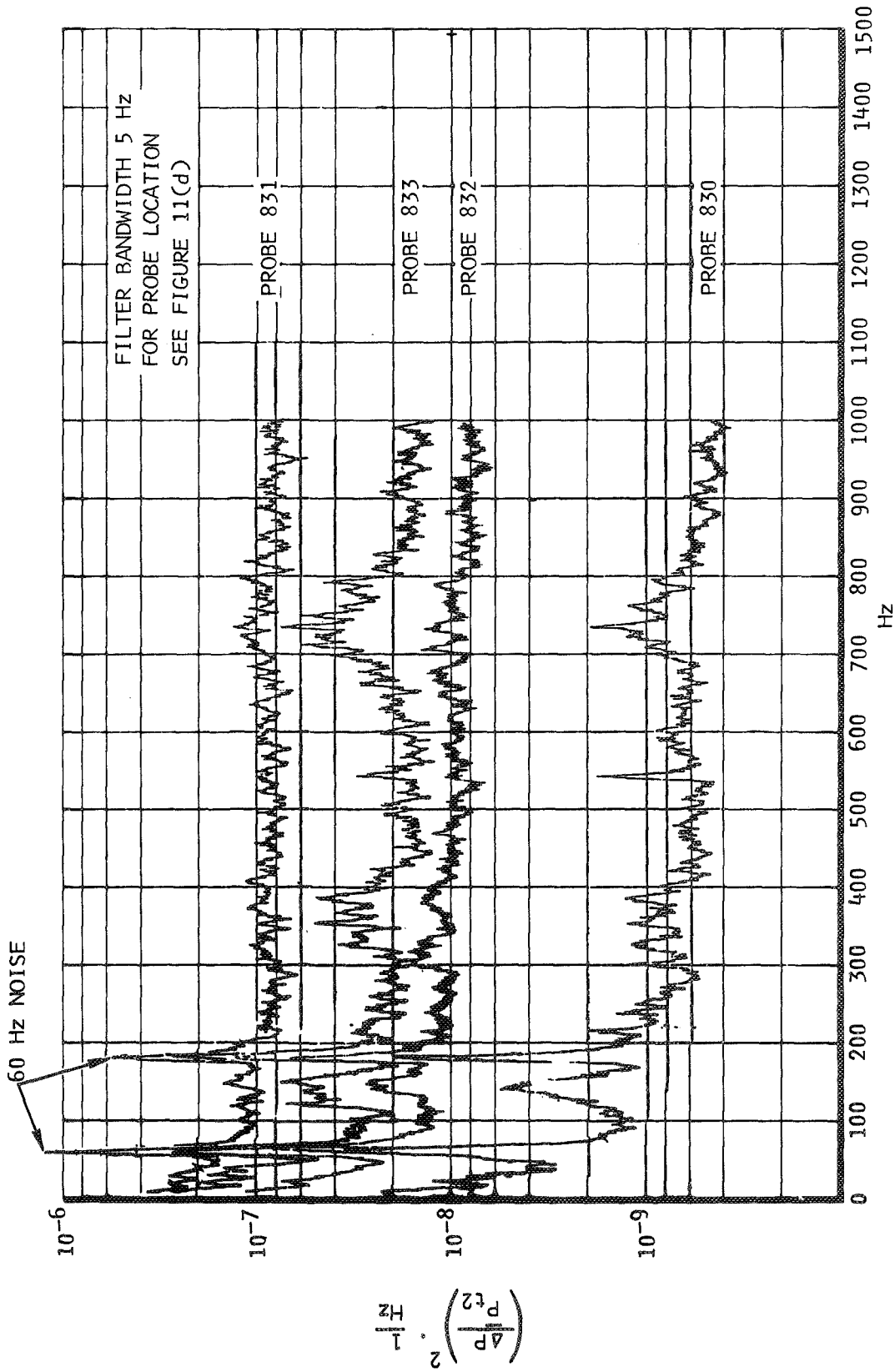


Figure 99.- Power spectral densities at rake MS 47.30, $M_0 = 3.0$, $\bar{P}_{t2}/P_{t0} = 0.565$.

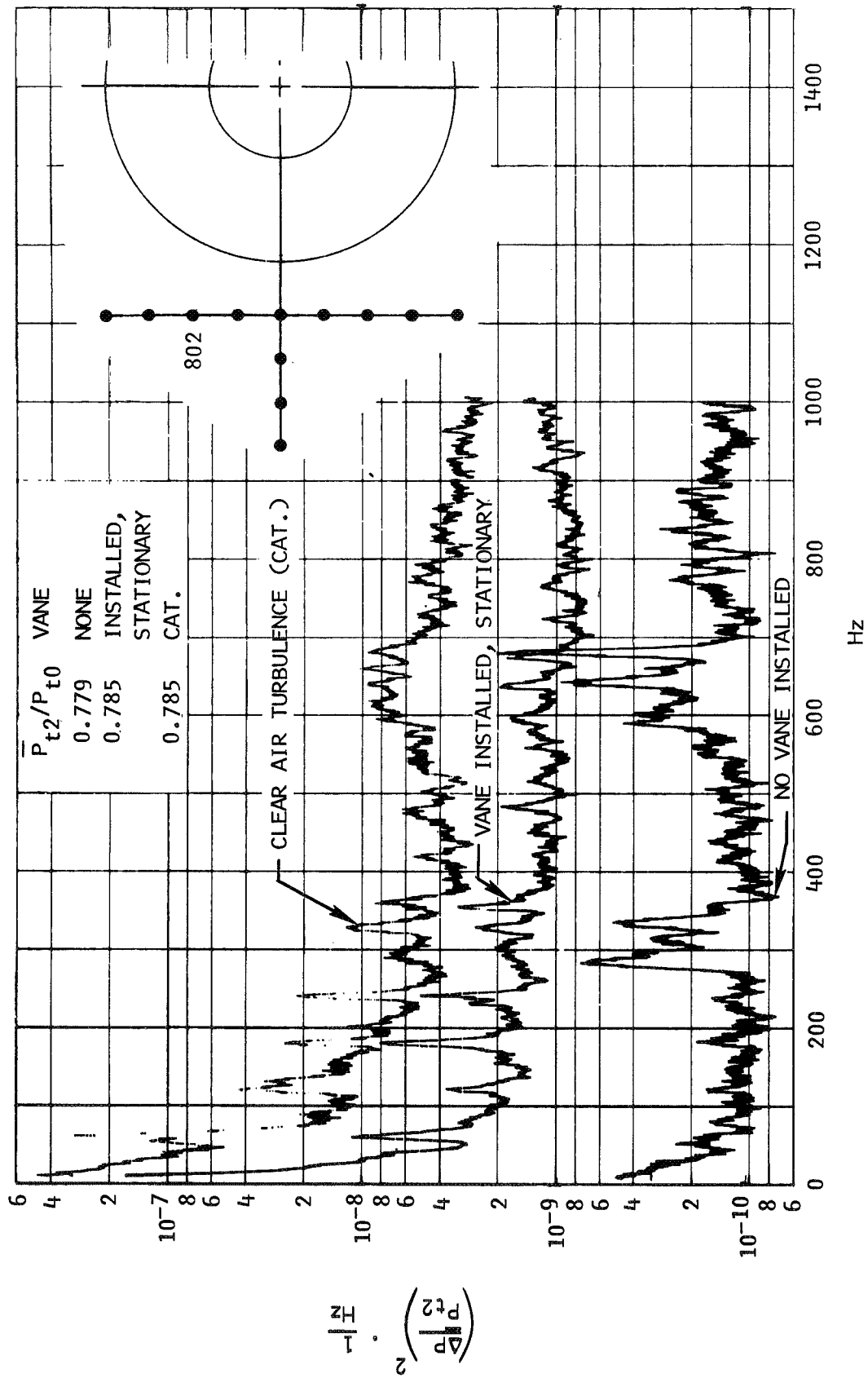


Figure 100.- Power spectral densities showing effects of disturbance vane, probe 802, $M_0 = 3.0$.

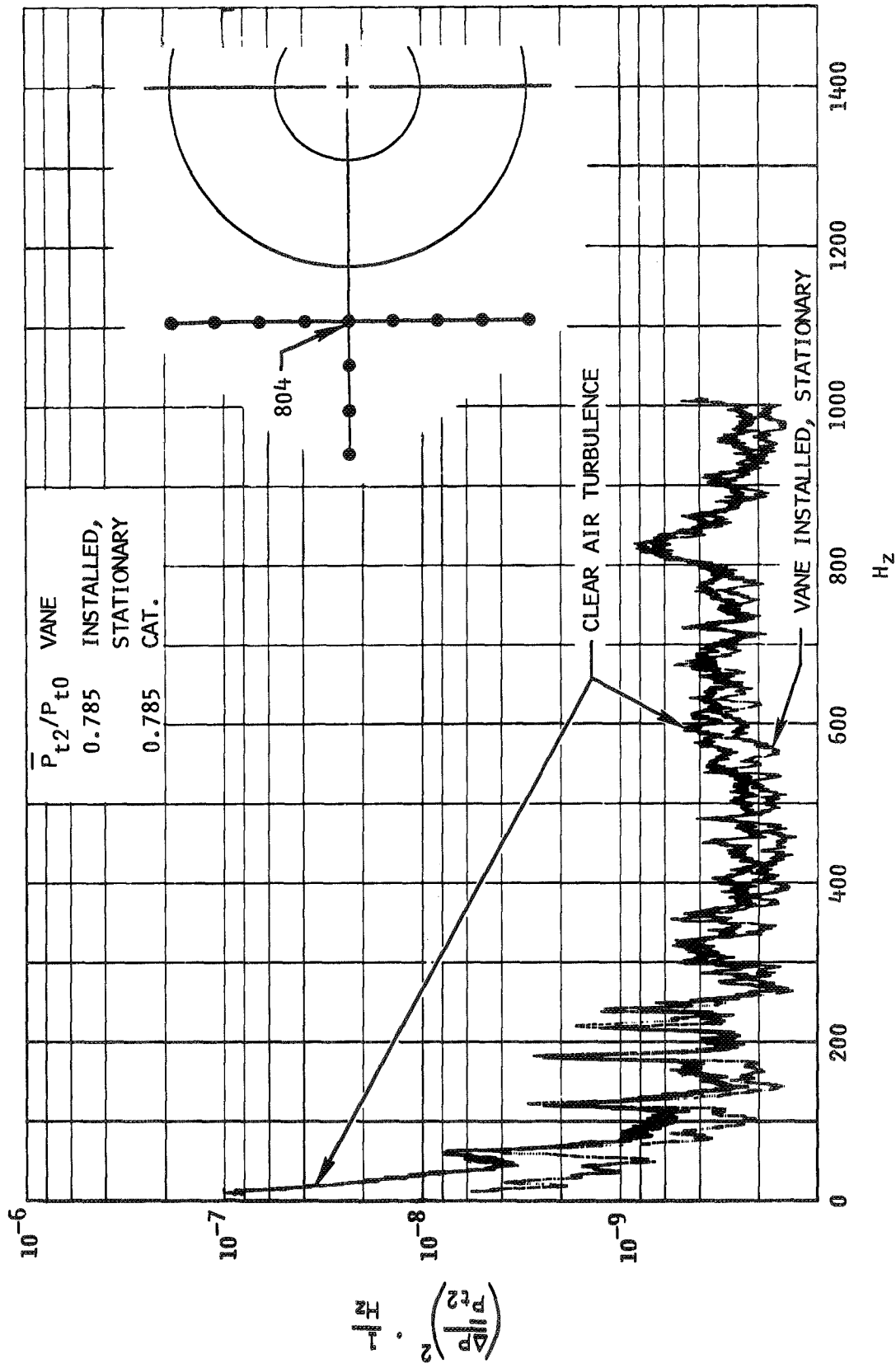


Figure 101.- Power spectral densities showing effects of disturbance vane, probe 804, $M_0 = 3.0$.

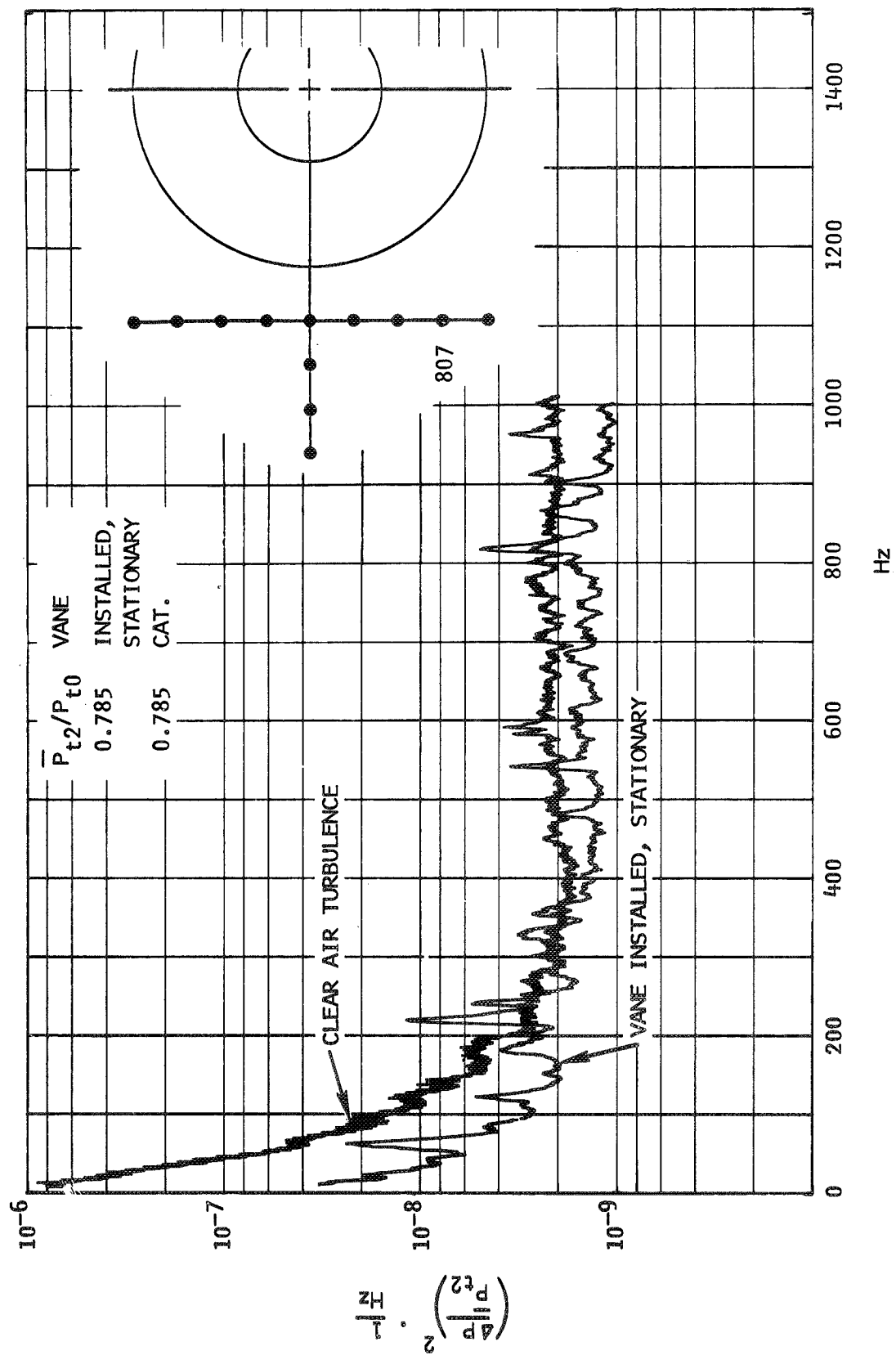


Figure 102.- Power spectral densities showing effects of disturbance vane, probe 807, $M_0 = 3.0$.

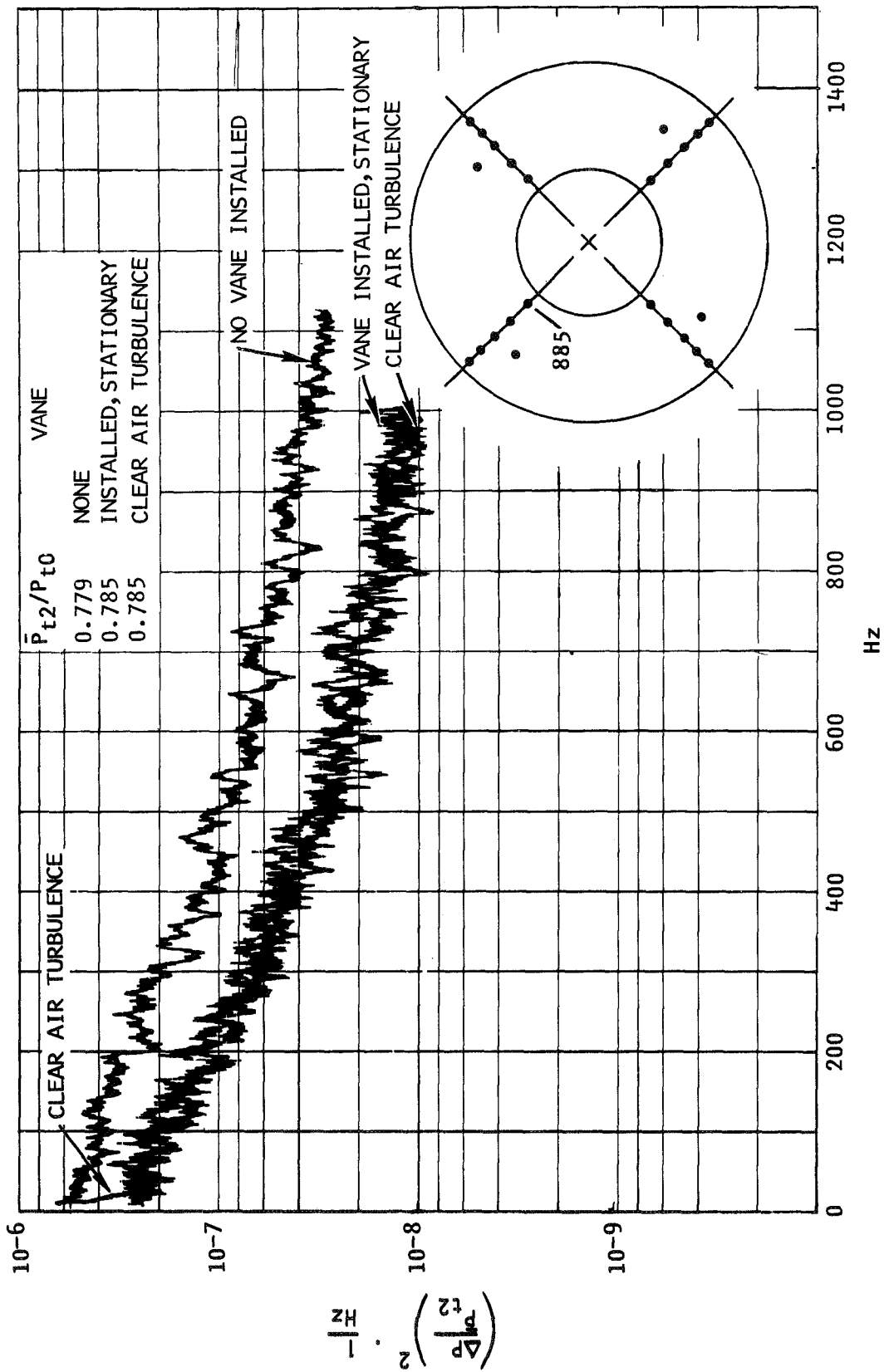


Figure 103.- Power spectral density showing effects of disturbance vane, probe 885, $M_0 = 3.0$.

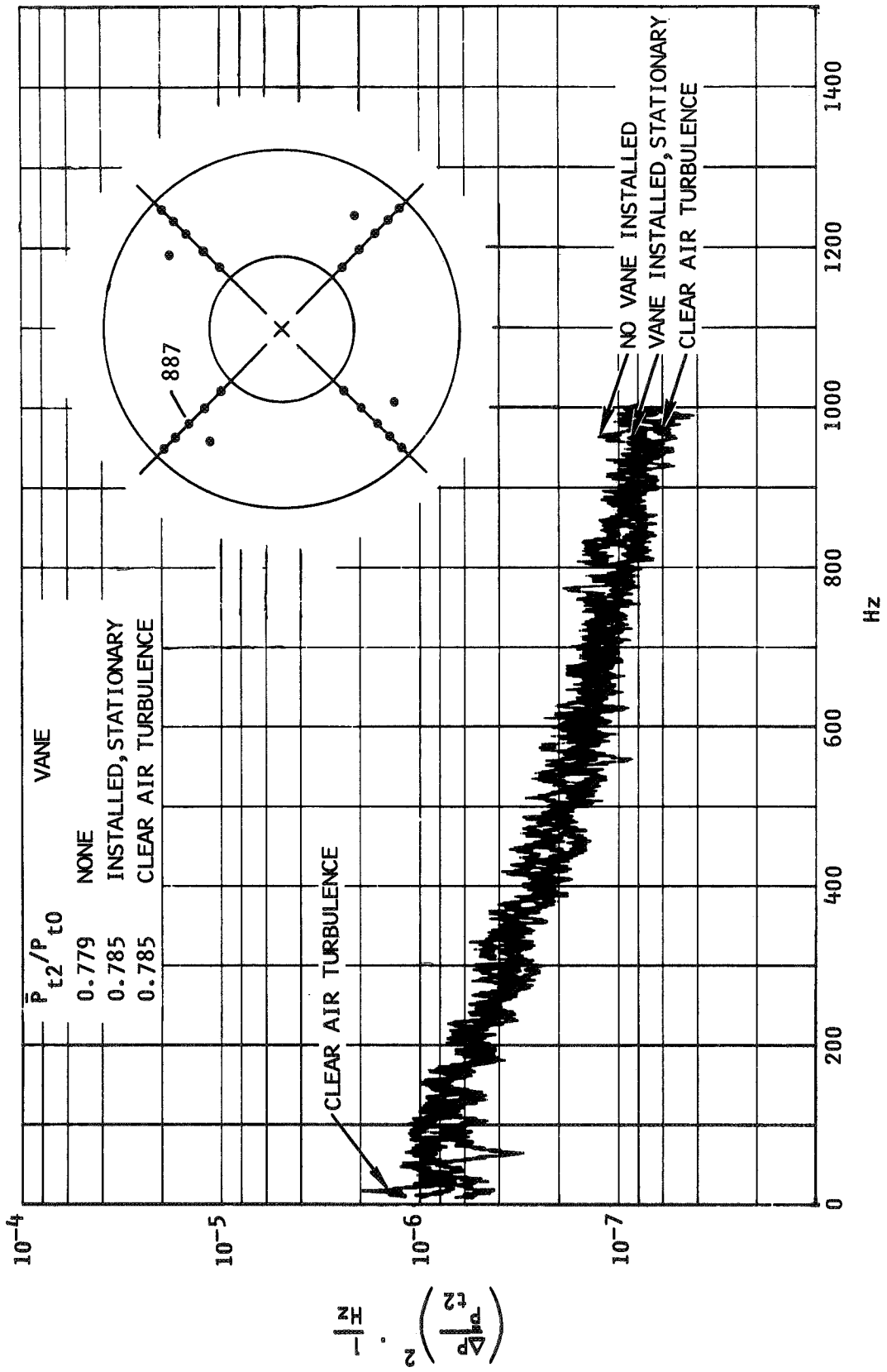


Figure 104.- Power spectral densities showing effects of disturbance vane, probe 887, $M_0 = 3.0$.

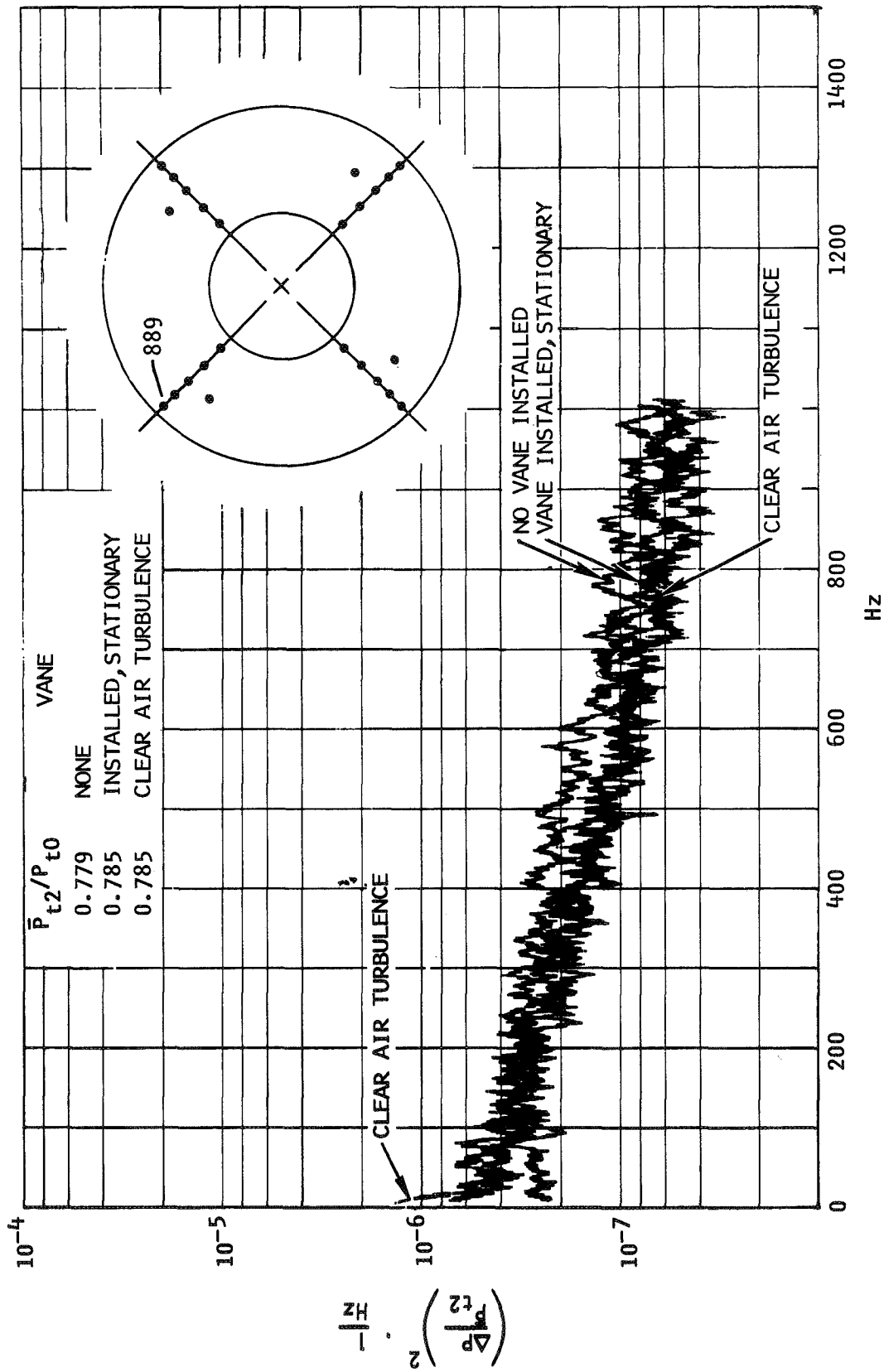
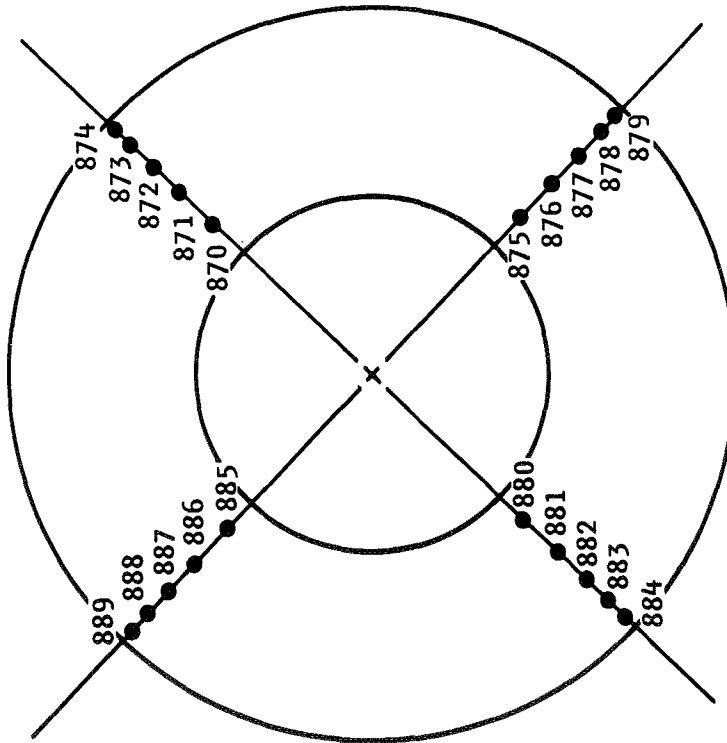


Figure 105.- Power spectral densities showing effects of disturbance vane, probe 889, $M_0 = 3.0$.



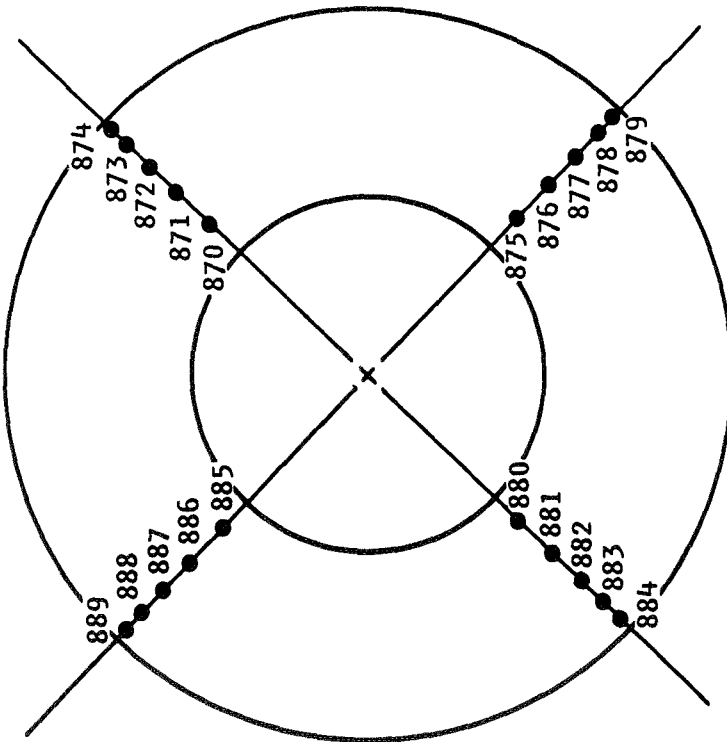
20 Hz

(a)

Probe No.	$\bar{P}_{t_2}/P_{t_0}=0.877$	$\bar{P}_{t_2}/P_{t_0}=0.565$
	COHERENCE FUNCTION	
870, 872	0.05	0.10
870, 874	-	0.09
870, 880	0.08	0.02
870, 885	0.03	0.03
871, 872	0.06	0.13
872, 873	0.10	0.42
872, 887	0.01	0.51
874, 884	0.29	0.01
874, 889	0.06	0.03
876, 877	0.17	0.78
877, 878	0.26	0.72
877, 882	0.02	-
880, 882	0.01	-
880, 884	-	0.19
881, 882	0.33	-
882, 883	0.09	-
886, 887	0.08	0.96
887, 888	0.04	0.87

Figure 106.- Engine face coherence, $M_0 = 3.0$.

Probe No.	$\bar{P}_{t_2/P_{t_0}=0.877}$	$\bar{P}_{t_2/P_{t_0}=0.565}$
	COHERENCE FUNCTION	
870,872	0.03	0.13
870,874	-	0
870,880	0.04	0
870,885	0	0.09
871,872	0.07	0.40
872,873	0.06	0.60
872,887	0.08	0.35
874,884	0.06	0
874,889	0.08	0
876,877	0.08	0.63
877,878	0.24	0.87
877,882	0.02	0.04
880,882	0.04	-
880,884	0.10	-
881,882	0.25	-
882,883	0.07	-
886,887	0.08	0.50
887,888	0.11	0.81

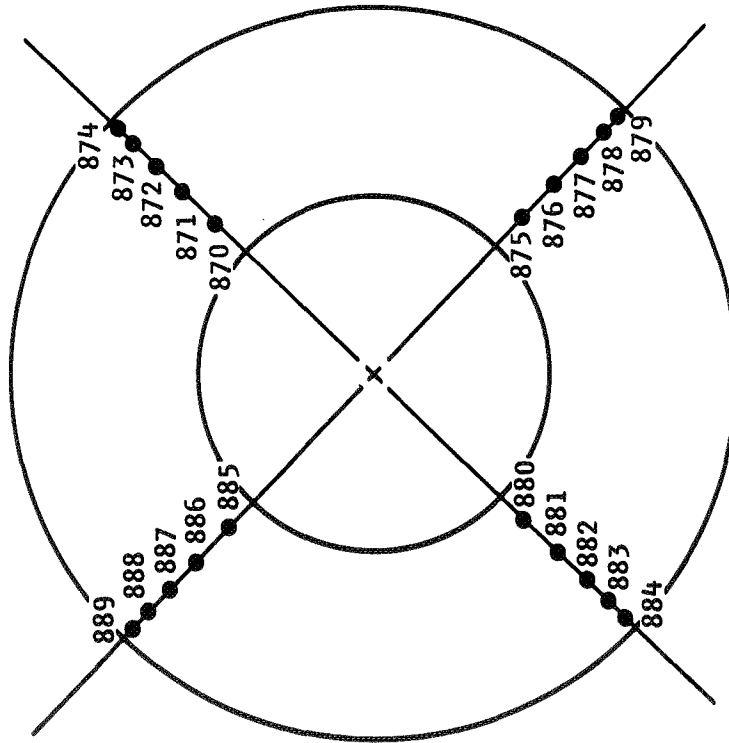


40 Hz

(b)

Figure 106.- Continued.

Probe No.	$\bar{P}_{t_2/P_{t_0}}=0.877$	$\bar{P}_{t_2/P_{t_0}}=0.565$
	COHERENCE FUNCTION	
870, 872	0.01	0.05
870, 874	-	0
870, 880	0.11	0.02
870, 885	0	0.01
871, 872	0.09	0.70
872, 873	0.08	0.96
872, 887	0.04	0.64
874, 884	0	0.06
874, 889	0.09	0.03
876, 877	0.09	0.61
877, 878	0.22	0.72
877, 882	0.004	0.08
880, 882	0	-
880, 884	-	0.26
881, 882	-	-
882, 883	0.06	-
886, 887	0.05	0.83
887, 888	0.25	1.0

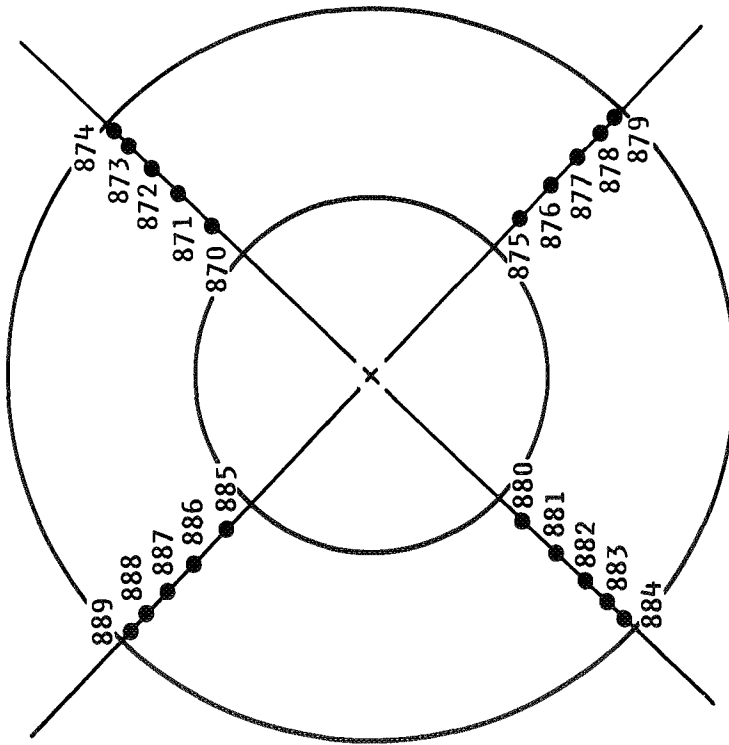


80 Hz

(c)

Figure 106.- Continued.

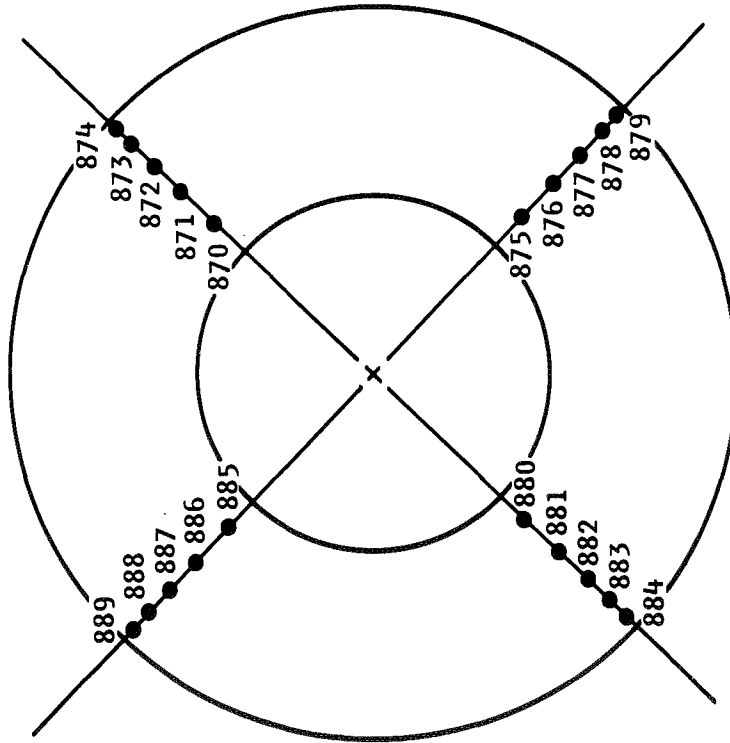
Probe No.	$\bar{P}_{t_2/P_{t_0}}=0.877$	$\bar{P}_{t_2/P_{t_0}}=0.565$
	COHERENCE FUNCTION	
870, 872	0	0
870, 874	-	0.18
870, 880	0	0.02
870, 885	0	0.15
871, 872	0.03	0.47
872, 873	0.14	0.80
872, 887	0.02	0.24
874, 884	0	0.15
874, 889	0	0.03
876, 877	0.05	0.70
877, 878	0.37	0.76
877, 882	0.02	0
880, 882	0.03	0
880, 884	-	0.25
881, 882	0.12	-
882, 883	0.13	-
886, 887	0.07	0.90
887, 888	0.17	1.0



100 Hz

(d)

Figure 106.- Continued.



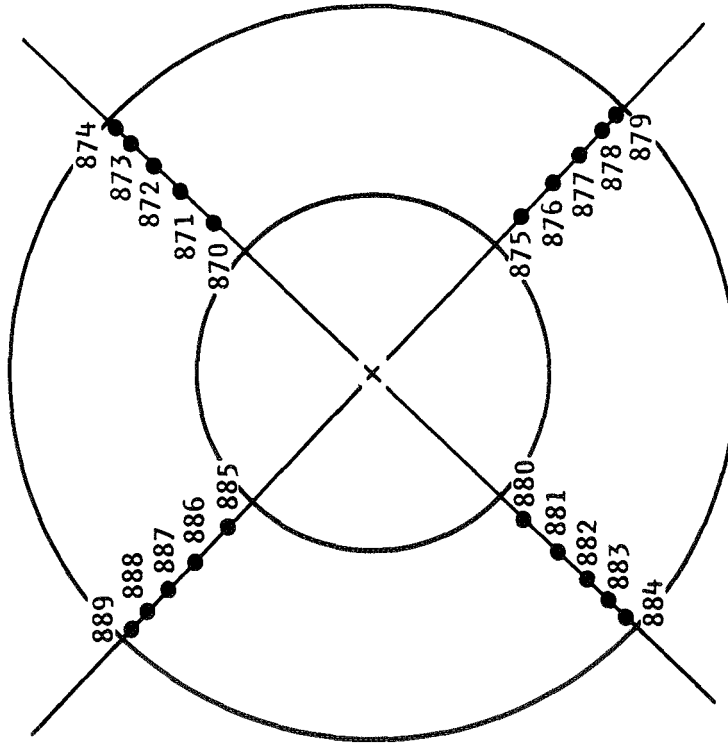
200 Hz

(e)

Probe No.	$\bar{P}_{t_2}/P_{t_0}=0.877$	$\bar{P}_{t_2}/P_{t_0}=0.565$
	COHERENCE FUNCTION	
870, 872	0.07	0
870, 874	-	-
870, 880	0	0
870, 885	0	0
871, 872	0.08	0.22
872, 873	0.10	0.21
872, 887	0.01	0
874, 884	0	0.10
874, 889	0	0.03
876, 877	0.03	0.57
877, 878	0.22	0.76
877, 882	0.01	0
880, 882	0.03	-
881, 882	0.14	-
882, 883	0.24	-
886, 887	0.04	0.55
887, 888	0.23	0.57

Figure 106.- Concluded.

Probe No.	$\bar{P}_{t2}/P_{t0}=0.918$	$\bar{P}_{t2}/P_{t0}=0.642$
	COHERENCE FUNCTION	
870, 872	0.03	0.31
870, 874	-	-
870, 880	0	0
870, 885	0	0.01
871, 872	0.14	0.39
872, 873	-	0.44
872, 887	0.04	0
874, 884	0	-
874, 889	0	-
876, 877	0.34	0.80
877, 878	0.01	0.59
877, 882	0.05	0.02
880, 882	0.32	0.02
880, 884	-	-
881, 882	0.63	0.30
882, 883	0.12	0.48
886, 887	0.20	0.76
887, 888	0	0

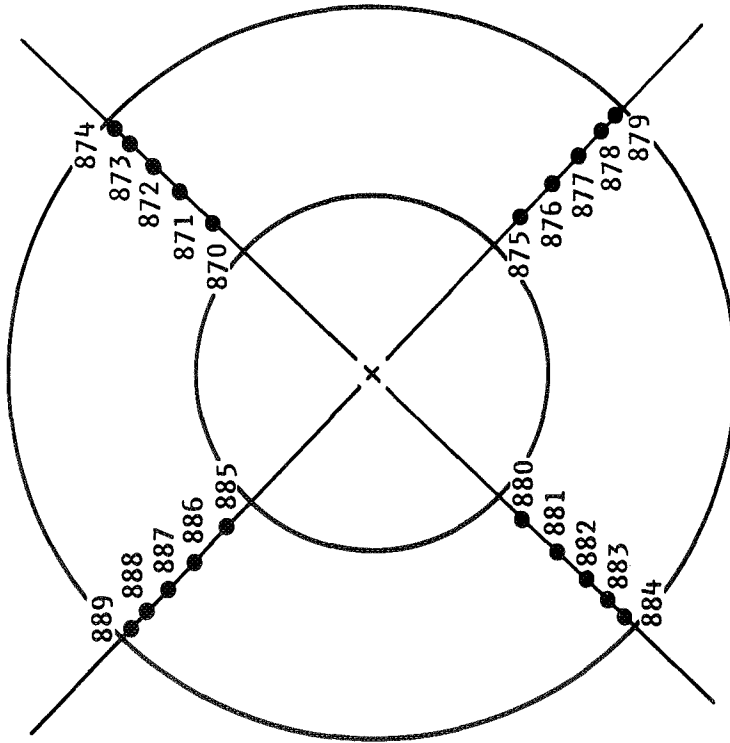


20 Hz

(a)

Figure 107.- Engine face coherence, $M_0 = 2.6$.

Probe No.	$\bar{P}_{t_2}/P_{t_0}=0.918$	$\bar{P}_{t_2}/P_{t_0}=0.642$
	COHERENCE FUNCTION	
870, 872	0.02	0.04
870, 874	-	-
870, 880	0	0.02
870, 885	0	0.08
871, 872	0.02	0.55
872, 873	-	0.57
872, 887	0.04	0.01
874, 884	0	-
874, 889	0	-
876, 877	0.26	0.63
877, 878	0.05	0.54
877, 882	0.03	0.06
880, 882	0.45	0.01
880, 884	-	-
881, 882	1.0	0.56
882, 883	0.17	0.66
886, 887	0.26	0.63
887, 888	0.35	0.62

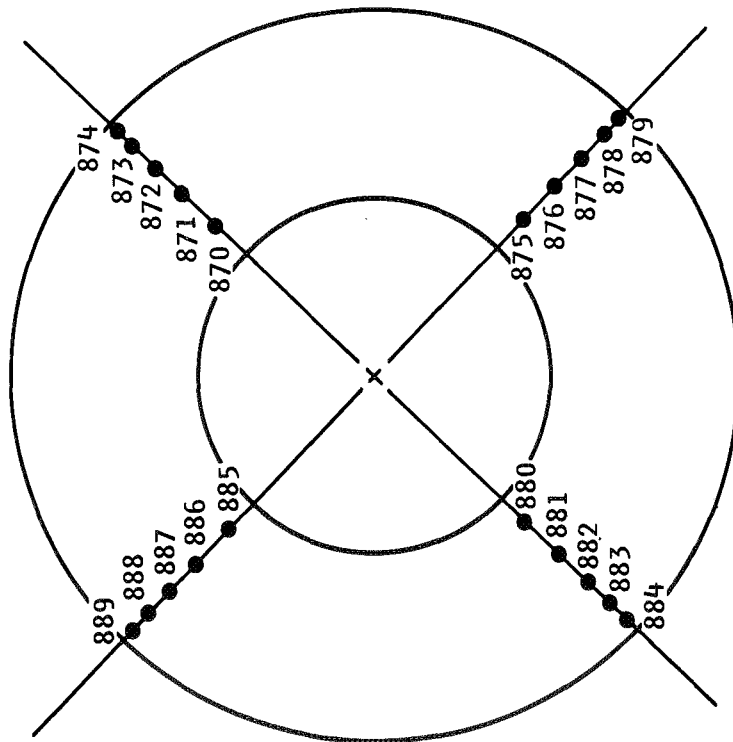


40 Hz

(b)

Figure 107. - Continued.

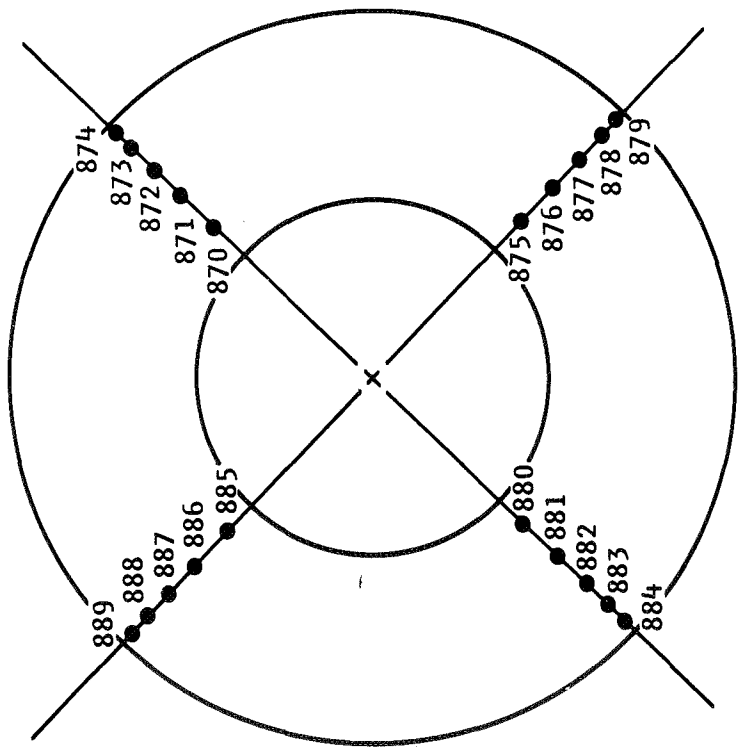
Probe No.	$\bar{P}_{t_2/P_{t_0}}=0.918$	$\bar{P}_{t_2/P_{t_0}}=0.642$
	COHERENCE FUNCTION	
870,872	0.02	0.17
870,874	-	-
870,880	0	0
870,885	0	0.13
871,872	0.10	-
872,873	-	0.83
872,887	0.03	0.03
874,884	0	-
874,889	0	-
876,877	0.33	0.77
877,878	0.16	0.67
877,882	0.01	0.03
880,882	0.23	0.04
880,884	-	-
881,882	0.83	0.29
882,883	0.02	0.67
886,887	0.29	0.53
887,888	0.19	0.51



80 Hz

(c)

Figure 107.- Continued.



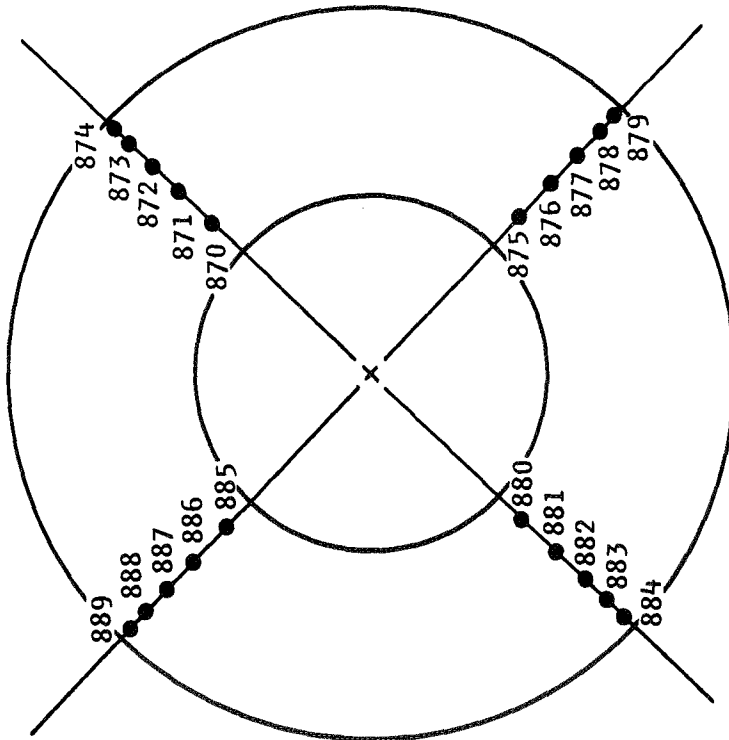
100 Hz

(d)

Probe No.	$\bar{P}_{t_2}/P_{t_0}=0.918$	$\bar{P}_{t_2}/P_{t_0}=0.642$
	COHERENCE FUNCTION	
870, 872	0.02	0.35
870, 874	-	-
870, 880	0	0
870, 885	0	0.16
871, 872	0.10	0.38
872, 873	-	-
872, 887	0.13	0.03
874, 884	0	0.02
874, 889	0	-
876, 877	0.33	0.47
877, 878	0.27	0.43
877, 882	0.17	0.04
880, 882	0.03	0.02
880, 884	-	-
881, 882	0.42	0.14
882, 883	0.01	0.70
886, 887	0.31	0.52
887, 888	0.33	0.94

Figure 107.- Continued.

Probe No.	$\bar{P}_{t_2}/P_{t_0}=0.918$	$\bar{P}_{t_2}/P_{t_0}=0.642$
	COHERENCE FUNCTION	
870,872	0	0.01
870,874	-	-
870,885	0	0.01
871,872	0.04	0.09
872,873	-	0.38
872,887	0.03	0
874,884	0	-
874,889	0	-
876,877	0.17	0.48
877,878	0.05	0.48
877,882	0.02	0
880,882	0	0.02
880,884	-	-
881,882	0.28	0.20
882,883	0.01	0.31
886,887	0.23	0.37
887,888	0.26	0.46



200 Hz

(e)

Figure 107.- Concluded.

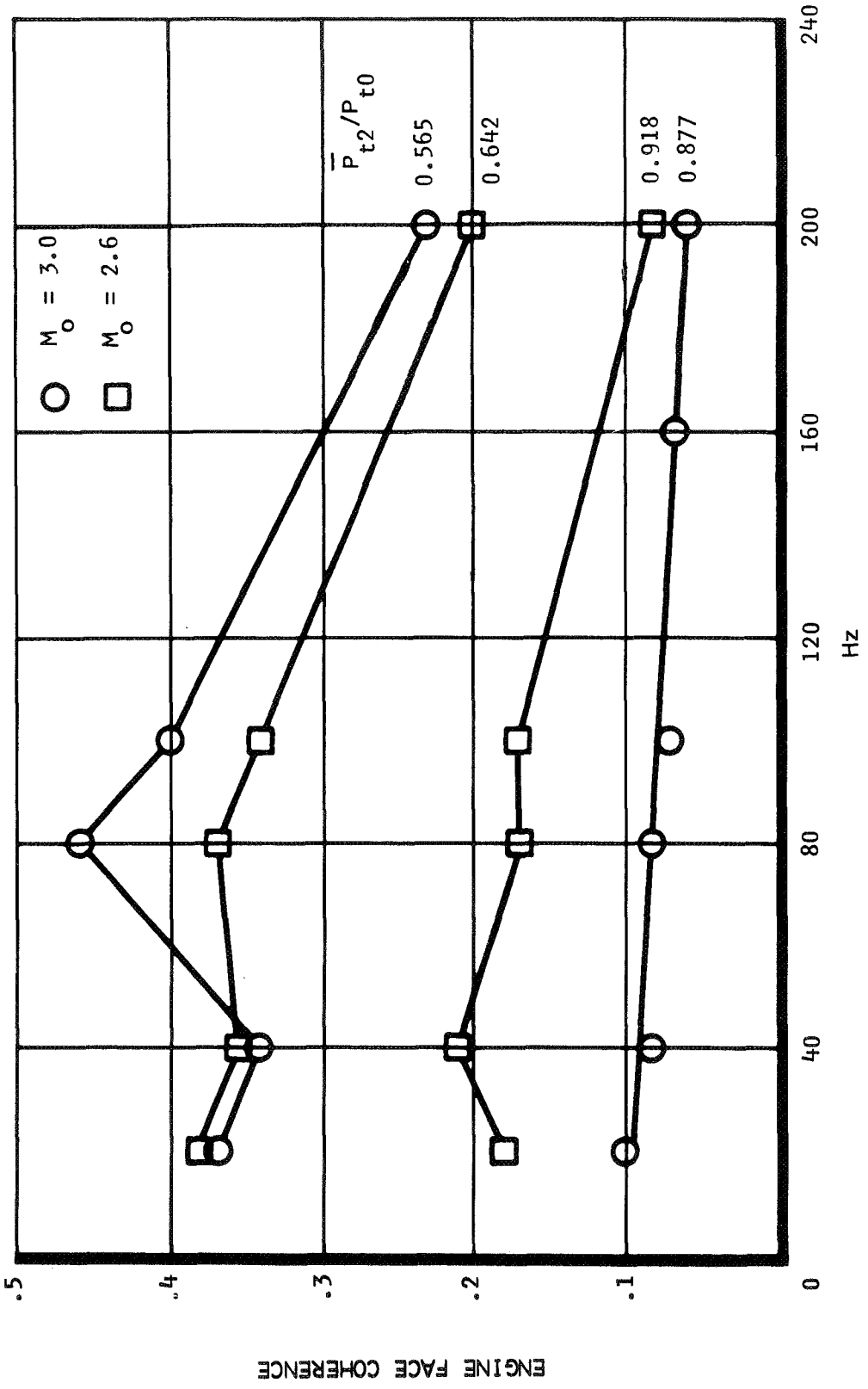
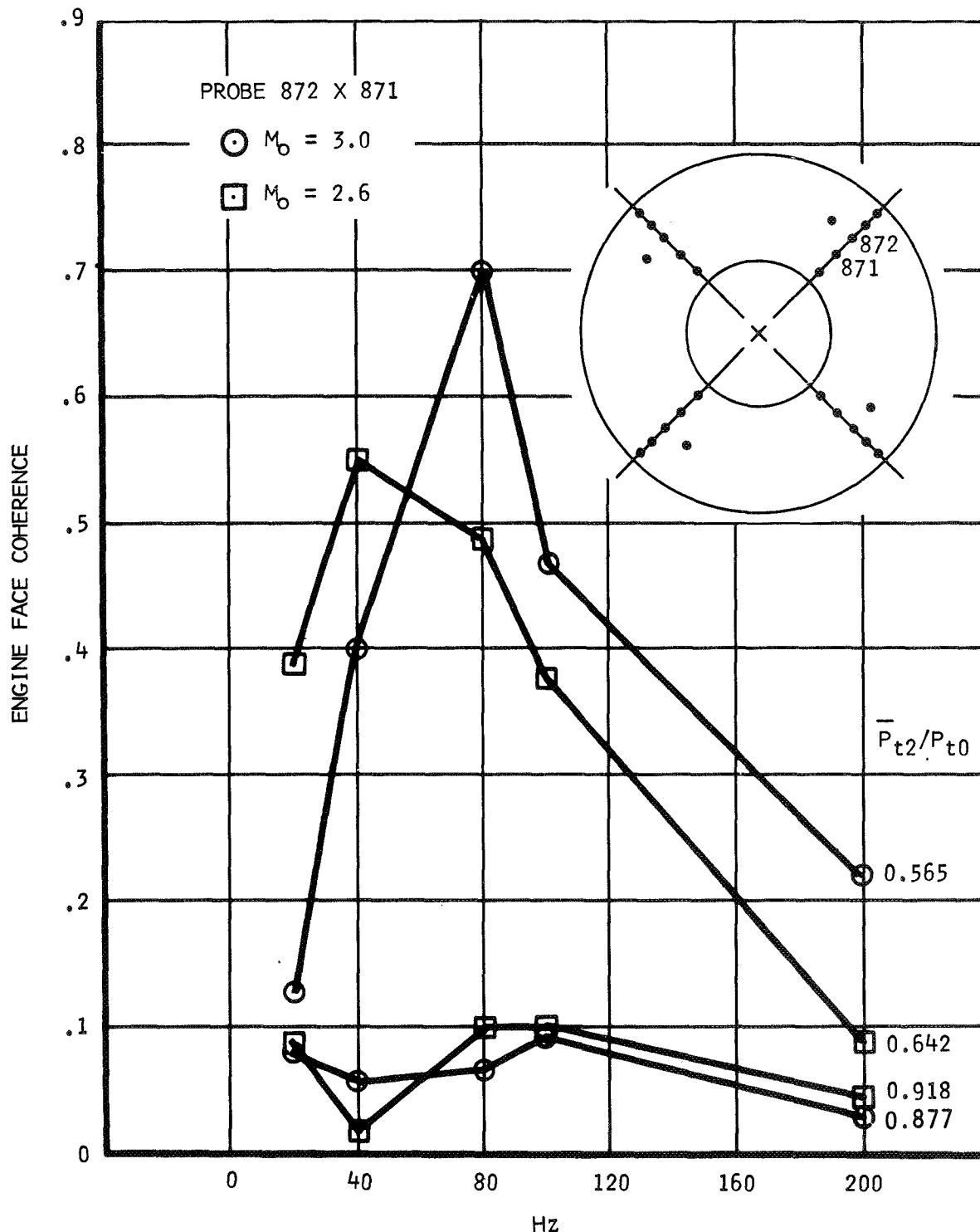
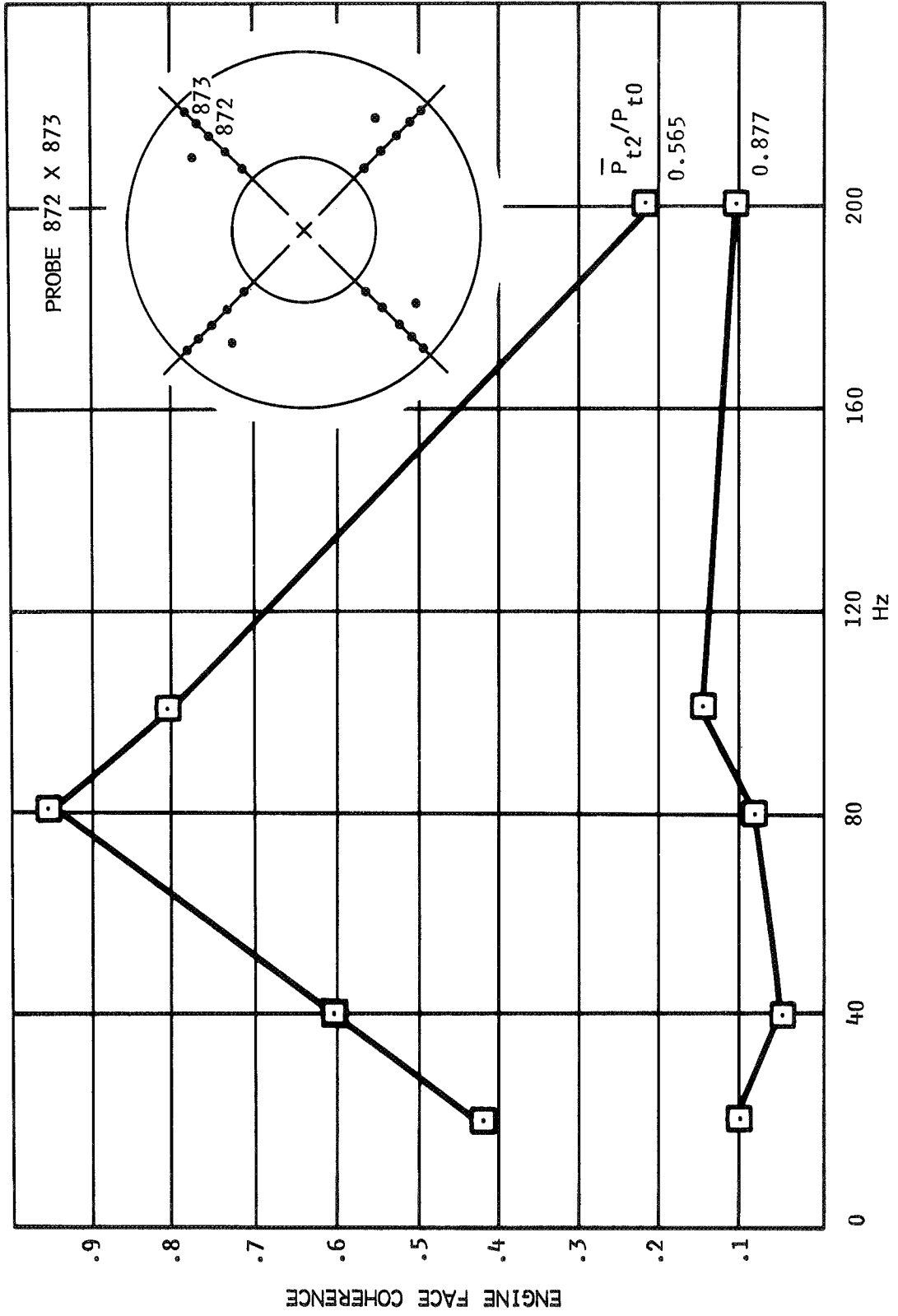


Figure 108.- Average coherence function - 13 engine face pairs.



(a)

Figure 109.- Coherence functions for adjacent probes on the same rake.



(b)
Figure 109.- Concluded

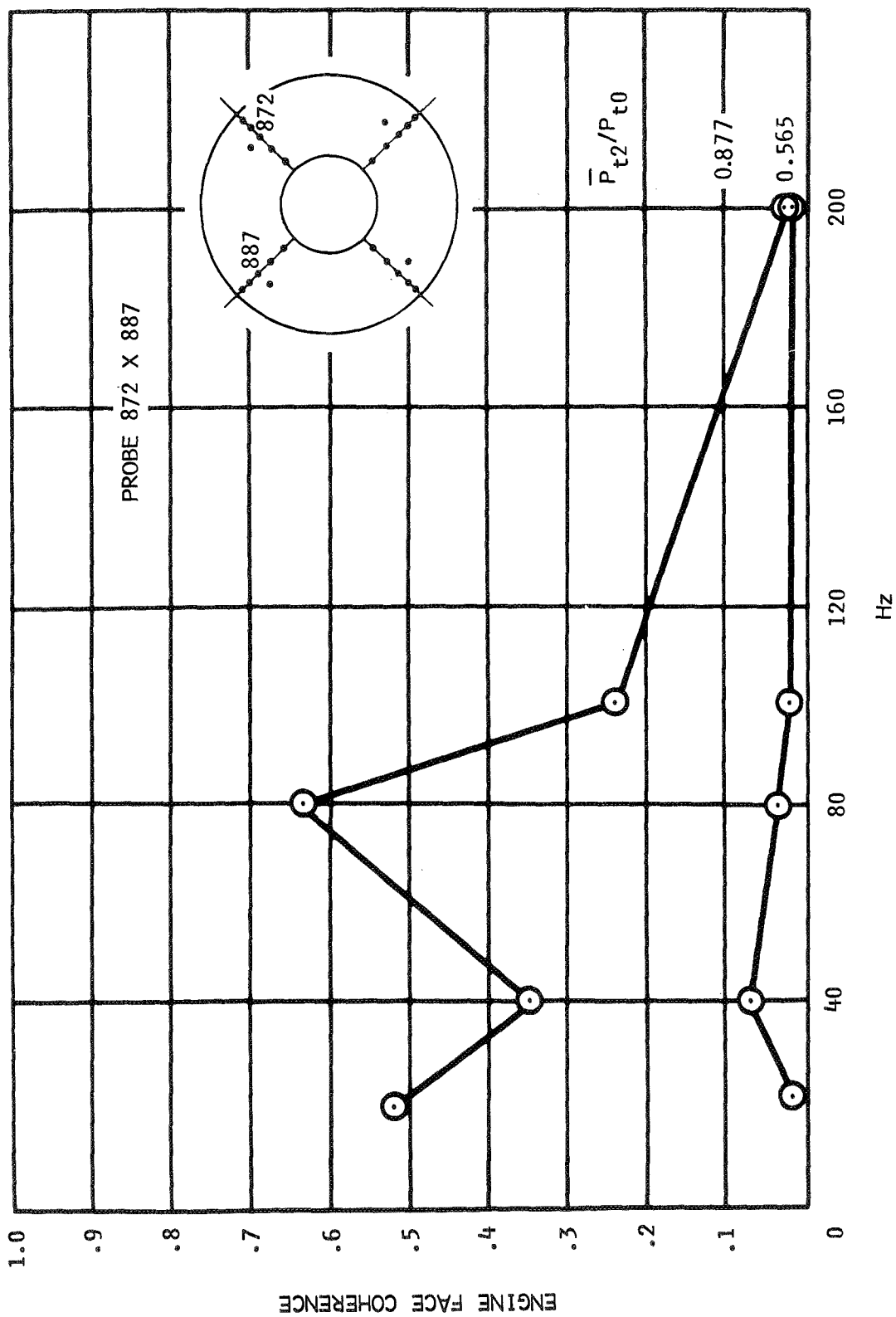


Figure 110.- Coherence function for equiradius probes on different rakes, $M_0 = 3.0$.

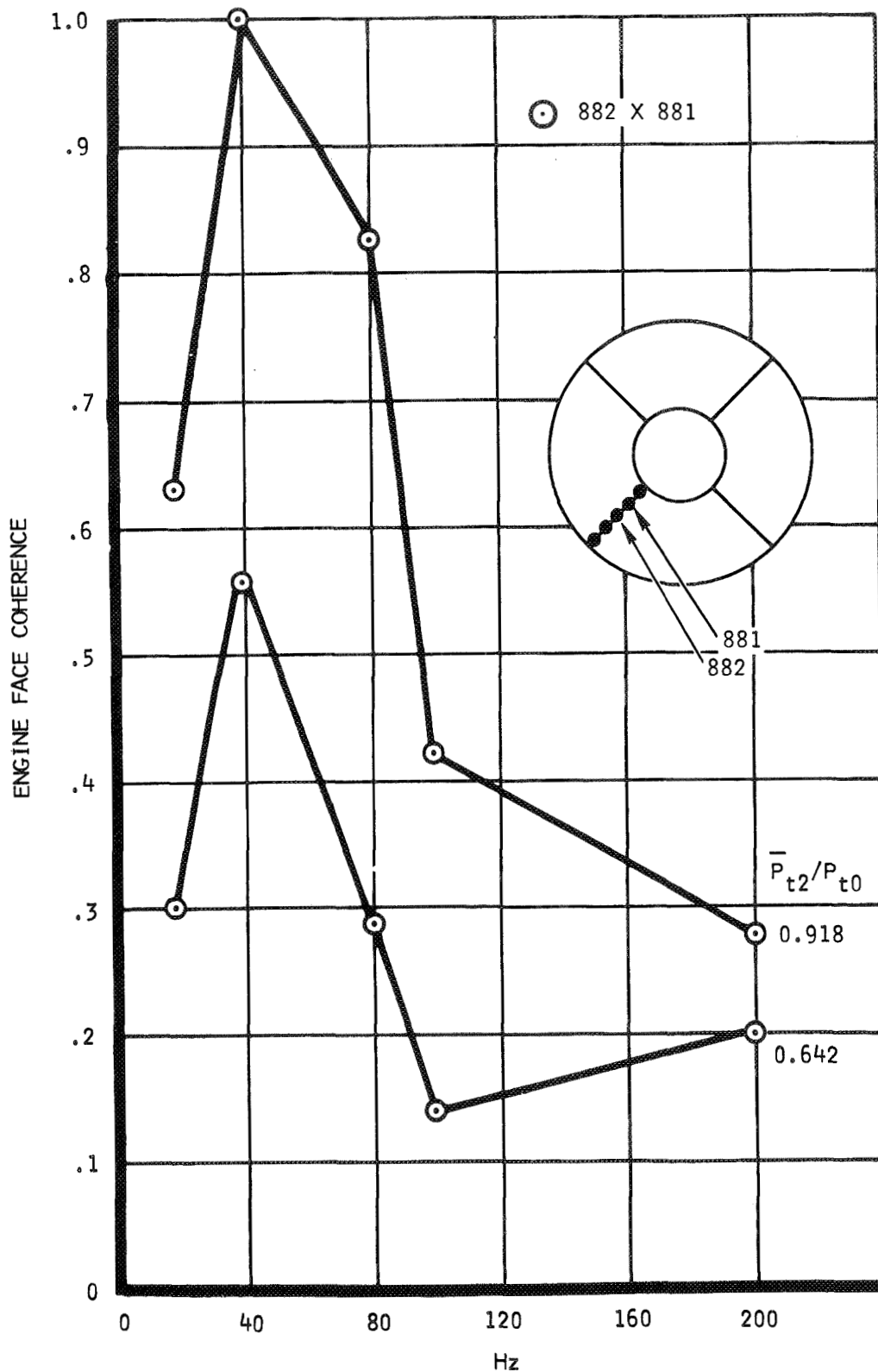


Figure 111. Coherence function inversion, $M_0 = 2.6$.

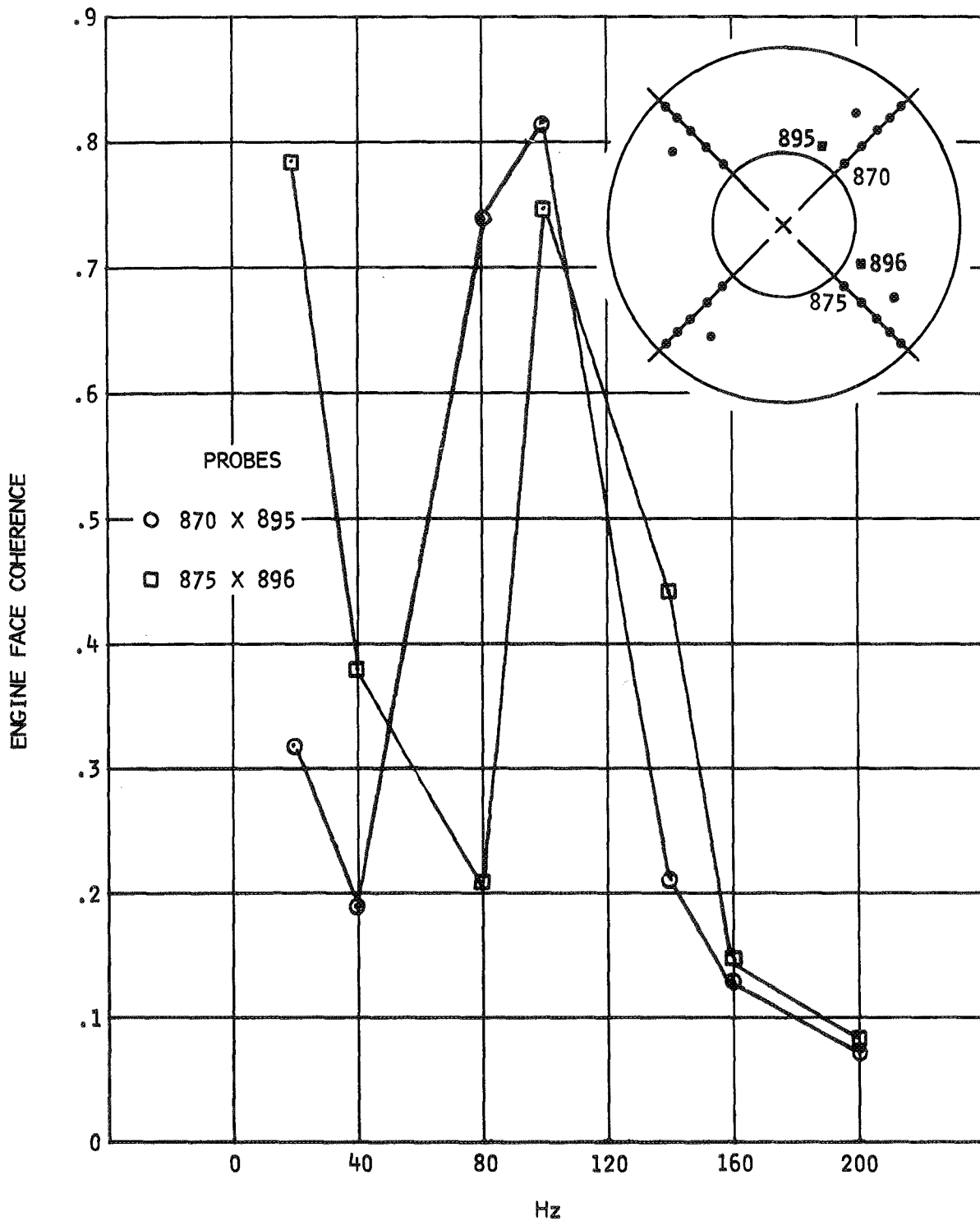


Figure 112.- Engine face coherence between static and total pressures, $M_0 = 3.0$, $\bar{P}_{t2}/P_{t0} = 0.565$.

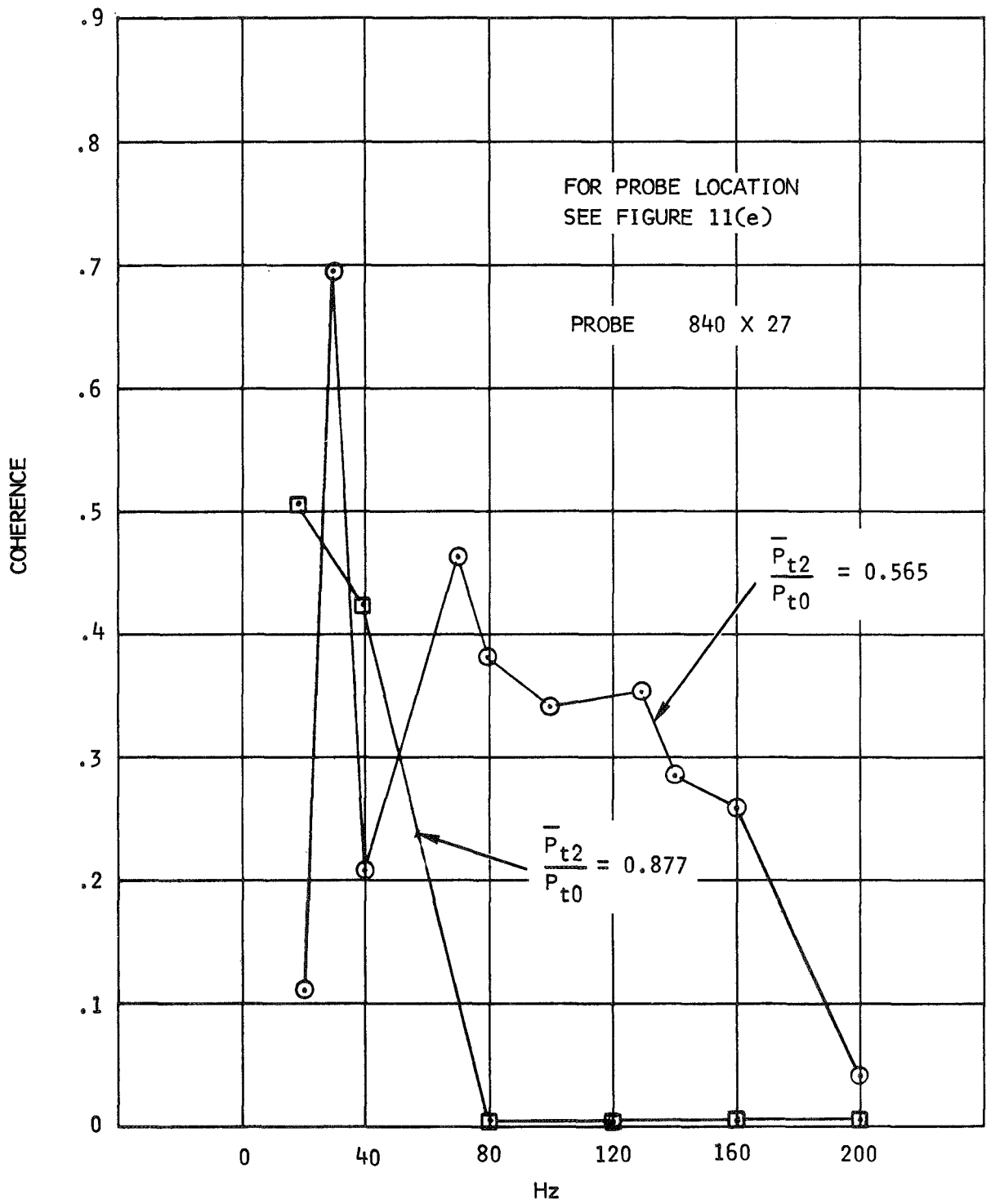


Figure 113.- Subsonic diffuser coherence function for probes on opposite sides of duct, MS 76.35, $M_0 = 3.0$.

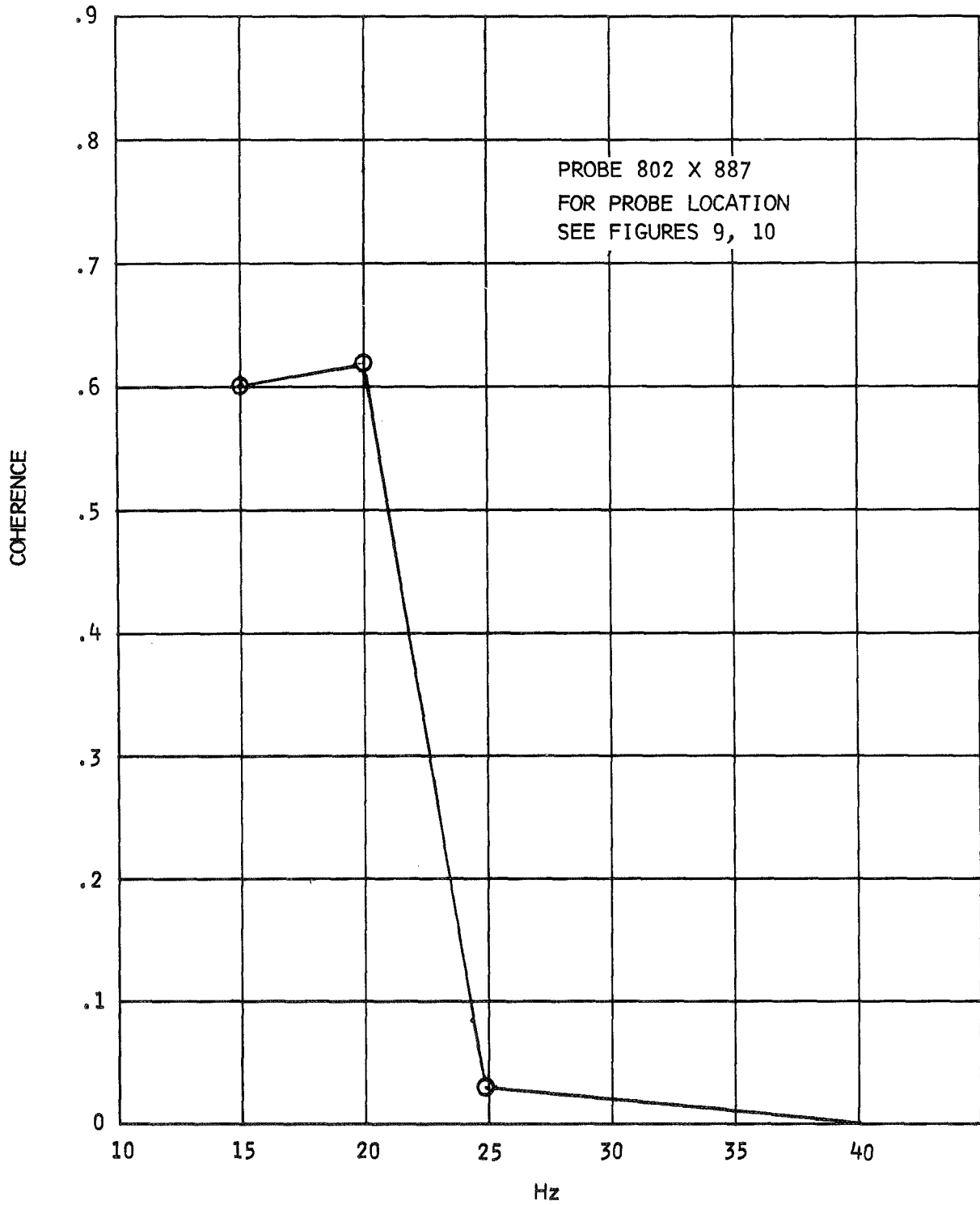


Figure 114.- External to engine face total pressure coherence with clear air turbulence, $M_0 = 3.0$, $\bar{P}_{t2}/P_{t0} = 0.785$.

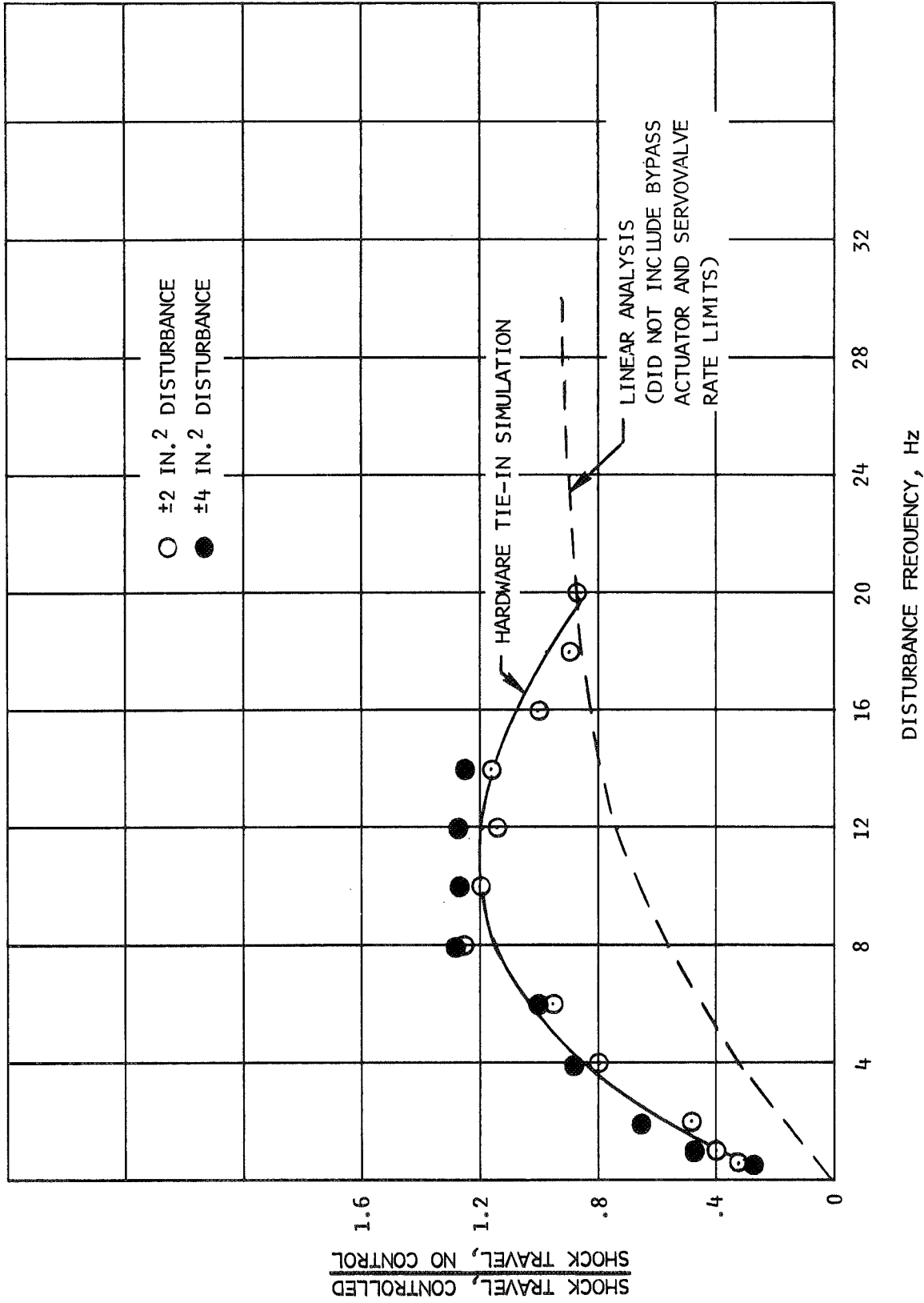


Figure 115.- Shock position control system performance with sinusoidal exit area disturbances, $M_0 = 3.0$.

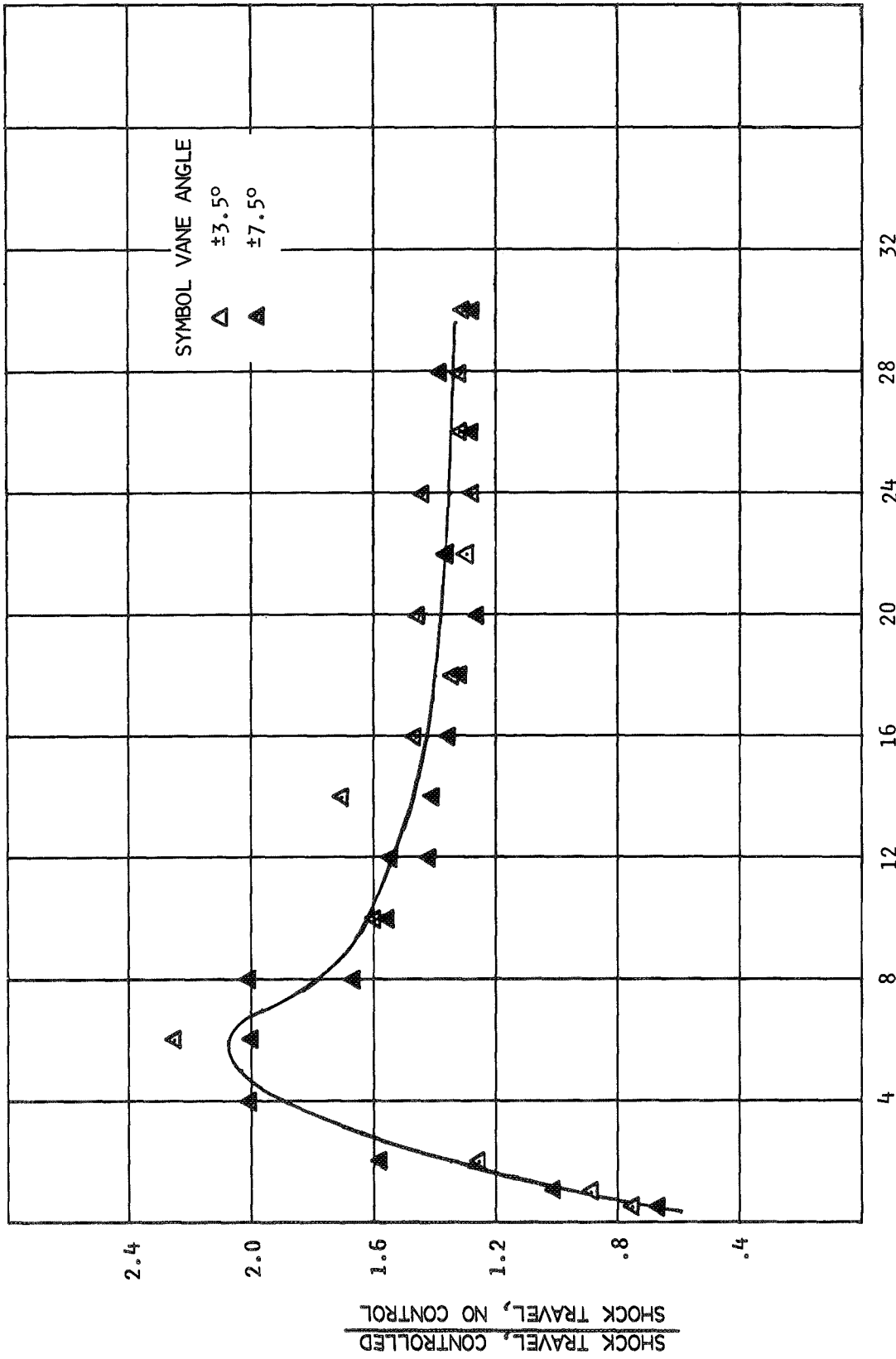


Figure 116. - Shock position control system performance with sinusoidal vane angle disturbances, $M_0 = 3.0$.

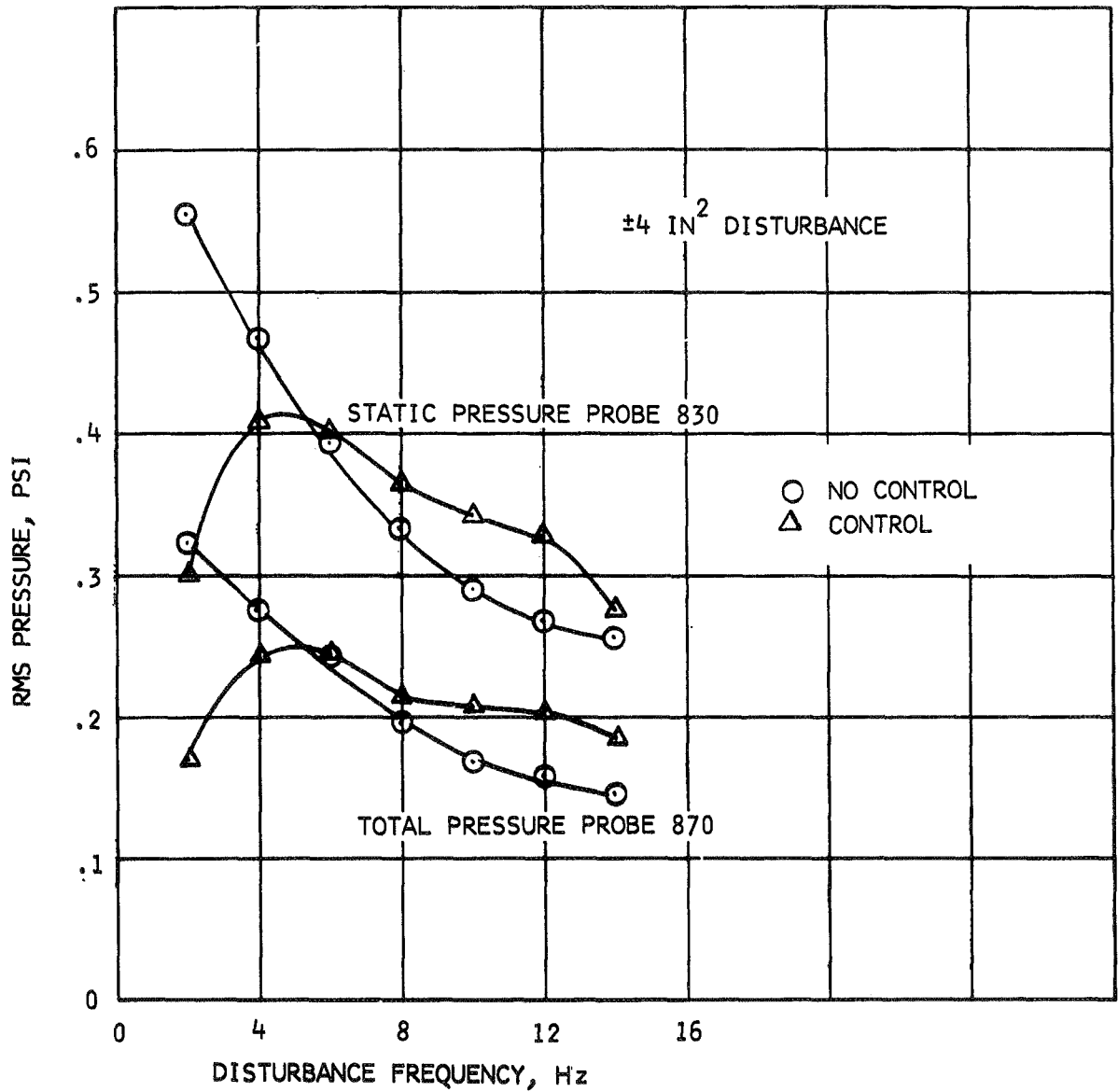


Figure 117. - Turbulence levels with sinusoidal exit area disturbances,
 $M_0 = 3.0$, $\bar{P}_{t2}/P_{t0} = 0.846$.

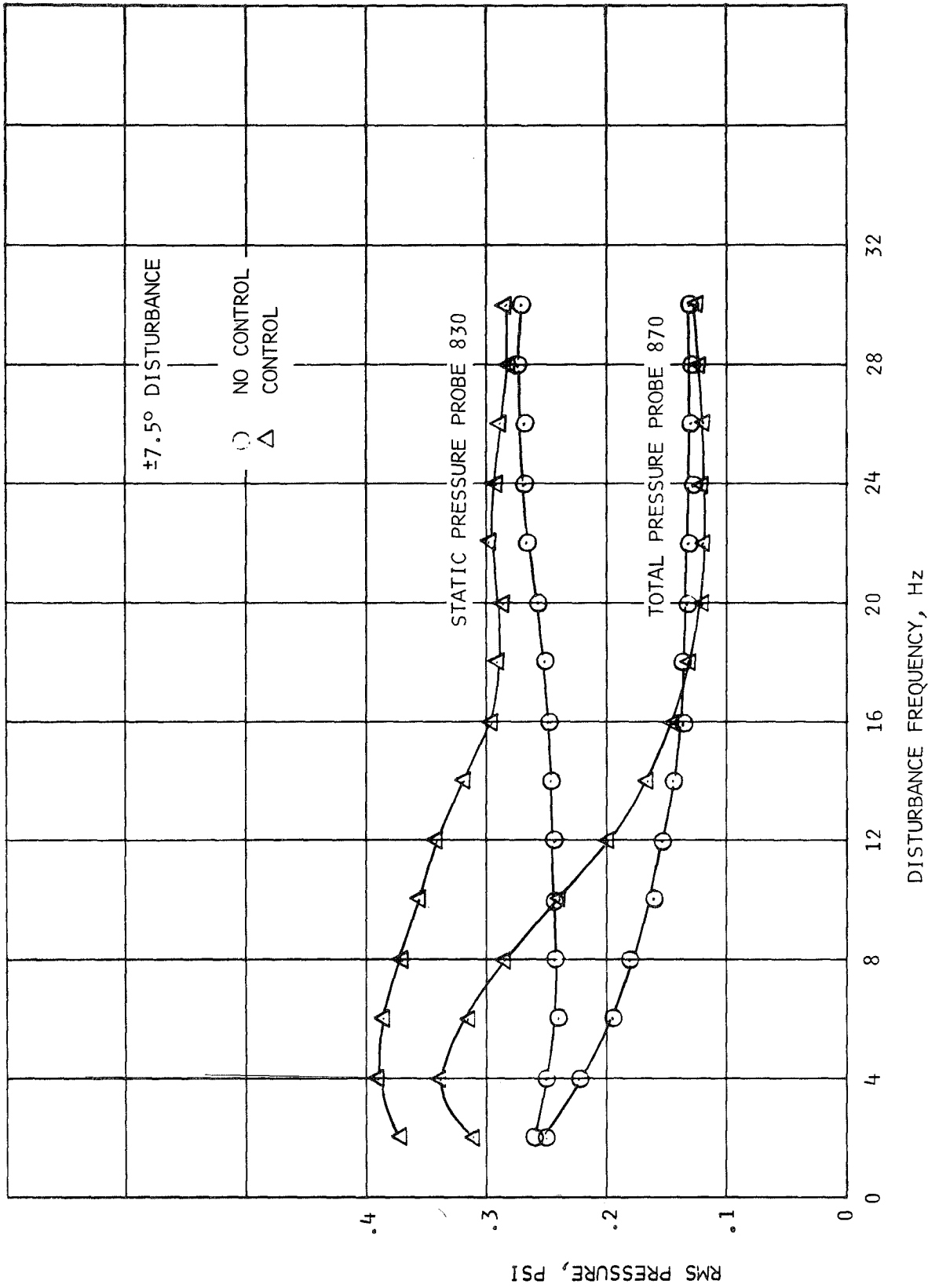


Figure 118. - Turbulence levels with sinusoidal vane angle disturbance, $M_0 = 3.0$, $\bar{P}_{t2}/P_{t0} = 0.778$.

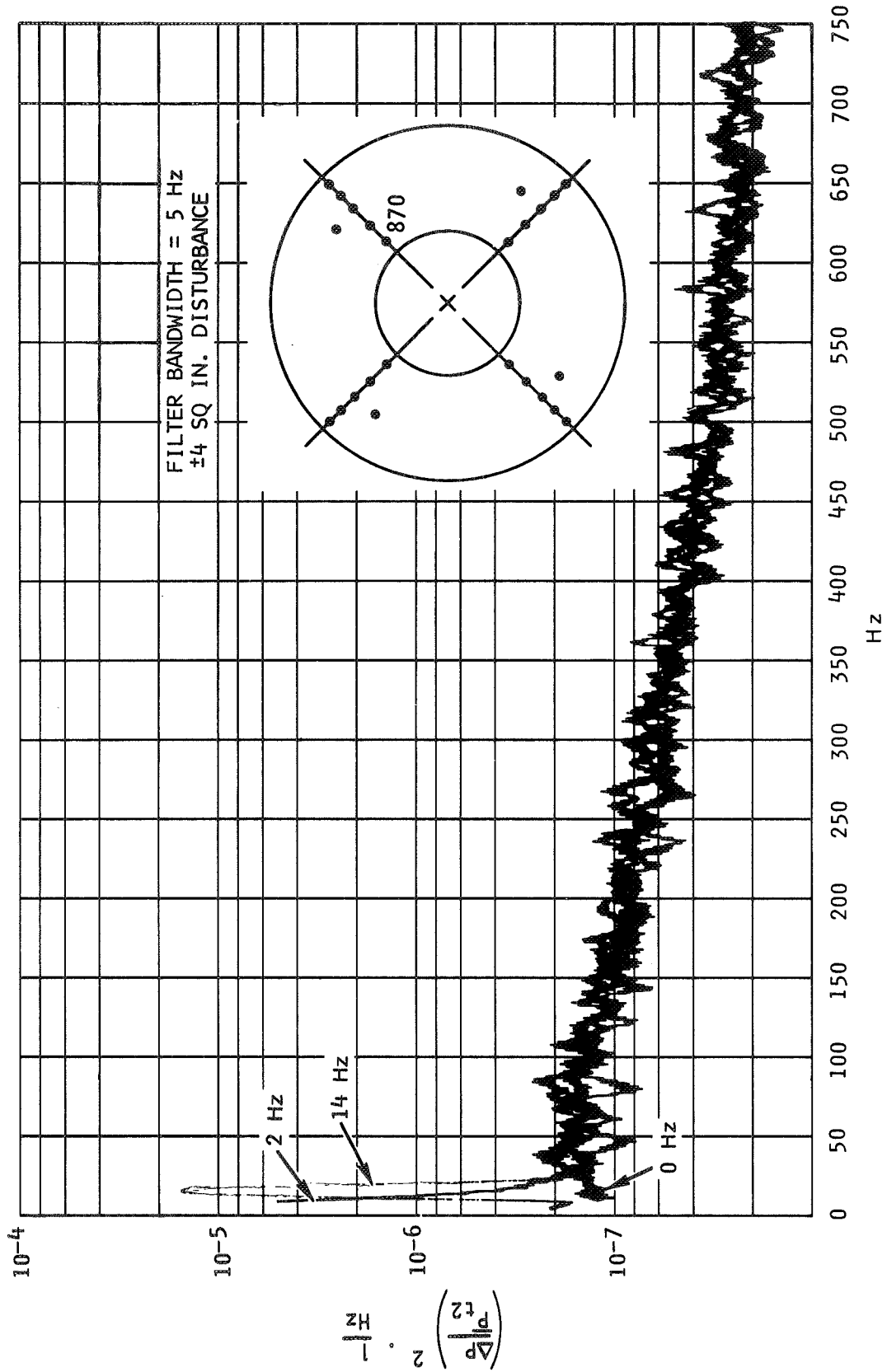


Figure 119.- Power spectral densities for 0, 2, and 14 Hz sinusoidal exit area disturbances, $M_0 = 3.0$, $\bar{P}_{t2}/P_{t0} = 0.846$.

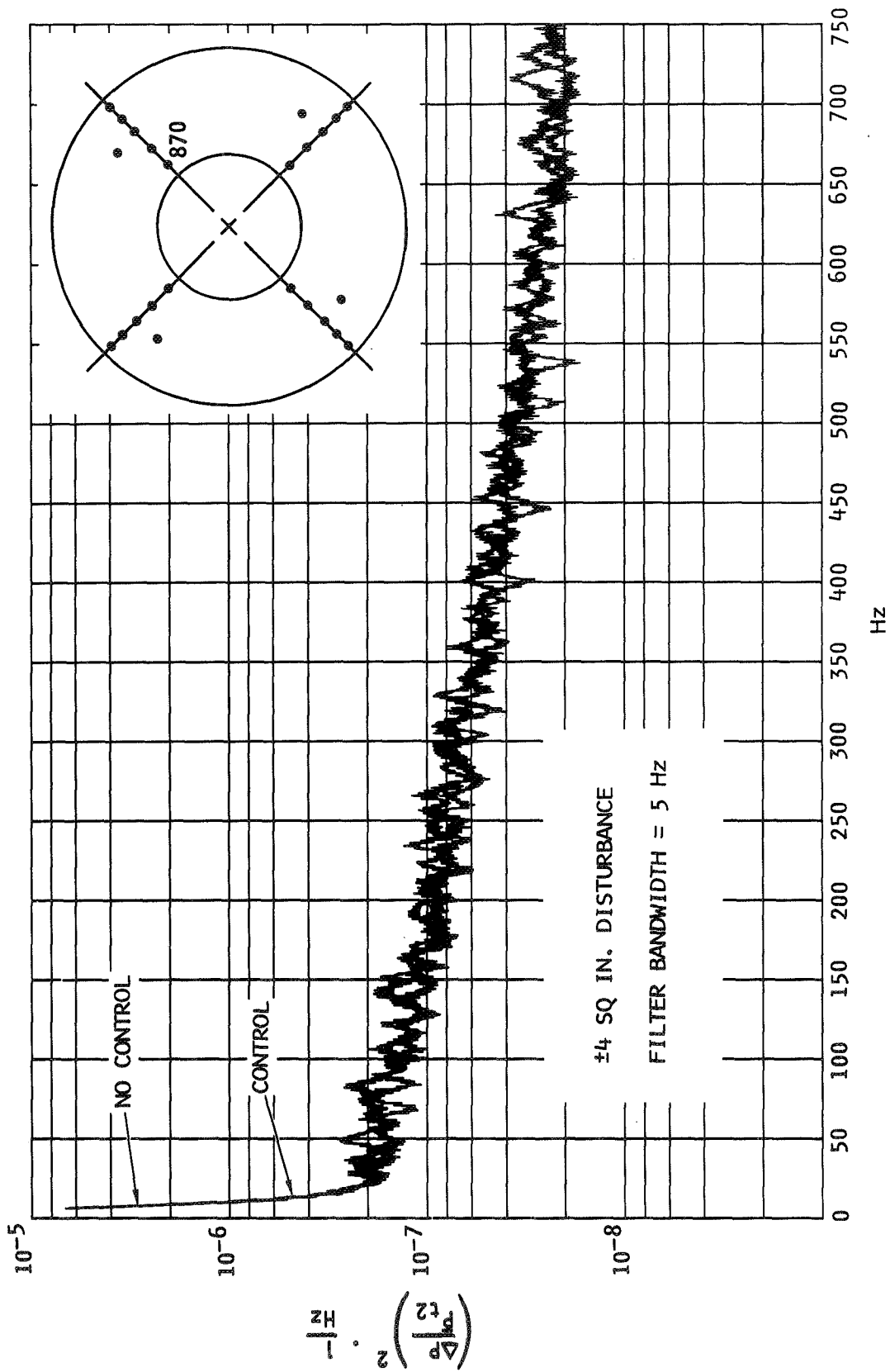


Figure 120.- Effect of control on PSD for a 2 Hz sinusoidal exit area disturbance, $M_0 = 3.0$, $\bar{P}_{t2}/P_{t0} = 0.846$.

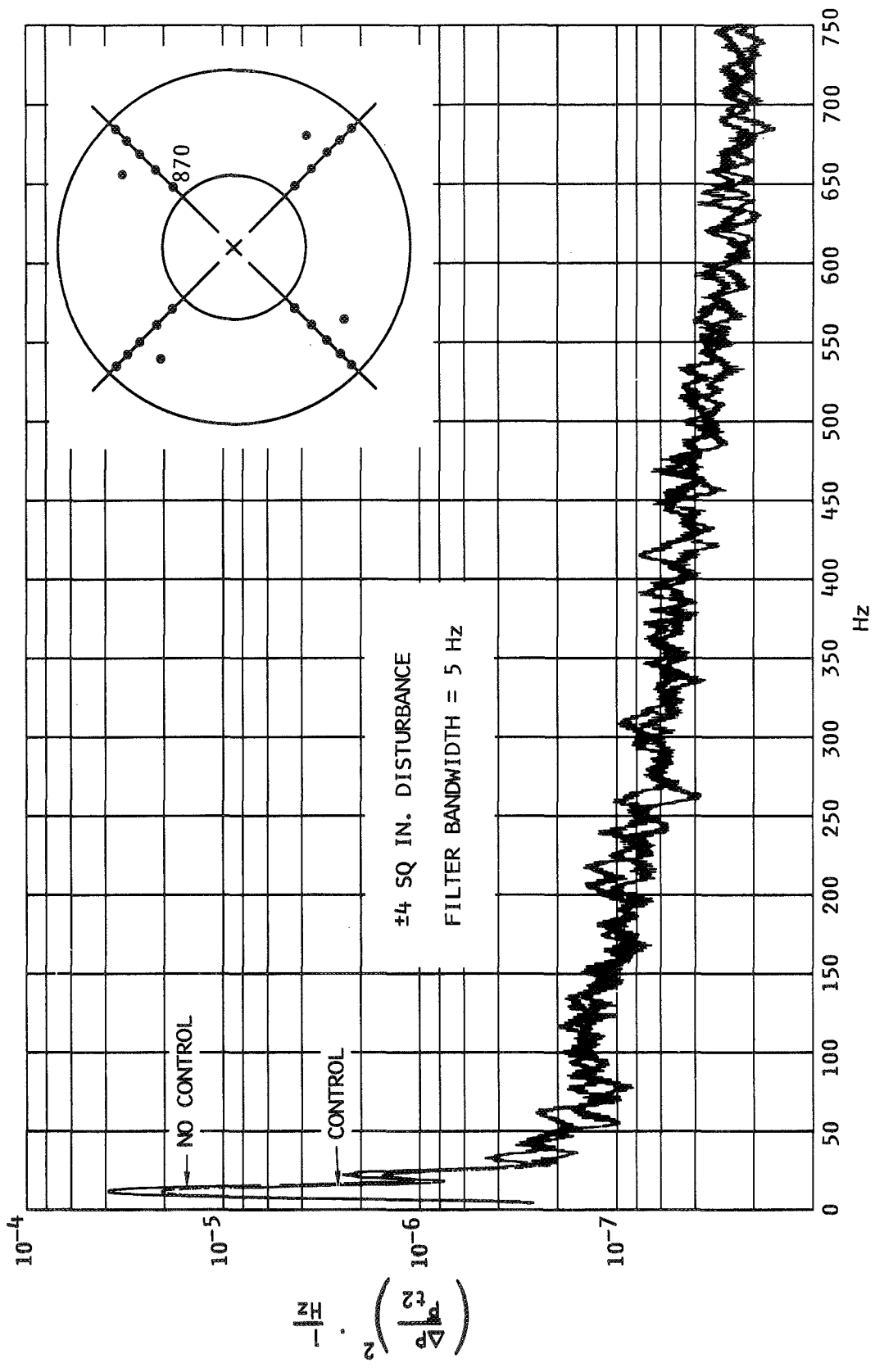


Figure 121.- Effect of control on PSD for a 10 Hz sinusoidal exit area disturbance, $M_0 = 3.0$, $\overline{P_{t2}/P_{t0}} = 0.846$.

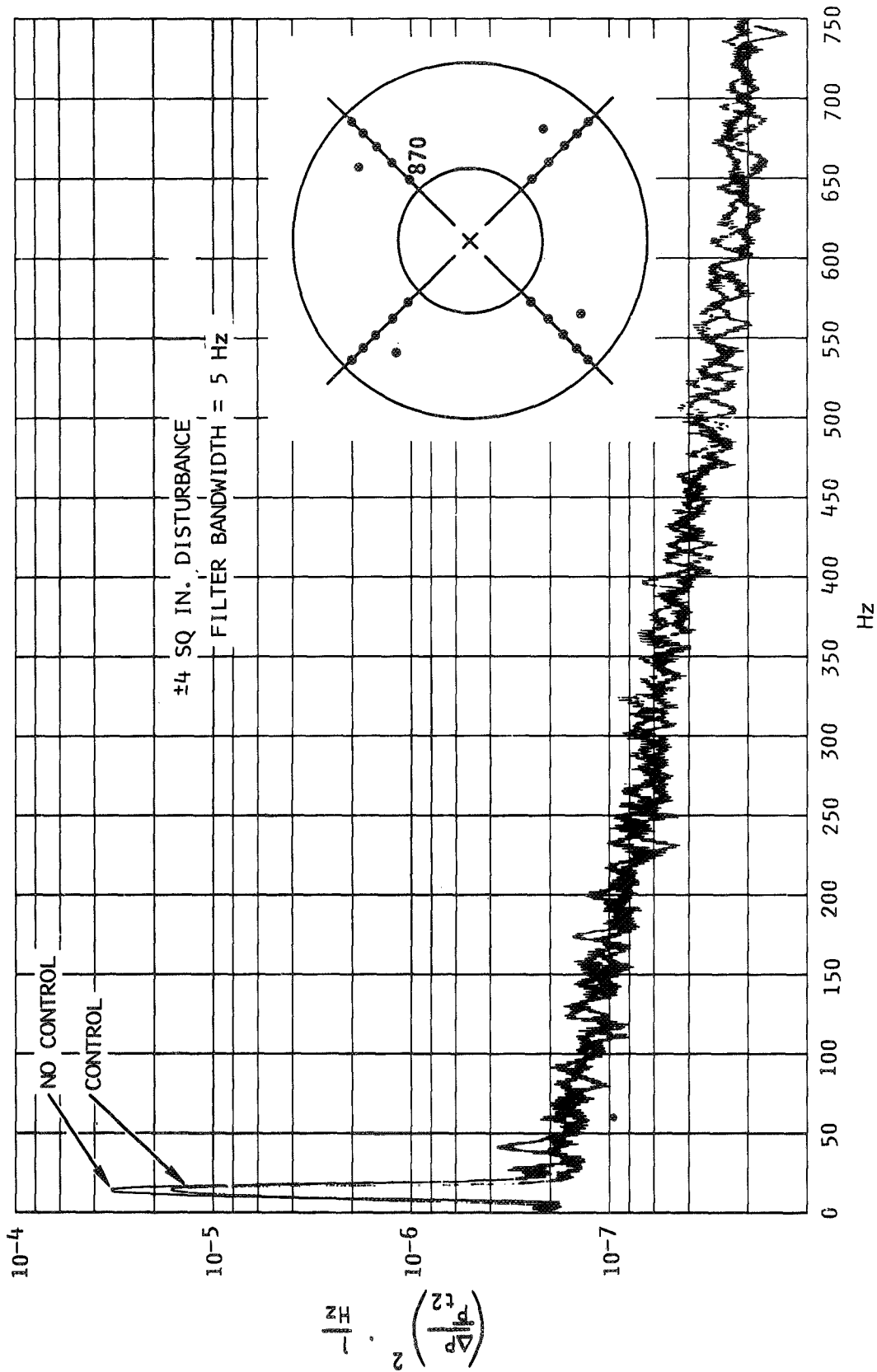


Figure 122.- Effect of control on PSD for a 14 Hz sinusoidal exit area disturbance,
 $M_0 = 3.0$, $\bar{P}_{t2}/P_{t0} = 0.846$.

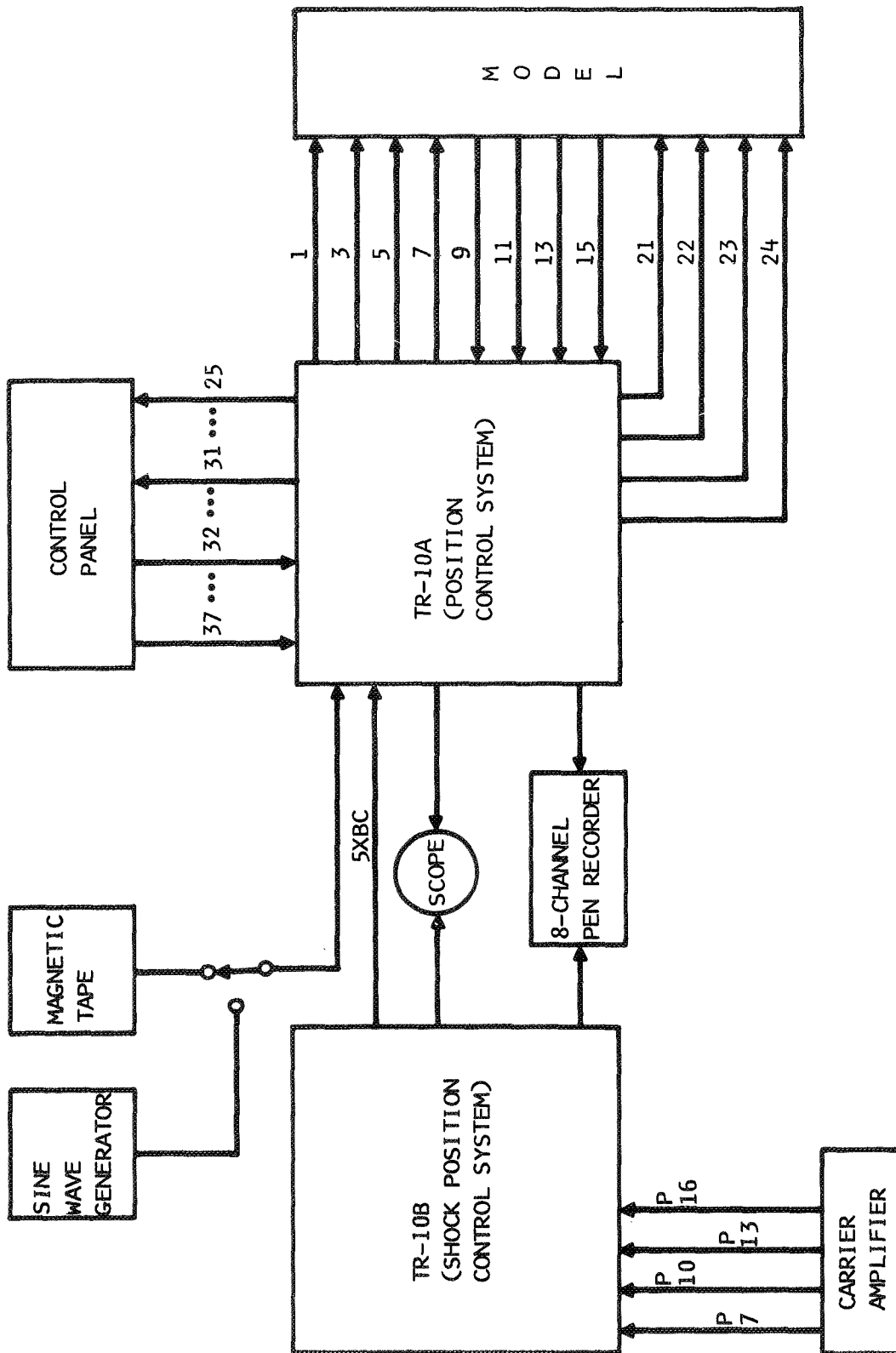


Figure 123.- Control system interfaces.

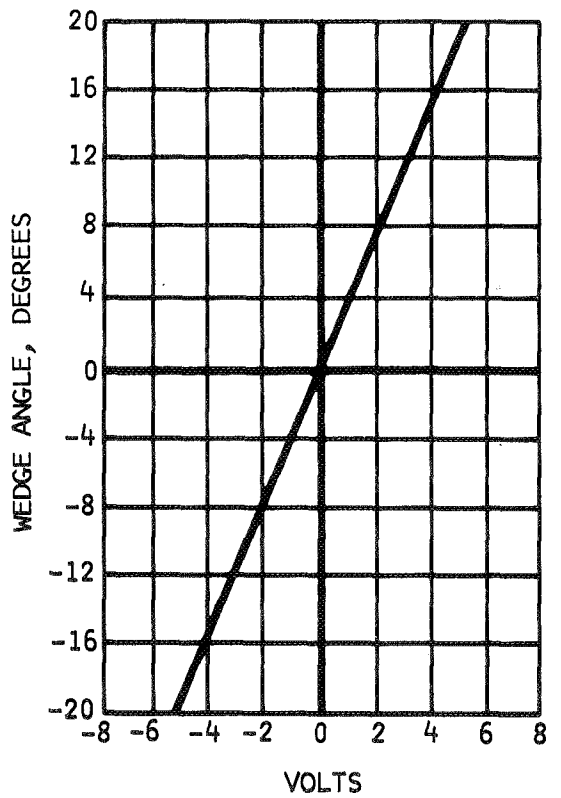
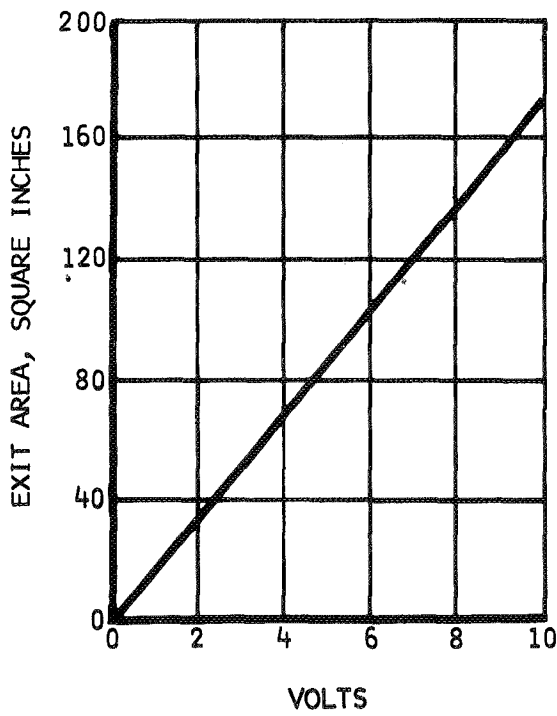
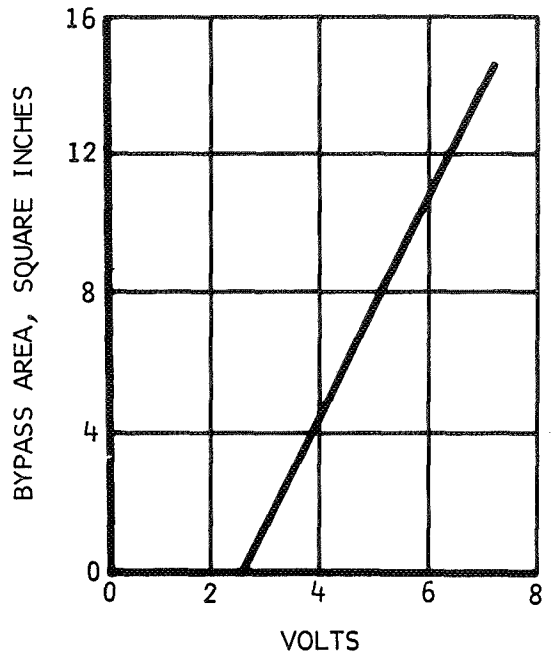
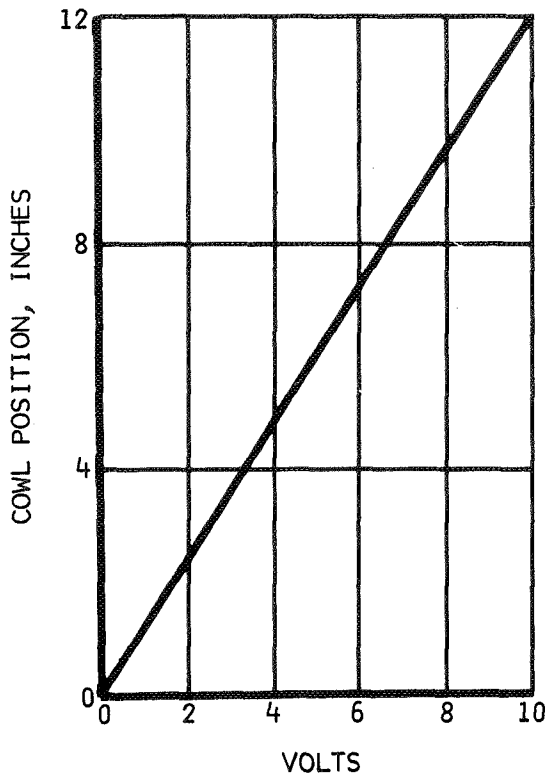


Figure 125.- Control system amplifier outputs versus actuator position.

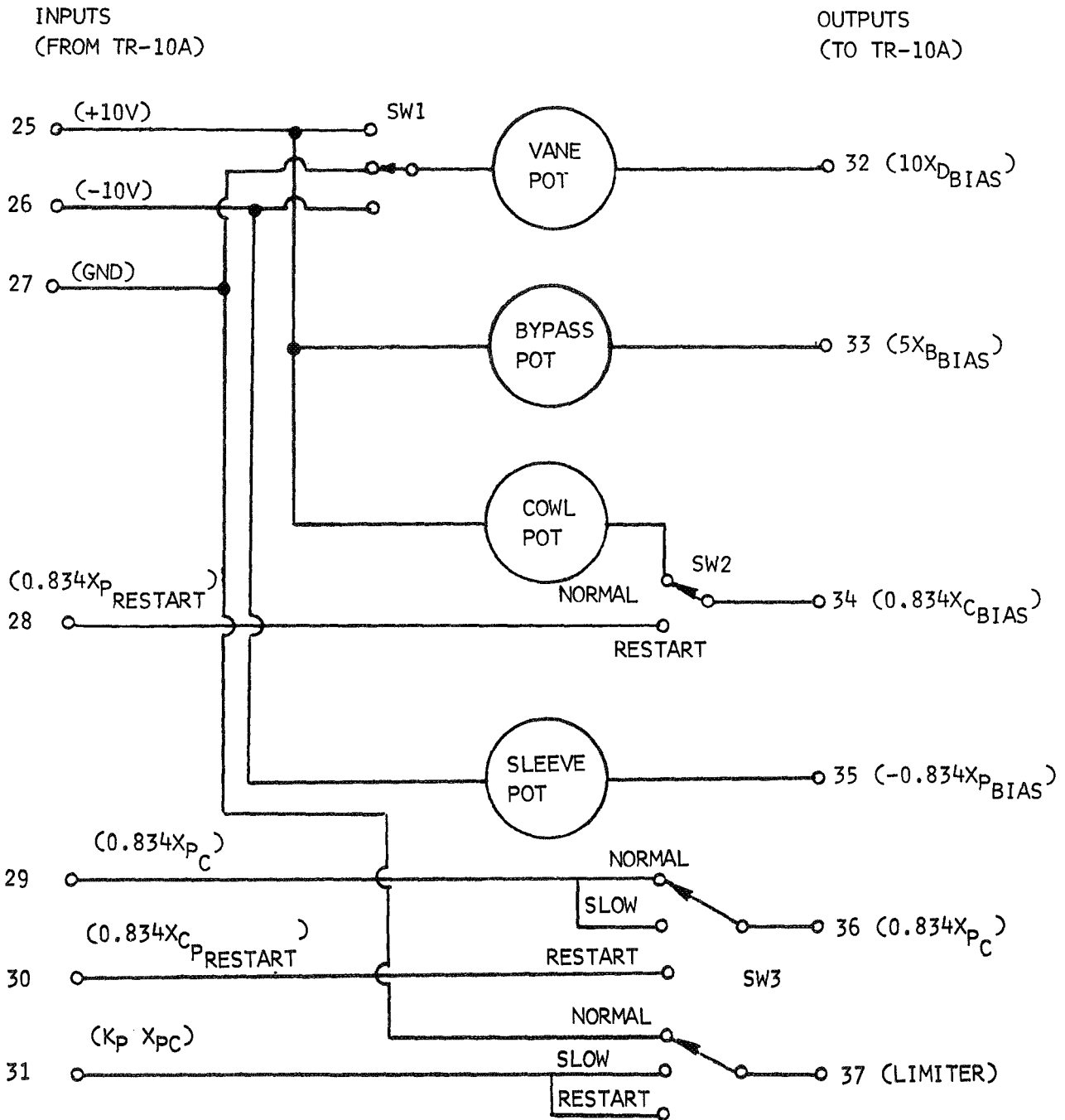


Figure 126.- Control panel wiring diagram.

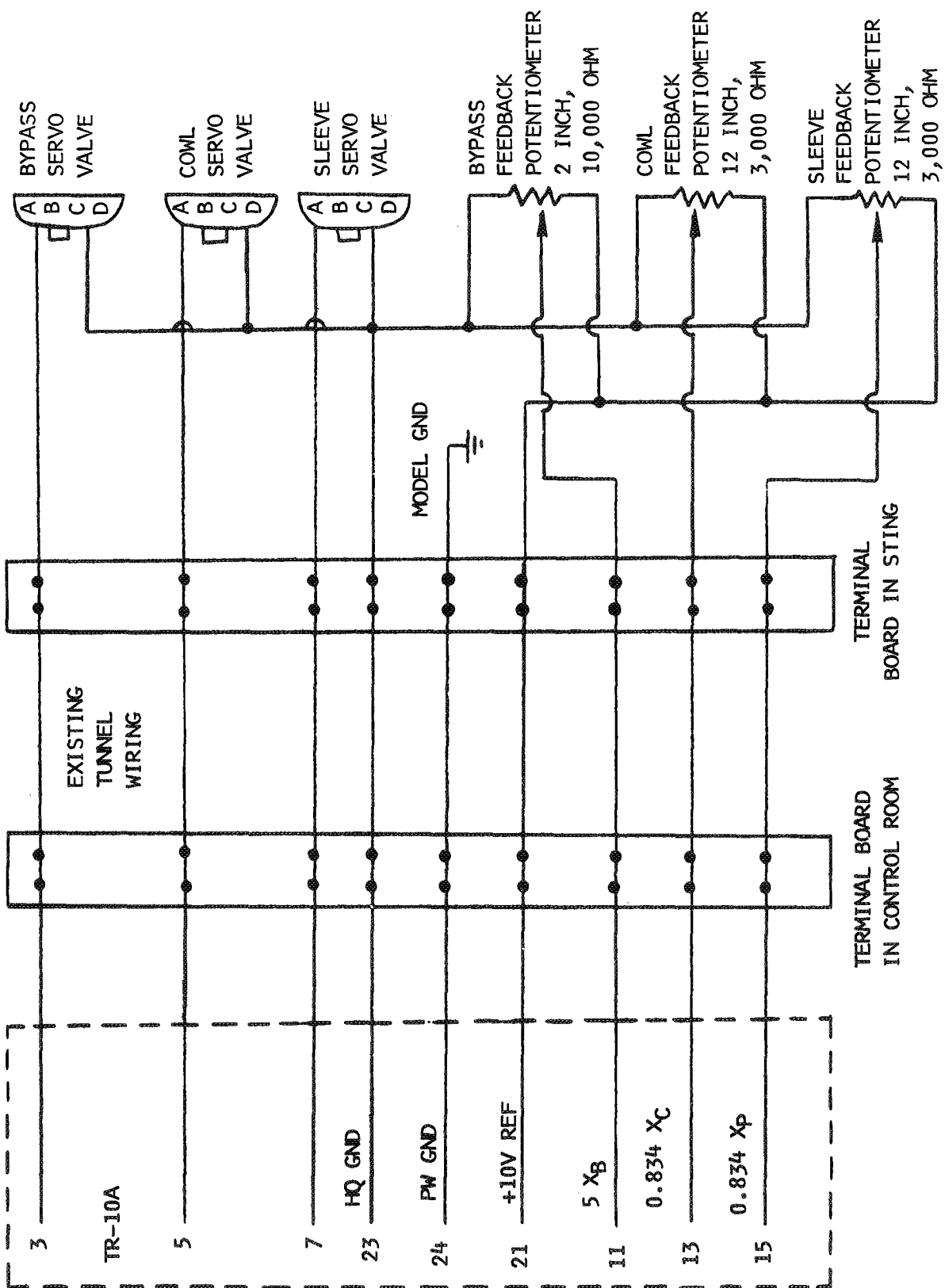


Figure 127.- Interface between TR-10A and model-mounted actuators.

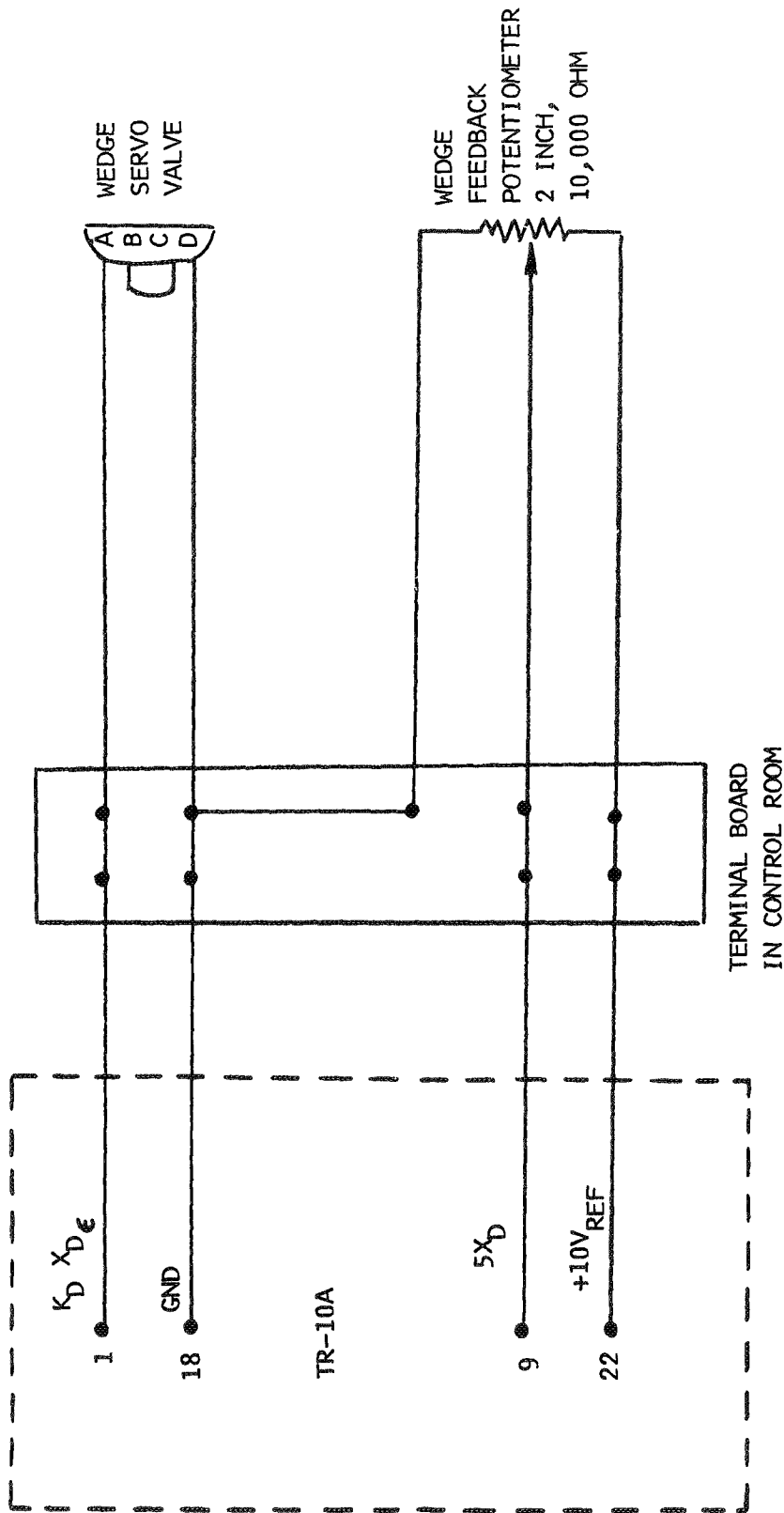


Figure 128.- Interface between TR-10A and disturbance vane actuator.

(FIGURE FROM REFERENCE 3)

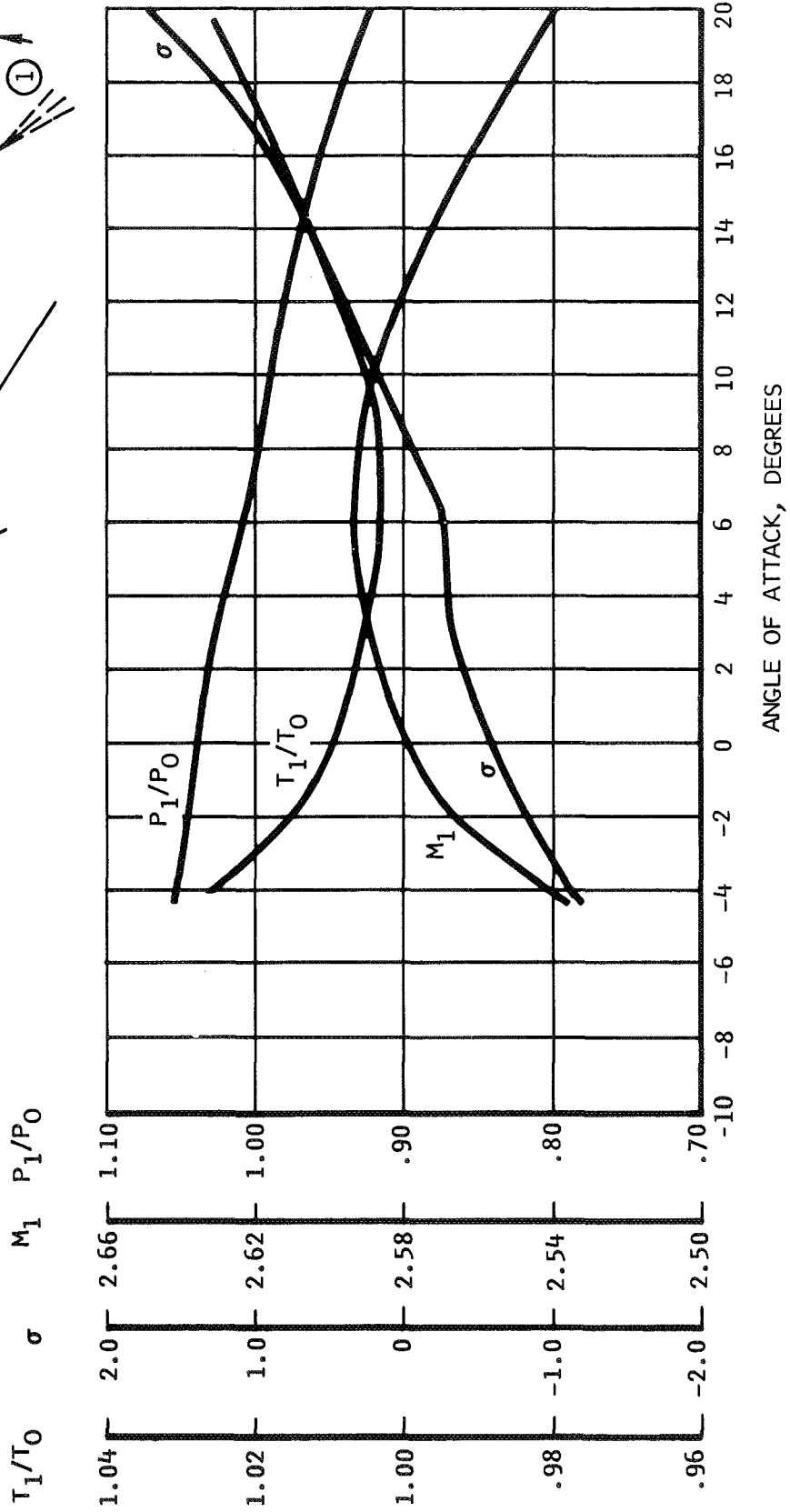
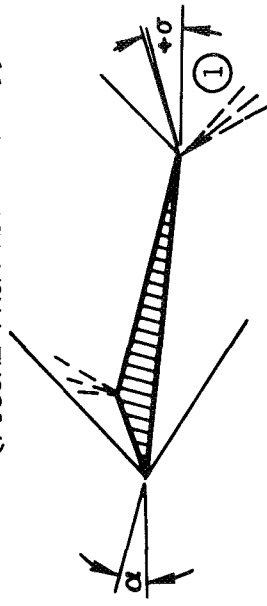


Figure 129.- Flow properties in the wake of a 25-degree leading edge and a 7.5-degree trailing edge wedge.

(FIGURE FROM REFERENCE 3)

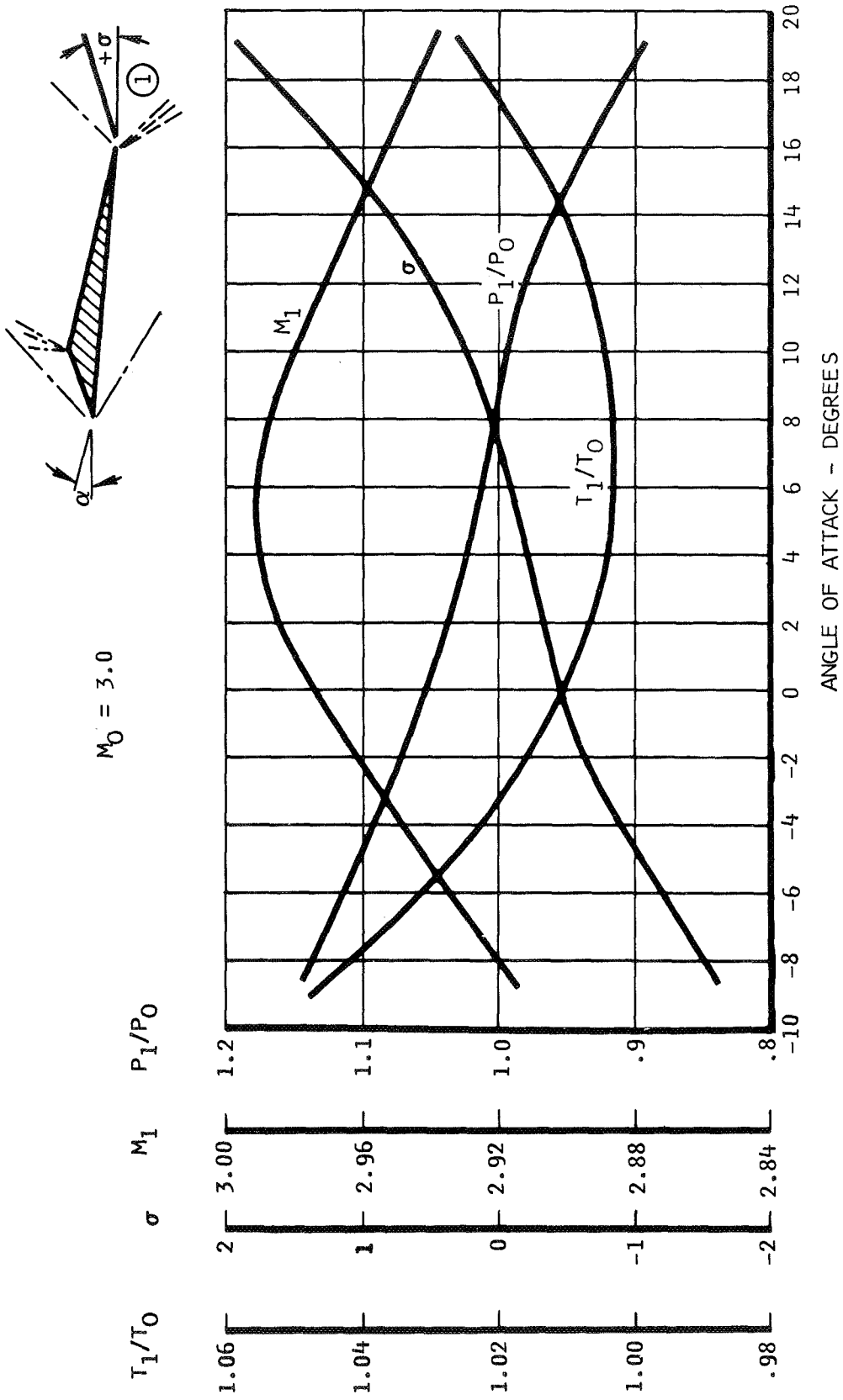


Figure 130.- Flow properties in the near wake of a 25-degree leading edge and a 7.5-degree trailing edge wedge.

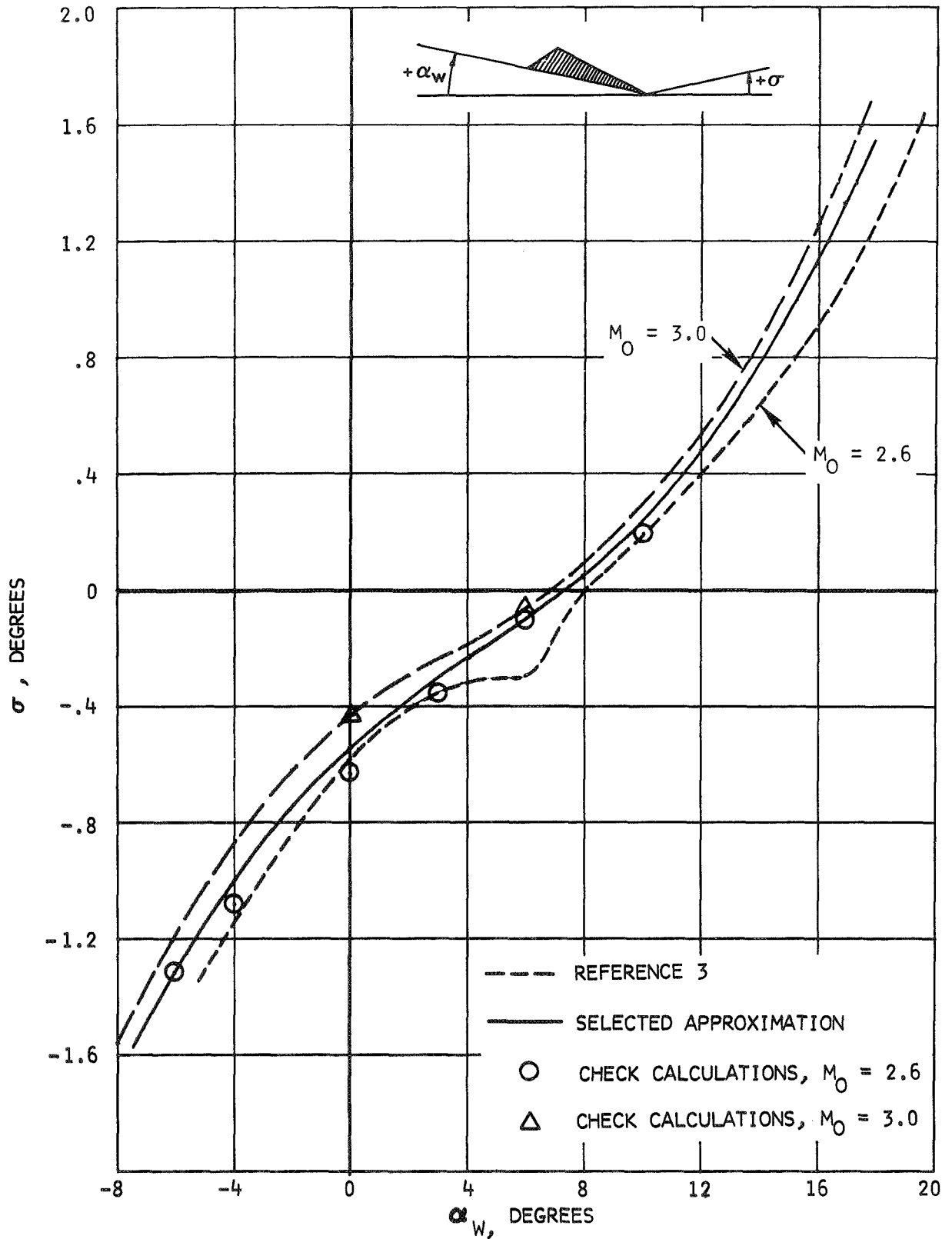


Figure 131. - Flow angle in the near wake of the disturbance wedge.

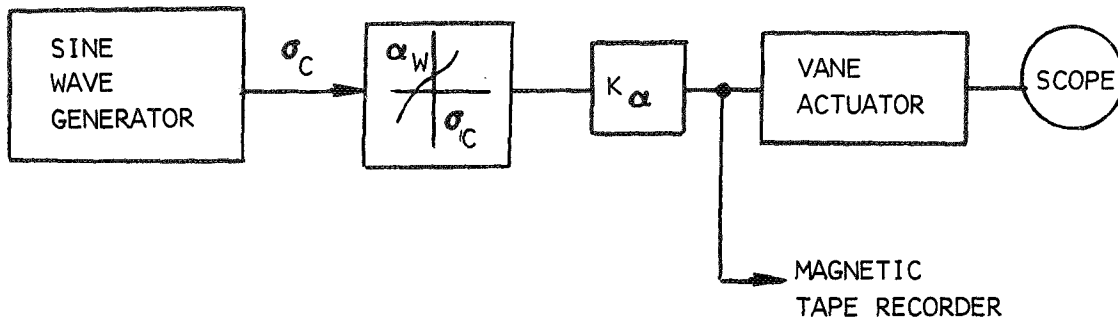


Figure 132. - Sinusoidal disturbance tape recording setup.

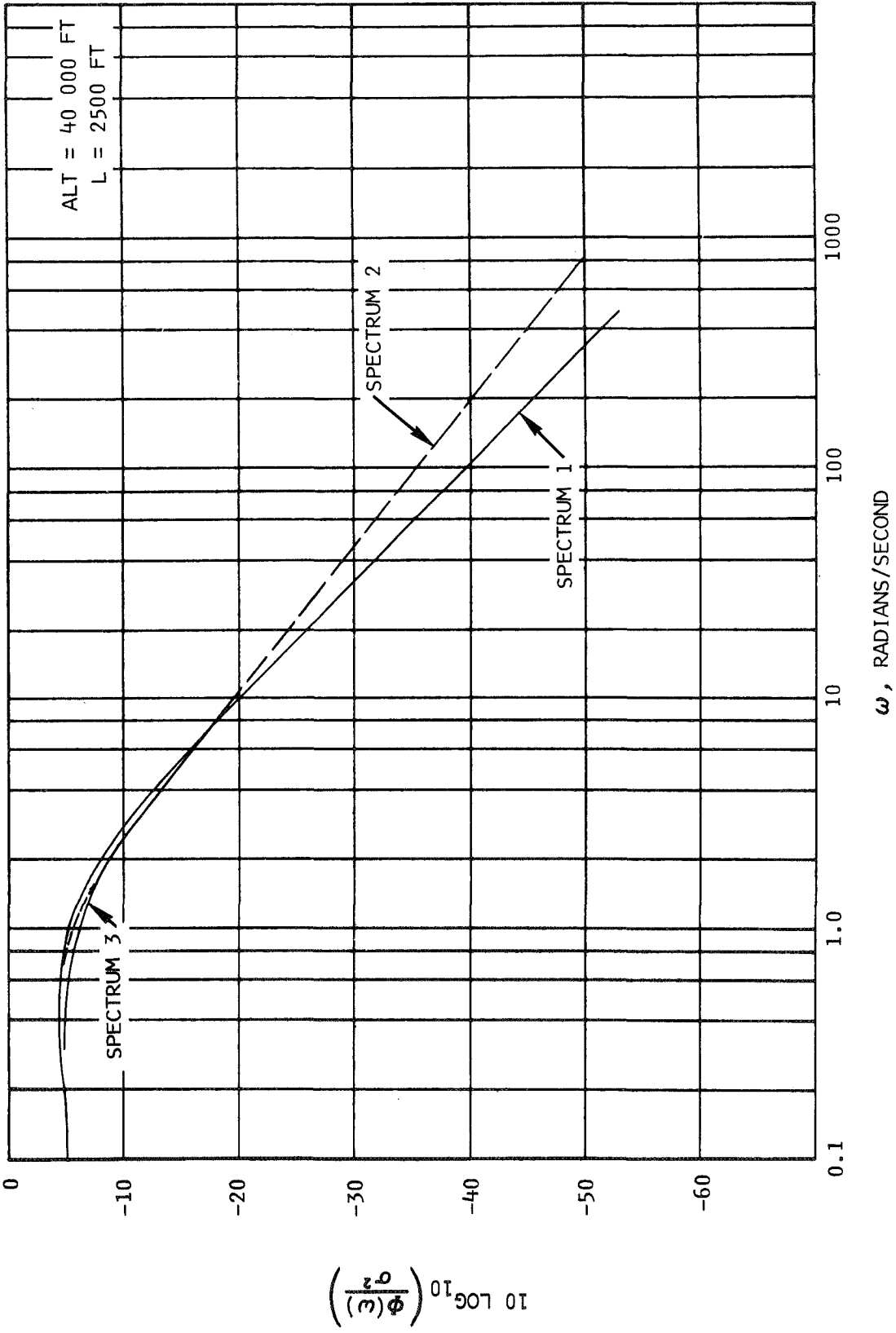


Figure 133. - CAT power spectral density, $M_0 = 2.6$.

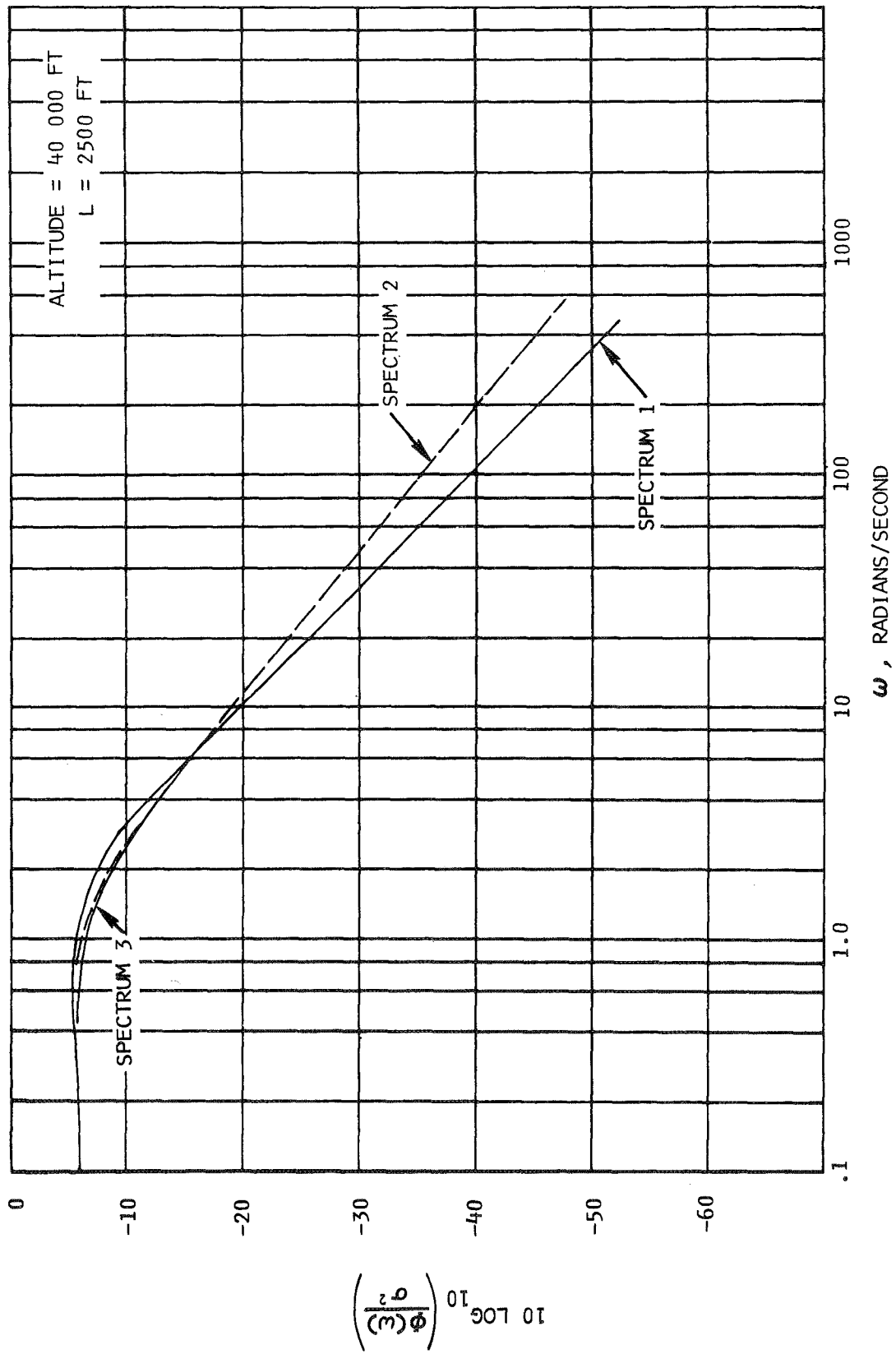


Figure 134. - CAT power spectral density, $M_0 = 3.0$.

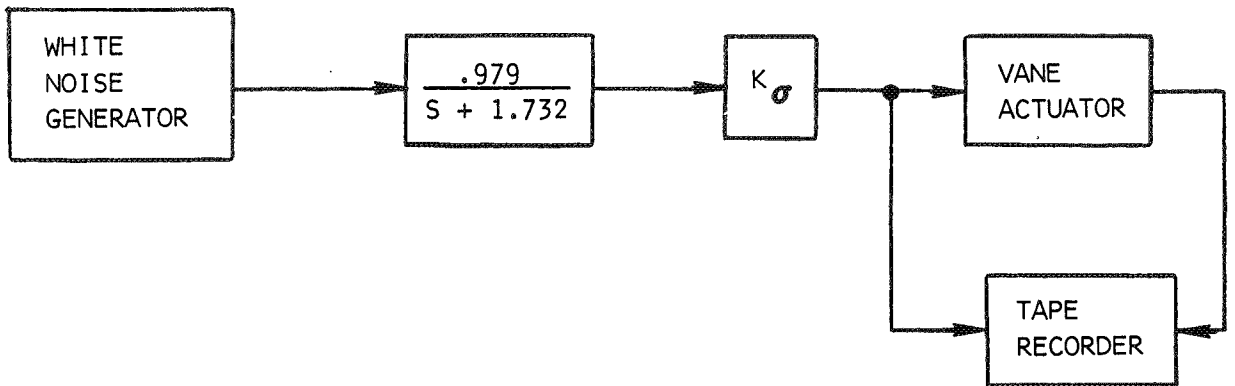


Figure 135. - CAT. input recording setup.

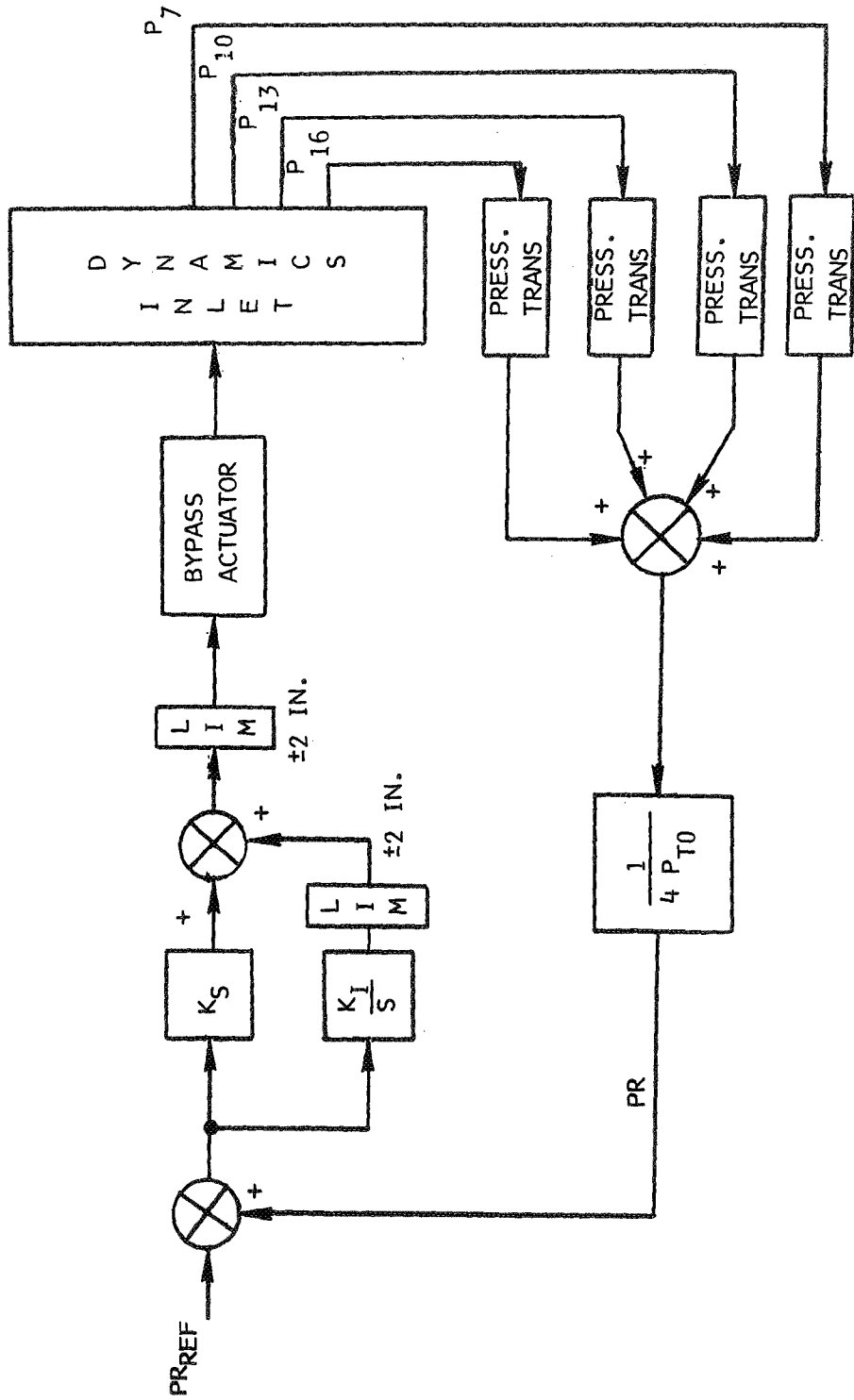


Figure 136. - Shock position control system block diagram.

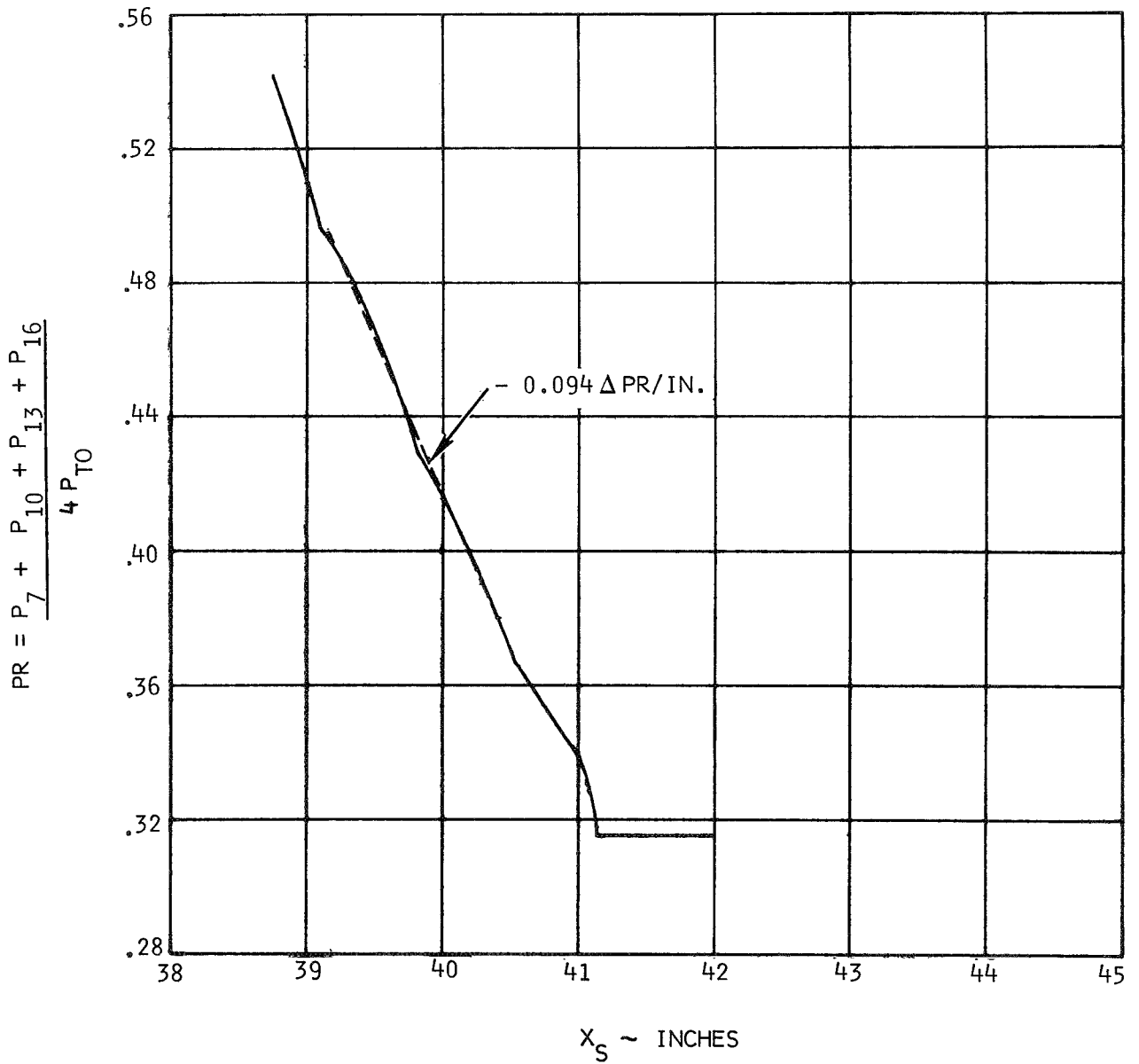


Figure 137. - Shock position pressure ratio versus shock position.

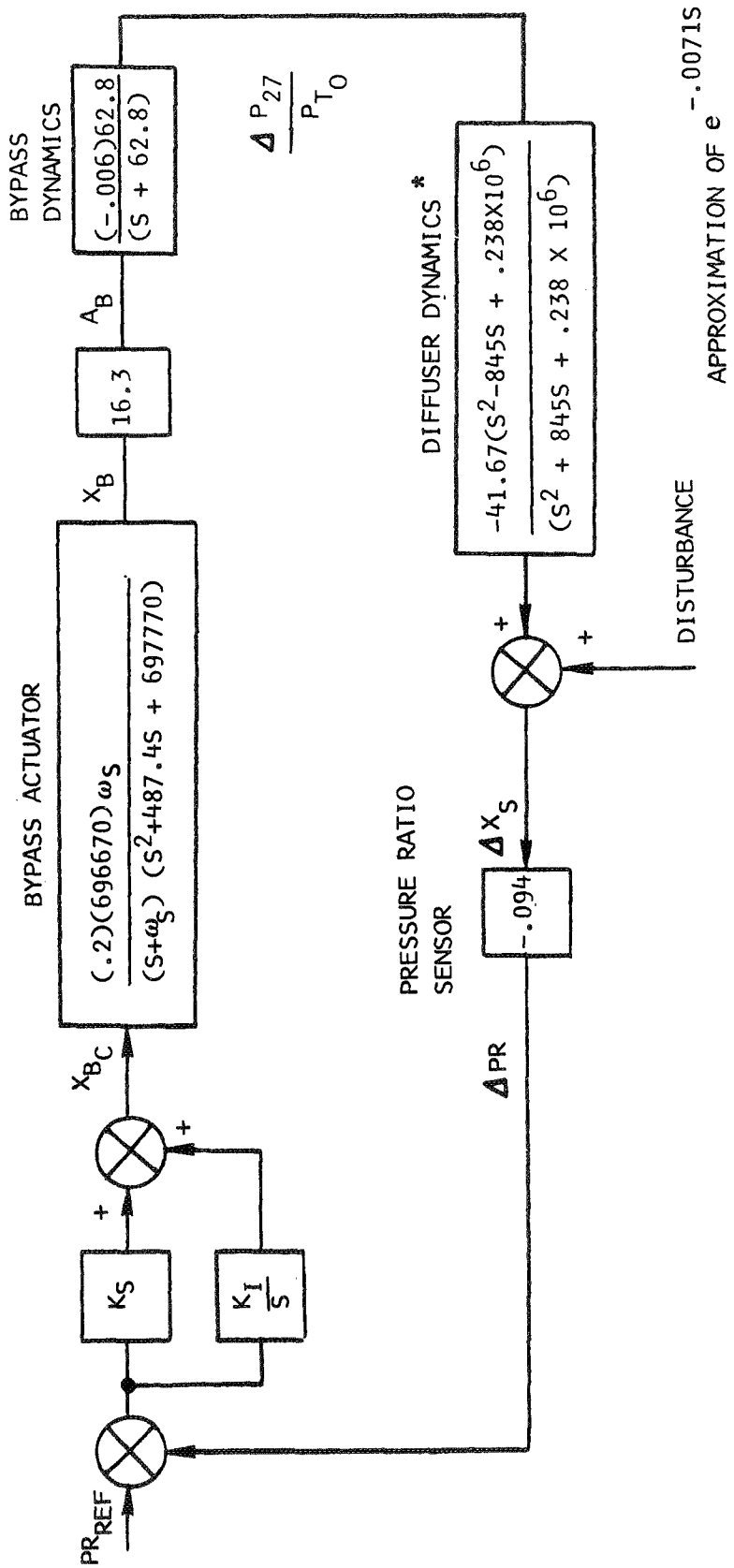


Figure 138. - Shock position control system linear mathematical model.

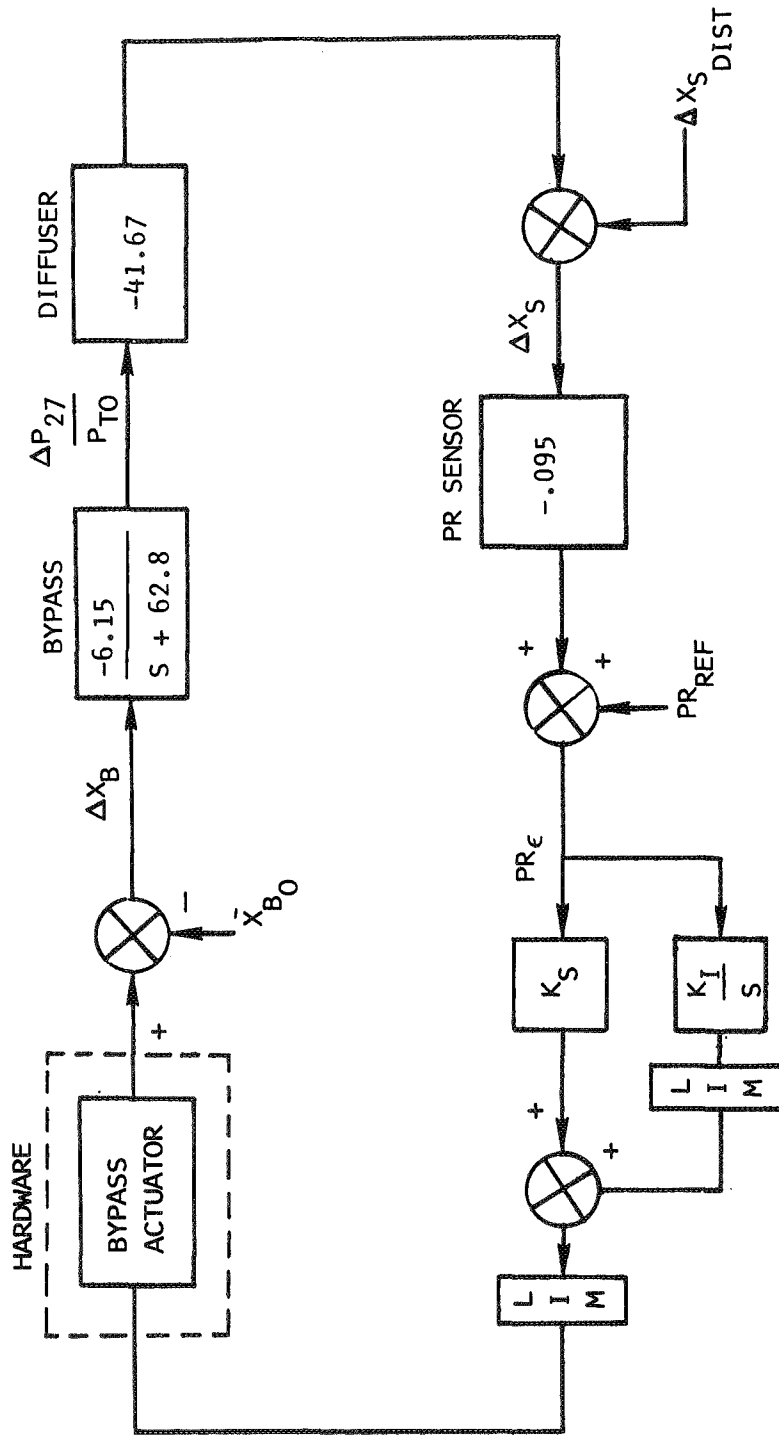
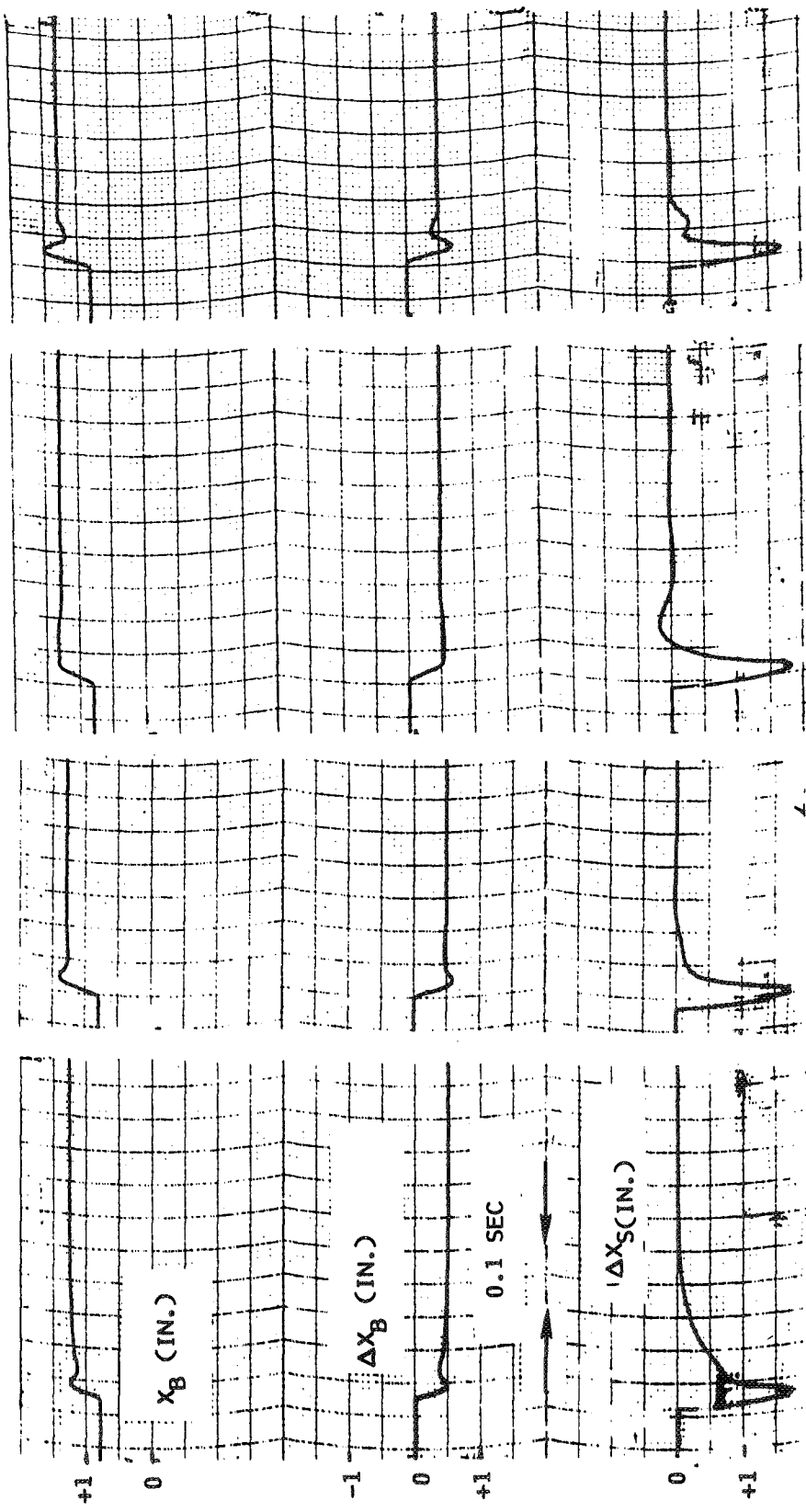


Figure 139. - Shock control system hardware tie-in simulation.



$K_S = 2.0$ $K_I = 55$ $K_S = 2.0$ $K_I = 100$ $K_S = 1.0$ $K_I = 100$ $K_S = 3.0$ $K_I = 100$

Figure 140. - Shock position control system responses to a 2-inch step change in ΔX_S Distance, hardware tie-in simulation.

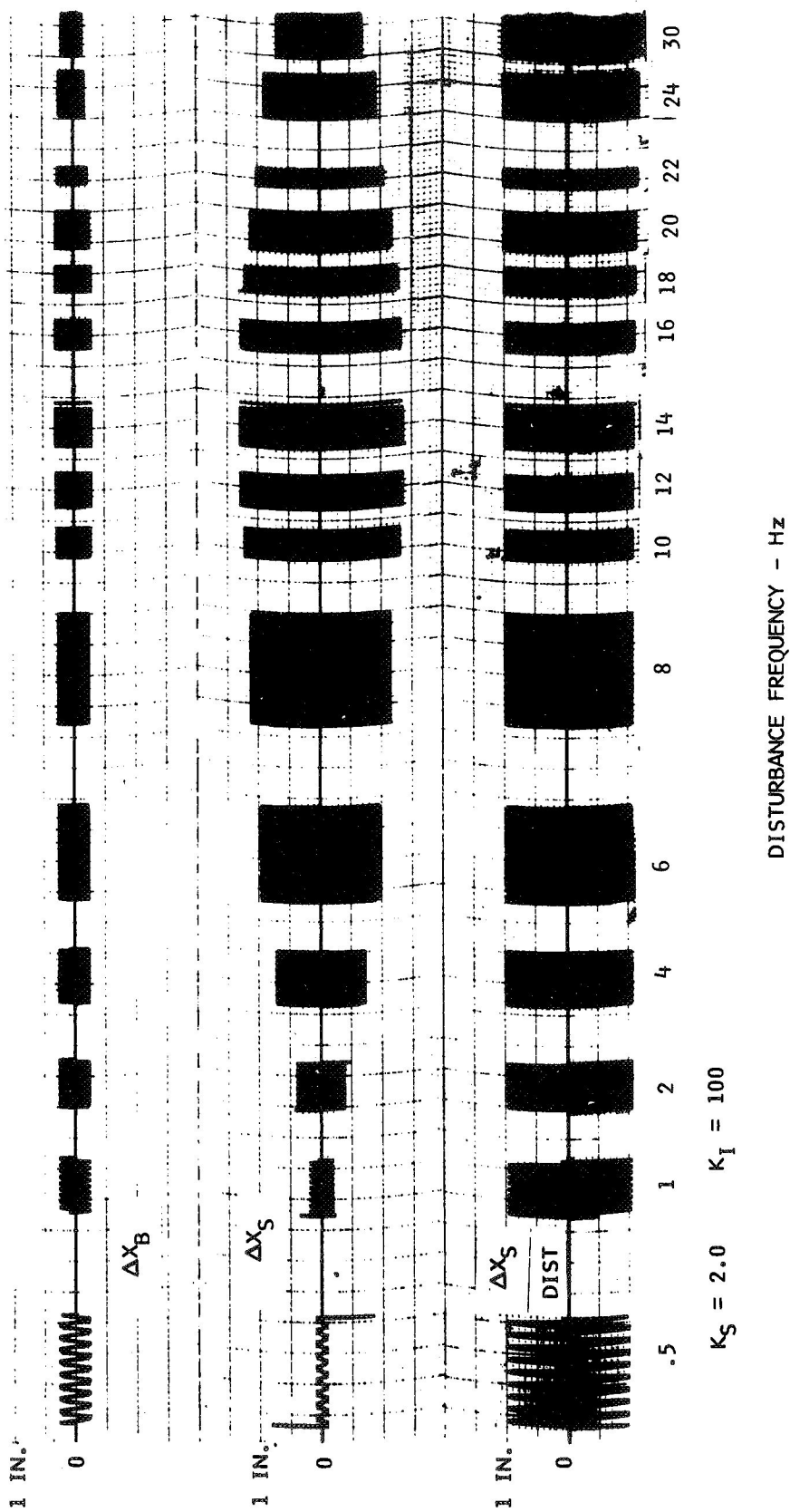


Figure 141. - Shock position control response to sinusoidal shock position disturbances, hardware tie-in simulation.

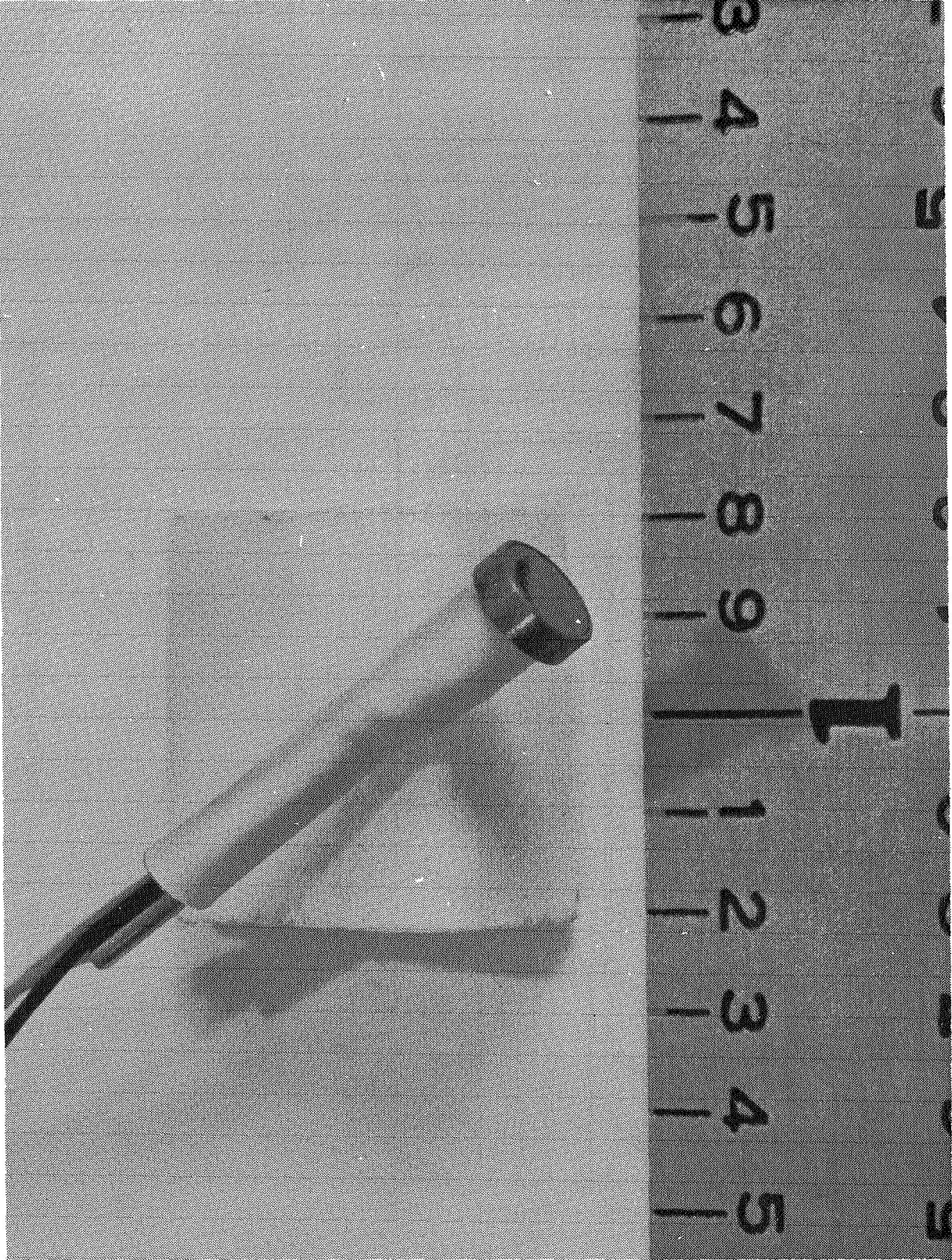


Figure 142. ~ Kulite CPL-125-25 pressure sensor.

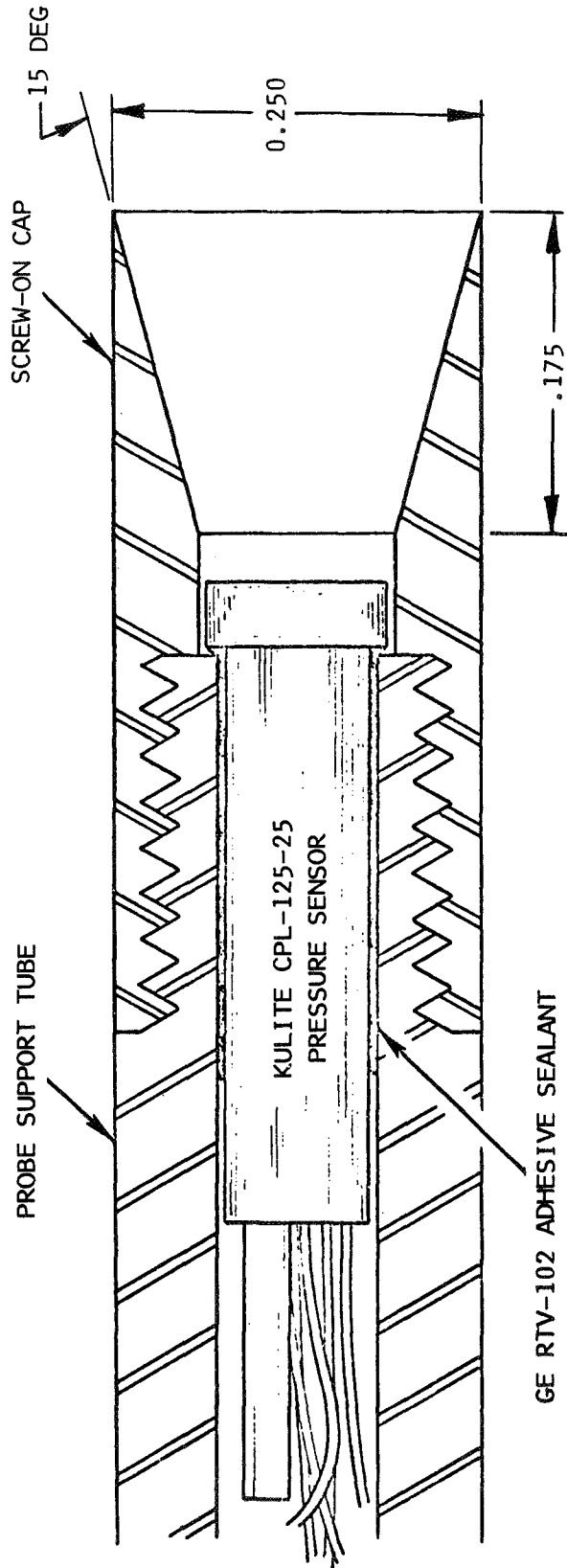


Figure 143. - Engine face rake total pressure probe.

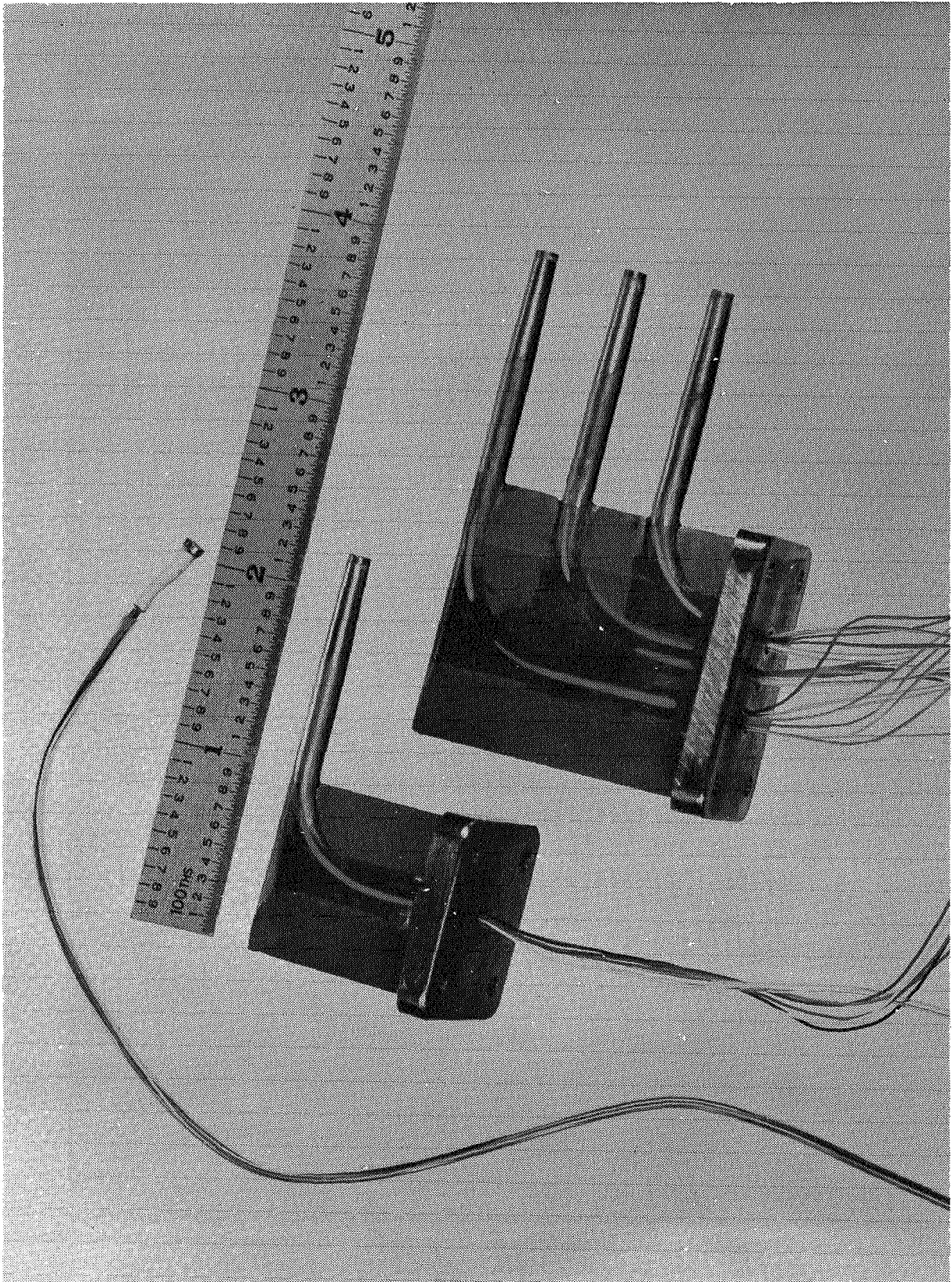


Figure 144. - Centerbody probes.



Figure 145. - Damaged diaphragm, pinhole failure.

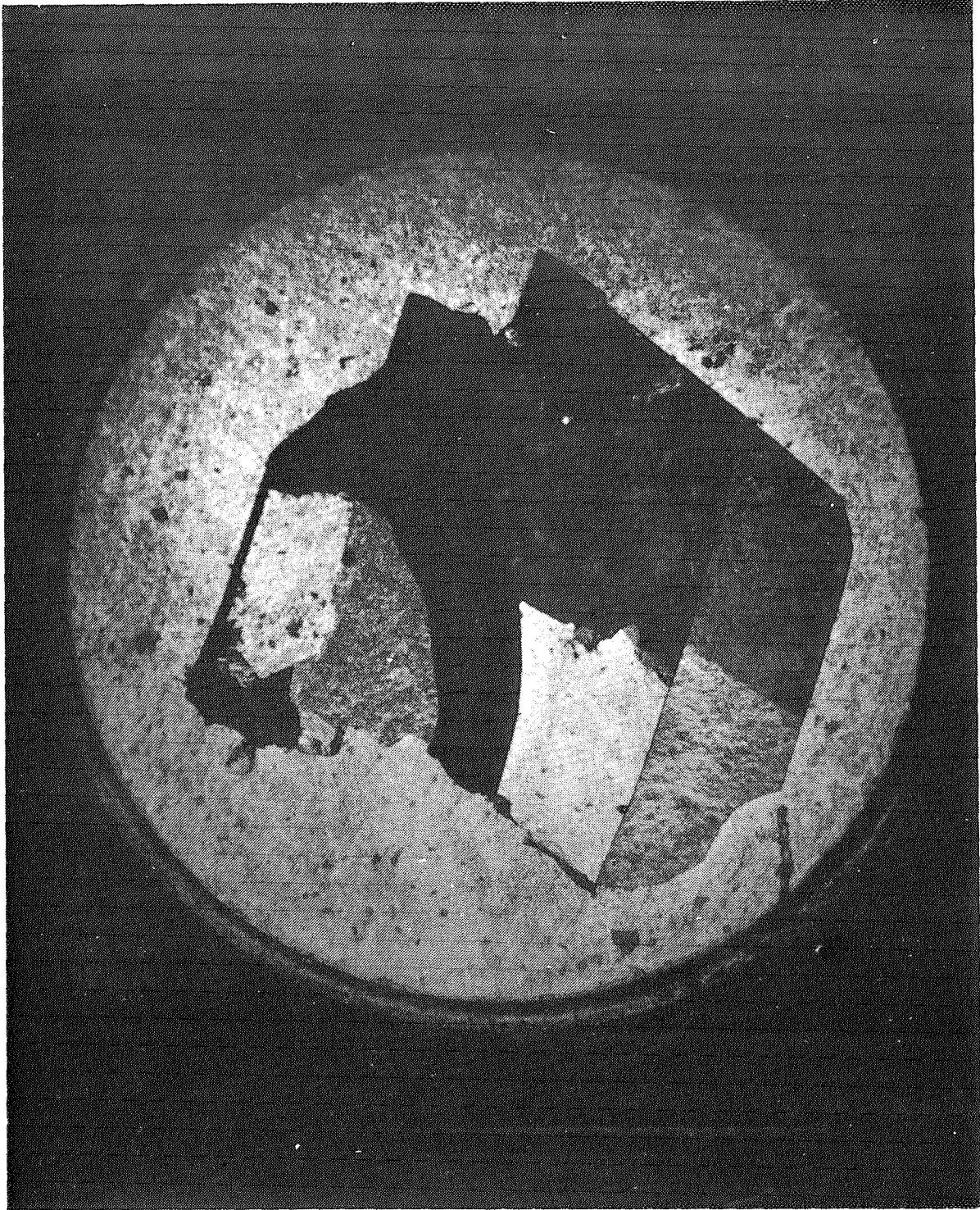
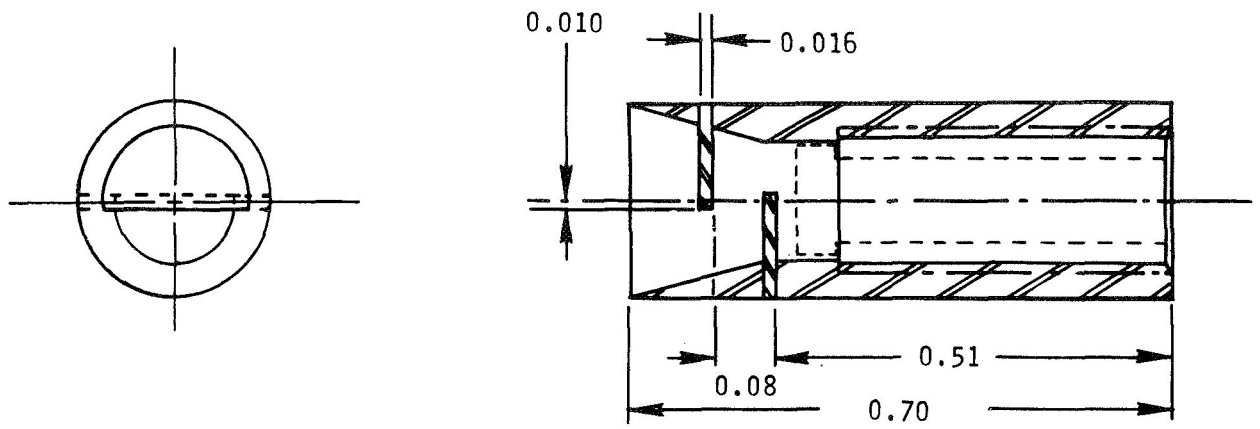
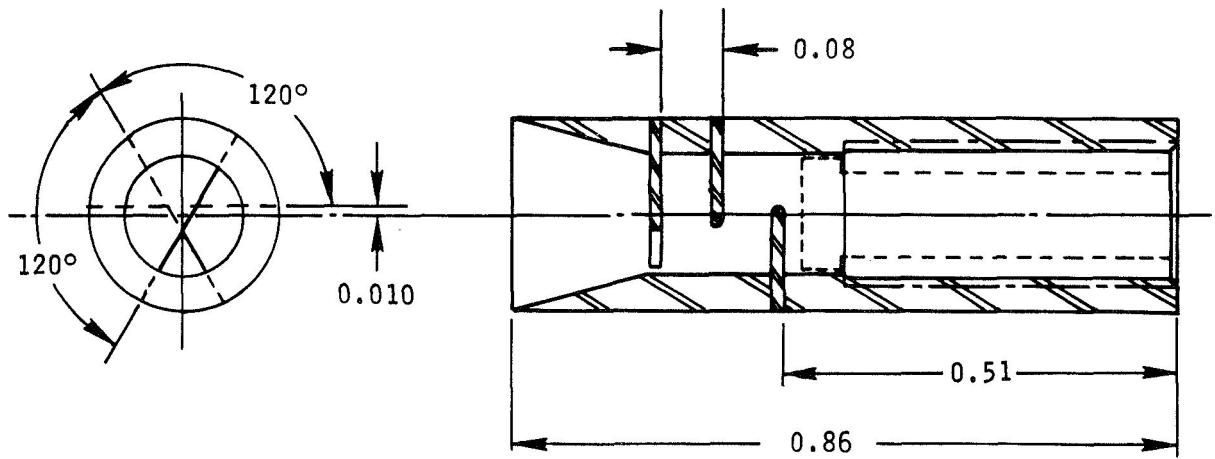


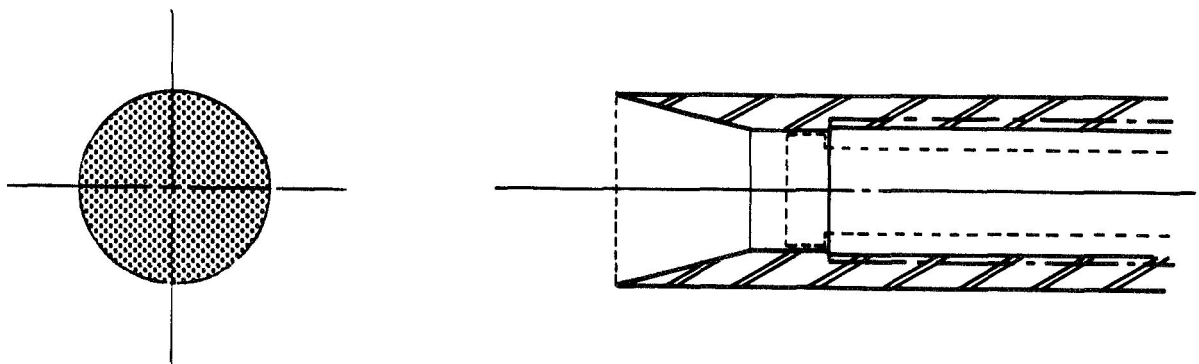
Figure 146.- Damaged diaphragm, "complete" failure.



TWO-BAFFLE CONFIGURATION

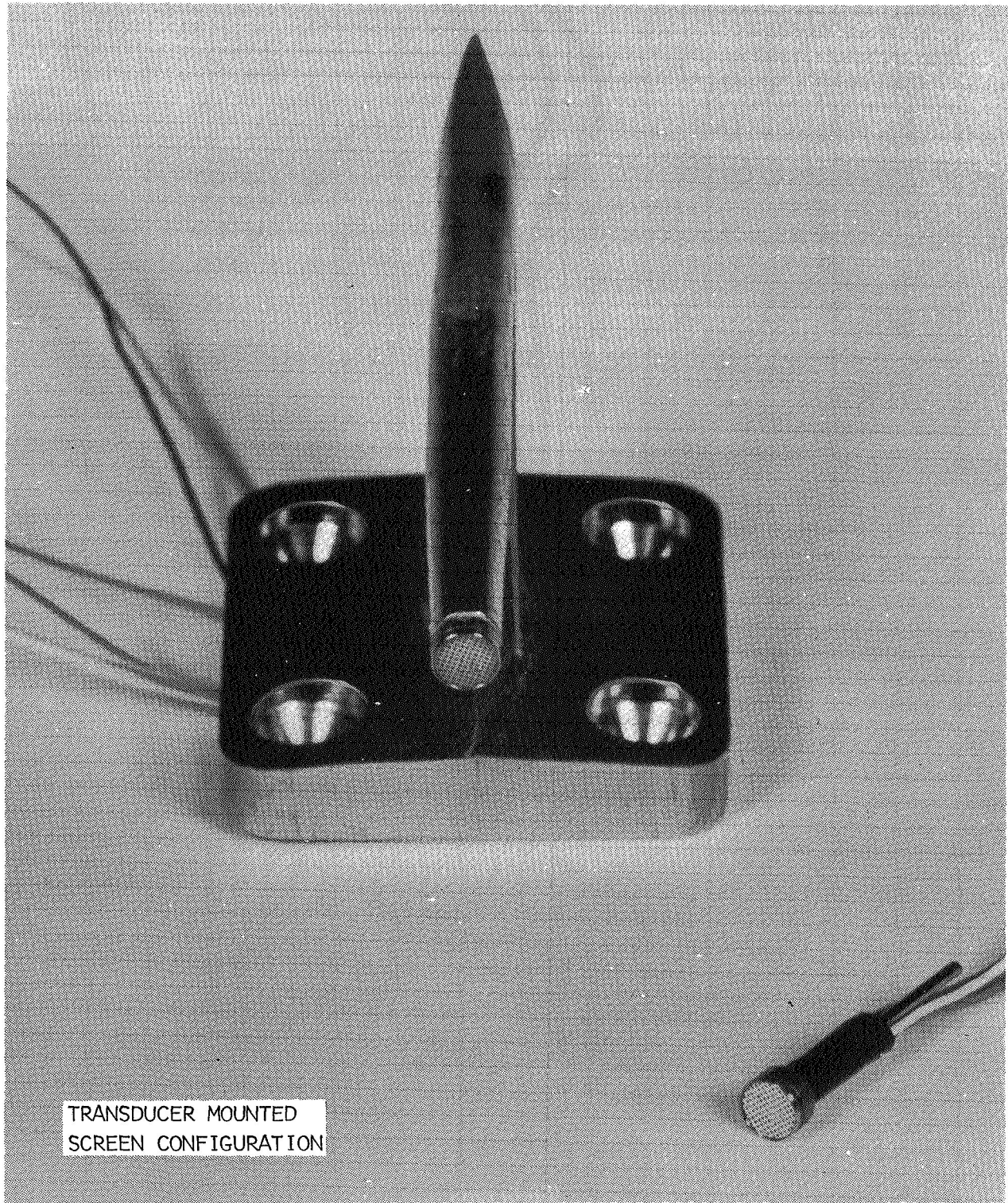


THREE-BAFFLE CONFIGURATION



SCREEN CONFIGURATION
(a)

Figure 147.- Probe modifications.



(b)
Figure 147.- Concluded.

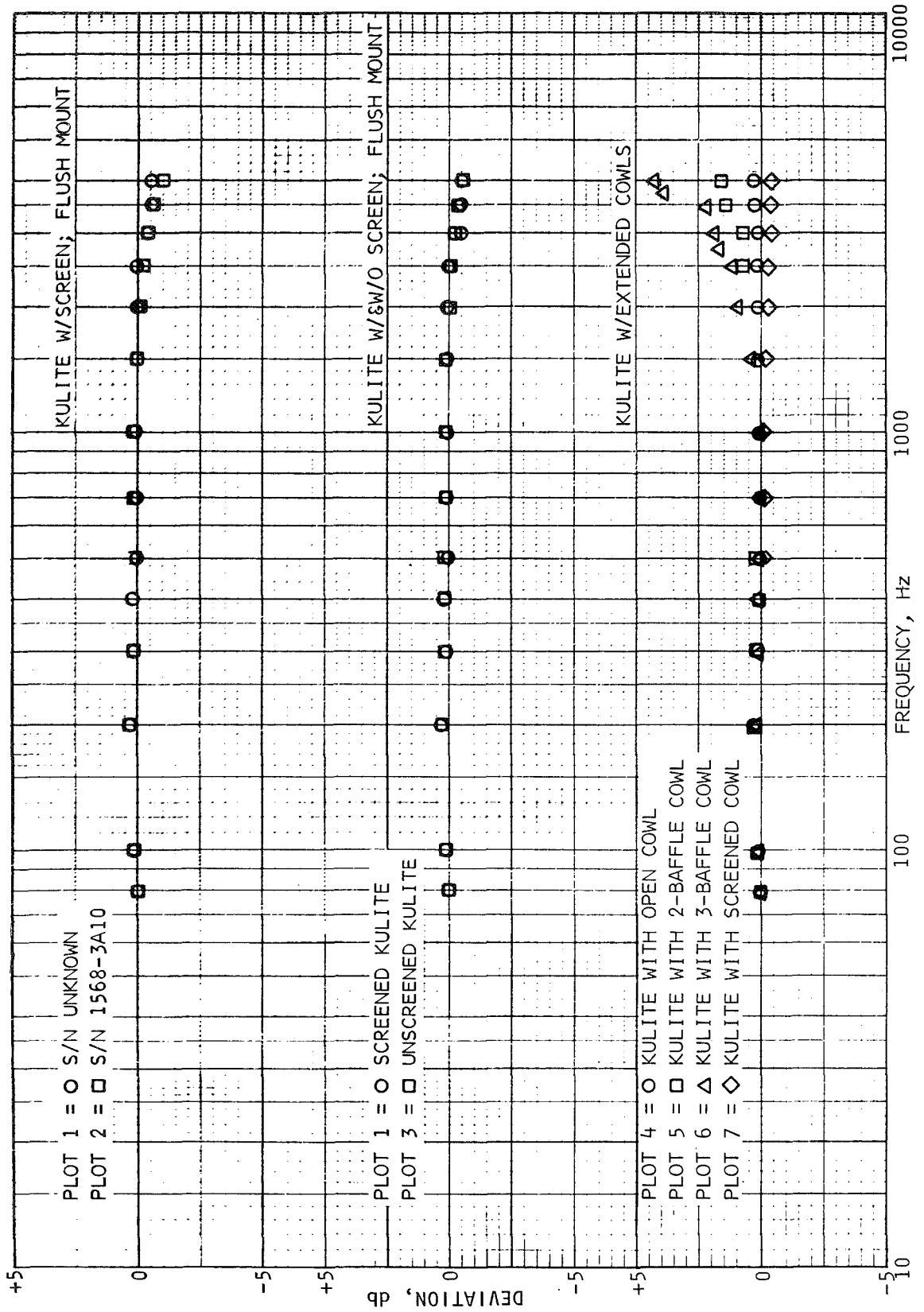


Figure 148.- Frequency calibration curve.

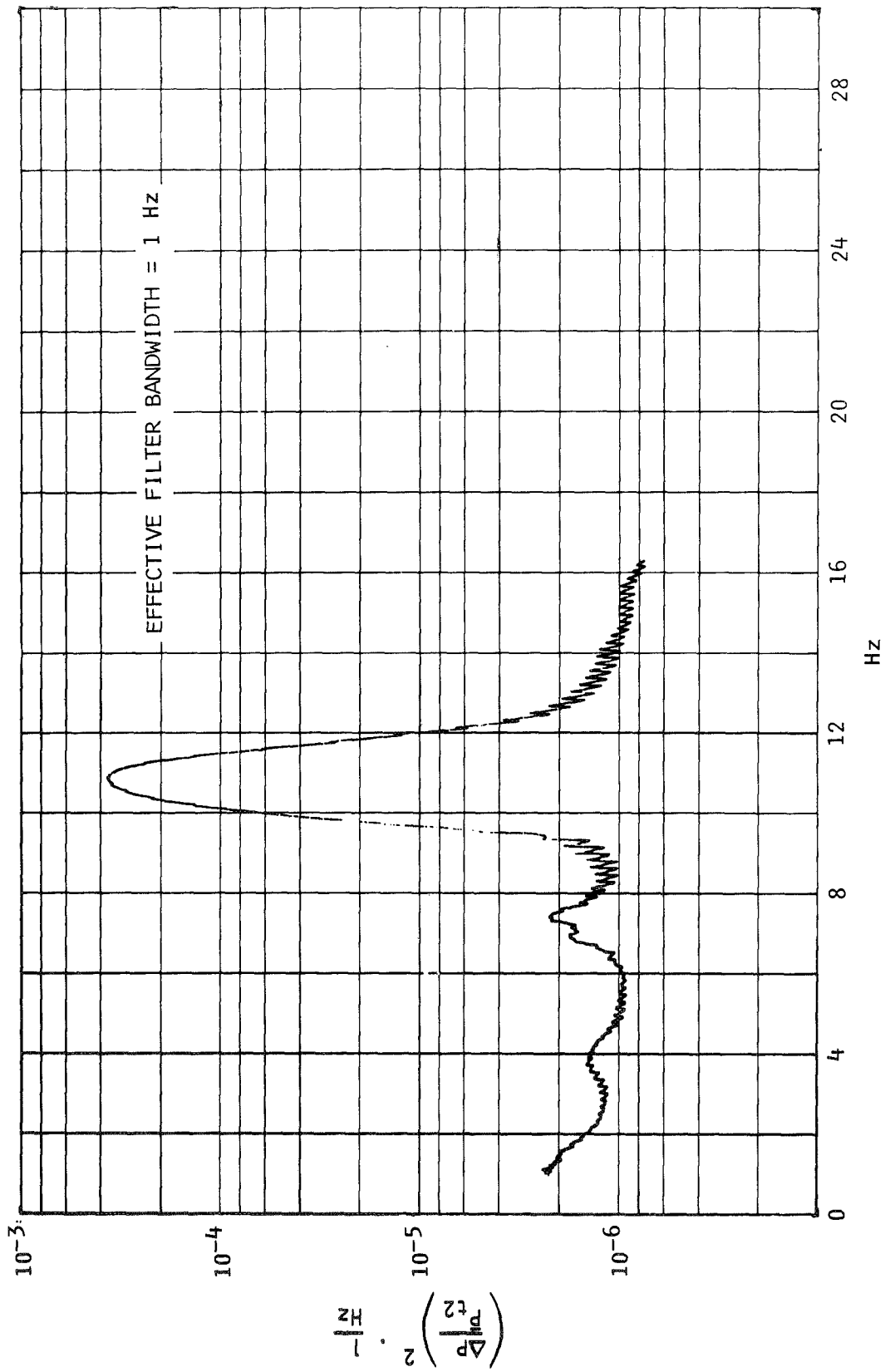


Figure 149.- Shock position parameter, power spectral density, 10 Hz excitation.

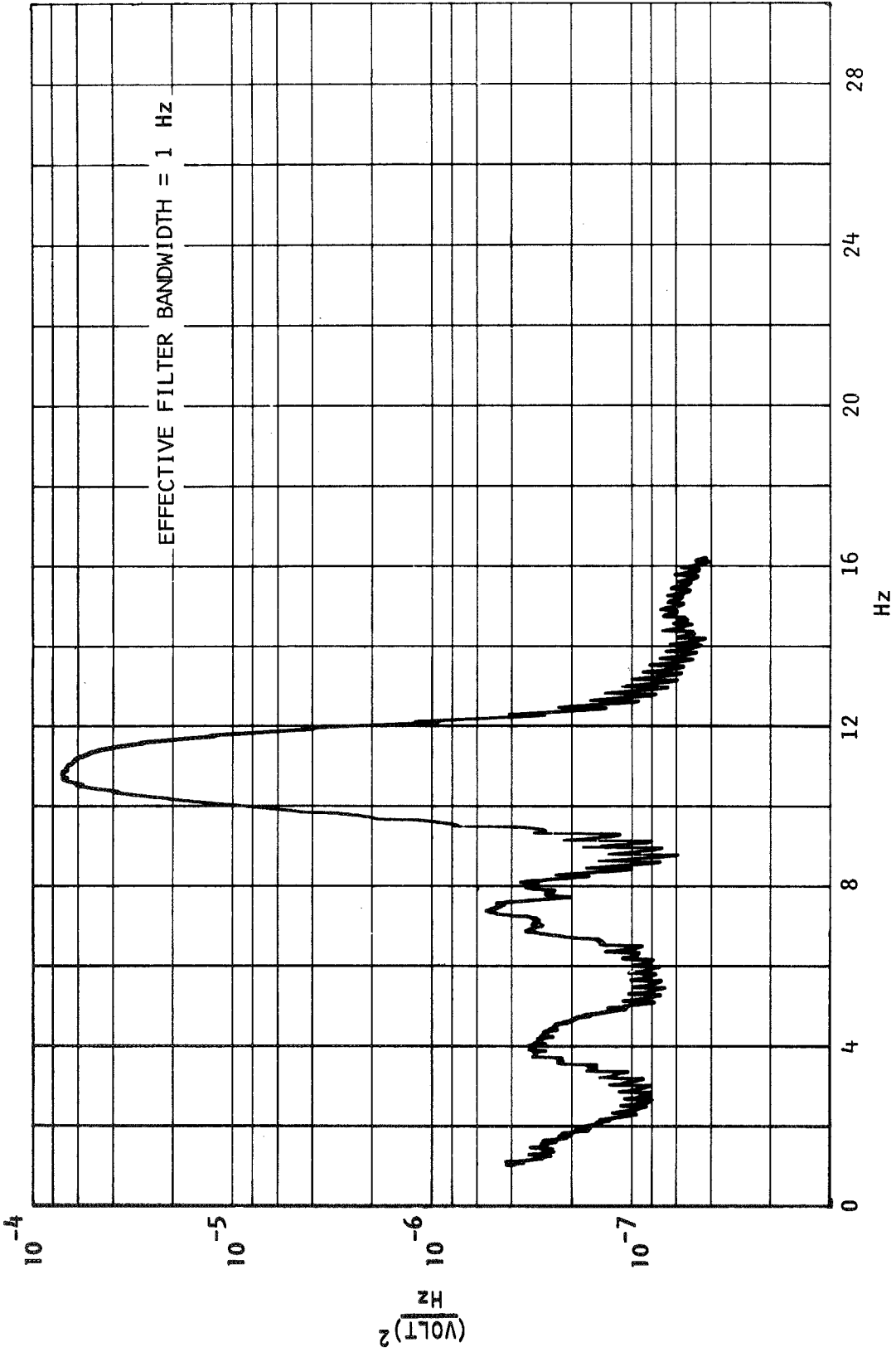


Figure 150.- Plug position parameter, power spectral density, 10 Hz excitation.

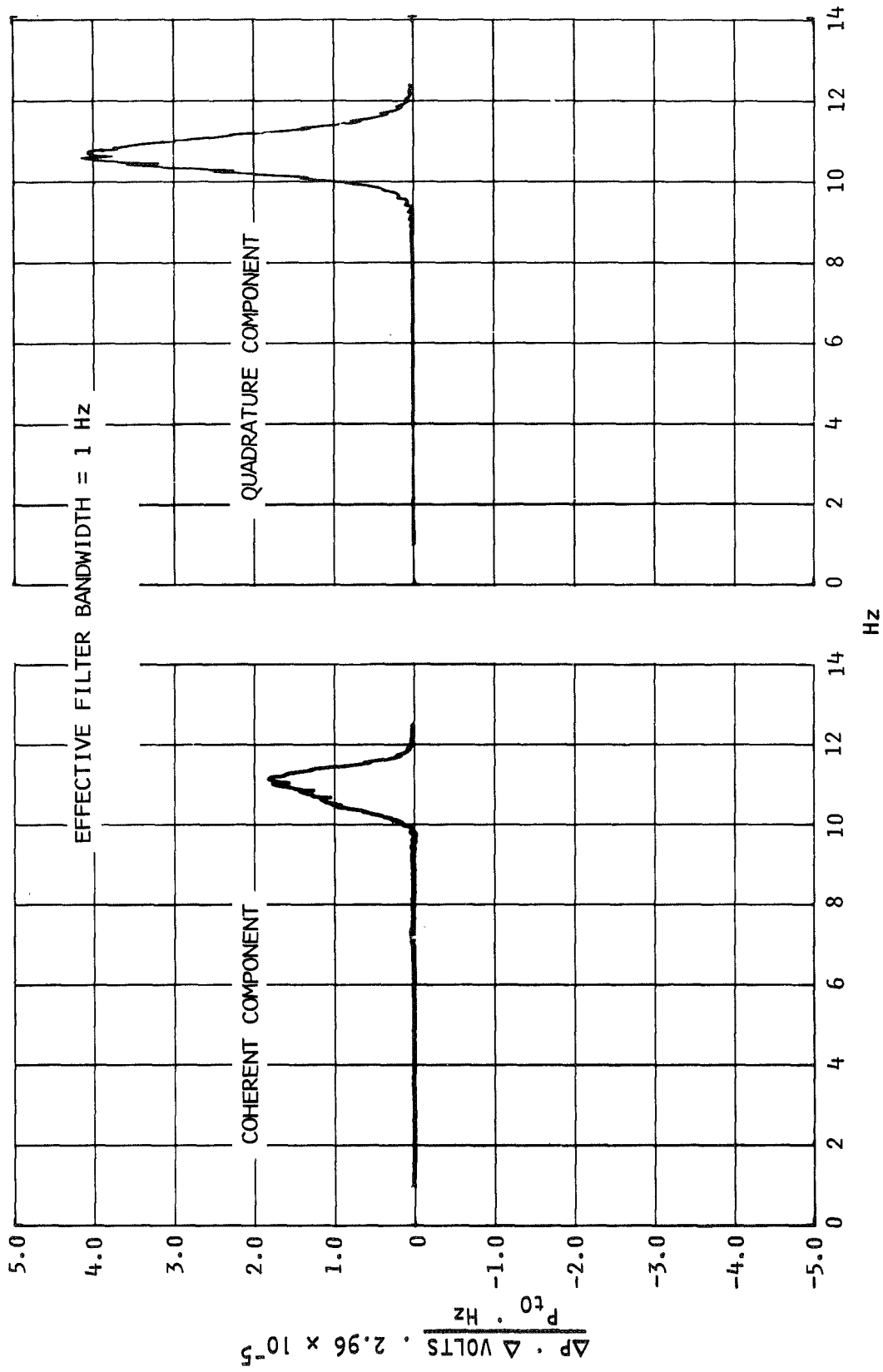


Figure 151.- Cross power spectral density, 10 Hz excitation.

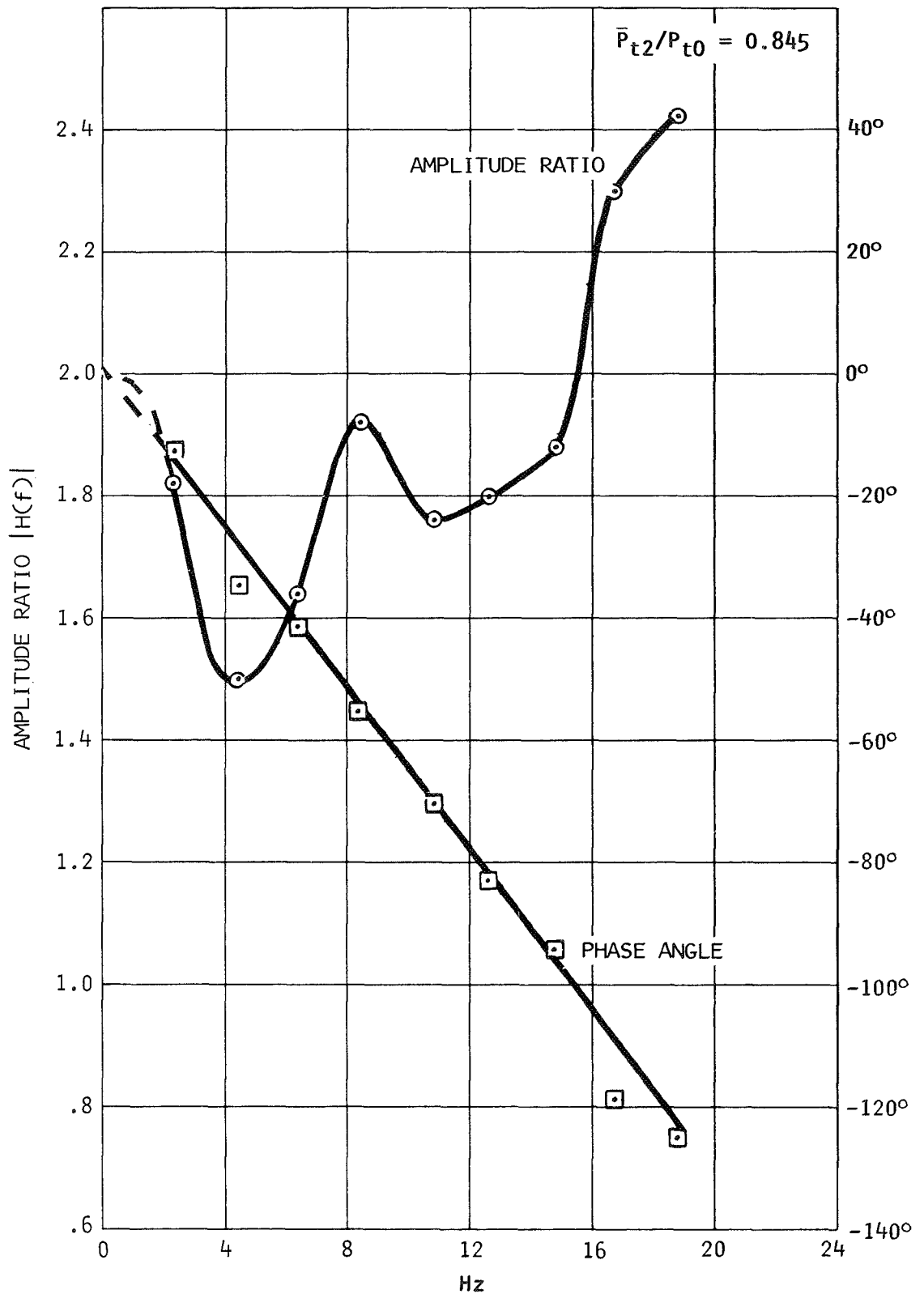


Figure 152.- Linear transfer function - $\frac{\text{shock position pressure change.}}{\text{exit area voltage change}}$

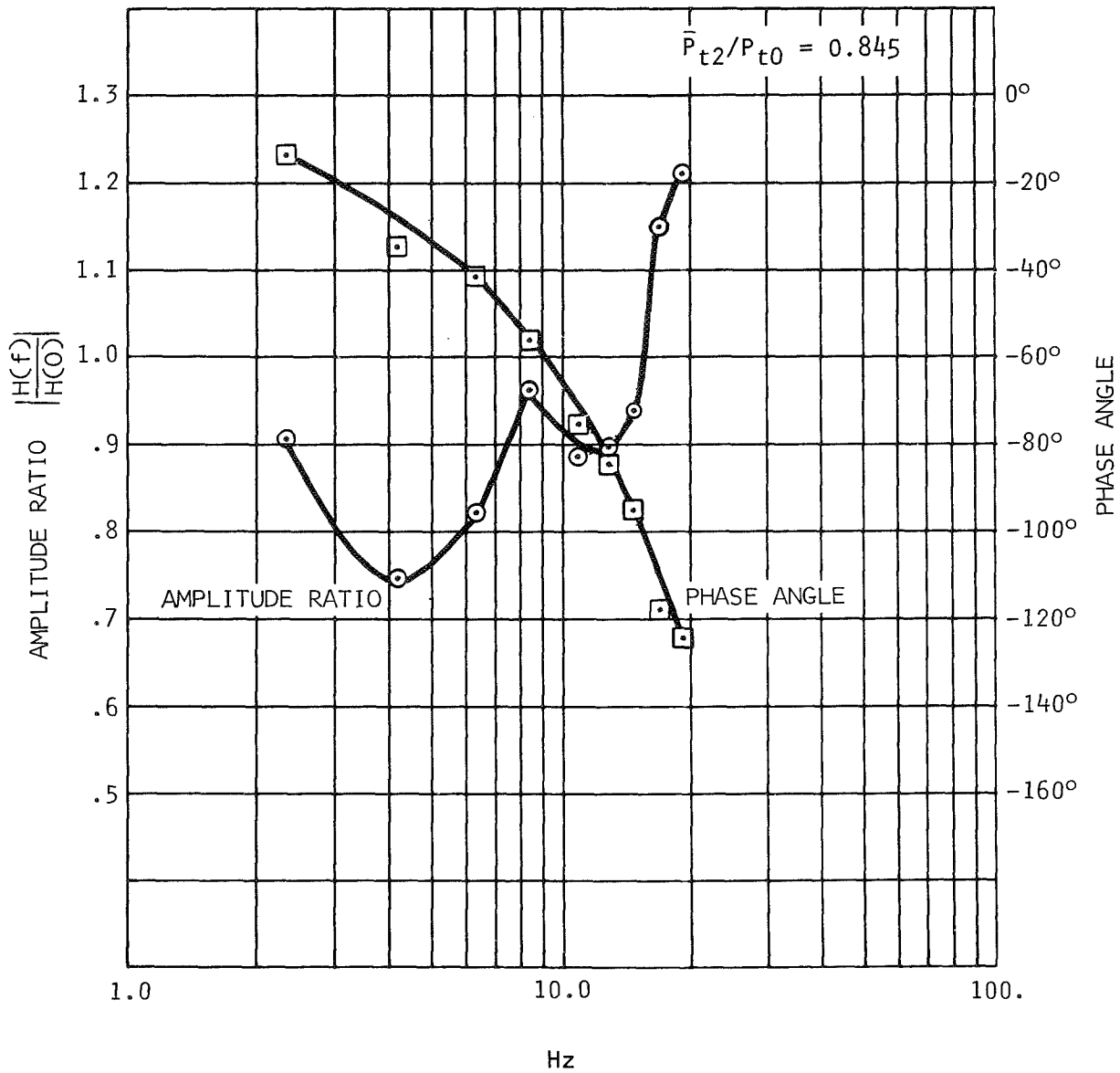


Figure 153.- Normalized transfer function - $\frac{\text{shock position change}}{\text{zero frequency shock position change}}$.

NATIONAL AERONAUTICS AND SPACE ADMINISTRATION
WASHINGTON, D. C. 20546
OFFICIAL BUSINESS

FIRST CLASS MAIL



POSTAGE AND FEES PAID
NATIONAL AERONAUTICS
SPACE ADMINISTRATION

POSTMASTER: if Undeliverable (Section 1
Postal Manual) Do Not Ret

"The aeronautical and space activities of the United States shall be conducted so as to contribute . . . to the expansion of human knowledge of phenomena in the atmosphere and space. The Administration shall provide for the widest practicable and appropriate dissemination of information concerning its activities and the results thereof."

—NATIONAL AERONAUTICS AND SPACE ACT OF 1958

NASA SCIENTIFIC AND TECHNICAL PUBLICATIONS

TECHNICAL REPORTS: Scientific and technical information considered important, complete, and a lasting contribution to existing knowledge.

TECHNICAL NOTES: Information less broad in scope but nevertheless of importance as a contribution to existing knowledge.

TECHNICAL MEMORANDUMS: Information receiving limited distribution because of preliminary data, security classification, or other reasons.

CONTRACTOR REPORTS: Scientific and technical information generated under a NASA contract or grant and considered an important contribution to existing knowledge.

TECHNICAL TRANSLATIONS: Information published in a foreign language considered to merit NASA distribution in English.

SPECIAL PUBLICATIONS: Information derived from or of value to NASA activities. Publications include conference proceedings, monographs, data compilations, handbooks, sourcebooks, and special bibliographies.

TECHNOLOGY UTILIZATION PUBLICATIONS: Information on technology used by NASA that may be of particular interest in commercial and other non-aerospace applications. Publications include Tech Briefs, Technology Utilization Reports and Technology Surveys.

Details on the availability of these publications may be obtained from:

SCIENTIFIC AND TECHNICAL INFORMATION DIVISION
NATIONAL AERONAUTICS AND SPACE ADMINISTRATION
Washington, D.C. 20546